Development of a coupled Monte Carlo code for charged particle transport through electromagnetic fields and bulk material for active radiation shielding

by

Luke Stegeman

B.S., Kansas State University, 2019

M.S., Kansas State University, 2022

AN ABSTRACT OF A DISSERTATION

submitted in partial fulfillment of the
requirements for the degree

DOCTOR OF PHILOSOPHY

Alan Levin Department of Mechanical and Nuclear Engineering
Carl R. Ice College of Engineering

KANSAS STATE UNIVERSITY
Manhattan, Kansas

2026

Abstract

Prolonged exposure to space radiation is one of the principal hazards of crewed missions beyond low Earth orbit, and the mass required to reduce exposure with passive shielding alone is large. Active radiation shielding proposes to use electromagnetic fields to deflect or decelerate charged particles before they reach a crewed volume. Any practical active shield will be a hybrid: the field acts on the incident radiation in vacuum, and the habitat or spacecraft structure acts on the particles that penetrate it. Evaluating such a hybrid requires transport through electromagnetic fields and through bulk matter within the same calculation, which no publicly available radiation transport code provided. This dissertation develops, verifies, and applies such a tool.

A transport equation for charged particles in externally applied electric and magnetic fields is derived in the kinetic energy and direction variables used in radiation protection, together with its adjoint and the boundary conditions under which the adjoint relation holds. The Active Shielding Particle Pusher (ASPP) is extended with Boolean geometry, material-dependent deceleration, an energy deposition tally, time-reversed propagation, additional field components, and closed-form reference potentials that relate applied voltage to stored energy. ASPP is validated against beamline measurements of ion deflection by an electric dipole at Brookhaven National Laboratory, with a mean relative error of 13.1 percent in the void area. The measurements show that a single dimensionless parameter, the ratio of field potential energy to ion kinetic energy, organizes shielding efficacy across dipole geometries, and that a single dipole is a poor shield in an isotropic environment.

G4-ASPP, a Geant4-based code, is then developed to combine the electromagnetic field transport of ASPP with the nuclear and electromagnetic interaction physics of Geant4 in a single self-consistent simulation. A distance-stepping analog of the Velocity-Verlet integrator is derived for G4-ASPP, and seven propagation methods are compared against analytic and reference trajectories. A fourth-order Runge–Kutta distance-stepping method gives relative errors no larger than 0.01 percent and is adopted for use in G4-ASPP.

G4-ASPP is applied to a lunar regolith habitat protected by an electrostatic "umbrella" over regolith thicknesses up to 50 grams per square centimeter and applied voltages up to 100 megavolts. On the unshielded lunar surface, its dose rates for the full solar-minimum galactic cosmic ray spectrum agree with published values to within a factor of 1.4, with the same mean quality factor and the same decrease in dose equivalent behind thin regolith. The applied voltage produces no resolvable change in dose. An independent combination model, coupling ASPP field transport, PHITS lunar albedo response functions, and HZETRN depth-dose responses, agrees that the voltage has no resolvable effect, shows that lunar albedo contributes less than 8 percent of the dose behind the habitat shell, and gives proton and alpha-particle dose rates of 0.57 to 0.94 times those of G4-ASPP. Building the combination model required three transport codes and a multi-stage normalization chain, while G4-ASPP evaluates each configuration in one simulation. For hybrid active–passive shielding, a single self-consistent simulation is therefore more tractable to develop, verify, and use than a pipeline of coupled single-purpose codes.

Development of a coupled Monte Carlo code for charged particle transport through electromagnetic fields and bulk material for active radiation shielding

by

Luke Stegeman

B.S., Kansas State University, 2019

M.S., Kansas State University, 2022

A DISSERTATION

submitted in partial fulfillment of the
requirements for the degree

DOCTOR OF PHILOSOPHY

Alan Levin Department of Mechanical and Nuclear Engineering
Carl R. Ice College of Engineering

KANSAS STATE UNIVERSITY
Manhattan, Kansas

2026

Approved by:

Major Professor
Amir A. Bahadori

Copyright

© Luke Stegeman 2026.

Abstract

Prolonged exposure to space radiation is one of the principal hazards of crewed missions beyond low Earth orbit, and the mass required to reduce exposure with passive shielding alone is large. Active radiation shielding proposes to use electromagnetic fields to deflect or decelerate charged particles before they reach a crewed volume. Any practical active shield will be a hybrid: the field acts on the incident radiation in vacuum, and the habitat or spacecraft structure acts on the particles that penetrate it. Evaluating such a hybrid requires transport through electromagnetic fields and through bulk matter within the same calculation, which no publicly available radiation transport code provided. This dissertation develops, verifies, and applies such a tool.

A transport equation for charged particles in externally applied electric and magnetic fields is derived in the kinetic energy and direction variables used in radiation protection, together with its adjoint and the boundary conditions under which the adjoint relation holds. The Active Shielding Particle Pusher (ASPP) is extended with Boolean geometry, material-dependent deceleration, an energy deposition tally, time-reversed propagation, additional field components, and closed-form reference potentials that relate applied voltage to stored energy. ASPP is validated against beamline measurements of ion deflection by an electric dipole at Brookhaven National Laboratory, with a mean relative error of 13.1 percent in the void area. The measurements show that a single dimensionless parameter, the ratio of field potential energy to ion kinetic energy, organizes shielding efficacy across dipole geometries, and that a single dipole is a poor shield in an isotropic environment.

G4-ASPP, a Geant4-based code, is then developed to combine the electromagnetic field transport of ASPP with the nuclear and electromagnetic interaction physics of Geant4 in a single self-consistent simulation. A distance-stepping analog of the Velocity-Verlet integrator is derived for G4-ASPP, and seven propagation methods are compared against analytic and reference trajectories. A fourth-order Runge–Kutta distance-stepping method gives relative errors no larger than 0.01 percent and is adopted for use in G4-ASPP.

G4-ASPP is applied to a lunar regolith habitat protected by an electrostatic "umbrella" over regolith thicknesses up to 50 grams per square centimeter and applied voltages up to 100 megavolts. On the unshielded lunar surface, its dose rates for the full solar-minimum galactic cosmic ray spectrum agree with published values to within a factor of 1.4, with the same mean quality factor and the same decrease in dose equivalent behind thin regolith. The applied voltage produces no resolvable change in dose. An independent combination model, coupling ASPP field transport, PHITS lunar albedo response functions, and HZETRN depth-dose responses, agrees that the voltage has no resolvable effect, shows that lunar albedo contributes less than 8 percent of the dose behind the habitat shell, and gives proton and alpha-particle dose rates of 0.57 to 0.94 times those of G4-ASPP. Building the combination model required three transport codes and a multi-stage normalization chain, while G4-ASPP evaluates each configuration in one simulation. For hybrid active–passive shielding, a single self-consistent simulation is therefore more tractable to develop, verify, and use than a pipeline of coupled single-purpose codes.

Table of Contents

List of Figures xiv

List of Tables xxvii

Acronyms xxviii

Acknowledgments xxxiii

1 Introduction 1

1.1 Motivation 1

1.2 Outline 5

1.3 Notation 6

1.3.1 Functions and Distributions 6

1.3.2 Other Mathematical Shorthand 6

2 Background 8

2.1 Radiation Protection 8

2.2 Space Radiation Environment 12

2.2.1 Solar Particle Events 12

2.2.2 Galactic Cosmic Rays 13

2.2.3 Magnetically Trapped Radiation 16

2.3 Space Radiation Exposure Limits 18

2.4 Active Radiation Shielding 19

2.4.1 Electrostatic Shielding 19

2.4.2 Magnetostatic Shielding 19

2.4.3 Plasma Shielding 20

2.4.4 Outlook 20

2.5 Space Radiation Transport 21

2.5.1 Derivation of the Charged Particle Transport Equation 23

2.5.2 Energy Differential 25

2.5.3 Direction Differential . . . 26
2.5.4 Position Differential . . . 27
2.5.5 Force and Streaming Terms of the Charged Particle Transport Equation . . . 27
2.5.6 Particle Phenomena Terms . . . 31
2.5.7 Compilation of Terms . . . 31
2.5.8 Adjoint Charged Particle Transport Equation . . . 32

3 Expansion and Experimental Validation of the Active Shielding Particle Pusher Code . . . 37
3.1 Active Shielding Particle Pusher Code . . . 37
3.2 Contributed Additions to ASPP . . . 38
3.2.1 Boolean Geometry . . . 38
3.2.2 Material Assignment . . . 40
3.2.3 Relativistic and Bethe-Bloch Deceleration . . . 40
3.2.4 Energy Deposition Tally . . . 43
3.2.5 Time-Reversed Particle Propagation . . . 44
3.2.6 Active Shielding Components . . . 46
3.2.6.1 Point Charge Element . . . 46
3.2.6.2 Line Segment Charge Element . . . 46
3.2.6.3 Rectangular Charge Element . . . 48
3.2.6.4 Rectangular Prism Bar Magnet . . . 49
3.3 Reference Potentials for Electrostatic Shielding Components . . . 50
3.4 Experimental Validation of ASPP . . . 52
3.5 Introduction . . . 52
3.6 Materials and Methods . . . 54
3.6.1 1d Shielding Efficacy Metric . . . 54
3.6.2 Measurement Setup . . . 55
3.6.3 Simulation Setup . . . 56
3.6.4 Parameter Space . . . 59
3.6.5 Void Area Calculation . . . 60
3.7 Results and Discussion . . . 61
3.7.1 Void Area without Dipole Rotation Results . . . 61
3.7.2 Beam Divergence Effects . . . 63
3.7.3 Void Area with Dipole Rotation Results . . . 64

3.7.4 Overall Measurement-Simulation Agreement . . . 65
3.8 Summary and Conclusion . . . 66

4 G4-ASPP Development . . . 73
4.1 Development and Benchmarking of Charged Particle Propagation Methods in G4-ASPP . . . 73
4.2 Introduction . . . 73
4.2.1 ASPP . . . 74
4.2.2 Geant4 . . . 75
4.2.3 G4-ASPP . . . 76
4.2.4 Objectives . . . 76
4.3 Mathematical Background . . . 77
4.3.1 Velocity-Verlet in Time and Space Coordinates . . . 77
4.3.2 Integrator Symplecticity and Phase-Space Preservation . . . 81
4.4 Materials and Methods . . . 84
4.4.1 Propagation Methods . . . 84
4.4.1.1 Semi-Analytical Propagation Method for Uniform Electric Field . . . 85
4.4.1.2 Boris Algorithm . . . 86
4.4.1.3 4th-order Runge-Kutta . . . 86
4.4.1.4 Euler Algorithm . . . 87
4.4.1.5 Geant4 Restricted and Unrestricted Stepping Methods . . . 88
4.4.2 Test Cases . . . 88
4.4.2.1 Case 1: Uniform Electric Field Only . . . 91
4.4.2.2 Case 2: Uniform Magnetic Field Only . . . 91
4.4.2.3 Case 3: Combined Uniform Electric and Magnetic Field . . . 92
4.4.2.4 Case 4: Line and Point Charge Combination Electric Field . . . 92
4.4.2.5 Case 5: Ideal Magnetic Dipole Field . . . 94
4.4.2.6 Case 6: Full Active Shielding Configuration . . . 95
4.4.3 Simulation Procedure . . . 97
4.4.4 Computation Time Study . . . 99
4.5 Trajectory Comparison and Analysis . . . 100
4.5.1 Test Cases . . . 100
4.5.1.1 Test Case 1 . . . 100
4.5.1.2 Test Case 2 . . . 100

4.5.1.3 Test Case 3 . . . 102
4.5.1.4 Test Case 4 . . . 103
4.5.1.5 Test Case 5 . . . 105
4.5.1.6 Test Case 6 . . . 105
4.5.2 Computation Time . . . 108
4.6 Conclusions . . . 109
4.7 Geant4 Particle Propagation Method . . . 113
4.8 Relativistic Acceleration Term Derivation . . . 115
4.9 Geant4 System of Units and Constants . . . 116

5 Validation of G4-ASPP using Combined Lunar Shielding Scenario . . . 118
5.1 Introduction . . . 118
5.1.1 G4-ASPP Methodology Summary . . . 120
5.2 Materials and Methods . . . 122
5.2.1 Lunar Habitat Scenario . . . 122
5.2.1.1 Active Shielding Configuration . . . 125
5.2.2 Albedo Response Functions . . . 126
5.2.2.1 PHITS Albedo Simulation Setup . . . 128
5.2.3 ASPP + PHITS + HZETRN Simulation Architecture . . . 130
5.2.3.1 Step 1: Compute Incident GCR Flux Distribution . . . 131
5.2.3.2 Step 2: Execute Primary ASPP Simulations . . . 131
5.2.3.3 Step 3: Albedo Response Function Convolution . . . 133
5.2.3.4 Step 4: Secondary ASPP Transport . . . 135
5.2.3.5 Step 5: Hit Accumulation . . . 136
5.2.3.6 Step 6: HZETRN Response Functions . . . 136
5.2.3.7 Step 7: Geometric Mapping and Chord-Averaged Response . . . 138
5.2.3.8 Step 8: Physical Normalization . . . 139
5.2.3.9 Step 9a: Dose Computation (Non-Photons) . . . 141
5.2.3.10 Step 9b: Dose Computation (Photons) . . . 142
5.2.3.11 Statistical Uncertainty . . . 143
5.3 Results and Discussion . . . 145
5.3.1 Albedo Response Functions . . . 145
5.3.2 Combination Model Radiation Response . . . 148

5.3.2.1 Dose and Dose Equivalent . . . 148
5.3.2.2 Dependence on Passive Shielding . . . 150
5.3.2.3 Dependence on Active Shielding . . . 150
5.3.2.4 Comparison with Blunier et al. (2025) . . . 151
5.3.3 G4-ASPP Radiation Response . . . 151
5.3.3.1 Dose and Dose Equivalent . . . 152
5.3.3.2 Dependence on Passive Shielding . . . 152
5.3.3.3 Dependence on Active Shielding . . . 159
5.3.3.4 Comparison with Blunier et al. (2025) . . . 159
5.3.4 Comparison of the Combination Model and G4-ASPP . . . 160
5.3.4.1 Passive Shielding Dependence . . . 161
5.3.4.2 Active Shielding Dependence . . . 161
5.3.4.3 Contributions by Primary Species . . . 162
5.3.4.4 Magnitude Difference . . . 163
5.3.5 Limitations and Future Work . . . 163
5.4 Conclusion . . . 165
5.5 Future Work . . . 166
5.6 Mistakes (and Corrections) . . . 168
5.6.1 Errors Found and Corrected . . . 169
5.6.2 Unresolved Issues . . . 172

6 Conclusion . . . 174
6.1 Summary . . . 174
6.1.1 Charged Particle Transport Formalism . . . 174
6.1.2 Extension and Experimental Validation of ASPP . . . 175
6.1.3 Charged Particle Propagation in G4-ASPP . . . 176
6.1.4 Combined Active and Passive Shielding of a Lunar Habitat . . . 176
6.2 Contributions . . . 177
6.2.1 Tools and Methodology . . . 177
6.2.2 General Knowledge . . . 179
6.3 Limitations . . . 180
6.4 Future Work . . . 180
6.4.1 Adjoint Transport for Configuration Design . . . 180

6.4.2 Field Physics and Design Tools . . . 181
6.4.3 Environments, Targets, and Validation . . . 181
6.5 Closing Remarks . . . 182

Bibliography . . . 183

A Albedo Response Functions . . . 191
A.0.1 Primary Flux Distribution at the Dome Surface . . . 343
A.0.1.1 Primary Hit Distribution—Azimuthal . . . 343
A.0.1.2 Primary Hit Distribution—Polar . . . 347
A.0.1.3 Primary Hit Distribution—Map . . . 347

List of Figures

2.1 Illustration of coronal mass ejection and subsequent solar particle event. 13

2.2 Angular flux time profile, October 1989. 14

2.3 Differential fluence spectrum, October 1989. 14

2.4 GCR differential flux spectra. 15

2.5 GCR isotopic distribution. 16

2.6 Illustration of Van Allen Belts. 18

3.1 Conceptual view of a charge q propagating through the electromagnetic field generated by Active Shielding Particle Pusher (ASPP) active shielding components. 38

3.2 Adjoint ASPP simulation results for protons with $T_0 = 10\,\text{MeV}$; the average initial kinetic energy required to reach the crew volume is $T = 25.0\,\text{MeV}$. 45

3.3 Adjoint ASPP simulation results for protons with $T_0 = 30\,\text{MeV}$; the average initial kinetic energy required to reach the crew volume is $T = 44.5\,\text{MeV}$. 46

3.4 Uniform line charge. 47

3.5 Geometric parameterization of rectangular charge sheet with constant surface charge density σ. 49

3.6 Parameterization of rectangular prism bar magnet of constant magnetization density $\vec{M}$. 50

3.7 Measured image data example; 2 MeV protons, $\pm 30\,\text{kV}$ applied voltage, sphere radius $a = 2.54\,\text{cm}$, center-to-center sphere separation $\ell_{CC} = 7.620\,\text{cm}$, dipole-detector distance $\ell_{DD} = 2\,\text{m}$. 55

3.8 Simplified cross section view of custom Brookhaven National Laboratory (BNL) test chamber with relevant components labeled. 55

3.9 Top cross section view of custom BNL test chamber with relevant components labeled and dimensions along the beam direction. 56

3.10 Simulation scenario; displayed parameters include the ion kinetic energy E_k, ion mass number A, ion proton number Z, ion electron number N_e, beam radius R_b, source-to-dipole distance ℓ_S, center-to-center sphere distance ℓ_{CC}, sphere charge Q, rod linear charge density λ, sphere radius a, rod radius R_r, and dipole-detector distance ℓ_{DD}; the reference coordinate system is oriented properly, but the origin is located at point $\mathcal{O}$, the center point between the two dipole spheres. 57

3.11 Example of sphere shadowing; sphere shadow is outlined using Fourier-fitted function from image analysis method. 59

3.12 Scaling law plots comparing measured and simulated images separated by sphere radius and center-to-center distance between spheres; a, ℓ_{CC}, and fitting parameters shown in Table 3.4; (a) $a = 1.27\,\text{cm}$, $\ell_{CC} = 5.715\,\text{cm}$; (b) $a = 1.27\,\text{cm}$, $\ell_{CC} = 11.430\,\text{cm}$; (c) $a = 2.54\,\text{cm}$, $\ell_{CC} = 7.620\,\text{cm}$; (d) $a = 2.54\,\text{cm}$, $\ell_{CC} = 11.430\,\text{cm}$; (e) $a = 3.81\,\text{cm}$, $\ell_{CC} = 11.430\,\text{cm}$. 68

3.13 Illustration of beam divergence assuming the beam steering magnet acts as a point source; ℓ_{PD} is the distance from the point source to the midsection of the dipole sphere and $2a'$ is the diameter of the dipole sphere's shadow projected on to the imaging screen. 69

3.14 Simulated image data illustrating how sphere shadowing effects diminish as applied dipole voltage V_{dip} (and scaling parameter f_s) increases; simulations conducted using 14 MeV protons with $V_{\text{dip}} \in (0, 70)$ kV where sphere radius $a = 2.54\,\text{cm}$ and center-to-center separation $\ell_{CC} = 7.620\,\text{cm}$; particles that intersected with either dipole sphere at any point during the simulation are plotted in orange; (a) $V_{\text{dip}} = 0\,\text{kV}$; (b) $V_{\text{dip}} = 10\,\text{kV}$; (c) $V_{\text{dip}} = 20\,\text{kV}$; (d) $V_{\text{dip}} = 30\,\text{kV}$; (e) $V_{\text{dip}} = 40\,\text{kV}$; (f) $V_{\text{dip}} = 50\,\text{kV}$; (g) $V_{\text{dip}} = 60\,\text{kV}$; (h) $V_{\text{dip}} = 70\,\text{kV}$. 69

3.15 Measured image data illustrating shape preservation between measured and simulated image data; measurements conducted using 14 MeV protons with $V_{\text{dip}} \in (0, 70)$ kV where sphere radius $a = 2.54\,\text{cm}$ and center-to-center separation $\ell_{CC} = 7.620\,\text{cm}$; (a) $V_{\text{dip}} = 0\,\text{kV}$; (b) $V_{\text{dip}} = 10\,\text{kV}$; (c) $V_{\text{dip}} = 20\,\text{kV}$; (d) $V_{\text{dip}} = 30\,\text{kV}$; (e) $V_{\text{dip}} = 40\,\text{kV}$; (f) $V_{\text{dip}} = 50\,\text{kV}$; (g) $V_{\text{dip}} = 60\,\text{kV}$; (h) $V_{\text{dip}} = 70\,\text{kV}$. 70

3.16 Plots comparing measured and simulated void areas as a function of dipole rotation angle α separated by dipole voltage configuration; dotted lines fit to measured void areas (data points are triangular), solid lines fit to simulated void areas (data points are square); fitting parameters for curve fits are shown in Table 3.5; (a) $V_+ = 0\,\text{kV}$, $V_- = 0\,\text{kV}$; (b) $V_+ = 0\,\text{kV}$, $V_- = -70\,\text{kV}$; (c) $V_+ = 70\,\text{kV}$, $V_- = 0\,\text{kV}$; (d) $V_+ = 70\,\text{kV}$, $V_- = -70\,\text{kV}$. . . 71

3.17 Comparison of simulated and measured void area data for $\alpha = 0$ in logarithmic- and linear-scale plots; the dotted line represents perfect agreement and the solid lines delineate the border of regions where measured and simulated void areas differ by a factor greater than two; (a) logarithmic comparison; (b) linear comparison. 72

4.1 Active shielding configuration; red components are positively charged; green components are negatively charged. 95
4.2 Case 1 results. 101
4.3 Case 2 results. 103
4.4 Case 3 results. 104
4.5 Case 4 results. 106
4.6 Case 5 results. 107
4.7 Case 6 results. 108
4.8 Computational time results as a function of Δt (and by extension, Δs) among all propagation methods for test cases 1, 4, and 6; refer to Figure 4.2b for legend. 110
4.9 High level step size selection flowchart in Geant4. 114

5.1 2D Lunar Habitat Schematic. 122
5.2 Transparent side, top, and 3D views of lunar habitat active-passive shielding configuration; depicts R_{ICRU}, R_{inner}, $R_{\text{outer}}(x)$, z_{rect}, R_{-}, z_{sphere}; R_{outer} depends on the chosen passive shielding thickness; in this case, $x = 50\,\text{g}\,\text{cm}^{-2}$. 123
5.3 Illustration of the radiation albedo concept. 127
5.4 Albedo response function, 17.09 GeV/n proton primary. 145
5.5 Albedo response function, 53.3 keV proton primary. 146
5.6 Albedo response function, 6.134 GeV/n alpha primary. 147
5.7 Integrated alpha-primary secondary yield vs. incident energy. 147
5.8 Combination model absorbed dose vs. shielding thickness. 149
5.9 Combination model ICRP-60 dose equivalent vs. shielding thickness. 149
5.10 Combination model NASA solid cancer dose equivalent vs. shielding thickness. 149
5.11 Combination model NASA leukemia dose equivalent vs. shielding thickness. 150
5.12 Geant4-ASPP (G4-ASPP) absorbed dose rate vs. passive shielding thickness, by active shielding voltage. 152
5.13 G4-ASPP International Commission on Radiological Protection (ICRP)-60 dose equivalent rate vs. passive shielding thickness, by active shielding voltage. 153

5.14 G4-ASPP National Aeronautics and Space Administration (NASA) solid cancer dose equivalent rate vs. passive shielding thickness, by active shielding voltage. 154
5.15 G4-ASPP NASA leukemia dose equivalent rate vs. passive shielding thickness, by active shielding voltage. 155
5.16 G4-ASPP absorbed dose rate vs. active shielding voltage, by passive shielding thickness. . 155
5.17 G4-ASPP ICRP-60 dose equivalent rate vs. active shielding voltage, by passive shielding thickness. 156
5.18 G4-ASPP NASA solid cancer dose equivalent rate vs. active shielding voltage, by passive shielding thickness. 157
5.19 G4-ASPP NASA leukemia dose equivalent rate vs. active shielding voltage, by passive shielding thickness. 158
5.20 Combination model and G4-ASPP absorbed dose by primary species. 160
5.21 Combination model and G4-ASPP ICRP-60 dose equivalent by primary species. 161
5.22 Combination model and G4-ASPP dose vs. applied voltage. 162
5.23 Comparison of pipeline complexities. 167

A.1 Integrated proton-primary secondary yield vs. incident energy. 191
A.2 Integrated alpha-primary secondary yield vs. incident energy. 192
A.3 Albedo response function, 10 keV/n proton primary. 193
A.4 Albedo response function, 14.1 keV/n proton primary. 194
A.5 Albedo response function, 19.8 keV/n proton primary. 194
A.6 Albedo response function, 27.8 keV/n proton primary. 195
A.7 Albedo response function, 38.8 keV/n proton primary. 196
A.8 Albedo response function, 53.3 keV/n proton primary. 197
A.9 Albedo response function, 72 keV/n proton primary. 197
A.10 Albedo response function, 95 keV/n proton primary. 198
A.11 Albedo response function, 122 keV/n proton primary. 199
A.12 Albedo response function, 154 keV/n proton primary. 200
A.13 Albedo response function, 189 keV/n proton primary. 200
A.14 Albedo response function, 228 keV/n proton primary. 201
A.15 Albedo response function, 271 keV/n proton primary. 202
A.16 Albedo response function, 320 keV/n proton primary. 203
A.17 Albedo response function, 374 keV/n proton primary. 203

A.18 Albedo response function, 434 keV/n proton primary. 204
A.19 Albedo response function, 501 keV/n proton primary. 205
A.20 Albedo response function, 575 keV/n proton primary. 206
A.21 Albedo response function, 659 keV/n proton primary. 206
A.22 Albedo response function, 754 keV/n proton primary. 207
A.23 Albedo response function, 860 keV/n proton primary. 208
A.24 Albedo response function, 979 keV/n proton primary. 209
A.25 Albedo response function, 1.112 MeV/n proton primary. 209
A.26 Albedo response function, 1.262 MeV/n proton primary. 210
A.27 Albedo response function, 1.43 MeV/n proton primary. 211
A.28 Albedo response function, 1.619 MeV/n proton primary. 212
A.29 Albedo response function, 1.832 MeV/n proton primary. 212
A.30 Albedo response function, 2.07 MeV/n proton primary. 213
A.31 Albedo response function, 2.338 MeV/n proton primary. 214
A.32 Albedo response function, 2.639 MeV/n proton primary. 215
A.33 Albedo response function, 2.976 MeV/n proton primary. 215
A.34 Albedo response function, 3.355 MeV/n proton primary. 216
A.35 Albedo response function, 3.779 MeV/n proton primary. 217
A.36 Albedo response function, 4.255 MeV/n proton primary. 218
A.37 Albedo response function, 4.789 MeV/n proton primary. 218
A.38 Albedo response function, 5.387 MeV/n proton primary. 219
A.39 Albedo response function, 6.057 MeV/n proton primary. 220
A.40 Albedo response function, 6.808 MeV/n proton primary. 221
A.41 Albedo response function, 7.65 MeV/n proton primary. 221
A.42 Albedo response function, 8.592 MeV/n proton primary. 222
A.43 Albedo response function, 9.648 MeV/n proton primary. 223
A.44 Albedo response function, 10.83 MeV/n proton primary. 224
A.45 Albedo response function, 12.15 MeV/n proton primary. 224
A.46 Albedo response function, 13.63 MeV/n proton primary. 225
A.47 Albedo response function, 15.3 MeV/n proton primary. 226
A.48 Albedo response function, 17.15 MeV/n proton primary. 227
A.49 Albedo response function, 19.23 MeV/n proton primary. 227
A.50 Albedo response function, 21.56 MeV/n proton primary. 228

A.51 Albedo response function, 24.17 MeV/n proton primary. 229
A.52 Albedo response function, 27.1 MeV/n proton primary. 230
A.53 Albedo response function, 30.37 MeV/n proton primary. 230
A.54 Albedo response function, 34.04 MeV/n proton primary. 231
A.55 Albedo response function, 38.15 MeV/n proton primary. 232
A.56 Albedo response function, 42.76 MeV/n proton primary. 233
A.57 Albedo response function, 47.93 MeV/n proton primary. 233
A.58 Albedo response function, 53.73 MeV/n proton primary. 234
A.59 Albedo response function, 60.24 MeV/n proton primary. 235
A.60 Albedo response function, 67.55 MeV/n proton primary. 236
A.61 Albedo response function, 75.77 MeV/n proton primary. 236
A.62 Albedo response function, 85.01 MeV/n proton primary. 237
A.63 Albedo response function, 95.41 MeV/n proton primary. 238
A.64 Albedo response function, 107.1 MeV/n proton primary. 239
A.65 Albedo response function, 120.4 MeV/n proton primary. 239
A.66 Albedo response function, 135.3 MeV/n proton primary. 240
A.67 Albedo response function, 152.2 MeV/n proton primary. 241
A.68 Albedo response function, 171.4 MeV/n proton primary. 242
A.69 Albedo response function, 193 MeV/n proton primary. 242
A.70 Albedo response function, 217.9 MeV/n proton primary. 243
A.71 Albedo response function, 246.2 MeV/n proton primary. 244
A.72 Albedo response function, 278.1 MeV/n proton primary. 245
A.73 Albedo response function, 314.7 MeV/n proton primary. 245
A.74 Albedo response function, 357.1 MeV/n proton primary. 246
A.75 Albedo response function, 405.3 MeV/n proton primary. 247
A.76 Albedo response function, 461.8 MeV/n proton primary. 248
A.77 Albedo response function, 526.8 MeV/n proton primary. 248
A.78 Albedo response function, 602.5 MeV/n proton primary. 249
A.79 Albedo response function, 691.3 MeV/n proton primary. 250
A.80 Albedo response function, 795.7 MeV/n proton primary. 251
A.81 Albedo response function, 919.2 MeV/n proton primary. 251
A.82 Albedo response function, 1.068 GeV/n proton primary. 252
A.83 Albedo response function, 1.246 GeV/n proton primary. 253

A.84 Albedo response function, 1.453 GeV/n proton primary. 254
A.85 Albedo response function, 1.71 GeV/n proton primary. 254
A.86 Albedo response function, 2.016 GeV/n proton primary. 255
A.87 Albedo response function, 2.397 GeV/n proton primary. 256
A.88 Albedo response function, 2.863 GeV/n proton primary. 257
A.89 Albedo response function, 3.444 GeV/n proton primary. 257
A.90 Albedo response function, 4.156 GeV/n proton primary. 258
A.91 Albedo response function, 5.04 GeV/n proton primary. 259
A.92 Albedo response function, 6.134 GeV/n proton primary. 260
A.93 Albedo response function, 7.488 GeV/n proton primary. 260
A.94 Albedo response function, 9.167 GeV/n proton primary. 261
A.95 Albedo response function, 11.26 GeV/n proton primary. 262
A.96 Albedo response function, 13.86 GeV/n proton primary. 263
A.97 Albedo response function, 17.09 GeV/n proton primary. 263
A.98 Albedo response function, 21.12 GeV/n proton primary. 264
A.99 Albedo response function, 26.15 GeV/n proton primary. 265
A.100 Albedo response function, 32.44 GeV/n proton primary. 266
A.101 Albedo response function, 40.23 GeV/n proton primary. 266
A.102 Albedo response function, 50 GeV/n proton primary. 267
A.103 Albedo response function, 10 keV/n alpha primary. 268
A.104 Albedo response function, 14.1 keV/n alpha primary. 269
A.105 Albedo response function, 19.8 keV/n alpha primary. 269
A.106 Albedo response function, 27.8 keV/n alpha primary. 270
A.107 Albedo response function, 38.8 keV/n alpha primary. 271
A.108 Albedo response function, 53.3 keV/n alpha primary. 272
A.109 Albedo response function, 72 keV/n alpha primary. 272
A.110 Albedo response function, 95 keV/n alpha primary. 273
A.111 Albedo response function, 122 keV/n alpha primary. 274
A.112 Albedo response function, 154 keV/n alpha primary. 275
A.113 Albedo response function, 189 keV/n alpha primary. 275
A.114 Albedo response function, 228 keV/n alpha primary. 276
A.115 Albedo response function, 271 keV/n alpha primary. 277
A.116 Albedo response function, 320 keV/n alpha primary. 278

A.117 Albedo response function, 374 keV/n alpha primary. 278
A.118 Albedo response function, 434 keV/n alpha primary. 279
A.119 Albedo response function, 501 keV/n alpha primary. 280
A.120 Albedo response function, 575 keV/n alpha primary. 281
A.121 Albedo response function, 659 keV/n alpha primary. 281
A.122 Albedo response function, 754 keV/n alpha primary. 282
A.123 Albedo response function, 860 keV/n alpha primary. 283
A.124 Albedo response function, 979 keV/n alpha primary. 284
A.125 Albedo response function, 1.112 MeV/n alpha primary. 284
A.126 Albedo response function, 1.262 MeV/n alpha primary. 285
A.127 Albedo response function, 1.43 MeV/n alpha primary. 286
A.128 Albedo response function, 1.619 MeV/n alpha primary. 287
A.129 Albedo response function, 1.832 MeV/n alpha primary. 287
A.130 Albedo response function, 2.07 MeV/n alpha primary. 288
A.131 Albedo response function, 2.338 MeV/n alpha primary. 289
A.132 Albedo response function, 2.639 MeV/n alpha primary. 290
A.133 Albedo response function, 2.976 MeV/n alpha primary. 290
A.134 Albedo response function, 3.355 MeV/n alpha primary. 291
A.135 Albedo response function, 3.779 MeV/n alpha primary. 292
A.136 Albedo response function, 4.255 MeV/n alpha primary. 293
A.137 Albedo response function, 4.789 MeV/n alpha primary. 293
A.138 Albedo response function, 5.387 MeV/n alpha primary. 294
A.139 Albedo response function, 6.057 MeV/n alpha primary. 295
A.140 Albedo response function, 6.808 MeV/n alpha primary. 296
A.141 Albedo response function, 7.65 MeV/n alpha primary. 296
A.142 Albedo response function, 8.592 MeV/n alpha primary. 297
A.143 Albedo response function, 9.648 MeV/n alpha primary. 298
A.144 Albedo response function, 10.83 MeV/n alpha primary. 299
A.145 Albedo response function, 12.15 MeV/n alpha primary. 299
A.146 Albedo response function, 13.63 MeV/n alpha primary. 300
A.147 Albedo response function, 15.3 MeV/n alpha primary. 301
A.148 Albedo response function, 17.15 MeV/n alpha primary. 302
A.149 Albedo response function, 19.23 MeV/n alpha primary. 302

A.150 Albedo response function, 21.56 MeV/n alpha primary. 303
A.151 Albedo response function, 24.17 MeV/n alpha primary. 304
A.152 Albedo response function, 27.1 MeV/n alpha primary. 305
A.153 Albedo response function, 30.37 MeV/n alpha primary. 305
A.154 Albedo response function, 34.04 MeV/n alpha primary. 306
A.155 Albedo response function, 38.15 MeV/n alpha primary. 307
A.156 Albedo response function, 42.76 MeV/n alpha primary. 308
A.157 Albedo response function, 47.93 MeV/n alpha primary. 308
A.158 Albedo response function, 53.73 MeV/n alpha primary. 309
A.159 Albedo response function, 60.24 MeV/n alpha primary. 310
A.160 Albedo response function, 67.55 MeV/n alpha primary. 311
A.161 Albedo response function, 75.77 MeV/n alpha primary. 311
A.162 Albedo response function, 85.01 MeV/n alpha primary. 312
A.163 Albedo response function, 95.41 MeV/n alpha primary. 313
A.164 Albedo response function, 107.1 MeV/n alpha primary. 314
A.165 Albedo response function, 120.4 MeV/n alpha primary. 314
A.166 Albedo response function, 135.3 MeV/n alpha primary. 315
A.167 Albedo response function, 152.2 MeV/n alpha primary. 316
A.168 Albedo response function, 171.4 MeV/n alpha primary. 317
A.169 Albedo response function, 193 MeV/n alpha primary. 317
A.170 Albedo response function, 217.9 MeV/n alpha primary. 318
A.171 Albedo response function, 246.2 MeV/n alpha primary. 319
A.172 Albedo response function, 278.1 MeV/n alpha primary. 320
A.173 Albedo response function, 314.7 MeV/n alpha primary. 320
A.174 Albedo response function, 357.1 MeV/n alpha primary. 321
A.175 Albedo response function, 405.3 MeV/n alpha primary. 322
A.176 Albedo response function, 461.8 MeV/n alpha primary. 323
A.177 Albedo response function, 526.8 MeV/n alpha primary. 323
A.178 Albedo response function, 602.5 MeV/n alpha primary. 324
A.179 Albedo response function, 691.3 MeV/n alpha primary. 325
A.180 Albedo response function, 795.7 MeV/n alpha primary. 326
A.181 Albedo response function, 919.2 MeV/n alpha primary. 326
A.182 Albedo response function, 1.068 GeV/n alpha primary. 327

A.183 Albedo response function, 1.246 GeV/n alpha primary. 328
A.184 Albedo response function, 1.453 GeV/n alpha primary. 329
A.185 Albedo response function, 1.71 GeV/n alpha primary. 329
A.186 Albedo response function, 2.016 GeV/n alpha primary. 330
A.187 Albedo response function, 2.397 GeV/n alpha primary. 331
A.188 Albedo response function, 2.863 GeV/n alpha primary. 332
A.189 Albedo response function, 3.444 GeV/n alpha primary. 332
A.190 Albedo response function, 4.156 GeV/n alpha primary. 333
A.191 Albedo response function, 5.04 GeV/n alpha primary. 334
A.192 Albedo response function, 6.134 GeV/n alpha primary. 335
A.193 Albedo response function, 7.488 GeV/n alpha primary. 335
A.194 Albedo response function, 9.167 GeV/n alpha primary. 336
A.195 Albedo response function, 11.26 GeV/n alpha primary. 337
A.196 Albedo response function, 13.86 GeV/n alpha primary. 338
A.197 Albedo response function, 17.09 GeV/n alpha primary. 338
A.198 Albedo response function, 21.12 GeV/n alpha primary. 339
A.199 Albedo response function, 26.15 GeV/n alpha primary. 340
A.200 Albedo response function, 32.44 GeV/n alpha primary. 341
A.201 Albedo response function, 40.23 GeV/n alpha primary. 341
A.202 Albedo response function, 50 GeV/n alpha primary. 342
A.203 Azimuthal angle distribution of grazing-incidence (zenith $> 80°$) dome hits for ^{1}H primaries at $0\,\mathrm{g\,cm^{-2}}$ passive shielding, by active shielding voltage. Dashed lines mark the eight perimeter point-charge azimuthal positions. 343
A.204 Azimuthal angle distribution of grazing-incidence (zenith $> 80°$) dome hits for ^{1}H primaries at $10\,\mathrm{g\,cm^{-2}}$ passive shielding, by active shielding voltage. Dashed lines mark the eight perimeter point-charge azimuthal positions. 344
A.205 Azimuthal angle distribution of grazing-incidence (zenith $> 80°$) dome hits for ^{1}H primaries at $20\,\mathrm{g\,cm^{-2}}$ passive shielding, by active shielding voltage. Dashed lines mark the eight perimeter point-charge azimuthal positions. 345
A.206 Azimuthal angle distribution of grazing-incidence (zenith $> 80°$) dome hits for ^{1}H primaries at $30\,\mathrm{g\,cm^{-2}}$ passive shielding, by active shielding voltage. Dashed lines mark the eight perimeter point-charge azimuthal positions. 346

A.207 Azimuthal angle distribution of grazing-incidence (zenith > 80°) dome hits for ^{1}H primaries at 50 g cm^{-2} passive shielding, by active shielding voltage. Dashed lines mark the eight perimeter point-charge azimuthal positions. . . . 347
A.208 Azimuthal angle distribution of grazing-incidence (zenith > 80°) dome hits for ^{1}H primaries at 5 g cm^{-2} passive shielding, by active shielding voltage. Dashed lines mark the eight perimeter point-charge azimuthal positions. . . . 348
A.209 Azimuthal angle distribution of grazing-incidence (zenith > 80°) dome hits for ^{4}He primaries at 0 g cm^{-2} passive shielding, by active shielding voltage. Dashed lines mark the eight perimeter point-charge azimuthal positions. . . . 349
A.210 Azimuthal angle distribution of grazing-incidence (zenith > 80°) dome hits for ^{4}He primaries at 10 g cm^{-2} passive shielding, by active shielding voltage. Dashed lines mark the eight perimeter point-charge azimuthal positions. . . . 350
A.211 Azimuthal angle distribution of grazing-incidence (zenith > 80°) dome hits for ^{4}He primaries at 20 g cm^{-2} passive shielding, by active shielding voltage. Dashed lines mark the eight perimeter point-charge azimuthal positions. . . . 351
A.212 Azimuthal angle distribution of grazing-incidence (zenith > 80°) dome hits for ^{4}He primaries at 30 g cm^{-2} passive shielding, by active shielding voltage. Dashed lines mark the eight perimeter point-charge azimuthal positions. . . . 352
A.213 Azimuthal angle distribution of grazing-incidence (zenith > 80°) dome hits for ^{4}He primaries at 50 g cm^{-2} passive shielding, by active shielding voltage. Dashed lines mark the eight perimeter point-charge azimuthal positions. . . . 353
A.214 Azimuthal angle distribution of grazing-incidence (zenith > 80°) dome hits for ^{4}He primaries at 5 g cm^{-2} passive shielding, by active shielding voltage. Dashed lines mark the eight perimeter point-charge azimuthal positions. . . . 354
A.215 Polar (zenith) angle distribution of dome hits for ^{1}H primaries at 0 g cm^{-2} passive shielding, by active shielding voltage. . . . 355
A.216 Polar (zenith) angle distribution of dome hits for ^{1}H primaries at 5 g cm^{-2} passive shielding, by active shielding voltage. . . . 355
A.217 Polar (zenith) angle distribution of dome hits for ^{1}H primaries at 10 g cm^{-2} passive shielding, by active shielding voltage. . . . 356
A.218 Polar (zenith) angle distribution of dome hits for ^{1}H primaries at 20 g cm^{-2} passive shielding, by active shielding voltage. . . . 356

A.219 Polar (zenith) angle distribution of dome hits for ^{1}H primaries at 30 g cm^{-2} passive shielding, by active shielding voltage. . . . 357
A.220 Polar (zenith) angle distribution of dome hits for ^{1}H primaries at 50 g cm^{-2} passive shielding, by active shielding voltage. . . . 357
A.221 Polar (zenith) angle distribution of dome hits for ^{4}He primaries at 0 g cm^{-2} passive shielding, by active shielding voltage. . . . 358
A.222 Polar (zenith) angle distribution of dome hits for ^{4}He primaries at 5 g cm^{-2} passive shielding, by active shielding voltage. . . . 358
A.223 Polar (zenith) angle distribution of dome hits for ^{4}He primaries at 10 g cm^{-2} passive shielding, by active shielding voltage. . . . 359
A.224 Polar (zenith) angle distribution of dome hits for ^{4}He primaries at 20 g cm^{-2} passive shielding, by active shielding voltage. . . . 359
A.225 Polar (zenith) angle distribution of dome hits for ^{4}He primaries at 30 g cm^{-2} passive shielding, by active shielding voltage. . . . 360
A.226 Polar (zenith) angle distribution of dome hits for ^{4}He primaries at 50 g cm^{-2} passive shielding, by active shielding voltage. . . . 360
A.227 Spatial distribution of dome hits (top view) for ^{1}H primaries at 0 g cm^{-2} passive shielding, by active shielding voltage. . . . 361
A.228 Spatial distribution of dome hits (top view) for ^{1}H primaries at 5 g cm^{-2} passive shielding, by active shielding voltage. . . . 361
A.229 Spatial distribution of dome hits (top view) for ^{1}H primaries at 10 g cm^{-2} passive shielding, by active shielding voltage. . . . 362
A.230 Spatial distribution of dome hits (top view) for ^{1}H primaries at 20 g cm^{-2} passive shielding, by active shielding voltage. . . . 362
A.231 Spatial distribution of dome hits (top view) for ^{1}H primaries at 30 g cm^{-2} passive shielding, by active shielding voltage. . . . 363
A.232 Spatial distribution of dome hits (top view) for ^{1}H primaries at 50 g cm^{-2} passive shielding, by active shielding voltage. . . . 363
A.233 Spatial distribution of dome hits (top view) for ^{4}He primaries at 0 g cm^{-2} passive shielding, by active shielding voltage. . . . 364
A.234 Spatial distribution of dome hits (top view) for ^{4}He primaries at 5 g cm^{-2} passive shielding, by active shielding voltage. . . . 364

A.235 Spatial distribution of dome hits (top view) for ^{4}He primaries at $10\,\mathrm{g\,cm^{-2}}$ passive shielding, by active shielding voltage. 365
A.236 Spatial distribution of dome hits (top view) for ^{4}He primaries at $20\,\mathrm{g\,cm^{-2}}$ passive shielding, by active shielding voltage. 365
A.237 Spatial distribution of dome hits (top view) for ^{4}He primaries at $30\,\mathrm{g\,cm^{-2}}$ passive shielding, by active shielding voltage. 366
A.238 Spatial distribution of dome hits (top view) for ^{4}He primaries at $50\,\mathrm{g\,cm^{-2}}$ passive shielding, by active shielding voltage. 366

List of Tables

2.1 GCR isotopic abundances. . . . 17

2.2 Space radiation exposure limits for space agencies around the world. . . . 18

3.1 Geometry in ASPP. . . . 39

3.2 List of parameters, associated symbols, and values contained within the measurements procured at BNL with no dipole rotation $\alpha = 0$ and constant dipole-detector distance $\ell_{DD} = 2\,\mathrm{m}$. 60

3.3 List of parameters, associated symbols, and values contained within the measurements procured at BNL with dipole rotation; all measurements were conducted with sphere radius $a = 2.54\,\mathrm{cm}$, center-to-center sphere separation $\ell_{CC} = 7.620\,\mathrm{cm}$, dipole-detector distance $\ell_{DD} = 2\,\mathrm{m}$, and 2 MeV protons. . . . 60

3.4 Table of fitting parameters (C_0, b_0, k_0, C_1, b_1) which correspond to the simulation and measurement void area data curve fits within the five plots of Figure 3.12 which correspond to various sphere radius a and center-to-center sphere separation ℓ_{CC} values; data type "s" refers to simulation, "m" refers to measurement; the coefficient of determination, R^2, (a goodness-of-fit measure) was included for each set of curve-fitted parameters. . . . 63

3.5 Fitting parameters ($\tilde{a}$, $\tilde{b}$) and coefficients of determination R^2 for rotation study; data type "s" refers to simulation, "m" refers to measurement. . . . 65

4.1 List of propagation methods considered for comparison. . . . 85

4.2 Condensed list of test cases. . . . 90

4.3 Parameters used to construct active shielding configuration shown in Figure 4.1. . . . 97

4.4 Comparison of base SI units and Geant4 system of default units. . . . 116

4.5 Geant4 physical constant definitions. . . . 117

5.1 Key geometric and material parameters of the lunar habitat simulation scenario. . . . 123

5.2 Lunar regolith composition by mass. . . . 124

5.3 Lunar regolith elemental composition by mass. . . . 124

5.4 ICRU four-element tissue elemental composition. . . . 125

5.5 Combination model and G4-ASPP dose rates for H and He primaries. . . . 160

Acronyms

ALARA

As Low As Reasonably Achievable. 9

ASPP

Active Shielding Particle Pusher. xiv, 3–5, 20, 23, 36–41, 43–46, 52, 54, 56–58, 61, 64, 66, 67, 74–77, 79, 93, 96, 113, 119–121, 126, 130, 131, 133, 135, 136, 138–140, 148, 151, 161, 163, 165, 166, 169–171, 175–181

BNL

Brookhaven National Laboratory. xiv, xxvii, 55, 56, 60, 61

BON

Badhwar-O'Neill. 15–17, 131, 139, 170

BT

Boris (Time). 97, 99–112

CSDA

Continuous Slowing-Down Approximation. 22, 162

DNA

deoxyribonucleic acid. 8

ES

Euler (Distance). 98–100, 102–105, 107, 109, 111, 112

ESPE

energetic solar particle event. 2, 13, 14

EVA

extravehicular activity. 13

FLUKA

FLUktuierende KAskade. 4, 75

G4-ASPP

Geant4-ASPP. xvi, xvii, 4, 5, 20, 23, 73, 74, 76, 77, 79, 84, 88, 93, 94, 96, 98, 99, 109–113, 118–123, 126, 130, 143, 150–167, 169–182

G4RS

Restricted Step Length, Geant4. 97–103, 105, 109, 111, 112

G4US

Unrestricted Step Length, Geant4. 97–103, 105, 109, 111, 112

GCR

galactic cosmic ray. 2, 3, 12, 13, 15–17, 19, 52, 53, 118, 119, 121, 126, 129, 131, 137, 139, 142, 143, 148, 150, 151, 159, 162–166, 168, 170, 176, 179–182, 191

Geant4

GEometry ANd Tracking 4. 4, 5

GOES

Geostationary Orbit Environmental Satellite. 13

GPU

Graphics Processing Unit. 4, 75

HZE

highly energetic, heavy charged particles. 52, 54, 73

HZETRN

High charge (Z) and Energy TRaNsport. 5, 22, 119–121, 123, 130, 131, 134, 137, 138, 141–143, 148, 150, 151, 163–166, 170, 171, 173–175, 177, 178, 180

IAEA

International Atomic Energy Agency. 9

ICRP

International Commission on Radiological Protection. xvi, xvii, 1, 2, 8, 9, 11, 12, 18, 120, 137, 144, 148–153, 156, 159–162, 165, 169, 173, 176–178

ICRU

International Commission on Radiation Units and Measurements. 125, 130, 131, 137–139, 141–143, 148–151, 159–165, 170, 171, 176, 177, 179–181

ISS

International Space Station. 1, 2, 18

JSC

Johnson Space Center. 12, 37

KSU

Kansas State University. 37

LEO

low-Earth orbit. 1, 2, 118

LET

linear energy transfer. 12, 137, 144, 169, 172, 173

MCNP

Monte Carlo N-Particle transport code. 4, 75

NASA

National Aeronautics and Space Administration. xvii, 1–3, 11–13, 18, 37, 120, 137, 144, 149, 150, 152, 154, 155, 157, 158, 169

NCRP

National Council on Radiation Protection. 18

NOAA

National Oceanic and Atmospheric Administration. 12

NRC

Nuclear Regulatory Commission. 2

NSCR

NASA Space Cancer Risk. 11

OLTARIS

On-Line Tool for the Assessment of Radiation In Space. 123

PHITS

Particle and Heavy Ion Transport code System. 4, 5, 75, 119–121, 123, 128–130, 134, 143, 145, 146, 148, 163–166, 172, 177–180, 191

RK4S

4th Order Runge-Kutta (Space). 86, 98–102, 105, 107, 109–112, 121, 176, 180

SAA

South Atlantic Anomaly. 1

SAT

Semi-Analytical (Time). 86, 91, 97, 99, 100

SEP

solar energetic particle. 12, 52

SEPEM

Solar Energetic Particle Environment Modeling application server. 13

SPE

solar particle event. 12, 13

SPEL

Spaceflight Permissible Exposure Limit. 2

SRAG

Space Radiation Analysis Group. 12

SWPC

Space Weather Prediction Center. 12

VVS

Momentum-Space-Verlet. 76, 79, 81, 84, 88, 98–103, 105, 107, 109–112, 176, 178, 180

VVT

Velocity-Verlet-Time. 75, 77, 79, 83, 84, 97, 99–103, 105, 107, 109–113

Acknowledgments

I would like to thank my advisor, Prof. Amir Bahadori, for nearly ten years of mentorship and for giving me the opportunity to pursue research in the first place. I joined his group in the summer of 2017 as an undergraduate research assistant through an undergraduate research program in nuclear engineering. At the end of that summer, he asked whether I would like to continue working with him during the academic year, and I accepted because I found the work interesting (and, truthfully, I needed to maintain *at least* one job to keep up with tuition payments). I continued working as an undergraduate research assistant until completing my undergraduate degree, and then continued directly into graduate school under his supervision.

The subjects I first encountered in Prof. Bahadori's courses, Radiation Protection and Shielding and Radiation and Human Health, eventually became central to my research and professional career. At the time, I had no particular reason to think that the material from those courses would form part of the foundation for my own doctoral research. It is interesting to look back and see how much of my education and career grew out of those early experiences.

I would also like to thank Dr. Dan Fry for giving me the opportunity to work on the NASA Active Shielding project. The overarching project originated with him, and I was not initially involved. I became interested in a problem that my office-mate was working on and started trying to solve it, which eventually led me to the project and to much of the research presented in this dissertation. Dan has also been a great mentor throughout this process. He encouraged me to pursue answers to difficult questions in practical ways. I am also grateful that I am able to continue working with him at NASA/JSC/SRAG.

I would also like to thank Prof. Bill Dunn and Prof. Jeremy Roberts, both of whom had a lasting influence on my technical education. Prof. Dunn passed away before I could complete this dissertation, but his contributions to my education remain an important part of this work. He taught my course in Monte Carlo Methods, while Prof. Roberts introduced me to Python. The subjects they taught have become integral parts of my research and professional work, and I am grateful for the foundation they provided.

I would also like to thank Prof. Matthew Berg and Prof. Arsen Iskhakov for serving on my dissertation committee and for taking the time to review and evaluate this work.

I am grateful to my colleagues at Kansas State University and NASA/JSC/SRAG for their support throughout my graduate studies. Although much of this dissertation was an independent effort, working alongside knowledgeable and supportive people provided an important source of technical insight, perspective, and encouragement. I am especially grateful to Dr. Katie Whitman for repeatedly asking for status updates and putting subtle pressure on me to make progress on the dissertation after finishing my daily work-related tasks. The conversations and occasional distractions made the process more manageable and, importantly, more enjoyable.

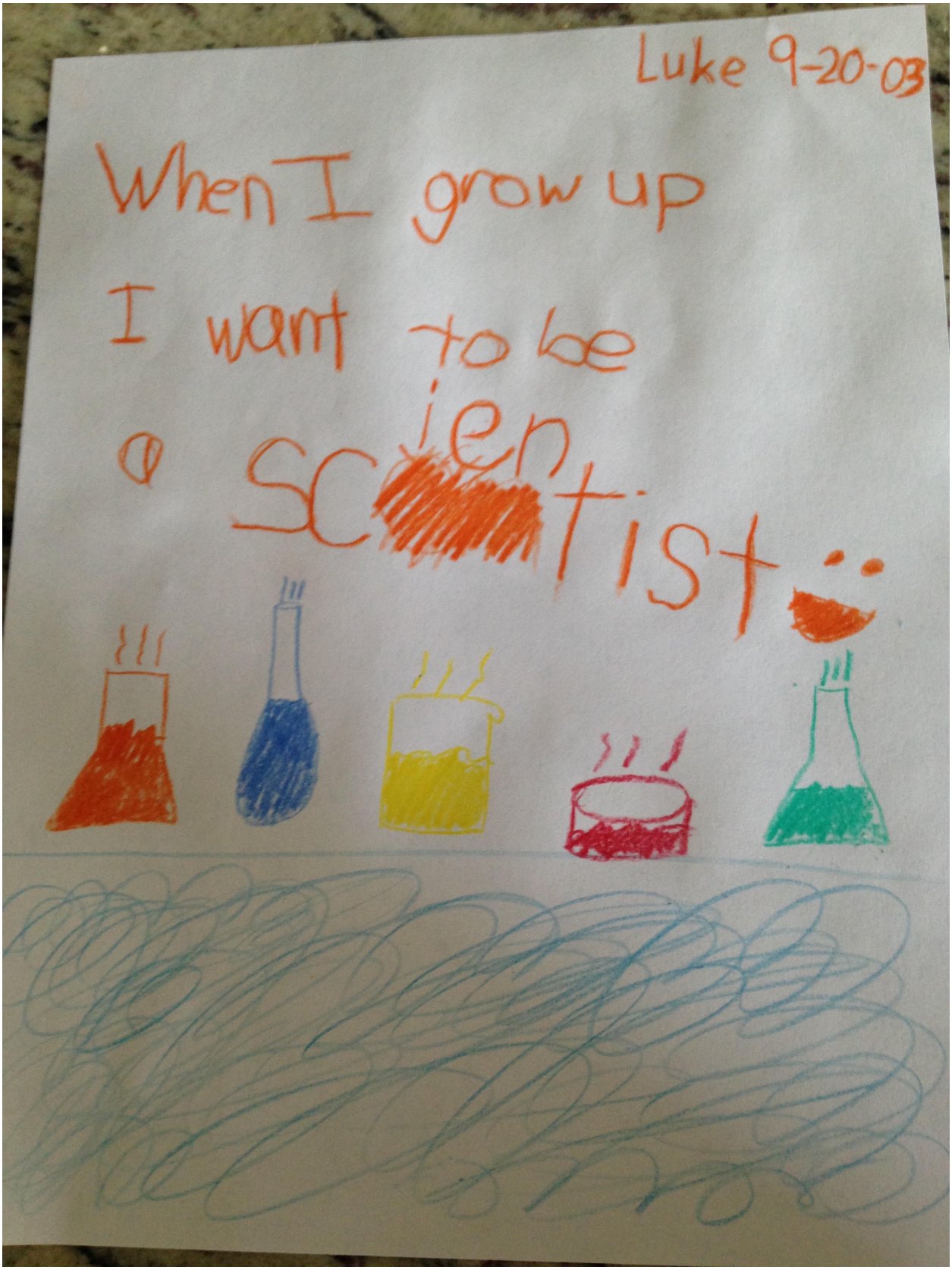
To my friends, I owe you an apology. This degree has taken far more of my time and attention than I initially intended. I am sorry for the times I was absent, for the plans I missed, and for the ways I may have made my work more important than our friendships.

At the same time, I am incredibly grateful to those of you who continued to invite me, check in on me, and make space for me even when I was difficult to reach. Your friendship survived a period of my life in which I was often consumed by this degree, and I do not take that for granted. I hope that finishing this dissertation gives me the opportunity to give some of that time back.

I am also grateful to my family. Completing a PhD demands a considerable amount of time, and I am grateful for your understanding throughout the years when this work seemed to consume most of my attention.

There is one final person I would like to acknowledge: my six-year-old self. Somewhere among my elementary school classwork is a drawing I made in first grade. It contains several vials of evaporating rainbow-colored materials (presumably caustic chemicals), and above them I wrote: "When I grow up I want to be a scientist." I had no idea then what a scientist was supposed to do, or where that ambition might take me. I certainly could not have imagined the path from that first-grade classroom to where I am now, finishing this dissertation and beginning the next chapter of my career.

Looking at that drawing now, I am struck less by how much has changed than by how much has remained the same. I still want to understand things. I still want to figure out how they work. I am grateful that that ambition survived all these years and all the things that could have taken me in a different direction. And although I am pleased that I eventually learned how to spell "scientist," I am even more pleased that six-year-old me was mostly right about what I wanted to become (although an engineer is not necessarily a scientist—just as a rectangle is not necessarily a square).


Luke 9-20-03
When I grow up
I want to be
a scientist

Funding for this work was supported in part by the NASA Human Health and Performance Contract NNJ15HK11B. Some of the computing for this work was performed on the Beocat Research Cluster at Kansas State University, which is funded in part by NSF grants CNS-1006860, EPS-1006860, EPS-0919443, ACI-1440548, CHE-1726332, and NIH P20GM113109.

Chapter 1

Introduction

1.1 Motivation

The NASA Artemis program is underway. In 2022, Artemis I launched, completed two orbits around the Moon, and returned to Earth safely after approximately 25.5 days. Artemis I was an uncrewed flight test. Artemis II—conducted over 10 days in April of 2026—was the first crewed mission to reach lunar orbit since Apollo 17 in December of 1972, over a half-century ago. Future Artemis missions are planned to carry astronauts into lunar orbit and to the lunar surface. They are also intended to establish Moon Base, a lunar surface outpost. The goal of the Artemis program is not simply to "return to the Moon". One of the overarching goals of the Artemis program is to develop the operational capacity for sustained human presence beyond low-Earth orbit (LEO) in preparation for missions to Mars [1].

Of course, space travel is not trivial. There are many risks that must be taken into account to ensure crew safety on any mission. Exposure to the harsh radiation environment in space is one of five major hazards identified by NASA that must be overcome to ensure safe, successful, and sustained human spaceflight beyond LEO [2]. The radiation environment in space is different in character compared to terrestrial radiation environments. Furthermore, the radiation environment varies greatly in different regions of space. For example, astronauts on the International Space Station (ISS) routinely receive significant radiation doses on orbit from the energetic protons trapped in the part of the Van Allen radiation belts that manifest at ISS altitudes as the South Atlantic Anomaly (SAA). A typical effective dose for an astronaut on a 180-day ISS mission, calculated using the ICRP 60 quality factor and tissue weighting factors, is approximately 70

to 80 mSv [3, 4]. For context, the Nuclear Regulatory Commission (NRC) limits the annual effective dose of nuclear radiation workers to 50 mSv y^{-1} (ignoring, for the moment, slight differences between the NRC's definition of effective dose and that of ICRP-60) [5, 6]. While the doses that astronauts receive are relatively large compared to terrestrial radiation workers, the risk of developing acute radiation-induced health effects is low except under extreme circumstances, like exposure to energetic solar particle events (ESPEs) with historically high fluxes. The primary health concern for astronauts, as it relates to radiation exposure, is the increase in the risk of cancer incidence and mortality later in life associated with prolonged low-dose-rate radiation exposures. While an 80 mSv effective dose accumulated over 180 days on the ISS is relatively benign, innovations in spaceflight operations and shielding technology are needed to protect astronauts from the greater cumulative galactic cosmic rays (GCRs) exposure expected during long-term, deep-space missions beyond LEO, like a sustained presence on the surface of the Moon or a mission to and from Mars.

Estimates for the effective dose accumulated over the course of a Mars transit mission vary, but a total NASA effective dose of about 1000 mSv is widely assumed [7, 8]. This 1000 mSv dose exceeds the current NASA Spaceflight Permissible Exposure Limit (SPEL) of 600 mSv [9]. An astronaut whose projected mission exposure exceeds the SPEL could require a formal waiver or other documented authorization acknowledging acceptance of the additional radiation risk before participating in a Mars mission. To avoid exceeding the agency limit, and potentially requiring such astronaut risk-acceptance documentation, radiation protection strategies in the spacecraft and planetary surface environments need to be improved. Typically, a radiation protection specialist would immediately resort to an optimization of one of the three canonical factors, oft repeated in medical training contexts: "time, distance, and shielding". Decreasing the time spent in a radiation field decreases the dose. Increasing the distance between a target and a source reduces the dose at the target location. And (in most situations) increasing the shielding mass between a target and source reduces the dose at the target.

For space applications, the picture is much more complicated due to the restrictions in place for spaceflight. It is expensive to add weight to spacecraft, and according to GCR modeling, there is a local minimum in the dose-equivalent-versus-shielding thickness curve at which point adding more shielding makes the internal radiation environment worse from a human health perspective [10]. The time spent in transit and on planetary surfaces could be reduced to reduce overall radiation exposure, but that would also limit science and exploration opportunities. It is impossible to increase the distance between the radiation source and

the target in space; the GCR-component of the space radiation environment is nearly isotropic and slightly increases in intensity with radial distance from the Sun [11], as far as is known. If these fundamental radiation protection parameters are so difficult to adjust, what can be done? It may not be feasible to introduce more shielding mass to a spacecraft design for radiation protection purposes alone. However, using electromagnetic fields to alter the local radiation environment around a spacecraft or a planetary habitat could provide some additional protection to astronauts with a smaller mass penalty. Electromagnetic fields can improve radiation protection by not only *slowing down* incident charged particles, but also by *diverting* their trajectories away from the inhabited volume. This concept is called active radiation shielding. Traditional forms of radiation shielding that involve placing mass between a source and a target will be referred to as *passive* radiation shielding, henceforth.

Active radiation shielding has never been deployed on a space mission, but plenty of conceptual and experimental work on the subject has been carried out since the 1960s. Investigations have explored electrostatic shielding [12–15], magnetostatic shielding [16], and plasma screening concepts, or the process of collecting interplanetary or artificially generated plasma to provide additional, coupled active and passive shielding outside of the spacecraft [17, 18]. Reviews dedicated to active shielding for radiation protection in space noted that previous studies had shown theoretical applicability but their schemes were beyond the range of current or even near-future technology [15, 19–21]. *There is a need to develop tools that can rapidly identify viable active shielding configurations, provide means to optimize those configurations for a variety of in-space scenarios, including in free space and on the surface of planetary bodies, and allow for an assessment of the technical feasibility of developing such an active shielding configuration that is compatible with other technical systems that form the in-space human habitat.* The 2015 NASA Technology Roadmaps and 2020 NASA Technology Taxonomy both cite the need to develop robust computational methods for the study and design of active radiation shielding systems for use on future long-term deep space missions for crew health and safety purposes [22, 23].

The development of the ASPP was a critical first step toward achieving these goals [24]. ASPP is a charged particle propagation code that allows the user to

- define the source particle distribution in terms of direction, energy, isotope, and charge state,
- define the location, orientation, extent, and electromagnetic properties of primitive geometric shapes

that ultimately generate an electromagnetic field defined by the superposition of analytic expressions for the electric ($\vec{E}(\vec{r})$) and magnetic ($\vec{B}(\vec{r})$) field vectors at all positions in space $\vec{r}$, and

- move these charged particles through space realistically, according to the electromagnetic field defined by the user, and tally quantities in a similar fashion to conventional Monte Carlo radiation transport codes.

ASPP's development was motivated by the fact that previous active radiation shielding simulation studies were typically confined to a single geometric configuration, and focused on one of either an electrostatic, magnetostatic, or plasma shield, but do not focus on establishing an *optimum* configuration [25]. ASPP addresses this issue by providing the means to build complicated active shielding configurations by defining physical shapes that ultimately produce the resultant electromagnetic field, opening the door to 1) rapid active shielding configuration prototyping and 2) large-scale parametric optimization studies. Examples of large scale optimization studies conducted using ASPP can be found in [26, 27], in which the authors describe the process of testing many variations of several active shielding configuration families and attempt to optimize these configurations to minimize incident fluence and dose to a hypothetical crew member.

ASPP is quite useful for prototyping and optimizing active radiation shielding configurations [24, 27–30]. However, *real* spacecraft designs *necessarily* include a passive radiation shielding component as well—this component being the spacecraft and the contents therein. ASPP is not equipped to handle passive shielding calculations as well as conventional radiation transport codes—HZETRN [31, 32], Monte Carlo N-Particle transport code (MCNP) [33], Particle and Heavy Ion Transport code System (PHITS) [34, 35], FLUktuierende KAskade (FLUKA) [36, 37], GEometry ANd Tracking 4 (Geant4) [38, 39]. ASPP lacks cross section data and does not consider physical interaction mechanisms. This deficiency is intentional to maintain ASPP as a fast, efficient, Graphics Processing Unit (GPU)-parallelizable code. Thus, to conduct more robust optimization studies that consider more aspects of the space habitat, including a potential active shielding *and* passive radiation shielding configuration, it would be prudent to develop a tool that can consider both at once. This concept motivated the development of a tool that combines the passive radiation transport capabilities of Geant4 with ASPP's ability to transport charged particles through electromagnetic fields. The resulting tool, G4-ASPP, forms the focus of this dissertation, with its development discussed in detail in the following chapters.

1.2 Outline

This dissertation encompasses much of the work undertaken as a Graduate Research Assistant during the author's time in the Graduate School.

- Chapter 2 discusses general background information on radiation protection, the space radiation environment, and particle transport methods. The neutral particle transport equation is discussed and an extension, the charged particle transport equation, is proposed in an effort to 1) mathematically describe the differences between neutral particle transport methods and charged particle transport methods and 2) derives the adjoint form of a proposed charged particle transport equation, to be considered for future work.

- Chapter 3 discusses the experimental validation of ASPP and some extraneous extensions to the ASPP codebase developed over the course of the Active Radiation Shielding project. This chapter also includes a discussion on how active radiation shielding effectiveness can be physically measured via void area calculation in a calibrated image.

- Chapter 4 discusses the development of G4-ASPP—particularly the benchmarking of the methods used to transport charged particles through electromagnetic fields in Geant4. It discusses a suite of established charged particle propagation schemes, and compares them among one another in terms of the accuracy of their trajectories compared to reference trajectories for analytically tractable cases, the degree to which they adhere to energy conservation laws, and computational time.

- Chapter 5 discusses an example utility of G4-ASPP: evaluating an active radiation shielding configuration meant to protect a proposed lunar surface habitat. This chapter compares the coupled charged particle transport methods G4-ASPP applies to a combined active-passive shielding scenario to that of a decoupled approach carried out with a combination of PHITS, ASPP, and High charge (Z) and Energy TRaNsport (HZETRN).

1.3 Notation

1.3.1 Functions and Distributions

The distinction between general functions and *distribution* functions can sometimes be subtle. This dissertation adopts the notation

$$f(a; b, c), \tag{1.1}$$

in which f is a function of a, which appears before the semi-colon, and a distribution in b and c, which follow the semi-colon. One important property of distribution functions is that the distributed parameters can be "integrated out" to recover a simple function of the non-distributed variables, i.e.,

$$\int_{c_0}^{c_1} \int_{b_0}^{b_1} f(a; b, c) \mathrm{d}b \mathrm{d}c = f(a), \tag{1.2}$$

where the bounds of integration cover the supports $b \in [b_0, b_1]$ and $c \in [c_0, c_1]$. The distribution function $f(a; b, c)$ can also be expressed in terms of partial derivatives,

$$f(a; b, c) = \frac{\partial^2 f(a, b, c)}{\partial b \partial c}. \tag{1.3}$$

1.3.2 Other Mathematical Shorthand

The sign function is typically defined as

$$\mathrm{sgn}(x) = \begin{cases} -1, & x < 0 \\ 0, & x = 0 \\ +1, & x > 0 \end{cases}. \tag{1.4}$$

In this work, the sign function is also corrupted for convenience purposes. There are instances in which it is convenient for the sign function to take an operator, like $+$ or $-$, as input. In this work,

$$\mathrm{sgn}(\mathrm{operator}) = \begin{cases} -1, & \text{operator is the subtraction operator} \\ +1, & \text{operator is the addition operator} \end{cases}, \tag{1.5}$$

is also used. Context should make this distinction obvious.

The Heaviside step function is defined as

$$\mathcal{H}(x) = \begin{cases} 0, & x < 0 \\ \\ 1, & x \geq 0 \end{cases}. \tag{1.6}$$

Note the convention $\mathcal{H}(0) = 1$; this is not consequential in this work, but is included to clarify that $\mathcal{H}(0) \neq 1/2$ as it is sometimes defined in other physics texts.

Chapter 2

Background

2.1 Radiation Protection

Ionizing radiation is a known carcinogen [40]. When cells are exposed to ionizing radiation, deoxyribonucleic acid (DNA) in the affected cells can be damaged directly or indirectly. When DNA is damaged directly, it is in the form of a single- or double-strand break, where one or both of the DNA polynucleotide chains are severed. This can lead to cell death, or possible mutation, which can manifest as cancer. Radiogenic free radicals (like $OH^{\bullet}$) in tissue can also damage DNA and induce mutagenesis [41].

There are two broad categories of ionizing radiation: directly ionizing and indirectly ionizing. Directly ionizing radiation includes charged particles; they *directly* ionize the medium they travel through by stripping away electrons from nearby atoms via Coulombic interactions, ultimately depositing energy (and slowing down) in the process. Indirectly ionizing radiation refers to uncharged particles, like photons and neutrons, that may interact with atomic nuclei in a medium to produce directly ionizing particles that then traverse and ionize the medium.

Modern radiation protection frameworks are built to implement the practice of justifying, optimizing, and limiting radiation exposures to humans. The 1990 ICRP recommendations on radiation protection summarize the foundational principles of radiation protection [4, 6]:

1. **Justification:** A cost-benefit analysis must be conducted to justify any intentional change to a radiation exposure scenario, and that change may only be justified if the individual and/or societal benefits of the exposure outweigh its detriments.

2. **Optimization:** The magnitude of individual and societal radiation doses should be maintained As Low As Reasonably Achievable (ALARA), considering economic and societal factors. The margin between benefit and detriment should be maximized to the extent to which the circumstances allow, within reason.

3. **Limitation:** Dose limits should be enforced. The magnitude of individual doses, except in the case of medical doses (in which the benefit outweighs the detriment), should be maintained below recommended dose limits.

Radiation protection takes on different forms for different applications. For members of the public, radiological protection is subject to substantially lower dose limits than for occupationally exposed workers, reflecting differences in the circumstances and benefits associated with exposure. The ICRP and International Atomic Energy Agency (IAEA) recommend an ICRP 103 effective dose limit of $1\,\mathrm{mSv\,y^{-1}}$ for public exposure from planned exposure situations, excluding exposure from natural background radiation and medical procedures [6, 42].

There exists a hierarchy of physical and dosimetric quantities used for radiation protection purposes, and all of these quantities can ultimately be related to the *amount of energy deposited* in a target (typically human tissue). The most fundamental dosimetric quantity is the absorbed dose (at a point), or the amount of energy deposited $\Delta\varepsilon$ per unit mass Δm,

$$D = \lim_{\Delta m \to 0} \frac{\Delta \varepsilon}{\Delta m}. \tag{2.1}$$

Absorbed dose is the central quantity linking the physical interaction of a particular type of ionizing radiation with matter to its potential to cause biological harm and forms the foundation for radiological protection. Another of the more basic quantities is the particle fluence, defined as the number of particles ΔN passing through a sphere centered at the point of interest per unit cross section of said sphere, ΔA, as ΔA approaches zero,

$$\Phi \equiv \lim_{\Delta A \to 0} \frac{\Delta N}{\Delta A}. \tag{2.2}$$

Equivalently, the fluence may also be defined as the sum of all particle path lengths s_i traversing a sphere

centered at the point of interest per unit volume ΔV, as ΔV approaches zero,

$$\Phi \equiv \lim_{\Delta V \to 0} \frac{\sum_i s_i}{\Delta V}. \tag{2.3}$$

The particle fluence is a fundamental measure of radiation field strength and forms the physical basis for computing the absorbed dose. The particle fluence is often described as a distribution function of kinetic energy T and solid angle direction $\vec{\Omega}$ (called the double-differential fluence) with possible dependence on position $\vec{r}$, time t and other parameters,

$$\Phi(\vec{r}, t; T, \vec{\Omega}) = \frac{\partial^2 \Phi}{\partial T \partial \Omega}(\vec{r}, t). \tag{2.4}$$

The particle fluence and absorbed dose, in general, can be related to one another through response functions $\mathcal{R}(T, \vec{\Omega})$ via the convolution

$$D = \int_{4\pi} \int_0^\infty \mathcal{R}(T, \vec{\Omega}) \Phi(\vec{r}, t; T, \vec{\Omega}) \mathrm{d}T \mathrm{d}\Omega. \tag{2.5}$$

$\Phi(\vec{r}, t; T, \vec{\Omega})$ is quite general. For a monoenergetic, monodirectional radiation field,

$$\Phi(\vec{r}, t; T, \vec{\Omega}) = \Phi(\vec{r}, t) \delta(T - T_0) \delta^3(\vec{\Omega} - \vec{\Omega}_0), \tag{2.6}$$

where $\delta(\cdot)$ is the Dirac delta function. In this case, Equation 2.5 simplifies to

$$D = \mathcal{R}(T_0, \vec{\Omega}_0) \Phi(\vec{r}, t). \tag{2.7}$$

While the absorbed dose provides a measure of the physical energy imparted to tissue, it does not account for the differing biological effectiveness of various types of radiation or the varying sensitivity of different organs and tissues. Occupations such as nuclear reactor technicians account for these effects via the organ equivalent dose $H_\mathcal{T}$. The organ equivalent dose is defined as,

$$H_\mathcal{T} = \sum_R w_R D_{\mathcal{T},R}, \tag{2.8}$$

where $D_{\mathcal{T},R}$ is the absorbed dose imparted to tissue $\mathcal{T}$ from radiation type R for stochastic effects, and w_R is the radiation weighting factor intended to reflect the relative biological effectiveness of radiation type R.

There are multiple definitions for the radiation weighting factors in common use, e.g., the values specified in [4] and [6]. The organ equivalent dose provides a biologically weighted dose to individual organs, accounting for differences in biological impacts of different radiation types. To extend this to an assessment of overall detriment from partial or non-uniform exposures and account for differences in radiosensitivity within the spectrum of human tissues, the ICRP effective dose $\mathcal{E}$ is defined as a weighted sum of organ equivalent doses,

$$\mathcal{E} = \sum_{\mathcal{T}} w_{\mathcal{T}} H_{\mathcal{T}}, \tag{2.9}$$

where each tissue $\mathcal{T}$ is scaled by a tissue weighting factor $w_{\mathcal{T}}$ that represents its relative contribution to the overall detriment from stochastic effects. The effective dose enables comparison of different exposure scenarios by expressing the total detriment as a single quantity, independent of the specific tissues or radiation types involved.

It is important to note that there are several different definitions of effective dose. All definitions take the form shown in Equation 2.9, but the results differ depending on which combination of tissue weighting factors and radiation weighting factors or quality factors prescribed by ICRP-60, ICRP-103, NASA Space Cancer Risk (NSCR), etc., are used to modify the physical quantity absorbed dose in each tissue $\mathcal{T}$ [4, 6, 43]; the detriment associated with 1 Sv of ICRP-103 effective dose is not equal to the detriment associated with 1 Sv of ICRP-60 effective dose. The detriment associated with 1 Sv of ICRP-103 effective dose might not even equate to the detriment associated with 1 Sv of ICRP-103 effective dose depending on whether $H_{\mathcal{T}}$ is the equivalent dose (uses radiation weighting factors) or the dose equivalent (uses quality factors). Stated in another way, for the same radiation exposure scenario, the use of different effective dose calculation methodologies will not necessarily result in identical numerical results. The NASA effective dose, $\mathcal{E}_{\text{NASA}}$, uses tissue weighting factors specified by the NSCR-2012 model, and does not adopt the radiation weighting factors defined in either [4] or [6], opting for an alternative quality factor definition. The NASA organ dose equivalent (note that these are *dose equivalent* values because they are calculated using a quality factor as opposed to a radiation weighting factor) is defined as

$$H_{\mathcal{T},\text{NASA}} = \frac{1}{\rho_{\mathcal{T}}} \int_0^\infty Q_{\text{NASA}}(Z, A, T) \Phi_{\mathcal{T}}(Z, A; T) L(Z, A, T) \mathrm{d}T, \tag{2.10}$$

where $\rho_{\mathcal{T}}$ is the density of the tissue in question (typically assumed to be $1\,\mathrm{g\,cm^{-3}}$), Q_{NASA} is the NASA

quality factor, and L is the linear energy transfer (LET) of an ion with charge Z, mass number A, and kinetic energy T. The NASA effective dose is better suited to account for the radiation quality of charged particle exposures where the particle kinetic energies range widely, such as the energies that are experienced in human spaceflight [9, 43, 44]. The NASA effective dose is also presumed to be less conservative than ICRP effective dose, which is important for space agencies that desire to send humans into space for increasingly longer periods of time.

2.2 Space Radiation Environment

Space radiation sources are typically divided into three broad categories and they are primarily focused on the radiation environment *within the heliosphere*: solar energetic particles (SEPs), GCRs, and charged particle radiation trapped in the Earth's magnetic field (trapped).

2.2.1 Solar Particle Events

The rapid outward acceleration of a collection of solar particulate matter is called a solar particle event (SPE). The solar dynamics involved in producing solar particle events are not fully understood. Over the course of approximately 11 years, the solar magnetic field changes polarity. The period when the solar magnetic polarity axis is approximately perpendicular to the solar rotational axis is known as solar maximum. During solar maximum, the number of sunspots visible on the solar surface increases, and so does the solar flare frequency. A more active Sun leads to a greater frequency of solar particle events, which are typically preceded by a solar flare, a coronal mass ejection, and Type II and Type IV radio bursts. A solar particle event accelerates charged particles—predominantly protons—away from the solar surface and into the heliosphere. SPEs are a concern for astronaut radiation exposure, especially for missions that travel outside the protection of Earth's magnetic field. A historically large SPE, though unlikely, could impart enough dose to induce acute tissue reactions (previously termed "deterministic effects"), such as mild acute radiation syndrome, under the right circumstances [45]. Figure 2.1 illustrates the progression of a solar particle event. Particles propagate away from a region on the Sun along heliospheric magnetic field lines.

The Space Radiation Analysis Group (SRAG) at NASA Johnson Space Center (JSC)—and the National Oceanic and Atmospheric Administration (NOAA) Space Weather Prediction Center (SWPC)—define a

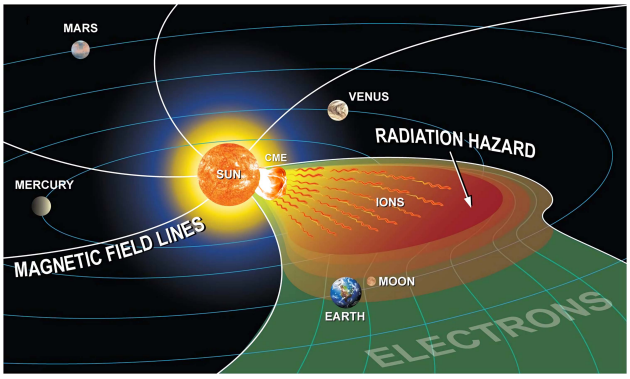


Figure 2.1: Illustration of coronal mass ejection and subsequent solar particle event. Source (courtesy NASA): [46]

.

solar particle event as a contiguous time period in which the >10 MeV integral proton flux at the primary Geostationary Orbit Environmental Satellite (GOES) instrument exceeds 10 protons $\mathrm{cm}^{-2}\,\mathrm{sr}^{-1}\,\mathrm{s}^{-1}$ [47, 48]. These events are typically only a concern for astronaut health during extravehicular activity (EVA); astronauts are well-shielded from protons less than approximately 30 MeV within crewed vehicles. ESPEs are defined as events in which the >100 MeV integral proton flux exceeds 1 proton $\mathrm{cm}^{-2}\,\mathrm{sr}^{-1}\,\mathrm{s}^{-1}$. These events are of greater concern for astronaut health due to the greater penetrative power of higher energy protons. For example, Figure 2.2 shows the angular proton flux time profile of the October 1989 ESPE as measured by GOES-7 and extracted from the Solar Energetic Particle Environment Modeling application server (SEPEM) database [49]. October 1989 is a significant event because of its long duration, high intensity, and its use in spacecraft shielding design. Figure 2.3 shows the differential fluence spectrum, or the differential flux spectra summed over the duration of the October 1989 event. Note that the magnitude of the peak ESPE differential flux is approximately 9–10 orders of magnitude higher than the peak GCR differential flux in shown in Figure 2.4, but the relevant particle energies with the greatest flux are much smaller for the ESPE than GCR. This suggests that optimal shielding strategies probably differ for SPEs/ESPEs and GCRs.

2.2.2 Galactic Cosmic Rays

GCRs consist of high-energy, heavy charged particles that originate from outside the solar system (likely from supernova remnants, quasars, active galactic cores, etc.) [51]. In contrast to SPEs, which are generally sporadic, high flux, transient episodes tied to solar activity, GCRs are ever-present, directionally isotropic, and relatively low flux radiation. GCRs are notoriously difficult to shield due to their high energies, isotopic

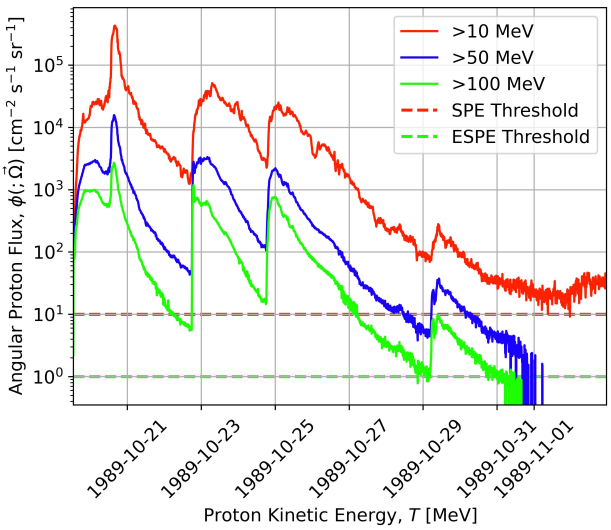


Figure 2.2: Angular flux time profiles from October 1989 ESPE; plot includes >10 MeV, >50 MeV, and >100 MeV integral proton flux profiles. Produced with data from [49]. Typical background proton flux is on the order of 0.1 protons cm^{-2} sr^{-1} s^{-1}.

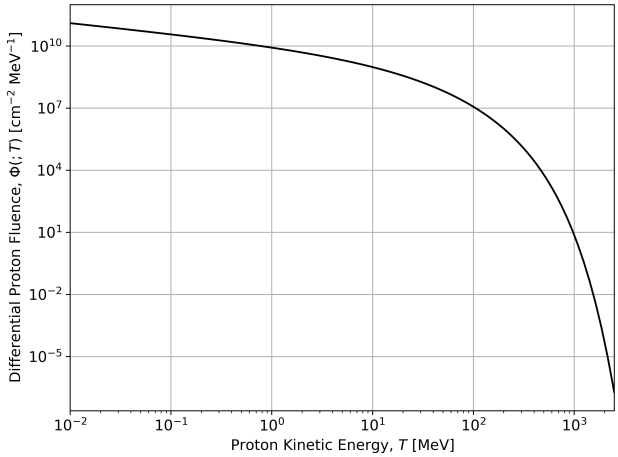


Figure 2.3: Differential fluence spectrum associated with October 1989 ESPE; produced with data from [50].

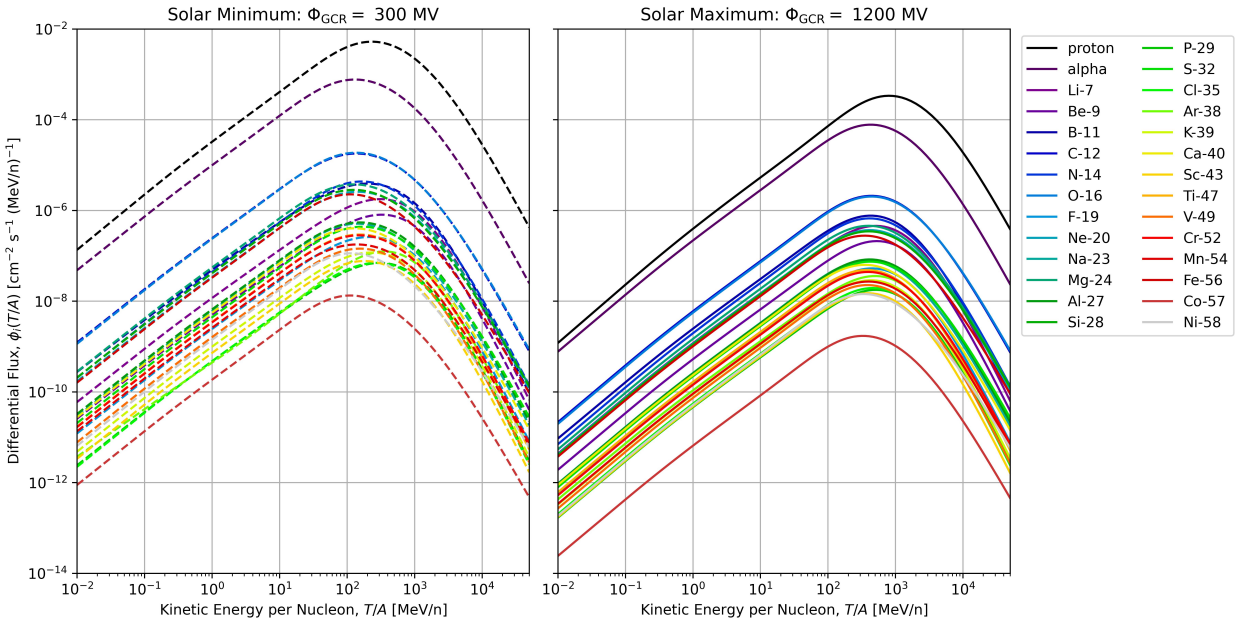


Figure 2.4: GCR differential flux spectra for each major particle species according to BON 2020 model. The left figure shows the GCR environment during representative solar minimum (assuming a solar modulation parameter of 300 MV) and the right figure shows the GCR environment during representative solar maximum (assuming a solar modulation parameter of 1200 MV).

diversity, and tendency to produce secondaries in shielding. GCRs are comprised of all ions with atomic numbers $1 \leq Z \leq 93$ with an approximate energy range of $1\,\mathrm{MeV\,n^{-1}}$ to a few $\mathrm{TeV\,n^{-1}}$. High quality estimates of the GCR differential flux spectrum can be extracted from the Badhwar-O'Neill (BON) 2020 model. Estimates of the GCR differential flux spectrum for representative solar minimum (assuming a solar modulation parameter of 300 MV) and solar maximum (assuming a solar modulation parameter of 1200 MV) are shown in Figure 2.4. Note that GCR flux is maximized during solar minimum and minimized during solar maximum—as solar activity increases, the solar wind becomes more intense and turbulent, which in turn reduces the intensity of GCRs within the heliosphere.

The isotopic distribution of GCRs is shown in Figure 2.5 and tabulated in Table 2.1. GCRs are dominated by protons (91% during solar minimum, 87% during solar maximum), followed by alpha particles (8% during solar minimum, 12% during solar maximum), with the remaining 1% comprised of heavier ions. Although the heavier ions are only a small fraction of the isotopic distribution, they can become important for estimating organ dose equivalents, effective dose, and radiation risk, due to the influence of ion charge on radiation quality [52]. In the absence of any historically intense solar particle events, GCRs will be the primary source of incident radiation exposure for the crew on any hypothetical long-duration space mission, and the primary

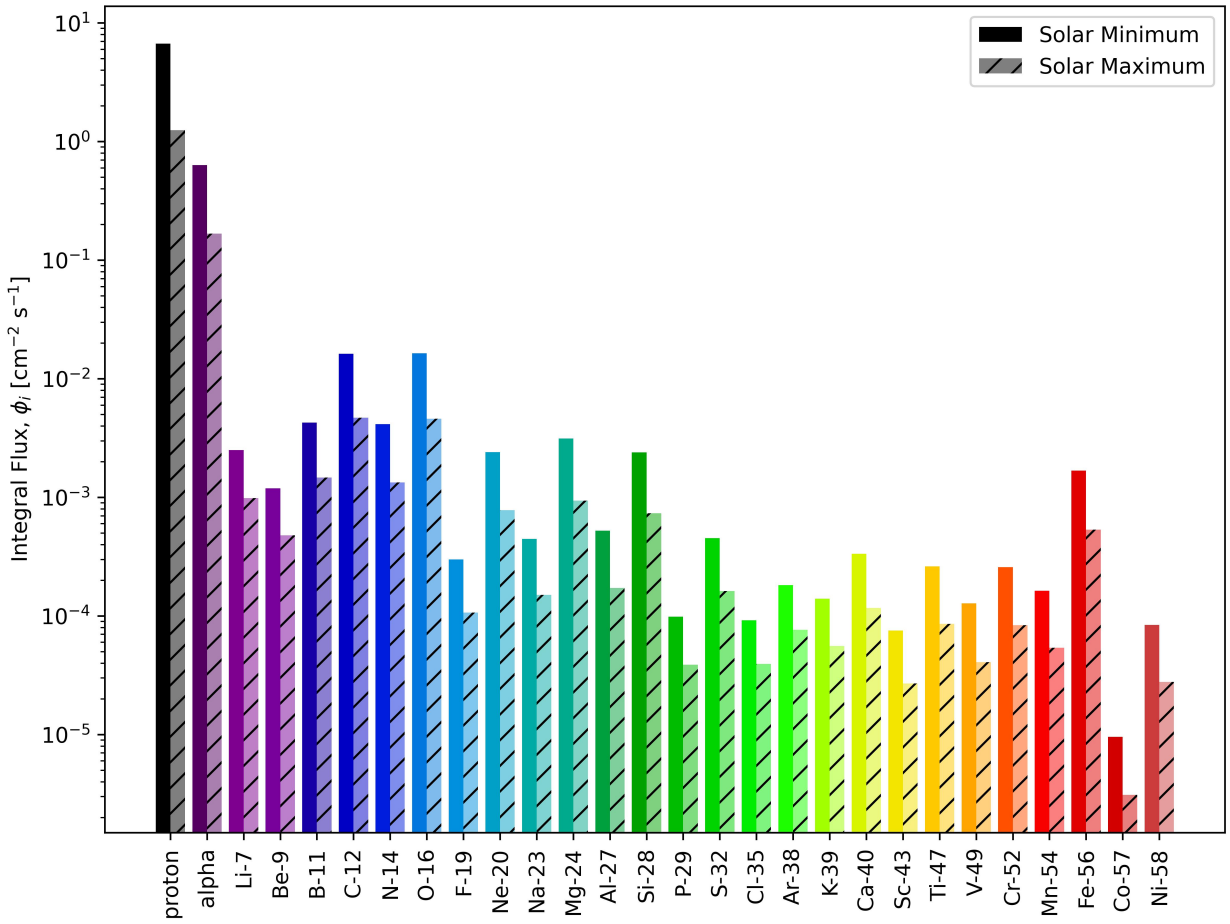


Figure 2.5: Isotopic distribution of major GCR species according to the BON 2020 model [52]. Solar minimum corresponds to $\Phi_{\text{GCR}} = 300\,\text{MV}$ while solar maximum corresponds to $\Phi_{\text{GCR}} = 1200\,\text{MV}$.

culprit for any increased risk of cancer incidence and mortality post-mission.

2.2.3 Magnetically Trapped Radiation

Magnetically trapped radiation belts refer to zones of energetic charged particles that have been "trapped" or "captured" by the magnetic field of a nearby planetary object. Earth has two trapped radiation belts (with occasional, temporary belts forming in response to space weather events or high-altitude nuclear weapon detonation tests), called the Van Allen Belts, named after their discoverer. Jupiter, Saturn, Uranus, Neptune, and Mercury also have magnetic fields of varying size and strength, which means they also have trapped radiation belts; Jupiter's is the strongest and most extensive. Figure 2.6 shows the toroidal nature of Earth's trapped radiation belts.

The Van Allen Belts consist of electrons and protons that originate from the solar wind and GCRs that

Particle	Flux (Solar Minimum) [$\mathrm{cm^{-2}\,s^{-1}}$]	Fraction (Solar Minimum)	Flux (Solar Maximum) [$\mathrm{cm^{-2}\,s^{-1}}$]	Fraction (Solar Maximum)
proton	6.677×10^{0}	9.063×10^{-1}	1.245×10^{0}	8.707×10^{-1}
alpha	6.325×10^{-1}	8.585×10^{-2}	1.670×10^{-1}	1.168×10^{-1}
O-16	1.640×10^{-2}	2.226×10^{-3}	4.599×10^{-3}	3.217×10^{-3}
C-12	1.619×10^{-2}	2.198×10^{-3}	4.679×10^{-3}	3.273×10^{-3}
B-11	4.266×10^{-3}	5.791×10^{-4}	1.471×10^{-3}	1.029×10^{-3}
N-14	4.141×10^{-3}	5.621×10^{-4}	1.336×10^{-3}	9.343×10^{-4}
Mg-24	3.130×10^{-3}	4.249×10^{-4}	9.379×10^{-4}	6.560×10^{-4}
Li-7	2.501×10^{-3}	3.394×10^{-4}	9.829×10^{-4}	6.875×10^{-4}
Ne-20	2.406×10^{-3}	3.266×10^{-4}	7.782×10^{-4}	5.443×10^{-4}
Si-28	2.391×10^{-3}	3.246×10^{-4}	7.347×10^{-4}	5.139×10^{-4}
Fe-56	1.676×10^{-3}	2.276×10^{-4}	5.343×10^{-4}	3.737×10^{-4}
Be-9	1.192×10^{-3}	1.618×10^{-4}	4.773×10^{-4}	3.338×10^{-4}
Al-27	5.223×10^{-4}	7.090×10^{-5}	1.722×10^{-4}	1.204×10^{-4}
S-32	4.523×10^{-4}	6.140×10^{-5}	1.623×10^{-4}	1.135×10^{-4}
Na-23	4.465×10^{-4}	6.061×10^{-5}	1.501×10^{-4}	1.050×10^{-4}
Ca-40	3.343×10^{-4}	4.538×10^{-5}	1.166×10^{-4}	8.158×10^{-5}
F-19	2.989×10^{-4}	4.058×10^{-5}	1.065×10^{-4}	7.449×10^{-5}
Cr-52	2.573×10^{-4}	3.493×10^{-5}	8.343×10^{-5}	5.836×10^{-5}
Ti-47	2.612×10^{-4}	3.546×10^{-5}	8.571×10^{-5}	5.995×10^{-5}
Ar-38	1.819×10^{-4}	2.469×10^{-5}	7.628×10^{-5}	5.336×10^{-5}
Mn-54	1.629×10^{-4}	2.211×10^{-5}	5.380×10^{-5}	3.764×10^{-5}
K-39	1.399×10^{-4}	1.899×10^{-5}	5.584×10^{-5}	3.906×10^{-5}
V-49	1.273×10^{-4}	1.728×10^{-5}	4.070×10^{-5}	2.847×10^{-5}
P-29	9.861×10^{-5}	1.339×10^{-5}	3.883×10^{-5}	2.716×10^{-5}
Cl-35	9.196×10^{-5}	1.248×10^{-5}	3.930×10^{-5}	2.749×10^{-5}
Ni-58	8.393×10^{-5}	1.139×10^{-5}	2.775×10^{-5}	1.941×10^{-5}
Sc-43	7.509×10^{-5}	1.019×10^{-5}	2.689×10^{-5}	1.881×10^{-5}
Co-57	9.545×10^{-6}	1.296×10^{-6}	3.093×10^{-6}	2.164×10^{-6}

Table 2.1: Isotopic abundances and integral fluxes for GCR according to BON 2020 model. Solar minimum corresponds to $\tilde{\Phi}_{\mathrm{GCR}} = 300\,\mathrm{MV}$ while solar maximum corresponds to $\tilde{\Phi}_{\mathrm{GCR}} = 1200\,\mathrm{MV}$. Isotopes are arranged by descending solar minimum abundance fraction.

become confined by the planet's magnetic field lines. Once captured, the charged particles spiral along the magnetic field lines, bouncing between the magnetic poles and drifting longitudinally to form toroidal regions of high flux density. The inner belt is dominated by protons between 10 MeV and a few hundred MeV. The outer belt is dominated by electrons with energies between 10 keV and 10 MeV. The high flux densities in these regions make loitering in the Van Allen Belts inadvisable from the perspective of both crew and instrument health, but do not pose serious risks to astronaut health for most realistic Lunar and Martian mission trajectories due to the short transit duration.

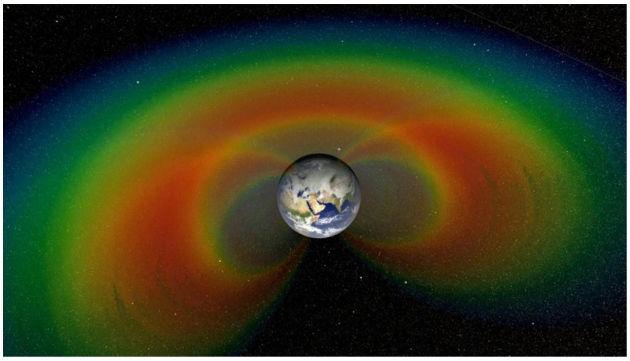


Figure 2.6: Illustration of Earth's trapped radiation belts: the Van Allen Belts [53].

2.3 Space Radiation Exposure Limits

While advisory bodies like the National Council on Radiation Protection (NCRP) and ICRP recommend relatively low yearly radiation exposure limits to terrestrial policymakers, space agencies are afforded more flexibility to apply their own space radiation specific exposure limits. Table 2.2 lists the career dose limits applied by agencies that operate on the ISS [54]. Exceedance of these limits by the agencies' respective astronauts carry various consequences, including (at maximum) preventing an astronaut that exceeds these limits from participating in future missions or (at minimum) requiring an acknowledgment of additional radiation-induced cancer risk on the part of the astronaut and/or their accompanying flight surgeon.

Table 2.2: Space radiation exposure limits for space agencies around the world [54].

Space Agency	Career Effective Dose Limit [mSv]	Effective Dose Methodology
Canadian Space Agency	1000	NASA Effective Dose
European Space Agency	1000	ICRP-103 Effective Dose
Japanese Aerospace Exploration Agency	500 to 1000*	ICRP-116 / ICRP-123 Effective Dose$
NASA	600	NASA Effective Dose
Roscosmos	1000	ICRP-60&

* Depends on sex and age at first mission.
$ ICRP-116 fluence-to-dose conversion factors for photons and electrons; ICRP-123 for protons, neutrons, and heavy ions.
& Includes multiplicative risk factors for dose rate, exposure distribution, and non-radiation biological effects.

2.4 Active Radiation Shielding

Active radiation shielding refers to the use of electromagnetic fields to protect astronauts from energetic charged particles by altering their trajectories or energies before they reach habitable volumes, whereas passive radiation shielding relies on shielding material composition and thickness to attenuate incident particle flux through Coulomb scattering and direct nuclear interaction. Active shielding systems have yet to be deployed on any spacecraft. Several conceptual approaches to active shielding have been investigated since the 1960s [12, 17, 19, 55]. These include electrostatic, magnetostatic, and plasma-based configurations.

2.4.1 Electrostatic Shielding

Electrostatic shielding aims to deflect incoming charged particles using electric fields generated by large potential differences. In principle, positively charged structures could be used to divert the trajectories of incident GCR particles and solar protons via the Lorentz force (no magnetic field component),

$$\frac{\mathrm{d}\vec{p}}{\mathrm{d}t} = q\vec{E}. \tag{2.11}$$

The practical realization of such systems faces formidable challenges. The required potentials for deflecting protons of tens to hundreds of MeV are on the order of gigavolts, far exceeding the breakdown limits of materials and the capabilities of power systems in spacecraft environments [17, 55]. Moreover, maintaining such large charge separations in the plasma environment of space would attract countercharges, leading to charge neutralization or arcing. For these reasons, electrostatic shielding is generally considered infeasible for high-energy galactic cosmic rays but might offer limited benefits against lower-energy solar energetic particles under specific configurations.

2.4.2 Magnetostatic Shielding

Magnetostatic shielding employs magnetic fields to bend the trajectories of charged particles via the Lorentz force. Superconducting coils or permanent magnets could, in principle, create regions of reduced particle flux near a habitat or spacecraft [55]. The radius of curvature for a charged particle in a magnetic field is given by

$$R_{\mathrm{mag}} = \frac{p}{qB}, \tag{2.12}$$

where p is the particle momentum, q its charge, and B the magnetic field strength. For a 1 GeV proton, the required field to achieve significant deflection over tens of meters is several teslas, implying large and massive superconducting systems. Additionally, the presence of such strong fields could interfere with onboard electronics and pose operational hazards to crew and instruments. Magnetic shielding remains an area of active research, particularly for configurations that use compact magnetic fields in combination with passive materials to achieve partial mitigation of the trapped or solar particle environment [19, 56].

2.4.3 Plasma Shielding

Plasma shielding represents a hybrid approach in which a magnetized plasma—either naturally occurring or artificially generated—interacts with incoming charged particles to produce a self-sustaining barrier. In principle, a plasma cloud maintained around a spacecraft could enhance the effective magnetic field via collective interactions, improving deflection efficiency beyond what static fields alone can achieve. Laboratory experiments and simulations have demonstrated partial deflection of low-energy ion beams using magnetized plasma plumes, but scaling such systems to space-relevant dimensions and energies remains a major challenge. The maintenance of plasma density, confinement, and stability in the solar wind environment requires continuous energy input and advanced plasma control technologies. Nevertheless, plasma-based concepts continue to attract interest as a potentially lightweight and adaptive form of active shielding.

2.4.4 Outlook

Active shielding remains a technically ambitious but potentially transformative approach to reducing astronaut radiation exposure, particularly during solar particle events or extended missions beyond Earth orbit. While significant challenges persist—including mass, power, field containment, and system integration—advances in superconducting materials, plasma control, and computational modeling tools such as ASPP and G4-ASPP enable continued exploration of feasible architectures. Integration of active and passive shielding concepts offers the most promising near-term strategy for comprehensive radiation protection in deep-space missions.

2.5 Space Radiation Transport

Radiation transport methods can be summarized as any attempt to approximate a solution to the Boltzmann transport equation to determine the particle flux distribution at some target point $\vec{r}_T$ or within some region $\vec{r} \in R$. The linearized Boltzmann transport equation, with the application of some important assumptions that will be addressed, fully describes the radiation field at all points within an arbitrary volume V, and is typically given by

$$\begin{aligned} \vec{\Omega} \cdot \nabla \phi_j(\vec{r}; T, \vec{\Omega}) + \mu_j(\vec{r}, T)\phi_j(\vec{r}; T, \vec{\Omega}) = \sum_k \int_0^\infty \int_{4\pi} \mu_{k\to j}(\vec{r}, T, \vec{\Omega}; T', \vec{\Omega}')\phi_k(\vec{r}; T', \vec{\Omega}')\, \mathrm{d}\Omega'\, \mathrm{d}T' \\ + S_j(\vec{r}, T, \vec{\Omega}), \end{aligned} \tag{2.13}$$

where $\phi_j(\vec{r}; T, \vec{\Omega})$ is the double-differential (that is, a distribution in particle kinetic energy T and solid angle direction $\vec{\Omega}$) particle flux distribution for particles of type j at position $\vec{r}$ in volume V, kinetic energy T, and solid angle direction $\vec{\Omega}$; $\mu_j(\vec{r}, T)$ is the total interaction coefficient for a particle of type j at position $\vec{r}$ with kinetic energy T; $S(\vec{r}, T, \vec{\Omega})$ represents particles born in volume V from some source; and $\mu_{k\to j}(\vec{r}, T, \vec{\Omega}; T', \vec{\Omega}')\mathrm{d}T'\mathrm{d}\Omega'$ is the interaction coefficient describing the probability per unit path length that a particle of type k, kinetic energy T, and solid angle direction $\vec{\Omega}$ interacts and produces a secondary particle of type j, kinetic energy in $\mathrm{d}T'$ about T' and solid angle direction in $\mathrm{d}\vec{\Omega}'$ about $\vec{\Omega}'$. There are some assumptions that are inherent in this formulation of the linearized Boltzmann transport equation: they are

1. the field is not self-interacting (this distinguishes the *linearized* Boltzmann transport equation from the general Boltzmann transport equation), and
2. particles are assumed to travel in *straight lines*.

Note that the number of source and sink terms varies with the specificity of the application.

For neutral particles, both of these assumptions generally hold true and Equation 2.13 is an appropriate description of the radiation field. The trajectories of neutrons are typically only affected by the short-range strong fundamental force (neutrons have mass and are affected by gravity, but gravity is so weak relative to the strong force that this force is neglected in most situations), so the straight-line assumption is valid. It is also exceedingly rare for two neutrons or two photons to interact with one another in non-laboratory settings.

Space radiation is primarily composed of high-energy charged particles (protons and heavier ions). In general, the assumptions above are *not* valid for charged particles. Charged particles constantly self-interact (via Coulombic forces) and they do not generally travel in straight lines in the presence of an electromagnetic field. Despite these limitations, approximate solutions are routinely employed while neglecting self-interactions and do not account for the presence of electromagnetic fields.

Space radiation transport calculations have been historically dominated by the application of deterministic methods to solve the Boltzmann transport equation. Deterministic heavy ion transport models, such as OLTARIS and HZETRN, are used by NASA for their analyses [32, 57]. HZETRN solves a form of the Boltzmann transport equation where an additional set of approximations are employed. They are:

1. excitation energies of atomic nuclei are small compared to the kinetic energy of incident ions,
2. the Continuous Slowing-Down Approximation (CSDA) accounts for all atomic collisions, and
3. there are no radiation sources within the volume of interest V; all particles enter V from the boundary ∂V.

When these approximations are applied to Equation 2.13, the meaning of $\mu_{k\to j}(\vec{r},T,\vec{\Omega};T',\vec{\Omega}')$ and $\mu_j(\vec{r},T)$ change from a combination of both atomic and nuclear collision cross sections, to only applying to nuclear collision cross sections, because an additional term involving the stopping power, $S_j(T)$, is included in the balance equation. The linearized Boltzmann transport equation, as applied in HZETRN, is given by

$$\begin{aligned}\vec{\Omega}\cdot\nabla\phi_j(\vec{r};T,\vec{\Omega}) - \frac{\partial}{\partial T}\left[S_j(T)\phi_j(\vec{r};T,\vec{\Omega})\right] + \mu_j(\vec{r},T)\phi_j(\vec{r};T,\vec{\Omega}) \\ = \sum_k \int_0^\infty \int_{4\pi} \mu_{k\to j}(\vec{r},T,\vec{\Omega};T',\vec{\Omega}')\phi_k(\vec{r},T',\vec{\Omega}')\mathrm{d}\Omega'\mathrm{d}T'.\end{aligned} \tag{2.14}$$

HZETRN provides rapid results at a single point for traditional, passive space radiation shielding applications due to its deterministic formulation. Unfortunately, active radiation shielding evaluation is incompatible with the linearized Boltzmann transport equation because, thus far, the Boltzmann equation variants that have been described implicitly assume that particle acceleration (a change in kinetic energy) only occurs during point-like, instantaneous particle interactions. Linearized Boltzmann transport equation variants only account for the strong nuclear force. The range of the strong force is very small, on the order

of 1×10^{-15} m. Active shielding leverages the electromagnetic force, which has an infinite range and can act on charged particles over longer timescales.

An attempt to expand the breadth of the Boltzmann transport equation, to allow for the consideration of forces beyond point-like interactions, is made in the following section, both to improve the reader's (and author's) understanding of the limitations of currently employed charged particle transport methods and to explore how active radiation shielding could be incorporated into efficient transport methods in the future. The adjoint form of the resulting equation—which would further enhance transport computational efficiency—is also developed. While the resulting equations are *not* directly employed in the present work beyond their derivations, it is sometimes useful to refer to them while discussing the results of transport codes ASPP and G4-ASPP, which in a sense attempt to *estimate* their solutions under various initial and boundary conditions.

2.5.1 Derivation of the Charged Particle Transport Equation

Let $N_j(t; \vec{r}, T, \vec{\Omega})\mathrm{d}\vec{r}\mathrm{d}T\mathrm{d}\vec{\Omega}$ be the number of particles of type j that exist in the phase space volume $\mathrm{d}\vec{r}\mathrm{d}T\mathrm{d}\vec{\Omega}$ at time t. All particles of type j within $\mathrm{d}\vec{r}\mathrm{d}T\mathrm{d}\vec{\Omega}$ have the same kinetic energy T, direction $\vec{\Omega}$, and position $\vec{r}$. Between interactions, each particle follows a trajectory $(\vec{r}(t), T(t), \vec{\Omega}(t))$ through phase space with phase space velocity $(\mathrm{d}\vec{r}/\mathrm{d}t, \mathrm{d}T/\mathrm{d}t, \mathrm{d}\vec{\Omega}/\mathrm{d}t)$. In the absence of all particle interactions (collisions with material, scatters, etc.), particles are neither created nor destroyed, so the number of particles of type j within any fixed region of phase space changes only through the net flow of particles across the boundary of that region. Applying conservation of particle number to an arbitrary region of phase space yields the phase space continuity equation,

$$\frac{\partial N_j}{\partial t} + \frac{\partial}{\partial \vec{r}} \cdot \left(N_j \frac{\mathrm{d}\vec{r}}{\mathrm{d}t} \right) + \frac{\partial}{\partial T} \left(N_j \frac{\mathrm{d}T}{\mathrm{d}t} \right) + \nabla_{S^2} \cdot \left(N_j \frac{\mathrm{d}\vec{\Omega}}{\mathrm{d}t} \right) = 0. \tag{2.15}$$

Because $|\vec{\Omega}| = 1$, the direction $\vec{\Omega}$ is confined to the unit sphere,

$$S^2 = \{(x, y, z) \in \mathbb{R}^3 | x^2 + y^2 + z^2 = 1\}. \tag{2.16}$$

Throughout this section, ∇_{S^2} denotes the *surface* gradient on the unit sphere and $\nabla_{S^2} \cdot$ denotes the corresponding *surface* divergence, rather than the conventional three-dimensional angular gradient $(\partial/\partial\vec{\Omega})$

and divergence $(\partial/\partial\vec{\Omega}\cdot)$. For a scalar function f and a vector field $\vec{W}$, the surface gradient is given by

$$\nabla_{S^2} f = \frac{\partial f}{\partial \vec{\Omega}} - \vec{\Omega}\left(\vec{\Omega}\cdot\frac{\partial f}{\partial \vec{\Omega}}\right), \tag{2.17}$$

and the surface divergence is given by

$$\nabla_{S^2}\cdot\vec{W} = \frac{\partial}{\partial \vec{\Omega}}\cdot\vec{W} - \vec{\Omega}\cdot\left(\vec{\Omega}\cdot\frac{\partial}{\partial \vec{\Omega}}\right)\vec{W}. \tag{2.18}$$

The conventional gradient and divergence operators account for variations in all three Cartesian directions, whereas the surface operators account only for variations tangent to the unit sphere, excluding the radial direction. Thus, only changes in particle direction contribute to the surface gradient and surface divergence. No component of $\nabla_{S^2} N_j$ may ever point parallel or anti-parallel to $\vec{\Omega}$, because this would imply that direction vectors can scale, which would contradict the requirement that solid angle direction vectors must be unit vectors. Equation 2.17 enforces this by construction: the surface gradient is always perpendicular to $\vec{\Omega}$,

$$\vec{\Omega}\cdot\nabla_{S^2} f = 0, \tag{2.19}$$

which is a useful identity used throughout this section.

Of course, the treatment of charged particle transport would be fairly mundane without the inclusion of any particle interactions. Including these interactions is as simple as replacing the right-hand side of Equation 2.15 with the rate of change in $N_j(t;\vec{r},T,\vec{\Omega})$ due to interactions,

$$\frac{\partial N_j}{\partial t} + \frac{\partial}{\partial \vec{r}}\cdot\left(N_j\frac{\mathrm{d}\vec{r}}{\mathrm{d}t}\right) + \frac{\partial}{\partial T}\left(N_j\frac{\mathrm{d}T}{\mathrm{d}t}\right) + \nabla_{S^2}\cdot\left(N_j\frac{\mathrm{d}\vec{\Omega}}{\mathrm{d}t}\right) = \sum_i\left(\frac{\partial N_j}{\partial t}\right)_i, \tag{2.20}$$

where $(\partial N_j/\partial t)_i$ can represent the time rate of change of the phase space distribution function due to any particle interaction type or transformation i, that is, collisions, scattering interactions, fragmentation, etc.

The phase space velocities in the left-hand side of Equation 2.20 follow from the equations of motion of a particle under an external force $\vec{F}$, and are derived in the following sections.

2.5.2 Energy Differential

The total kinetic energy of a particle is given by

$$T = \sqrt{(pc)^2 + (mc^2)^2} - mc^2, \tag{2.21}$$

where c is the speed of light, m is the particle rest mass, and p is the magnitude of the particle momentum. The derivative of T with respect to t is

$$\frac{\mathrm{d}T}{\mathrm{d}t} = \frac{pc^2}{\sqrt{(pc)^2 + (mc^2)^2}} \frac{\mathrm{d}p}{\mathrm{d}t}. \tag{2.22}$$

The derivative of the momentum magnitude with respect to time can be rewritten in terms of the external force $\vec{F}$ and the direction vector $\vec{\Omega}$ experienced by a particle using the following series of steps,

$$\frac{\mathrm{d}p}{\mathrm{d}t} = \frac{\mathrm{d}}{\mathrm{d}t}\left[\sqrt{p_x^2 + p_y^2 + p_z^2}\right], \tag{2.23}$$

$$\frac{\mathrm{d}p}{\mathrm{d}t} = \frac{p_x \frac{\mathrm{d}p_x}{\mathrm{d}t} + p_y \frac{\mathrm{d}p_y}{\mathrm{d}t} + p_z \frac{\mathrm{d}p_z}{\mathrm{d}t}}{\sqrt{p_x^2 + p_y^2 + p_z^2}}, \tag{2.24}$$

$$\frac{\mathrm{d}p}{\mathrm{d}t} = \frac{\vec{p} \cdot \vec{F}}{p}, \tag{2.25}$$

$$\frac{\mathrm{d}p}{\mathrm{d}t} = \vec{\Omega} \cdot \vec{F}. \tag{2.26}$$

It should be noted that $\vec{F} = \mathrm{d}\vec{p}/\mathrm{d}t$ and $\vec{\Omega} = \vec{p}/p$. Now the kinetic energy total differential can be written in terms of $\mathrm{d}t$,

$$\mathrm{d}T = \frac{pc^2}{\sqrt{(pc)^2 + (mc^2)^2}} (\vec{\Omega} \cdot \vec{F}) \mathrm{d}t. \tag{2.27}$$

This expression can also be written in terms of T instead of p using Equation 2.21,

$$\mathrm{d}T = \frac{c\sqrt{T(T + 2mc^2)}}{T + mc^2} (\vec{\Omega} \cdot \vec{F}) \mathrm{d}t. \tag{2.28}$$

Note that assuming classical mechanics,

$$T = \frac{p^2}{2m}, \tag{2.29}$$

yields

$$\mathrm{d}T = \frac{p}{m}(\vec{\Omega} \cdot \vec{F})\mathrm{d}t, \tag{2.30}$$

and

$$\mathrm{d}T = \sqrt{\frac{2T}{m}}(\vec{\Omega} \cdot \vec{F})\mathrm{d}t. \tag{2.31}$$

2.5.3 Direction Differential

The direction of travel of a particle is denoted with $\vec{\Omega}$, which can be equivalently expressed in multiple forms,

$$\vec{\Omega} = \frac{\vec{p}}{p} = \frac{\vec{v}}{v}. \tag{2.32}$$

The direction differential, $\mathrm{d}\vec{\Omega}$, is a vector differential quantity defined as

$$\mathrm{d}\vec{\Omega} = \langle \mathrm{d}\Omega_x, \mathrm{d}\Omega_y, \mathrm{d}\Omega_z \rangle, \tag{2.33}$$

where $\mathrm{d}\Omega_x$ refers to a differential change in the x-component of the particle's direction vector. $\mathrm{d}\Omega_y$ and $\mathrm{d}\Omega_z$ are defined similarly. $\mathrm{d}\vec{\Omega}$ may be related to $\mathrm{d}t$ by taking the derivative of both sides of Equation 2.32 with respect to time t,

$$\frac{\mathrm{d}\vec{\Omega}}{\mathrm{d}t} = \frac{\mathrm{d}}{\mathrm{d}t}\left[\frac{\vec{p}}{p}\right], \tag{2.34}$$

$$\frac{\mathrm{d}\vec{\Omega}}{\mathrm{d}t} = \frac{p\frac{\mathrm{d}\vec{p}}{\mathrm{d}t} - \vec{p}\frac{\mathrm{d}p}{\mathrm{d}t}}{p^2}, \tag{2.35}$$

$$\frac{\mathrm{d}\vec{\Omega}}{\mathrm{d}t} = \frac{\vec{F}}{p} - \frac{\vec{p}(\vec{p} \cdot \vec{F})}{p^3}, \tag{2.36}$$

$$\frac{\mathrm{d}\vec{\Omega}}{\mathrm{d}t} = \frac{\vec{F} - \vec{\Omega}(\vec{\Omega} \cdot \vec{F})}{p}. \tag{2.37}$$

The numerator is the component of the force perpendicular to the direction of travel. The parallel component of the force changes the momentum magnitude, and the perpendicular component changes the direction. Rewriting p in terms of kinetic energy T yields

$$\mathrm{d}\vec{\Omega} = c\frac{\vec{F} - \vec{\Omega}(\vec{\Omega} \cdot \vec{F})}{\sqrt{T(T + 2mc^2)}}\mathrm{d}t. \tag{2.38}$$

Note that under the assumptions of classical mechanics,

$$\mathrm{d}\vec{\Omega} = \frac{\vec{F} - \vec{\Omega}(\vec{\Omega} \cdot \vec{F})}{\sqrt{2mT}}\mathrm{d}t. \tag{2.39}$$

2.5.4 Position Differential

The position of a particle $\vec{r}$ is related to particle velocity $\vec{v}$ via

$$\frac{\mathrm{d}\vec{r}}{\mathrm{d}t} = \vec{v}, \tag{2.40}$$

which is trivially rewritten in terms of kinetic energy T

$$\mathrm{d}\vec{r} = \vec{\Omega}\frac{c\sqrt{T(T+2mc^2)}}{T+mc^2}\mathrm{d}t. \tag{2.41}$$

Under the assumptions of classical mechanics,

$$\mathrm{d}\vec{r} = \vec{\Omega}\sqrt{\frac{2T}{m}}\mathrm{d}t. \tag{2.42}$$

2.5.5 Force and Streaming Terms of the Charged Particle Transport Equation

The left-hand side of Equation 2.20 can be rewritten in a form that is more meaningful by substituting the phase space velocities developed in the last few sections,

$$\frac{\partial N_j}{\partial t} + \frac{\partial}{\partial \vec{r}} \cdot \left(\vec{\Omega} L N_j\right) + \frac{\partial}{\partial T}\left[(\vec{\Omega} \cdot \vec{F}) L N_j\right] + \nabla_{S^2} \cdot \left[\left[\vec{F} - \vec{\Omega}(\vec{\Omega} \cdot \vec{F})\right] K N_j\right] = \sum_i \left(\frac{\partial N_j}{\partial t}\right)_i, \tag{2.43}$$

where $L(T)$ and $K(T)$ represent coefficients that are functions of kinetic energy T,

$$L = L(T) = \begin{cases} c\frac{\sqrt{T(T+2mc^2)}}{T+mc^2}, v/c \sim 1 \\ \sqrt{\frac{2T}{m}}, v/c \ll 1, \end{cases} \tag{2.44}$$

$$K = K(T) = \begin{cases} \frac{c}{\sqrt{T(T+2mc^2)}}, v/c \sim 1 \\ \frac{1}{\sqrt{2mT}}, v/c \ll 1. \end{cases} \tag{2.45}$$

Note that L is the particle speed v and K is the reciprocal of the momentum magnitude, $1/p$.

At this point, it is possible to reformulate Equation 2.43 in the more familiar terms of the flux density distribution function $\phi_j = \phi_j(t; \vec{r}, T, \vec{\Omega})$. Let

$$\phi_j(t; \vec{r}, T, \vec{\Omega}) = L(T) N_j(t; \vec{r}, T, \vec{\Omega}), \tag{2.46}$$

where $L(T)$ is the particle speed. Because L and K depend only on T, and $\vec{\Omega}$ does not depend on $\vec{r}$, each term on the left-hand side of Equation 2.43 converts directly to the flux density distribution form,

$$\frac{\partial N_j}{\partial t} = \frac{1}{L}\frac{\partial \phi_j}{\partial t}, \tag{2.47}$$

$$\frac{\partial}{\partial \vec{r}} \cdot \left(\vec{\Omega} L N_j \right) = \vec{\Omega} \cdot \frac{\partial \phi_j}{\partial \vec{r}}, \tag{2.48}$$

$$\frac{\partial}{\partial T}\left[(\vec{\Omega} \cdot \vec{F}) L N_j \right] = \frac{\partial}{\partial T}\left[(\vec{\Omega} \cdot \vec{F}) \phi_j \right], \tag{2.49}$$

and

$$\nabla_{S^2} \cdot \left\{ \left[\vec{F} - \vec{\Omega}(\vec{\Omega} \cdot \vec{F}) \right] K N_j \right\} = \frac{K}{L} \nabla_{S^2} \cdot \left\{ \left[\vec{F} - \vec{\Omega}(\vec{\Omega} \cdot \vec{F}) \right] \phi_j \right\}. \tag{2.50}$$

The force and streaming terms of the charged particle transport equation can therefore be written in terms of ϕ_j and T,

$$\frac{\partial}{\partial T}\left[(\vec{\Omega} \cdot \vec{F}) \phi_j \right] + \frac{K}{L} \nabla_{S^2} \cdot \left\{ \left[\vec{F} - \vec{\Omega}(\vec{\Omega} \cdot \vec{F}) \right] \phi_j \right\} + \vec{\Omega} \cdot \frac{\partial \phi_j}{\partial \vec{r}} + \frac{1}{L}\frac{\partial \phi_j}{\partial t} = \sum_i \left(\frac{\partial N_j}{\partial t} \right)_i. \tag{2.51}$$

Equation 2.51 applies to any particle flux density distribution function, under the influence of any external force field $\vec{F}$. For charged particles, it is assumed that the only non-local forces of significance are electromagnetic forces (gravitational forces are ignored). Let $\vec{F}$ be the Lorentz force,

$$\vec{F} = q_j(\vec{E} + L\vec{\Omega} \times \vec{B}), \tag{2.52}$$

where q_j is the charge of particle type j, $\vec{E}$ is the electric field vector, and $\vec{B}$ is the magnetic field vector. Two vector properties simplify the substitution: (1) the dot product of two orthogonal vectors is zero, and (2) the cross product of two vectors is mutually orthogonal to both vectors, i.e., $\vec{\Omega} \cdot (\vec{\Omega} \times \vec{B}) = 0$. Thus $\vec{\Omega} \cdot \vec{F} = q_j(\vec{\Omega} \cdot \vec{E})$, which does not depend on T, and $\vec{F} - \vec{\Omega}(\vec{\Omega} \cdot \vec{F}) = q_j[\vec{E} - \vec{\Omega}(\vec{\Omega} \cdot \vec{E}) + L\vec{\Omega} \times \vec{B}]$. Substituting

Equation 2.52 into the left-hand side of Equation 2.51 yields

$$q_j(\vec{\Omega}\cdot\vec{E})\frac{\partial\phi_j}{\partial T}+q_j\frac{K}{L}\nabla_{S^2}\cdot\left\{\left[\vec{E}-\vec{\Omega}(\vec{\Omega}\cdot\vec{E})+L\vec{\Omega}\times\vec{B}\right]\phi_j\right\}+\vec{\Omega}\cdot\frac{\partial\phi_j}{\partial\vec{r}}+\frac{1}{L}\frac{\partial\phi_j}{\partial t}. \tag{2.53}$$

The angular term of Equation 2.53 may be expanded with the product rule,

$$\nabla_{S^2}\cdot\left(\vec{V}_\perp\phi_j\right)=\nabla_{S^2}\phi_j\cdot\vec{V}_\perp+\phi_j\nabla_{S^2}\cdot\vec{V}_\perp, \tag{2.54}$$

where

$$\vec{V}_\perp=\vec{E}_\perp+L\vec{\Omega}\times\vec{B} \tag{2.55}$$

is the part of $\vec{E}+L\vec{\Omega}\times\vec{B}$ perpendicular to $\vec{\Omega}$, and is therefore tangent to the unit sphere, and

$$\vec{E}_\perp=\vec{E}-\vec{\Omega}(\vec{\Omega}\cdot\vec{E}) \tag{2.56}$$

is the part of $\vec{E}$ perpendicular to $\vec{\Omega}$. In the first term of Equation 2.54, the surface gradient $\nabla_{S^2}\phi_j$ is also perpendicular to $\vec{\Omega}$ (Equation 2.19), so the component $-\vec{\Omega}(\vec{\Omega}\cdot\vec{E})$ contributes nothing,

$$\nabla_{S^2}\phi_j\cdot\vec{V}_\perp=\nabla_{S^2}\phi_j\cdot(\vec{E}+L\vec{\Omega}\times\vec{B}). \tag{2.57}$$

The second term requires the surface divergence of each part of $\vec{V}_\perp$. For $\vec{E}_\perp$, choose spherical coordinates with the polar axis aligned with $\vec{E}$, and let θ be the angle between $\vec{E}$ and $\vec{\Omega}$ and ψ the azimuthal angle. Then

$$E_{\perp,\theta}=-E\sin\theta \tag{2.58}$$

and

$$E_{\perp,\psi}=0, \tag{2.59}$$

where $E = |\vec{E}|$. Applying the standard spherical-coordinate divergence formula at unit radius gives

$$\begin{aligned}
\nabla_{S^2} \cdot \vec{E}_\perp &= \frac{1}{\sin\theta} \frac{\partial}{\partial\theta} \Big(\sin\theta \, E_{\perp,\theta} \Big) + \frac{1}{\sin\theta} \frac{\partial E_{\perp,\psi}}{\partial\psi} \\
&= -\frac{E}{\sin\theta} \frac{\partial}{\partial\theta} \sin^2\theta \\
&= -2E\cos\theta \\
&= -2(\vec{\Omega} \cdot \vec{E}).
\end{aligned} \tag{2.60}$$

For $\vec{\Omega} \times \vec{B}$, choose the polar axis aligned with $\vec{B}$ instead. Then $(\vec{\Omega} \times \vec{B})_\theta = 0$ and $(\vec{\Omega} \times \vec{B})_\psi = -B\sin\theta$, which does not depend on ψ, so both terms of the divergence formula vanish. Because L depends only on T, the same holds for $L\vec{\Omega} \times \vec{B}$. Together,

$$\nabla_{S^2} \cdot \vec{E}_\perp = -2(\vec{\Omega} \cdot \vec{E}) \tag{2.61}$$

and

$$\nabla_{S^2} \cdot \Big(\vec{\Omega} \times \vec{B} \Big) = 0, \tag{2.62}$$

so $\nabla_{S^2} \cdot \vec{V}_\perp = -2(\vec{\Omega} \cdot \vec{E})$.

The final, simplified form of the left-hand-side of the charged particle transport equation is

$$q_j \left[\frac{\partial \phi_j}{\partial T} - 2\frac{K}{L}\phi_j \right] (\vec{\Omega} \cdot \vec{E}) + q_j \frac{K}{L} \nabla_{S^2}\phi_j \cdot (\vec{E} + L\vec{\Omega} \times \vec{B}) + \vec{\Omega} \cdot \frac{\partial \phi_j}{\partial \vec{r}} + \frac{1}{L}\frac{\partial \phi_j}{\partial t}. \tag{2.63}$$

Each term has a direct physical interpretation. The first term is the rate at which the electric field moves particles through kinetic energy: $q_j(\vec{\Omega} \cdot \vec{E})$ is the work done on the particle per unit path length. The second term arises from the compression of phase space in direction. Along a collisionless trajectory, $\phi_j = vN_j$, so the flux density grows when the field accelerates the particle. In a uniform field, this is the narrowing of the solid angle occupied by a group of particles whose momentum perpendicular to the field is conserved while v grows. The coefficient $2K/L = 2/(pv)$ reduces to $1/T$ in the classical limit. The third term is the rotation of particle direction by the electric and magnetic fields, and the remaining terms are the familiar streaming and time-dependence terms.

2.5.6 Particle Phenomena Terms

The right-hand side of Equation 2.20 accounts for all particle "births" and "deaths" that occur within the differential phase space volume $\mathrm{d}\vec{r}\mathrm{d}T\mathrm{d}\vec{\Omega}$ alongside any additional source terms. Let the birth operator be denoted $\mathcal{B}[\phi_k(t;\vec{r},T,\vec{\Omega})]$. The birth operator accounts for particles of type j born in the differential phase space volume $\mathrm{d}\vec{r}\mathrm{d}T\mathrm{d}\vec{\Omega}$ at time t due to the flux density of particle type k and can be written as

$$\mathcal{B}[\phi_k] = \int_{4\pi}\int_{0}^{\infty} \mu_{k\to j}(\vec{r};T'\to T,\vec{\Omega}'\to\vec{\Omega})\phi_k(t;\vec{r},T',\vec{\Omega}')\mathrm{d}T'\mathrm{d}\vec{\Omega}', \tag{2.64}$$

where $\mu_{k\to j}(\vec{r};T'\to T,\vec{\Omega}'\to\vec{\Omega})$ is the double-differential macroscopic cross section for particles of type k, initial energy T', and initial direction $\vec{\Omega}'$ that ultimately interact within the phase space volume $\mathrm{d}\vec{r}\mathrm{d}T'\mathrm{d}\vec{\Omega}'$ to produce a particle of type j with energy T traveling in direction $\vec{\Omega}$. Let the death operator be denoted $\mathcal{D}[\phi_j(t;\vec{r},T,\vec{\Omega})]$. The death operator accounts for all particles of type j that exit the differential phase space volume $\mathrm{d}\vec{r}\mathrm{d}T\mathrm{d}\vec{\Omega}$ at time t and can be written as

$$\mathcal{D}[\phi_j] = \mu_j(\vec{r},T)\phi_j(t;\vec{r},T,\vec{\Omega}), \tag{2.65}$$

where $\mu_j(\vec{r},T)$ is the macroscopic cross section for all particles of type j with kinetic energy T that interact in the medium at $\vec{r}$ and result in the particle of type j leaving $\mathrm{d}\vec{r}\mathrm{d}T$ and/or becoming a particle that is *not* type j. The particle birth and death terms can be made unambiguous on a per application basis. The general expression for the right-hand side of Equation 2.20 can be written as

$$\sum_i \left(\frac{\partial N_j}{\partial t}\right)_i = \sum_k \mathcal{B}[\phi_k] - \mathcal{D}[\phi_j] + \dot{S}(t;\vec{r},T,\vec{\Omega}), \tag{2.66}$$

where $\dot{S}(t;\vec{r},T,\vec{\Omega})$ is an arbitrary source term for particles of type j.

2.5.7 Compilation of Terms

It is possible to rewrite Equation 2.63 and 2.66 in terms of the flux density for all particle types as a coupled system of partial differential equations,

$$q_j\left[\frac{\partial\phi_j}{\partial T} - 2\frac{K}{L}\phi_j\right](\vec{\Omega}\cdot\vec{E}) + q_j\frac{K}{L}\nabla_{S^2}\phi_j\cdot(\vec{E}+L\vec{\Omega}\times\vec{B}) + \vec{\Omega}\cdot\frac{\partial\phi_j}{\partial\vec{r}} + \frac{1}{L}\frac{\partial\phi_j}{\partial t} = \sum_k \mathcal{B}[\phi_k] - \mathcal{D}[\phi_j] + \dot{S}_j(t;\vec{r},T,\vec{\Omega}). \tag{2.67}$$

Equation 2.67 is evidently a more general form of the Boltzmann equations commonly found throughout textbooks on particle physics and nuclear engineering. If $q_j = 0$, then Equation 2.67 reduces to the same form as neutral particle (e.g., neutron and photon) transport equations. If the electromagnetic field is absent or negligible but $q_j \neq 0$, Equation 2.67 can still be expressed in a form that accounts for deceleration of charged particles in bulk material, like the transport equation that forms the backbone of HZETRN (Equation 3.1 from [58]).

2.5.8 Adjoint Charged Particle Transport Equation

An adjoint form of Equation 2.67 can be constructed when certain boundary conditions are applied. The adjoint equation will be derived term-by-term. Let an arbitrary operator be denoted $\mathcal{O}[\cdot]$. Let the inner product over the support $\vec{P} \in \mathcal{R}$ of arbitrary functions $\mathcal{O}[f]$ and $g^\dagger$ be

$$(g^\dagger, \mathcal{O}[f]) \equiv \int_{\mathcal{R}} g^\dagger(\vec{P}) \mathcal{O}[f(\vec{P})] \mathrm{d}\vec{P}. \tag{2.68}$$

The appropriate boundary conditions required to form an adjoint equation can be determined by equating this inner product to the (yet unknown) inner product of the adjoint operator $\mathcal{O}^\dagger$ acting on $g^\dagger$ and f,

$$(\mathcal{O}^\dagger[g^\dagger], f) \equiv \int_{\mathcal{R}} f(\vec{P}) \mathcal{O}^\dagger[g^\dagger(\vec{P})] \mathrm{d}\vec{P}, \tag{2.69}$$

plus the boundary condition terms, where physical properties of f and/or $g^\dagger$ can be reasonably selected to force these terms to zero. It is assumed that f and $g^\dagger$ are real-valued. The appropriate boundary conditions and adjoint operators for each term in Equation 2.67 are determined below.

Let $\phi_j^\dagger$ be the adjoint flux density distribution of particle type j. Express the first term of Equation 2.67 as

$$q_j(\vec{\Omega} \cdot \vec{E}) \frac{\partial \phi_j}{\partial T},$$

and the adjoint form is determined via the inner product

$$\int_0^\infty q_j(\vec{\Omega} \cdot \vec{E}) \frac{\partial \phi_j}{\partial T} \phi_j^\dagger \mathrm{d}T = \int_0^\infty q_j(\vec{\Omega} \cdot \vec{E}) \frac{\partial}{\partial T} \left(\phi_j^\dagger \phi_j \right) \mathrm{d}T - \int_0^\infty q_j(\vec{\Omega} \cdot \vec{E}) \frac{\partial \phi_j^\dagger}{\partial T} \phi_j \mathrm{d}T, \tag{2.70}$$

which trivially reduces to

$$\int_0^\infty \frac{\partial \phi_j}{\partial T}\phi_j^\dagger \mathrm{d}T = \left(\phi_j \phi_j^\dagger\right)\Big|_0^\infty + \int_0^\infty -\frac{\partial \phi_j^\dagger}{\partial T}\phi_j \mathrm{d}T, \tag{2.71}$$

because $\vec{\Omega}\cdot\vec{E}$ does not depend on T.

For the first term of Equation 2.67, the adjoint operator is $-q_j(\vec{\Omega}\cdot\vec{E})\partial/\partial T$ (where the original operator on ϕ_j was $q_j(\vec{\Omega}\cdot\vec{E})\partial/\partial T$) subject to the requirement that

$$\phi_j(T\to\infty)\phi_j^\dagger(T\to\infty) - \phi_j(T=0)\phi_j^\dagger(T=0) = 0, \tag{2.72}$$

which is easily accomplished with the reasonable assumptions that (1) the flux density is zero for particles with no kinetic energy, $\phi_j(T=0)=0$, and (2) there are no particles with infinite kinetic energy, $\phi_j(T\to\infty)=0$.

Express the second term of Equation 2.67 as

$$-2q_j\frac{K}{L}(\vec{\Omega}\cdot\vec{E})\phi_j,$$

and note that multiplication is a self-adjoint operator, so the adjoint operator for this term is simply $-2q_j(K/L)(\vec{\Omega}\cdot\vec{E})$ and subject to no additional requirements.

Express the third term of Equation 2.67 as

$$q_j\frac{K}{L}\nabla_{S^2}\phi_j\cdot\vec{V}_\perp,$$

where $\vec{V}_\perp$ is the component of $\vec{E}+L\vec{\Omega}\times\vec{B}$ tangent to the unit sphere (Equation 2.55). Only this component contributes, because the surface gradient $\nabla_{S^2}\phi_j$ is perpendicular to $\vec{\Omega}$ (Equation 2.19). The adjoint form of this term is determined via the inner product

$$\begin{aligned} q_j\frac{K}{L}\int_{4\pi}\nabla_{S^2}\phi_j\cdot\vec{V}_\perp\phi_j^\dagger\,\mathrm{d}\vec{\Omega} = {} & q_j\frac{K}{L}\int_{4\pi}\nabla_{S^2}\cdot\left(\phi_j\phi_j^\dagger\vec{V}_\perp\right)\mathrm{d}\vec{\Omega} \\ & - q_j\frac{K}{L}\int_{4\pi}\nabla_{S^2}\phi_j^\dagger\cdot\vec{V}_\perp\phi_j\,\mathrm{d}\vec{\Omega} \\ & - q_j\frac{K}{L}\int_{4\pi}\phi_j\phi_j^\dagger\nabla_{S^2}\cdot\vec{V}_\perp\,\mathrm{d}\vec{\Omega}. \end{aligned} \tag{2.73}$$

The Divergence Theorem on the unit sphere can be exploited to reduce the first term on the right-hand side,

$$q_j \frac{K}{L} \int_{4\pi} \nabla_{S^2} \cdot \left(\phi_j \phi_j^\dagger \vec{V}_\perp \right) \mathrm{d}\vec{\Omega} = q_j \frac{K}{L} \int_{\partial\Omega} \phi_j \phi_j^\dagger \vec{V}_\perp \cdot \hat{n}_\Omega \mathrm{d}(\partial\Omega), \tag{2.74}$$

where $\hat{n}_\Omega$ is the normal to the "boundary" $\partial\Omega$. Conceptually, the integral $\int_{4\pi} \mathrm{d}\vec{\Omega}$ represents the solid angle subtended by a sphere: 4π steradians. Equivalently, the solid angle direction can represent the set of all points constrained to the unit sphere. Topologically, the boundary of this set of points is *empty*, and because $\vec{V}_\perp$ is tangent to the sphere, the integral over this empty boundary is *zero*, leading to

$$q_j \frac{K}{L} \int_{4\pi} \nabla_{S^2} \cdot \left(\phi_j \phi_j^\dagger \vec{V}_\perp \right) \mathrm{d}\vec{\Omega} = 0. \tag{2.75}$$

The final term of Equation 2.73 does not vanish. Although $\vec{E}$ and $\vec{B}$ do not depend on particle direction, the tangential field $\vec{V}_\perp$ does, and by Equations 2.61 and 2.62,

$$\nabla_{S^2} \cdot \vec{V}_\perp = -2(\vec{\Omega} \cdot \vec{E}). \tag{2.76}$$

Thus, the adjoint form of the third term of Equation 2.67 is

$$-q_j \frac{K}{L} \nabla_{S^2} \phi_j^\dagger \cdot (\vec{E} + L\vec{\Omega} \times \vec{B}) + 2q_j \frac{K}{L} (\vec{\Omega} \cdot \vec{E}) \phi_j^\dagger,$$

and no additional boundary conditions are required. The multiplicative part of this result cancels the adjoint of the second term, so the second and third terms of Equation 2.67 are together skew-adjoint. This is expected: together, they are the surface divergence $q_j(K/L)\nabla_{S^2} \cdot (\vec{V}_\perp \phi_j)$ of Equation 2.53, and the adjoint of a divergence of a flux is the corresponding derivative along the flow. Express the fourth term of Equation 2.67 (the streaming term) as

$$\vec{\Omega} \cdot \frac{\partial \phi_j}{\partial \vec{r}},$$

and the adjoint form is determined via the inner product

$$\int_V \phi_j^\dagger \vec{\Omega} \cdot \frac{\partial \phi_j}{\partial \vec{r}} \mathrm{d}V = \int_V \frac{\partial}{\partial \vec{r}} \cdot \left(\vec{\Omega} \phi_j \phi_j^\dagger \right) \mathrm{d}V - \int_V \phi_j \vec{\Omega} \cdot \frac{\partial \phi_j^\dagger}{\partial \vec{r}} \mathrm{d}V. \tag{2.77}$$

Note that the Divergence Theorem states that the volume integral over the divergence of a vector field is

equal to the volume *boundary* integral over the vector field component parallel to the surface normal, i.e.,

$$\int_V \frac{\partial}{\partial \vec{r}} \cdot \left(\vec{\Omega} \phi_j \phi_j^\dagger \right) \mathrm{d}V = \int_{\partial V} \vec{\Omega} \cdot \hat{n} \phi_j \phi_j^\dagger \mathrm{d}(\partial V). \tag{2.78}$$

The adjoint operator for this term is $-\partial/\partial \vec{r} \cdot \vec{\Omega}$ subject to the requirement

$$\int_{\partial V} \vec{\Omega} \cdot \hat{n} \phi_j \phi_j^\dagger \mathrm{d}(\partial V) = 0, \tag{2.79}$$

which is accomplished by ensuring

$$\phi_j(\vec{r} \in \partial V) = 0, \vec{\Omega} \cdot \hat{n} < 0, \tag{2.80}$$

and

$$\phi_j^\dagger(\vec{r} \in \partial V) = 0, \vec{\Omega} \cdot \hat{n} \geq 0. \tag{2.81}$$

Equation 2.80 states that particles must not enter V (the problem domain or volume) from *outside* V. Equation 2.81 states that adjoint particles have *no importance* after they exit V. These two requirements are met by simply defining the problem domain V such that the external particle source is initialized within V, and adjoint particle detectors are defined within V (typically near the boundary ∂V).

The fifth term of Equation 2.67 is given by

$$\frac{1}{L} \frac{\partial \phi_j}{\partial t},$$

and this term is treated nearly identically to the first term to obtain the adjoint form (skew-adjoint),

$$-\frac{1}{L} \frac{\partial \phi_j^\dagger}{\partial t}, \tag{2.82}$$

where the additional requirement

$$\frac{1}{L} \left(\phi_j(t = t_1) \phi_j^\dagger(t = t_1) - \phi_j(t = t_0) \phi_j^\dagger(t = t_0) \right) = 0, \tag{2.83}$$

provided that the temporal boundary contribution vanishes. Specifically, integration by parts requires

$$\frac{\phi_j(t = t_1) \phi_j^\dagger(t = t_1) - \phi_j(t = t_0) \phi_j^\dagger(t = t_0)}{L} = 0. \tag{2.84}$$

This condition is satisfied by assuming that the forward flux distribution in the region of interest vanishes at both temporal boundaries, $\phi_j(t = t_0) = \phi_j(t = t_1) = 0$. This is practical for Monte Carlo simulations, where simulation times are finite.

The adjoint of the birth operator $\mathcal{B}[\phi_k]$ defined in Equation 2.64 follows from exchanging the roles of the incident and produced particles. In the adjoint equation for particle type j, the birth operator becomes

$$\mathcal{B}^\dagger[\phi_k^\dagger] = \int_{4\pi}\int_0^\infty \mu_{j\to k}(\vec{r}; T \to T', \vec{\Omega} \to \vec{\Omega}')\phi_k^\dagger(t; \vec{r}, T', \vec{\Omega}')\mathrm{d}T'\mathrm{d}\vec{\Omega}' : \tag{2.85}$$

the importance of a particle of type j at $(T, \vec{\Omega})$ includes the importance of every particle of type k it can produce.

The death operator $\mathcal{D}[f]$ defined in Equation 2.65 is self-adjoint, thus

$$\mathcal{D}^\dagger[f] = \mu_j(\vec{r}, T)f. \tag{2.86}$$

Recompiling all terms, the final adjoint form of the charged particle transport equation is

$$-q_j(\vec{\Omega}\cdot\vec{E})\frac{\partial\phi_j^\dagger}{\partial T} - q_j\frac{K}{L}\nabla_{S^2}\phi_j^\dagger\cdot(\vec{E} + L\vec{\Omega}\times\vec{B}) - \frac{\partial\phi_j^\dagger}{\partial\vec{r}}\cdot\vec{\Omega} - \frac{1}{L}\frac{\partial\phi_j^\dagger}{\partial t} = \sum_k \mathcal{B}^\dagger[\phi_k^\dagger] - \mathcal{D}^\dagger[\phi_j^\dagger] + \dot{S}^\dagger(t; \vec{r}, T, \vec{\Omega}), \tag{2.87}$$

where $\dot{S}^\dagger(t; \vec{r}, T, \vec{\Omega})$ is the adjoint source term, which is chosen by the user depending on the quantity of interest. Equation 2.87 is subject to the following boundary conditions:

- $\phi_j(T = 0) = 0$ (particles with zero energy do not contribute flux),
- $\phi_j(T \to \infty) = 0$ (particles cannot be infinitely energetic),
- $\phi_j(\vec{r} \in \partial V) = 0, \vec{\Omega}\cdot\hat{n} < 0$ (particles must not enter the problem domain V from outside V),
- $\phi_j^\dagger(\vec{r} \in \partial V) = 0, \vec{\Omega}\cdot\hat{n} \geq 0$ (adjoint particles have no importance after exiting V), and
- $\phi_j(t = t_0) = \phi_j(t = t_1) = 0$ (the initial and final flux distributions in the problem domain are zero).

The left-hand side of Equation 2.87 is $-1/L$ times the rate of change of $\phi_j^\dagger$ along a particle trajectory, with the phase space velocities of Equation 2.43. In the absence of interactions and adjoint sources, the adjoint flux is therefore constant along the same trajectories that carry the forward flux, which is the property exploited by the time-reversed particle propagation of ASPP.

Chapter 3

Expansion and Experimental Validation of the Active Shielding Particle Pusher Code

3.1 Active Shielding Particle Pusher Code

The ASPP code is a charged particle propagation software tool developed specifically for the rapid-prototyping of active radiation shielding configurations for spacecraft [24, 28]. ASPP was developed through a collaboration between NASA JSC, University of Utah, and Kansas State University (KSU). In ASPP, users can define electromagnetic fields by placing active shielding components around a "crew volume" that represents a generic volume within which it is assumed crew members are allowed to roam. Figure 3.1 broadly illustrates the placement of active shielding components in space and how the electromagnetic field influences the motion of charged particles.

Charged particle propagation in electromagnetic fields is governed by the Lorentz force, which is shown in Equation 2.52, but is more commonly written

$$\vec{F} = q(\vec{E} + \vec{v} \times \vec{B}). \tag{3.1}$$

Equation 3.1 governs charged particle transport in ASPP. Several particle propagation methods are imple-

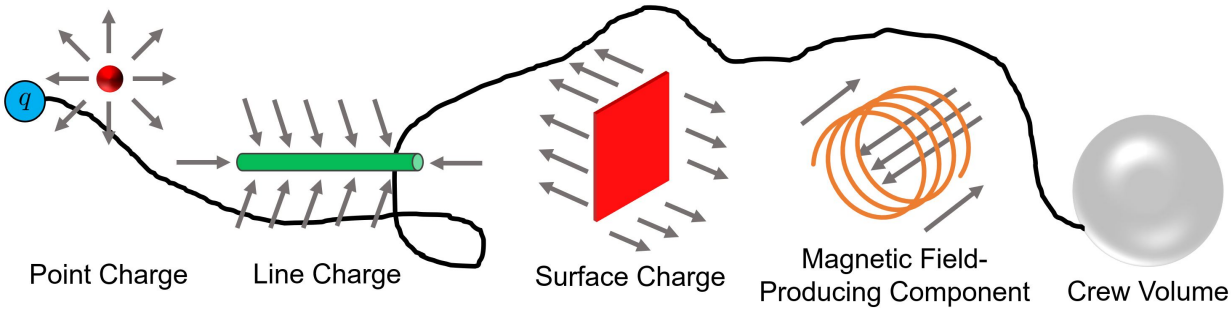


Figure 3.1: Conceptual view of a charge q propagating through the electromagnetic field generated by ASPP active shielding components.

mented in ASPP and are selectable by the user prior to simulation. These propagation methods will be discussed in detail in the next chapter. All propagation methods implemented in ASPP essentially work by incrementing time forward by a small Δt, recomputing the force imparted to the charged particle given its current position (and perhaps its previous position), and computing the next position of the particle at time $t + \Delta t$. All methods implemented in ASPP are constant time step methods.

3.2 Contributed Additions to ASPP

3.2.1 Boolean Geometry

ASPP's geometry system supports two operations: 1) enabling or disabling the field within a region, and 2) flagging particles that pass through a geometric object.

ASPP includes the ability to confine certain particle-affecting phenomena (electromagnetic fields) to regions of space bounded by simple and/or combinations of simple three-dimensional shapes (primitives) using constructive solid geometry, also known as Boolean geometry. Boolean geometry allows the program to "test" if a particle is on the "positive" or "negative" half-space of any mathematically defined boundary. Boundaries are defined via one or more functions $f_i(x, y, z, \vec{\zeta}) = 0$, where (x, y, z) describes the location of a particle and $\vec{\zeta}$ is a vector that contains all necessary parameters that define the bounding shape. For example, a general plane is defined via

$$f(x, y, z, \vec{\zeta}) = Ax + By + Cz + D = 0. \tag{3.2}$$

Here, $\vec{\zeta} = \langle A, B, C, D \rangle$ and defines the orientation and location of the plane. For a particle located at $(\tilde{x}, \tilde{y}, \tilde{z})$,

the particle is said to be in the positive half-space relative to the plane if $f(\tilde{x}, \tilde{y}, \tilde{z}, \vec{\zeta}) > 0$, in the negative half-space relative to the plane if $f(\tilde{x}, \tilde{y}, \tilde{z}, \vec{\zeta}) < 0$, and coincident with the plane if $f(\tilde{x}, \tilde{y}, \tilde{z}, \vec{\zeta}) = 0$. Similar logic can be applied to any well-defined surface embedded in three-dimensional space (useful for determining if a particle is inside or outside of a sphere). Table 3.1 describes the primitives available for use in ASPP.

Table 3.1: Geometric objects available for use in ASPP. Parameters in the $\vec{\zeta}$ column are specified by the user and x, y, z are the spatial variables.

Surface	ID	$f(x, y, z, \vec{\zeta}) = 0$	$\vec{\zeta}$
General plane	P	$Ax + By + Cz - D = 0$	A, B, C, D
Plane normal to x-axis	PX	$x - D = 0$	D
Plane normal to y-axis	PY	$y - D = 0$	D
Plane normal to z-axis	PZ	$z - D = 0$	D
General sphere	S	$(x - x_0)^2 + (y - y_0)^2 + (z - z_0)^2 - R^2 = 0$	x_0, y_0, z_0, R
Sphere centered on origin	SO	$x^2 + y^2 + z^2 - R^2 = 0$	R
Sphere centered x-axis	SX	$(x - x_0)^2 + y^2 + z^2 - R^2 = 0$	x_0, R
Sphere centered y-axis	SY	$x^2 + (y - y_0)^2 + z^2 - R^2 = 0$	y_0, R
Sphere centered z-axis	SZ	$x^2 + y^2 + (z - z_0)^2 - R^2 = 0$	z_0, R
Cylinder parallel to x-axis	C/X	$(y - y_0)^2 + (z - z_0)^2 - R^2 = 0$	y_0, z_0, R
Cylinder parallel to y-axis	C/Y	$(x - x_0)^2 + (z - z_0)^2 - R^2 = 0$	x_0, z_0, R
Cylinder parallel to z-axis	C/Z	$(x - x_0)^2 + (y - y_0)^2 - R^2 = 0$	x_0, y_0, R
Cylinder parallel to x-axis	CX	$y^2 + z^2 - R^2 = 0$	R
Cylinder parallel to y-axis	CY	$x^2 + z^2 - R^2 = 0$	R
Cylinder parallel to z-axis	CZ	$x^2 + y^2 - R^2 = 0$	R
Cone parallel to x-axis	K/X	$\sqrt{(y - y_0)^2 + (z - z_0)^2} + k\lvert t\rvert(x - x_0) = 0$	$x_0, y_0, z_0, \lvert t\rvert^2, k$
Cone parallel to y-axis	K/Y	$\sqrt{(x - x_0)^2 + (z - z_0)^2} + k\lvert t\rvert(y - y_0) = 0$	$x_0, y_0, z_0, \lvert t\rvert^2, k$
Cone parallel to z-axis	K/Z	$\sqrt{(x - x_0)^2 + (y - y_0)^2} + k\lvert t\rvert(z - z_0) = 0$	$x_0, y_0, z_0, \lvert t\rvert^2, k$
Cone along x-axis	KX	$\sqrt{y^2 + z^2} + k\lvert t\rvert(x - x_0) = 0$	$x_0, \lvert t\rvert^2, k$
Cone along y-axis	KY	$\sqrt{x^2 + z^2} + k\lvert t\rvert(y - y_0) = 0$	$y_0, \lvert t\rvert^2, k$
Cone along z-axis	KZ	$\sqrt{x^2 + y^2} + k\lvert t\rvert(z - z_0) = 0$	$z_0, \lvert t\rvert^2, k$

Beyond these primitives, it is also possible to construct more complicated boundaries via logical operations. If A and B represent two solids, and $f_A(x, y, z, \vec{\zeta}_A)$ and $f_B(x, y, z, \vec{\zeta}_B)$ are their respective boundary-defining functions, then a more complex shape can be constructed by applying *union*, *intersection*, and/or *difference* operations to construct a new boundary-defining function. To define the boundary associated with the union of A and B, $A \cup B$,

$$f_{A\cup B}(x, y, z, \vec{\zeta}_A, \vec{\zeta}_B) = \min\left(f_A(x, y, z, \vec{\zeta}_A), f_B(x, y, z, \vec{\zeta}_B)\right) = 0. \tag{3.3}$$

To define the boundary associated with the intersection of A and B, $A \cap B$,

$$f_{A\cap B}(x, y, z, \vec{\zeta}_A, \vec{\zeta}_B) = \max\left(f_A(x, y, z, \vec{\zeta}_A), f_B(x, y, z, \vec{\zeta}_B)\right) = 0. \tag{3.4}$$

To define the boundary associated with the set of points in A but not in B (a difference), $A \setminus B$,

$$f_{A\setminus B}(x, y, z, \vec{\zeta}_A, \vec{\zeta}_B) = \max\left(f_A(x, y, z, \vec{\zeta}_A), -f_B(x, y, z, \vec{\zeta}_B)\right) = 0. \tag{3.5}$$

3.2.2 Material Assignment

Boolean geometry allows all of three-dimensional space, $\mathbb{R}^3$, to be divided into well-defined subspaces $S_i \in \mathbb{R}^3$. In ASPP, each subspace can be assigned specific material properties by specifying five parameters. There are three "switches" that tell the program to either consider or ignore

1. the local electric field, $\vec{E}(\vec{r} \in S_i)$,
2. the local magnetic field, $\vec{B}(\vec{r} \in S_i)$, and
3. local stopping power effects, $\langle -\frac{\mathrm{d}T}{\mathrm{d}s}\rangle(\vec{r} \in S_i)$,

and two additional numerical parameters that define the mean proton-to-nucleon ratio of the material, $\langle Z/A\rangle$, and the mean effective excitation energy of the medium I_{eff}. One major limitation of ASPP is that nuclear interactions (i.e., non-Coulombic slowing down) between incident particles and materials are not considered.

3.2.3 Relativistic and Bethe-Bloch Deceleration

The mean energy loss per unit path length, or the mean stopping power, $\langle -\mathrm{d}T/\mathrm{d}s\rangle$, of a charged particle traversing some medium can be modeled by the Bethe-Bloch formula, which states

$$\left\langle -\frac{\mathrm{d}T}{\mathrm{d}s}\right\rangle = \left\langle \frac{Z}{A}\right\rangle \frac{N_a \rho z^2 e^4}{4\pi M_u \beta^2 m_e c^2 \epsilon_0^2}\left[\ln\left(\frac{2m_e c^2 \beta^2 \gamma^2}{I_{\text{eff}}}\right) - \beta^2 + \frac{f(\gamma)}{2} - \frac{C(\gamma)}{Z} - \frac{\delta_F}{2} + \Delta L^{\text{LS}} + \Delta L^{\text{B}}(a)\right], \tag{3.6}$$

where N_a is Avogadro's number, $\langle Z/A\rangle$ is the mean proton-to-nucleon ratio of the medium, $M_u = 1\,\mathrm{g\,mol^{-1}}$ (the atomic mass constant), ρ is the density of the medium, ze is the charge of the particle, e is the elementary charge, $\beta = v/c$, where v is the particle speed and c is the speed of light, γ is the Lorentz factor, m_e is the mass of an electron, ϵ_0 is the vacuum permittivity, and I_{eff} is the mean effective excitation energy of the medium [59, 60]. While the terms in black in Equation 3.6 represent the *uncorrected* Bethe-Bloch equation, the black terms combined with the red terms represent the *corrected* Bethe-Bloch equation. $f(\gamma)$ represents

a relativistic collision-kinematic contribution to the stopping power expression and is given by

$$f(\gamma) = \ln(R) + \left[\frac{m_e}{m}\gamma\beta^2 R\right]^2, \tag{3.7}$$

where m is the mass of the charged particle traversing the medium and R is given by

$$R = \left[1 + \left(\frac{m_e}{m}\right)^2 + 2\gamma\frac{m_e}{m}\right]^{-1}, \tag{3.8}$$

and is only valid for $m > m_e$ [60]. $C(\gamma)/Z$ is the shell correction associated with the medium which accounts for the fact that atomic electrons are bound as opposed to free, which the uncorrected Bethe-Bloch assumes. δ_F is the density-effect correction, which accounts for polarization of the medium by the electric field of the traversing charged particle and the resulting reduction in energy transfer from distant collisions. ΔL^{LS} is the Lindhard-Sørensen correction, which accounts for the modification of the charged particle's electromagnetic field due to the finite size and quantum-mechanical structure of the target atoms. $\Delta L^{\mathrm{B}}(a)$ is the Barkas correction, which accounts for higher-order effects in the projectile-target interaction that depend on the sign of the projectile charge, where a is the cutoff impact parameter [60].

$\langle Z/A \rangle$ for a homogeneous mixture or compound is computed via

$$\left\langle \frac{Z}{A} \right\rangle = \sum_i w_i \frac{Z_i}{A_i}, \tag{3.9}$$

where w_i, Z_i, and A_i are the weight fraction, atomic number, and mass number of constituent atom i, respectively. I_{eff} for a homogeneous mixture or compound is given by

$$I_{\mathrm{eff}} = \exp\left(\left\langle \frac{Z}{A} \right\rangle^{-1} \sum_i w_i \left(\frac{Z_i}{A_i}\right) \ln\left(f_i I_i\right)\right), \tag{3.10}$$

where I_i is the mean excitation energy for constituent atom i, $f_i = 1.13$ if atom i is part of a compound, and $f_i = 1$ otherwise [61].

The energy loss mechanism is implemented into ASPP as part of the acceleration term in the velocity-Verlet propagation method [62, 63]. The approximate acceleration attributable to the mean stopping power is derived below. Let s be a variable distance, T the kinetic energy of the particle, and m_0 the rest mass of

the particle. The kinetic energy T is re-expressed in terms of γ, m_0, and c,

$$\left\langle -\frac{\mathrm{d}T}{\mathrm{d}s}\right\rangle \approx -\frac{\mathrm{d}T}{\mathrm{d}s} = -\frac{\mathrm{d}}{\mathrm{d}s}\Big((\gamma-1)m_0c^2\Big) = -m_0c^2\frac{\mathrm{d}\gamma}{\mathrm{d}s}. \tag{3.11}$$

Multiply both sides by $v = \mathrm{d}s/\mathrm{d}t$ to obtain a $\mathrm{d}\gamma/\mathrm{d}t$ term,

$$\left\langle -\frac{\mathrm{d}T}{\mathrm{d}s}\right\rangle \frac{\mathrm{d}s}{\mathrm{d}t} = -m_0c^2\frac{\mathrm{d}s}{\mathrm{d}t}\frac{\mathrm{d}\gamma}{\mathrm{d}s} = -m_0c^2\frac{\mathrm{d}\gamma}{\mathrm{d}t}. \tag{3.12}$$

Rewrite, isolating $\langle -\mathrm{d}T/\mathrm{d}s\rangle$ and replacing $\mathrm{d}s/\mathrm{d}t$ with v,

$$\left\langle -\frac{\mathrm{d}T}{\mathrm{d}s}\right\rangle = -\frac{m_0c^2}{v}\frac{\mathrm{d}\gamma}{\mathrm{d}t}. \tag{3.13}$$

Note that

$$\frac{\mathrm{d}\gamma}{\mathrm{d}t} = \frac{v}{c^2}\left(1-\frac{v^2}{c^2}\right)^{-3/2}\frac{\mathrm{d}v}{\mathrm{d}t}, \tag{3.14}$$

so

$$\left\langle -\frac{\mathrm{d}T}{\mathrm{d}s}\right\rangle = -m_0\left(1-\frac{v^2}{c^2}\right)^{-3/2}\frac{\mathrm{d}v}{\mathrm{d}t}. \tag{3.15}$$

Equation 3.15 relates the derivative of the speed, dv/dt, to the mean stopping power. From here, the acceleration term can be derived. First, assume that the charged particle acceleration vector $d\vec{v}/dt$ is exactly anti-parallel to the velocity vector $\vec{v}$ when the particle of interest is in a non-vacuum medium, $\vec{v} \parallel -d\vec{v}/dt$. As a result, the direction vector $\vec{\Omega}$ is equivalently defined by two distinct quantities,

$$\vec{\Omega} = \frac{\vec{v}}{v} = -\frac{\frac{\mathrm{d}\vec{v}}{\mathrm{d}t}}{\left|\frac{\mathrm{d}\vec{v}}{\mathrm{d}t}\right|}. \tag{3.16}$$

Note that

$$\frac{\mathrm{d}v}{\mathrm{d}t} = \frac{\vec{v}}{v}\cdot\frac{\mathrm{d}\vec{v}}{\mathrm{d}t} = \vec{\Omega}\cdot\frac{\mathrm{d}\vec{v}}{\mathrm{d}t} = -\frac{\frac{\mathrm{d}\vec{v}}{\mathrm{d}t}\cdot\frac{\mathrm{d}\vec{v}}{\mathrm{d}t}}{\left|\frac{\mathrm{d}\vec{v}}{\mathrm{d}t}\right|} = -\frac{\left|\frac{\mathrm{d}\vec{v}}{\mathrm{d}t}\right|^2}{\left|\frac{\mathrm{d}\vec{v}}{\mathrm{d}t}\right|} = -\left|\frac{\mathrm{d}\vec{v}}{\mathrm{d}t}\right|. \tag{3.17}$$

The acceleration vector can now be expressed in terms of the derivative of the speed,

$$\frac{\mathrm{d}\vec{v}}{\mathrm{d}t} = \frac{\vec{v}}{v}\frac{\mathrm{d}v}{\mathrm{d}t}, \tag{3.18}$$

and ultimately, the mean stopping power,

$$\frac{\mathrm{d}\vec{v}}{\mathrm{d}t} = -\frac{\vec{\Omega}}{\gamma^3 m_0}\left\langle -\frac{\mathrm{d}T}{\mathrm{d}s}\right\rangle. \tag{3.19}$$

The expression for acceleration shown in Equation 3.19 was added to ASPP's existing acceleration term to form

$$\frac{\mathrm{d}\vec{v}}{\mathrm{d}t} = \frac{q}{\gamma m_0}\left[\vec{E} + \vec{v}\times\vec{B} - \frac{\vec{v}}{c^2}(\vec{E}\cdot\vec{v}) - \frac{\vec{\Omega}}{\gamma^2 q}\left\langle -\frac{\mathrm{d}T}{\mathrm{d}s}\right\rangle\right]. \tag{3.20}$$

$\langle -\mathrm{d}T/\mathrm{d}s\rangle$ is computed each time the electromagnetic field vectors ($\vec{E}$ and $\vec{B}$) are computed. Note that $\langle -\mathrm{d}T/\mathrm{d}s\rangle = 0$ in a vacuum. There is an argument to be made that the third and fourth terms of Eq. 3.20 describe the same phenomenon at different scales: the third term describe deceleration due to an external electric field, whereas the fourth term describes deceleration due to the accumulation of electrostatic forces imparted on a particle as it traverses the relatively small space between atoms in bulk material. Finally, note that ASPP implements the *uncorrected* form of the Bethe-Bloch equation (Equation 3.6) to compute $\langle -\mathrm{d}T/\mathrm{d}s\rangle$.

3.2.4 Energy Deposition Tally

An energy deposition tallying feature was added to ASPP. The user can specify a cell in which to estimate the mean energy deposited per source particle via charged particle deceleration along with its associated relative error. The mean energy deposited per source particle in some cell is given by

$$\bar{\mathcal{E}} = \frac{S_1}{N}, \tag{3.21}$$

and the associated relative error is given by

$$\tilde{R}(\bar{\mathcal{E}}) = \frac{1}{S_1}\sqrt{\frac{NS_2 - S_1^2}{N-1}}, \tag{3.22}$$

where N is the total number of source particles, and S_1 and S_2 are standard accumulator functions,

$$S_1 = \sum_i^N W_i \mathcal{E}_i, \tag{3.23}$$

and

$$S_2 = \sum_i^N (W_i \mathcal{E}_i)^2. \tag{3.24}$$

W_i is the weight of particle i.

3.2.5 Time-Reversed Particle Propagation

To evaluate the shielding performance of an active shielding configuration using the 'forward' transport mode in ASPP, an isotropic particle field with kinetic energy T is generated within a sphere of radius R_L that fully encloses all relevant components, including the crew volume and shielding elements, following the method of [64]. Particles entering the crew volume—typically a 5 m radius sphere—are tallied to estimate flux and related quantities. This approach works well for "grid-search" optimization but is computationally expensive. The cost grows quickly with complexity because the number of variables increases the spacing between grid points and the total points required, reflecting the *curse of dimensionality*.

A more efficient active shielding configuration optimization approach is desired. ASPP's 'adjoint' transport mode was added to identify weaknesses in candidate active shielding configurations. The implementation essentially relies upon time-reversed particle propagation. N "impact" points are evenly distributed over the surface of the crew volume using the method from [65]. At each impact point, M particles are initialized with directions $\vec{\Omega}$ uniformly distributed over the inward-pointing subspace (i.e., directions for which $\vec{\Omega} \cdot \hat{n} < 0$, where $\hat{n}$ is the normal to the crew volume boundary at position $\vec{r}$). Each particle is also assigned an impact kinetic energy T_0 by the user, representing the maximum energy that a particle could impart to the crew volume in a forward simulation (ASPP currently does not account for nuclear interactions in bulk media). Particles are then propagated backward in time using the time-reversed Velocity-Verlet algorithm. The simulation ends when particles exit the problem domain, which by default is a sphere of radius $R = \sqrt{2}R_L + 1\,\mathrm{m}$ centered at the origin. The positions and kinetic energies of all exiting particles are recorded.

The outputs of an adjoint ASPP simulation indicate the original positions and initial kinetic energies of particles that ultimately impact the crew volume. Specifically, the exit positions correspond to locations from which impacting particles originate, and the exit kinetic energies indicate the initial kinetic energy T required for a particle to reach the crew volume with energy T_0. These results can be used to guide the placement of additional shielding to either a) reduce the flux from specific directions or b) increase the initial

energy required for particles to reach the crew volume with energy T_0.

Figures 3.2 and 3.3 show example results from the "orthogonal" configuration family described in [26, 27]. This configuration consists of 18 positively charged square plates and 8 negatively charged rods. Two different impact energies T_0 are considered. The figures depict the positions and kinetic energies of protons exiting the problem domain at the end of the simulation, with the problem-domain radius set to 100 m in each case.

In Figure 3.2, the particle distribution reveals clear "holes" corresponding to the arrangement of the active shielding configuration. The stacks of positively charged plates create regions where particles of a given initial energy do not penetrate. The negatively charged rods tend to focus particles toward the corners of the configuration. Particles impacting the crew volume with $T_0 = 10\,\text{MeV}$ are more likely to reach it if their initial trajectories pass through the gaps in the shielding. This suggests that adding positive charges in these locations could further improve protection.

Figure 3.3 shows the distribution for a higher T_0. The initial position distribution is nearly isotropic, indicating that the configuration is less effective at deflecting higher-energy particles than lower-energy ones. In both cases, the differences between the average initial kinetic energy T and the impact energy T_0 is approximately 15 MeV. This implies that an average potential-energy barrier of about 15 MeV must be overcome for particles to reach the crew volume for this particular shielding configuration.

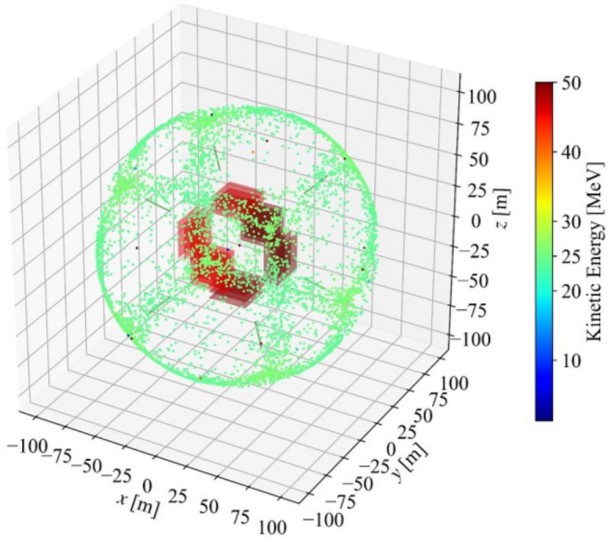


Figure 3.2: Adjoint ASPP simulation results for protons with $T_0 = 10\,\text{MeV}$; the average initial kinetic energy required to reach the crew volume is $T = 25.0\,\text{MeV}$ (from [66]).

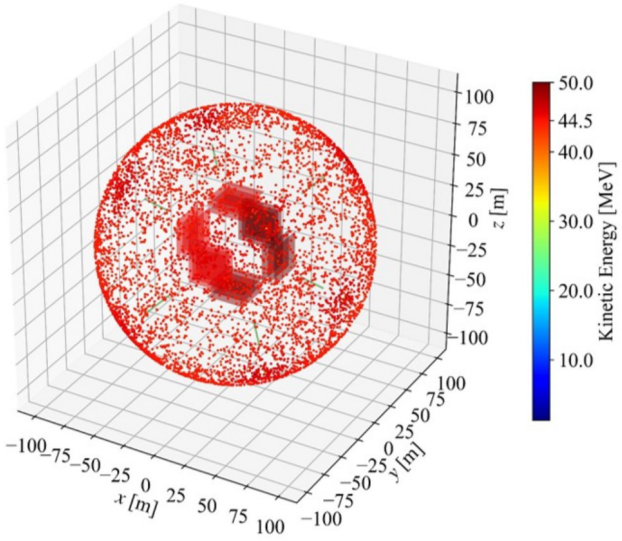


Figure 3.3: Adjoint ASPP simulation results for protons with $T_0 = 30\,\text{MeV}$; the average initial kinetic energy required to reach the crew volume is $T = 44.5\,\text{MeV}$ (from [66]).

3.2.6 Active Shielding Components

3.2.6.1 Point Charge Element

The electric field at $\vec{r}$ due to a point charge Q located at $\vec{r}_0$ is given by

$$\vec{E}(\vec{r}) = \frac{Q}{4\pi\epsilon_0}\frac{\vec{r}-\vec{r}_0}{|\vec{r}-\vec{r}_0|^3}, \tag{3.25}$$

where ϵ_0 is the permittivity of free space. The electric potential at $\vec{r}$ is given by

$$V(\vec{r}) = \frac{Q}{4\pi\epsilon_0|\vec{r}-\vec{r}_0|}. \tag{3.26}$$

3.2.6.2 Line Segment Charge Element

The electric field at $\vec{r}$ due to a finite line charge of constant linear charge density λ with endpoints $\vec{r}_1$ and $\vec{r}_2$ is given by

$$\vec{E}(\vec{r}) = \frac{\lambda}{2\pi\epsilon_0}\left(\frac{|\vec{r}_2-\vec{r}_1|}{(|\vec{r}-\vec{r}_1|+|\vec{r}-\vec{r}_2|)^2-|\vec{r}_2-\vec{r}_1|^2}\right)\left(\frac{\vec{r}-\vec{r}_1}{|\vec{r}-\vec{r}_1|}+\frac{\vec{r}-\vec{r}_2}{|\vec{r}-\vec{r}_2|}\right). \tag{3.27}$$

Note that the potential field is generally given by

$$V(\vec{r}) = -\int_{\infty}^{\vec{r}} \vec{E}(\vec{\ell})\cdot \mathrm{d}\vec{\ell}. \tag{3.28}$$

This path integral represents the work per unit charge required to bring a positive test charge q from infinity to $\vec{r}$. Note that the integral is also path independent because $\vec{E}(\vec{r})$ is a conservative field. For convenience, we select the test charge path to be a straight line from infinity to $\vec{r}$, i.e., $\vec{\ell}(t) = \vec{r}_1 + t(\vec{r} - \vec{r}_1)$ where $t \in [1, \infty)$. As a result of this selection, $\mathrm{d}\vec{\ell} = (\vec{r} - \vec{r}_1)\mathrm{d}t$ and $\vec{\ell}(1) = \vec{r}$. Substituting $\vec{\ell}(t)$ and Equation 3.27 into Equation 3.28 eventually yields

$$V(\vec{r}) = -\int_{\infty}^{1} \frac{\lambda|\vec{r}_2 - \vec{r}_1|}{2\pi\epsilon_0} \frac{|\vec{r} - \vec{r}_1|\left(1 + \frac{t|\vec{r} - \vec{r}_1| + \frac{(\vec{r}_1 - \vec{r}_2)\cdot(\vec{r} - \vec{r}_1)}{|\vec{r} - \vec{r}_1|}}{|\vec{\ell}(t) - \vec{r}_2|}\right)}{(|\vec{\ell}(t) - \vec{r}_1| + |\vec{\ell}(t) - \vec{r}_2|)^2 - |\vec{r}_2 - \vec{r}_1|^2}\mathrm{d}t. \tag{3.29}$$

Note that

$$\frac{\mathrm{d}}{\mathrm{d}t}\left(|\vec{\ell}(t) - \vec{r}_1| + |\vec{\ell}(t) - \vec{r}_2|\right) = |\vec{r} - \vec{r}_1|\left(1 + \frac{t|\vec{r} - \vec{r}_1| + \frac{(\vec{r}_1 - \vec{r}_2)\cdot(\vec{r} - \vec{r}_1)}{|\vec{r} - \vec{r}_1|}}{|\vec{\ell}(t) - \vec{r}_2|}\right). \tag{3.30}$$

We can exploit this to obtain a standard integration form that can be simplified. Let $k(t) = |\vec{\ell}(t) - \vec{r}_1| + |\vec{\ell}(t) - \vec{r}_2|$ and substitute again,

$$V(\vec{r}) = -\frac{\lambda|\vec{r}_2 - \vec{r}_1|}{2\pi\epsilon_0}\int_{\infty}^{1} \frac{1}{[k(t)]^2 - |\vec{r}_2 - \vec{r}_1|^2}\frac{\mathrm{d}k}{\mathrm{d}t}\mathrm{d}t = -\frac{\lambda|\vec{r}_2 - \vec{r}_1|}{2\pi\epsilon_0}\int_{\infty}^{k(1)} \frac{\mathrm{d}k}{k^2 - |\vec{r}_2 - \vec{r}_1|^2}. \tag{3.31}$$

Evaluate the integral.

$$V(\vec{r}) = -\frac{\lambda}{4\pi\epsilon_0}\left[\ln\left(\frac{k - |\vec{r}_2 - \vec{r}_1|}{k + |\vec{r}_2 - \vec{r}_1|}\right)\right]_{\infty}^{k(1)} = -\frac{\lambda}{4\pi\epsilon_0}\ln\left(\frac{k(1) - |\vec{r}_2 - \vec{r}_1|}{k(1) + |\vec{r}_2 - \vec{r}_1|}\right). \tag{3.32}$$

Note that $k(1) = |\vec{r} - \vec{r}_1| + |\vec{r} - \vec{r}_2|$ and substitute to obtain the electric potential at $\vec{r}$,

$$V(\vec{r}) = \frac{\lambda}{4\pi\epsilon_0}\ln\left(\frac{|\vec{r} - \vec{r}_1| + |\vec{r} - \vec{r}_2| + |\vec{r}_2 - \vec{r}_1|}{|\vec{r} - \vec{r}_1| + |\vec{r} - \vec{r}_2| - |\vec{r}_2 - \vec{r}_1|}\right). \tag{3.33}$$

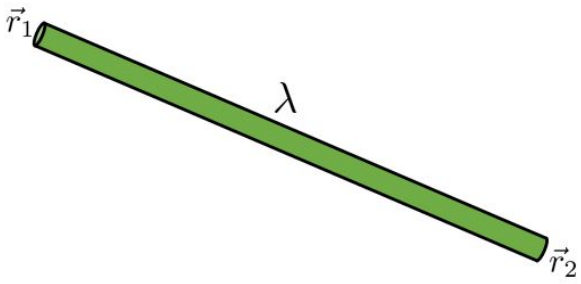


Figure 3.4: Visualization of a uniformly charged line of linear charge density λ and endpoints $\vec{r}_1$ and $\vec{r}_2$.

3.2.6.3 Rectangular Charge Element

The electric field due to a rectangular sheet of constant surface charge density σ is given by a considerably more complicated set of equations. Let the midpoint of the rectangular sheet be $\vec{r}_0$, let the unit normal vector be $\hat{w}$, define the unit "orientation vector" $\hat{u}$ and dimensions $[\Delta u \times \Delta v]$ such that Δu is the length of the edge parallel to $\hat{u}$ and Δv is the length of the edge parallel to $\hat{v} = \hat{w} \times \hat{u}$. Figure 3.5 defines these parameters visually. For additional convenience, define the in-plane coordinates $u = (\vec{r} - \vec{r}_0) \cdot \hat{u}$, $v = (\vec{r} - \vec{r}_0) \cdot \hat{v}$ and $w = (\vec{r} - \vec{r}_0) \cdot \hat{w}$. The electric field at $\vec{r}$ is given by

$$\vec{E}(\vec{r}) = \begin{bmatrix} E_x(\vec{r}) \\ E_y(\vec{r}) \\ E_z(\vec{r}) \end{bmatrix} = \begin{bmatrix} \hat{u} & \hat{v} & \hat{w} \end{bmatrix} \begin{bmatrix} E_u(\vec{r}) \\ E_v(\vec{r}) \\ E_w(\vec{r}) \end{bmatrix}, \tag{3.34}$$

where

$$\begin{bmatrix} \hat{u} & \hat{v} & \hat{w} \end{bmatrix} = \begin{bmatrix} u_x/u & v_x/v & w_x/w \\ u_y/u & v_y/v & w_y/w \\ u_z/u & v_z/v & w_z/w \end{bmatrix}, \tag{3.35}$$

$$\begin{bmatrix} E_u(\vec{r}) \\ E_v(\vec{r}) \\ E_w(\vec{r}) \end{bmatrix} = \frac{\sigma}{4\pi\epsilon_0} \begin{bmatrix} \sum_{i\in\{+,-\}} \sum_{j\in\{+,-\}} \operatorname{sgn}(i) \operatorname{sgn}(j) \ln(\eta_{ij} - \beta_j) \\ \sum_{i\in\{+,-\}} \sum_{j\in\{+,-\}} \operatorname{sgn}(i) \operatorname{sgn}(j) \ln(\eta_{ij} - \alpha_i) \\ \sum_{i\in\{+,-\}} \sum_{j\in\{+,-\}} \operatorname{sgn}(i) \operatorname{sgn}(j) \arctan\left(\frac{\alpha_i \beta_j}{2w\eta_{ij}}\right) \end{bmatrix}. \tag{3.36}$$

The various α, β, and η parameters are simply placeholders for

$$\begin{bmatrix} \alpha_- \\ \alpha_+ \\ \beta_- \\ \beta_+ \end{bmatrix} = \begin{bmatrix} 2u - \Delta u \\ 2u + \Delta u \\ 2v - \Delta v \\ 2v + \Delta v \end{bmatrix}, \tag{3.37}$$

and

$$\begin{bmatrix} \eta_{--} \\ \eta_{+-} \\ \eta_{-+} \\ \eta_{++} \end{bmatrix} = \begin{bmatrix} \sqrt{\alpha_-^2 + \beta_-^2 + 4w^2} \\ \sqrt{\alpha_+^2 + \beta_-^2 + 4w^2} \\ \sqrt{\alpha_-^2 + \beta_+^2 + 4w^2} \\ \sqrt{\alpha_+^2 + \beta_+^2 + 4w^2} \end{bmatrix}. \tag{3.38}$$

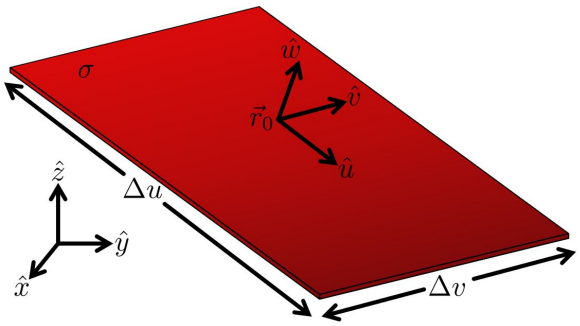


Figure 3.5: Geometric parameterization of rectangular charge sheet with constant surface charge density σ.

The potential field is determined similarly to the finite line charge. Let $\vec{\ell}(t) = \vec{r}_0 + t(\vec{r} - \vec{r}_0)$ where $t \in [1, \infty)$. Eventually, one obtains

$$V(\vec{r}) = \frac{\sigma}{8\pi\epsilon_0} \sum_{i\in\{+,-\}} \sum_{j\in\{+,-\}} \left\{ \operatorname{sgn}(i)\operatorname{sgn}(j) \left[\alpha_i \operatorname{arcsinh}\left(\frac{\beta_j}{\sqrt{\alpha_i^2 + 4w^2}} \right) + \beta_j \operatorname{arcsinh}\left(\frac{\alpha_i}{\sqrt{\beta_j^2 + 4w^2}} \right) - 2w \arctan\left(\frac{\alpha_i \beta_j}{2\eta_{ij} w} \right) \right] \right\}. \quad (3.39)$$

3.2.6.4 Rectangular Prism Bar Magnet

The magnetic field at $\vec{r}$ due to a bar magnet in the form of rectangular prism of constant magnetization density $\vec{M}$, with dimensions $[\Delta u \times \Delta v \times \Delta w]$, a midpoint located at $\vec{r}_0$, is given by

$$\vec{B} = \begin{bmatrix} B_x(\vec{r}) \\ B_y(\vec{r}) \\ B_z(\vec{r}) \end{bmatrix} = \begin{bmatrix} \hat{u} & \hat{v} & \hat{w} \end{bmatrix} \begin{bmatrix} B_u(\vec{r}) \\ B_v(\vec{r}) \\ B_w(\vec{r}) \end{bmatrix}, \quad (3.40)$$

where

$$\begin{bmatrix} B_u(\vec{r}) \\ B_v(\vec{r}) \\ B_w(\vec{r}) \end{bmatrix} = \frac{\mu_0 |\vec{M}|}{4\pi} \begin{bmatrix} -\sum_{n=0}^{7} F_1\left((-1)^{\lfloor n/4 \rfloor} \tau_u, (-1)^{\lfloor n/2 \rfloor} \tau_v, (-1)^n \tau_w \right) \\ \ln\left(\frac{F_2(-\tau_u,\tau_v,\tau_w) F_2(\tau_u,\tau_v,\tau_w)}{F_2(-\tau_u,\tau_v,\tau_w) F_2(\tau_u,-\tau_v,\tau_w)} \right) \\ \ln\left(\frac{F_2(-\tau_u,-\tau_w,\tau_v) F_2(\tau_u,\tau_w,\tau_v)}{F_2(-\tau_u,\tau_w,\tau_v) F_2(\tau_u,-\tau_w,\tau_v)} \right) \end{bmatrix}, \quad (3.41)$$

$$F_1(x_1, x_2, x_3) = \arctan\left(\frac{(\frac{\Delta v}{2} + x_2)(\frac{\Delta w}{2} + x_3)}{(\frac{\Delta u}{2} + x_1)\sqrt{(\frac{\Delta u}{2} + x_1)^2 + (\frac{\Delta v}{2} + x_2)^2 + (\frac{\Delta w}{2} + x_3)^2}} \right), \quad (3.42)$$

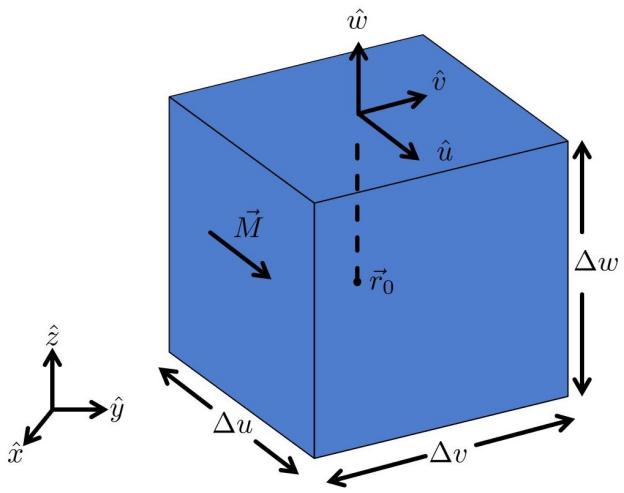


Figure 3.6: Parameterization of rectangular prism bar magnet of constant magnetization density $\vec{M}$.

$$F_2(x_1, x_2, x_3) = \frac{\sqrt{(\frac{\Delta u}{2} + x_1)^2 + (\frac{\Delta v}{2} + x_2)^2 + (\frac{\Delta w}{2} - x_3)^2} + (\frac{\Delta w}{2} - x_3)}{\sqrt{(\frac{\Delta u}{2} + x_1)^2 + (\frac{\Delta v}{2} + x_2)^2 + (\frac{\Delta w}{2} + x_3)^2} - (\frac{\Delta w}{2} + x_3)}, \tag{3.43}$$

$$\tau_u = (\vec{r} - \vec{r}_0) \cdot \hat{u}, \tag{3.44}$$

and τ_v and τ_w are defined similarly. Figure 3.6 visually defines the variables used to compute $\vec{B}(\vec{r})$.

3.3 Reference Potentials for Electrostatic Shielding Components

For engineering purposes, it is useful to consider the amount of energy required to maintain a specified potential on each electrostatic shielding element. In general, the energy stored in a single electrostatic shielding component charged to a reference potential V_{self} at its own surface is given by

$$W = \frac{1}{2} Q V_{\text{self}} = \frac{1}{2} C_{\text{self}} V_{\text{self}}^2, \tag{3.45}$$

where Q is the total charge on the component and C_{self} is its self-capacitance, or the ratio of charge to surface potential for that component in isolation. The power required to maintain this potential against leakage is then

$$\dot{W} = \frac{W}{\tau}, \tag{3.46}$$

where τ is the characteristic discharge time of the system. This formulation does not account for dissipative losses caused by negatively charged plasma interacting with electrostatic shielding components.

The self-capacitance for each configuration is determined via

$$C_{\text{self}} = \frac{Q}{V_{\text{self}}}. \tag{3.47}$$

In general, the reference potential is defined via Equation 3.28. Note that the point, line, and rectangular electrostatic shielding components cannot be practically manufactured; a finite volume is required. For a point charge, the finite volume analog is a sphere of radius R. The reference potential is determined by evaluating the electric potential via Equation 3.26 at a point on the surface of the constructed sphere, $\vec{r} = \vec{r}_0 + R\hat{n}$, where $\hat{n}$ is any unit direction vector. This gives

$$V_{\text{self}} = \frac{Q}{4\pi\epsilon_0 R}. \tag{3.48}$$

For a line charge, the finite volume analog is a cylinder of radius R and length L. The reference potential is determined by evaluating the electric potential via Equation 3.33 at any point on the curved surface of the cylinder that is halfway between the two end-caps, $\vec{r} = (\vec{r}_1 + \vec{r}_2)/2 + R\hat{n}$, where $\hat{n}$ is any direction orthogonal to the axis of the cylinder, $\vec{r}_2 - \vec{r}_1$. This gives

$$V_{\text{self}} = \frac{\lambda}{4\pi\epsilon_0} \ln\left(\frac{\sqrt{L^2 + 4R^2} + L}{\sqrt{L^2 + 4R^2} - L}\right). \tag{3.49}$$

For a rectangular charge, the finite volume analog is a rectangular prism of thickness Δw, length Δu, and width Δv. The reference potential is determined by evaluating the electric potential via Equation 3.39 at the midpoint of the rectangular prism, projected to the nearest "broad-face" surface (it is assumed that $\Delta w \ll \Delta u$ and $\Delta w \ll \Delta v$), i.e., $\vec{r} = \vec{r}_0 + \hat{w}\Delta w/2$. This gives

$$\begin{aligned} V_{\text{self}} = \frac{\sigma}{2\pi\epsilon_0}\Bigg[&\Delta u \operatorname{arcsinh}\left(\frac{\Delta v}{\sqrt{(\Delta u)^2 + (\Delta w)^2}}\right) \\ &+ \Delta v \operatorname{arcsinh}\left(\frac{\Delta u}{\sqrt{(\Delta v)^2 + (\Delta w)^2}}\right) \\ &- \Delta w \arctan\left(\frac{\Delta u \Delta v}{\Delta w\sqrt{(\Delta u)^2 + (\Delta v)^2 + (\Delta w)^2}}\right)\Bigg]. \end{aligned} \tag{3.50}$$

Going forward, when it is said that a potential was applied to an electrostatic shielding component, the relevant characteristic dimensions of the component will be cited alongside V_{self} to fully define the system—eventually allowing for an estimate of the energy required to operate the active shield.

3.4 Experimental Validation of ASPP

ASPP was experimentally validated using beamline measurements conducted at the Tandem Van de Graaff facility of Brookhaven National Laboratory [28].[1] In this study, shielding efficacy was assessed for a simple dipole shielding configuration as a function of several variables including particle type, particle energy, dipole voltage, dipole geometry, and dipole orientation, in an attempt to validate the mechanics underpinning ASPP.

Abstract

Passive radiation shielding alone is insufficient for protecting astronauts from galactic cosmic ray exposure. Active shields, utilizing electromagnetic fields to deflect heavy charged ions in space, could be used to supplement conventional passive shielding. Due to experimental limitations, simulation capability is crucial for designing effective active shields. The purpose of this work is to validate the ASPP code, used to characterize active shielding efficacy, using beamline measurements conducted at Brookhaven National Laboratory. Emphasis is placed on 1) comparing shielding efficacy as a function of a scaled dimensionless parameter among various electric dipole sphere sizes and center-to-center distances, 2) comparing shielding efficacy as a function of dipole rotation angle as the voltage applied to each sphere is varied independently, and 3) comparing shielding efficacy observed in measurements and simulations to broaden the validation domain of ASPP. Simulated and measured shielding efficacy data are shown to agree to within a factor of 1.10 on average. The results of this work demonstrate that dimensionless scaling of parameters characteristic of the active shield and incident radiation can be used to create scaling laws for a range of ion species relevant for protecting astronauts from galactic cosmic ray exposure at beamline energies.

3.5 Introduction

The risks associated with space radiation on crewed, long-duration, deep-space missions limit our ability to execute these missions beyond low-Earth orbit while remaining in compliance with applicable National Aeronautics and Space Administration (NASA) standards [9]. GCRs and SEPs, which make up the bulk of the interplanetary radiation field capable of impacting astronaut health, are composed of highly energetic,

[1] Part of this chapter is reproduced from L. Stegeman, R. Pal Chowdhury, D. Fry, M. L. Lund, S. Madzunkov, A. Belousov, and A. A. Bahadori, "Experimental validation of the Active Shielding Particle Pusher code," Journal of Applied Physics 129, 024902 (2021), https://doi.org/10.1063/5.0031460, with the permission of AIP Publishing.

heavy charged particless (HZEs) [67]. Mass requirements for astronaut radiation protection are too great for passive shielding alone to provide adequate protection. GCRs in particular are capable of penetrating large material thicknesses, rendering practical passive shielding thicknesses ineffective for astronaut protection [10, 68]. In response to these excessive mass requirements, efforts are underway to explore the applicability of active shielding to space radiation shielding problems. In contrast with passive shielding, which relies on the use of bulk material to reduce the energy of and potentially stop energetic particles, active shielding employs electromagnetic fields to shield incident charged particle radiation, either by slowing them down or diverting them away from the crew volume altogether.

Full-scale active shielding design evaluation presents a set of problems. The space radiation environment is impossible to fully replicate on Earth. It is also prohibitively expensive to send vehicles outfitted with active shielding designs into space for testing on a frequent basis. The most feasible approach is to instead test scaled-down active shielding designs using ion species and energies available on Earth. A one-dimensional scaling approach was developed by Fry *et al.*, enabling one to relate a measure of the shielding efficacy of an electric dipole active shielding configuration in the presence of a beam of charged particle radiation to a dimensionless scaling parameter, f_s [25]. The dimensionless scaling parameter, f_s, is defined as

$$f_s = \frac{(Z - N_e)eV_{\text{dip}}}{(\gamma^2 - 1)E_0/\gamma}, \tag{3.51}$$

where e is the elementary charge, V_{dip} is the dipole voltage (voltage applied to the positively charged portion of the electric dipole structure), Z is the atomic number, N_e is the number of bound electrons, E_0 is the rest-mass energy, and γ is the Lorentz factor of the incident charged particle beam. f_s is fundamentally the ratio of the potential energy of the electromagnetic field generated by the active shield to the kinetic energy of the incident charged particle. This dimensionless scaling parameter effectively collapses several independent variables into a single parameter. These independent variables include Z, N_e, ion mass number A (contained within the rest-mass energy E_0), ion kinetic energy E_k (contained within the Lorentz factor γ), and V_{dip}. The dimensionless scaling parameter f_s facilitates comparison among electric dipoles with significant geometric variations, like those tested in this study, and others better suited for in-space shielding, such as those discussed in Ref. [30] and [26]. The objectives of this work were to 1) compare shielding efficacy as a function of f_s among various electric dipole sphere radii (a) and center-to-center distances between spheres

(ℓ_{CC}), 2) compare shielding efficacy as a function of dipole rotation angle (α) as the voltage applied to each sphere was varied independently, and 3) compare shielding efficacy observed in measurements versus analogous simulations in order to broaden the existing validation domain of the ASPP to include ion species relevant for protecting astronauts from galactic cosmic ray exposure. It is important to note that a single electric dipole shielding configuration is *not* intended to work as an effective active shield. Instead, the electric dipole shielding configuration is used as a simple test article to compare ASPP simulations with beamline measurements.

3.6 Materials and Methods

3.6.1 1d Shielding Efficacy Metric

The efficacy of passive radiation shields can be characterized in terms of flux density reduction or absorbed dose reduction, which can vary as a function of parameters such as shielding thickness, material, and incident energy, observed at some point of interest behind the shield. [69] A more recent approach specific to space radiation shielding employs a ratio of mass stopping powers between the shield of interest and some reference shield. [70] These measures of shielding efficacy succinctly describe the degree to which the radiation field is affected by the shield. However, problems arise when similar approaches are used to evaluate the shielding efficacy of active radiation shielding configurations.

Traditional metrics for shielding efficacy are less useful for active shielding analysis. In the passive shielding case, interactions between energetic particles and the atoms comprising the passive shield occur over atomic scale distances and on very short timescales. In the active shielding case, electromagnetic interactions occur over relatively long periods of time, much larger distances, and the phenomenon of absorption is absent, unless the HZE ions encounter matter. The absence of absorption implies, through phase space volume conservation, that any region experiencing a reduction in flux density due to the presence of an active shield is compensated by another region in space where flux density is *enhanced*. The generation of enhancement regions is what makes metrics averaged over large regions of space, like flux density reduction, much less useful for active shielding analysis. For the simplified electric dipole active shield, it is possible to select regions of space that are largely devoid of radiation. These regions are called void areas, and they appear in images of the beam profile downstream from where the dipole is located. The void area is defined as

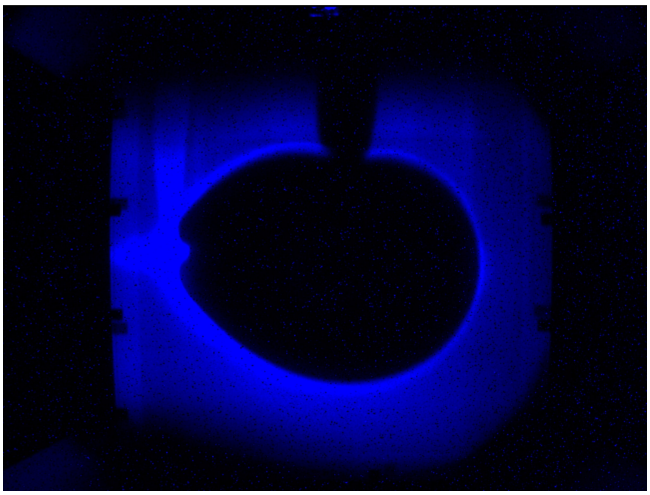


Figure 3.7: Measured image data example; 2 MeV protons, ±30 kV applied voltage, sphere radius $a = 2.54$ cm, center-to-center sphere separation $\ell_{CC} = 7.620$ cm, dipole-detector distance $\ell_{DD} = 2$ m.

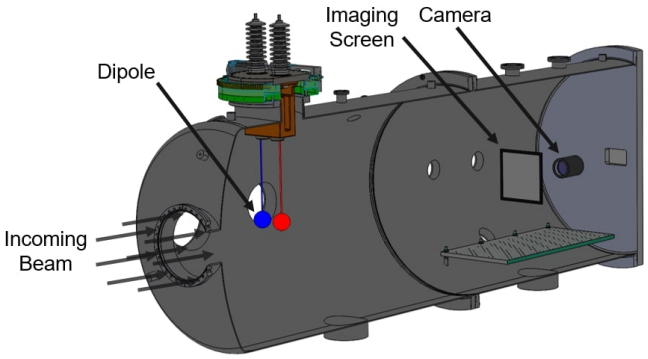


Figure 3.8: Simplified cross section view of custom BNL test chamber with relevant components labeled.

the region in which the radiation intensity is significantly reduced and is clearly encompassed by an area of higher radiation intensity. An example void area is shown in Figure 3.7.

3.6.2 Measurement Setup

A custom-built vacuum chamber was constructed within BNL's Tandem Van de Graaff Facility. [71] This vacuum chamber is operated around 1×10^{-7} Torr. Figures 3.8 and 3.9 show the components of the vacuum chamber relevant to this work. The imaging screen is a custom made 22.86-by-22.86 cm vacuum phosphor screen deposited on glass, built by Kimball Physics (model no. 68-632800). The camera is a USB3.0 Color 1.2MP Complementary Metal-Oxide-Semiconductor Camera, built by Mightex (model no. SMN-C050-U).

Prior to entering the vacuum chamber, the ion beam is swept horizontally and vertically to produce a wider, less intense beam with an area that matches or exceeds the area of the entrance port. The swept

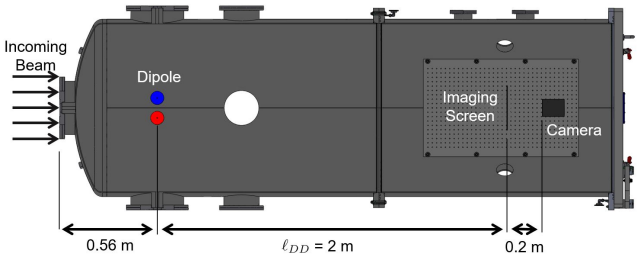


Figure 3.9: Top cross section view of custom BNL test chamber with relevant components labeled and dimensions along the beam direction.

beam enters from the entrance port on the left and impacts the imaging screen on the right, all while being influenced by the presence of the electric field. When charged particle interactions occur in the imaging screen, visible light is emitted. The photons generated from the imaging screen are then captured by the camera and integrated into a single image over a user-defined shutter-time, typically 750 ms. An example of measured image data is shown in Figure 3.7.

As in Fry *et al.*, an electric dipole field was selected to serve as the active shield for validation purposes [25]. The physical electric dipole consists of two conductive, spherical shells attached to independent voltage sources via conductive rods. The positive and negative voltage sources are connected to a mounting plate within the chamber that is equipped with several slots to which dipole spheres may attach, allowing for controlled variation in center-to-center distance (ℓ_{CC}). Three dipole sphere sizes were tested, allowing for variation in sphere radii, a. The conductive rods that connect the spheres to the voltage sources all had radii of $R_r = 2.555\,\text{mm}$.

Some features of the chamber are not shown in Figure 3.8 for illustration purposes. The imaging screen is attached to a translation stage which can be moved both along and orthogonal to the beam axis. The distance from the center of the dipole to the imaging screen was kept constant at $\ell_{DD} = 2\,\text{m}$ for all measurements. The camera was rigidly attached to the imaging screen, ensuring consistency in relative positioning of the two components.

3.6.3 Simulation Setup

ASPP is a charged particle propagation software tool developed specifically for rapid-prototyping active shielding configurations [24]. ASPP allows the user to propagate relativistic and non-relativistic charged particles characterized by Z, A, N_e, and E_k through electromagnetic fields. Transport is governed by the

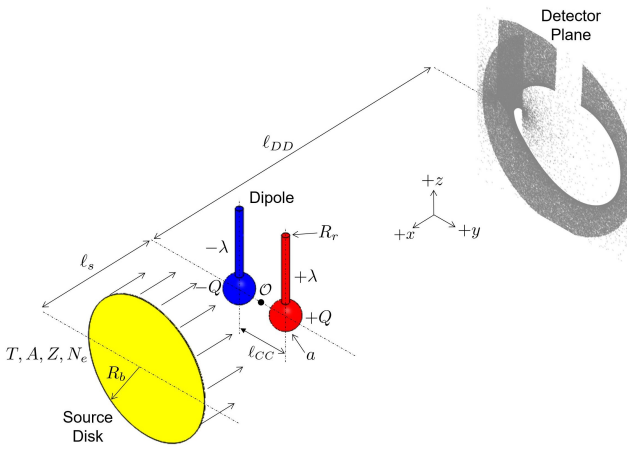


Figure 3.10: Simulation scenario; displayed parameters include the ion kinetic energy E_k, ion mass number A, ion proton number Z, ion electron number N_e, beam radius R_b, source-to-dipole distance ℓ_S, center-to-center sphere distance ℓ_{CC}, sphere charge Q, rod linear charge density λ, sphere radius a, rod radius R_r, and dipole-detector distance ℓ_{DD}; the reference coordinate system is oriented properly, but the origin is located at point $\mathcal{O}$, the center point between the two dipole spheres.

Lorentz force law [24]. Among other features, electric fields can be specified directly, by giving electric field components at points on a grid, or indirectly, by specifying a charge distribution according to location and magnitude. While the open-source general-purpose Monte Carlo radiation transport toolkit Geant4 could be used in this application, ASPP is strongly preferred due to relative ease of use, GPU compatibility, increased computational efficiency, and the implementation of symplectic electromagnetic propagators (as opposed to Geant4's default Runge-Kutta electromagnetic propagator) [72].

ASPP simulations were set up to reflect the measurement scenario as closely as possible. Figure 3.10 depicts how laminar beamline simulations are conducted in ASPP. The source is modeled as a monodirectional disk source with maximum beam radius[2] of $R_b = 15\,\text{cm}$. This source disk emits a single ion type characterized by its initial kinetic energy E_k, mass number A, atomic number Z, and number of bound electrons N_e. Source ions are initially directed in the $-x$-direction. The distance from the source to the center of the dipole structure was set to $\ell_S = 2\,\text{m}$. This distance was selected after preliminary tests showed that initializing source ions any greater than 2 m upstream of the dipole structure did not significantly affect the results of the simulation (in terms of positions at which source ions intersect with the detector plane); minimizing the distance between source ion initial positions and the dipole structure minimizes the necessary simulation run-time. Energy losses in the diffuse residual air in the chamber are considered negligible and are not accounted for in simulations.

[2]The size of the source disk is irrelevant as long as the physical dipole is completely encompassed by the beam.

While the physical active shield is comprised of conductive ball-and-rod structures, the active shield was modeled in ASPP with a combination of line and point charges. Point charge magnitudes and linear charge densities were computed using the voltage applied to each conductor. The point charge magnitude was calculated accounting for the sphere separation factor, as in Ref. [25], by

$$Q = \frac{4\pi\epsilon_0 a V_{\text{dip}}}{1 - \frac{1}{1+\delta}}, \tag{3.52}$$

where δ is the ratio of the sphere radius to the minimum surface-to-surface distance between spheres, so

$$\delta = \frac{\ell_{CC} - 2a}{a}. \tag{3.53}$$

ASPP can generate the electric field due to a finite line of charge given the linear charge density λ and the endpoints of the line segment $\vec{r}_1$ and $\vec{r}_2$. The line segment endpoints for the positive rod were set to $\vec{r}_{1+} = \langle 0, \ell_{CC}/2, a\rangle$ and $\vec{r}_{2+} = \langle 0, \ell_{CC}/2, a + 30.48\,\text{cm}\rangle$. The line segment endpoints for the negative rod were set to $\vec{r}_{1-} = \langle 0, -\ell_{CC}/2, a\rangle$ and $\vec{r}_{2-} = \langle 0, -\ell_{CC/2}, a + 30.48\,\text{cm}\rangle$. The linear charge density used to represent each charged rod was determined by assuming a constant surface charge density for each ball-and-rod structure. Setting $Q/4\pi a^2 = \lambda L_r/2\pi R_r L_r$ and solving for λ gives

$$\lambda = \frac{Q R_r}{2a^2}, \tag{3.54}$$

where R_r is the rod radius.

Ion trajectories that intersect with the charged spheres and rods contribute to the void area seen on the imaging screen and captured by the camera as in Figure 3.11, where no voltage is applied. This "shadowing" effect has a significant impact on the size of the void area in the low f_s region, to the point where only shadowing effects (passive shielding effects) are observed for $V_{\text{dip}} = 0$. ASPP is equipped to account for these shadowing effects. For any point charge, a sphere radius can be specified as an input. Any particle trajectory that intersects with the virtual sphere surrounding the point charge is flagged, signaling that the ion would have been stopped by an equivalent physical sphere. Flagged particles can then be ignored when calculating the void area.

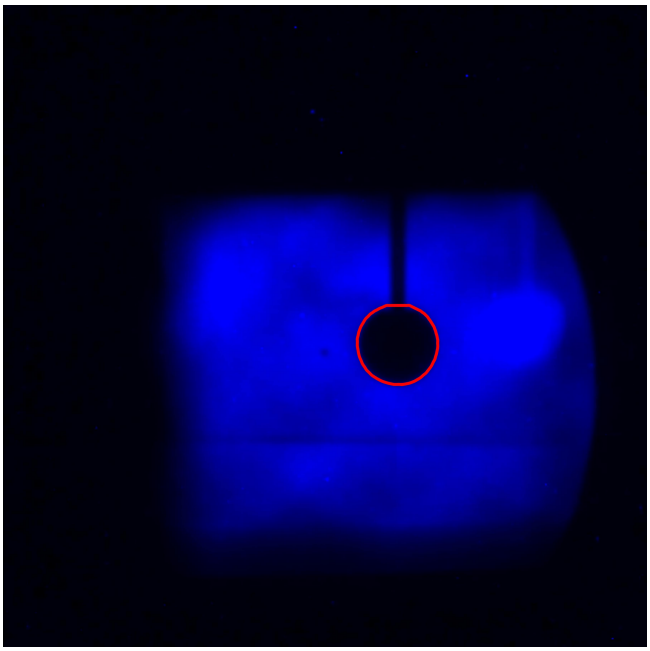


Figure 3.11: Example of sphere shadowing; sphere shadow is outlined using Fourier-fitted function from image analysis method.

3.6.4 Parameter Space

Several physical properties of the experimental setup were varied, resulting in a broad parameter space. These parameters include ion species (characterized by atomic number Z, mass number A, charge state $Z - N_e$), ion kinetic energy E_k, dipole voltage V_{dip} (voltage on positive sphere), sphere radius a, center-to-center sphere distance ℓ_{CC}, and dipole rotation angle α ($\alpha = 0$ is the "neutral position", shown in Figure 3.10). This parameter space is highly multidimensional, and the shielding efficacy of the active shield is dependent upon all of these variables, though the use of the dimensionless scaling parameter f_s collapses several independent variables contributing to the void area (Z, A, N_e, E_k, V_{dip}) into a single number.[3] Ultimately, the experimental parameter space selection was guided by beamline availability, equipment availability, and the desire to cover a wide range of f_s values. Table 3.2 illustrates the parameter space used to compare the effects of a and ℓ_{CC} on the shielding efficacy as a function of f_s.

Table 3.3 illustrates the parameter space used to determine the effect that rotating the dipole structure by angle α with respect to its center point has on void area. Four different applied voltage configurations were considered. Let sphere A be the ball-and-rod structure connected to the positive voltage source and

[3]The variables that were collapsed into f_s may still contribute to the void area in a minor, possibly second order way (especially for low f_s values), but these effects appear to be small.

let sphere B be the ball-and-rod structure connected to the negative voltage source. Sphere A corresponds to the red sphere while sphere B corresponds to the blue sphere, as shown in Figure 3.10. The four applied voltage combinations are as follows: 1) 0 kV applied to both sphere A and sphere B, 2) 70 kV applied to sphere A and −70 kV applied to sphere B, 3) 70 kV applied to sphere A and 0 kV applied to sphere B, and 4) 0 kV applied to sphere A and −70 kV applied to sphere B.

Table 3.2: List of parameters, associated symbols, and values contained within the measurements procured at BNL with no dipole rotation $\alpha = 0$ and constant dipole-detector distance $\ell_{DD} = 2\,\text{m}$.

Parameter [Unit]	Symbol	Domain				
Dipole Voltage [kV]	V_{dip}	0, 10, 20, 30, 40, 50, 60, 70				
Sphere Radius [cm]	a	1.27, 2.54, 3.81				
Center-to-Center Distance [cm]	ℓ_{CC}	5.715, 7.620, 11.430				
		$^{1}H^{+}$	$^{4}He^{2+}$	$^{12}C^{6+}$	$^{56}Fe^{4+}$	$^{56}Fe^{6+}$
Ions, Initial Kinetic Energies [MeV]	Z, A, T	2	4	10	10	22.5
		6	6	14		
		10	10			
		14				
		22				

Table 3.3: List of parameters, associated symbols, and values contained within the measurements procured at BNL with dipole rotation; all measurements were conducted with sphere radius $a = 2.54\,\text{cm}$, center-to-center sphere separation $\ell_{CC} = 7.620\,\text{cm}$, dipole-detector distance $\ell_{DD} = 2\,\text{m}$, and 2 MeV protons.

Parameter [Unit]	Symbol	Domain
Dipole Rotation Angle [rad]	α	$-\pi/2$ to $\pi/2$; $\Delta\alpha = \pi/18$ rad
Dipole Voltage Configuration [kV]	(V_+, V_-)	(0, 0), (+70, 0), (0, -70), (+70, -70)

3.6.5 Void Area Calculation

The void areas produced by each simulation or measurement were used as the metric for the shielding efficacy. The void area is defined as the region in which the radiation intensity is significantly less than elsewhere and is clearly encompassed by an area of higher radiation intensity. The void area *does not* include the area devoid of radiation outside of the ovate shape generated by the presence of the charged spheres; see Figure 3.11 to observe how the void area outlines the shadow generated by the sphere and *not* the shadow of the supporting rod.

An image analysis script was written in Python to partially automate void area calculations. This script uses a combination of Canny edge detection [73] and watershed transformations [74] to find and fit the edge of the void area to a $2N + 1$-term Fourier series $f(\theta)$ using a non-linear least squares algorithm. More detail

on this image analysis method can be found in Ref. [75]. The Fourier series that best fits the void edge is given by

$$f(\theta) = c + \sum_{n=1}^{N} \Big[a_n \cos(n\theta) + b_n \sin(n\theta) \Big] \tag{3.55}$$

where a_n, b_n, and c are the fitting coefficients determined by the non-linear least squares algorithm provided in Ref. [76]. The area enclosed by the curve $f(\theta)$ can be determined analytically by integrating the square of $f(\theta)$ over all angles θ (one revolution) and halving the result. The void area, A_0, is

$$A_0 = \pi \bigg(c^2 + \frac{1}{2} \sum_{n=1}^{N} (a_n^2 + b_n^2) \bigg). \tag{3.56}$$

The utility of the Fourier fitting method extends past calculating the void area. The perimeter of the void area, P_0, can be determined by calculating the arc length of $f(\theta)$,

$$P_0 = \int_{2\pi} \sqrt{\Big[f(\theta) \Big]^2 + \Big[f'(\theta) \Big]^2} \, \mathrm{d}\theta. \tag{3.57}$$

The average center-to-curve distance of the void area, D_0, can also be determined by finding the average value of $f(\theta)$,

$$D_0 = \frac{1}{2\pi} \int_{2\pi} f(\theta) \mathrm{d}\theta. \tag{3.58}$$

3.7 Results and Discussion

The following section discusses a number of comparisons made between void areas obtained from BNL measurement image data and ASPP simulation image data. First, simulated and measured void areas are compared as a function of f_s, a, and ℓ_{CC}. Deviation between simulation and measurement at low f_s values due to non-negligible beam divergence and sphere shadowing are discussed. Measured and simulated void areas are compared as a function of dipole rotation angle α. Finally, simulated and measured void areas are compared directly.

3.7.1 Void Area without Dipole Rotation Results

Figure 3.12 depicts the void areas of all measurements and simulations conducted where $\alpha = 0$ as a function of f_s. In general, measured void areas agree well with simulated void areas. Five plots are shown, separated

by geometric properties of the electric dipole–the sphere radii a and the center-to-center distances ℓ_{CC}. Each plot includes two curves: one for simulations and one for measurements.

Observing the overall differences in magnitude between Figures 3.12b, 3.12d, and 3.12e, it is immediately apparent that larger dipole sphere sizes give larger void areas for the same f_s value. This is due to the fact that larger surface areas can hold greater amounts of charge at the same applied voltage, increasing the strength and extent of the electric field, which in turn improves the shielding efficacy.

While the effects of sphere size on the void area are straightforward, the effect of the center-to-center distance between spheres is more subtle. Comparing Figures 3.12a and 3.12b and Figures 3.12c and 3.12d, it is observed that the slope of the function changes at different values of f_s when ℓ_{CC} is varied while a is held constant. Other than the difference in the location along the f_s-axis at which the slope changes (also referred to as the 'knee' or $f_{s,\text{knee}}$), A_0 versus f_s with the same a but different ℓ_{CC} are quite similar.

All curves of Figure 3.12 are well described by the function

$$A_0(f_s) = \begin{cases} C_0 f_s^{b_0} + k_0 \text{ for } f_s < f_{s,\text{knee}} \\ C_1 f_s^{b_1} \text{ for } f_s > f_{s,\text{knee}} \end{cases} . \tag{3.59}$$

Note that the fitted function was forced to be continuous at $f_{s,\text{knee}}$, i.e.,

$$\lim_{f_s \to f_{s,\text{knee}}^-} A_0(f_s) = \lim_{f_s \to f_{s,\text{knee}}^+} A_0(f_s) = A_0(f_{s,\text{knee}}).$$

Table 3.4 shows fitting parameters C_0, b_0, k_0, C_1, and b_1 for the curve-fits shown in Figure 3.12 (simulated and measured). The coefficient of determination, R^2, is also shown to provide a goodness-of-fit measure. R^2 is calculated via

$$R^2 = 1 - \frac{\sum_i [y_i - g(x_i; \vec{v})]^2}{\sum_i [y_i - \bar{y}]^2}, \tag{3.60}$$

where y_i values are generic data points, $\bar{y}$ is the mean of those data points, and $g(x_i; \vec{v})$ is the functional fit evaluated at values x_i with fitting parameters contained within $\vec{v}$.

A linear relationship is observed for $f_s < f_{s,\text{knee}}$, while a sublinear relationship (exponent of approximately 2/3) is observed for $f_s > f_{s,\text{knee}}$. The value of $f_{s,\text{knee}}$ was determined by visually inspecting the plots shown in Figure 3.12 for sudden changes in slope. This change from linear to sublinear dependence on f_s appears to occur when the extent of the void area expands past center point of each sphere. This is sensible, as the shift

Table 3.4: Table of fitting parameters (C_0, b_0, k_0, C_1, b_1) which correspond to the simulation and measurement void area data curve fits within the five plots of Figure 3.12 which correspond to various sphere radius a and center-to-center sphere separation ℓ_{CC} values; data type "s" refers to simulation, "m" refers to measurement; the coefficient of determination, R^2, (a goodness-of-fit measure) was included for each set of curve-fitted parameters.

Figure	a [cm]	ℓ_{CC} [cm]	$f_{s,\text{knee}} \times 10^3$	Type	C_0 [m^2]	b_0	$k_0 \times 10^4$ [m^2]	C_1 [m^2]	b_1	R^2
3.12a	1.27	5.715	8.63	s	1.39	1.10	4.545	0.21	0.70	0.99628
				m	2.00	1.20	7.744	0.23	0.71	0.99795
3.12b	1.27	11.430	27.8	s	1.73	1.18	4.953	-	-	0.99419
				m	1.58	1.19	7.808	-	-	0.99947
3.12c	2.54	7.620	10.6	s	2.01	1.00	17.21	0.44	0.66	0.99823
				m	2.98	1.12	29.81	0.32	0.60	0.99894
3.12d	2.54	11.430	18.3	s	3.03	1.14	18.11	0.20	0.45	0.99910
				m	3.99	1.22	31.36	0.29	0.54	0.99795
3.12e	3.81	11.430	12.8	s	4.07	1.07	41.83	0.73	0.65	0.99875
				m	5.00	1.16	67.60	0.62	0.64	0.99963

from linear to sublinear dependence also corresponds to a change in the shape of the void area from circular to cardioid-like. Essentially, once the void area exceeds an area that is roughly the size of a circle that would fully encompass both spheres/point charges, the negative pole appears to attract more ions toward the void from a greater distance. This observation is buttressed by the fact that as ℓ_{CC} increases, $f_{s,\text{knee}}$ also increases (or even disappears completely outside of the domain of f_s covered by ground measurements).

3.7.2 Beam Divergence Effects

While strong agreement between simulation and measurement is observed at higher f_s values, deviation between the two is substantial for low f_s values. Two factors likely contribute to this difference: greater penetration due to a high kinetic energy-to-electrostatic potential energy ratio, and the fact that there is non-negligible beam divergence occurring in measurements not represented in simulations. If measurements were conducted with a laminar, monodirectional beam, then measured void areas at $f_s = 0$ would be much closer to the cross sectional area of the spheres. Consider Figure 3.13, which illustrates how the void area may be approximated when considering beam divergence for the $f_s = 0$ case. Assuming the sphere is a perfect ion absorber and position of the beam steering magnet is assumed to be a point source, the void area of the sphere projected onto the imaging screen in the presence of beam divergence can be determined using a similar triangles approach. From $\ell_{PD}/2a = (\ell_{PD} + \ell_{DD})/2a'$, one can deduce a beam divergence magnification factor M, which scales the simulated void area to account for beam divergence, in terms of

ℓ_{PD} and ℓ_{DD},

$$M = \frac{(\ell_{PD} + \ell_{DD})^2}{\ell_{PD}^2}, \tag{3.61}$$

where ℓ_{PD} is the distance from the point source to the point centered between the two dipole spheres.

Consider the following example calculation that illustrates how beam divergence could account for differences in simulated and measured void areas for low f_s values. For 6 MeV proton irradiation and no voltage applied to the 2.54 cm-radius dipole spheres with 7.620 cm center-to-center distance, the image analysis algorithm found that the simulated void area was $A_{0,\text{sim}} = 2.03 \times 10^{-3}\,\text{m}^2$ (essentially the cross-sectional area of the sphere) and that the measured void area was $A_{0,\text{meas}} = 3.08 \times 10^{-3}\,\text{m}^2$. The distance from the beam steering magnet (treated as a point source here) and the dipole was $\ell_{PD} = 8.656\,\text{m}$, so for this example, $M = 1.691$. The simulated void area, accounting for beam divergence, is approximately $MA_{0,\text{sim}} = 3.43 \times 10^{-3}\,\text{m}^2$. This value overpredicts the measured image area, but is a) three times closer than if beam divergence were not considered for simulated image data, and b) assumes the sphere is a perfect absorber.

The effects of beam divergence naturally diminish as f_s increases. Electrostatic shielding eventually dominates in terms of its contribution to the void area compared to the void contribution from sphere shielding. Figure 3.14 shows ASPP simulations where particles that intersected either dipole sphere were flagged as they were transported. On the detector plane, these 'shadowed' particles are plotted in a different color. It is clear that, as V_{dip} (a surrogate for f_s) increases, the fraction of the void area created by sphere shadowing effects decreases, to the point where at $V_{\text{dip}} = 70\,\text{kV}$ the shadow nearly lines up with the void edge created by non-shadowed particles alone. Figure 3.15 shows measured image data which corresponds to the simulated image data in Figure 3.14, experimentally demonstrating both particle shadowing effects and shape preservation between simulation and measurement.

3.7.3 Void Area with Dipole Rotation Results

Figure 3.16 depicts the void areas of all measurements and simulations taken as part of the dipole field rotation study. Table 3.3 shows the parameter space for these simulations and measurements. When two void regions were observed in the same image (e.g., $V_+ = V_- = 0$ and the projection of the sphere cross sections on to the imaging screen do not overlap), *both* void areas were calculated and summed to produce a single data point.

Table 3.5: Fitting parameters ($\tilde{a}$, $\tilde{b}$) and coefficients of determination R^2 for rotation study; data type "s" refers to simulation, "m" refers to measurement.

Figure	Voltage [kV]	Type	$\tilde{a} \times 10^3$ [m^2]	$\tilde{b}$	R^2
3.16a	(0, 0)	s	4.255	0.615	0.87351
		m	6.510	0.589	0.74483
3.16b	(0, -70)	s	1.771	1.165	0.93866
		m	9.671	1.065	0.98469
3.16c	(+70, 0)	s	24.50	0.265	0.81486
		m	26.84	0.576	0.97871
3.16d	(+70, -70)	s	30.98	0.874	0.99640
		m	28.87	0.873	0.99745

Figure 3.16 is separated into four plots according to how the voltage on each dipole sphere was configured. All eight data sets (four groups corresponding to the four voltage configurations, with one measurement data set and one simulation data set for each group) can be approximated by the function

$$A_0 = \tilde{a} \cos(\tilde{b}\alpha) \tag{3.62}$$

where $\tilde{a}$ and $\tilde{b}$ are fitting parameters. Table 3.5 shows fitting parameters for the curve-fits shown in Figure 3.16 (simulated and measured), alongside the coefficient of determination for each curve.

Simulated and measured void areas appear to follow the same general trends (with varying degrees of magnitude agreement), except for the case where $V_+ = 70\,\text{kV}$ and $V_- = 0$; measured void areas appear relatively constant for all α. This behavior may result from a combination of beam divergence effects in the measurement as well as a change in magnification factor as the distance between the positively charged sphere and the imaging detector changes as a function of α.

3.7.4 Overall Measurement-Simulation Agreement

Figure 3.17 shows a comparison of all simulated void area data with corresponding measured void area data using two-dimensional histograms which show the concentration of $(A_{0,\text{sim}}, A_{0,\text{meas}})$ data points on 40×40 grids. The mean relative error over all N measured/simulated void area pairs,

$$\text{MRE} = \frac{1}{N} \sum_{i}^{N} \frac{|A_{0,\text{sim},i} - A_{0,\text{meas},i}|}{A_{0,\text{meas}}}, \tag{3.63}$$

was 13.1 %. Observing the ratio $A_{0,\text{sim}}/A_{0,\text{meas}}$, simulated and measured void areas differ by an average factor of 1.10 and 1.75 at maximum. As expected, worse agreement is observed for smaller void areas due

to the dominating effects of beam divergence in this domain. Figure 3.17b shows that about three or four of the largest void areas are overestimated by ASPP simulation. These overestimates are likely due to the fact that very large voids either exceed the size of the incident beam or exceed the bounds of the phosphor screen, leading to "broken" void edges. The image analysis technique employed is able to handle "broken" voids, but the resulting measured void area is slightly smaller than it would be if the void were fully closed. This explains why these simulated void areas appear to marginally outsize the measured void areas.

3.8 Summary and Conclusion

The objectives of this work were to 1) compare shielding efficacy as a function of f_s among various electric dipole sphere sizes and center-to-center distances, 2) compare shielding efficacy as a function of dipole rotation angle as the voltage applied to each sphere was varied independently, and 3) compare shielding efficacy observed in measurements versus analogous simulations in order to broaden the validation domain of ASPP.

Measurements and simulations demonstrated that the shielding efficacy metric–the void area–could be expressed as a function of f_s using the form shown in Equation 3.59. Observing the fitting parameters in Table 3.4 and the graphs of Figure 3.12, it is shown that increasing the size of the dipole spheres improves the shielding efficacy for the same value of f_s. Increasing the center-to-center distance between dipole spheres for the same sphere radius appears to increase the value of f_s at which the relationship between A_0 and f_s transitions from a linear relationship to a sublinear relationship. This transition, which occurs at $f_{s,\text{knee}}$, is due to a change in shape of the void area. The void area grows linearly when the void area is circular, and grows sublinearly (with an exponent of approximately 2/3) when the void area is cardioid-like. Small differences between measured and simulated void areas are exacerbated at low f_s values due to beam divergence and ion penetration which exist in measurements and not in simulations.

Measurements and simulations were less consistent with one another in the context of the dipole rotation study. Figure 3.16 shows how A_0 changes with rotation angle α. The case where $V_+ = V_- = 70\,\text{kV}$ showed the best shielding efficacy when $\alpha = 0$, but performed poorly when $\alpha \to \pm\pi/2$ (on par with $V_+ = 0$, $V_- = 70\,\text{kV}$ and $V_+ = V_- = 0$ cases). This implies that the electric dipole is largely ineffective as a shield if the radiation field is not predominantly perpendicular to the dipole axis, meaning an electric dipole would

likely make for a poor shield in a 3d, isotropic radiation environment. The case where $V_+ = 70\,\mathrm{kV}$ and $V_- = 0$ gave the most consistent shielding efficacy, presumably due to the absence of an actual "dipole" altogether, coupled with the additional passive shielding provided by the neutral sphere. Beam divergence in measurement may be to blame for the large differences between measured and simulated void areas, especially for the $V_+ = V_- = 0$ and $V_+ = 0$, $V_- = 70\,\mathrm{kV}$ cases.

A direct comparison between simulated and measured void areas for all $\alpha = 0$ data showed that ASPP simulations reflect the analogous measurements remarkably well. The mean relative error between measured and simulated void areas was 13.1%. Simulated and measured void areas differed by a factor of 1.10 on average and a factor of 1.75 in the most extreme case.

The validation domain of ASPP has broadened to include multiple ion species and an energy range up to at least $22\,\mathrm{MeV/n}$. Future work will focus on using ASPP to develop a one-dimensional scaling law for in-space ion energies and extend shielding efficacy evaluations to three-dimensional active shielding configurations. Additional work includes a more thorough analysis of how the threshold value $f_{s,\mathrm{knee}}$ relates to the shape of the void, shielding efficacy analyses of planar charged arrays, and the exploration of a relationship between the flux reduction experienced within an actively shielded volume and the volume of various equipotential surfaces.

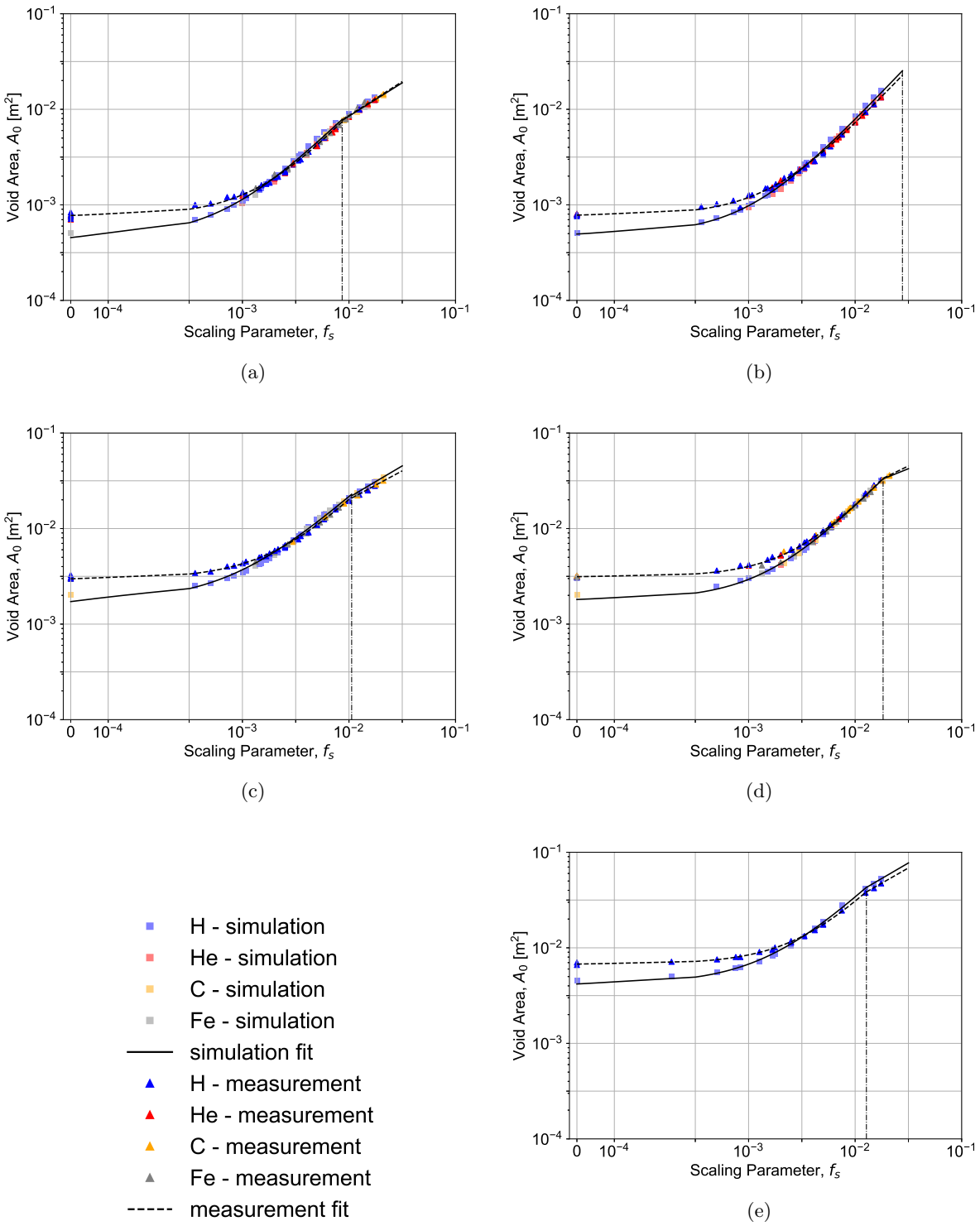


Figure 3.12: Scaling law plots comparing measured and simulated images separated by sphere radius and center-to-center distance between spheres; a, ℓ_{CC}, and fitting parameters shown in Table 3.4; (a) $a = 1.27\,\text{cm}$, $\ell_{CC} = 5.715\,\text{cm}$; (b) $a = 1.27\,\text{cm}$, $\ell_{CC} = 11.430\,\text{cm}$; (c) $a = 2.54\,\text{cm}$, $\ell_{CC} = 7.620\,\text{cm}$; (d) $a = 2.54\,\text{cm}$, $\ell_{CC} = 11.430\,\text{cm}$; (e) $a = 3.81\,\text{cm}$, $\ell_{CC} = 11.430\,\text{cm}$.

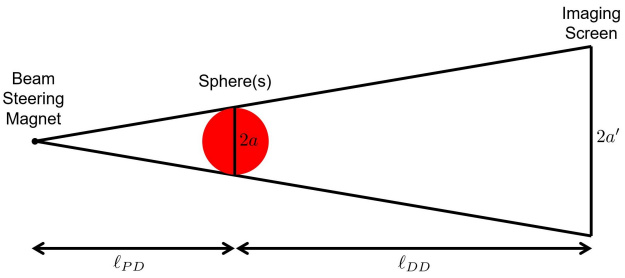


Figure 3.13: Illustration of beam divergence assuming the beam steering magnet acts as a point source; ℓ_{PD} is the distance from the point source to the midsection of the dipole sphere and $2a'$ is the diameter of the dipole sphere's shadow projected on to the imaging screen.

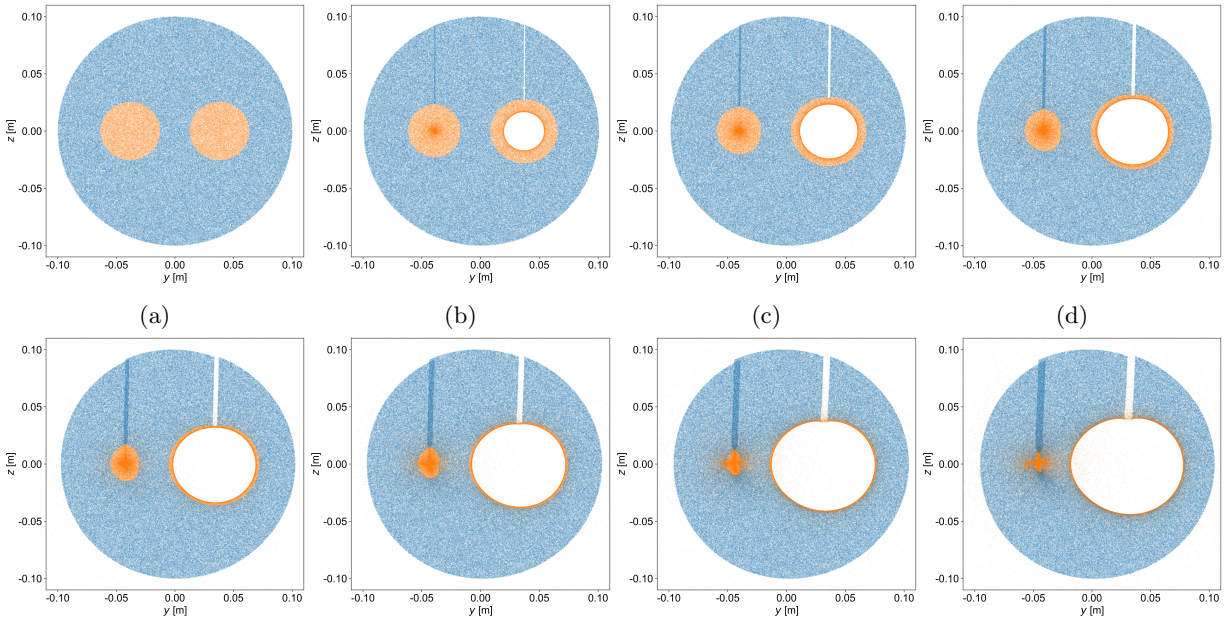


Figure 3.14: Simulated image data illustrating how sphere shadowing effects diminish as applied dipole voltage V_{dip} (and scaling parameter f_s) increases; simulations conducted using 14 MeV protons with $V_{\text{dip}} \in (0, 70)$ kV where sphere radius $a = 2.54$ cm and center-to-center separation $\ell_{CC} = 7.620$ cm; particles that intersected with either dipole sphere at any point during the simulation are plotted in orange; (a) $V_{\text{dip}} = 0$ kV; (b) $V_{\text{dip}} = 10$ kV; (c) $V_{\text{dip}} = 20$ kV; (d) $V_{\text{dip}} = 30$ kV; (e) $V_{\text{dip}} = 40$ kV; (f) $V_{\text{dip}} = 50$ kV; (g) $V_{\text{dip}} = 60$ kV; (h) $V_{\text{dip}} = 70$ kV.

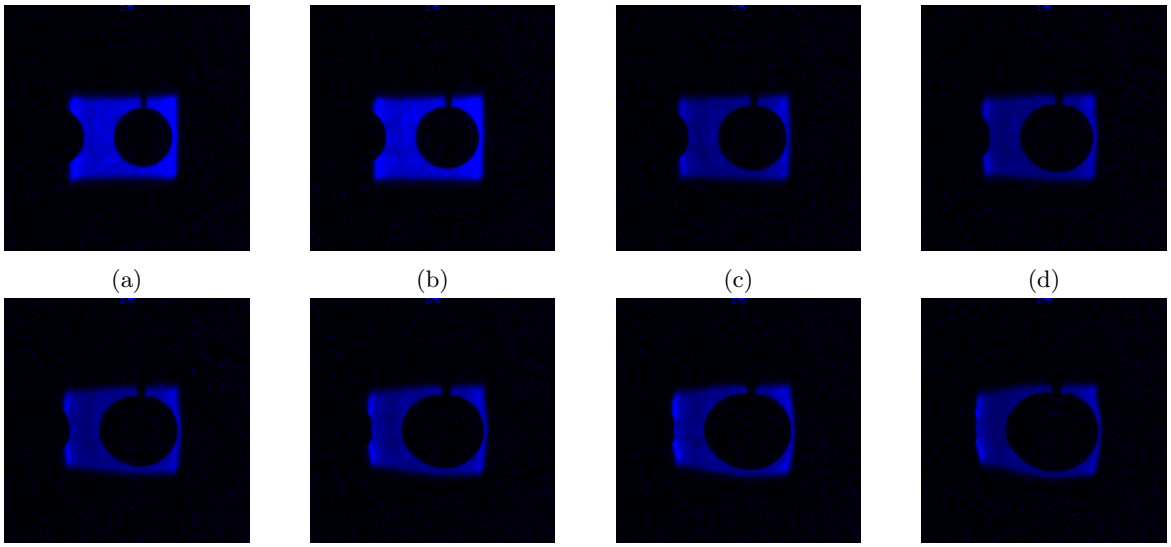


Figure 3.15: Measured image data illustrating shape preservation between measured and simulated image data; measurements conducted using 14 MeV protons with $V_{\text{dip}} \in (0, 70)$ kV where sphere radius $a = 2.54\,\text{cm}$ and center-to-center separation $\ell_{CC} = 7.620\,\text{cm}$; (a) $V_{\text{dip}} = 0\,\text{kV}$; (b) $V_{\text{dip}} = 10\,\text{kV}$; (c) $V_{\text{dip}} = 20\,\text{kV}$; (d) $V_{\text{dip}} = 30\,\text{kV}$; (e) $V_{\text{dip}} = 40\,\text{kV}$; (f) $V_{\text{dip}} = 50\,\text{kV}$; (g) $V_{\text{dip}} = 60\,\text{kV}$; (h) $V_{\text{dip}} = 70\,\text{kV}$.

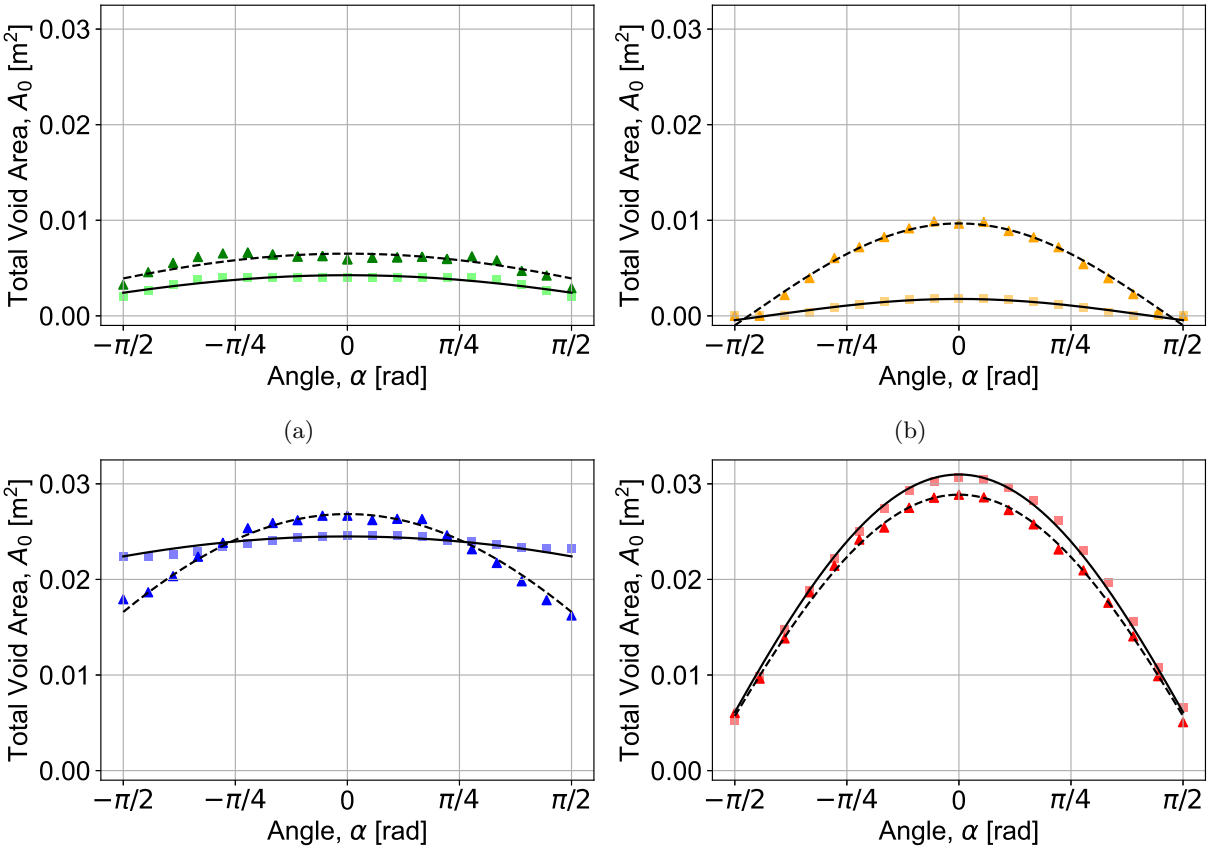


Figure 3.16: Plots comparing measured and simulated void areas as a function of dipole rotation angle α separated by dipole voltage configuration; dotted lines fit to measured void areas (data points are triangular), solid lines fit to simulated void areas (data points are square); fitting parameters for curve fits are shown in Table 3.5; (a) $V_+ = 0\,\text{kV}$, $V_- = 0\,\text{kV}$; (b) $V_+ = 0\,\text{kV}$, $V_- = -70\,\text{kV}$; (c) $V_+ = 70\,\text{kV}$, $V_- = 0\,\text{kV}$; (d) $V_+ = 70\,\text{kV}$, $V_- = -70\,\text{kV}$.

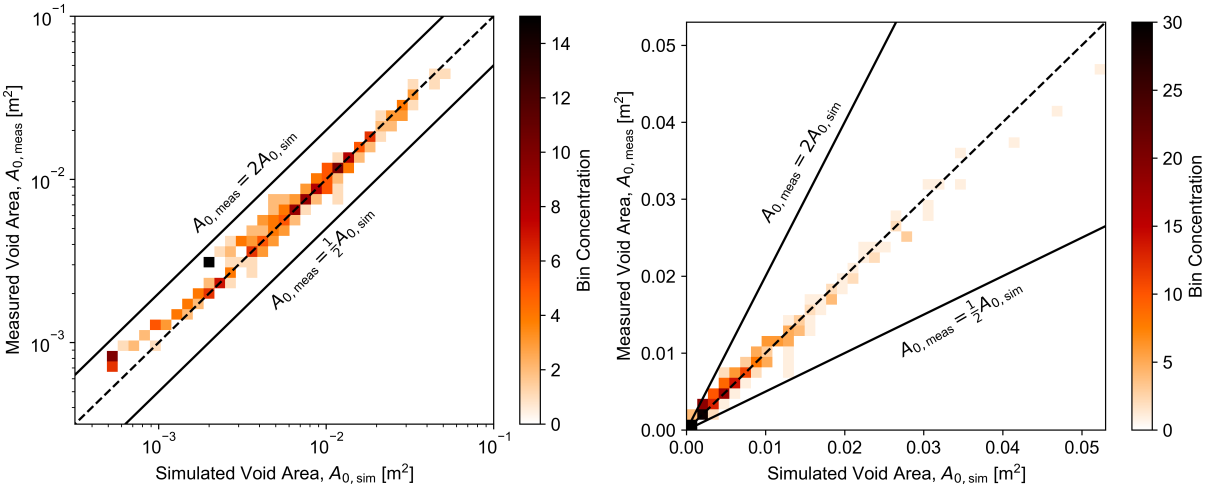


Figure 3.17: Comparison of simulated and measured void area data for $\alpha = 0$ in logarithmic- and linear-scale plots; the dotted line represents perfect agreement and the solid lines delineate the border of regions where measured and simulated void areas differ by a factor greater than two; (a) logarithmic comparison; (b) linear comparison.

Chapter 4

G4-ASPP Development

4.1 Development and Benchmarking of Charged Particle Propagation Methods in G4-ASPP

A new transport tool that simultaneously accounts for the impacts of external electromagnetic fields and bulk shielding material on charged particle dynamics, G4-ASPP, was developed to streamline active radiation shielding assessment and design for spacecraft.[1] Transport simulations were performed to assess accuracy and speed of G4-ASPP particle propagation methods in electromagnetic fields against standard methods. The time-step-based Velocity-Verlet propagation method and an analogous distance-stepping method used in G4-ASPP were derived. The symplecticity and phase-space conservation properties of each method are discussed. Results suggest implementation of a 4th-order Runge-Kutta distance-stepping method into G4-ASPP to improve trajectory accuracy without sacrificing much speed.

4.2 Introduction

Radiation exposure is a limiting factor for human space exploration and operations [78]. The space radiation environment is a harsh carcinogen—teeming with HZE particles—and must be mitigated to ensure safe, successful, and regulation compliant missions [79]. On crewed missions, crew safety is of paramount importance. In extreme cases, incident space radiation can result in loss of crew during the mission, or result

[1] Part of this chapter is an original manuscript [77] of an article published by Taylor & Francis in Journal of Computational and Theoretical Transport on August 3, 2023, available online: https://doi.org/10.1080/23324309.2023.2240578.

in latent health effects [9]. Radiation shielding and protection on space missions has historically focused on passive shielding, where short-range material interactions are exploited to reduce overall crew dose. In certain environments, such as during interplanetary travel outside of low-Earth orbit, adequate protection of the spacecraft is infeasible with passive shielding alone given the mass restrictions associated with spaceflight [80]. Furthermore, additional mass can eventually lead to a decrease in passive shielding effectiveness where secondary particle doses resulting from HZE particle interactions overcome the benefits of shielding lower energy particles [10, 80].

Active radiation shielding methods, an alternative to passive shielding methods, have been and are a current subject of investigation to supplement passive shielding techniques for space radiation protection [25, 27–30, 66, 81]. In active shielding methods, electromagnetic fields are deployed to deflect incoming charged particles away from the spacecraft altogether, prior to material interactions. Active shielding can reduce the particle flux incident on the spacecraft, in turn reducing exposure and risk to crew members. Combined shielding methods incorporate both active and passive shielding methods. In practice, any deployed active shielding system for space exploration purposes will be coupled with the passive shielding provided by the spacecraft and astronauts [82].

Particle transport simulations are necessary for developing optimal spacecraft shielding distributions. Adding external active shielding to a vehicle only further increases the importance of reliable particle transport results. Currently, there are no broadly applicable, publicly available radiation transport codes suitable for combined active and passive radiation shielding analysis. The development of a code dedicated to combined shielding transport (G4-ASPP) is underway and the charged particle propagation methods used for transport through complicated, component-based electromagnetic fields are fully developed, implemented, and complete. One aim of this work is to benchmark the charged particle transport capabilities of G4-ASPP.

4.2.1 ASPP

ASPP is an experimentally-validated charged particle transport code developed and used for rapidly prototyping active shielding configurations [24, 28]. In ASPP, users can specify electromagnetic fields directly, by providing electric and/or magnetic field components at points on a grid, or indirectly, by specifying the positioning and orientation of charged, current-carrying, and/or magnetized objects (active shielding components). The contributions of each field-producing component are superimposed to produce the final

field, computed analytically at particle location $\vec{r}$, at least once per particle step operation, depending on the integration method applied. ASPP propagates particles using the relativistic form of the Lorentz force equation. The governing equations of motion are

$$\frac{\mathrm{d}\vec{p}}{\mathrm{d}t} = q\left(\vec{E} + \vec{v} \times \vec{B}\right), \tag{4.1}$$

and

$$\frac{\mathrm{d}\vec{r}}{\mathrm{d}t} = \vec{v}, \tag{4.2}$$

where $\vec{p}$ is the particle momentum, t is time, q is the particle charge, $\vec{E}$ is the electric field vector, $\vec{v}$ is the particle velocity, $\vec{B}$ is the magnetic field, and $\vec{r}$ is the particle position. ASPP's primary advantage over other charged particle propagation tools, including Geant4 [39], is that ASPP is capable of GPU parallelization/acceleration. This comes at the expense of some features of more traditional Monte Carlo particle transport codes [83–85], such as tracking asynchronous particle interactions within shielding material. By default, ASPP uses the Velocity-Verlet-Time (VVT) method to push particles through space.

4.2.2 Geant4

Geant4, or "**GE**ometry **AN**d **T**racking 4", is a widely utilized radiation transport toolkit for particle transport simulations in detailed geometry [39, 86–89]. Unlike other commonly used Monte Carlo radiation transport codes—like MCNP, PHITS, FLUKA, and others—Geant4 is not a rigid *black box* but a flexible *glass box*, meaning the source code is meant to be visible to the user (but also modifiable, or even *breakable* by a careless developer) [83–85]. Geant4 is written in C++ and allows the user to customize many aspects of the program. In return, Geant4 expects the user to compile executables that accurately carry out the physical processes that the user desires to assess. Geant4 facilitates program development by providing a variety of built-in physical interaction processes and code examples developers can choose from to construct simulations that account for the effects relevant to specific irradiation scenarios. Among these include electromagnetic and hadronic particle interaction models, optical physics models, particle decay models, thermal neutron interaction models, low-energy particle interaction models, etc. The need to simultaneously track short-range particle interactions in passive shielding material and long-range particle interactions with external electromagnetic fields led to the implementation of ASPP charged particle propagation methods in

Geant4 source code. This combination of particle transport programs is called G4-ASPP.

4.2.3 G4-ASPP

G4-ASPP is a radiation transport code built from the Geant4 toolkit that combines the charged particle transport methods and active shielding component specification of ASPP with the built-in capabilities of Geant4. In G4-ASPP, the user can specify passive shielding components with attachable material properties in the form of constructive solid geometry alongside active shielding components. The physical objects that create the active shield are also modeled as solid geometric objects with attachable material properties. The primary difference between ASPP and G4-ASPP charged particle transport through electromagnetic fields is the form of the equations of motion. ASPP makes use of the traditional form of the Lorentz force and velocity in Equations 4.1 and 4.2, where *time* is the discretized variable. G4-ASPP represents the Lorentz force as a spatial (s) derivative of momentum,

$$\frac{\mathrm{d}\vec{\tilde{p}}}{\mathrm{d}s} = \frac{qc}{v}\left(\vec{E} + \vec{v} \times \vec{B}\right), \tag{4.3}$$

where c is the speed of light, ds represents an infinitesimal distance or path length, and $\vec{\tilde{p}} = \vec{p}c$ is the *pseudo-momentum*. Particle positions are updated by way of the relation

$$\frac{\mathrm{d}\vec{r}}{\mathrm{d}s} = \frac{\vec{\tilde{p}}}{\tilde{p}}. \tag{4.4}$$

The equations of motion related to charged particle propagation in Geant4 are treated as functions of s rather than t because most commonly used Geant4 particle transport processes, e.g. particle stopping power, are typically expressed as functions of distance. Computational efficiency and adaptive step size control also contribute to this development choice. Both sets of equations are equally valid and are related by a factor of c/v (note that $\frac{\mathrm{d}t}{\mathrm{d}s} = \frac{1}{v}$). To keep G4-ASPP as consistent with ASPP as possible, a new distance-based version of the Velocity-Verlet method was derived and implemented as the default charged particle propagation mode, called the Momentum-Space-Verlet (VVS) (VVS stands for **V**elocity-**V**erlet-**S**pace) method.

4.2.4 Objectives

The objectives of this work were to

- derive a distance-stepping propagation method analogous to the time-step-based Velocity-Verlet propagation method,
- verify the charged particle propagation capabilities of G4-ASPP in comparison to well-established methods across various electromagnetic field geometries,
- determine the time-integrated relative error of trajectories obtained via different propagation methods with respect to a reference propagation method, and
- assess the relative computational efficiency of each propagation method.

4.3 Mathematical Background

4.3.1 Velocity-Verlet in Time and Space Coordinates

The VVT method is a numerical integration scheme commonly used in particle propagation simulations to generate particle states $(\vec{r}_n, \vec{v}_n)$ (or some surrogate thereof) at a series of time steps t_n. The VVT is simple, stable over a long duration, time-reversible [66, 90], and the default propagation method for ASPP particle transport [24]. The VVT is constructed as follows:

The position $\vec{r}$ and velocity $\vec{v}$ of the particle of interest as a function of time t are desired. The position at time $t + \Delta t$ is expressed as a Taylor expansion of $\vec{r}(t + \Delta t)$ about t,

$$\vec{r}(t + \Delta t) = \vec{r}(t) + \Delta t \frac{\mathrm{d}\vec{r}}{\mathrm{d}t}\bigg|_t + \frac{(\Delta t)^2}{2} \frac{\mathrm{d}^2\vec{r}}{\mathrm{d}t^2}\bigg|_t + \mathcal{O}\Big((\Delta t)^3\Big), \tag{4.5}$$

where Δt is the propagation time step. Noting the usual derivatives of position with respect to time, i.e.,

$$\vec{v} = \frac{\mathrm{d}\vec{r}}{\mathrm{d}t}, \text{ and } \vec{a} = \frac{\mathrm{d}^2\vec{r}}{\mathrm{d}t^2},$$

Equation 4.5 is rewritten as

$$\vec{r}(t + \Delta t) = \vec{r}(t) + \Delta t \vec{v}(t) + \frac{(\Delta t)^2}{2} \vec{a}(t) + \mathcal{O}\Big((\Delta t)^3\Big). \tag{4.6}$$

A Taylor expansion of $\vec{v}(t+\Delta t)$ about t gives

$$\vec{v}(t+\Delta t) = \vec{v}(t) + \Delta t \frac{\mathrm{d}\vec{v}}{\mathrm{d}t}\bigg|_t + \frac{(\Delta t)^2}{2}\frac{\mathrm{d}^2\vec{v}}{\mathrm{d}t^2}\bigg|_t + \mathcal{O}\Big((\Delta t)^3\Big). \tag{4.7}$$

Taking the derivative of Equation 4.7 with respect to t and ignoring 2nd-order-and-higher Δt terms gives

$$\frac{\mathrm{d}\vec{v}}{\mathrm{d}t}\bigg|_{t+\Delta t} = \frac{\mathrm{d}\vec{v}}{\mathrm{d}t}\bigg|_t + \Delta t \frac{\mathrm{d}^2\vec{v}}{\mathrm{d}t^2}\bigg|_t + \mathcal{O}\Big((\Delta t)^2\Big). \tag{4.8}$$

Rearranging to isolate $\frac{\mathrm{d}^2\vec{v}}{\mathrm{d}t^2}$ gives

$$\frac{\mathrm{d}^2\vec{v}}{\mathrm{d}t^2}\bigg|_t = \frac{1}{\Delta t}\left(\frac{\mathrm{d}\vec{v}}{\mathrm{d}t}\bigg|_{t+\Delta t} - \frac{\mathrm{d}\vec{v}}{\mathrm{d}t}\bigg|_t\right) - \frac{1}{\Delta t}\mathcal{O}\Big(\Delta t\Big). \tag{4.9}$$

This expression can be substituted into Equation 4.7 to obtain

$$\vec{v}(t+\Delta t) = \vec{v}(t) + \frac{\Delta t}{2}\Big(\vec{a}(t+\Delta t) + \vec{a}(t)\Big) + \mathcal{O}\Big((\Delta t)^2\Big). \tag{4.10}$$

When $\vec{a}(t+\Delta t)$ is velocity-dependent, $\vec{a}(t+\Delta t)$ must be approximated using the updated position $\vec{r}(t+\Delta t)$ and velocity $\vec{v}(t)$. This has implications in the symplecticity and phase-space volume conservation of the VVT method. The acceleration term computed given the updated position $\vec{r}(t+\Delta t)$ and current velocity $\vec{v}(t)$ is denoted

$$\vec{a}(t+\Delta t) \approx \vec{a}'(t) = \vec{a}(\vec{r}(t+\Delta t), \vec{v}(t)). \tag{4.11}$$

It is important to note that when special relativity is considered, the acceleration term is generally velocity-dependent (the only exception being the case where no external forces $\vec{F}$ are present), i.e.,

$$\vec{a} = \frac{1}{\gamma m_0}\left(\vec{F} - \frac{\vec{v}(\vec{v}\cdot\vec{F})}{c^2}\right). \tag{4.12}$$

A full derivation of the relativistic acceleration equation is given in Section 4.8.

All of the information gleaned from the derivation above can be condensed into a simple format called a

one-step map [91]. The one-step map for the VVT method is given by

$$\Psi_{\text{VVT}} : \begin{cases} \vec{r}_{n+1} = \vec{r}_n + \Delta t \vec{v}_n + \frac{(\Delta t)^2}{2} \vec{a}_n \\ \vec{v}_{n+1} = \vec{v}_n + \frac{\Delta t}{2}(\vec{a}'_n + \vec{a}_n) \end{cases}, \tag{4.13}$$

where

$$\vec{r}_n = \vec{r}(t_n), \tag{4.14}$$

$$\vec{v}_n = \vec{v}(t_n), \tag{4.15}$$

$$\vec{a}_n = \vec{a}(\vec{r}(t_n), \vec{v}(t_n)), \tag{4.16}$$

$$\vec{a}'_n = \vec{a}(\vec{r}(t_{n+1}), \vec{v}(t_n)), \tag{4.17}$$

and

$$t_n = n\Delta t. \tag{4.18}$$

ASPP uses the VVT method to propagate particles through electromagnetic fields by default. The VVT is a *time-stepping* integration method. G4-ASPP, built using the Geant4 toolkit, propagates particles through electromagnetic fields via an adaptive *distance-stepping* method, where many small steps of length Δs are taken to trace the particle's trajectory.

In order to properly compare the particle propagation results between ASPP propagation methods, like the VVT, and G4-ASPP propagation methods, a particle propagation method analogous to the VVT method, the VVS method, was derived in terms of $\vec{r}(s)$ and $\vec{\tilde{p}}(s)$, the position and pseudo-momentum as a function of distance parameter s. Again, the position at distance $s + \Delta s$ is expressed as a Taylor expansion of $\vec{r}(s + \Delta s)$ about s,

$$\vec{r}(s + \Delta s) = \vec{r}(s) + \Delta s \frac{\mathrm{d}\vec{r}}{\mathrm{d}s}\bigg|_s + \frac{(\Delta s)^2}{2} \frac{\mathrm{d}^2\vec{r}}{\mathrm{d}s^2}\bigg|_s + \mathcal{O}\Big((\Delta s)^3\Big). \tag{4.19}$$

Note that

$$\frac{\mathrm{d}\vec{r}}{\mathrm{d}s} = \frac{\mathrm{d}\vec{r}}{\mathrm{d}t}\frac{\mathrm{d}t}{\mathrm{d}s} = \frac{\vec{v}}{v} = \frac{\vec{\tilde{p}}}{\tilde{p}}, \tag{4.20}$$

and

$$\frac{\mathrm{d}^2\vec{r}}{\mathrm{d}s^2} = \frac{\mathrm{d}}{\mathrm{d}s}\left(\frac{\mathrm{d}\vec{r}}{\mathrm{d}s}\right) = \frac{\mathrm{d}}{\mathrm{d}s}\left(\frac{\vec{\tilde{p}}}{\tilde{p}}\right) = \frac{1}{\tilde{p}}\left(\frac{\mathrm{d}\vec{\tilde{p}}}{\mathrm{d}s} - \frac{\vec{\tilde{p}}}{\tilde{p}}\frac{\mathrm{d}\tilde{p}}{\mathrm{d}s}\right). \tag{4.21}$$

The terms $\frac{\mathrm{d}\vec{\tilde{p}}}{\mathrm{d}s}$ and $\frac{\mathrm{d}\tilde{p}}{\mathrm{d}s}$ are calculable and directly related to the force $\vec{F}$ acting on the particle. $\frac{\mathrm{d}\vec{\tilde{p}}}{\mathrm{d}s}$ is given by

$$\frac{\mathrm{d}\vec{\tilde{p}}}{\mathrm{d}s} = c\frac{\mathrm{d}\vec{p}}{\mathrm{d}t}\frac{\mathrm{d}t}{\mathrm{d}s} = \frac{c}{v}\vec{F} = \frac{U}{\tilde{p}}\vec{F}, \tag{4.22}$$

where U is the sum of the particle rest mass energy $\tilde{m}_0$ and the kinetic energy T,

$$U = \tilde{m}_0 + T, \tag{4.23}$$

which can be expressed in terms of $\tilde{p}$ as

$$U = \sqrt{\tilde{m}_0^2 + \tilde{p}^2}. \tag{4.24}$$

$\frac{\mathrm{d}\tilde{p}}{\mathrm{d}s}$ is given by

$$\frac{\mathrm{d}\tilde{p}}{\mathrm{d}s} = \frac{\vec{\tilde{p}}}{\tilde{p}} \cdot \frac{\mathrm{d}\vec{\tilde{p}}}{\mathrm{d}s} = \frac{U}{\tilde{p}^2}(\vec{\tilde{p}} \cdot \vec{F}). \tag{4.25}$$

The position update equation is now

$$\vec{r}(s + \Delta s) \approx \vec{r}(s) + \Delta s\frac{\vec{\tilde{p}}(s)}{\tilde{p}(s)} + \frac{(\Delta s)^2}{2\tilde{p}(s)}\left(\frac{\mathrm{d}\vec{\tilde{p}}}{\mathrm{d}s}\bigg|_s - \frac{\vec{\tilde{p}}}{\tilde{p}}\frac{\mathrm{d}\tilde{p}}{\mathrm{d}s}\bigg|_s\right) \tag{4.26}$$

A Taylor expansion of $\vec{\tilde{p}}(s + \Delta s)$ about s gives

$$\vec{\tilde{p}}(s + \Delta s) = \vec{\tilde{p}}(s) + \Delta s\frac{\mathrm{d}\vec{\tilde{p}}}{\mathrm{d}s}\bigg|_s + \frac{(\Delta s)^2}{2}\frac{\mathrm{d}^2\vec{\tilde{p}}}{\mathrm{d}s^2}\bigg|_s + \mathcal{O}\Big((\Delta s)^3\Big). \tag{4.27}$$

Taking the derivative of Equation 4.27 with respect to s and ignoring 2nd-order-and-above Δs terms gives

$$\frac{\mathrm{d}\vec{\tilde{p}}}{\mathrm{d}s}\bigg|_{s+\Delta s} = \frac{\mathrm{d}\vec{\tilde{p}}}{\mathrm{d}s}\bigg|_s + \Delta s\frac{\mathrm{d}^2\vec{\tilde{p}}}{\mathrm{d}s^2}\bigg|_s + \mathcal{O}\Big(\Delta s\Big). \tag{4.28}$$

Rearranging to isolate $\frac{\mathrm{d}^2\vec{\tilde{p}}}{\mathrm{d}s^2}$ gives

$$\frac{\mathrm{d}^2\vec{\tilde{p}}}{\mathrm{d}s^2} = \frac{1}{\Delta s}\left(\frac{\mathrm{d}\vec{\tilde{p}}}{\mathrm{d}s}\bigg|_{s+\Delta s} - \frac{\mathrm{d}\vec{\tilde{p}}}{\mathrm{d}s}\bigg|_s\right) - \frac{1}{\Delta s}\mathcal{O}\Big(\Delta s\Big). \tag{4.29}$$

This expression can be substituted into Equation 4.27 to obtain

$$\vec{\tilde{p}}(s + \Delta s) = \vec{\tilde{p}}(s) + \frac{\Delta s}{2}\left(\frac{\mathrm{d}\vec{\tilde{p}}}{\mathrm{d}s}\bigg|_s + \frac{\mathrm{d}\vec{\tilde{p}}}{\mathrm{d}s}\bigg|_{s+\Delta s}\right) + \mathcal{O}\Big((\Delta s)^2\Big). \tag{4.30}$$

Similar to the $\vec{a}(t+\Delta t)$ term discussed earlier, when $\left.\frac{\mathrm{d}\vec{\tilde{p}}}{\mathrm{d}s}\right|_{s+\Delta s}$ depends on the pseudo-momentum, it must be approximated using the updated position $\vec{r}(s+\Delta s)$ and the pseudo-momentum $\vec{\tilde{p}}(s)$. Again, this has implications for the symplecticity and phase-space volume conservation of the VVS method. The pseudo-momentum derivative with respect to s at distance $s+\Delta s$, computed using $\vec{r}(s+\Delta s)$ and $\vec{\tilde{p}}(s)$, is approximated via

$$\left.\frac{\mathrm{d}\vec{\tilde{p}}}{\mathrm{d}s}\right|_{s+\Delta s} \approx \left(\left.\frac{\mathrm{d}\vec{\tilde{p}}}{\mathrm{d}s}\right|_{s}\right)' = \left.\frac{\mathrm{d}\vec{\tilde{p}}}{\mathrm{d}s}\right|_{\vec{r}(s+\Delta s),\vec{\tilde{p}}(s)}. \tag{4.31}$$

The results of the preceding derivation are summarized in the one-step map Ψ_{VVS},

$$\Psi_{\mathrm{VVS}}: \begin{cases} \vec{r}_{n+1} = \vec{r}_n + \Delta s \frac{\vec{\tilde{p}}_n}{\tilde{p}_n} + \frac{(\Delta s)^2}{2\tilde{p}_n}\left[\left(\frac{\mathrm{d}\vec{\tilde{p}}}{\mathrm{d}s}\right)_n - \frac{\vec{\tilde{p}}_n}{\tilde{p}_n}\left(\frac{\mathrm{d}\tilde{p}}{\mathrm{d}s}\right)_n\right] \\ \vec{\tilde{p}}_{n+1} = \vec{\tilde{p}} + \frac{\Delta s}{2}\left[\left(\frac{\mathrm{d}\vec{\tilde{p}}}{\mathrm{d}s}\right)_n + \left(\frac{\mathrm{d}\vec{\tilde{p}}}{\mathrm{d}s}\right)'_n\right] \end{cases} \tag{4.32}$$

where

$$\vec{r}_n = \vec{r}(s_n), \tag{4.33}$$

$$\vec{\tilde{p}}_n = \vec{\tilde{p}}(s_n), \tag{4.34}$$

$$\left(\frac{\mathrm{d}\vec{\tilde{p}}}{\mathrm{d}s}\right)_n = \left.\frac{\mathrm{d}\vec{\tilde{p}}}{\mathrm{d}s}\right|_{s_n}, \tag{4.35}$$

$$\left(\frac{\mathrm{d}\vec{\tilde{p}}}{\mathrm{d}s}\right)'_n = \left.\frac{\mathrm{d}\vec{\tilde{p}}}{\mathrm{d}s}\right|_{\vec{r}(s_{n+1}),\vec{\tilde{p}}(s_n)}, \tag{4.36}$$

$$\left(\frac{\mathrm{d}\tilde{p}}{\mathrm{d}s}\right)_n = \left.\frac{\mathrm{d}\tilde{p}}{\mathrm{d}s}\right|_{s_n}, \tag{4.37}$$

and

$$s_n = n\Delta s. \tag{4.38}$$

4.3.2 Integrator Symplecticity and Phase-Space Preservation

The properties of *symplectic integrators* are desirable for particle transport in electromagnetic fields. In symplectic integrators, the Hamiltonian,

$$\mathcal{H} = V + T, \tag{4.39}$$

or the sum of potential energy V and kinetic energy T of a system, is conserved (or approximately conserved) throughout the simulation. Symplectic integrators are especially useful for extended particle simu-

lations where particles are tracked over long distances and time-scales because the error in particle energy is bounded by nature of the propagation method [91]. The phase-space volume is also preserved by symplectic integrators [91, 92].

Define a one-step map, say Ψ, that maps the particle state at step n, $S_n \equiv (\vec{r}_n, \vec{v}_n)$ to the particle state at step $n+1$, $S_{n+1} \equiv (\vec{r}_{n+1}, \vec{v}_{n+1})$, as

$$\Psi : S_n \to S_{n+1}. \tag{4.40}$$

The Jacobian of the $(n+1)$-th state with respect to the n-th state, $\frac{\partial S_{n+1}}{\partial S_n}$ is used to determine both symplecticity and phase-space preservation of the stepping algorithm [91]. This Jacobian is written explicitly as a matrix of Jacobians,

$$\frac{\partial S_{n+1}}{\partial S_n} = \begin{bmatrix} \frac{\partial \vec{r}_{n+1}}{\partial \vec{r}_n} & \frac{\partial \vec{r}_{n+1}}{\partial \vec{v}_n} \\ \frac{\partial \vec{v}_{n+1}}{\partial \vec{r}_n} & \frac{\partial \vec{v}_{n+1}}{\partial \vec{v}_n} \end{bmatrix}. \tag{4.41}$$

Note that a Jacobian expression $\frac{\partial \vec{a}}{\partial \vec{b}}$ where $\vec{f} = \langle f_x, f_y, f_z \rangle$ and $\vec{g} = \langle g_1, g_2, g_3 \rangle$, is explicitly written as

$$\frac{\partial \vec{f}}{\partial \vec{g}} = \begin{bmatrix} \frac{\partial f_x}{\partial g_1} & \frac{\partial f_x}{\partial g_2} & \frac{\partial f_x}{\partial g_3} \\ \frac{\partial f_y}{\partial g_1} & \frac{\partial f_y}{\partial g_2} & \frac{\partial f_y}{\partial g_3} \\ \frac{\partial f_z}{\partial g_1} & \frac{\partial f_z}{\partial g_2} & \frac{\partial f_z}{\partial g_3} \end{bmatrix}. \tag{4.42}$$

The condition for symplecticity [91] is

$$\left(\frac{\partial S_{n+1}}{\partial S_n}\right)^{\mathrm{T}} \begin{bmatrix} 0 & \mathbf{I} \\ -\mathbf{I} & 0 \end{bmatrix} \left(\frac{\partial S_{n+1}}{\partial S_n}\right) = \begin{bmatrix} 0 & \mathbf{I} \\ -\mathbf{I} & 0 \end{bmatrix}. \tag{4.43}$$

Phase-space preservation is confirmed if the determinant of the Jacobian is equal to unity,

$$\left|\frac{\partial S_{n+1}}{\partial S_n}\right| = 1. \tag{4.44}$$

For illustration, recall the one-step map developed in Section 4.3.1 for the Velocity-Verlet integration method in time coordinates, Ψ_{VVT}. It is well-known that the Velocity-Verlet integration method is symplectic when the acceleration depends only on particle position [63]. It will be shown a) *why* this integration method is *not* symplectic for velocity-dependent forces, b) that this integration method *is* symplectic for position-dependent forces, and c) that this integration method does *not* strictly conserve phase-space, though it does

so approximately. The Jacobian associated with Ψ_{VVT} is given by

$$\frac{\partial S_{n+1}}{\partial S_n} = \begin{bmatrix} \frac{\partial \vec{r}_{n+1}}{\partial \vec{r}_n} & \frac{\partial \vec{r}_{n+1}}{\partial \vec{v}_n} \\ \frac{\partial \vec{v}_{n+1}}{\partial \vec{r}_n} & \frac{\partial \vec{v}_{n+1}}{\partial \vec{v}_n} \end{bmatrix} = \begin{bmatrix} \mathbf{I} + \Delta t \frac{\partial \vec{v}_n}{\partial \vec{r}_n} + \frac{(\Delta t)^2}{2} \frac{\partial \vec{a}_n}{\partial \vec{r}_n} & \frac{\partial \vec{r}_n}{\partial \vec{v}_n} + \Delta t \mathbf{I} + \frac{(\Delta t)^2}{2} \frac{\partial \vec{a}_n}{\partial \vec{v}_n} \\ \frac{\partial \vec{v}_n}{\partial \vec{r}_n} + \frac{\Delta t}{2} \left(\frac{\partial \vec{a}'_n}{\partial \vec{r}_n} + \frac{\partial \vec{a}_n}{\partial \vec{r}_n} \right) & \mathbf{I} + \frac{\Delta t}{2} \left(\frac{\partial \vec{a}'_n}{\partial \vec{v}_n} + \frac{\partial \vec{a}_n}{\partial \vec{v}_n} \right) \end{bmatrix}. \tag{4.45}$$

Note that, without losing generality,

$$\frac{\partial \vec{r}_n}{\partial \vec{v}_n} = 0, \ \frac{\partial \vec{v}_n}{\partial \vec{r}_n} = 0, \text{ and } \frac{\partial \vec{a}'_n}{\partial \vec{r}_n} = 0.$$

After rewriting,

$$\frac{\partial S_{n+1}}{\partial S_n} = \begin{bmatrix} \mathbf{I} + \frac{(\Delta t)^2}{2} \frac{\partial \vec{a}_n}{\partial \vec{r}_n} & \Delta t \mathbf{I} + \frac{(\Delta t)^2}{2} \frac{\partial \vec{a}_n}{\partial \vec{v}_n} \\ \frac{\Delta t}{2} \frac{\partial \vec{a}_n}{\partial \vec{r}_n} & \mathbf{I} + \frac{\Delta t}{2} \left(\frac{\partial \vec{a}'_n}{\partial \vec{v}_n} + \frac{\partial \vec{a}_n}{\partial \vec{v}_n} \right) \end{bmatrix}. \tag{4.46}$$

Evaluating the left-hand side of Equation 4.43, it follows that

$$LHS_{4.43} = \begin{bmatrix} 0 & \mathbf{I} + \frac{\Delta t}{2} \left(\frac{\partial \vec{a}'_n}{\partial \vec{v}_n} + \frac{\partial \vec{a}_n}{\partial \vec{v}_n} \right) + \frac{(\Delta t)^3}{4} \frac{\partial \vec{a}_n}{\partial \vec{r}_n} \frac{\partial \vec{a}'_n}{\partial \vec{v}_n} \\ -\mathbf{I} - \frac{\Delta t}{2} \left(\frac{\partial \vec{a}'_n}{\partial \vec{v}_n} + \frac{\partial \vec{a}_n}{\partial \vec{v}_n} \right) - \frac{(\Delta t)^3}{4} \frac{\partial \vec{a}'_n}{\partial \vec{v}_n} \frac{\partial \vec{a}_n}{\partial \vec{r}_n} & \frac{(\Delta t)^3}{4} \left(\frac{\partial \vec{a}_n}{\partial \vec{v}_n} \frac{\partial \vec{a}'_n}{\partial \vec{v}_n} - \frac{\partial \vec{a}'_n}{\partial \vec{v}_n} \frac{\partial \vec{a}_n}{\partial \vec{v}_n} \right) \end{bmatrix}. \tag{4.47}$$

In general, $LHS_{4.43} \neq \begin{bmatrix} 0 & \mathbf{I} \\ -\mathbf{I} & 0 \end{bmatrix}$, and thus, the VVT method, as currently described, is *not* symplectic. The phase-space volume is also generally *not* preserved. However, for velocity-independent acceleration functions (i.e., velocity-independent *forces*),

$$\frac{\partial \vec{a}_n}{\partial \vec{v}_n} = \frac{\partial \vec{a}'_n}{\partial \vec{v}_n} = 0,$$

and under this condition, $LHS_{4.43} = \begin{bmatrix} 0 & \mathbf{I} \\ -\mathbf{I} & 0 \end{bmatrix}$, and the VVT method *is* symplectic. Under this same condition, it is also easily shown that the VVT preserves phase-space volume, as

$$\left| \frac{\partial S_{n+1}}{\partial S_n} \right| = \begin{vmatrix} \mathbf{I} + \frac{(\Delta t)^2}{2} \frac{\partial \vec{a}_n}{\partial \vec{r}_n} & \Delta t \mathbf{I} \\ \frac{\Delta t}{2} \frac{\partial \vec{a}_n}{\partial \vec{r}_n} & \mathbf{I} \end{vmatrix} = \left| \mathbf{I} + \frac{(\Delta t)^2}{2} \frac{\partial \vec{a}_n}{\partial \vec{r}_n} - (\Delta t \mathbf{I})(\mathbf{I})^{-1} \frac{\Delta t}{2} \frac{\partial \vec{a}_n}{\partial \vec{r}_n} \right| \left| \mathbf{I} \right| = 1. \tag{4.48}$$

Now, contrast this with the VVS method. The Jacobian associated with Ψ_{VVS} is given by

$$\frac{\partial S_{n+1}}{\partial S_n} = \begin{bmatrix} \mathbf{I} + \frac{(\Delta s)^2}{2\tilde{p}_n}\left(\frac{\partial \vec{k}_n}{\partial \vec{r}_n} - \frac{\vec{p}_n}{\tilde{p}_n}\frac{\partial k_n}{\partial \vec{r}_n}\right) & \frac{\Delta s}{\tilde{p}_n}\left(\mathbf{I} - \vec{\Omega}_n \otimes \vec{\Omega}_n\right) - \frac{(\Delta s)^2}{2\tilde{p}_n}\left(\frac{\vec{\Omega}_n \otimes \vec{k}_n}{\tilde{p}_n} + \frac{\partial \vec{k}_n}{\partial \vec{p}_n} - \mathbf{I}\frac{k_n}{\tilde{p}_n} - \vec{\Omega} \otimes \frac{\partial k_n}{\partial \vec{p}_n}\right) \\ \frac{\Delta s}{2}\left(\frac{\partial \vec{k}_n}{\partial \vec{r}_n} + \frac{\partial \vec{k}'_n}{\partial \vec{r}_n}\right) & \mathbf{I} + \frac{\Delta s}{2}\left(\frac{\partial \vec{k}_n}{\partial \vec{p}_n} + \frac{\partial \vec{k}'_n}{\partial \vec{p}_n}\right) \end{bmatrix}, \tag{4.49}$$

where

$$\vec{k}_n = \left(\frac{\partial \vec{p}}{\partial s}\right)_n, \tag{4.50}$$

and $\otimes$ represents an outer product of two 3-vectors (resulting in a 3×3 matrix). Using a similar treatment as applied to the VVT method, it can be shown that the Jacobian associated with the VVS method satisfies neither the symplecticity definition (Equation 4.43) nor the phase-space volume conservation condition (Equation 4.44) in general. Additionally, even when forces are velocity-independent, the VVS remains *non*-symplectic and does *not* conserve phase-space volume. Symplectic integrators are desirable because they tend to be more accurate over long integration times than non-symplectic integrators, and thus can replicate real-world phenomena without drift, such as the periodic orbit of a planet around a star, or the cyclical nature of a charged particle moving in a magnetic field. Phase-space conservation is a desirable property for an integrator because it is often associated with time reversibility, which is a necessary (but not sufficient) condition for a system to be energy-conserving [93]. Differences between the VVT and VVS method results, alongside the adaptive step size VVS method implemented in G4-ASPP, a 4th-order Runge-Kutta integration method, an Euler integration method, and the Boris integration method, will be compared in terms of *trajectory accuracy*, *energy conservation*, and *computational time*.

4.4 Materials and Methods

4.4.1 Propagation Methods

In this section, all charged particle propagation methods used for comparison purposes, except for the previously-described VVT and VVS, are briefly described. Table 4.1 summarizes all propagation methods discussed.

Table 4.1: List of propagation methods considered for comparison.

Propagation Method	Abbreviation	Global Error (Position)	Global Error (Velocity/Pseudo-momentum)
Restricted Step Length, G4	G4RS	$\mathcal{O}\left((\Delta s)^2\right)$	$\mathcal{O}\left(\Delta s\right)$
Unrestricted Step Length, G4	G4US	$\mathcal{O}\left((\Delta s)^2\right)$	$\mathcal{O}\left(\Delta s\right)$
Boris (Time)	BT	$\mathcal{O}\left((\Delta t)^2\right)$	$\mathcal{O}\left((\Delta t)^2\right)$
Velocity Verlet (Time)	VVT	$\mathcal{O}\left((\Delta t)^2\right)$	$\mathcal{O}\left(\Delta t\right)$
Velocity Verlet (Distance)	VVS	$\mathcal{O}\left((\Delta s)^2\right)$	$\mathcal{O}\left(\Delta s\right)$
4th-order Runge-Kutta (Distance)	RK4S	$\mathcal{O}\left((\Delta s)^4\right)$	$\mathcal{O}\left((\Delta s)^3\right)$
Euler (Distance)	ES	$\mathcal{O}\left(\Delta s\right)$	$\mathcal{O}\left(\Delta s\right)$
Semi-Analytical (Time)	SAT	$\mathcal{O}\left(\Delta t\right)$	Exact

4.4.1.1 Semi-Analytical Propagation Method for Uniform Electric Field

In general, it is not possible to determine the analytical trajectory of a charged particle influenced by an electromagnetic field when considering relativistic effects. Consider the simplest possible case, where $\vec{E}$ is a uniform electric field and the magnetic field is zero. Starting from Equations 4.1 and 4.2, the exact momentum is obtained by integrating Equation 4.1 directly from initial time t_0 to current time t,

$$\int_{t_0}^{t} \frac{\mathrm{d}\vec{p}}{\mathrm{d}t'} dt' = \int_{t_0}^{t} q\vec{E} dt' \Rightarrow \vec{p}(t) = \vec{p}(t_0) + (t - t_0) q\vec{E}.$$

This equation leads to the position-momentum relation,

$$\frac{\mathrm{d}\vec{r}}{\mathrm{d}t} = \frac{\vec{p}(t)c^2}{\gamma(t)\tilde{m}_0} = \frac{\vec{p}(t)c^2}{\sqrt{\tilde{m}_0^2 + (p(t)c)^2}} = c^2 \frac{\vec{p}(t_0) + (t - t_0)q\vec{E}}{\sqrt{\tilde{m}_0^2 + |\vec{p}(t_0) + (t - t_0)q\vec{E}|^2 c^2}}.$$

There are no closed-form expressions for the integral over t of this expression, so an analytical solution to the particle trajectory at this level of generality does not exist when relativistic effects are considered. A "semi-analytical" solution for $\vec{r}(t)$ can be obtained via a number of numerical integration methods, e.g., a simple Euler scheme,

$$\vec{r}(t) = \vec{r}(t_0) + \sum_{n=0}^{N} \Delta t \left.\frac{\mathrm{d}\vec{r}}{\mathrm{d}t}\right|_{t_n}, \tag{4.51}$$

where $\left.\frac{\mathrm{d}\vec{r}}{\mathrm{d}t}\right|_{t_n}$ is exact. The semi-analytical time-stepping method (Semi-Analytical (Time) (SAT)) described here will be utilized only for test case 1, in which a uniform electric field is applied. It will also be used to justify the use of the Boris method as the "reference propagation method" for other test cases.

4.4.1.2 Boris Algorithm

The Boris propagation algorithm is well-known for its accuracy in long-term charged particle simulations in electromagnetic fields despite its non-symplecticity [91, 94]. The popularity of the Boris algorithm for conducting electromagnetic charged particle propagation simulations persists because it requires only one force evaluation per time step, it is second-order accurate in position and velocity, and has a tendency to preserve conserved quantities. It is typically cited as the accepted standard numerical integration method for charged particle propagation in electromagnetic fields [91, 94–96]. Given initial position $\vec{r}_n$, velocity $\vec{u}_n = \gamma_n \vec{v}_n$, and step length Δt, the Boris algorithm is carried out as follows:

$$\Psi_{\mathrm{BT}}: \begin{cases} \vec{r}_{n+1/2} = \vec{r}_n + \frac{\Delta t \vec{u}_n}{2\gamma_n} \\ \vec{u}^- = \vec{u}_n + \frac{q\vec{E}_{n+1/2}}{2m_0} \\ \vec{t} = \tan\left(\frac{q\Delta t B_{n+1/2}}{2m_0\gamma_n}\right)\frac{\vec{B}_{n+1/2}}{B_{n+1/2}} \\ \vec{u}' = \vec{u}^- + \vec{u}^- \times \vec{t} \\ \vec{u}^+ = \vec{u}^- + \frac{2\vec{u}'\times\vec{t}}{1+\vec{t}^2} \\ \vec{u}_{n+1} = \vec{u}^+ + \frac{q\vec{E}_{n+1/2}}{2m_0} \\ \vec{r}_{n+1} = \vec{r}_{n+1/2} + \frac{\Delta t \vec{u}_{n+1}}{2\gamma_{n+1}} \end{cases} . \tag{4.52}$$

4.4.1.3 4th-order Runge-Kutta

A 4th-order Runge-Kutta distance-stepping algorithm (4th Order Runge-Kutta (Space) (RK4S)) was considered. Equation 4.53 details the method. 4th-order Runge-Kutta is a staple numerical method for solving ordinary differential equations, and its popularity stems from its ease of implementation, numerical stability, and lack of a requirement for high-order derivatives to achieve high-order accuracy.

$$\Psi_{\text{RK4S}}: \begin{cases} \left(\frac{\mathrm{d}\vec{r}}{\mathrm{d}s}\right)_1 = \frac{\vec{\tilde{p}}_n}{\tilde{p}_n} \\ \left(\frac{\mathrm{d}\vec{\tilde{p}}}{\mathrm{d}s}\right)_1 = \frac{qU_n}{\tilde{p}_n}\left(\vec{E}_n + \frac{c\vec{\tilde{p}}_n}{U_n} \times \vec{B}_n\right) \\ \vec{r}_1 = \vec{r}_n + \frac{\Delta s}{2}\left(\frac{\mathrm{d}\vec{r}}{\mathrm{d}s}\right)_1 \\ \vec{\tilde{p}}_1 = \vec{\tilde{p}}_n + \frac{\Delta s}{2}\left(\frac{\mathrm{d}\vec{\tilde{p}}}{\mathrm{d}s}\right)_1 \\ \left(\frac{\mathrm{d}\vec{r}}{\mathrm{d}s}\right)_2 = \frac{\vec{\tilde{p}}_1}{\tilde{p}_1} \\ \left(\frac{\mathrm{d}\vec{\tilde{p}}}{\mathrm{d}s}\right)_2 = \frac{qU_1}{\tilde{p}_1}\left(\vec{E}_1 + \frac{c\vec{\tilde{p}}_1}{U_1} \times \vec{B}_1\right) \\ \vec{r}_2 = \vec{r}_1 + \frac{\Delta s}{2}\left(\frac{\mathrm{d}\vec{r}}{\mathrm{d}s}\right)_2 \\ \vec{\tilde{p}}_2 = \vec{\tilde{p}}_n + \frac{\Delta s}{2}\left(\frac{\mathrm{d}\vec{\tilde{p}}}{\mathrm{d}s}\right)_2 \\ \left(\frac{\mathrm{d}\vec{r}}{\mathrm{d}s}\right)_3 = \frac{\vec{\tilde{p}}_2}{\tilde{p}_2} \\ \left(\frac{\mathrm{d}\vec{\tilde{p}}}{\mathrm{d}s}\right)_3 = \frac{qU_2}{\tilde{p}_2}\left(\vec{E}_2 + \frac{c\vec{\tilde{p}}_2}{U_2} \times \vec{B}_2\right) \\ \vec{r}_3 = \vec{r}_n + \Delta s\left(\frac{\mathrm{d}\vec{r}}{\mathrm{d}s}\right)_3 \\ \vec{\tilde{p}}_3 = \vec{\tilde{p}}_n + \Delta s\left(\frac{\mathrm{d}\vec{\tilde{p}}}{\mathrm{d}s}\right)_3 \\ \left(\frac{\mathrm{d}\vec{r}}{\mathrm{d}s}\right)_4 = \frac{\vec{\tilde{p}}_3}{\tilde{p}_3} \\ \left(\frac{\mathrm{d}\vec{\tilde{p}}}{\mathrm{d}s}\right)_4 = \frac{qU_3}{\tilde{p}_3}\left(\vec{E}_3 + \frac{c\vec{\tilde{p}}_3}{U_3} \times \vec{B}_3\right) \\ \vec{r}_{n+1} = \vec{r}_n + \frac{\Delta s}{6}\left[\left(\frac{\mathrm{d}\vec{r}}{\mathrm{d}s}\right)_1 + 2\left(\frac{\mathrm{d}\vec{r}}{\mathrm{d}s}\right)_2 + 2\left(\frac{\mathrm{d}\vec{r}}{\mathrm{d}s}\right)_3 + \left(\frac{\mathrm{d}\vec{r}}{\mathrm{d}s}\right)_4\right] \\ \vec{\tilde{p}}_{n+1} = \vec{\tilde{p}}_n + \frac{\Delta s}{6}\left[\left(\frac{\mathrm{d}\vec{\tilde{p}}}{\mathrm{d}s}\right)_1 + 2\left(\frac{\mathrm{d}\vec{\tilde{p}}}{\mathrm{d}s}\right)_2 + 2\left(\frac{\mathrm{d}\vec{\tilde{p}}}{\mathrm{d}s}\right)_3 + \left(\frac{\mathrm{d}\vec{\tilde{p}}}{\mathrm{d}s}\right)_4\right] \end{cases} \tag{4.53}$$

4.4.1.4 Euler Algorithm

The Euler method is the most basic of all numerical integration methods and is not particularly reliable. However, it is useful to observe the complexity necessary to adequately track particles through different types of electromagnetic fields. The Euler integration scheme is implemented as follows, given initial position $\vec{r}_n$, pseudo-momentum $\vec{\tilde{p}}_n$, and distance step Δs,

$$\Psi_{\text{ES}}: \begin{cases} \vec{r}_{n+1} = \vec{r}_n + \Delta s \frac{\vec{\tilde{p}}_n}{\tilde{p}_n} \\ \vec{\tilde{p}}_{n+1} = \vec{\tilde{p}}_n + \Delta s \frac{qU_n}{\tilde{p}_n}\left(\vec{E}_n + \frac{c\vec{\tilde{p}}_n}{U_n} \times \vec{B}_n\right) \end{cases} . \tag{4.54}$$

4.4.1.5 Geant4 Restricted and Unrestricted Stepping Methods

Geant4 is a general-purpose Monte Carlo particle transport toolkit with the capability of simulating charged particle transport in electromagnetic fields, though some aspects of the functionality are implemented by the user. In this case, the VVS method was implemented into Geant4's particle propagation scheme. Significant differences arise between the VVS method described and the VVS method incorporated in Geant4 because Geant4 has a default *adaptive* distance-stepping method implemented. This adaptive method is quite complex and is under-described in Geant4 documentation. A high-level description of the Geant4 adaptive step size method are included in Section 4.7. Generically, the one-step map for the Geant4 VVS method is given by

$$\Psi_{\text{G4*S}} : \begin{cases} \Delta s_n = f(\vec{r}_n, \tilde{\vec{p}}_n, \vec{E}_n, \vec{B}_n, \text{geometry}) \\ \vec{r}_{n+1} = \vec{r}_n + \Delta s_n \frac{\tilde{\vec{p}}_n}{\tilde{p}_n} + \frac{(\Delta s_n)^2}{2\tilde{p}_n} \left[\left(\frac{\mathrm{d}\vec{p}}{\mathrm{d}s} \right)_n - \frac{\tilde{\vec{p}}_n}{\tilde{p}_n} \left(\frac{\mathrm{d}\tilde{p}}{\mathrm{d}s} \right)_n \right] \\ \tilde{\vec{p}}_{n+1} = \tilde{\vec{p}} + \frac{\Delta s_n}{2} \left[\left(\frac{\mathrm{d}\vec{p}}{\mathrm{d}s} \right)_n + \left(\frac{\mathrm{d}\vec{p}}{\mathrm{d}s} \right)'_n \right] \end{cases} . \tag{4.55}$$

Here, the function f denotes the process by which the step size is determined for each step. This process is dependent on many parameters, including the cell geometry specified by the user. A flow chart of the process for determining Δs_n is given in Section 4.7. There are two variations of this method included in this work, *restricted* and *unrestricted*. The difference is that the *restricted* version sets the maximum step size as

$$\Delta s_{\max} = c\Delta t, \tag{4.56}$$

where, in this study, $\Delta t = 1 \times 10^{-10}$ s, and the *unrestricted* version removes this limitation by ensuring that the maximum step size is

$$\Delta s_{\max} = \mathcal{D}_{\max}, \tag{4.57}$$

where $\mathcal{D}_{\max}$ is the largest double precision number representable in C++.

4.4.2 Test Cases

Six test cases were evaluated to assess G4-ASPP's ability to properly propagate particles through electromagnetic fields. The parameters that define each test case are summarized in Table 4.2. The details of each

test were selected so as to avoid numerical instabilities. Some properties are common among the test cases. The test particle is always a proton with charge $+e$ and mass m_p. The entire volume is specified as a vacuum for the non-Geant4 propagators. In Geant4, implementing a *perfect* vacuum causes computational issues, so the "vacuum" material in Geant4 is approximated as a "galactic" material—highly-diffuse hydrogen in a micro-pressure, near-absolute zero temperature environment, which is an even more accurate representation of the deep-space environment. Specifically, the pressure is $3 \times 10^{-18}\,\mathrm{Pa}$, the density is $1 \times 10^{-25}\,\mathrm{g\,cm^{-3}}$, and the temperature is $2.73\,\mathrm{K}$ [39]. Even in cases where physical active shielding components *are* specified, the interior of the volumes are still specified as this "galactic" material.

Table 4.2: Condensed list of test cases.

Case	Description	Parameters	Initial Location, $\vec{r}_0$ [m]	Initial Direction, $\vec{\Omega}_0$	Initial Kinetic Energy, T_0 [MeV]
1	Uniform $\vec{E}$	$\frac{2}{\sqrt{3}} \times 10^4 \langle 1,1,1 \rangle$ V m^{-1}	$\langle 1,1,0 \rangle$	$\left\langle -\frac{1}{\sqrt{2}}, -\frac{1}{\sqrt{2}}, 0 \right\rangle$	1
2	Uniform $\vec{B}$	$\frac{1}{100\sqrt{3}} \langle 1,1,1 \rangle$ T	$\langle 1,1,0 \rangle$	$\left\langle -\frac{1}{\sqrt{2}}, -\frac{1}{\sqrt{2}}, 0 \right\rangle$	1
3	Uniform $\vec{E}$ and $\vec{B}$	$\vec{E} = \frac{1}{50} \langle 1,0,0 \rangle$ V m^{-1} $\vec{B} = \frac{1}{50} \langle 0,1,0 \rangle$ T	$\langle 1,1,0 \rangle$	$\left\langle -\frac{1}{\sqrt{2}}, -\frac{1}{\sqrt{2}}, 0 \right\rangle$	1
4	Point and Line Charge	$Q = 5 \times 10^{-4}$ C $\vec{r}_p = \langle 0,0,0 \rangle$ m $\lambda = -5 \times 10^{-4}$ C m^{-1} $\vec{r}_{\ell,1} = \langle -1,-1,0 \rangle$ m $\vec{r}_{\ell,2} = \langle 1,-1,0 \rangle$ m	$\langle 1,1,1 \rangle$	$\langle 1,0,0 \rangle$	0.75
5	Ideal Magnetic Dipole	$M_0 = 10^8$ A m^2 $\vec{r}_d = \langle 0,0,0 \rangle$ $\hat{M} = \langle 0,0,1 \rangle$	$\langle 20,25,30 \rangle$	$\left\langle -\frac{1}{\sqrt{3}}, -\frac{1}{\sqrt{3}}, -\frac{1}{\sqrt{3}} \right\rangle$	1
6	Active Shielding Configuration	Table 4.3; Figure 4.1 and Figure 3.5.	$\langle 90,75,60 \rangle$	$\left\langle -\frac{1}{\sqrt{3}}, -\frac{1}{\sqrt{3}}, -\frac{1}{\sqrt{3}} \right\rangle$	15

4.4.2.1 Case 1: Uniform Electric Field Only

In this case, a uniform electric field is applied,

$$\vec{E}(\vec{r}) = \left(\frac{2}{\sqrt{3}} \times 10^4\right)\langle 1, 1, 1\rangle \text{ V m}^{-1}.$$

The initial state of the test proton in this case is

$$\vec{r}_0 = \langle 1, 1, 0\rangle \text{ m},$$

$$\vec{\Omega}_0 = \frac{1}{\sqrt{2}}\langle -1, -1, 0\rangle,$$

and

$$T_0 = 1 \,\text{MeV}.$$

This test case was formulated to ensure all methods properly propagate a charged particle through a simple electric field. The reference propagation method for this case is the SAT method, as it is only applicable for a uniform electric field and no magnetic field when considering relativistic effects. Additionally, this case was used to establish the Boris propagation method as the most reliably accurate method via comparison with SAT and justified its use as a reference for the remaining test cases.

4.4.2.2 Case 2: Uniform Magnetic Field Only

In this case, a uniform magnetic field is applied,

$$\vec{B}(\vec{r}) = \frac{1}{100\sqrt{3}}\langle 1, 1, 1\rangle \text{ T}.$$

The initial state of the test proton in this case is

$$\vec{r}_0 = \langle 1, 1, 0\rangle \text{ m},$$

$$\vec{\Omega}_0 = \frac{1}{\sqrt{2}}\langle -1, -1, 0\rangle,$$

and

$$T_0 = 1\,\mathrm{MeV}.$$

This test case was formulated to ensure all methods properly propagate a charged particle through a simple magnetic field.

4.4.2.3 Case 3: Combined Uniform Electric and Magnetic Field

In this case, perpendicular electric and magnetic fields were applied,

$$\vec{E}(\vec{r}) = \frac{1}{50}\langle 1, 0, 0\rangle \ \mathrm{V\,m^{-1}},$$

and

$$\vec{B}(\vec{r}) = \frac{1}{50}\langle 0, 1, 0\rangle \ \mathrm{T}.$$

The initial state of the test proton in this case is

$$\vec{r}_0 = \langle 1, 1, 0\rangle \ \mathrm{m},$$

$$\vec{\Omega}_0 = \frac{1}{\sqrt{2}}\langle -1, -1, 0\rangle,$$

and

$$T_0 = 1\,\mathrm{MeV}.$$

This test case was formulated to ensure electric and magnetic fields could be simultaneously applied and result in a successful propagation. It also serves to display the relative strength of magnetic fields over electric fields.

4.4.2.4 Case 4: Line and Point Charge Combination Electric Field

In this case, a charge distribution consisting of a point charge with magnitude

$$Q = 5 \times 10^{-4} \ \mathrm{C},$$

located at

$$\vec{r}_p = \langle 0, 0, 0 \rangle \text{ m},$$

and a line charge with linear charge density

$$\lambda = -5 \times 10^{-4} \,\text{C}\,\text{m}^{-1},$$

with endpoints located at

$$\vec{r}_{\ell,1} = \langle -1, -1, 0 \rangle \text{ m},$$

and

$$\vec{r}_{\ell,2} = \langle 1, -1, 0 \rangle \text{ m},$$

is applied. Here, the acceleration term is no longer constant with respect to position and velocity. The electric field at point $\vec{r}$ in free space, due to a point charge Q located at $\vec{r}_p$ is given by

$$\vec{E}(\vec{r}) = \frac{Q(\vec{r} - \vec{r}_p)}{4\pi\epsilon_0 |\vec{r} - \vec{r}_p|^3}, \tag{4.58}$$

where ϵ_0 is the permittivity of free space. The electric field at point $\vec{r}$ in free space due to a line charge with linear charge density λ spanning from $\vec{r}_{\ell,1}$ to $\vec{r}_{\ell,2}$ is given by

$$\vec{E}(\vec{r}) = \frac{\lambda |\vec{r}_2 - \vec{r}_1| \left(\frac{\vec{r} - \vec{r}_1}{|\vec{r} - \vec{r}_1|} + \frac{\vec{r} - \vec{r}_2}{|\vec{r} - \vec{r}_2|} \right)}{2\pi\epsilon_0 \left[\left(|\vec{r} - \vec{r}_1| + |\vec{r} - \vec{r}_2| \right)^2 - |\vec{r}_2 - \vec{r}_1|^2 \right]}, \tag{4.59}$$

as shown in [24, 97]. The total electric field is obtained via superposition. In reality, two charges set so close to one another would exhibit electrostatic induction effects. Electrostatic induction and other modes of intra-surface charge redistribution are ignored throughout this work. This is a known deficiency of both ASPP and G4-ASPP. The initial state of the test proton in this case is

$$\vec{r}_0 = \langle 1, 1, 1 \rangle \text{ m},$$

$$\vec{\Omega}_0 = \langle 1, 0, 0 \rangle,$$

and

$$T_0 = 0.75\,\text{MeV}.$$

This case was formulated to show that G4-ASPP is capable of successfully conducting charged particle transport for electric fields that vary with position. The kinetic energy was changed from 1 MeV to 0.75 MeV to facilitate a clearer presentation of the trajectories.

4.4.2.5 Case 5: Ideal Magnetic Dipole Field

In this case, an ideal magnetic dipole field is applied. The magnetic field acting at $\vec{r}$ in free space due to an ideal magnetic dipole pointing along

$$\hat{M} = \langle 0, 0, 1 \rangle,$$

with strength

$$M_0 = 1 \times 10^8\,\text{A}\,\text{m}^2,$$

located at

$$\vec{r}_d = \langle 0, 0, 0 \rangle,$$

is given by

$$\vec{B}(\vec{r}) = \frac{\mu_0 M_0}{4\pi}\left[\frac{3(\vec{r}-\vec{r}_d)\Big((\vec{r}-\vec{r}_d)\cdot\hat{M}\Big)}{|\vec{r}-\vec{r}_d|^5} - \frac{\hat{M}}{|\vec{r}-\vec{r}_d|^3} + \frac{8\pi}{3}\hat{M}\delta^3(\vec{r}-\vec{r}_d)\right], \tag{4.60}$$

where μ_0 is the permeability of free space. The initial state of the test proton in this case is

$$\vec{r}_0 = \langle 20, 25, 30 \rangle\ \text{m},$$

$$\vec{\Omega}_0 = \frac{1}{\sqrt{3}}\langle -1, -1, -1 \rangle,$$

and

$$T_0 = 1\,\text{MeV}.$$

This case was formulated to show that G4-ASPP is capable of successfully conducting charged particle transport in position-dependent magnetic fields.

4.4.2.6 Case 6: Full Active Shielding Configuration

In this case, a full three-dimensional active shielding configuration, shown in Figure 4.1, is integrated into the simulation space. This active shielding configuration, similar to those discussed in [26, 27, 30], consists

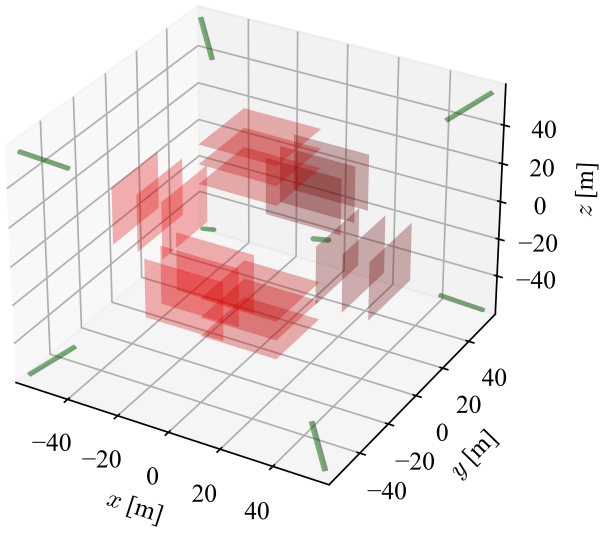


Figure 4.1: Active shielding configuration; red components are positively charged; green components are negatively charged.

of an arrangement of positive, uniformly charged rectangles and negative, uniformly charged line segments which sum to a total charge of zero. The electric field produced by a uniformly charged, arbitrarily oriented rectangular surface is given below [24]. Figure 3.5 defines all parameters associated with the size and orientation of a single rectangular charge. To construct the electric field at $\vec{r}$ in free space due to a single rectangular charge component given rectangle surface charge σ, side lengths Δu and Δv, midpoint $\vec{r}_r$, normal vector $\hat{w}$, orientation vector $\hat{u}$, first define

$$\eta_1 = \sqrt{(2(\vec{r}-\vec{r}_r)\cdot\hat{u}-\Delta u)^2+(2(\vec{r}-\vec{r}_r)\cdot\hat{v}-\Delta v)^2+(2(\vec{r}-\vec{r}_r)\cdot\hat{w})^2}, \tag{4.61}$$

$$\eta_2 = \sqrt{(2(\vec{r}-\vec{r}_r)\cdot\hat{u}+\Delta u)^2+(2(\vec{r}-\vec{r}_r)\cdot\hat{v}-\Delta v)^2+(2(\vec{r}-\vec{r}_r)\cdot\hat{w})^2}, \tag{4.62}$$

$$\eta_3 = \sqrt{(2(\vec{r}-\vec{r}_r)\cdot\hat{u}-\Delta u)^2+(2(\vec{r}-\vec{r}_r)\cdot\hat{v}+\Delta v)^2+(2(\vec{r}-\vec{r}_r)\cdot\hat{w})^2}, \tag{4.63}$$

and

$$\eta_4 = \sqrt{(2(\vec{r}-\vec{r}_r)\cdot\hat{u}+\Delta u)^2+(2(\vec{r}-\vec{r}_r)\cdot\hat{v}+\Delta v)^2+(2(\vec{r}-\vec{r}_r)\cdot\hat{w})^2}, \tag{4.64}$$

for convenience. Then, compute the electric field components at point $\vec{r}$ projected onto the $\hat{u}$, $\hat{v}$, and $\hat{w}$ directions (the coordinate system associated with the rectangle component),

$$E_u = \frac{\sigma}{4\pi\epsilon_0} \ln\left[\frac{(\eta_1 + \Delta v - 2(\vec{r}-\vec{r}_r)\cdot\hat{v})(\eta_4 - \Delta v - 2(\vec{r}-\vec{r}_r)\cdot\hat{v})}{(\eta_2 + \Delta v - 2(\vec{r}-\vec{r}_r)\cdot\hat{v})(\eta_3 - \Delta v - 2(\vec{r}-\vec{r}_r)\cdot\hat{v})}\right], \tag{4.65}$$

$$E_v = \frac{\sigma}{4\pi\epsilon_0} \ln\left[\frac{(\eta_1 + \Delta u - 2(\vec{r}-\vec{r}_r)\cdot\hat{u})(\eta_4 - \Delta u - 2(\vec{r}-\vec{r}_r)\cdot\hat{u})}{(\eta_2 - \Delta u - 2(\vec{r}-\vec{r}_r)\cdot\hat{u})(\eta_3 + \Delta u - 2(\vec{r}-\vec{r}_r)\cdot\hat{u})}\right], \tag{4.66}$$

and

$$\begin{aligned} E_w = \frac{\sigma}{4\pi\epsilon_0}\Bigg[&\arctan\left(\frac{2((\vec{r}-\vec{r}_r)\cdot\hat{u} - \Delta u)((\vec{r}-\vec{r}_r)\cdot\hat{v} - \Delta v)}{\eta_1(\vec{r}-\vec{r}_r)\cdot\hat{w}}\right) \\ &+ \arctan\left(\frac{-2((\vec{r}-\vec{r}_r)\cdot\hat{u} + \Delta u)((\vec{r}-\vec{r}_r)\cdot\hat{v} - \Delta v)}{\eta_2(\vec{r}-\vec{r}_r)\cdot\hat{w}}\right) \\ &- \arctan\left(\frac{2((\vec{r}-\vec{r}_r)\cdot\hat{u} - \Delta u)((\vec{r}-\vec{r}_r)\cdot\hat{v} + \Delta v)}{\eta_3(\vec{r}-\vec{r}_r)\cdot\hat{w}}\right) \\ &- \arctan\left(\frac{2((\vec{r}-\vec{r}_r)\cdot\hat{u} + \Delta u)((\vec{r}-\vec{r}_r)\cdot\hat{v} + \Delta v)}{\eta_4(\vec{r}-\vec{r}_r)\cdot\hat{w}}\right)\Bigg]. \end{aligned} \tag{4.67}$$

Finally, revert to the standard frame of reference via the inner product

$$\vec{E}(\vec{r}) = \begin{bmatrix} E_u & E_v & E_w \end{bmatrix} \begin{bmatrix} u_x & u_y & u_z \\ v_x & v_y & v_z \\ w_x & w_y & w_z \end{bmatrix}. \tag{4.68}$$

Again, the total electric field is obtained via superposition with no consideration of electrostatic induction or equilibrating charge distributions. The full active shielding configuration is detailed in Table 4.3.

The initial state of the test proton in this case is

$$\vec{r}_0 = \langle 90, 75, 60\rangle \text{ m},$$

$$\vec{\Omega}_0 = \frac{1}{\sqrt{3}}\langle -1, -1, -1\rangle,$$

and

$$T_0 = 15\,\text{MeV}.$$

This case was formulated to showcase that, like ASPP, G4-ASPP is capable of handling charged particle

Table 4.3: Parameters used to construct active shielding configuration shown in Figure 4.1.

Rectangle Charges					
σ [C m^{-2}]	Δu [m]	Δv [m]	$\vec{r}_r$ [m]	$\hat{w}$	$\hat{u}$
7.5722×10^{-6}	30	30	$\langle 30, 0, 0\rangle$	$\langle 1, 0, 0\rangle$	$\langle 0, 1, 0\rangle$
			$\langle 40, 0, 0\rangle$	$\langle 1, 0, 0\rangle$	$\langle 0, 1, 0\rangle$
			$\langle 50, 0, 0\rangle$	$\langle 1, 0, 0\rangle$	$\langle 0, 1, 0\rangle$
			$\langle 0, 30, 0\rangle$	$\langle 0, 1, 0\rangle$	$\langle -1, 0, 0\rangle$
			$\langle 0, 40, 0\rangle$	$\langle 0, 1, 0\rangle$	$\langle -1, 0, 0\rangle$
			$\langle 0, 50, 0\rangle$	$\langle 0, 1, 0\rangle$	$\langle -1, 0, 0\rangle$
			$\langle -30, 0, 0\rangle$	$\langle -1, 0, 0\rangle$	$\langle 0, -1, 0\rangle$
			$\langle -40, 0, 0\rangle$	$\langle -1, 0, 0\rangle$	$\langle 0, -1, 0\rangle$
			$\langle -50, 0, 0\rangle$	$\langle -1, 0, 0\rangle$	$\langle 0, -1, 0\rangle$
			$\langle 0, -30, 0\rangle$	$\langle 0, -1, 0\rangle$	$\langle 1, 0, 0\rangle$
			$\langle 0, -40, 0\rangle$	$\langle 0, -1, 0\rangle$	$\langle 1, 0, 0\rangle$
			$\langle 0, -50, 0\rangle$	$\langle 0, -1, 0\rangle$	$\langle 1, 0, 0\rangle$
			$\langle 0, -30, 0\rangle$	$\langle 0, 0, 1\rangle$	$\langle 0, 1, 0\rangle$
			$\langle 0, -40, 0\rangle$	$\langle 0, 0, 1\rangle$	$\langle 0, 1, 0\rangle$
			$\langle 0, -50, 0\rangle$	$\langle 0, 0, 1\rangle$	$\langle 0, 1, 0\rangle$
			$\langle 0, 30, 0\rangle$	$\langle 0, 0, 1\rangle$	$\langle 0, 1, 0\rangle$
			$\langle 0, 40, 0\rangle$	$\langle 0, 0, 1\rangle$	$\langle 0, 1, 0\rangle$
			$\langle 0, 50, 0\rangle$	$\langle 0, 0, 1\rangle$	$\langle 0, 1, 0\rangle$
Line Charges					
λ [C m^{-1}]			$\vec{r}_{\ell,1}$ [m]	$\vec{r}_{\ell,2}$ [m]	
-7.66685×10^{-4}			$46.188\langle 1, 1, 1\rangle$	$57.735\langle 1, 1, 1\rangle$	
			$46.188\langle -1, -1, -1\rangle$	$57.735\langle -1, -1, -1\rangle$	
			$46.188\langle -1, 1, 1\rangle$	$57.735\langle -1, 1, 1\rangle$	
			$46.188\langle 1, -1, 1\rangle$	$57.735\langle 1, -1, 1\rangle$	
			$46.188\langle 1, 1, -1\rangle$	$57.735\langle 1, 1, -1\rangle$	
			$46.188\langle -1, -1, 1\rangle$	$57.735\langle -1, -1, 1\rangle$	
			$46.188\langle 1, -1, -1\rangle$	$57.735\langle 1, -1, -1\rangle$	
			$46.188\langle -1, 1, -1\rangle$	$57.735\langle -1, 1, -1\rangle$	

transport through electric fields defined by many active shielding components. In this case, the kinetic energy was changed from 1 MeV to 15 MeV because the average kinetic energy required by a proton to overcome the potential barrier produced by this particular active shielding configuration is approximately 15 MeV [66]. It was anticipated that a proton that makes a closer approach to the center of the active shielding configuration would produce a more interesting trajectory.

4.4.3 Simulation Procedure

Each simulation is conducted in a similar fashion. First, time-stepping propagation methods (Boris (Time) (BT), VVT, SAT) are utilized to propagate a test proton with the provided initial state over $N = 10^5$ time steps with step duration $\Delta t = 1 \times 10^{-10}$ s. These trajectories are saved. Next, the distance-stepping propagation methods (Restricted Step Length, Geant4 (G4RS), Unrestricted Step Length, Geant4 (G4US),

VVS, RK4S, Euler (Distance) (ES)) are utilized. For methods VVS, RK4S, and ES, the distance-step length is constant and set to be

$$\Delta s = c\Delta t = 0.029\,979\,245\,8\,\mathrm{m} \approx 30\,\mathrm{mm}.$$

This choice of Δs represents the maximum distance any particle could travel over a duration Δt. Given the choice of Δt, preliminary simulations show that the impact of a Δs—which is typically significantly longer than the true distance traveled during one time step Δt—on trajectory accuracy is negligible. The G4-ASPP propagation methods adapt the step length over the course of the simulation. For the G4RS method, $c\Delta t$ is the maximum possible step length. For the G4US method, there is no practical maximum step length. The total time elapsed over the course of each distance-stepping propagation method is tracked via the relation

$$\frac{\mathrm{d}t}{\mathrm{d}s} = \frac{1}{v} = \frac{T}{\tilde{p}c},$$

where the total simulation time associated with each distance simulation is

$$t_{\mathrm{total}} = \sum_{n=0}^{N-1} \frac{\Delta s_n}{v_n}.$$

The total simulation time for each distance-stepping simulation is used to determine when each simulation should stop. That is, for the minimum n such that

$$t_{\mathrm{total}} \geq N\Delta t,$$

subsequent particle positions $\vec{r}_n$ are discarded to cleanly compare all trajectories, regardless of simulation method.

Three time-series data products are extracted from each simulation: the position, kinetic energy, and time-integrated relative error of the trajectory with respect to a reference propagation method. The kinetic energy is computed via

$$T = (\gamma - 1)\tilde{m}_0, \tag{4.69}$$

at each step, where $\tilde{m}_0$ is the rest mass energy of the particle. Comparing the kinetic energy time-profile of each method provides qualitative information regarding relative propagation method stability. The time-

integrated relative error is a metric that represents the accuracy of one trajectory $\vec{r}(t)$ with respect to some reference trajectory $\vec{r}_{\text{ref}}(t)$ (in this work, usually the trajectory produced by the BT method). The time-integrated relative error is obtained via

$$R_r(t) = \frac{1}{t}\int_0^t \frac{|\vec{r}(t') - \vec{r}_{\text{ref}}(t')|}{|\vec{r}_{\text{ref}}(t')|}\mathrm{d}t'. \tag{4.70}$$

Smaller values of $R_r(t)$ imply better consistency between the trajectory of the propagation method in question and the reference method at time t. To obtain $\vec{r}(t)$ from distance-stepping propagation methods (which provide $\vec{r}(s)$ and $t(s)$ values), linear interpolation was used to convert $\vec{r}(s)$ data to $\vec{r}(t)$ data, which are used to directly compare all trajectories, regardless of whether the associated propagation method is distance- or time-based.

4.4.4 Computation Time Study

The amount of real time necessary to execute each propagation method was evaluated for test cases 1, 4, and 6. The time step Δt was varied over four values—10^{-11} s, 10^{-10} s, 10^{-9} s, and 10^{-8} s—to observe how computational time changes as a function of

1. time step Δt, for time-stepping methods (BT, VVT, SAT),
2. distance step Δs, for simple distance-stepping methods (VVS, RK4S, ES), and
3. maximum allowable distance step $\Delta s_{\max}$ for the restricted G4-ASPP stepping method (G4RS).

Note that the unrestricted G4-ASPP stepping method, G4US, is not expected to change as Δt changes, because the distance-step in G4US is not given a practical upper bound. The initial conditions of each test case remain the same here. Each propagation method was computed over propagation times $t \in [0, 10]$ µs and the computational time t_c was tracked during code execution. To ensure a fair comparison, all propagation methods, including G4US and G4RS, were fully replicated in Python. Python is known to be considerably slower than C++—the language Geant4 is written in—so focus is placed on the relationships between computational times among different propagation methods rather than the raw computational time itself. Test cases 1, 4, and 6 were selected for computational time analysis because of the gradual increase in electric field complexity from case 1 to case 4 to case 6. Test case 1 contains a simple uniform electric field,

test case 4 contains a position-dependent field generated from a point charge and a line charge, and test case 6 contains a more complex position-dependent field generated by a proposed active shielding configuration with many charged components.

4.5 Trajectory Comparison and Analysis

4.5.1 Test Cases

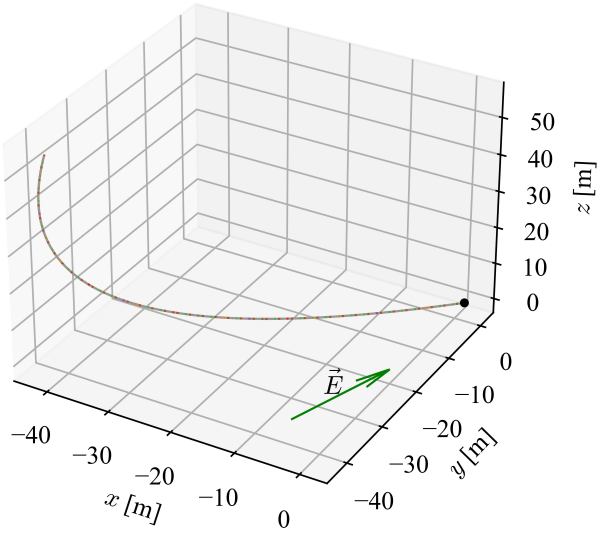
Figure 4.2-4.7 show all test case results, including a trajectory plot, a kinetic energy timeline, and the time-integrated relative error in position for all methods applied.

4.5.1.1 Test Case 1

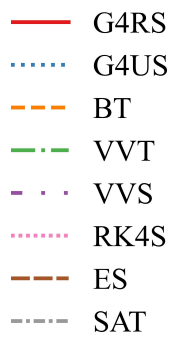
Figure 4.2 shows the results of test case 1, where a uniform electric field is applied to the simulation space. At the scale shown, all trajectory results are indistinguishable from one another. Kinetic energy profiles decrease as the test proton is decelerated by the opposing electric field and then begins to increase again as the direction changes around $t = 6\,\mu s$. For this case only, the reference propagation method was the SAT method. Figure 4.2d shows that the BT, RK4S, and VVT methods produced trajectories that are nearly coincident and maintain the smallest overall time-integrated relative error with respect to the trajectory produced by the SAT method. The G4RS, VVS, ES, and G4US methods produce trajectories that increasingly diverge from that of the SAT method, with G4RS being the closest match among this group, followed by VVS, ES, and G4US in descending order of similarity. Figure 4.2d shows that all propagation methods produced time-integrated relative errors less than 1% for all t. Based on its widespread use in the field, and small $R_r(t)$ with respect to the SAT-produced trajectory, the BT method was chosen as the reference method for all other test cases [91, 94, 98].

4.5.1.2 Test Case 2

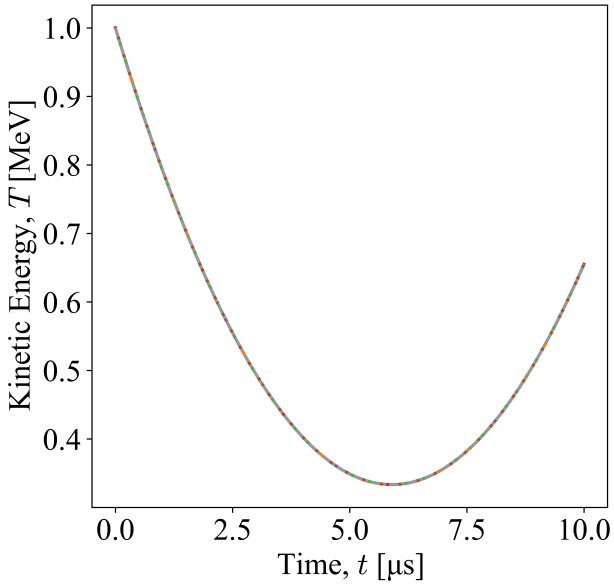
Figure 4.3 shows the results of test case 2, where a uniform magnetic field is applied to the simulation space. Again, trajectory results are indistinguishable from one another. The test particle moves in a helical trajectory, as expected. Note that the kinetic energy timelines differ among the various propagation methods, when, theoretically, the kinetic energy should remain constant because magnetic fields do no work



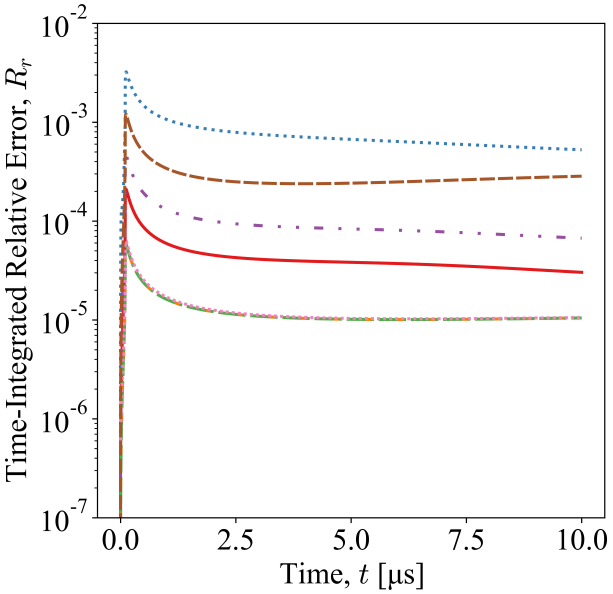
(a) Particle trajectory with uniform field applied; test particle starts at black dot.



(b) Universal legend; refer to Table 4.1 for propagation method abbreviations.



(c) Particle kinetic energy timeline.



(d) Time-integrated relative error in position with respect to SAT position.

Figure 4.2: Case 1 results.

on charged particles. The G4US, ES, VVS, and G4RS kinetic energy timelines clearly increase linearly as t increases. Over long durations, these methods would increase the particle kinetic energy *ad infinitum*. The kinetic energy profile associated with the VVT method *very slightly* increases as t increases. The BT and RK4S kinetic energy profiles appear steady at $T = 1\,\text{MeV}$ for all t. The energy conservation properties of the VVT, BT, and RK4S relate to their phase-space preservation properties. Note that none of these

propagation methods are symplectic in this case, as the applied force is (strongly) velocity-dependent. The reference method in this case is the BT method. The time-integrated relative error with respect to the BT method trajectory is smallest for the RK4S trajectory at steady state, defined as

$$t \to N\Delta t.$$

From here, the VVT, G4RS, VVS, ES, and G4US are respectively less accurate.

4.5.1.3 Test Case 3

Figure 4.4 shows the results of test case 3, where orthogonal electric and magnetic fields are applied to the simulation space. In this case, the trajectories are noticeably less coincident, and some trajectories, like ES, start to clearly separate from the other trajectories. The test particle moves in a helical motion again. The influence of the electric field is much less pronounced. This is a consequence of the relative strength of magnetic fields versus electric fields. Consider a 1 T magnetic field orthogonal to the direction of motion of a charged particle. The magnitude of the force acting on this particle is given by

$$F_B = qvB.$$

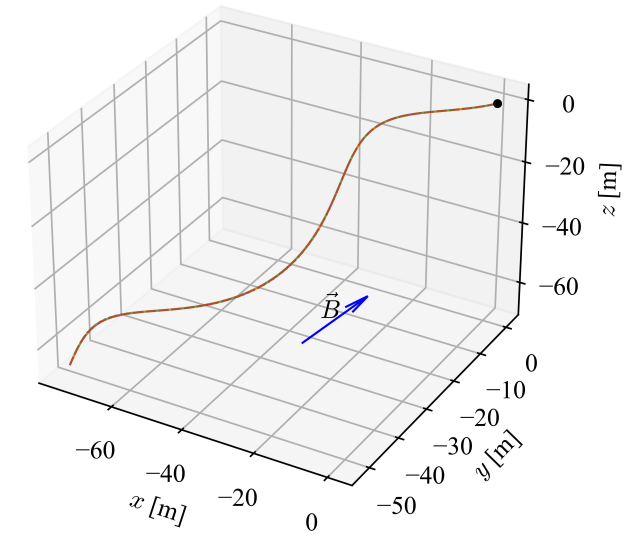
Now, consider a $1\,\mathrm{V\,m^{-1}}$ electric field influencing the motion of a charged particle. The magnitude of the force acting on this particle is given by

$$F_E = qE.$$

The unit magnetic field is stronger than the unit electric field (in base SI units) by a factor of the particle speed v,

$$\frac{F_B}{F_E} = \frac{vB}{E} = v\frac{1\,\mathrm{T}}{1\,\mathrm{V\,m^{-1}}}.$$

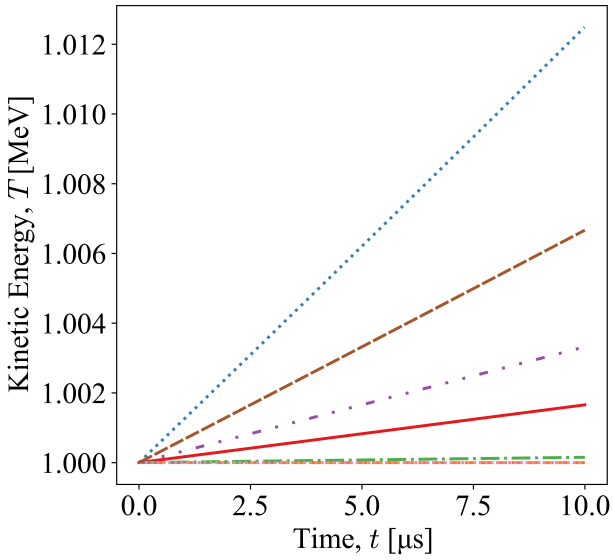
Charged particles generally travel at very high speeds, and can approach the speed of light. This explains why the influence of the electric field is less pronounced in this test case. Note that the kinetic energy timelines again greatly differ among the various propagation methods. The G4US, ES, VVS, and G4RS kinetic energy timelines again increase linearly as t increases. The trends among different propagation methods are the same as they are in test case 2, where RK4S exhibits the smallest relative error with respect to BT, followed



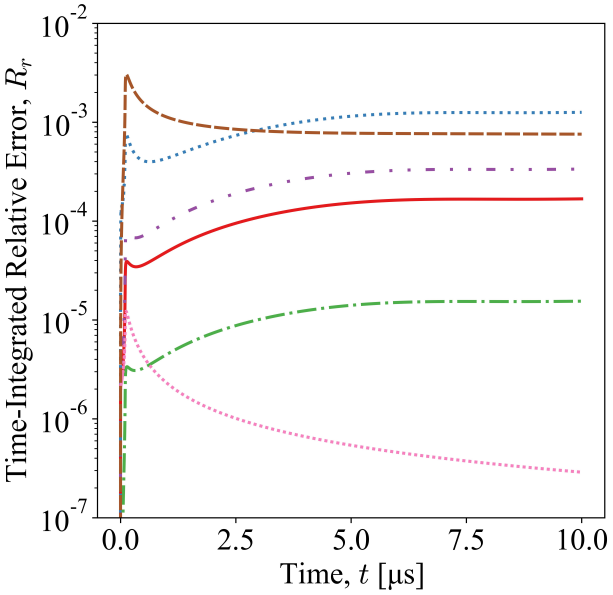
(a) Particle trajectory with uniform magnetic field applied; test particle starts at black dot.



(b) Universal legend; refer to Table 4.1 for propagation method abbreviations.



(c) Particle kinetic energy timeline.



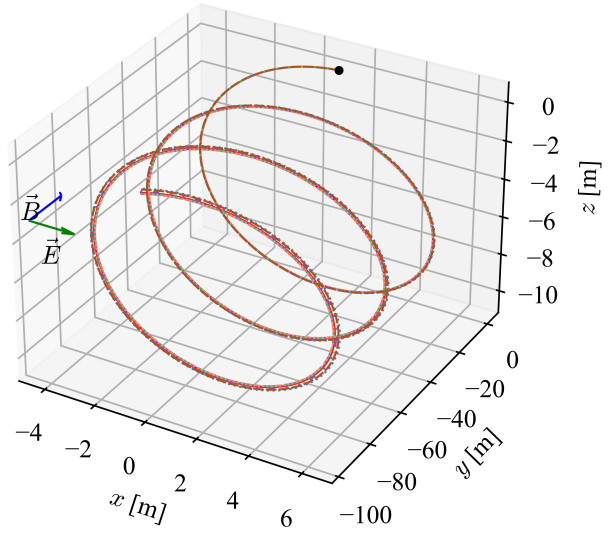
(d) Time-integrated relative error in position with respect to BT position.

Figure 4.3: Case 2 results.

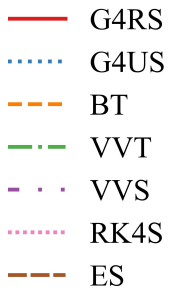
by VVT, G4RS, VVS, ES, and G4US.

4.5.1.4 Test Case 4

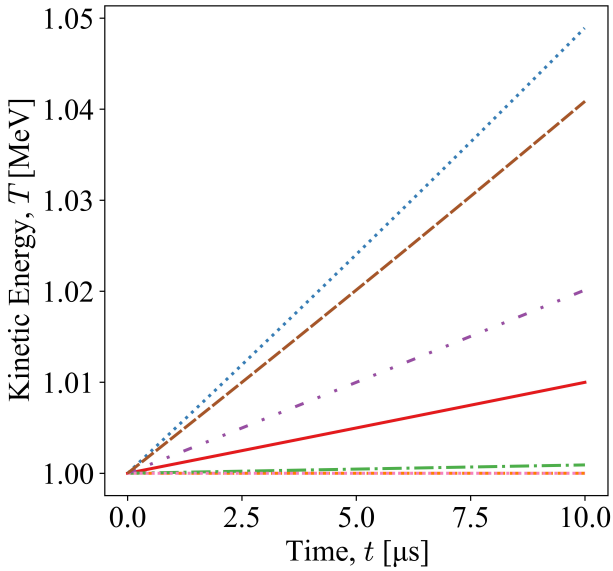
Figure 4.5 shows the results of test case 4, where a negative line charge (shown in green) and a positive point charge (shown in red) generate an electric field that varies with particle position. Differences in trajectory are



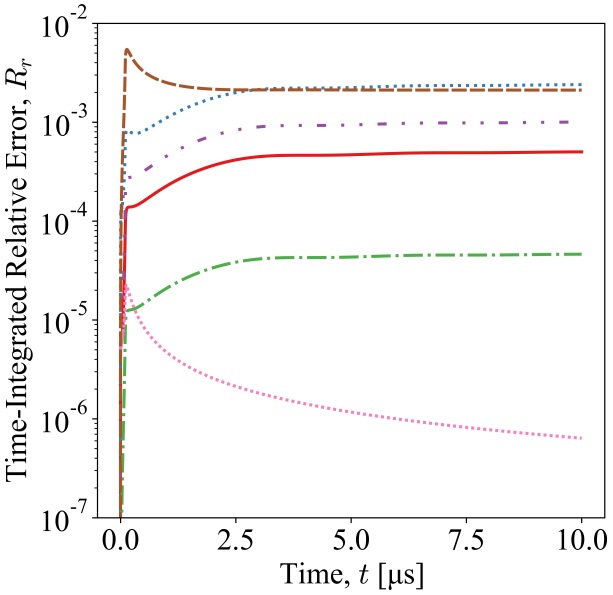
(a) Particle trajectory with uniform electric and magnetic field applied; test particle starts at black dot.



(b) Universal legend; refer to Table 4.1 for propagation method abbreviations.



(c) Particle kinetic energy timeline.



(d) Time-integrated relative error in position with respect to BT position.

Figure 4.4: Case 3 results.

obvious for this test case. All particle trajectories follow nearly identical paths except for the one produced by the ES method. The ES method noticeably diverges from the other trajectories while still exhibiting generally similar behavior as the other trajectories. This divergence is likely related to an overestimation of $\vec{p}_{n+1}$. All other propagation methods discussed in this work, except for the SAT method, compute the $\vec{v}_{n+1}$ or $\vec{p}_{n+1}$ with a combination of $\frac{\mathrm{d}\vec{v}}{\mathrm{d}t}$ or $\frac{\mathrm{d}\vec{p}}{\mathrm{d}s}$ terms computed at more than one t or s, leading to a Δs coefficient

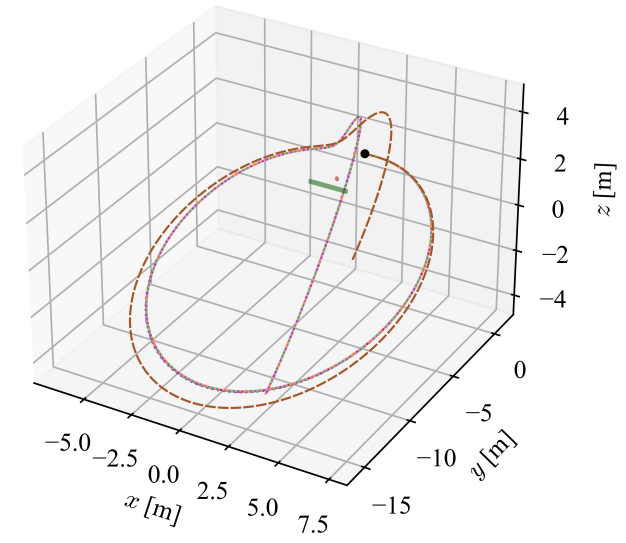
that is typically *smaller* than $\left(\frac{\mathrm{d}\vec{v}}{\mathrm{d}t}\right)_n$ or $\left(\frac{\mathrm{d}\vec{p}}{\mathrm{d}s}\right)_n$. The ES method does not, leading to an overestimation of $\vec{\tilde{p}}_{n+1}$ and thus a more drastic change in direction $\frac{\vec{\tilde{p}}_{n+1}}{\tilde{p}_{n+1}}$ during the calculation of $\vec{r}_{n+2}$, etc. The kinetic energy timeline shows that the ES method's tendency to overstep leads to a delay in changes to the test particle's kinetic energy. In terms of error with respect to the BT method, VVT and RK4S display the smallest time-integrated relative error. At first, the VVT trajectory follows the BT trajectory more closely, but as time progresses, the RK4S trajectory follows the BT trajectory better than the VVT trajectory. The G4RS, VVS, G4US, and ES methods follow in order of decreasing accuracy. There is a noticeable rapid increase in the $R_r(t)$ plots around $t = 8\,\mu\mathrm{s}$ associated with the location at which the test particle is intensely accelerated by the nearby point-and-line charge combination. This indicates that simulation accuracy is expected to decrease when particles enter regions where the electromagnetic field changes quickly over short distances.

4.5.1.5 Test Case 5

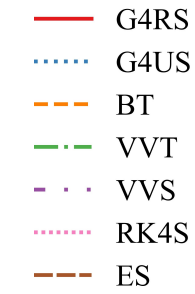
Figure 4.6 shows the results of test case 5, where an ideal magnetic dipole (represented in blue) generates a magnetic field that varies with particle position. Differences in trajectory are apparent again, particularly after the test particle is deflected away from the magnetic dipole location. This reinforces the idea that strong fields yield the greatest disparity in trajectory results among different propagation methods. The kinetic energy timelines show that the BT and RK4S methods appear to properly conserve energy throughout the simulation, as magnetic fields do no work on charged particles. VVT also performs well in this regard. The G4RS, G4US, VVS, and ES methods perform progressively worse in energy conservation. In terms of relative error, the RK4S method shows the smallest time-integrated relative error with respect to the BT method at steady state. VVT, G4RS, VVS, G4US, and ES follow in order of decreasing accuracy.

4.5.1.6 Test Case 6

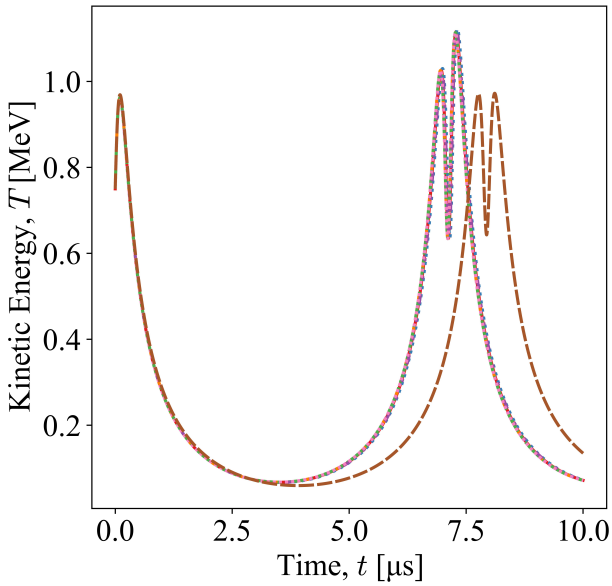
Figure 4.7 shows the results of test case 6, where a charge-neutral active shielding configuration composed of several rectangular and line charges was used to generate a position-dependent electric field. In this case, trajectory differences only distinguish the adaptive step size (Geant4) propagation methods from the other propagation methods. The trajectories associated with the G4US and G4RS methods begin to change direction sooner than those produced by the BT, VVT, RK4S, VVS, and ES methods. This occurs because



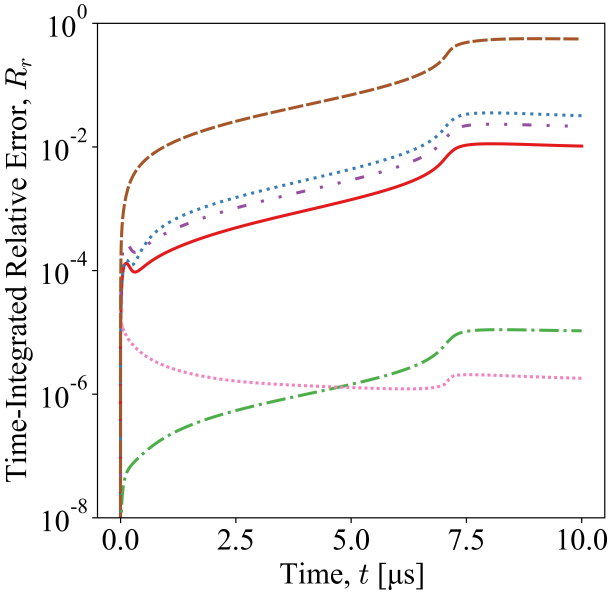
(a) Particle trajectory with line-and-point charge produced electric field applied; test particle starts at black dot.



(b) Universal legend; refer to Table 4.1 for propagation method abbreviations.



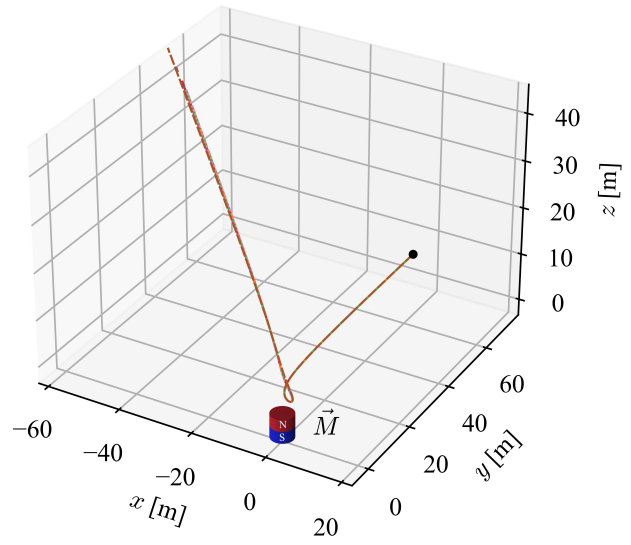
(c) Particle kinetic energy timeline.



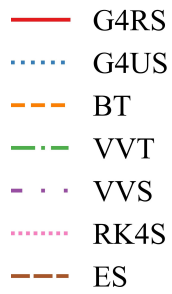
(d) Time-integrated relative error in position with respect to BT position.

Figure 4.5: Case 4 results.

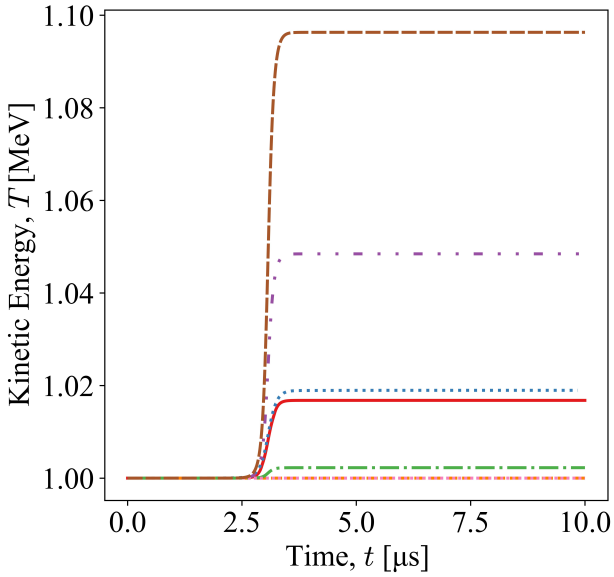
the adaptive step size procedures in Geant4 are designed such that smaller steps are taken near regional boundaries. The rectangular charges and line charges are modeled as constructive solid geometry objects in Geant4, so particles that approach these objects naturally start to take smaller and smaller steps. At some point, the force exerted becomes very large due to the diminishing distance between the test particle and charged object, and the test particle is deflected away. In contrast, in the non-adaptive propagation



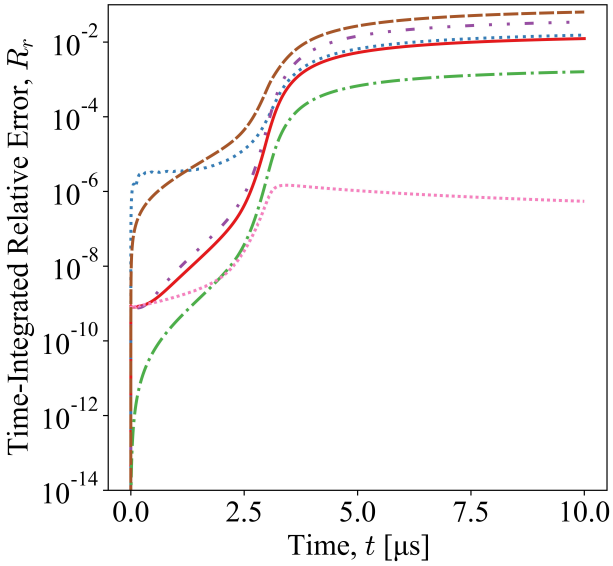
(a) Particle trajectory with ideal magnetic dipole field applied; test particle starts at black dot.



(b) Universal legend; refer to Table 4.1 for propagation method abbreviations.



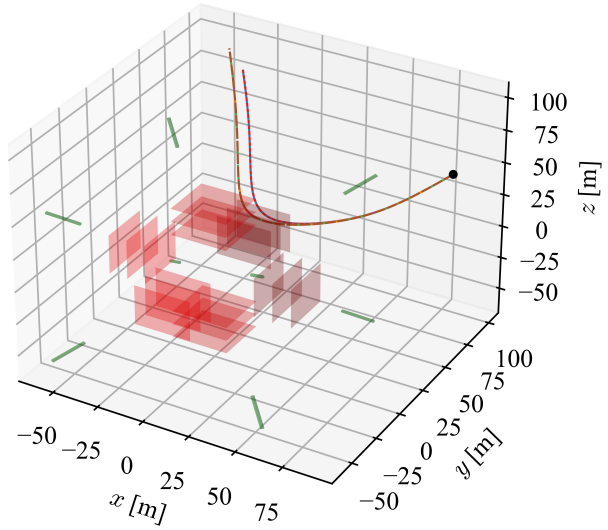
(c) Particle kinetic energy timeline.



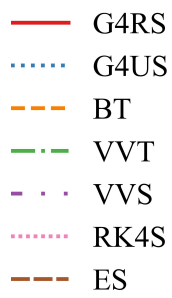
(d) Time-integrated relative error in position with respect to BT position.

Figure 4.6: Case 5 results.

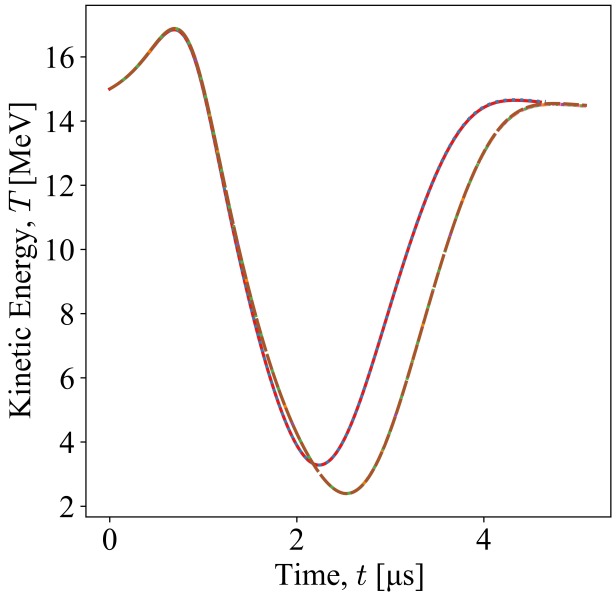
methods, the step size is fixed, and thus it is possible for the test particle to "skip over" the charged object (in this case, a positively charged rectangle). The differences in kinetic energy profiles are explained similarly. The time-integrated relative error for the Geant4 propagation methods is overstated in Figure 4.7d for the same reason. Otherwise, the time-integrated relative error with respect to BT trajectory at steady state is smallest for RK4S, followed by VVT, VVS, and ES.



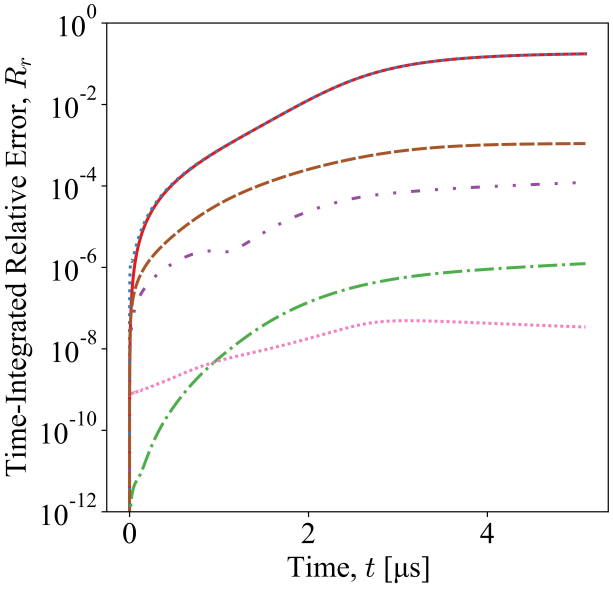
(a) Particle trajectory with electric field produced by active shielding configuration applied; test particle starts at black dot.



(b) Universal legend; refer to Table 4.1 for propagation method abbreviations.



(c) Particle kinetic energy timeline.



(d) Time-integrated relative error in position with respect to BT position.

Figure 4.7: Case 6 results.

4.5.2 Computation Time

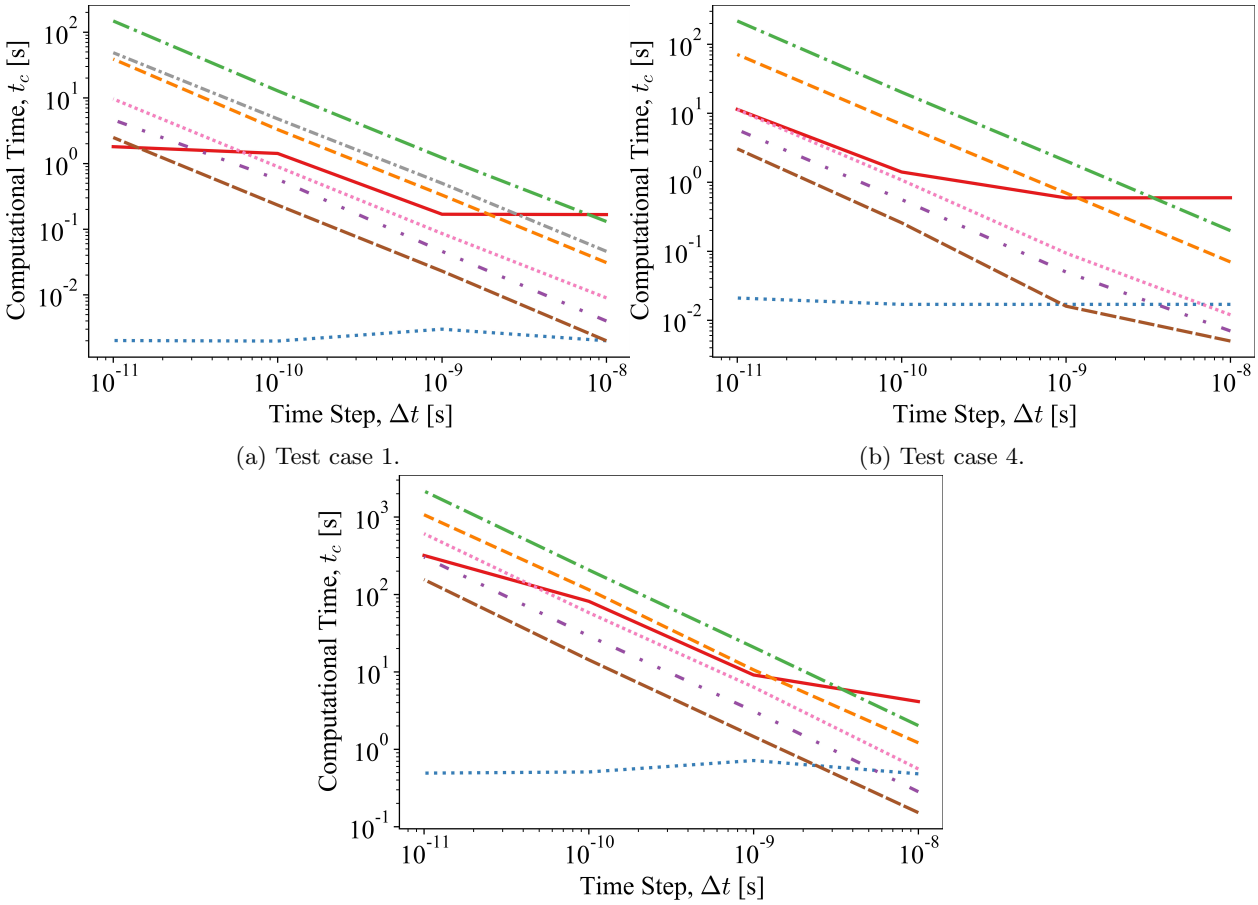
Figure 4.8a, 4.8b, and 4.8c show the computational time t_c as a function of time step duration Δt for test cases 1, 4 and 6, respectively. The relationships between computational time performances remain consistent among the non-adaptive propagation methods in each test case. Overall, test case 4 consumes slightly more

computational time than test case 1, and test case 6 consumes approximately one order of magnitude more computational time than test cases 1 and 4. In test case 1, the field is constant with respect to position, while in test cases 4 and 6, the field is position-dependent due to the presence of electric field-generating components. In test case 4, one positive point charge and one negative line charge are present. In test case 6, 18 positive rectangular charges and 8 negative line charges are present; 13 times more charged objects than test case 4. It is expected that the computational time increases as the number of field-generating components increases. It is also expected that rectangular charges are more computationally expensive than line charges, and line charges are more computationally expensive than point charges, as rectangular charges have more complex electric field functions than line charges, and line charges have more complex electric field functions than point charges. Shifting focus to the relationships between propagation methods, the time-stepping methods (VVT, SAT, BT) consume more computational time than the non-adaptive distance-stepping methods (RK4S, VVS, ES). The computational time required to run the G4RS method is comparable to the non-adaptive distance-stepping methods for small Δt because the upper bound of Δs in G4RS is $c\Delta t$. The additional computational time separating the VVS method and the G4RS method is simply the computational time required to compute an appropriate Δs. It is also worth noting that the G4-ASPP stepping procedure was *not* written with computational efficiency in mind. Note that the curve associated with the unrestricted G4-ASPP adaptive distance-stepping method generally does not vary with Δt because the upper bound on Δs present in G4RS is no longer applied in G4US. Finally, note that the G4RS method appears to flatten as Δt becomes larger.

4.6 Conclusions

The objectives of this work were to

- derive a distance-stepping propagation method analogous to the time-step-based Velocity-Verlet propagation method,
- verify the charged particle propagation capabilities of G4-ASPP in comparison to well-established methods across various electromagnetic field geometries,
- determine the time-integrated relative error of trajectories obtained via different propagation methods with respect to a reference propagation method, and



(a) Test case 1.

(b) Test case 4.

(c) Test case 6.

Figure 4.8: Computational time results as a function of Δt (and by extension, Δs) among all propagation methods for test cases 1, 4, and 6; refer to Figure 4.2b for legend.

- assess the relative computational efficiency of each propagation method.

In Section 4.3.1, a distance-stepping method analogous to the time-step-based Velocity-Verlet propagation method was derived, called the Momentum-Verlet Method, or VVS. This method, unlike VVT, is *not* symplectic, even for velocity-independent forces. However, propagation method symplecticity does not appear to be a major factor for propagation accuracy *over the time-scale studied in this work*, given that BT and RK4S are non-symplectic and each method consistently outperforms VVT in terms of accurately conserving energy in the presence of pure magnetic fields. This suggests that RK4S or a distance-stepping analog of BT should be implemented into G4-ASPP to improve energy tracking capabilities and, possibly, overall trajectory accuracy. It is worth noting that BT *does* conserve phase-space, which is a necessary (but not sufficient) condition to be an energy-conserving propagation method. It is unlikely that RK4S is energy-conserving or phase-space conserving. The energy conservation properties exhibited by RK4S in this

work are likely a result of the high-order of accuracy of the propagator itself relative to other methods. Five out of six test cases show that both G4-ASPP particle propagation methods, G4RS and G4US, produce trajectories that closely resemble trajectories produced by standard propagation methods. In the sixth case, the G4-ASPP particle propagation methods follow a slightly altered trajectory compared to the standard propagation methods because G4-ASPP propagation methods tend to decrease step sizes when approaching physical boundaries. In the sixth case, the test particle was on a collision course with one of the rectangular charge components that make up the active shielding configuration. G4-ASPP step sizes appropriately decreased as the test particle approached the rectangular charge component in question–the other propagation methods maintained a constant step size (in time or distance), and intersected the rectangular charge by traveling too far in one step.

Time-integrated relative errors computed for each particle propagation method with respect to trajectories produced from the BT method vary widely among test case/propagation method combinations, but the comparative accuracy of each propagation method is consistent across test cases, except for the case where the active shielding configuration is present. In general, and at steady state, the following list of propagation methods shows the hierarchy of propagation methods in terms of accuracy with respect to the BT method, from best to worst, with an associated maximum time-integrated relative error at steady state across all test cases listed in parentheses:

1. BT (0 %),
2. RK4S ($\leq 0.01\%$),
3. VVT ($\leq 0.1\%$),
4. G4RS ($\leq 1\%$),
5. VVS ($\leq 1\%$),
6. G4US ($\leq 10\%$), and
7. ES ($\leq 100\%$).

The computational time consumed by each propagation method was also evaluated for test cases 1 and 4 as a function of Δt (BT, VVT), or analogously Δs (RK4S, VVS, ES), or equivalently the maximum allowable

step distance (G4RS). The relationships between all constant step size propagation methods are consistent across test cases. The following list displays each non-adaptive size step propagation method in order of shortest to longest execution time:

1. ES,
2. VVS,
3. RK4S,
4. BT,
5. SAT, and
6. VVT.

The performances of the adaptive step size propagation methods, G4US and G4RS, do not decrease with Δt in power law fashion as the non-adaptive step size propagation methods do. G4RS, the restricted adaptive step size propagation method in G4-ASPP that utilizes VVS for stepping procedures, appears to consume less computational time as Δt increases, but eventually asymptotically approaches a lower bound computational time that cannot be improved upon by changing Δt. Δt controls the maximum allowable distance step size in G4RS via the relation $\Delta s_{\max} = c\Delta t$. G4RS can take steps smaller than $\Delta s_{\max}$, but not larger. G4US, the unrestricted adaptive step size propagation method implemented with VVS integration in G4-ASPP, is generally unaffected by Δt because the maximum allowable distance step size is instead set to the maximum double-precision value representable in C++, meaning there is no practical maximum step size. G4US is generally much faster than G4RS (a factor of around 100 to 1000 times faster), though G4RS allows for greater step size control and accuracy in trajectory. Reviewing the computational time results in concert with the time-integrated relative error results suggests that the trajectory accuracy of the RK4S method over the VVS method may justify the implementation of the RK4S method in G4-ASPP over VVS, despite an expected increase in computational time.

As part of future work, a 4th-order Runge-Kutta distance-stepping integration method (and perhaps a distance-stepping analog to the Boris integration method) will be implemented to improve trajectory accuracy, computational time, and energy tracking/conservation in G4-ASPP. Several Runge-Kutta methods are already available in the Geant4 source code; implementation in G4-ASPP framework will be simple. In

addition, the time-reversibility of the VVT method will be exploited to explore adjoint transport methods in G4-ASPP. A known deficiency of ASPP and G4-ASPP is that electrostatic charge induction effects are ignored, so configurations with many nearby charged components may generate inaccurate resultant fields (especially those between charged components) because the charge distributions on each component are not allowed to equilibrate. A solution to this issue which leverages a numerical Laplace equation solver is in development. Ultimately, G4-ASPP is meant to serve as a combined active-passive radiation shielding design and simulation tool. Future work will primarily focus on assessing G4-ASPP's ability to determine shielding efficacy in combined shielding environments. Since no such open source code currently exists, combinations of existing computational tools will be needed to assess charged particle transport through electromagnetic fields and transport through bulk media in a segmented fashion at first, before cleverly combining the results to imitate the all-in-one simulation carried out by G4-ASPP for comparison. This future study will address passive shielding associated with active shielding components and other aspects of the space environment such as spacecraft geometry, space radiation spectra, and planetary surfaces, such as the Moon, Mars, etc.

4.7 Geant4 Particle Propagation Method

In Section 4.4.1.5, the step size selection method used in Geant4 is referenced in Equation 4.55 as a generic function f of current position $\vec{r}_n$, current pseudo-momentum $\vec{\tilde{p}}_n$, local electric field, $\vec{E}_n$, local magnetic field $\vec{B}_n$, and the simulation geometry. The step size selection method utilized by default in Geant4 is extremely complicated. To the authors' knowledge, detailed documentation on the entirety of this method does not appear to exist [39, 86–89, 99]. For instance, one component (Compute "Valid Endpoint" Flag) of this procedure is loosely detailed in a public PowerPoint document [87], but other action items, such as the step size refinement procedures, are not. Providing meticulous documentation for this step selection method is left for future work. However, a high-level, generic explanation of this process is provided for those interested. Figure 4.9 displays a high-level overview of the process Geant4 goes through when selecting the next step length, Δs_n, for a charged particle in a vacuous medium with an electromagnetic field present. Actions are labeled in yellow, high-importance actions in black, and decisions in purple diamonds.

Each step begins with initialization, which occurs at the start of the simulation or immediately after a previous step. Let the initial state of the particle be $\vec{r}_n$, $\vec{\tilde{p}}_n$. A step size is proposed, either depending on

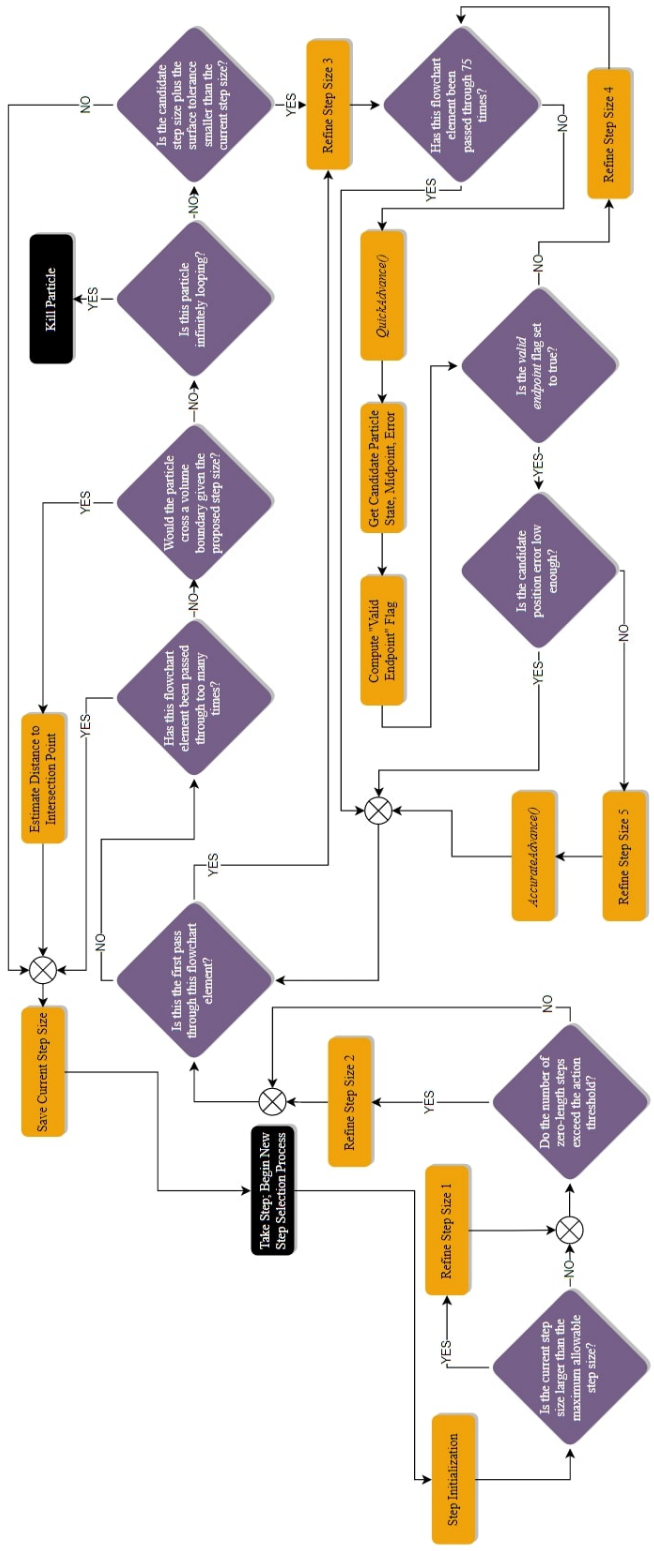


Figure 4.9: High level step size selection flowchart in Geant4.

the length of the previous step, or if at the beginning of a simulation, the initial step length. From here, this proposed step length is filtered through a series of conditional statements and "step size refinement" processes. For example, if the proposed step length is greater than the maximum allowable step size, which is either a default or user-defined distance, then the proposed step length is refined (Refine Step Size 1) such that the new proposed step size is equal to the maximum allowable step size.

In general, the step selection algorithm used in Geant4 is meant to decrease step size (and thus improve simulation fidelity) near volume boundaries and during drastic changes in direction, while also ensuring that simulation time is not wasted in large regions of low-to-zero deflection and/or material homogeneity. In the flowchart, two methods are italicized. These are the *QuickAdvance()* and *AccurateAdvance()* methods. The *QuickAdvance()* method should be thought of as a single-step instance of a standard numerical integration procedure. Given the current step size Δs_n, current position $\vec{r}_n$, and current pseudo-momentum $\vec{p}_n$, a candidate $n+1$ particle state is obtained, alongside new particle midpoint values, chord lengths, and step error metrics. *QuickAdvance()* makes no attempt to modify Δs_n. The *AccurateAdvance()* method is an iterative procedure that continues to refine the step size Δs_n until the error associated with the integration step is less than a predefined acceptable value. As a result, *AccurateAdvance()* could conceivably call *QuickAdvance()* many times before finding a suitable Δs_n.

4.8 Relativistic Acceleration Term Derivation

Relativistic effects are significant in high-energy particle transport. When considering relativistic effects [100], the algebraic form of Newton's Second Law is not applicable, i.e.,

$$\frac{\mathrm{d}\vec{p}}{\mathrm{d}t} = \vec{F} \neq m_0\vec{a}. \tag{4.71}$$

The correct acceleration term is derived as follows: note

$$\vec{F} = \frac{\mathrm{d}\vec{p}}{\mathrm{d}t} = \frac{\mathrm{d}}{\mathrm{d}t}\left(\gamma m_0 \vec{v}\right) = m_0\left(\vec{v}\frac{\mathrm{d}\gamma}{\mathrm{d}t} + \gamma\frac{\mathrm{d}\vec{v}}{\mathrm{d}t}\right). \tag{4.72}$$

The derivative of the Lorentz factor is given by

$$\frac{\mathrm{d}\gamma}{\mathrm{d}t} = \frac{\gamma^3 v}{c^2}\frac{\mathrm{d}v}{\mathrm{d}t}. \tag{4.73}$$

Note that for $v \neq 0$,

$$v\frac{\mathrm{d}v}{\mathrm{d}t} = \vec{v} \cdot \frac{\mathrm{d}\vec{v}}{\mathrm{d}t}. \tag{4.74}$$

Thus,

$$\vec{F} = m_0 \left[\frac{\gamma^3 \vec{v}}{c^2} \left(\vec{v} \cdot \frac{\mathrm{d}\vec{v}}{\mathrm{d}t} \right) + \gamma \frac{\mathrm{d}\vec{v}}{\mathrm{d}t} \right]. \tag{4.75}$$

To isolate $\frac{\mathrm{d}v}{\mathrm{d}t}$, an alternative expression for $\vec{v} \cdot \frac{\mathrm{d}\vec{v}}{\mathrm{d}t}$ is needed. Take the dot product of both sides of Equation 4.75 and solve for $\vec{v} \cdot \frac{\mathrm{d}\vec{v}}{\mathrm{d}t}$,

$$\vec{v} \cdot \frac{\mathrm{d}\vec{v}}{\mathrm{d}t} = \frac{\vec{v} \cdot \vec{F}}{m_0 \gamma^3}. \tag{4.76}$$

Substitute this expression into Equation 4.75 and isolate $\frac{\mathrm{d}\vec{v}}{\mathrm{d}t}$ to obtain the true relativistic acceleration term,

$$\vec{a} = \frac{\mathrm{d}\vec{v}}{\mathrm{d}t} = \frac{1}{\gamma m_0} \left(\vec{F} - \frac{\vec{v}(\vec{v} \cdot \vec{F})}{c^2} \right). \tag{4.77}$$

4.9 Geant4 System of Units and Constants

Geant4 uses—by default—a unique system of units. Table 4.4 displays the units assumed for "naked" numbers, or numbers that are unaccompanied by Geant4's built-in unit conversion coefficients.

Table 4.4: Comparison of base SI units and Geant4 system of default units.

Quantity	Base SI Unit	Geant4 Unit
Length	m	mm
Time	s	ns
Energy	J	MeV
Charge	C	e^+
Temperature	K	K
Amount	mol	mol
Luminous Intensity	cd	cd
Angle	rad	rad
Solid Angle	sr	sr

Physical and computational constants are generally defined with a limited precision. Table 4.5 displays the exact floating point values used for each physical constant relevant to Geant4 electromagnetic field transport and/or computing processes.

Table 4.5: Geant4 physical constant definitions.

Constant	Symbol	Value	Units
Pi	π	3.14159265358979312	–
Speed of light	c	299.792458	$\mathrm{mm\,ns^{-1}}$
Elementary charge	e	$1.602176634 \times 10^{-19}$	C
Proton rest mass energy	$\tilde{m}_p$	938.272013	MeV
Maximum C++ double value	$\mathcal{D}_{\max}$	$1.7976931348623157 \times 10^{308}$	–
Minimum C++ double value	$\mathcal{D}_{\min}$	$2.2250738585072014 \times 10^{-308}$	–
Large value	$\mathcal{K}$	9.0×10^{99}	–

Chapter 5

Validation of G4-ASPP using Combined Lunar Shielding Scenario

5.1 Introduction

The Artemis and Moon-to-Mars programs aim to develop a reliable method for sustained long-duration exploration missions to the Moon and eventually to Mars. The human health risks associated with space radiation exposure during these missions will be elevated significantly due to the extended time spent beyond the Earth's protective magnetosphere (an active shield itself). Under nominal conditions, astronauts will incur slightly higher GCR doses beyond LEO. If an extreme solar particle event were to occur, astronauts could receive proton doses that approach operational safety limits. Risk mitigation is a critical consideration in mission planning. Mission planning becomes more complicated for long-duration missions because the probability of encountering a rare, adverse event is inflated due to the increased duration in the spacecraft. Additionally, the accumulation of GCR dose contributions is more likely to approach established career dose limits.

The goal of this study is to evaluate charged particle radiation transport results of G4-ASPP against analogous results generated by a combination of previously validated radiation transport tools. In [77], charged particle transport methods through electromagnetic fields developed for G4-ASPP were verified against well-established propagation methodologies and showed good agreement. The next step in the validation process for G4-ASPP is to evaluate its ability to conduct charged particle transport considering

both active shielding and passive shielding components.

For every validation study, there must be a suitable basis for comparison. Unfortunately, there are no known publicly available radiation transport tools that are capable of simultaneous charged particle transport through electromagnetic fields *and* traditional radiation transport in bulk media. Therefore, a comparison between G4-ASPP and results from a combination of particle transport codes was pursued; multiple previously established transport codes to handle each component of transport that G4-ASPP attempts to simulate (active shielding and passive shielding). This combination is referred to as the "combination model".

The three programs that make up the combination model are ASPP, PHITS, and HZETRN, each covering a distinct piece of the overall transport problem.

ASPP—which is the primary inspiration behind G4-ASPP and has been validated against experimental beamline measurements in [28]—conducts charged particle transport through the electromagnetic fields generated by the active shielding components. ASPP numerically integrates the relativistic Lorentz force equation of motion for each source particle through the combined electrostatic field of the active shielding configuration until that source particle either

1. exits the problem domain, or

2. exceeds the maximum number of timesteps allotted to it according to its initial speed and the size of the problem domain.

ASPP does not model nuclear interactions, energy loss, or scattering within bulk media, and is therefore restricted to vacuum propagation between the source, the active shielding elements, and either the habitat outer surface or the bare lunar surface.

PHITS—a well-established general-purpose Monte Carlo transport code [84, 101]—is used to generate albedo response functions that account for the secondary particles produced when primary GCR ions interact with the lunar regolith surface. PHITS models the full range of nuclear and atomic interaction physics relevant to space radiation transport in bulk media, including hadron-nucleus and nucleus-nucleus reactions, spallation and fragmentation product generation, and electromagnetic (photon/electron/positron) transport, using its internal library of nuclear reaction and evaporation/fragmentation models. Because ASPP has no bulk-media transport capability, PHITS is the only component of the combination model that resolves what happens to a particle once it enters the regolith at the lunar surface.

HZETRN—a deterministic, one-dimensional, straight-ahead Boltzmann transport code developed by NASA and validated for space radiation applications [32]—transports the combined primary and secondary fluence distributions through the shielding of the habitat dome and computes the resulting dose and dose equivalent within the habitat interior. HZETRN solves the coupled linearized Boltzmann transport equations for neutrons, light ions, heavy ions, pions, muons, and electromagnetic cascade particles through a user-specified slab geometry, using the NUCFRG3 heavy-ion fragmentation model [102] and the Serber intranuclear cascade model [103] for nucleon-induced light-particle production, and computes absorbed dose and dose equivalent internally at each transport depth using the NASA and ICRP-60 quality factor implementations.

Together, ASPP handles the electromagnetic-field transport that PHITS and HZETRN cannot, while PHITS and HZETRN handle the bulk-media nuclear transport physics that ASPP cannot; no single one of the three codes is capable of modeling the complete hybrid shielding problem on its own. This is the gap G4-ASPP is intended to close within a single, self-consistent simulation.

The comparison between G4-ASPP and the combination model was carried out in the context of a simple lunar habitat and a simple active radiation shielding configuration intended to reduce the incident radiation exposure to hypothetical crew members within the habitat. This simple test scenario was designed such that a) both the electromagnetic field and bulk media transport capabilities of G4-ASPP could be demonstrated and b) the scenario was not so complicated as to prevent the combination model from adequately representing the physics.

The primary purpose of G4-ASPP is to evaluate the benefits of combined active-passive shielding configurations with respect to dosimetric outcomes. Thus, the quantities of interest when it comes to comparing G4-ASPP with the combination model are dosimetric shielding effectiveness metrics: the absorbed dose rate $\dot{D}$ and the dose equivalent rate $\dot{H}$ to a tissue target inside the habitat, and their dependence on passive shielding thickness and applied voltage used to power an active shield.

5.1.1 G4-ASPP Methodology Summary

G4-ASPP is built on top of the Geant4 Monte Carlo toolkit and is intended to model, within a single self-consistent simulation, the combination of charged-particle transport through the active shielding's electromagnetic field and subsequent nuclear/atomic transport through bulk shielding media. This is the same

overall transport problem that the combination model delegates across ASPP, PHITS, and HZETRN. G4-ASPP's electromagnetic field transport is verified against analytic and well-established charged-particle propagation methods in [77]; this chapter attempts to extend that verification to the combined hybrid shielding case addressed here. G4-ASPP uses the same active shielding geometry description (real and image charge/-plate positions, derived from the applied voltage via the self-potential relations of Section 5.2.1.1) as the ASPP stage of the combination model, so that both approaches are evaluated against an identical shielding configuration.

A full description of G4-ASPP's charged particle transport treatment is given in [77]. For the G4-ASPP results shown in this chapter, charged particle propagation through the active shielding electromagnetic field used the RK4S distance-stepping method, following the recommendation of [77] based on its favorable trajectory accuracy relative to computational cost.

For nuclear and atomic transport through the passive regolith and habitat dome shielding, G4-ASPP uses the Geant4 reference physics list `FTFP_INCLXX_HP`. In this physics list, hadron-nucleus inelastic scattering below approximately 3 GeV is handled by the Liège intranuclear cascade model (INCL++), which replaces the default Bertini cascade used in the more commonly applied `FTFP_BERT_HP` list. INCL++ additionally treats reactions induced by light nuclei up to $A = 18$ [104], which covers the highest-dose-contributing GCR primaries considered in this chapter. INCL++ is used in the intermediate range of approximately 3–15 GeV, and the Fritiof (FTF) string model is used above approximately 15 GeV for the high-energy tail of the GCR spectrum [105]. Nuclear de-excitation following intranuclear cascade is handled by Geant4's excitation handler, which invokes the Generalized Evaporation Model, multifragmentation, Fermi breakup, and fission models as appropriate [106]. The `_HP` designation activates the high-precision neutron cross section model, which uses evaluated nuclear data libraries (G4NDL) in place of parameterized cross sections for neutron elastic, inelastic, capture, and fission interactions below 20 MeV [105]. Electromagnetic transport of photons, electrons, positrons, and muons is handled by the standard Geant4 electromagnetic physics constructor, `G4EmStandardPhysics` [105].

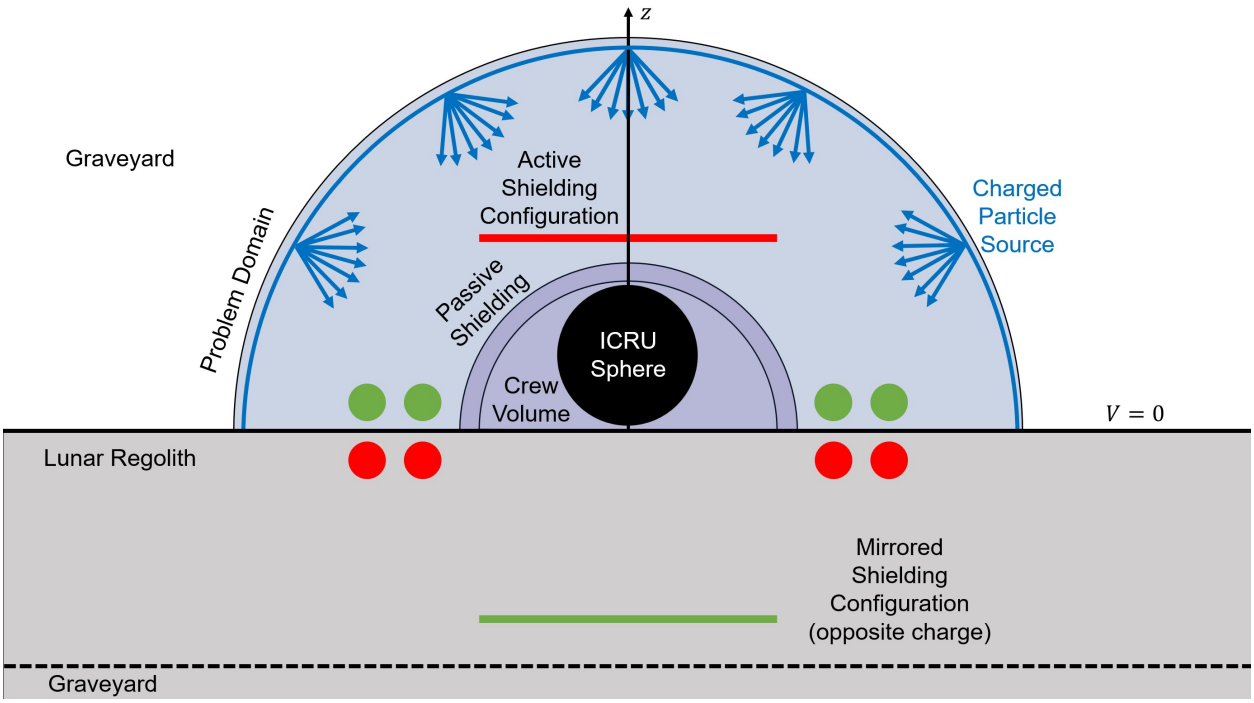


Figure 5.1: Two-dimensional schematic of a simple lunar habitat augmented with a simple active radiation shielding configuration; elements are not necessarily to-scale.

5.2 Materials and Methods

5.2.1 Lunar Habitat Scenario

Figure 5.1 presents a schematic of the simplified lunar habitat used to compare G4-ASPP with the combination model. The figure also suggests the different pathways by which radiation propagates from the source regions into the habitat volume. From top to bottom (exterior to interior), the schematic includes:

- the problem domain, defined as the geometric union of
  - a large hemisphere containing both the active shielding configuration and the lunar habitat, and
  - a semi-infinite slab of lunar regolith, which also includes a mirrored copy of the active shielding configuration to enforce a zero electric potential at the lunar surface;
- a hemispherical source of charged particles with a radius R_{src} just smaller than that of the problem domain, from which particles are emitted with a cosine angular distribution to approximate the half-space isotropy of the space radiation environment incident on the lunar surface.

The key geometric and material parameters of the scenario are summarized in Table 5.1, with selected

parameters shown in Figure 5.2. The habitat is modeled as a hemispherical shell of lunar regolith with a density of $\rho_{\text{reg}} = 1.6\,\text{g}\,\text{cm}^{-3}$. The regolith composition is based on the Apollo 17 lunar regolith material composition used in On-Line Tool for the Assessment of Radiation In Space (OLTARIS) [50], which is reproduced in Table 5.2.

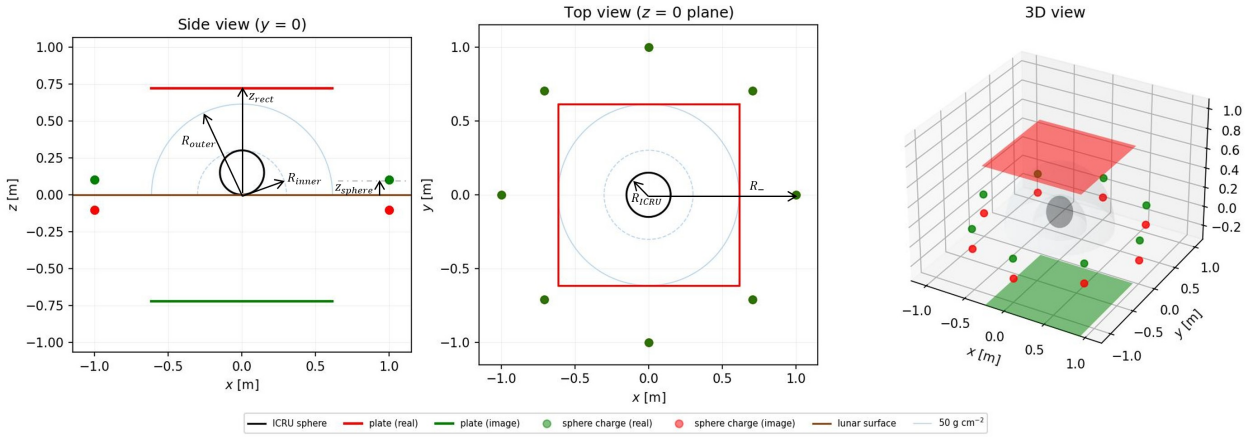


Figure 5.2: Transparent side, top, and 3D views of lunar habitat active-passive shielding configuration; depicts R_{ICRU}, R_{inner}, $R_{\text{outer}}(x)$, z_{rect}, R_{-}, z_{sphere}; R_{outer} depends on the chosen passive shielding thickness; in this case, $x = 50\,\text{g}\,\text{cm}^{-2}$.

Table 5.1: Key geometric and material parameters of the lunar habitat simulation scenario.

Parameter	Value	Description
R_{ICRU}	15.0 cm	ICRU sphere radius
R_{inner}	30.2 cm	Habitat inner radius ($= 2R_{\text{ICRU}} + 2\delta$)
$R_{\text{outer}}(x)$	$R_{\text{inner}} + x/\rho_{\text{reg}}$	Habitat outer radius at shielding x
ρ_{reg}	$1.6\,\text{g}\,\text{cm}^{-3}$	Regolith density
x	$0, 5, 10, 20, 30, 50$ g cm^{-2}	Passive shielding sweep
R_{surf}	20 m	Lunar regolith cylinder / scoring disk radius (G4-ASPP)
R_{tally}	200 m	PHITS albedo tally disk radius
δ	0.1 cm	Geometric tolerance
$z_{\text{rect,standoff}}$	10 cm	Standoff distance between dome apex and center of plate
Δw	1 cm	Thickness of charged plate in z-direction

The molecular composition by mass was converted to an elemental mass-fraction composition for use in G4-ASPP, PHITS, and HZETRN. Element number densities were also calculated for the HZETRN material definition. For HZETRN, the most naturally abundant isotope of each element was selected when generating the material cross sections. The resulting elemental composition and number densities are given in Table 5.3.

The elemental mass fraction for element j of molecule i, f_{ij}, is given by

$$f_{ij} = \frac{n_{ij}\mathcal{M}_j}{\sum_j n_{ij}\mathcal{M}_j}, \tag{5.1}$$

Molecule	Mass Fraction
MgO	0.095
MnO	0.0024
FeO	0.177
Cr_2O_3	0.0046
Al_2O_3	0.109
O_2Ti	0.096
S	0.0012
O_5P_2	0.0007
O	0.00352
Na_2O	0.0038
CaO	0.107
K_2O	0.00078
O_2Si	0.399

Table 5.2: Lunar regolith molecular composition by mass ($\rho_{\text{reg}} = 1.6\,\text{g}\,\text{cm}^{-3}$) [50].

Element	Mass Fraction	$(Z,\, A)$	Number Density [atoms cm^{-3}]
O	0.416942	(8, 16)	$1.569\,402 \times 10^{22}$
Si	0.186507	(14, 28)	$3.999\,191 \times 10^{21}$
Fe	0.137584	(26, 56)	$1.483\,658 \times 10^{21}$
Ca	0.076472	(20, 40)	$1.149\,079 \times 10^{21}$
Al	0.057689	(13, 27)	$1.287\,577 \times 10^{21}$
Ti	0.057537	(22, 48)	$7.238\,784 \times 10^{20}$
Mg	0.057289	(12, 24)	$1.419\,470 \times 10^{21}$
Cr	0.003147	(24, 52)	$3.645\,244 \times 10^{19}$
Na	0.002819	(11, 23)	$7.384\,480 \times 10^{19}$
Mn	0.001859	(25, 55)	$2.037\,461 \times 10^{19}$
S	0.001200	(16, 32)	$2.254\,076 \times 10^{19}$
K	0.000648	(19, 39)	$9.973\,501 \times 10^{18}$
P	0.000306	(15, 31)	$5.939\,706 \times 10^{18}$

Table 5.3: Lunar regolith elemental composition by mass, most naturally abundant isotope, and atomic number density ($\rho_{\text{reg}} = 1.6\,\text{g}\,\text{cm}^{-3}$) [50].

where n_{ij} is the stoichiometric coefficient attached to element j of molecule i and $\mathcal{M}_j$ is the atomic weight of element j. The elemental mass fractions of the composite material, $\mathcal{W}_j$, are given by

$$\mathcal{W}_j = \frac{\sum_i y_i f_{ij}}{\sum_j \sum_i y_i f_{ij}}, \tag{5.2}$$

where y_i is the mass fraction associated with molecule i for the composite material. The number density of element j is given by

$$N_j = \frac{\rho \mathcal{W}_j N_A}{\mathcal{M}_j}, \tag{5.3}$$

where ρ is the density of the composite material and N_A is Avogadro's number.

The passive shielding areal density x of the hemispherical shell is swept over six values (0, 5, 10, 20, 30,

and $50\,\mathrm{g\,cm^{-2}}$) in both models, to characterize the dose reduction afforded by the regolith shell alone and together with the active shielding. The International Commission on Radiation Units and Measurements (ICRU) tissue sphere [107] ($R_{\mathrm{ICRU}} = 15\,\mathrm{cm}$) is centered at $\vec{r}_c = (R_{\mathrm{ICRU}} + \delta)\hat{z}$, the vertical midpoint of the habitat cavity, leaving a clearance of $\delta = 0.1\,\mathrm{cm}$ between the sphere and both the habitat floor and the inner dome surface. The ICRU sphere serves as the scoring volume for all simulations and is composed of ICRU four-element tissue (aka, soft tissue, or simply tissue) with density $\rho_{\mathrm{tis}} = 1\,\mathrm{g\,cm^{-3}}$. This composition is given in Table 5.4.

Element	Mass Fraction	$(Z,\ A)$	Number Density [atoms $\mathrm{cm^{-3}}$]
O	0.762	(8, 16)	2.87×10^{22}
C	0.111	(6, 12)	5.57×10^{21}
H	0.101	(1, 1)	6.04×10^{22}
N	0.026	(7, 14)	1.12×10^{21}

Table 5.4: ICRU four-element tissue elemental composition [107]; $\rho_{\mathrm{tis}} = 1\,\mathrm{g\,cm^{-3}}$. Note that the ICRU sphere is technically defined as a mixture of *natural-abundance* O, C, H, and N. For simplicity, each element is assumed to be entirely composed of its single most abundant isotope. This is a good approximation because the dominant isotopes comprise approximately 99.7% of natural O, 98.9% of natural C, 99.99% of natural H, and 99.6% of natural N.

5.2.1.1 Active Shielding Configuration

The active shielding configuration studied here is referred to as a "lunar umbrella". It consists of two types of charged conductors arranged to deflect incoming positively charged ions upward and away from the habitat before they reach the passive shielding of the lunar habitat. The first element is a positively charged rectangular plate positioned above the habitat dome, while the second consists of negatively charged spherical electrodes distributed around the outside of the habitat.

The first element is a horizontally oriented square conducting plate of side length

$$\Delta u = \Delta v = 2R_{\mathrm{outer}}\left(50\,\mathrm{g\,cm^{-2}}\right), \tag{5.4}$$

where $R_{\mathrm{outer}}(x)$ is defined as

$$R_{\mathrm{outer}}(x) = R_{\mathrm{inner}} + \frac{x}{\rho_{\mathrm{reg}}}. \tag{5.5}$$

The plate is centered above the dome apex at a height of

$$z_{\mathrm{rect}} = R_{\mathrm{outer}}(50\,\mathrm{g\,cm^{-2}}) + z_{\mathrm{rect,standoff}} + \frac{\Delta w}{2}, \tag{5.6}$$

where $z_{\text{rect,standoff}}$ is the distance along the z-axis from the dome apex to the center of the positively charged plate, and Δw is the thickness of the plate in the z-direction. The plate is held at potential V. According to the self-potential standard laid out in Equation 3.50, this corresponds to a surface charge density of

$$\sigma = \frac{2\pi\epsilon_0 V}{\Delta u \operatorname{arcsinh}\left(\frac{\Delta v}{\sqrt{(\Delta u)^2+(\Delta w)^2}}\right) + \Delta v \operatorname{arcsinh}\left(\frac{\Delta u}{\sqrt{(\Delta v)^2+(\Delta w)^2}}\right) - \Delta w \arctan\left(\frac{\Delta u \Delta v}{\Delta w\sqrt{(\Delta u)^2+(\Delta v)^2+(\Delta w)^2}}\right)}. \tag{5.7}$$

The second element consists of $N_{\text{elec}} = 8$ spherical conducting electrodes of radius $R_{\text{sphere}} = 10\,\text{cm}$, arranged uniformly azimuthally at radius $R_{-} = 100\,\text{cm}$ from the z-axis, with centers at height $z_{\text{sphere}} = R_{\text{sphere}} + \delta$ above the lunar surface. Each electrode carries charge $Q_{\text{point}} = -Q_{\text{rect}}/N_{\text{elec}}$, chosen to make the configuration charge neutral. ASPP represents each electrode as a point charge at the sphere center, whereas G4-ASPP also models the electrode as a solid sphere.

It is well-known that the lunar surface experiences differential charging as a result of exposure to solar ultraviolet light (which leads to photoelectron production) and the ambient solar wind [108–110]. The electric potential across the lunar surface is neither uniform nor constant, but it is small ($\pm 1\,\text{V}$–$1\,\text{kV}$) relative to the electric potentials produced by the proposed active shielding configuration ($\sim$MVs). In this work, differential lunar surface charging is neglected.

To enforce zero electric potential at the lunar surface ($z = 0$), the method of images is applied. Image charges are introduced below the $z = 0$ plane as mirror reflections of the real charges with their signs reversed [111]. These image charges do not represent physical conductors; they are a mathematical device to satisfy the boundary condition imposed by the grounded conducting lunar surface ($V(z = 0) = 0$). The full set of charges (real and image) is written into the simulation configuration file and passed directly to both the ASPP and G4-ASPP workflows.

The applied voltage V is swept over eight values (0, 1, 2, 5, 10, 20, 50, and 100 MV), yielding 6 shielding $\times$ 8 voltage = 48 distinct (shielding, voltage) combinations per primary GCR species in each model.

5.2.2 Albedo Response Functions

Generically, radiation albedo refers to the ratio of the number of emergent particles to the number of particles incident on a surface. The differential number albedo, $\alpha(Z, T, \vec{\Omega}; Z', T', \vec{\Omega}')$, can be defined as the ratio of (1) the total number of particles of type Z' emerging from a differential surface element $\mathrm{d}A$ with energies in $\mathrm{d}T'$

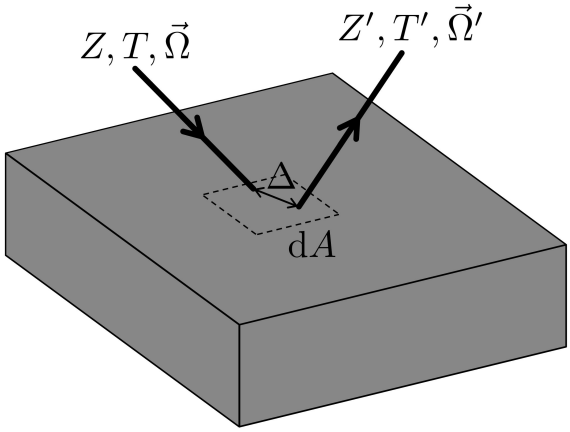


Figure 5.3: Illustration of the radiation albedo concept; adapted from Figure 7.14 of [61].

about T' and with directions in $\mathrm{d}\Omega'$ about $\vec{\Omega}'$ to (2) the total number of particles initially incident upon the same differential surface element $\mathrm{d}A$ of type Z, energy T, and direction $\vec{\Omega}$. Figure 5.3 illustrates the concept and the variables involved. There are some implicit assumptions that accompany albedo approximations. It is assumed that the distance between the particle entry location and the exit location, Δ, is smaller than the differential surface area element width, i.e. $\Delta < \sqrt{\mathrm{d}A}$. It is also assumed that the reflecting medium is sufficiently deep, to ensure that it is unlikely that particles will pass through the medium without interacting. Finally, it is assumed that there is little to no material impeding the path between the reflecting medium and the source. This assumption is easily justifiable by considering the state of a particle *just outside* the reflecting medium as the initial particle state. In certain scenarios, such as on the lunar surface where the atmosphere is negligible, there is practically nothing standing between the source and reflecting medium (the lunar regolith). In mathematical form,

$$\alpha(Z, T, \vec{\Omega}; Z', T', \vec{\Omega}') = \frac{J_{\mathrm{out}}(Z, T, \vec{\Omega}; Z', T', \vec{\Omega}')}{\int_{4\pi}\int_{0}^{\infty}\sum_{\tilde{Z}\in\mathcal{Z}} J_{\mathrm{in}}(;\tilde{Z}, \tilde{T}, \tilde{\vec{\Omega}})\mathrm{d}\tilde{T}\mathrm{d}\tilde{\Omega}}, \tag{5.8}$$

where $\mathcal{Z}$ is the set of all possible particle types, $J_{\mathrm{out}}(Z, T, \vec{\Omega}; Z', T', \vec{\Omega}')$ is the net particle current out of the surface as a distribution function of Z', T', and $\vec{\Omega}'$, and $J_{\mathrm{in}}(;Z, T, \vec{\Omega})$ is the net particle current into the surface as a distribution function of Z, T and $\vec{\Omega}$. Both currents have dimensions of particles per unit area per unit energy per unit solid angle. To obtain the differential number albedo *response function*, let the

incident particle current be of a single particle type $\tilde{Z}$, single energy $\tilde{T}$, and single direction $\tilde{\Omega}$,

$$J_{\text{in}}(Z,T,\vec{\Omega};\tilde{Z},\tilde{T},\vec{\tilde{\Omega}}) = \frac{N_{\text{inc}}(\tilde{Z},\tilde{T},\vec{\tilde{\Omega}})\delta_{\tilde{Z},Z}\delta(\tilde{T}-T)\delta^2(\vec{\tilde{\Omega}}-\vec{\Omega})}{A}, \tag{5.9}$$

where $N_{\text{inc}}(\tilde{Z},\tilde{T},\vec{\tilde{\Omega}})$ is the total number of particles entering the surface of area A as a function of $\tilde{Z}$, $\tilde{T}$, and $\vec{\tilde{\Omega}}$. Note that $\delta_{a,b}$ represents the Kronecker delta function, which is zero everywhere except for $a = b$, where its value is unity. Also note that, in spherical coordinates, the shorthand $\delta^2(\vec{\tilde{\Omega}}-\vec{\Omega})$ is defined as

$$\delta^2(\vec{\tilde{\Omega}}-\vec{\Omega}) \equiv \frac{\delta(\tilde{\theta}-\theta)\delta(\tilde{\psi}-\psi)}{\sin\theta}. \tag{5.10}$$

Inserting the result of equation 5.9 into equation 5.8 yields the differential number albedo response function,

$$\alpha(Z,T,\vec{\Omega};Z',T',\vec{\Omega}') = \frac{J_{\text{out}}(Z,T,\vec{\Omega};Z',T',\vec{\Omega}')A}{N_{\text{inc}}(Z,T,\vec{\Omega})}. \tag{5.11}$$

In words, the number albedo is the outgoing current multiplied by the area over which it is scored, per incident particle. When constructing albedo response functions, $J_{\text{out}}(Z,T,\vec{\Omega};Z',T',\vec{\Omega}')$ refers to the outgoing current distribution that arises from incident particles of type Z, energy T, and direction $\vec{\Omega}$. To *utilize* these albedo response functions, the outgoing current $J_{\text{out}}(Z,T,\vec{\Omega};Z',T',\vec{\Omega}')$, which may be ordinarily dependent on any set of variables $\vec{P}$ that the incident current distribution is also dependent upon (which also includes Z, T, and $\vec{\Omega}$), is determined by folding the albedo response function with the incident current distribution,

$$J_{\text{out}}(\vec{P};Z',T',\vec{\Omega}') = \int_{4\pi}\int_{0}^{\infty}\sum_{Z\in\mathcal{Z}}\alpha(Z,T,\vec{\Omega};Z',T',\vec{\Omega}')J_{\text{in}}(\vec{P};Z,T,\vec{\Omega})\mathrm{d}T\mathrm{d}\Omega. \tag{5.12}$$

In this case, $J_{\text{in}}(\vec{P};Z,T,\vec{\Omega})$ is an arbitrary incident current distribution.

5.2.2.1 PHITS Albedo Simulation Setup

The albedo response functions for the lunar regolith were computed using PHITS version 3.17 [101]. A semi-infinite slab of lunar regolith 20 m deep was modeled, which is sufficient to ensure that no primary particle traverses the slab without interaction. The regolith composition was modeled as shown in Tables 5.2 and 5.3. The density was set to $\rho_{\text{reg}} = 1.6\,\text{g}\,\text{cm}^{-3}$.

Separate PHITS runs were performed for each combination of incident particle species Z, incident kinetic

energy per nucleon T, and incident polar cosine $\omega = \cos\theta$. The energy grid consisted of 100 logarithmically spaced points from 0.01 MeV/n to 5×10^4 MeV/n, and the angular grid consisted of 10 uniformly spaced cosine bins from $\omega = -1$ (normal incidence) to $\omega = 0$ (parallel to surface). Outgoing particles were tallied using a `t-cross` surface crossing tally (`a-curr` output, unit 5, [cm^2/MeV/n/sr/source]) over a disk of radius $R_{\text{tally}} = 200$ m centered at the entry point, so the number albedo of Equation 5.11 is the tallied current multiplied by $A_{\text{tally}} = \pi R_{\text{tally}}^2$. The tally resolved 100 outgoing energy bins and 20 outgoing cosine bins, and recorded 60 outgoing particle species spanning $Z = 0$ (neutrons and photons) through $Z = 28$ (Ni). The 100 energies $\times$ 10 angles $\times$ 2 species = 2000 independent PHITS runs each targeted 3×10^7 source particles. Each run was executed on 16 cores with a limit of 168 hours per job, and a run that did not finish within a job was resubmitted in the PHITS restart mode, which continues the existing tallies. The median run completed 3×10^7 source particles. At incident energies above 1×10^4 MeV/n, where each history is most expensive, the median was 2×10^6 for ^{1}H and 1×10^6 for ^{4}He, and the smallest run completed 2.3×10^5. Of the 2000 runs, 74 produced no tally output: 71 ^{4}He runs above 4000 MeV/n, including every incident angle at the three highest energies, and three ^{1}H runs. The combination model treats the albedo response at these grid points as zero (Section 5.6). Incident particle species were limited to protons and alpha particles, as they make up the vast majority of the incident GCR spectrum. Heavier particles are more efficient when it comes to inducing albedo secondaries, but the incident flux of protons and alphas overwhelms the incident flux of heavier ions.

The nuclear reaction models used to generate the albedo response functions followed the PHITS default configuration with two explicit overrides. Nucleon-induced and light-ion-induced reactions used the JQMD-2.0 intranuclear cascade/molecular dynamics model (`irqmd=1`), selected in place of the legacy JQMD implementation for improved accuracy in nucleon-nucleon interactions [101]. Nucleus-nucleus and nucleon-nucleus reaction cross sections used the "Sato formula" (`icxsni=2`) [101]. De-excitation of the reaction residuals following intranuclear cascade was handled by the Generalized Evaporation Model (GEM) [112]. Coulomb (angular) straggling of charged particles was modeled using the first-order Moliere formulation (`nspred=2`) [101]. Photon, electron, and positron transport was enabled via EGS5 mode (`negs=1`), rather than PHITS's default of omitting electromagnetic cascade transport entirely, so that the albedo response functions capture bremsstrahlung and electromagnetic cascade contributions from the primary hadronic interactions [101].

5.2.3 ASPP + PHITS + HZETRN Simulation Architecture

The quantities used to compare the ASPP+PHITS+HZETRN combination model with G4-ASPP are the absorbed dose rate, $\dot{D}$, and the dose equivalent rate, $\dot{H}$, in the ICRU sphere located inside the lunar habitat.

The combination model requires a sequence of simulations because no individual code in the workflow models all of the relevant transport processes. The workflow begins with an ASPP simulation that transports the source particles from the source region to one of two interfaces:

1. the lunar surface–vacuum interface, or

2. the outer surface of the lunar habitat–vacuum interface.

Because ASPP does not model transport through bulk media, the subsequent transport depends on either PHITS or HZETRN, depending on the interface reached by the particle.

At the lunar surface, ASPP tallies the incident differential particle current distribution $J_{\text{in}}(\vec{r}; Z, T, \vec{\Omega})$, where $\vec{r}$ is a crossing location on the regolith surface ($\vec{r} \cdot \hat{z} = 0$) and $\vec{\Omega} \cdot \hat{z} < 0$ for every particle entering the regolith. The albedo response functions are applied to this distribution through the folding relation of Equation 5.12, with the position on the lunar surface taking the place of the generic parameter vector $\vec{P}$,

$$J_{\text{out}}(\vec{r}; Z', T', \vec{\Omega}') = \sum_{Z \in \mathcal{Z}} \int_{\vec{\Omega} \cdot \hat{z} < 0} \int_0^\infty \alpha(Z, T, \vec{\Omega}; Z', T', \vec{\Omega}') J_{\text{in}}(\vec{r}; Z, T, \vec{\Omega}) \mathrm{d}T \mathrm{d}\Omega, \tag{5.13}$$

to obtain the differential distribution of particles emerging from the lunar regolith. Each factor in Equation 5.13 has a direct physical meaning. The product $J_{\text{in}}(\vec{r}; Z, T, \vec{\Omega})\mathrm{d}T\mathrm{d}\Omega$ is the number of particles of species Z entering the regolith per unit surface area at $\vec{r}$ with kinetic energy per nucleon in $\mathrm{d}T$ about T and direction in $\mathrm{d}\Omega$ about $\vec{\Omega}$. By Equation 5.11, $\alpha(Z, T, \vec{\Omega}; Z', T', \vec{\Omega}')\mathrm{d}T'\mathrm{d}\Omega'$ is the number of particles of species Z' that emerge with kinetic energy per nucleon in $\mathrm{d}T'$ about T' and direction in $\mathrm{d}\Omega'$ about $\vec{\Omega}'$ per incident particle in state $(Z, T, \vec{\Omega})$. Summing the product over all incident states gives the outgoing current, which carries the same units as J_{in}. Only the inward hemisphere contributes to the solid-angle integral because J_{in} vanishes for $\vec{\Omega} \cdot \hat{z} \geq 0$. Using the incident current at $\vec{r}$ to produce the outgoing current at the same $\vec{r}$ is the locality assumption stated with Equation 5.8: the separation Δ between entry and exit points is small compared with the spatial resolution at which J_{in} is constructed.

This outgoing distribution is used as the source distribution for a second ASPP simulation, which trans-

ports the albedo particles toward the lunar habitat. Expressed in the same form as the primary source term of Equation 5.41, the albedo source is

$$S_{\mathrm{alb}}(\vec{r}, Z', T', \vec{\Omega}') = J_{\mathrm{out}}(\vec{r}; Z', T', \vec{\Omega}')\delta(\vec{r}\cdot\hat{z})\,\mathcal{H}\big(|\vec{r}\times\hat{z}| - R_{\mathrm{fp}}\big)\,\mathcal{H}(\vec{\Omega}'\cdot\hat{z}). \tag{5.14}$$

The δ-function confines emission locations to the regolith surface, the first unit step function removes emission from beneath the habitat footprint (Step 3), and the second unit step function restricts emission directions to the outgoing hemisphere. No outer limit is needed, because J_{out} vanishes wherever no primary particle reaches the surface. Unlike Equation 5.41, Equation 5.14 contains no additional factor of $|\vec{\Omega}'\cdot\hat{n}|$, because J_{out} is already a current (a surface-crossing rate per unit area) rather than an intensity. Integrating S_{alb} over position, energy, and outgoing direction gives the total number of albedo particles emitted per primary source particle, $C^{\mathrm{total}}(Z')$ (Step 3).

Particles that reach the outer surface of the lunar habitat are instead transported through the habitat shielding using depth-dose response functions developed with HZETRN, which give the absorbed dose rate and dose equivalent rate within the ICRU sphere.

The entire end-to-end workflow is carried out as detailed in Sections 5.2.3.1–5.2.3.11.

5.2.3.1 Step 1: Compute Incident GCR Flux Distribution

The incident GCR flux is defined using BON2020 [52] outputs. BON2020 produces the omnidirectional differential flux for 28 species from hydrogen through nickel over the energy range 0.01–50,000 MeV/n. Dividing by 4π gives the isotropic differential flux per unit solid angle, $\phi_{\mathrm{GCR}}(Z;T)$, in units of $[\mathrm{MeV/n^{-1}\,m^{-2}\,s^{-1}\,sr^{-1}}]$. Integrating over the hemisphere of incident directions and converting from $\mathrm{m^{-2}}$ to $\mathrm{cm^{-2}}$ gives the boundary condition fluxes for each species in units of $[\mathrm{cm^{-2}\,s^{-1}\,MeV/n^{-1}}]$. The solar modulation parameter was set to $\tilde{\Phi} = 300\,\mathrm{MV}$ to emulate solar minimum-like conditions. Figure 2.4 shows the differential flux spectrum produced by BON2020 with $\tilde{\Phi} = 300\,\mathrm{MV}$ (solar minimum) and $\tilde{\Phi} = 1200\,\mathrm{MV}$ (solar maximum).

5.2.3.2 Step 2: Execute Primary ASPP Simulations

An ASPP simulation is performed for each combination of primary GCR species Z and incident kinetic energy per nucleon T_k on a 100-point logarithmic grid, and applied voltage V. The source is distributed over the curved surface of the upper hemisphere of radius R_{src}. The initial position is sampled uniformly

in azimuth and uniformly in polar cosine, with $\psi_{\rm pos} \in [0, 2\pi)$ and $\omega_{\rm pos} = \cos\theta_{\rm pos} \in [0, 1]$. Thus, the initial position is

$$\vec{r}_0 = R_{\rm src} \left\langle \sin\theta_{\rm pos}\cos\psi_{\rm pos}, \sin\theta_{\rm pos}\sin\psi_{\rm pos}, \cos\theta_{\rm pos} \right\rangle . \tag{5.15}$$

The initial particle direction is sampled relative to the local inward source surface normal,

$$\hat{n}_{\rm in} = -\frac{\vec{r}_0}{|\vec{r}_0|}. \tag{5.16}$$

The local polar cosine, $\omega_{\rm dir} = \cos\theta_{\rm dir}$, is sampled according to the cosine distribution,

$$\omega_{\rm dir} = \sqrt{1 - u^2}, \qquad u \sim \mathcal{U}(0, 1), \tag{5.17}$$

while the local azimuth, $\psi_{\rm dir}$, is sampled uniformly over $[0, 2\pi)$. The resulting initial direction is therefore directed into the problem domain with the required cosine angular distribution. The initial speed of the ion, v_0, is determined from the initial kinetic energy per nucleon associated with run k, T_k, via

$$v_0 = c\sqrt{1 - \left(1 + \frac{AT_k}{m_0 c^2}\right)^{-2}}, \tag{5.18}$$

where c is the speed of light, m_0 is the rest mass of the ion, and A is the mass number of the ion. Two mutually orthogonal unit vectors that are also orthogonal to $\hat{n}_{\rm in}$ are

$$\hat{e}_{\theta_{\rm dir}} = \left\langle \cos\theta_{\rm pos}\cos\psi_{\rm pos}, \cos\theta_{\rm pos}\sin\psi_{\rm pos}, -\sin\theta_{\rm pos} \right\rangle , \tag{5.19}$$

and

$$\hat{e}_{\psi_{\rm dir}} = \left\langle -\sin\psi_{\rm pos}, \cos\psi_{\rm pos}, 0 \right\rangle . \tag{5.20}$$

$\hat{e}_{\theta_{\rm dir}}$ points along the source surface in the direction of increasing $\theta_{\rm pos}$ and $\hat{e}_{\psi_{\rm dir}}$ points along the source surface in the direction of increasing $\psi_{\rm pos}$. This constructs the orthonormal basis $\{\hat{e}_{\theta_{\rm dir}}, \hat{e}_{\psi_{\rm dir}}, \hat{n}_{\rm in}\}$ at the source position $\vec{r}_0$. The corresponding initial ion velocity is then

$$\vec{v}_0 = v_0 \begin{bmatrix} \hat{e}_{\theta_{\rm dir}} & \hat{e}_{\psi_{\rm dir}} & \hat{n}_{\rm in} \end{bmatrix} \begin{bmatrix} \sin\theta_{\rm dir}\cos\psi_{\rm dir} \\ \sin\theta_{\rm dir}\sin\psi_{\rm dir} \\ \cos\theta_{\rm dir} \end{bmatrix} . \tag{5.21}$$

Each run transports $N = 10^5$ source particles and each run is seeded with an independent random-number sequence. After initialization, each ion is propagated through the electromagnetic field of the active shielding configuration with a velocity-Verlet integrator. A particle is tracked until it reaches a scoring surface or enters the graveyard, defined as the semi-infinite volume that is the logical complement of the box described by the intersection $(|x| \leq R_{\mathrm{src}}) \cap (|y| \leq R_{\mathrm{src}}) \cap (-R_{\mathrm{src}} \leq z \leq R_{\mathrm{src}})$ (i.e., the graveyard is all of space that is not within said box). Particles reaching the lunar surface at $z = 0$ are recorded as surface hits, and particles reaching the habitat are recorded as dome hits; in both cases the position and velocity at the crossing are recorded. Particles that leave the box without reaching either scoring interface are discarded.

To bound the cost of any trajectory that remains inside the box, each particle is allowed at most

$$N_{\mathrm{steps}} = f \frac{d_{\mathrm{box}}}{v_0 \Delta t} \tag{5.22}$$

integration steps, where d_{box} is the length of the diagonal of the box and Δt is the integration time step. d_{box}/v_0 is the time required for a particle to traverse the box diagonal in a straight line. The factor f allows for trajectories that are slowed or turned by the field. In this work, $f = 2$.

The outer surface of the habitat is represented by eight concentric hemispherical scoring shells, one at $R_{\mathrm{outer}}(x)$ for each passive shielding thickness. A particle is scored at every shell it enters, with the entry point located within the integration step in which it occurs, and is terminated at the innermost shell. All eight shielding thicknesses are scored within a single ASPP transport simulation.

5.2.3.3 Step 3: Albedo Response Function Convolution

This step converts the surface hits of each primary run into a source of albedo particles for each outgoing species Z'. The kinetic energy per nucleon T and direction $\vec{\Omega}$ of each surface hit follow from its velocity $\vec{v}$ at the surface crossing,

$$T = \frac{m_0 c^2}{A} \left(\frac{1}{\sqrt{1 - |\vec{v}|^2/c^2}} - 1 \right), \tag{5.23}$$

with polar cosine $\omega = \vec{\Omega} \cdot \hat{z}$ and azimuth $\psi = \mathrm{atan2}(\Omega_y, \Omega_x)$, where $\vec{\Omega} = \vec{v}/|\vec{v}|$.

Surface hits inside a footprint of radius $R_{\mathrm{fp}} = 92.7\,\mathrm{cm}$, larger than the outer radius of every dome considered, $|\vec{r}| \leq R_{\mathrm{fp}}$, are discarded, because these primaries would first have reached the dome prior to reaching $z = 0$. The same footprint is used for every shielding thickness, so one albedo source is generated

per primary run. This also discards the annulus between $R_{\mathrm{outer}}(x)$ and R_{fp}, which is less than 0.2 % of the lunar surface area within the source radius.

Because the albedo response is local, the lunar surface is divided into n_b square spatial bins of equal area A_b, whose bounding box is the spatial extent of the surface hits in the run. Within each spatial bin, the surface hits are binned on the incident grid of the PHITS response functions (Section 5.2.2.1): energy bin j, of width ΔT_j, contains the grid energy T_j, and cosine bin q, of width $\Delta\omega_q$, contains the grid cosine ω_q. The incident current in spatial bin b, per primary source particle, is estimated as

$$J_{\mathrm{in}}(b; Z, T_j, \omega_q) = \frac{n_{b,jq}}{N\, A_b\, \Delta T_j\, 2\pi\, \Delta\omega_q}, \tag{5.24}$$

where $n_{b,jq}$ is the number of surface hits in spatial bin b with kinetic energy per nucleon in energy bin j and polar cosine in cosine bin q, N is the number of primary source particles in the run, and $2\pi\Delta\omega_q$ is the solid angle of cosine bin q. Every primary source particle carries unit weight, so each surface hit counts once. Z is the primary species of the run. The current does not resolve the incident azimuth ψ, because the regolith slab is symmetric about $\hat{z}$ and the PHITS tally resolves only the outgoing polar cosine, so the response depends on the incident and outgoing directions only through ω and ω'. Only surface hits enter Equation 5.24. Dome hits are passed to the HZETRN stage (Steps 5–9).

Folding this current with the albedo response, the discrete form of Equation 5.12, gives the outgoing current from bin b, per unit area and per primary source particle,

$$J_{\mathrm{out}}(b; Z', T', \omega') = 2\pi \sum_j \sum_q \alpha(Z, T_j, \omega_q; Z', T', \omega')\, J_{\mathrm{in}}(b; Z, T_j, \omega_q)\, \Delta T_j \Delta\omega_q. \tag{5.25}$$

The product $2\pi J_{\mathrm{in}} \Delta T_j \Delta\omega_q = n_{b,jq}/(N A_b)$ is the number of particles entering bin b per unit area per primary source particle in incident state (T_j, ω_q), and α converts each of them into outgoing particles per unit T' and per unit solid angle. Each surface hit is simply assigned the response of the grid point whose energy and cosine bins contain it, without interpolation.

The total outgoing current from bin b is

$$C_b^{\mathrm{spatial}}(Z') = \int_{\omega'>0} \int_0^\infty J_{\mathrm{out}}(b; Z', T', \omega') \mathrm{d}T'\, \mathrm{d}\Omega', \tag{5.26}$$

the number of outgoing particles of species Z' per unit area per primary source particle. Multiplying by the bin area and summing over bins gives the number of outgoing particles of species Z' per primary source particle,

$$C^{\text{total}}(Z') = \sum_b C_b^{\text{spatial}}(Z')\, A_b. \tag{5.27}$$

The outgoing distribution is then sampled into an ASPP source file (`source.txt`) for each outgoing species. For each spatial bin, n_{draw} energy–angle pairs are sampled from the bin's outgoing distribution by inverse-transform sampling, and each pair is replicated at n_{az} azimuthal angles about the surface normal. Source positions are sampled uniformly within the bin; a position that falls inside the dome footprint is resampled within the same bin, because the current assigned to the bin originates from surface hits outside the footprint. The source particle ℓ, sampled from bin b, is assigned the weight

$$w_\ell = \frac{C_b^{\text{spatial}}(Z')\, A_b}{C^{\text{total}}(Z')} \frac{1}{n_{\text{draw}}\, n_{\text{az}}}. \tag{5.28}$$

The weights of each source file sum to unity, so w_ℓ is the fraction of the outgoing albedo of species Z' that particle ℓ represents, while $C^{\text{total}}(Z')$ carries the absolute number of albedo particles per primary source particle. The two factors are combined with the physical source strength of the parent primary run in Step 9a.

5.2.3.4 Step 4: Secondary ASPP Transport

A secondary ASPP simulation is performed for each primary simulation and outgoing particle species using the corresponding `source.txt` file generated in Step 3. The secondary particles are initialized at their sampled positions on the lunar surface with the sampled energies and directions from the albedo response convolution. Each secondary particle retains the statistical weight assigned in Equation 5.28. The secondary particles are then propagated through the same electrostatic field configuration used in the corresponding primary ASPP simulation and are scored at all eight hemispherical shells exactly as in Step 2. Secondary trajectories that return to the lunar surface are discarded, such that only a single albedo generation is modeled.

Only outgoing species for which a dose response is available are transported: ^{1}H, ^{4}He, neutrons, ^{16}O, ^{24}Mg, ^{28}Si, and ^{56}Fe (Step 6), together with photons (Step 9b). Neutrons and photons feel no electric field

and cross no material between the lunar surface and the habitat, so their shell crossings are computed exactly by intersecting each source particle's straight-line path with the shells, using the same entry conditions as the ASPP scoring.

The source file generated in Step 3 for a given primary run and outgoing species contains $n = n_{b'} n_{\mathrm{draw}} n_{\mathrm{az}}$ particles, where $n_{b'}$ is the number of spatial bins with non-zero outgoing current (typically $n = 10^6$). To keep the secondary transport tractable, each charged secondary source file is subsampled uniformly without replacement to $m = 10^4$ particles for ^{1}H and ^{4}He and $m = 10^3$ particles for heavier ions, and each retained weight is multiplied by n/m. Source files with $n \leq m$ are used unchanged, and neutral secondaries, whose shell crossings are computed analytically, are not subsampled. Because the secondary transport contains no material, the contribution of each source particle to a tally is a fixed function of its initial position, energy, and direction. The rescaled subsample is identical to the "expansion estimator" of simple random sampling without replacement, which is unbiased for the tally of the full source file and preserves C^{total} in expectation [113]. Subsampling adds variance but no bias: on average, a source subsampled to m particles has the same precision as m particles drawn directly from the albedo distribution. Fewer particles are retained for the heavier ions because their albedo yields are several orders of magnitude below the proton yield (Figure 5.7) and their transport cost per particle is the highest.

5.2.3.5 Step 5: Hit Accumulation

Dome crossings from the primary and secondary simulations are kept individually rather than binned. For each crossing i, the position $\vec{r}_i$, velocity $\vec{v}_i$, and shell index are recorded, together with the source energy T_k of the primary run to which it belongs. The species and kinetic energy per nucleon at the crossing, Z_i and T_i, select the response function used in Steps 7 and 9. T_k sets the physical normalization of Step 8. For a secondary crossing, the index ℓ of its source particle links it to its weight w_ℓ.

5.2.3.6 Step 6: HZETRN Response Functions

A single normal-incidence slab transport evaluated at a single representative depth does not fully represent the geometry of particle transport through the hemispherical habitat. In particular, two geometric effects must be accounted for. First, particles incident upon the outer dome surface at oblique angles traverse a greater physical path length through the regolith than the nominal areal density x of the shielding shell.

Second, only a fraction of particles that enter the inner cavity intersect the finite-volume ICRU sphere; particles with sufficiently large impact parameters pass through the cavity without intersecting the scoring volume. These effects are incorporated on a per-particle basis using a two-dimensional HZETRN response function.

For each primary GCR species and each energy T on HZETRN's internal GCR transport energy grid, HZETRN [32] is executed once in "interpolation" mode using a two-layer slab geometry. The first layer consists of lunar regolith and is swept over a fine grid of areal densities from 0 to $400\,\mathrm{g\,cm^{-2}}$, which extends several times beyond the largest nominal passive shielding thickness considered in this study. The second layer consists of `icru_soft_tissue` and is swept over the full diameter of the ICRU sphere, from 0 to $2R_{\mathrm{ICRU}}$.

The resulting response grid,

$$\mathcal{R}(x_1, x_2 \mid Z, T), \tag{5.29}$$

gives the absorbed dose or dose equivalent per unit incident fluence for a particle of species Z and kinetic energy per nucleon T as a function of the regolith areal density x_1 and tissue areal density x_2. For a given crossing, the response is taken from the grid energy bin that contains the particle's energy.

At each response grid point, HZETRN computes the fluence response $\mathcal{R}_\phi(x_1, x_2, Z', T' \mid Z, T)$, the transported fluence spectrum of particles of species Z' and kinetic energy per nucleon T' at depths (x_1, x_2) per unit incident fluence of species Z and energy T. The fluence response includes both the incident boundary-condition species and all secondary particles generated by HZETRN as the radiation field propagates through the regolith and tissue. The absorbed dose response follows from the fluence response according to

$$\mathcal{R}_D(x_1, x_2 \mid Z, T) = \frac{1}{\rho_{\mathrm{tis}}} \sum_{Z' \in \mathcal{Z}} \int_0^\infty L(Z', T')\, \mathcal{R}_\phi(x_1, x_2, Z', T' \mid Z, T)\, \mathrm{d}T', \tag{5.30}$$

and the dose equivalent response according to

$$\mathcal{R}_H(x_1, x_2 \mid Z, T) = \frac{1}{\rho_{\mathrm{tis}}} \sum_{Z' \in \mathcal{Z}} \int_0^\infty Q(Z', T')\, L(Z', T')\, \mathcal{R}_\phi(x_1, x_2, Z', T' \mid Z, T)\, \mathrm{d}T', \tag{5.31}$$

where $L(Z', T')$ is the unrestricted LET in tissue and $Q(Z', T')$ is the applicable quality factor. Depending on the response quantity being computed, Q is taken from either the ICRP-60 formulation or the NASA solid cancer/leukemia quality factor formulation defined in [43].

Equations 5.30 and 5.31 describe the calculation performed internally by HZETRN for each response-grid point. The subsequent aggregation of these responses over the particle population transported by ASPP is described below.

5.2.3.7 Step 7: Geometric Mapping and Chord-Averaged Response

To apply the response function to an individual dome hit, the particle trajectory is related to the habitat geometry. Let particle i intersect the outer dome surface at position $\vec{r}_i$, where $|\vec{r}_i| = R_{\text{outer}}(x)$, with velocity $\vec{v}_i$. The particle direction is

$$\vec{\Omega}_i = \frac{\vec{v}_i}{|\vec{v}_i|}. \tag{5.32}$$

At the outer dome surface, the active shielding transport has already been completed. The particle is assumed to propagate in a straight line through the passive shielding.

The ICRU sphere is centered at $\vec{r}_c = (R_{\text{ICRU}} + \delta)\hat{z}$ (the vertical midpoint within the cavity of the lunar habitat). The perpendicular distances from the habitat center (the origin) and from the center of the ICRU sphere, $\vec{r}_c$, to the straight-line trajectory are

$$b_i = \left|\vec{r}_i \times \vec{\Omega}_i\right|, \tag{5.33}$$

and

$$b_i^c = \left|(\vec{r}_i - \vec{r}_c) \times \vec{\Omega}_i\right|. \tag{5.34}$$

The trajectory intersects the ICRU sphere if and only if $b_i^c \leq R_{\text{ICRU}}$. Because the sphere lies within the habitat cavity, any trajectory that intersects it necessarily crosses the inner surface of the habitat first. Trajectories with $b_i^c > R_{\text{ICRU}}$ do not contribute to the dose in the scoring volume, even if they enter the cavity. For particles satisfying $b_i^c \leq R_{\text{ICRU}}$, the physical path length through the regolith is the distance from the outer dome crossing to the inner dome surface,

$$s_{1,i} = -\vec{r}_i \cdot \vec{\Omega}_i - \sqrt{R_{\text{inner}}^2 - b_i^2}, \tag{5.35}$$

which corresponds to the regolith areal density

$$x_{1,i} = \rho_{\text{reg}} s_{1,i}. \tag{5.36}$$

The corresponding chord length through the ICRU sphere is

$$s_{2,i} = 2\sqrt{R_{\text{ICRU}}^2 - (b_i^c)^2}, \tag{5.37}$$

and the corresponding tissue areal density is

$$x_{2,i} = \rho_{\text{tis}} s_{2,i}. \tag{5.38}$$

Because the particle traverses a finite chord through the ICRU sphere, rather than terminating at a single tissue depth, the appropriate response is the response averaged over the particle's chord:

$$\overline{\mathcal{R}}_i = \frac{1}{x_{2,i}} \int_0^{x_{2,i}} \mathcal{R}(x_{1,i}, x_2 \mid Z_i, T_i) \mathrm{d}x_2. \tag{5.39}$$

5.2.3.8 Step 8: Physical Normalization

The ASPP simulations themselves are time-independent: each simulation represents a statistical realization of the specified incident radiation field rather than a finite-duration exposure. The physical normalization is introduced only when the simulation results are scaled to the incident GCR flux. For a generic differential source distribution $S(\vec{r}, Z, T, \vec{\Omega})$, the corresponding physical source strength is

$$\mathcal{N} = \sum_{Z \in \mathcal{Z}} \int_V \int_0^\infty \int_{4\pi} S(\vec{r}, Z, T, \vec{\Omega}) \mathrm{d}\Omega \, \mathrm{d}T \mathrm{d}\vec{r}. \tag{5.40}$$

For the cosine-law-sampled, inward-facing hemisphere source used here (Step 2, radius R_{src}, Table 5.1), the source term can be written as a combination of delta-functions and Heaviside step functions,

$$S(\vec{r}, Z, T, \vec{\Omega}) = \phi_{\text{GCR}}(Z; T) \delta(|\vec{r}| - R_{\text{src}}) \mathcal{H}(\vec{r} \cdot \hat{z}) \mathcal{H}\left(-\vec{\Omega} \cdot \frac{\vec{r}}{|\vec{r}|}\right) \left(-\vec{\Omega} \cdot \frac{\vec{r}}{|\vec{r}|}\right), \tag{5.41}$$

where $\phi_{\text{GCR}}(Z; T)$ is the BON2020 flux per unit solid angle of Step 1, converted to units of $[\text{cm}^{-2}\,\text{d}^{-1}\,\text{MeV/n}^{-1}\,\text{sr}^{-1}]$. It does not depend on $\vec{\Omega}$ because the GCR flux is isotropic. The "per day" unit

belongs to the physical normalization of the radiation environment and does not represent a time variable in the transport simulation.

Equation 5.40 can be evaluated directly. First, note that $-\vec{\Omega}\cdot\vec{r}/|\vec{r}| = \vec{\Omega}\cdot\hat{n}_{\rm in} = \cos\theta_{\rm dir}$, the local polar cosine of Step 2, and is thus technically independent of $\vec{r}$. Then, evaluate the volume integral and the double integral over solid angle and energy separately, noting that $\mathrm{d}\vec{r} = |\vec{r}|^2\sin\theta_{\rm pos}\mathrm{d}|\vec{r}|\mathrm{d}\theta_{\rm pos}\mathrm{d}\psi_{\rm pos}$ and $\mathrm{d}\Omega = \sin\theta_{\rm dir}\mathrm{d}\theta_{\rm dir}\mathrm{d}\psi_{\rm dir}$,

$$\begin{aligned}\mathcal{N} = \sum_{Z\in\mathcal{Z}}&\left(\int_0^{2\pi}\mathrm{d}\psi_{\rm pos}\right)\left(\int_0^{\pi}\sin\theta_{\rm pos}\int_0^{\infty}\mathcal{H}(\vec{r}\cdot\hat{z})\delta(|\vec{r}|-R_{\rm src})|\vec{r}|^2\mathrm{d}|\vec{r}|\mathrm{d}\theta_{\rm pos}\right)\\ &\times\left(\int_0^{\infty}\phi_{\rm GCR}(Z;T)\mathrm{d}T\right)\left(\int_0^{2\pi}\mathrm{d}\psi_{\rm dir}\right)\\ &\times\left(\int_0^{\pi}\cos\theta_{\rm dir}\sin\theta_{\rm dir}\mathcal{H}(\cos\theta_{\rm dir})\mathrm{d}\theta_{\rm dir}\right).\end{aligned} \tag{5.42}$$

Integrating over the radial dimension $|\vec{r}|$ replaces all $|\vec{r}|$ with $R_{\rm src}$. The positional and directional azimuthal integrals each evaluate to 2π. Also, the Heaviside step functions may be simplified via integration bound replacement by noting that $\vec{r}\cdot\hat{z} = \cos\theta_{\rm pos} \geq 0$ for $\theta_{\rm pos}\in[0,\pi/2)$ and $\cos\theta_{\rm dir}\geq 0$ for $\theta_{\rm dir}\in[0,\pi/2]$. These simplifications yield

$$\mathcal{N} = \sum_{Z\in\mathcal{Z}} 4\pi^2 R_{\rm src}^2\left(\int_0^{\pi/2}\sin\theta_{\rm pos}\mathrm{d}\theta_{\rm pos}\right)\left(\int_0^{\pi/2}\cos\theta_{\rm dir}\sin\theta_{\rm dir}\mathrm{d}\theta_{\rm dir}\right)\left(\int_0^{\infty}\phi_{\rm GCR}(Z;T)\mathrm{d}T\right). \tag{5.43}$$

The integral over $\theta_{\rm pos}$ yields unity and the integral over $\theta_{\rm dir}$ yields $1/2$. Finally, the full normalization term is

$$\mathcal{N} = 2\pi^2 R_{\rm src}^2\sum_{Z\in\mathcal{Z}}\int_0^{\infty}\phi_{\rm GCR}(Z;T)\mathrm{d}T \tag{5.44}$$

An ASPP run at energy T_k represents the source energy bin $(T_{k-1},T_k]$ of width $\Delta T_k = T_k - T_{k-1}$, so the energy integral is restricted to that bin. The physical source strength associated with a run for primary species Z and energy T_k is

$$\mathcal{N}(Z,T_k) = 2\pi^2 R_{\rm src}^2\phi_{\rm GCR}(Z;T_k)\Delta T_k. \tag{5.45}$$

If $N(Z,T_k)$ source particles are simulated for this run, a raw per-source-particle tally $\mathcal{K}(Z,T_k)$ is converted to its physical value according to

$$\mathcal{K}_{\rm phys}(Z,T_k) = \frac{\mathcal{N}(Z,T_k)}{N(Z,T_k)}\mathcal{K}(Z,T_k). \tag{5.46}$$

5.2.3.9 Step 9a: Dose Computation (Non-Photons)

Each dome crossing i that reaches the ICRU sphere deposits energy along its chord. Within the straight-ahead approximation underlying HZETRN, a broad, normally incident beam of fluence Φ produces dose $\Phi\mathcal{R}(x_1, x_2 \mid Z, T)$ at tissue areal density x_2. The energy deposited in a column of cross-sectional area $\mathrm{d}A$ and areal density $\mathrm{d}x_2$ is $\Phi\mathcal{R}\mathrm{d}A\mathrm{d}x_2$, and $\Phi\mathrm{d}A$ particles traverse that column, so each particle (together with the secondaries it produces, which remain on its line in the straight-ahead approximation) deposits $\mathcal{R}\mathrm{d}x_2$. Dome crossing i deposits

$$\varepsilon_i = \int_0^{x_{2,i}} \mathcal{R}(x_{1,i}, x_2 \mid Z_i, T_i)\mathrm{d}x_2 = x_{2,i}\overline{\mathcal{R}}_i, \tag{5.47}$$

in the sphere. Dividing by the sphere mass, $\rho_{\mathrm{tis}}V_{\mathrm{ICRU}}$ with $V_{\mathrm{ICRU}} = \frac{4}{3}\pi R_{\mathrm{ICRU}}^3$, and using $x_{2,i} = \rho_{\mathrm{tis}}\, s_{2,i}$, crossing i contributes $s_{2,i}\,\overline{\mathcal{R}}_i/V_{\mathrm{ICRU}}$ per simulated particle. The factor $s_{2,i}/V_{\mathrm{ICRU}}$ is the track-length estimator of the fluence inside the sphere.

Each crossing also represents a physical number of particles per unit time, $\mathcal{N}_i$. For a primary crossing from run k, this is the run's source strength divided by its number of source particles,

$$\mathcal{N}_i = \frac{\mathcal{N}(Z, T_k)}{N(Z, T_k)}. \tag{5.48}$$

For a secondary crossing of species Z', produced by source particle ℓ of the albedo source of run k,

$$\mathcal{N}_i = \mathcal{N}(Z, T_k)C^{\mathrm{total}}(Z')w_\ell. \tag{5.49}$$

There is no division by $N(Z, T_k)$ here, because $C^{\mathrm{total}}(Z')$ is already a number per primary source particle, and the weights w_ℓ, including the factor n/m of Step 4 for subsampled sources, sum to unity on average. In both cases Z and T_k refer to the parent primary run, not to the species or energy of the particle at the crossing. The dose rate (absorbed dose $\dot{D}$, dose equivalent $\dot{H}$, or another response quantity, denoted generically $\dot{\mathcal{X}}$, with $\overline{\mathcal{R}}_i$ chosen accordingly) is the sum over all crossings at the shell for the shielding thickness considered,

$$\dot{\mathcal{X}} = \sum_{i\,:\,b_i^c \le R_{\mathrm{ICRU}}} \mathcal{N}_i \,\frac{s_{2,i}}{V_{\mathrm{ICRU}}}\,\overline{\mathcal{R}}_i. \tag{5.50}$$

Written out for the primary crossings alone, using Equation 5.45,

$$\dot{\mathcal{X}}_{\text{primary}}(Z) = \sum_k \frac{2\pi^2 R_{\text{src}}^2 \, \phi_{\text{GCR}}(Z; T_k) \, \Delta T_k}{N(Z, T_k)} \sum_{\substack{i \in \text{run } k \\ b_i^c \le R_{\text{ICRU}}}} \frac{s_{2,i}}{V_{\text{ICRU}}} \, \overline{\mathcal{R}}_i. \tag{5.51}$$

Each crossing is normalized by the source energy T_k of its run, whereas its response is evaluated at species and energy associated with the crossing, Z_i and T_i.

5.2.3.10 Step 9b: Dose Computation (Photons)

The photon is not a valid HZETRN `user-gcr` boundary condition species, so photon secondaries are not transported through HZETRN. Instead, photon dose is estimated analytically via the photon absorbed dose response method, valid under charged-particle equilibrium. For a photon of kinetic energy T traversing regolith depth x_1 and tissue depth x_2, the dose response is

$$\mathcal{R}_\gamma(x_1, x_2 \mid T) = T \left(\frac{\mu_{\text{en}}(T)}{\rho} \right)_{\text{tis}} \exp\left[- \left(\frac{\mu(T)}{\rho} \right)_{\text{reg}} x_1 - \left(\frac{\mu(T)}{\rho} \right)_{\text{tis}} x_2 \right], \tag{5.52}$$

where μ/ρ is the mass attenuation coefficient (narrow-beam, accounting for beam attenuation through the regolith and tissue traversed before the interaction point) and μ_{en}/ρ is the mass energy-absorption coefficient (the fraction of interaction energy retained locally, rather than escaping as bremsstrahlung or scattered photons). Mass attenuation coefficients for lunar regolith and ICRU soft tissue were obtained from NIST XCOM [114], using the elemental compositions of Table 5.3 and the four-element ICRU tissue composition respectively, combined via the Bragg additivity rule. The tissue mass energy-absorption coefficient was obtained from NIST's tabulated X-ray mass attenuation and energy-absorption coefficients for ICRU soft tissue [115], which cover 1 keV to 20 MeV; values above 20 MeV are extrapolated log-log-linearly from the last two tabulated points, since GCR-driven secondary photon spectra are expected to concentrate well below this range.

As with ion species, the relevant quantity for a photon traversing the ICRU sphere along a chord is the response averaged along that chord rather than evaluated at a single depth. Because Equation 5.52 is a simple exponential in x_2, this average has closed form,

$$\overline{\mathcal{R}}_\gamma(x_1 \mid T, x_{2,\text{chord}}) = T \left(\frac{\mu_{\text{en}}(T)}{\rho} \right)_{\text{tis}} e^{-(\mu(T)/\rho)_{\text{reg}} x_1} \frac{1 - e^{-(\mu(T)/\rho)_{\text{tis}} x_{2,\text{chord}}}}{(\mu(T)/\rho)_{\text{tis}} \, x_{2,\text{chord}}}, \tag{5.53}$$

using the same chord length $x_{2,\mathrm{chord}} = \rho_{\mathrm{tis}} s_{2,i}$ (Equation 5.37) as the ion-species calculation. This average is obtained by integrating $\mathcal{R}_\gamma(x_1, x_2, \mid T)$ from 0 to $x_{2,\mathrm{chord}}$ and dividing by $x_{2,\mathrm{chord}}$. For photons, $Q = 1$, so the photon contribution to dose equivalent is numerically equal to its contribution to absorbed dose.

The tissue coefficients are tabulated from 1 keV to 20 MeV, while albedo photons reach energies of a few GeV [115]. Below 1 keV and above 20 MeV, the coefficients are extrapolated logarithmically. This can lead to an overestimate in the contribution of photons to dose.

5.2.3.11 Statistical Uncertainty

Both models report the statistical uncertainty of a mean over independent source histories. Neither includes systematic uncertainties from the GCR environment model, nuclear interaction cross sections, the HZETRN and PHITS transport models, or the photon coefficient tables.

The G4-ASPP simulations with ^{1}H and ^{4}He primaries were performed with two independent sets of random-number seeds. The first set used the Geant4 default seed for every run. The second set assigned one seed pair to each combination of primary species and regolith thickness, shared by all applied voltages. In both sets, the runs at different voltages for a given species and thickness transport the same primary particles and differ only where the field alters a trajectory, so the comparison between voltages at fixed thickness is paired. The two sets are independent of each other, and the ^{1}H and ^{4}He results reported in this chapter are their mean,

$$\bar{X} = \frac{X_1 + X_2}{2}, \tag{5.54}$$

with uncertainty

$$\sigma_{\bar{X}} = \frac{1}{2}\sqrt{\sigma_1^2 + \sigma_2^2}, \tag{5.55}$$

where X_1 and X_2 are the results of the two sets and σ_1 and σ_2 are their statistical uncertainties. The full 28-species results use the first set only. The consequences of the shared default seed are described in Section 5.6.

In G4-ASPP, the energy ε_n deposited in the ICRU sphere by event n is accumulated together with ε_n^2. For N events, the relative uncertainty of the absorbed dose is

$$\frac{\sigma_D}{D} = \frac{1}{\langle\varepsilon\rangle}\sqrt{\frac{\langle\varepsilon^2\rangle - \langle\varepsilon\rangle^2}{N}}, \tag{5.56}$$

where

$$\langle \varepsilon \rangle = \frac{1}{N} \sum_{n=1}^{N} \varepsilon_n, \tag{5.57}$$

and

$$\langle \varepsilon^2 \rangle = \frac{1}{N} \sum_{n=1}^{N} \varepsilon_n^2. \tag{5.58}$$

For dose equivalent, the quality-weighted energy

$$h_n = \sum_j Q_j \, \varepsilon_{n,j} \tag{5.59}$$

deposited by event n is accumulated together with h_n^2. Here, $\varepsilon_{n,j}$ is the energy deposited by event n in steps whose LET, taken as the energy deposited in the step divided by the step length, falls in bin j, and Q_j is the ICRP-60 quality factor evaluated at the arithmetic center of that bin. The bins are logarithmically spaced, 20 per decade, over $0.1\,\mathrm{keV\,\mu m^{-1}}$ to $1 \times 10^5\,\mathrm{keV\,\mu m^{-1}}$. The relative uncertainty of the dose equivalent is given by Equation 5.56 with ε_n replaced by h_n. A single event deposits energy in many LET bins, and the per-event estimator retains the correlation between those deposits. The NASA dose equivalents are accumulated in the same way, with the quality factor evaluated for each energy deposit from the charge, mass number, and kinetic energy of the depositing particle. The ICRP-60 dose-equivalent uncertainties of the full 28-species results were instead computed by combining the LET bins in quadrature, $\sigma_H^2 = \sum_j Q_j^2 \, \sigma_{D,j}^2$, which omits that correlation and underestimates the uncertainty (Section 5.6). Contributions from different primary species are combined in quadrature. This treats the species as independent, which holds for the second seed set but not strictly for the first set or for the full 28-species results, in which runs of different species begin from the same random-number sequence and share their source positions (Section 5.6).

In the combination model, let $c_i = \mathcal{N}_i \, s_{2,i} \, \overline{\mathcal{R}}_i / V_{\mathrm{ICRU}}$ be the contribution of crossing i to Equation 5.50. Each primary history crosses the sphere once (at most) for a given shell, so within a run of N histories, the per-history score is c_i for a history that produces crossing i and zero otherwise. The variance of the run total is then

$$\sigma_k^2 = \sum_{i \,\in\, \mathrm{run}\, k} c_i^2 - \frac{1}{N} \Big(\sum_{i \,\in\, \mathrm{run}\, k} c_i \Big)^2. \tag{5.60}$$

5.3 Results and Discussion

5.3.1 Albedo Response Functions

Figures 5.4–5.7 show representative examples of the differential number albedo response functions $\alpha(Z, T, \vec{\Omega}; Z', T', \vec{\Omega}')$ generated from the PHITS simulations described in Section 5.2.2.1. The examples are selected to illustrate several notable features of the response function set, including its dependence on incident species, incident energy, and incidence angle. The complete set of response functions spanning all simulated incident species, energies, and angles is used in the albedo convolution of Equation 5.11. All albedo response function figures are shown individually in Appendix A.

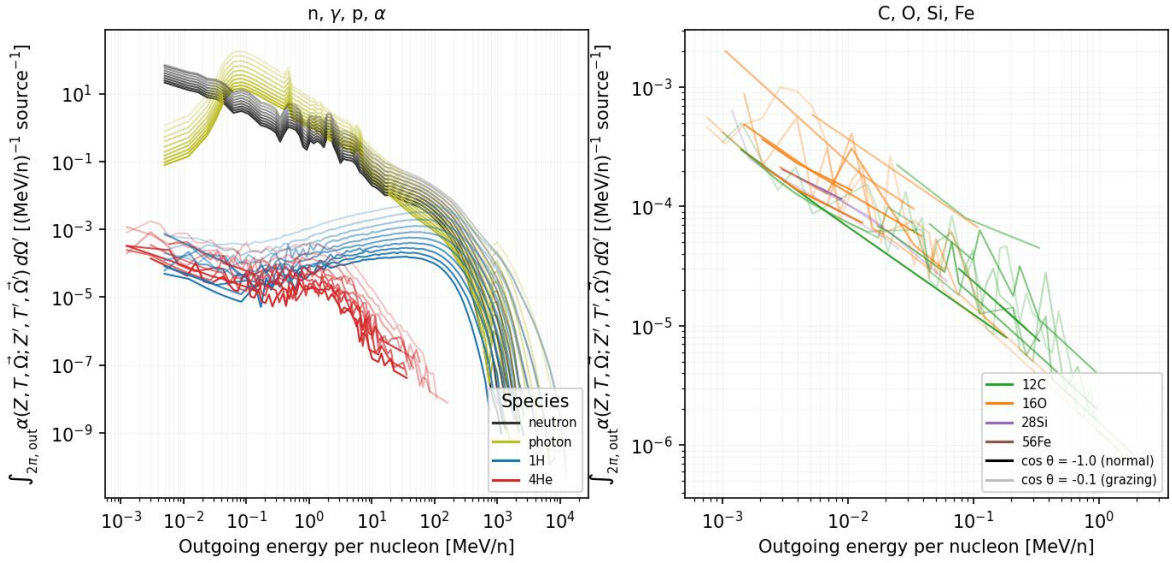


Figure 5.4: Differential number albedo response function for a 17.09 GeV n^{-1} proton primary, shown for all ten simulated incident polar cosine bins ($\cos\theta = -1.0$ to -0.1, indicated by line shading). Left: neutron, photon, ^{1}H, and ^{4}He outgoing secondaries. Right: ^{12}C, ^{16}O, ^{28}Si, and ^{56}Fe outgoing secondaries at normal ($\cos\theta = -1.0$) and grazing ($\cos\theta = -0.1$) incidence.

At high incident proton energy (Figure 5.4), the outgoing spectrum is dominated by neutrons and photons, whose yields exceed those of charged secondaries by several orders of magnitude across much of the outgoing energy range. This behavior is consistent with high-energy nuclear interactions in the regolith producing an intranuclear cascade followed by nuclear de-excitation, which generates substantial neutron and photon emission. Charged secondaries undergo continuous electromagnetic energy loss and may be stopped before reaching the surface, whereas neutrons and photons are not subject to the same charged-particle stopping mechanism and can escape the regolith more readily [116, 117]. The heavy-fragment yields in the right panel

decrease rapidly with increasing outgoing energy per nucleon and exhibit greater statistical fluctuations than the light secondary spectra, consistent with the lower production probability of these channels given the 10^6 source histories simulated per PHITS run.

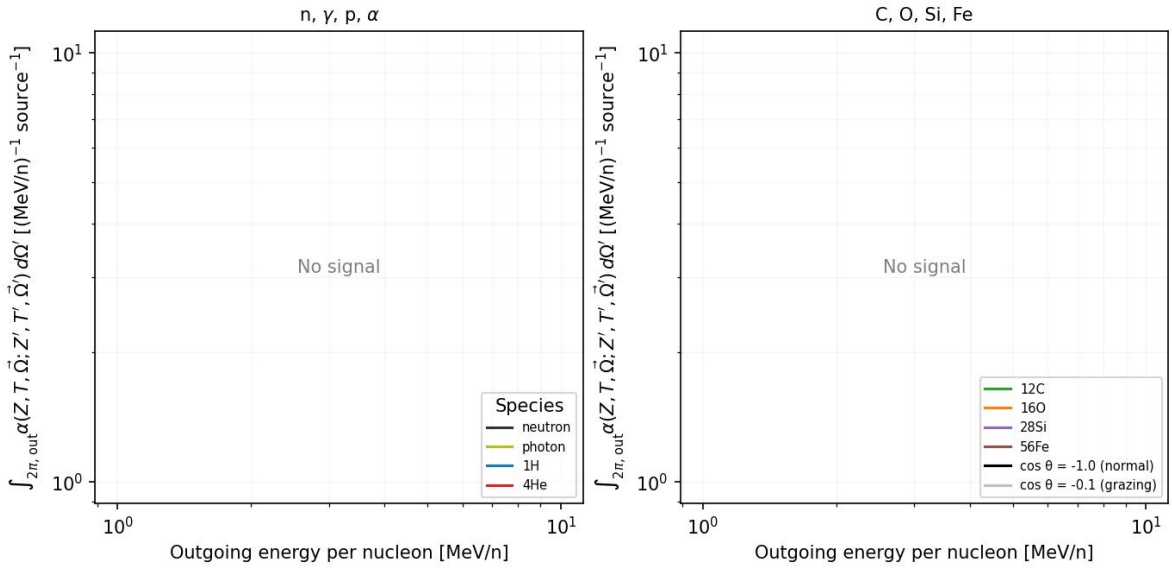


Figure 5.5: Differential number albedo response function for a 53.3 keV proton primary, showing no scored secondaries at any outgoing energy, species, or incident polar cosine bin.

At low incident proton energy (Figure 5.5), no secondaries are scored at any outgoing energy, species, or incident angle. At 53.3 keV, the incident proton kinetic energy is far below the energy scale required for nuclear reactions with the constituent nuclei of the regolith. Consequently, no nuclear reaction secondaries are produced, providing a useful lower-energy bound on the response function set.

Figure 5.6 shows a representative primary alpha response. The qualitative structure is similar to that of the high-energy proton response, with neutron- and photon-dominated outgoing spectra and comparatively noisy heavy-fragment yields. The alpha-primary response also demonstrates the production of multiple secondary particles per incident alpha through nuclear fragmentation.

Figure 5.7 shows the integrated secondary yield per incident ^{4}He primary as a function of incident energy per nucleon for each simulated incident angle. Neutron and proton yields increase smoothly with incident energy, with the rate of increase decreasing at the highest energies. The ^{4}He secondary yield exhibits a non-monotonic decrease of approximately one to two orders of magnitude between roughly 10 and 100 MeV n^{-1}, followed by an increase at higher incident energies. The physical origin of this feature is not established in the present study. Possible explanations include changes in the relative importance of competing nuclear reaction

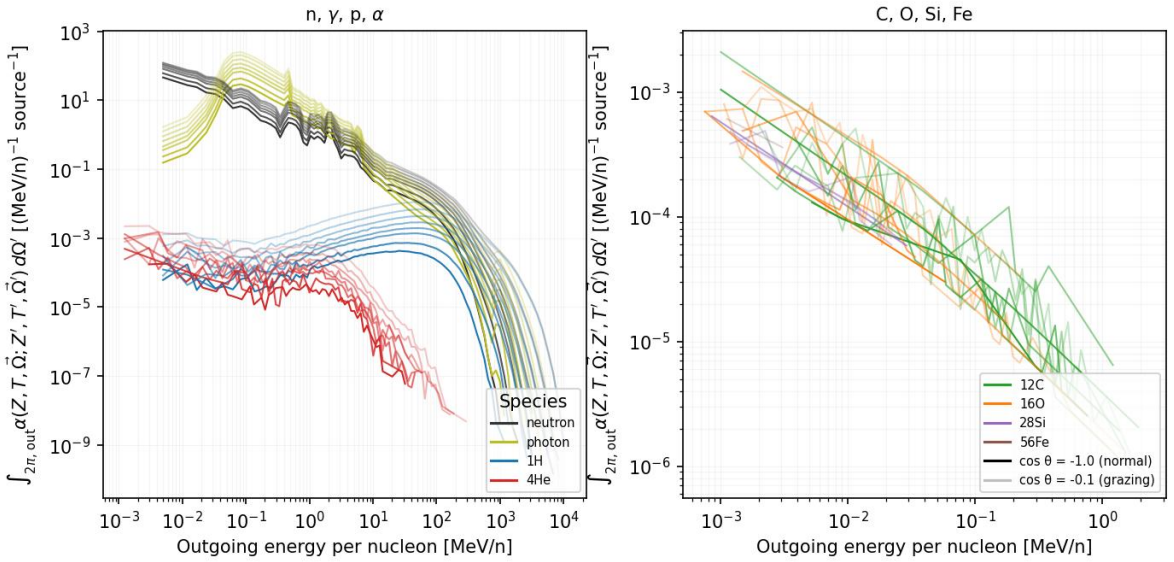


Figure 5.6: Differential number albedo response function for a 6.134 GeV n^{-1} ^{4}He primary, shown for all ten simulated incident polar cosine bins ($\cos\theta = -1.0$ to -0.1).

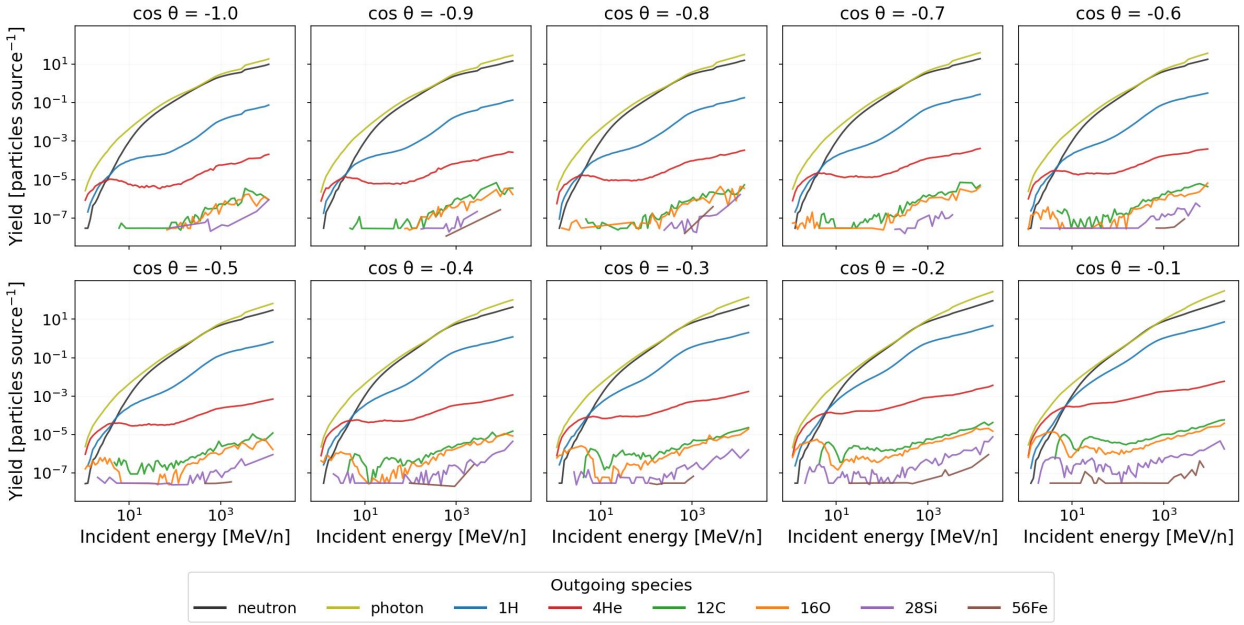


Figure 5.7: Integrated outgoing secondary particle yield per source ^{4}He primary as a function of incident energy per nucleon, shown separately for each of the ten simulated incident polar cosine bins ($\cos\theta_{\mathrm{dir}} = -1.0$ to -0.1).

and fragmentation channels with incident energy; identifying the mechanism would require examination of the underlying PHITS reaction model and reaction-channel contributions.

Heavy-fragment yields (^{12}C, ^{16}O, and ^{28}Si) become nonzero only above approximately a few MeV n^{-1} and remain statistically noisier than the light-secondary yields over much of the simulated energy range. Yields generally increase as the incidence angle becomes shallower ($\cos\theta_{\mathrm{dir}} \to -0.1$), consistent with the greater regolith path length traversed by the incident primary before reaching the surface.

5.3.2 Combination Model Radiation Response

The combination model results presented in this section include both primary GCR transport (^{1}H, ^{4}He) and secondary albedo particles generated from those primaries via the ASPP+PHITS+HZETRN method of Section 5.2.3, including the analytical photon dose contribution described in Section 5.2.3.10.

For the shielding and voltage conditions evaluated here, the secondary and photon contributions are small relative to the primary ^{1}H/^{4}He contribution. At zero passive shielding and zero applied voltage, secondary particles contribute 5.9 % of the absorbed dose rate and 7.9 % of the ICRP-60 dose equivalent rate. Their share decreases with shielding thickness, to 2.2 % and 3.6 % at 50 g cm^{-2}, as the regolith shell attenuates the albedo before it reaches the habitat interior. The secondary share is small because the dome subtends a small solid angle as viewed from most of the lunar surface from which albedo particles are emitted, so only a small fraction of secondary trajectories intersect the habitat.

5.3.2.1 Dose and Dose Equivalent

Total absorbed dose and dose equivalent rates to the ICRU sphere, computed via the chord geometry method of Section 5.2.3.7 and summed over both primary GCR species simulated (^{1}H, ^{4}He), are shown in Figures 5.8–5.11 as a function of regolith shielding thickness x for each applied active shielding voltage V. At zero passive shielding and zero applied voltage, the ^{1}H+^{4}He absorbed dose rate is 0.199 ± 0.012 mGy d^{-1} and the ICRP-60 dose equivalent rate is 0.326 ± 0.020 mSv d^{-1}. The statistical uncertainty of an individual shielding–voltage combination is 6–7 % (1σ, Section 5.2.3.11).

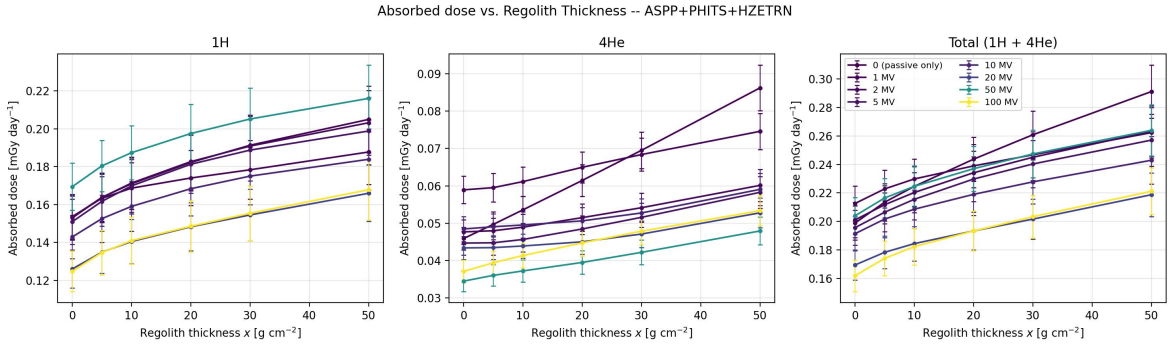


Figure 5.8: Absorbed dose rate to the ICRU sphere vs. regolith shielding thickness, computed via the combination model. Panels show ^{1}H, ^{4}He, and the total (species-summed) contribution; line color indicates applied active shielding voltage. Error bars indicate the 1σ statistical uncertainty.

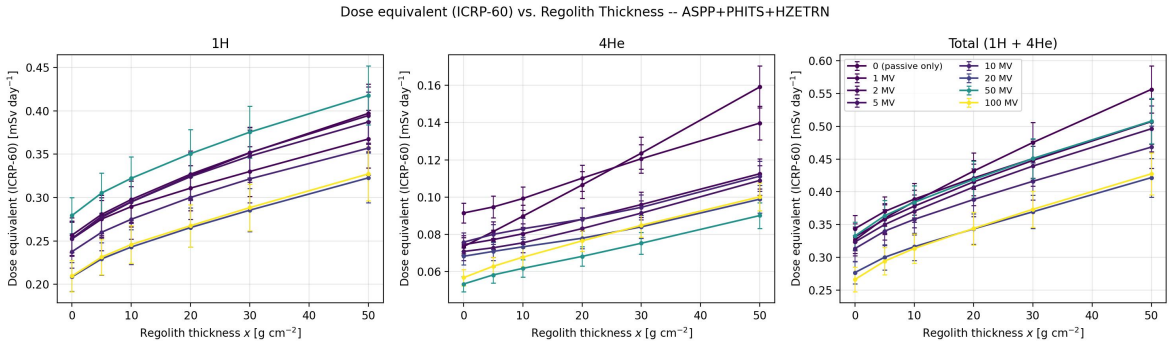


Figure 5.9: Dose equivalent rate (ICRP-60 quality factor) to the ICRU sphere vs. regolith shielding thickness, computed via the combination model. Panels show ^{1}H, ^{4}He, and the total (species-summed) contribution; line color indicates applied active shielding voltage. Error bars indicate the 1σ statistical uncertainty.

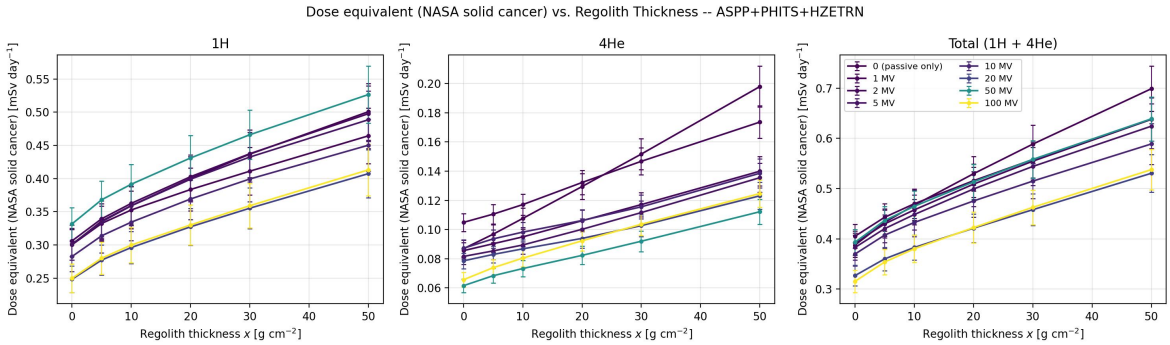


Figure 5.10: Dose equivalent rate (NASA solid cancer quality factor) to the ICRU sphere vs. regolith shielding thickness, computed via the combination model. Panels show ^{1}H, ^{4}He, and the total (species-summed) contribution; line color indicates applied active shielding voltage. Error bars indicate the 1σ statistical uncertainty.

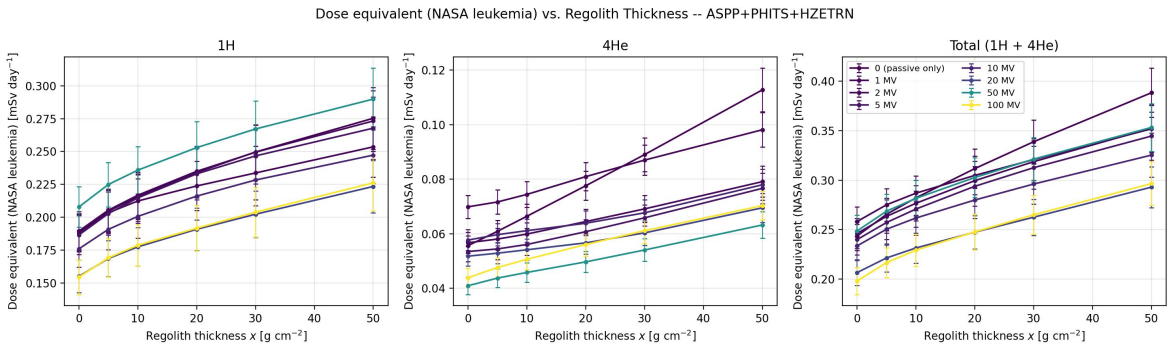


Figure 5.11: Dose equivalent rate (NASA leukemia quality factor) to the ICRU sphere vs. regolith shielding thickness, computed via the combination model. Panels show ^{1}H, ^{4}He, and the total (species-summed) contribution; line color indicates applied active shielding voltage. Error bars indicate the 1σ statistical uncertainty.

5.3.2.2 Dependence on Passive Shielding

Both ^{1}H and ^{4}He dose contributions increase with regolith shell thickness over the full range considered. At zero applied voltage, the ^{1}H+^{4}He absorbed dose rate increases from 0.199 ± 0.012 to 0.291 ± 0.019 mGy d^{-1} between 0 and 50 g cm^{-2}, and the ICRP-60 dose equivalent rate increases from 0.326 to 0.556 mSv d^{-1}. For light primaries, the dose carried by secondary particles produced in the regolith, which is contained in the HZETRN response through Equation 5.30, evidently grows faster over this range than the primaries are attenuated. The decrease in dose equivalent rate at low shielding thickness reported for the full GCR spectrum is driven by fragmentation of high-quality-factor heavy ions [118], which are not primaries in this calculation (omitted for the sake of time). The shielding dependence of the ^{1}H+^{4}He contribution is compared with G4-ASPP in Section 5.3.4.

5.3.2.3 Dependence on Active Shielding

The combination model shows no systematic dependence on applied voltage. At zero passive shielding, the ^{1}H+^{4}He absorbed dose rate varies between 0.162 and 0.213 mGy d^{-1} over 0–100 MV. It decreases from 1 to 20 MV, but the 50 MV result is higher than those at 10 and 20 MV, and the variation at 50 g cm^{-2} is similar. The pattern of the scatter supports the same reading. A potential of 1 MV can turn back only protons below about 1 MeV, which carry a negligible share of the GCR dose, yet the 1 MV result differs from the passive result by +7 % at zero passive shielding and −10 % at 50 g cm^{-2}, approximately 1σ of the difference in opposite directions. Results at different shielding thicknesses are correlated by construction, because the

same ASPP runs are scored at every shell. Agreement between thicknesses is not independent evidence. Within the statistical precision of the present calculation, the combination model resolves no effect of the active shield on the ^{1}H+^{4}He dose.

5.3.2.4 Comparison with Blunier et al. (2025)

A recent study by Blunier et al. (2025) compiled radiation-protection results from several studies examining absorbed dose and dose equivalent as functions of passive shielding thickness for lunar habitat configurations [119]. Their study considers a hemispherical lunar-regolith dome surrounding either a human phantom or an ICRU sphere, making the geometry closely comparable to that considered here. Figure 7 of [119] summarizes the dose and dose equivalent results obtained in their study alongside results from several previous investigations using similar configurations. This compilation provides a useful reference for evaluating both the magnitude and shielding-dependent trends observed in the present work.

At zero passive shielding and zero applied voltage, the ^{1}H+^{4}He absorbed dose rate of 0.199 mGy d^{-1} is 80 % of the 0.25 mGy d^{-1} reported for the full GCR spectrum on the lunar surface by Matthiä and Berger [118]. They attribute approximately 60 % of the absorbed dose to protons, with alpha particles and heavier ions each contributing between 15 % and 20 %, at regolith shielding up to 20 g cm^{-2} [118]; the corresponding ^{1}H+^{4}He share of 75–80 % agrees with the present result. The ICRP-60 dose equivalent rate of 0.326 mSv d^{-1} is approximately 40 % of the full-spectrum value of approximately 0.8 mSv d^{-1} [118, 119]. A smaller share in dose equivalent than in absorbed dose is expected, because heavy ions, which are absent here, contribute disproportionately to dose equivalent through their high quality factors [118].

The additional depth-dose response species available in HZETRN—including neutrons, ^{16}O, ^{24}Mg, ^{28}Si, and ^{56}Fe—do not represent additional primary GCR species in this calculation. Instead, they extend the dose response treatment to secondary albedo particles generated when ^{1}H and ^{4}He primaries interact with the lunar surface. Extending the primary ASPP transport to the heavier species is required for a full-spectrum comparison with [119], particularly for the *shape* of the dose equivalent versus shielding curves.

5.3.3 G4-ASPP Radiation Response

This section presents G4-ASPP dose and dose equivalent rates for the same habitat configuration and shielding/voltage sweep evaluated for the combination model above. Unlike the combination model, G4-

ASPP computes dose directly within a single self-consistent simulation with no separate response function convolution or chord geometry aggregation step.

5.3.3.1 Dose and Dose Equivalent

Figures 5.12–5.15 show the G4-ASPP absorbed dose, ICRP-60 dose equivalent, NASA solid cancer dose equivalent, and NASA leukemia dose equivalent rates as functions of passive shielding thickness for several active shielding voltages. Figures 5.16–5.19 show the same four quantities as functions of active shielding voltage for several fixed passive shielding thicknesses. Error bars represent Monte Carlo statistical uncertainty.

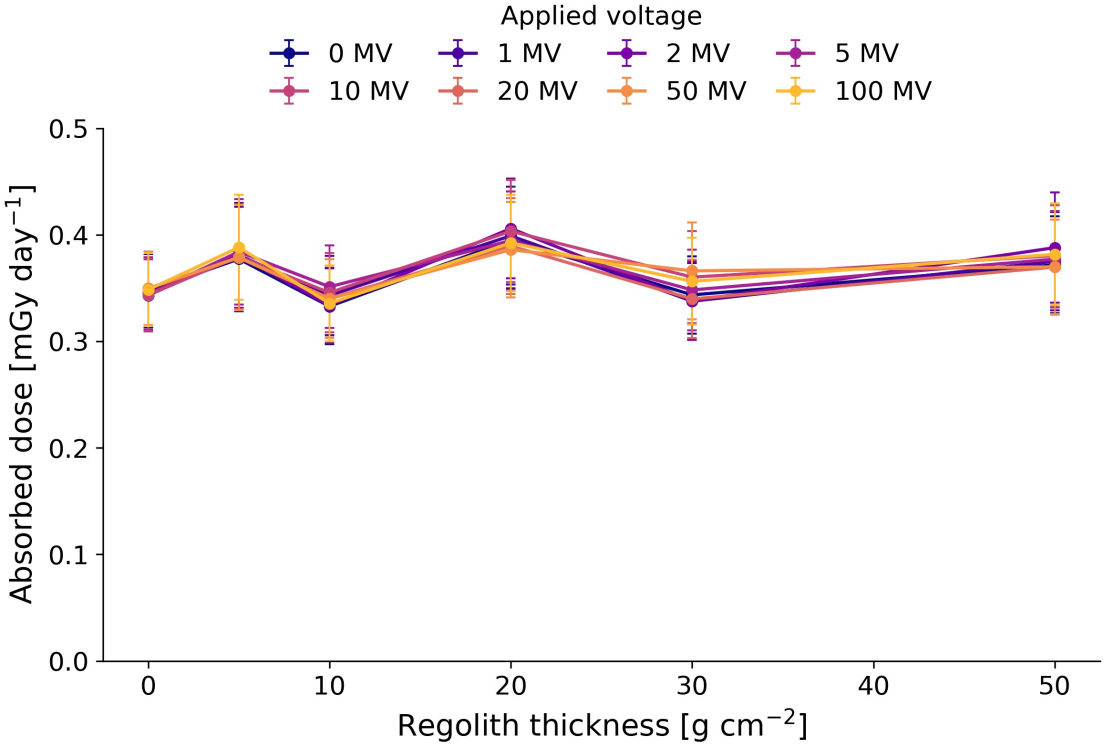


Figure 5.12: G4-ASPP absorbed dose rate vs. passive shielding thickness, by active shielding voltage.

5.3.3.2 Dependence on Passive Shielding

For the full 28-species spectrum, the G4-ASPP dose equivalent rate decreases with increasing passive shielding at low thickness. At zero applied voltage, the ICRP-60 dose equivalent rate decreases from 1.21 mSv d^{-1} at zero shielding to 0.95 mSv d^{-1} at 5 g cm^{-2} and 0.82 mSv d^{-1} at 10 g cm^{-2}, reaches its lowest value at

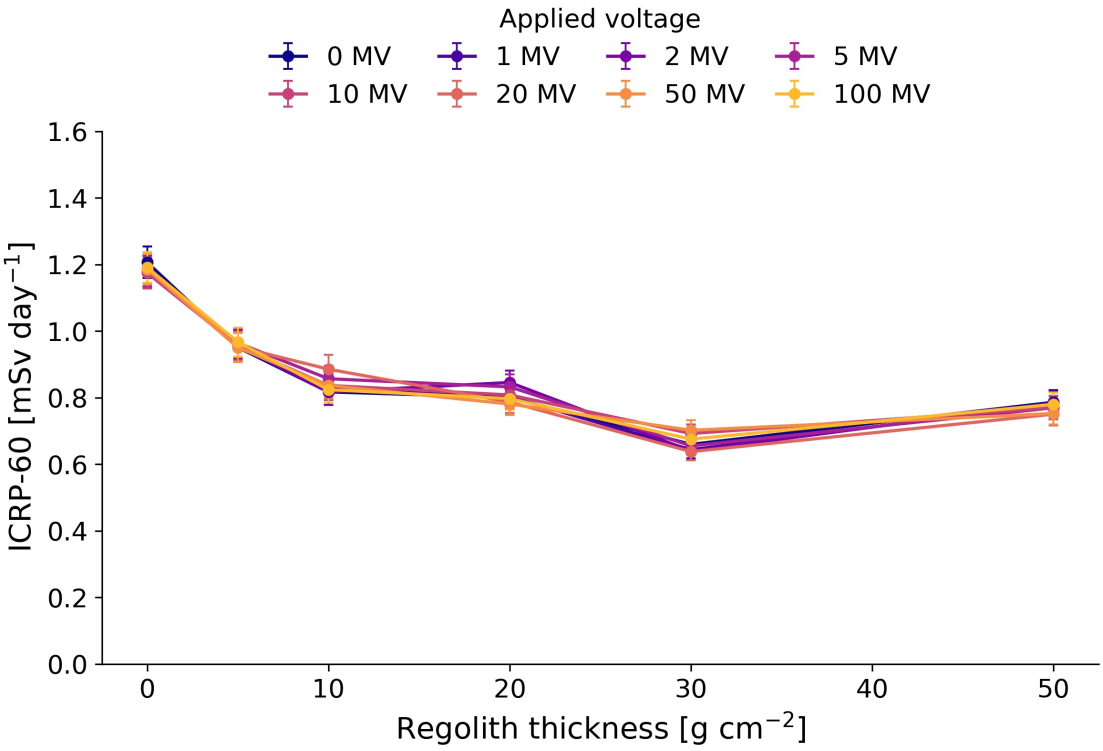


Figure 5.13: G4-ASPP ICRP-60 dose equivalent rate vs. passive shielding thickness, by active shielding voltage.

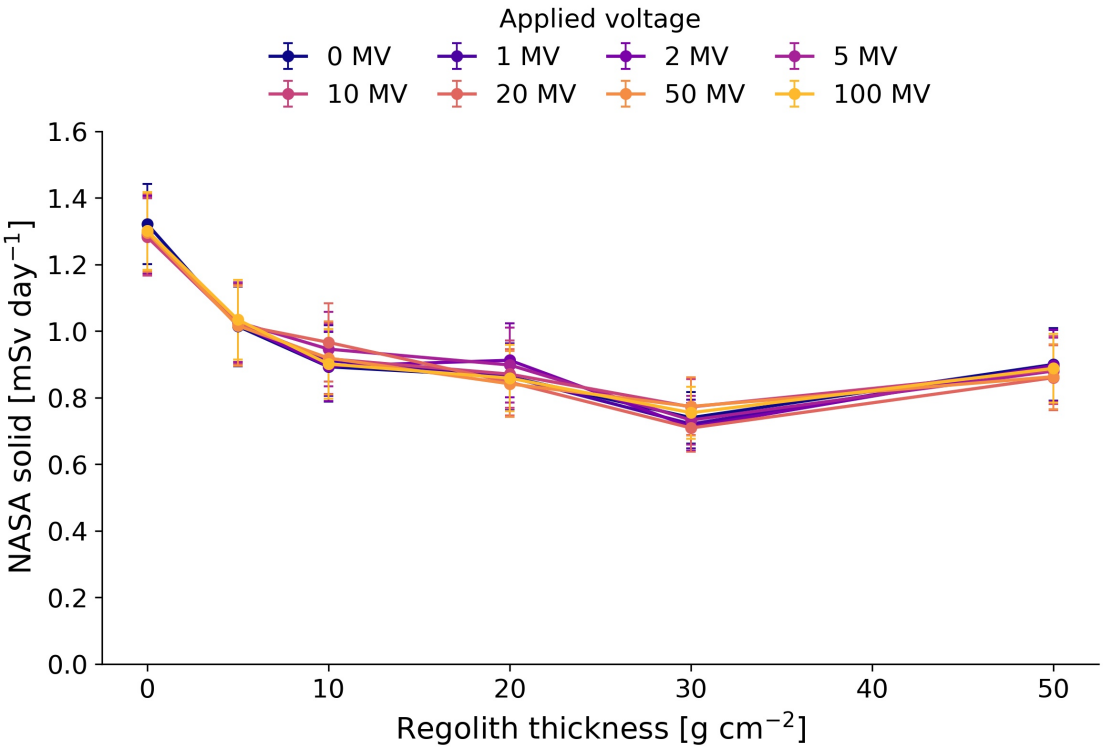


Figure 5.14: G4-ASPP NASA solid cancer dose equivalent rate vs. passive shielding thickness, by active shielding voltage.

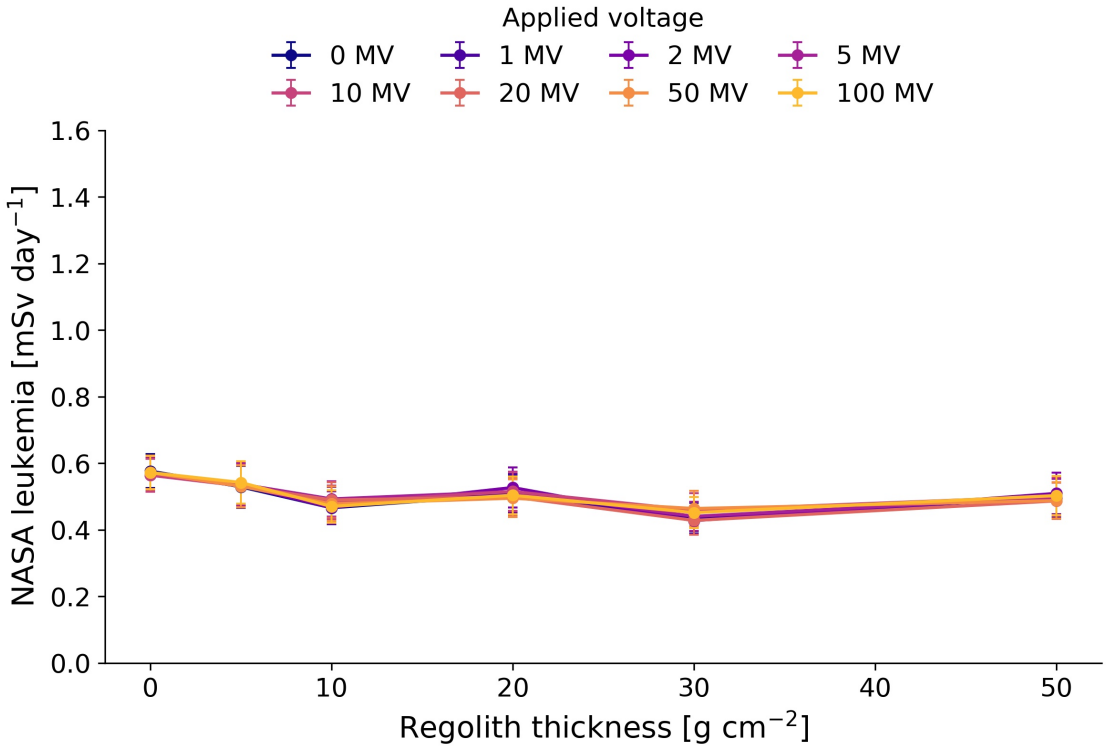


Figure 5.15: G4-ASPP NASA leukemia dose equivalent rate vs. passive shielding thickness, by active shielding voltage.

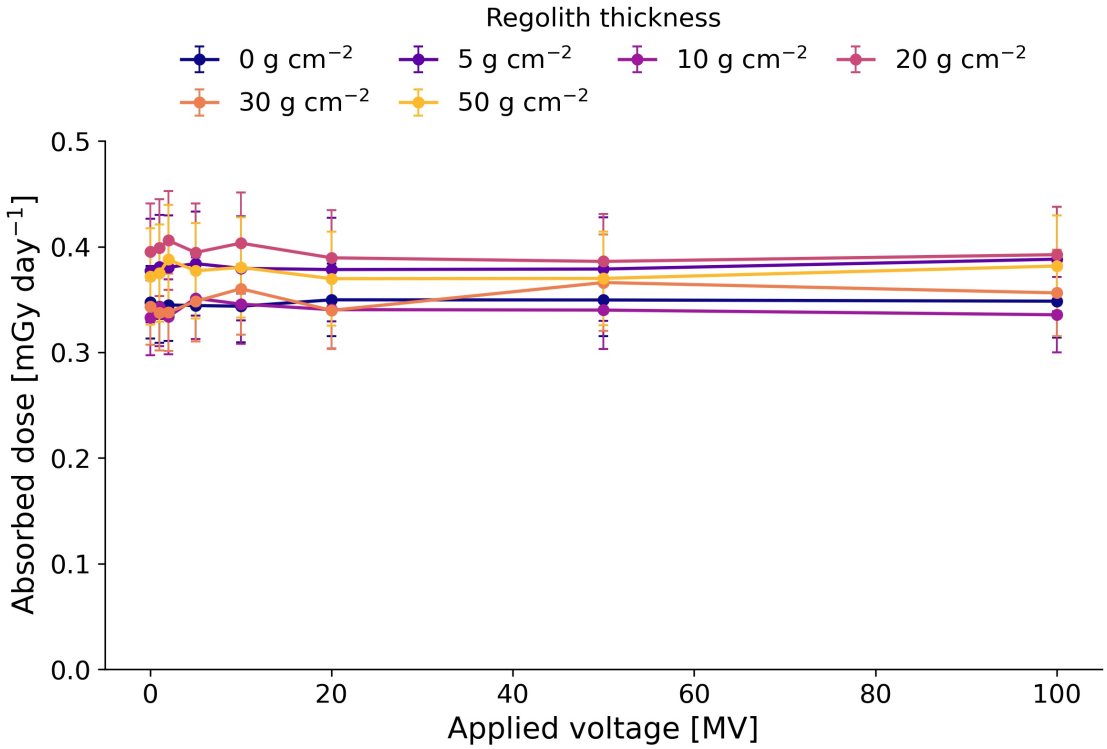


Figure 5.16: G4-ASPP absorbed dose rate vs. active shielding voltage, by passive shielding thickness.

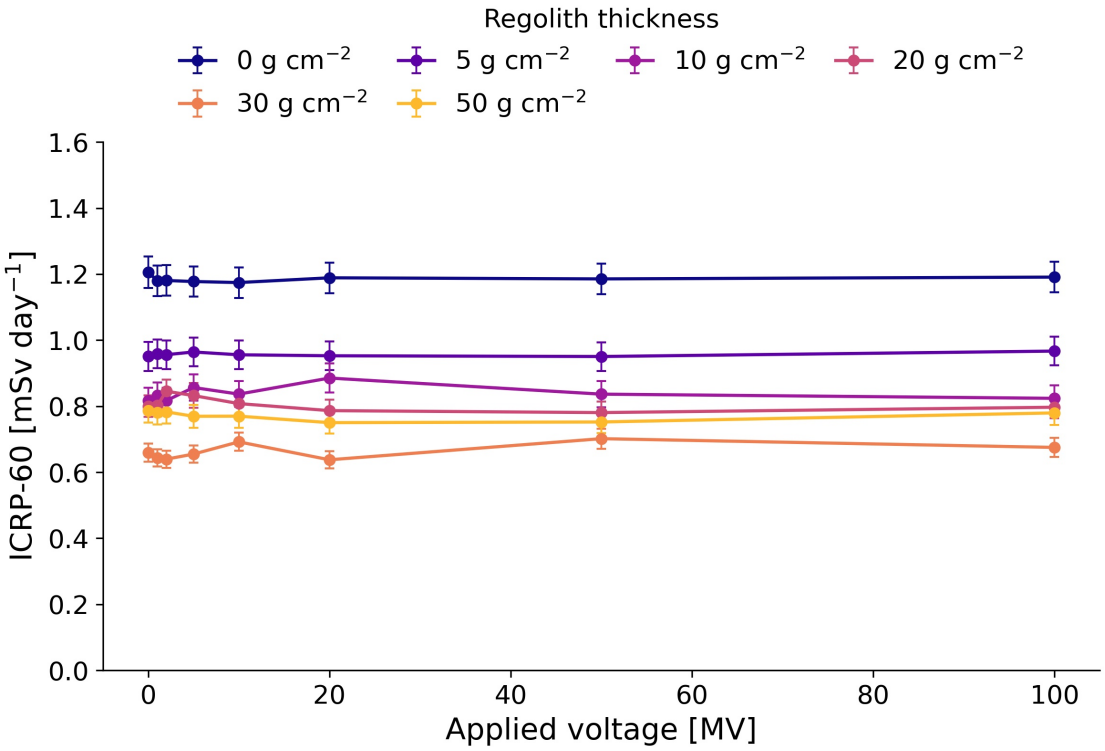


Figure 5.17: G4-ASPP ICRP-60 dose equivalent rate vs. active shielding voltage, by passive shielding thickness.

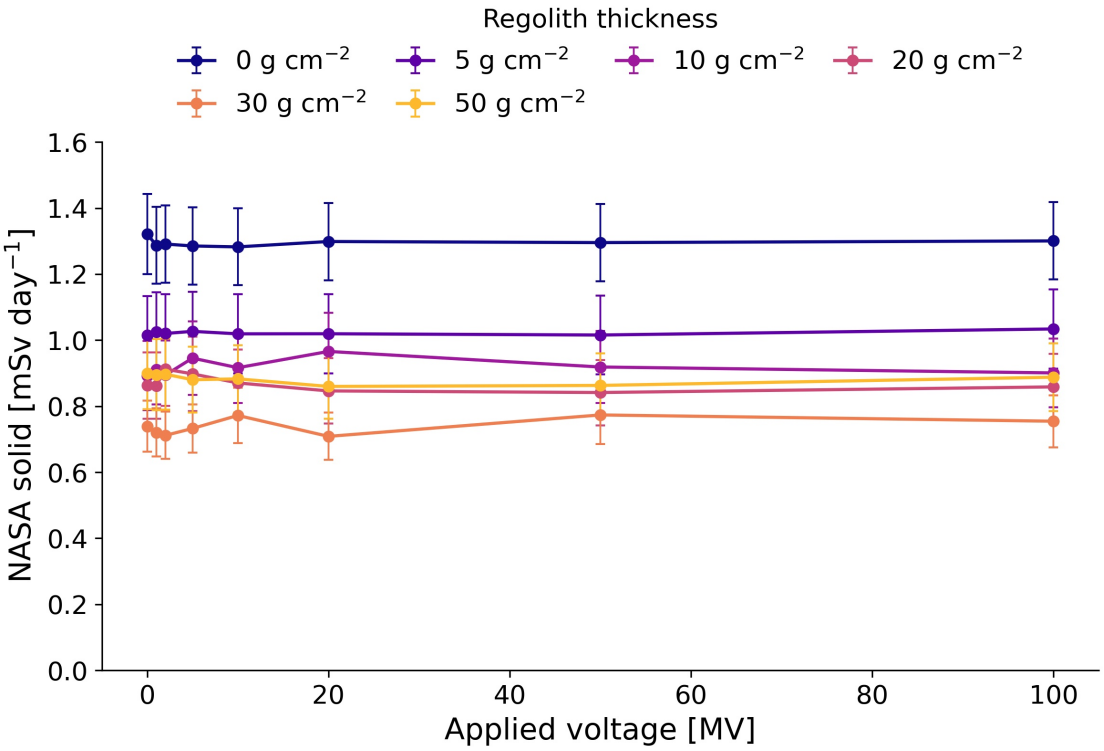


Figure 5.18: G4-ASPP NASA solid cancer dose equivalent rate vs. active shielding voltage, by passive shielding thickness.

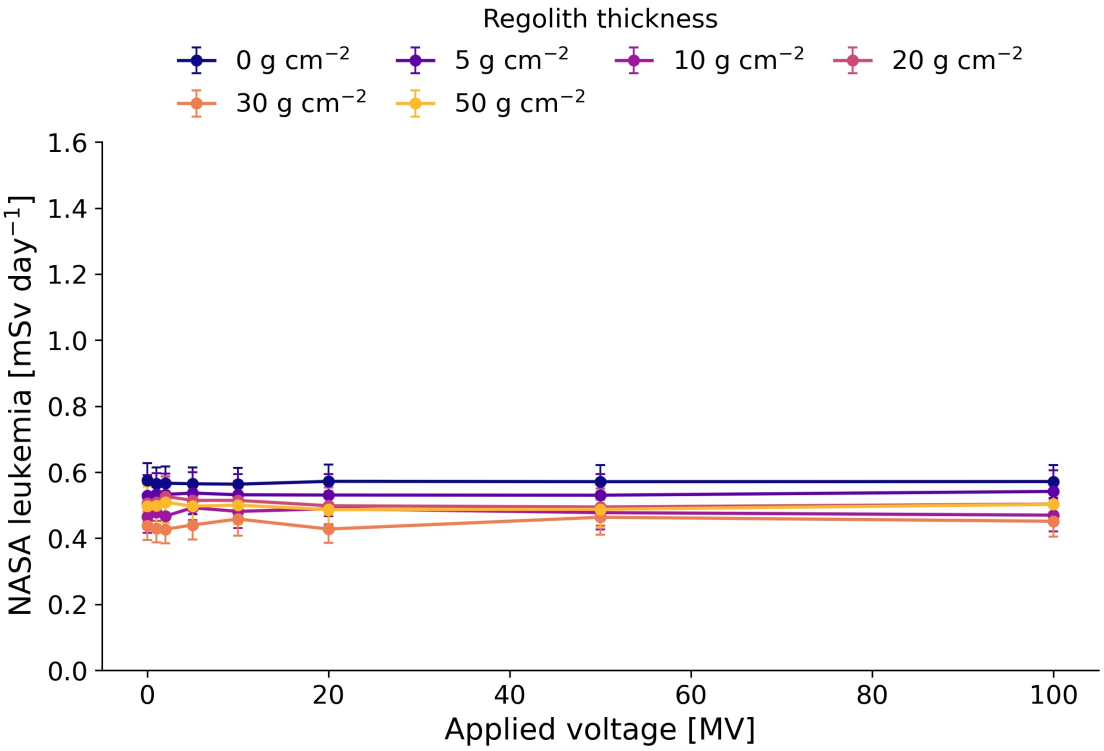


Figure 5.19: G4-ASPP NASA leukemia dose equivalent rate vs. active shielding voltage, by passive shielding thickness.

$30\,\mathrm{g\,cm^{-2}}$, and increases again at $50\,\mathrm{g\,cm^{-2}}$; the other dose equivalent rate quantities follow the same pattern. The absorbed dose rate remains constant to within its statistical uncertainty of approximately 10 % over the same range. Both behaviors agree with the mechanism identified for the lunar surface: thin regolith fragments high-quality-factor heavy ions, which lowers dose equivalent while leaving absorbed dose nearly unchanged, and secondary production increases the dose at larger thickness [118]. The non-monotonic dependence is also qualitatively consistent with that reported for GCR environments more generally [10].

5.3.3.3 Dependence on Active Shielding

The dependence on active shielding is generally weaker than the dependence on passive shielding. At fixed passive shielding thickness, the G4-ASPP dose and dose equivalent rates remain approximately constant over the 0–100 MV voltage range. This behavior is consistent across the different passive shielding thicknesses and all four dose quantities considered. The runs at different voltages for a given species and thickness transport the same primary particles (Section 5.2.3.11), so the ratio of each result to the zero-voltage result at the same thickness is less affected by statistical fluctuation than the individual values. These ratios lie between 0.977 and 1.066 for absorbed dose and between 0.954 and 1.084 for the three dose equivalent quantities, without a consistent sign: at 5 and $10\,\mathrm{g\,cm^{-2}}$, every voltage gives a result at or above the zero-voltage result, whereas at zero passive shielding every voltage gives a dose equivalent at or below it. The spread is larger than that of the ^{1}H+^{4}He contribution alone (Section 5.3.4), and no resolvable voltage dependence can be established from these results.

5.3.3.4 Comparison with Blunier et al. (2025)

At zero passive shielding and zero applied voltage, the G4-ASPP full 28-species result is an absorbed dose rate of $0.348\,\mathrm{mGy\,d^{-1}}$ and an ICRP-60 dose equivalent rate of $1.21\,\mathrm{mSv\,d^{-1}}$, a mean ICRP-60 quality factor of 3.5. Matthiä and Berger report $0.25\,\mathrm{mGy\,d^{-1}}$ and $0.84\,\mathrm{mSv\,d^{-1}}$ for the lunar surface at solar minimum, a mean ICRP-60 quality factor of 3.4 [118], and the unshielded dose equivalent rate compiled by Blunier et al. is of the same magnitude [119]. The G4-ASPP values are higher by a factor of approximately 1.4 in both quantities. Because the factor is the same for absorbed dose and dose equivalent, the difference lies in the amount of energy deposited rather than in its radiation quality, consistent with the different targets: the 15 cm ICRU sphere has less self-shielding than the organs of an anthropomorphic phantom. The dependence

on thin shielding also agrees. Between 0 and 10 g cm^{-2}, G4-ASPP gives a 32 % decrease in ICRP-60 dose equivalent and an absorbed dose that is constant within uncertainty; between 0.5 and 10.5 g cm^{-2} of regolith, Matthiä and Berger report a 22 % decrease in dose equivalent (0.85 to 0.66 mSv d^{-1}) and a constant absorbed dose rate of 0.25 mGy d^{-1} [118].

5.3.4 Comparison of the Combination Model and G4-ASPP

A like-for-like comparison requires the same primary species in both calculations. G4-ASPP records the dose by primary species, so its ^{1}H and ^{4}He contributions can be compared directly with the combination model. The comparison covers the six thicknesses from 0 to 50 g cm^{-2} simulated in both methods. Table 5.5 lists both at zero applied voltage, and Figures 5.20 and 5.21 show them by primary species.

Table 5.5: Absorbed dose rate $\dot{D}$ [mGy d^{-1}] and ICRP-60 dose equivalent rate $\dot{H}$ [mSv d^{-1}] to the ICRU sphere from ^{1}H and ^{4}He primaries at zero applied voltage, from the combination model and G4-ASPP, with their ratio (combination model / G4-ASPP). The G4-ASPP values are the mean of two independent seed sets (Equation 5.54), with 1σ statistical uncertainties. The statistical uncertainty of the combination model is 6–7 %, and that of the ratio is 10–13 %.

	Combination model		G4-ASPP		Ratio	
x [g cm^{-2}]	$\dot{D}$	$\dot{H}$	$\dot{D}$	$\dot{H}$	$\dot{D}$	$\dot{H}$
0	0.199	0.326	0.266 ± 0.022	0.508 ± 0.054	0.75	0.64
5	0.214	0.360	0.330 ± 0.031	0.636 ± 0.068	0.65	0.57
10	0.225	0.385	0.334 ± 0.027	0.660 ± 0.064	0.67	0.58
20	0.244	0.432	0.355 ± 0.036	0.705 ± 0.084	0.69	0.61
30	0.261	0.475	0.277 ± 0.023	0.521 ± 0.041	0.94	0.91
50	0.291	0.556	0.339 ± 0.029	0.714 ± 0.064	0.86	0.78

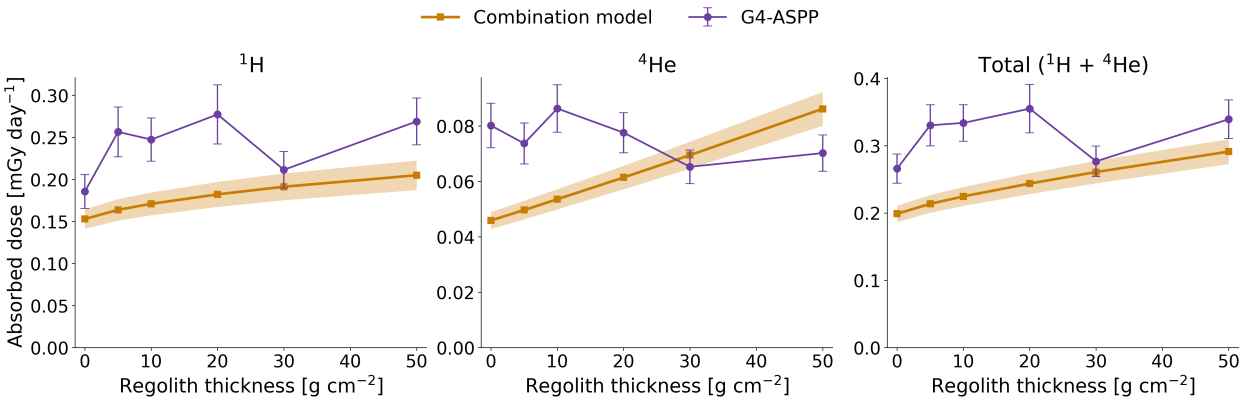


Figure 5.20: Absorbed dose rate to the ICRU sphere vs. regolith thickness at zero applied voltage for ^{1}H primaries (left), ^{4}He primaries (center), and their sum (right). The combination model is shown as a line with a shaded 1σ statistical uncertainty band; G4-ASPP is shown as markers with 1σ statistical error bars and is the mean of two independent seed sets.

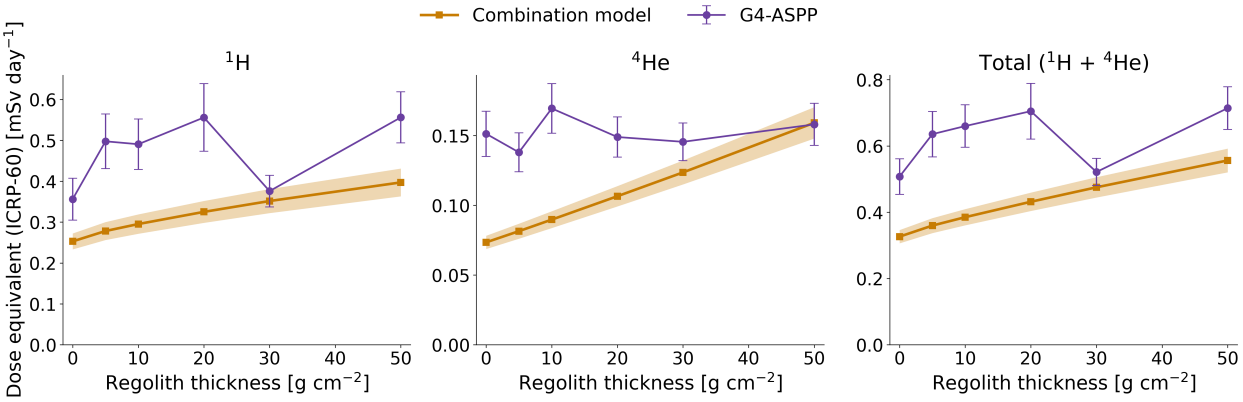


Figure 5.21: ICRP-60 dose equivalent rate to the ICRU sphere vs. regolith thickness at zero applied voltage, shown as in Figure 5.20.

5.3.4.1 Passive Shielding Dependence

Restricted to ^{1}H and ^{4}He primaries, both methods give dose rates that increase with regolith thickness, unlike the full-spectrum dose equivalent of Section 5.3.3.2. That decrease at low shielding thicknesses comes from the heavy ions. At zero applied voltage, the increase is steeper in the combination model. Between 0 and 50 g cm^{-2}, its absorbed dose rate increases by 46 % and its dose equivalent rate by 71 %, against 28 ± 15 % and 41 ± 20 % for G4-ASPP. At applied voltages from 1 to 100 MV, the corresponding increases are 23–37 % and 48–61 % in the combination model and 26–32 % and 41–48 % in G4-ASPP, consistent within the uncertainty of the G4-ASPP values. The steeper increase at zero voltage comes from the combination model's ^{4}He contribution, whose absorbed dose rate increases by 88 % between 0 and 50 g cm^{-2} at zero voltage and by 22–44 % at the other voltages. The G4-ASPP values at 30 g cm^{-2} lie below those at the neighboring thicknesses in both seed sets, by approximately 2σ in absorbed dose and 3σ in dose equivalent.

5.3.4.2 Active Shielding Dependence

The two methods differ in how precisely they resolve an effect of the applied voltage (Figure 5.22). In G4-ASPP, the runs at different voltages for a given species and thickness transport the same primary particles (Section 5.2.3.11), so their ratio to the zero-voltage result changes only through histories whose trajectories the field alters. For ^{1}H+^{4}He, these ratios lie between 0.97 and 1.04 for absorbed dose and between 0.94 and 1.05 for dose equivalent at every thickness and voltage. In the combination model, each voltage is an independent ASPP sample, and the same sample is scored at every thickness. Its results at a given thickness scatter by approximately 9 % about their mean over voltage, against a quoted uncertainty of 6–7 %. They

decrease from 0 to 20 MV, and the 50 MV result is out of that order. A 100 MV barrier can turn back protons only below approximately 100 MeV, whose CSDA range in water is 7.718 g cm^{-2} [120], while most of the GCR dose is delivered by particles of higher energy. Together with the paired G4-ASPP result, this makes the combination model's variation more consistent with statistical scatter larger than its quoted uncertainty than with an effect of the field. For this electrode configuration, the dose to the ICRU sphere is just insensitive to the applied voltage up to 100 MV in both calculations.

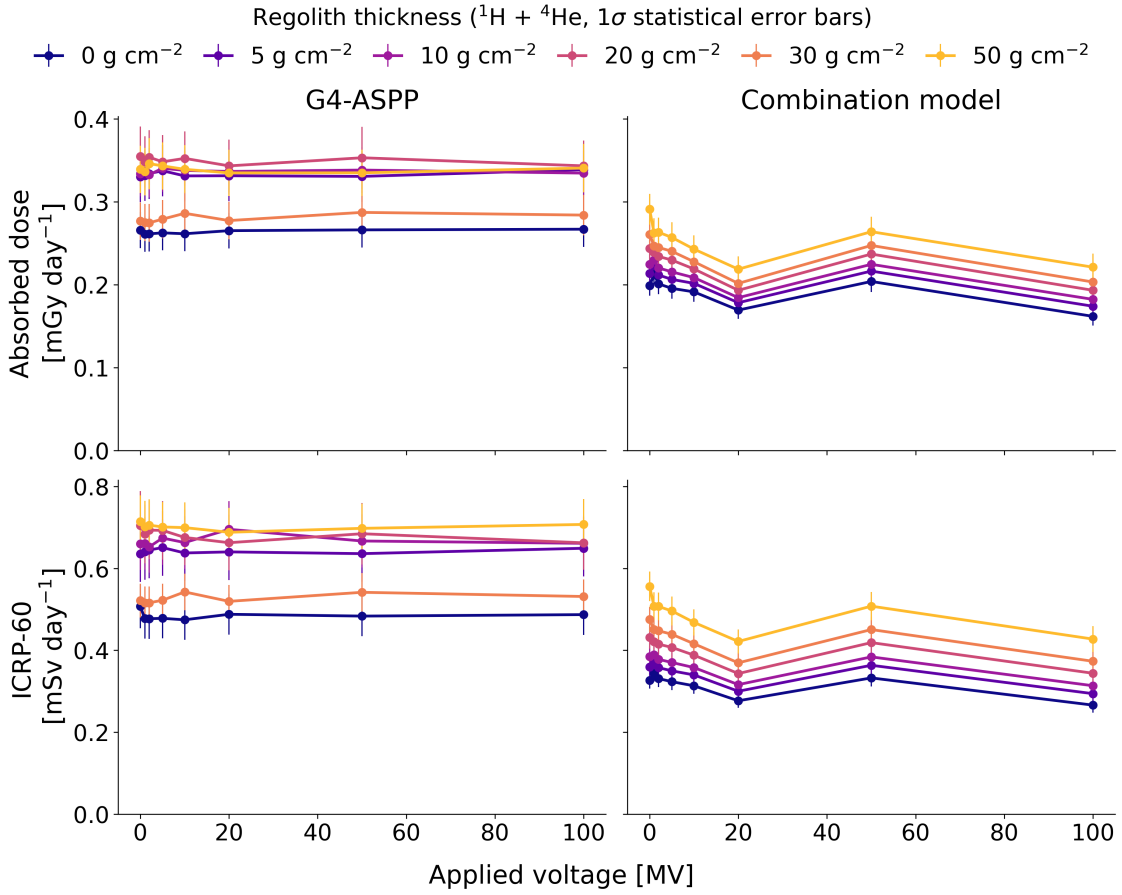


Figure 5.22: ^{1}H+^{4}He absorbed dose rate (top) and ICRP-60 dose equivalent rate (bottom) to the ICRU sphere vs. applied voltage, for G4-ASPP (left, mean of two independent seed sets) and the combination model (right). Line color indicates regolith thickness. Error bars indicate the 1σ statistical uncertainty.

5.3.4.3 Contributions by Primary Species

The two primary species differ in how the methods compare (Figures 5.20 and 5.21). For ^{1}H, the combination model is lower than G4-ASPP at every thickness, with an absorbed dose ratio of 0.64 to 0.90 at zero applied voltage and no trend with thickness. Both methods give a ^{1}H dose that increases with regolith thickness

at rates consistent within uncertainty: between 0 and 50 g cm^{-2}, the ^{1}H absorbed dose rate increases by 34 % in the combination model and by 45 ± 22 % in G4-ASPP. For ^{4}He, the trends differ. Over the same range, the G4-ASPP ^{4}He absorbed dose rate changes by −12 ± 12 % at zero voltage and by −5 to −11 % at the other voltages, whereas that of the combination model increases by 88 % at zero voltage and by 22 to 44 % at the other voltages. At 1 to 100 MV, the two trends differ by 28 to 55 percentage points, against a combined uncertainty of 17 to 20 percentage points; the G4-ASPP results at different voltages share their primaries and are not independent tests. As a result, the combination model's ^{4}He absorbed dose rate at zero voltage is 0.57 times that of G4-ASPP at zero passive shielding and 1.23 times at 50 g cm^{-2}, and the ^{4}He contribution accounts for most of the increase with thickness of the ratios in Table 5.5. The results of this work do not identify the cause of the difference in the ^{4}He trends.

5.3.4.4 Magnitude Difference

The combination model is lower than G4-ASPP by a factor between 0.57 and 0.94 (Table 5.5), with the difference largest at 5 to 20 g cm^{-2} and larger for dose equivalent than for absorbed dose at every thickness. Several structural differences between the methods could contribute, and the results of this work do not separate them. First, in the straight-ahead approximation of HZETRN, the secondaries produced by a primary remain on the primary's ray, so only primaries whose rays intersect the ICRU sphere contribute. In three-dimensional transport, neutrons and charged secondaries produced in the dome by primaries whose rays miss the sphere can also reach it. This would lower the combination model more for dose equivalent, to which neutrons contribute disproportionately. Second, the combination model excludes albedo produced beneath the habitat footprint, which in G4-ASPP reaches the sphere through the habitat floor. Third, the combination model omits secondary species without a dose response and uses different nuclear interaction models (PHITS for the albedo and HZETRN for the shield) from G4-ASPP. A G4-ASPP calculation that tallies the dose by the origin of the depositing particle (dome secondary, albedo secondary, or primary) would isolate the first two contributions.

5.3.5 Limitations and Future Work

Several limitations of the present analysis constrain the completeness of the radiation dose response estimates. Primary ASPP transport was performed only for ^{1}H and ^{4}He rather than the full GCR spectrum because

of the computational time and storage requirements. Several unrepresented species, particularly ^{16}O, ^{24}Mg, ^{28}Si, and ^{56}Fe, contribute disproportionately to dose equivalent relative to their particle abundance because of their high-LET interactions. Dose response coverage for these species is already available in the HZETRN volume dose calculation, but extending the combination model to them would also require PHITS albedo response functions for each heavy primary species. The present library required at least 3×10^5 core-hours for each of ^{1}H and ^{4}He, most of it at incident energies above 100 MeV/n, and the cost per ^{4}He history was several times that per ^{1}H history; a library for each heavier species would be expected to cost at least as much. This limitation accounts for the lower full-spectrum dose equivalent of the combination model relative to the benchmarks of [118, 119], and it prevents the combination model from reproducing the decrease in dose equivalent with thin shielding.

A second limitation identified during the validation of the combination model is the energy convention used by the PHITS albedo response functions. The `e-type=1` tally convention and the lack of `iMeVperu=1` in the `[Parameters]` section resulted in a misrepresentation of the energy axis for tracked species (primary and secondary) with mass number $A > 1$. The input files generated for PHITS were meant to be in MeV/n. Correcting and validating this energy convention is another well-defined task for future work. Since response functions would need to be regenerated, and this process takes an enormous amount of computational time, it would also be prudent to use the most recent version of PHITS, instead of repeating with PHITS version 3.17.

The active shielding configuration investigated here was deliberately limited to a single geometry and a voltage sweep at that geometry. Consequently, the results do not establish how the observed radiation response changes across the much larger design space of electrode geometries, voltages, passive shielding configurations, and materials. Exploring this space with forward transport would require a large number of computationally expensive simulations. An adjoint transport formulation offers one potential aid. An adjoint solution for the ICRU sphere can be reused for any source spectrum, and, combined with the forward solution, it gives the first-order sensitivity of the dose to changes in the field or the shielding materials. A finite change of electrode geometry or voltage, however, still requires new transport solutions. Applying this approach to active shielding would require an adjoint formulation that incorporates charged particle transport in the electrostatic field, representing an important extension of G4-ASPP.

The present analysis is also restricted to steady-state GCR exposure. Solar particle events represent a

distinct source of acute radiation exposure and are not considered here. Because active shielding performance depends on the incident particle energy and spectrum, its effectiveness against the softer spectra characteristic of solar particle events may differ from its effectiveness against GCR. Magnetically trapped proton and electron environments, such as those encountered near Earth and Jupiter, provide additional environments in which active shielding responses could be evaluated (though these would necessarily extend beyond a lunar habitat configuration).

Finally, the systematic difference in magnitude between the two methods for ^{1}H and ^{4}He primaries (Section 5.3.4.4) is not yet totally explained, nor is the difference in their ^{4}He trends with thickness (Section 5.3.4.3), though the results are at least within a factor of two. A G4-ASPP calculation that tallies the dose by the origin of the depositing particle, combined with a combination-model calculation that includes the albedo produced beneath the habitat footprint, would separate the contributions of three-dimensional secondary transport and albedo.

5.4 Conclusion

This chapter presented two independent approaches for estimating radiation dose behind an actively and passively shielded lunar habitat: a direct Geant4-based transport model (G4-ASPP) and a combination model coupling ASPP electrostatic transport, PHITS albedo response functions, and HZETRN depth-dose response curves. The combination model determines dose to the ICRU sphere from the chord length traversed by each particle and uses response functions normalized to the physical GCR source emission rate. The G4-ASPP approach produces dose estimates that are of the same general magnitude as independent literature results. For the full GCR spectrum, G4-ASPP gives an unshielded absorbed dose rate of $0.348\,\mathrm{mGy\,d^{-1}}$ and an ICRP-60 dose equivalent rate of $1.21\,\mathrm{mSv\,d^{-1}}$, a factor of approximately 1.4 above published lunar-surface values for an anthropomorphic phantom, with the same mean quality factor and the same decrease in dose equivalent behind thin shielding. For ^{1}H and ^{4}He primaries, the combination model reproduces the published share of absorbed dose carried by these species, and lies a factor of 0.57 to 0.94 below G4-ASPP. Both methods give a ^{1}H+^{4}He dose that increases with regolith thickness, and secondary albedo particles contribute less than 8 % of the dose behind the habitat shell over 0 to $50\,\mathrm{g\,cm^{-2}}$.

Neither approach provides a definitive quantitative basis for concluding whether active electrostatic

shielding improves or worsens the radiation environment for the habitat configuration investigated here. The G4-ASPP results show no dependence of dose on applied voltage: because the runs at different voltages share their primary particles, the ^{1}H+^{4}He dose at each voltage is within 6 % of its zero-voltage value. The combination model's variation with voltage is larger than its quoted statistical uncertainty but has no physical ordering. For this active shielding configuration, a potential of up to 100 MV is too small to deflect the particles that deliver most of the GCR dose. Explaining the systematic difference in magnitude between the two methods, together with extending primary GCR transport beyond ^{1}H and ^{4}He, is left as future work.

The two approaches also differ massively in their computational and operational complexity. The combination model requires three independent transport codes—ASPP, PHITS, and HZETRN—connected through a multistage pipeline involving primary transport, albedo response folding, secondary particle resampling and transport, and depth-dose aggregation. Each interface introduces opportunities for normalization, unit convention, and data format errors. Establishing and verifying the physical normalization of the source and the chord geometry calculations required more development and validation effort. By contrast, G4-ASPP evaluates a shielding configuration within a single self-consistent Geant4 simulation, eliminating the need for manual data transfer between independent transport codes.

This difference has practical consequences for both development and application. A new G4-ASPP configuration can be evaluated without reproducing the intermediate processing required by the combination model, reducing both turnaround time and the number of external interfaces that must be maintained. It also lowers the barrier to use because a user does not need to manage three separate transport codes and their associated input and output conventions. These advantages are independent of the magnitude difference between the two methods and provide an important motivation for continued development of G4-ASPP. The relative operational complexity of the two approaches is illustrated in Figure 5.23.

5.5 Future Work

The most direct extension of this work is to broaden the primary ASPP transport from ^{1}H and ^{4}He to the remaining important GCR species. This would provide a more complete assessment of the combination model and directly address the species-scope limitation. Completing the missing PHITS secondary runs and correcting the heavy-ion energy-axis convention would likewise improve the completeness and reliability of

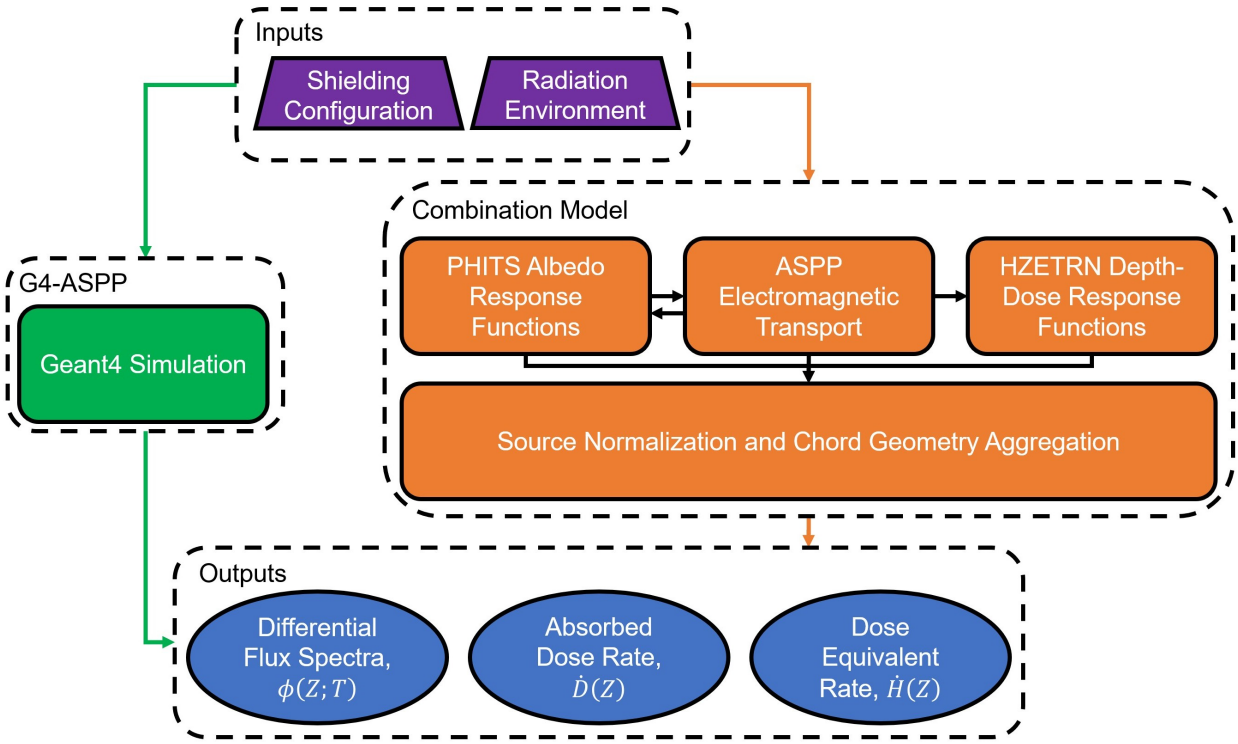


Figure 5.23: Comparison of the computational pipelines used by G4-ASPP and the combination model. G4-ASPP performs transport and dose calculation within a single simulation, whereas the combination model requires multiple transport and post-processing stages connected through intermediate data products.

the albedo response functions, which could easily serve other purposes outside of this work.

A longer-term objective is to make active shielding configuration optimization computationally practical. The single geometry investigated here represents only one point in a much larger design space. An adjoint transport formulation, combined with the forward solution, would give the first-order sensitivity of the dose to the electrode geometry and voltage from one pair of calculations, which could guide the search through that space, although each configuration selected in this way would still require independent transport calculations. For active shielding, this would require incorporating the electrostatic field into the adjoint transport formulation rather than relying on the field-free formulations commonly used in deterministic transport.

A complementary design tool could provide interactive visualization of the electromagnetic field while a shielding configuration is being constructed. Electrode geometry and applied voltage could be modified while the resulting field is displayed in real time. Coupling such a tool with an adjoint transport calculation would provide a framework for interactive shielding design in which field visualization guides configuration selection and the adjoint solution provides an estimate of the corresponding dosimetric response.

The radiation environments considered in this work could also be expanded beyond steady-state GCR. Solar particle events should be evaluated separately because their softer energy spectra may produce a different active shielding response than the GCR spectrum considered here. Magnetically trapped proton and electron populations, including those encountered near Earth and Jupiter, provide additional environments for evaluating the generality of the active shielding approach.

5.6 Mistakes (and Corrections)

This section records the errors found during the work reported in this chapter, how each was found, how it was corrected, and how it affected the results. It also lists the issues that remain open and the lines of investigation that were pursued without changing the results. Every correction listed here is included in the results of the preceding sections. Smaller errors in plotting and parsing scripts that did not affect any reported value are not listed.

5.6.1 Errors Found and Corrected

Two errors affected the G4-ASPP results. No G4-ASPP run in the original set specified a random-number seed, so every run started from the Geant4 default seed. Re-running a few events of selected runs with tracking output enabled and comparing the initial state of each primary showed what this implied. Runs at different voltages for the same species and thickness transported identical primary particles, runs at different thicknesses transported nearly the same sequence of primaries offset by one event, and runs of different species began from the same source positions. The first of these makes the comparison between voltages paired, which is useful. The other two mean that the results at different thicknesses, and the contributions of different species, are not independent samples, although they had been treated as independent when compared or added in quadrature. A second set of ^{1}H and ^{4}He runs was performed with one new seed pair for each species and thickness, and the two sets are averaged (Section 5.2.3.11). The averaging changed the comparison with the combination model. With the original set alone, the ratio of the combination model to G4-ASPP was 0.56 to 0.83, and the ^{1}H+^{4}He absorbed dose and dose equivalent of G4-ASPP increased by 20 % and 24 % between 0 and 50 g cm^{-2}. The step in absorbed dose from 5 to 10 g cm^{-2}, −11 % in the original set, was +14 % in the second. The full 28-species results were not repeated and still use the default seed.

The second error concerned the ICRP-60 dose-equivalent uncertainty, which was originally computed by combining the uncertainties of the individual LET bins in quadrature. A single event deposits energy in many bins, so the bin contributions are positively correlated and the quadrature sum underestimates the uncertainty. The estimator was replaced with the per-event estimator of Equation 5.59. The ^{1}H and ^{4}He runs were repeated with the default seed and the corrected executable. Every dose value was reproduced exactly, and the dose-equivalent uncertainties were 2.4 to 3.4 times larger, for example from 8.2 to 19.6 % for the unshielded ^{1}H run at zero voltage. The full 28-species dose-equivalent uncertainties were not recomputed. The NASA dose equivalents were always computed with a per-event estimator and were not affected.

The remaining errors were in the combination model. The first combination-model ASPP runs intended for ^{4}He primaries specified an unphysical ion with $Z = 4$ and $A = 2$. The charge and mass number had been entered in the reverse of the order ASPP expects, and ASPP accepted the unphysical combination without a warning. Such an ion has four times the charge-to-mass ratio of ^{4}He, so the field deflected it far more

strongly than it would a real ^{4}He ion. The error was found by inspecting the order of the input parameters in ASPP, before the combination-model results were incorporated into this dissertation, and the ^{4}He primary runs were repeated with the correct ion.

The normalization of the combination model was corrected in several stages. The normalization connecting the number of simulated source particles to the physical GCR source rate initially omitted the factor $2\pi^2 R^2$ of Equation 5.44, and the unit conversion applied to the BON flux included an additional factor of 4π. Without the first factor, the combination-model dose rates were several orders of magnitude too small. Both errors were found by re-deriving the normalization from the cosine-law current of an isotropic flux through the source hemisphere and by comparison with the G4-ASPP normalization. The conversion now changes units only, and the angular integration is carried entirely by $2\pi^2 R^2$. Separately, each ASPP hit contributes $w_i/(\cos\theta_i S)$ to the fluence estimate of its run, and that contribution must be divided by the number of source particles N launched in the run. Three successive implementations of this division were wrong. The first divided by the number of hits in the run instead of N, which overestimated the dose by roughly the square of N divided by the number of hits and produced an implausible spike in dose at low voltage. The second omitted the division entirely, so the dose was too low by a factor of $N \approx 10^5$. The third divided the sum of the dose contributions by the sum of the estimator contributions, which computes a weighted average of the dose per hit instead of a weighted sum; it was too low and was identified by comparison with the magnitude of the G4-ASPP result. The current implementation divides each contribution by the N associated with the same run.

After these corrections, and the correction of the HZETRN boundary condition described below, the combination model was still about two orders of magnitude below G4-ASPP. A further error lay in the estimator itself. The combination model originally scored each hit that reached the ICRU sphere with the surface-crossing estimator averaged over the whole dome, $w_i/(\cos\theta_i A_S)$ with $A_S = 2\pi R_{\mathrm{outer}}^2$. Restricting that estimator to the hits that reach the sphere applies the geometric probability of reaching the sphere twice, once through the selection of hits and once through the normalization by the dome area. It underestimated the dose by approximately $A_S/(\pi R_{\mathrm{ICRU}}^2)$, a factor of about 8 for the unshielded dome and larger for thicker domes, which accounts for a factor of approximately 8 of the remaining difference at zero passive shielding. It was replaced with the track-length estimator of Equation 5.50. At the same time, it was found that the impact parameters of Equations 5.33 and 5.34 had both been measured from the origin, which placed half

of the ICRU sphere below the lunar surface. The sphere is now centered at $R_{\mathrm{ICRU}} + \delta$ above the floor, as in G4-ASPP.

Two errors in the bookkeeping of the combination model discarded or reused data. The script that combines the ASPP runs into binned fluences assigned each run's fluence to its (species, voltage) entry instead of adding it. Because each ASPP run is monoenergetic and the 100 runs of an energy grid share the same entry, only the last run processed was retained. The error was found when the ^{4}He contribution disappeared from the combined fluence, because its last-processed run had no hits, and the ^{1}H contribution was also undercounted. The assignment operator was replaced with an accumulation operator. In a similar way, the total outgoing albedo yield C^{total} of a primary run was cached by run directory only. Because the multi-radius primary runs are scored at every shielding thickness from the same directory, the yield computed for the first thickness was reused at the others. The cache key was changed to paired indices that represent the run directory and thickness.

Three errors affected the HZETRN responses. The response for one incident energy was first computed with a boundary-condition flux concentrated at a single point of the HZETRN energy grid. HZETRN integrates the dose with a ten-point Gauss–Legendre quadrature on each grid segment and interpolates the flux at the quadrature nodes with a cubic Lagrange interpolation that falls back to linear interpolation when the cubic would overshoot. No node lies at a grid point, so a flux concentrated at one grid point is severely under-sampled. Reproducing this scheme independently of HZETRN predicted that a single-point boundary condition recovers 8.24 % of the intended flux and a seven-point boundary condition 85.58 %, a ratio of 10.38, against a measured ratio of 10.18. The boundary condition was changed to spread each unit flux over seven adjacent grid points, and all 875 HZETRN responses (7 species, 125 energies) were regenerated. The corrected depth-dose responses also show a Bragg peak that was absent before. The regolith composition passed to HZETRN listed atomic masses, for example 15.999 for oxygen, where HZETRN expects integer mass numbers. HZETRN truncates the value to an integer, so the requested isotopes (for example, $A = 15$ for oxygen) did not match the cross-section files. The composition was changed to the integer mass number of the dominant isotope of each of the 13 regolith elements, matching the names of the cross-section files. Finally, several array tasks generated the shared HZETRN cross-section file for the ICRU tissue simultaneously and corrupted it. File locking did not prevent this reliably, so the file is now generated once, serially, before the array of HZETRN runs is submitted.

5.6.2 Unresolved Issues

Several issues remain open. The largest is the magnitude of the difference between the methods: for ^{1}H and ^{4}He primaries, the combination model is 0.57 to 0.94 times G4-ASPP. Section 5.3.4.4 lists the structural differences that could contribute, but the present results do not separate them. The methods also differ in the ^{4}He trend with thickness, which decreases slightly in G4-ASPP and increases in the combination model (Section 5.3.4.3), and the cause is not identified. Within G4-ASPP, the ^{1}H+^{4}He result at $30\,\mathrm{g\,cm^{-2}}$ lies below those at the neighboring thicknesses by approximately 2σ in absorbed dose and 3σ in dose equivalent, in both seed sets. Because the two sets are independent, this is unlikely to be a fluctuation of one sample, but the cause is not known.

The uncertainty of the combination model is underestimated. Its results at different voltages scatter by approximately 9 % about their mean at each thickness, against a quoted uncertainty of 6–7 %. The quoted uncertainty treats each primary history as independent and omits several correlated or unpropagated contributions. Albedo particles generated from the same primary share its yield and weights, the secondary sources of every primary run are resampled from the same random-number seed, and the statistical uncertainty of the PHITS albedo responses is not propagated. Which of these accounts for the excess scatter has not been determined.

The PHITS albedo library is incomplete in two respects. Of the 2000 PHITS runs, 74 produced no tally output: 71 ^{4}He runs above 4000 MeV/n, including every incident angle at the three highest energies, and three ^{1}H runs. The routine that reads the library fills a missing response with zeros and issues a warning instead of stopping, so the combination model has no ^{4}He albedo at incident energies of 32 000 MeV/n and above, and only part of the angular range from 4000 to 26 000 MeV/n. The effect is bounded by the ^{4}He share of the albedo dose, which is itself less than 8 % of the total, but it has not been quantified. In addition, the `e-type=1` convention described in Section 5.3.5 bins the outgoing energy of secondaries with $A > 1$ by total kinetic energy on a grid defined per nucleon. The energy axis can be corrected after the fact, but secondaries above $5 \times 10^{4}/A$ MeV/n were never scored, and the response functions would have to be regenerated to recover them.

Finally, the two methods define LET differently. G4-ASPP assigns each energy deposit the LET of its step, the deposited energy divided by the step length, and deposits with a step LET outside $0.1\,\mathrm{keV\,\mu m^{-1}}$

to $1 \times 10^5\,\mathrm{keV}\,\mu\mathrm{m}^{-1}$ do not contribute to the ICRP-60 dose equivalent. HZETRN uses the unrestricted LET. The mean quality factor of the G4-ASPP full-spectrum result, 3.5, is close to the 3.4 of Matthiä and Berger [118], which suggests that neither difference is large, but neither has been evaluated directly.

Chapter 6

Conclusion

Active radiation shielding proposes to use electromagnetic fields to deflect or decelerate charged particles before they reach a specified target, like a crewed volume. Any practical implementation will be a hybrid shield that includes both active and passive shielding. Evaluating such a hybrid shield requires a transport calculation that treats long-range electromagnetic forces and short-range interactions in bulk matter together. This dissertation developed such a tool, G4-ASPP, verified its charged particle propagation, and applied it to a lunar habitat. This chapter summarizes the work, states what it has added to the field, identifies its limitations, and describes possible future work.

6.1 Summary

6.1.1 Charged Particle Transport Formalism

Chapter 2 reviewed radiation protection frameworks, the space radiation environment, and the deterministic transport methods used for passive shielding analysis. The linearized Boltzmann transport equation, in the form solved by HZETRN, assumes that particles change energy only through point-like interactions and otherwise travel in straight lines. Neither assumption holds for a charged particle in an externally applied electromagnetic field. Starting from conservation of particles in phase space, Chapter 2 derived a charged particle transport equation (Equation 2.67) in the kinetic energy and solid angle direction variables used throughout space radiation shielding practice, with explicit terms for the work done by the electric field on the particle energy and for the rotation of the particle direction by the electric and magnetic fields.

Equation 2.67 reduces to the neutral-particle transport equation for $Z = 0$. Equation 2.67 reduces to the continuous-slowing-down form underlying HZETRN when the field $\vec{F}$ is absent. The adjoint of Equation 2.67 was then constructed term-by-term (Equation 2.87), together with the appropriate boundary conditions on kinetic energy, position, and time required for the adjoint relation to hold. The derivation was not used directly in later chapters, but it defines the quantity that ASPP and G4-ASPP estimate by Monte Carlo and establishes the form an adjoint method for active shielding must take.

6.1.2 Extension and Experimental Validation of ASPP

Chapter 3 described ASPP, a charged particle propagation code for the rapid prototyping of active shielding configurations, and the capabilities added to it during this work. These additions include Boolean geometry for confining fields and flagging particles; per-region material assignment, which switches the local electric field, magnetic field, and stopping power on or off and specifies the mean charge-to-mass ratio and mean excitation energy of the medium; relativistic deceleration using the uncorrected Bethe-Bloch formula; and an energy deposition tally with its associated relative error. The code was also extended with a time-reversed propagation mode that traces particles from a crew volume back to their origins on the source sphere. Additional field-generating components were added, including finite line charges, rectangular charges, and a rectangular-prism bar magnet. Closed-form reference potentials and self-capacitances were also added for the finite-volume analogs of these components, which relate the applied voltage to the stored energy and power required to operate an active shield.

Applied to an orthogonal plate-and-rod configuration, the time-reversed mode showed that protons reaching a spherical crew volume had crossed a mean potential energy barrier of approximately 15 MeV. It also revealed the directions through which the configuration admits particles.

The second half of Chapter 3 presented the experimental validation of ASPP against beamline measurements at the Tandem Van de Graaff facility of Brookhaven National Laboratory [28]. Shielding efficacy was quantified as the void area produced by an electric dipole in a calibrated phosphor-screen image and expressed as a function of the dimensionless scaling parameter f_s (Equation 3.51), the ratio of the potential energy of the field to the kinetic energy of the incident ion. Simulated and measured void areas agreed with a mean relative error of 13.1 %, differing by a factor of 1.10 on average and 1.75 at most. The void area grew linearly with f_s while the void remained circular, and grew sublinearly with an exponent near 2/3 once the

void reformed into a cardioid-like shape. The dipole rotation study showed that a single electric dipole loses most of its efficacy when the incident radiation is not perpendicular to the dipole axis, so a dipole alone would be a poor shield in an isotropic environment. The validation extended the demonstrated domain of ASPP to multiple ion species at energies up to at least 22 MeV/n.

6.1.3 Charged Particle Propagation in G4-ASPP

Chapter 4 described the construction of G4-ASPP on the Geant4 toolkit and the verification of its charged particle propagation methods [77]. Because Geant4 advances particles in distance rather than time, a distance-stepping analog of the Velocity-Verlet method (VVS) was derived so that G4-ASPP could reproduce the default ASPP integrator, and its symplecticity and phase-space properties were analyzed. Seven propagation methods were compared across six test cases with analytically tractable or reference trajectories, in terms of trajectory error, energy conservation, and computational time. Relative to the Boris integrator, the fourth-order Runge–Kutta distance stepping method (RK4S) produced time-integrated relative errors no larger than 0.01 %, compared with 0.1 % for time-stepping Velocity-Verlet and 1 % for VVS. The adaptive Geant4 stepping in G4-ASPP correctly reduced its step size near physical boundaries, which the constant-step methods did not. On this basis, RK4S was recommended for G4-ASPP, and it was the propagation method used in Chapter 5.

6.1.4 Combined Active and Passive Shielding of a Lunar Habitat

Chapter 5 applied G4-ASPP to a scenario that exercises both of its transport capabilities: a hemispherical lunar regolith habitat containing an ICRU tissue sphere, protected by an electrostatic "umbrella" consisting of a positively charged plate above the dome and a ring of negatively charged spheres, with image charges enforcing a grounded lunar surface. Passive shielding thickness and applied voltage were swept from 0 $\mathrm{g\,cm^{-2}}$ to 50 $\mathrm{g\,cm^{-2}}$ and 0 MV to 100 MV, respectively, under a solar minimum GCR spectrum.

At zero passive shielding and zero voltage, G4-ASPP gave an absorbed dose rate of 0.348 $\mathrm{mGy\,d^{-1}}$ and an ICRP-60 dose equivalent rate of 1.21 $\mathrm{mSv\,d^{-1}}$ for the full GCR spectrum. Both are a factor of approximately 1.4 above the values reported by Matthiä and Berger for the unshielded lunar surface with an anthropomorphic phantom, with nearly the same mean quality factor (3.5 and 3.4, respectively) [118]. The dose equivalent rate decreased by 32 % over the first 10 $\mathrm{g\,cm^{-2}}$ of regolith while the absorbed dose rate

remained constant within uncertainty, the behavior Matthiä and Berger attribute to the fragmentation of heavy ions [118]. The applied voltage produced no resolvable change in any of the four dose quantities: at each shielding thickness, every voltage gave a result within 7 % of the zero-voltage result for absorbed dose and within 9 % for the dose equivalent quantities, without a consistent sign.

To provide an independent comparison, Chapter 5 also constructed a combination model in which ASPP transports primary particles through the field, PHITS albedo response functions convert the particles reaching the lunar surface into albedo sources, a second ASPP simulation transports the albedo particles, and HZETRN response functions convert the particles reaching the dome into dose in the ICRU sphere. For ^{1}H and ^{4}He primaries at zero shielding and zero voltage, the combination model gave an absorbed dose rate of $0.199\,\mathrm{mGy\,d^{-1}}$, consistent with the share of the published lunar-surface absorbed dose carried by these species [118], and an ICRP-60 dose equivalent rate of $0.326\,\mathrm{mSv\,d^{-1}}$. These values are a factor between 0.57 and 0.94 of the corresponding ^{1}H and ^{4}He contribution in G4-ASPP over the shielding thicknesses compared. Both methods gave a ^{1}H+^{4}He dose rate that increases with regolith thickness, and neither resolved a dependence on applied voltage. The methods differ in the ^{4}He contribution, which increases with regolith thickness in the combination model and decreases slightly in G4-ASPP.

6.2 Contributions

The principal scientific contributions of this dissertation are broken into two groups: tools and methodology that others can use, and general knowledge about active shielding for space radiation protection applications.

6.2.1 Tools and Methodology

1. G4-ASPP transports charged particles through component-defined electromagnetic fields and through bulk shielding media within a single Geant4 simulation, using the active shielding component definitions of ASPP and the nuclear and electromagnetic interactions physics of Geant4. To the author's knowledge, no other publicly available code performs both functions in one self-consistent calculation. A shielding configuration that would otherwise require several codes and intermediate data products is evaluated in one run, with dose scored directly as energy deposited per unit mass in the target volume. A tagged version of this code will eventually be available publicly at

https://github.com/lukestegeman/G4-ASPP. Applied to the unshielded lunar surface, G4-ASPP's full-spectrum dose rates agreed with published values to within a factor of approximately 1.4, with the same mean ICRP-60 quality factor, and it reproduced the decrease in dose equivalent behind thin regolith that is attributed to heavy-ion fragmentation [118, 119].

2. The capabilities added to ASPP—Boolean geometry, per-region material assignment, relativistic deceleration, an energy deposition tally, time-reversed propagation, additional field components, and closed-form reference potentials and self-capacitances—made it possible to model the active shielding stage of the lunar habitat scenario, to trace the particles a configuration admits back to their source origins, and to estimate the stored energy and power of a configuration from its geometry and voltage. The beamline comparison established its accuracy against measurement for multiple ion species [28]. This code exists at https://github.com/lukestegeman/ASPP and requires prior institutional permission for access.

3. The VVS integrator was derived so that a code that advances particles in distance, such as Geant4, can reproduce the Velocity-Verlet method, and its symplecticity and phase-space properties were analyzed. The verification framework of six test cases with analytically tractable or reference trajectories can be reused to assess any new propagation method [77].

4. Constructing the combination model documented methods that apply beyond this comparison: the physical source strength of a cosine-law hemispherical source (Equation 5.44); a per-particle chord geometry that maps each surface crossing onto a regolith path and a chord through the target; a track-length estimator that converts those chords into dose in a target smaller than the scoring surface (Equation 5.50); a normalization of folded albedo currents into weighted secondary sources that carries the absolute albedo yield per primary particle; and a library of 2000 PHITS lunar regolith albedo response functions for incident protons and alpha particles, subject to the energy-axis correction noted in the limitations below. The combination model infrastructure, excluding ASPP, HZETRN, and PHITS, will eventually be available publicly at https://github.com/lukestegeman/combination_model.

5. Chapter 2 expressed the effect of electric and magnetic forces on particle kinetic energy and direction in the variables used by space radiation transport codes and constructed the corresponding adjoint equation and boundary conditions. The force terms have the same origin as those in the collisional

Boltzmann equation of kinetic theory. The contribution added here is their formulation in kinetic energy and direction, where they connect directly to the deterministic methods used for passive shielding and indicate how an adjoint active shielding evaluation method could be formulated.

6.2.2 General Knowledge

1. Two independent methods agree that the dose to the ICRU sphere does not depend on the applied voltage within statistical uncertainty for the "lunar umbrella" configuration studied here. In G4-ASPP, the ^{1}H+^{4}He absorbed dose rate at zero passive shielding varies by less than 3 % between 0 and 100 MV. A 100 MV potential can turn back protons only below approximately 100 MeV, which carry a small share of the GCR dose. Potentials of the order considered here therefore act only on the low-energy part of the spectrum.

2. The combination model required three transport codes, 2000 PHITS albedo simulations, 1600 primary ASPP simulations, over 10,000 secondary ASPP simulations, and a multi-stage normalization workflow to link them all together. For the same primaries, the combination model gave dose equivalent rates as low as 0.57 times those from G4-ASPP, with the largest difference at 5 to 20 g cm^{-2}. The straight-ahead treatment of secondaries produced in the dome and the exclusion of albedo from beneath the habitat are candidate causes for this discrepancy (Section 5.3.4). G4-ASPP treats these secondaries identically to all other transported particles. Together, the effort and the approximations support a central argument of the dissertation: for hybrid active–passive shielding, a single self-consistent simulation tool is more tractable to develop, verify, and use than a coupled pipeline of single-purpose codes. This justifies the motivation for the development of G4-ASPP and G4-ASPP provides a path forward for serious active–passive shielding configuration optimization efforts.

3. Simulated and measured void areas agreed with a mean relative error of 13.1 % [28]. The dimensionless parameter f_s organizes shielding efficacy across dipoles of different sizes and separation, with a void area that grows linearly with f_s and then sublinearly, with an exponent of approximately 2/3, as the void changes shape. A single electric dipole loses most of its efficacy for radiation that is not perpendicular to its axis, and is thus a poor shield in an isotropic environment. For an orthogonal plate-and-rod configuration, protons reaching the crew volume had crossed a mean potential energy

barrier of approximately 15 MeV.

4. Of seven methods compared, RK4S produced time-integrated relative errors no larger than 0.01 % relative to the Boris integrator, compared to 0.1 % for time-stepping Velocity-Verlet and 1 % for VVS, which led to its adoption in G4-ASPP [77]. Geant4's boundary-aware adaptive stepping reduced the step size near physical boundaries, which constant-step methods did not.

6.3 Limitations

Several limitations bound the conclusions above. The statement that the "lunar umbrella" configuration provides no benefit rests on paired comparisons at fixed thickness, which bound the change in dose between 0 and 100 MV to within 6 % for ^{1}H+^{4}He and within 9 % for the full spectrum at the simulated statistics; smaller effects are not excluded. Only one active shielding geometry was evaluated, and only steady-state solar minimum GCR exposure was considered. Dose was scored in an ICRU sphere rather than an anthropomorphic phantom, which limits direct comparison with whole-body or effective dose estimates. Both ASPP and G4-ASPP superimpose analytic fields of individual components and therefore neglect charge induction between nearby conductors, and differential charging of the lunar surface was neglected.

The combination model carries additional limitations. Its primary transport was restricted to ^{1}H and ^{4}He. Its PHITS albedo tallies misrepresent the energy axis for tracked species with $A > 1$. Only a single albedo generation is modeled, the albedo produced beneath the habitat footprint is excluded, and secondary species without a dose response are omitted. Its electrodes are point charges without physical extent, and at the thickest regolith shell considered, the physical electrodes would intersect the dome. Finally, HZETRN's one-dimensional, straight-ahead transport is applied to a thin, curved regolith shell and a 15 cm tissue sphere, a geometry far from the slab for which it is formulated.

6.4 Future Work

6.4.1 Adjoint Transport for Configuration Design

A single configuration is one point in a design space of electrode geometries, voltages, materials, and passive shielding layouts. Forward transport, in which each candidate configuration requires a complete simulation,

scales poorly to searching that space. The elements of an adjoint approach are present in this dissertation, including the adjoint charged particle transport equation and its boundary conditions (Chapter 2), the time-reversed propagation mode of ASPP (Chapter 3), and the time-reversibility of the Velocity-Verlet integrator (Chapter 4). Developing an adjoint mode in G4-ASPP that combines reversed electromagnetic transport with adjoint transport in bulk media would compute, for a given configuration, the importance of each source region and energy for the dose in the crew volume once, so that any source spectrum could be evaluated against it, and, combined with the forward solution, would give the first-order sensitivity of the dose to changes in the field. A substantially different configuration would still require new transport calculations. Such a method would also identify the trajectories through which a configuration admits charged particles, as the time-reversed ASPP results did qualitatively for the orthogonal configuration.

6.4.2 Field Physics and Design Tools

Treating each field component as an isolated analytic source ignores the redistribution of charge on nearby conductors. A numerical solution of Laplace's equation for the conductor geometry, used either to correct component charges or to supply the field directly, would remove that approximation for configurations with closely spaced components. A complementary tool that displays the electrostatic field while a configuration is being constructed, coupled to an adjoint dose estimate, would let a designer adjust electrode geometry and voltage interactively rather than through repeated forward simulations. The reference potentials and self-capacitances of Chapter 3 could be attached to such a tool to report the stored energy and power associated with each design alongside its dosimetric effect, allowing for optimization.

6.4.3 Environments, Targets, and Validation

Because active shielding acts more strongly on lower-energy particles, its effect on the softer spectra of solar particle events may differ substantially from its effect on GCR, and those events should be evaluated separately. Trapped proton and electron environments near Earth and Jupiter, free-space transit, and the Martian surface would test the generality of the conclusions drawn here. Replacing the ICRU sphere with an anthropomorphic phantom would allow organ dose and effective dose to be computed and compared directly with whole-body estimates such as those of [119] and [118]. Finally, the beamline methodology of Chapter 3 could be extended to a combined test article, an electrode configuration placed upstream of a

passive absorber and a target detector, providing experimental data against which the coupled transport in G4-ASPP could be validated directly.

6.5 Closing Remarks

This dissertation set out to make hybrid active–passive radiation shielding something that can be evaluated with the same confidence as passive shielding. G4-ASPP now performs that evaluation within a single simulation. G4-ASPP's electromagnetic propagation has been verified against reference methods, the propagation code from which it descends has been validated against measurement, and its first application produced dose estimates for a lunar habitat that are consistent with independent literature values. The same application showed that a plausible electrostatic configuration provides no resolvable benefit against GCR, and that obtaining an independent answer by coupling established codes requires a laborious multi-stage workflow that rests on approximations that a single simulation avoids. Progress on active shielding will depend on evaluating many configurations quickly and with confidence in each result. A self-consistent combined transport tool, eventually paired with adjoint methods, appears to be a practical way to do so.

Bibliography

[1] "Artemis plan: NASA's lunar exploration program overview," Tech. Rep. NP-2020-05-2853-HQ, National Aeronautics and Space Administration, 2020. https://www.lpi.usra.edu/lunar/strategies/Artemis-Plan_NP-2020-05-2853-HQ.pdf.

[2] National Aeronautics and Space Administration, "5 hazards of human spaceflight." https://www.nasa.gov/hrp/hazards/, Jan 2024.

[3] F. A. Cucinotta, M.-H. Y. Kim, V. Willingham, and K. A. George, "Physical and biological organ dosimetry analysis for International Space Station astronauts," *Radiation Research*, vol. 170, pp. 127–138, Jul 2008.

[4] ICRP, "1990 recommendations of the International Commission on Radiological Protection," *Annals of the ICRP*, vol. 21, no. 1-3, 1991.

[5] U.S. Nuclear Regulatory Commission, "Standards for protection against radiation." Title 10, Part 20, https://www.ecfr.gov/current/title-10/chapter-I/part-20.

[6] ICRP, "The 2007 recommendations of the International Commission on Radiological Protection," *Annals of the ICRP*, vol. 37, no. 2-4, 2007.

[7] D. M. Hassler *et al.*, "Mars' surface radiation environment measured with the Mars Science Laboratory's Curiosity rover," *Science*, vol. 343, no. 6169, p. 1244797, 2014.

[8] L. C. Simonsen, T. C. Slaba, P. Guida, and A. Rusek, "NASA's first ground-based galactic cosmic ray simulator: Enabling a new era in space radiobiology research," *PLOS Biology*, vol. 18, May 2020.

[9] NASA, "NASA space flight human-system standard: Volume 1: Crew health," Technical Standard NASA-STD-3001, National Aeronautics and Space Administration, 2022.

[10] T. C. Slaba, A. A. Bahadori, B. D. Reddell, R. C. Singleterry, M. S. Clowdsley, and S. R. Blattnig, "Optimal shielding thickness for galactic cosmic ray environments," *Life Sciences in Space Research*, vol. 12, pp. 1–15, 2017.

[11] J. S. Rankin *et al.*, "Galactic cosmic rays throughout the heliosphere and in the very local interstellar medium," *Space Science Reviews*, vol. 218, p. 42, July 2022.

[12] F. H. Vogler, "Analysis of an electrostatic shield for space vehicles," *AIAA Journal*, vol. 2, pp. 872–878, May 1964.

[13] W. Frisina, "Optimizing electrostatic radiation shielding for manned space vehicles," *Acta Astronautica*, vol. 12, pp. 995–1003, Dec. 1985.

[14] P. Metzger, R. Youngquist, and J. Lane, "Asymmetric electrostatic radiation shielding for spacecraft," in *2004 IEEE Aerospace Conference Proceedings*, IEEE, 2004.

[15] R. Tripathi, "Meeting the grand challenge of protecting astronaut's health: Electrostatic active space radiation shielding for deep space missions," Tech. Rep. NIAC Final Report, NASA, Hampton, VA, 2011.

[16] K. Ferrone, F. Guan, J. Ma, L. Peterson, C. Willis, and S. Kry, "Reducing space radiation cancer risk with magnetic shielding," *Advances in Space Research*, vol. 68, pp. 153–160, July 2021.

[17] R. Levy and G. Janes, "Plasma radiation shielding," *AIAA J.*, vol. 2, no. 10, pp. 1835–1838, 1964.

[18] R. Levy and F. French, "Plasma radiation shield - concept and applications to space vehicles," *J. Spacecr. Rockets*, vol. 5, no. 5, pp. 570–577, 1968.

[19] K. Ferrone, C. Willis, F. Guan, J. Ma, L. Peterson, and S. Kry, "A review of magnetic shielding technology for space radiation," *Radiation*, vol. 3, no. 1, pp. 46–57, 2023.

[20] R. Tripathi, J. Wilson, and R. Youngquist, "Electrostatic active radiation shielding - revisited," in *2006 IEEE Aerospace Conference*, 2006.

[21] L. Townsend, "Critical analysis of active shielding methods for space radiation protection," in *2005 IEEE Aerospace Conference*, pp. 724–730, 2005.

[22] "TA 6: Human health, life support, and habitation systems," tech. rep., National Aeronautics and Space Administration, Jul 2015. https://www.nasa.gov/wp-content/uploads/2016/08/2015_nasa_technology_roadmaps_ta_6_human_health_life_support_habitation_final.pdf.

[23] "2020 NASA technology taxonomy," tech. rep., National Aeronautics and Space Administration, 2020. https://www3.nasa.gov/sites/default/files/atoms/files/2020_nasa_technology_taxonomy.pdf.

[24] D. Fry, M. Lund, A. A. Bahadori, R. Pal Chowdhury, L. Stegeman, and S. Madzunkov, "Active Shielding Particle Pusher (ASPP): Charged-particle tracking through electromagnetic fields," tech. rep., NASA Lyndon B. Johnson Space Center, Houston, TX, 2020.

[25] D. Fry, S. Madzunkov, J. Simcic, and A. Hunt, "Application of scaling methods to foster ground development of active shielding concepts for space exploration," *Acta Astronautica*, vol. 178, pp. 296–307, 2021.

[26] R. Pal Chowdhury, *Hybrid Methods of Space Radiation Shielding for Astronauts against Deep-Space Radiation*. PhD thesis, Kansas State University, 2020.

[27] R. Pal Chowdhury, L. Stegeman, M. L. Lund, S. M. Madzunkov, D. Fry, and A. A. Bahadori, "Hybrid methods of radiation shielding against deep-space radiation," *Life Sciences in Space Research*, vol. 38, pp. 67–78, 2023.

[28] L. Stegeman *et al.*, "Experimental validation of the Active Shielding Particle Pusher code," *Journal of Applied Physics*, vol. 129, p. 024902, 2021.

[29] R. Pal Chowdhury *et al.*, "Space radiation electrostatic shielding scaling laws: Beam-like and isotropic angular distributions," *Journal of Applied Physics*, vol. 130, no. 3, p. 034903, 2021.

[30] R. Pal Chowdhury *et al.*, "Three-dimensional charge distribution for electrostatic space radiation shielding," in *Transactions of the American Nuclear Society*, vol. 120, (Minneapolis, MN), pp. 744–747, 2019.

[31] NASA, "HZETRN2020." NASA Software Catalog, 2020. LAR-19979-1.

[32] T. Slaba, J. Wilson, C. Werneth, and K. Whitman, "Updated deterministic radiation transport for future deep space missions," *Life Sciences in Space Research*, vol. 27, pp. 6–18, 2020.

[33] J. A. Kulesza *et al.*, "MCNP® Code Version 6.3.2 Theory & User Manual," Tech. Rep. LA-UR-26-23119, Rev. 1, Los Alamos National Laboratory, Los Alamos, NM, USA, May 2026.

[34] Japan Atomic Energy Agency, "Particle and Heavy Ion Transport code System (PHITS)." https://phits.jaea.go.jp/, Sept. 2026. Released: 2026-09-01.

[35] T. Sato *et al.*, "Recent improvements of the particle and heavy ion transport code system – PHITS version 3.33," *Journal of Nuclear Science and Technology*, vol. 61, no. 1, pp. 127–135, 2024.

[36] FLUKA.CERN Collaboration, "FLUKA particle transport code, version 4-5.2." https://fluka.cern, 2026. Accessed: 2026-09-15.

[37] The FLUKA Collaboration *et al.*, "The FLUKA code: Overview and new developments," *EPJ Nuclear Sci. Technol.*, vol. 10, p. 16, 2024.

[38] Geant4 Collaboration, "Geant4 simulation toolkit, release 11.4.2." https://cern.ch, June 2026.

[39] J. Allison *et al.*, "Recent developments in Geant4," *Nuclear Instruments and Methods in Physics Research Section A: Accelerators, Spectrometers, Detectors and Associated Equipment*, vol. 835, pp. 186–225, 2016.

[40] National Center for Biotechnology Information, "Radiation," 2012. Accessed: 2024-10-14.

[41] National Research Council (US) Committee on the Biological Effects of Ionizing Radiation (BEIR V), *Health Effects of Exposure to Low Levels of Ionizing Radiation: BEIR V*. Washington (DC): National Academies Press (US), 1990.

[42] International Atomic Energy Agency, *Radiation Protection and Safety of Radiation Sources: International Basic Safety Standards, General Safety Requirements Part 3*. Vienna, Austria: International Atomic Energy Agency, 2014.

[43] L. J. Chappel, C. M. Milder, and S. R. Elgart, "NASA space cancer risk model: 2020 operational implementation," tech. rep., NASA, 2021.

[44] F. A. Cucinotta, M. Y. Kim, and L. J. Chappell, "Space radiation cancer risk projections and uncertainties – 2010," tech. rep., NASA, 2011.

[45] International Commission on Radiological Protection, "ICRP publication 118: ICRP statement on tissue reactions and early and late effects of radiation in normal tissues and organs – threshold doses for tissue reactions in a radiation protection context," 2012. International Commission on Radiological Protection, Oxford.

[46] T. Phillips, "Illustration of coronal mass ejection and subsequent solar particle event." https://soho.nascom.nasa.gov/hotshots/2007_05_25/. Accessed: 2025-01-08.

[47] NOAA Space Weather Prediction Center, "Solar radiation storms." https://www.swpc.noaa.gov/phenomena/solar-radiation-storm, 2024. Accessed: 2025-04-07.

[48] NASA Space Radiation Analysis Group, "What is space radiation?." https://srag.jsc.nasa.gov/spaceradiation/what/what.cfm, 2024. Accessed: 2025-04-07.

[49] "Solar Energetic Particle Environment Modelling (SEPEM) application server." http://www.sepem.eu/, 2025. Accessed: 2025-04-29.

[50] NASA Langley Research Center, "On-Line Tool for the Assessment of Radiation in Space (OLTARIS)." https://oltaris.nasa.gov/, 2025. Accessed: 2025-04-29.

[51] A. W. Strong, I. V. Moskalenko, and V. S. Ptuskin, "Cosmic-ray propagation and interactions in the Galaxy," *Annual Review of Nuclear and Particle Science*, vol. 57, pp. 285–327, Nov. 2007.

[52] T. C. Slaba and K. Whitman, "The Badhwar-O'Neill 2020 GCR model," *Space Weather*, vol. 18, no. 6, p. e2020SW002456, 2020. e2020SW002456 2020SW002456.

[53] NASA, "What are the Van Allen belts and why do they matter?." https://science.nasa.gov/biological-physical/stories/van-allen-belts/. Accessed: 2025-04-12.

[54] M. Shavers *et al.*, "Space agency-specific standards for crew dose and risk assessment of ionising radiation exposures for the International Space Station," *Z Med Phys*, vol. 34, pp. 14–30, Feb 2024. Epub 2023 Jul 27.

[55] P. Spillantini *et al.*, "Shielding from cosmic radiation for interplanetary missions: Active and passive methods," *Radiat. Meas.*, vol. 42, no. 1, pp. 14–23, 2007.

[56] L. Simonsen, J. Wilson, M. Kim, and F. Cucinotta, "Radiation exposure for human Mars exploration," *Health Physics*, vol. 79, pp. 515–525, 2000.

[57] J. W. Norbury *et al.*, "Advances in space radiation physics and transport at NASA," *Life Sciences in Space Research*, vol. 22, pp. 98–124, 2019.

[58] J. W. Wilson *et al.*, "HZETRN: Description of a free-space ion and nucleon transport and shielding computer program," May 1995.

[59] D. R. Grimes, D. R. Warren, and M. Partridge, "An approximate analytical solution of the Bethe equation for charged particles in the radiotherapeutic energy range," *Scientific Reports*, vol. 7, no. 1, 2017.

[60] F. Salvat, "Bethe stopping-power formula and its corrections," *Phys. Rev. A*, vol. 106, p. 032809, Sep 2022.

[61] J. K. Shultis and R. E. Faw, *Radiation Shielding*. La Grange Park, IL: American Nuclear Society, March 2000.

[62] L. Verlet, "Computer "experiments" on classical fluids. i. thermodynamical properties of Lennard-Jones molecules," *Physical Review*, vol. 159, pp. 98–103, July 1967.

[63] E. Hairer, C. Lubich, and G. Wanner, "Geometric numerical integration illustrated by the Störmer–Verlet method," *Acta Numerica*, vol. 12, pp. 399–450, 2003.

[64] D. Rajon and W. Bolch, "Interactions with 3D isotropic and homogeneous radiation fields: a Monte Carlo simulation algorithm," *Computer Methods and Programs in Biomedicine*, vol. 70, no. 2, pp. 167–177, 2003.

[65] M. Deserno, "How to generate equidistributed points on the surface of a sphere," technical report, Max Planck Institute for Polymer Research, Mainz, Germany, 2004.

[66] L. Stegeman, S. M. Madzunkov, D. Fry, and A. A. Bahadori, "Outlook on adjoint radiation transport tool for active-passive shielding analysis," in *Transactions of the American Nuclear Society*, vol. 125, (Washington, D.C.), pp. 1088–1092, 2021.

[67] J. C. McPhee and J. B. Charles, *Human health and performance risks of space exploration missions: evidence reviewed by the NASA human research program*, vol. 3405. US National Aeronautics & Space Administration, 2009.

[68] R. C. Singleterry, "Radiation Engineering Analysis of Shielding Materials to Assess their Ability to Protect Astronauts in Deep Space from Energetic Particle Radiation," *Acta Astronautica*, no. 91, pp. 49–54, 2013.

[69] S. Guetersloh *et al.*, "Polyethylene as a Radiation Shielding Standard in Simulated Cosmic-Ray Environments," *Nuclear Instruments and Methods in Physics Research Section B: Beam Interactions with Materials and Atoms*, no. 252, pp. 319–332, 2006.

[70] A. Bahadori, E. Semones, M. Ewert, J. Broyan, and S. Walker, "Measuring Space Radiation Shielding Effectiveness," in *EPJ Web of Conferences*, vol. 153, p. 04001, 2017.

[71] "BNL Tandem Van de Graaff Capabilities." https://www.bnl.gov/tandem/capabilities/. Accessed: 2020-05-30.

[72] M. U. Bug *et al.*, "Effect of a Magnetic Field on the Track Structure of Low-energy Electrons: a Monte Carlo Study," *European Physical Journal D*, vol. 60, pp. 85–92, 2010.

[73] J. Canny, "A Computational Approach to Edge Detection," *IEEE Trans. Pattern Anal. Mach. Intell.*, vol. 8, pp. 679–698, June 1986.

[74] S. Beucher and F. Meyer, "The Morphological Approach to Segmentation: The Watershed Transformation," in *Mathematical Morphology in Image Processing* (E. R. Dougherty, ed.), vol. 34, ch. 12, pp. 433–481, CRC Press, 01 1993.

[75] L. Stegeman, R. Pal Chowdhury, M. L. Lund, D. J. Fry, S. M. Madzunkov, and A. A. Bahadori, "Assessment of Electrostatic Radiation Shielding Efficacy via Void Area Calculation," in *Transactions of the American Nuclear Society*, vol. 122, pp. 584–587, 2020.

[76] "scipy.optimize.curve_fit." https://docs.scipy.org/doc/scipy.reference/generated/scipy.optimize.curve_fit.html. Accessed: 2019-12-31.

[77] L. Stegeman, D. J. Fry, and A. A. Bahadori, "Development and benchmarking of charged particle propagation methods in G4-ASPP," *Journal of Computational and Theoretical Transport*, vol. 52, no. 4, pp. 269–313, 2023.

[78] A. Fogtman *et al.*, "Towards sustainable human space exploration—priorities for radiation research to quantify and mitigate radiation risks," *npj Microgravity*, vol. 9, no. 1, 2023.

[79] J. Chancellor, G. Scott, and J. Sutton, "Space radiation: The number one risk to astronaut health beyond low Earth orbit," *Life*, vol. 4, no. 3, pp. 491–510, 2014.

[80] J. W. Wilson, J. Miller, A. Konradi, and F. A. Cucinotta, "Shielding strategies for human space exploration," Tech. Rep. 19980137598, National Aeronautics and Space Administration, 1997.

[81] B. Kim *et al.*, "Systematic modeling of electrostatic radiation shields for deep space flight," *Radiation Physics and Chemistry*, vol. 193, p. 110007, 2022.

[82] A. A. Bahadori, M. V. Baalen, M. R. Shavers, C. Dodge, E. J. Semones, and W. E. Bolch, "The effect of anatomical modeling on space radiation dose estimates: a comparison of doses for NASA phantoms and the 5th, 50th, and 95th percentile male and female astronauts," *Physics in Medicine & Biology*,

vol. 56, p. 1671, Feb. 2011.

[83] C. J. Werner, "MCNP users manual - code version 6.2," tech. rep., Los Alamos National Laboratory, 2017.

[84] T. Sato *et al.*, "Features of Particle and Heavy Ion Transport code System (PHITS) version 3.02," *Journal of Nuclear Science and Technology*, vol. 55, pp. 684–690, 2018.

[85] A. Ferrari, P. R. Sala, A. Fasso, and J. Ranft, "FLUKA: A multi-particle transport code (program version 2021)," tech. rep., Office of Scientific and Technical Information (OSTI), 2021.

[86] S. Agostinelli *et al.*, "Geant4—a simulation toolkit," *Nuclear Instruments and Methods in Physics Research Section A: Accelerators, Spectrometers, Detectors and Associated Equipment*, vol. 506, no. 3, pp. 250–303, 2003.

[87] J. Apostolakis, "Field propagation in Geant4," May 2005.

[88] K. Amako *et al.*, "Geant4 and its validation," *Nuclear Physics B - Proceedings Supplements*, vol. 150, pp. 44–49, 2006. Proceedings of the 9th Topical Seminar on Innovative Particle and Radiation Detectors.

[89] Q. Xie, S. Wenzel, and J. Apostolakis, "Modernizing field propagation in Geant4: Report from a Google Summer of Code project 2014," Oct 2014.

[90] D. Malament, "On the time reversal invariance of classical electromagnetic theory," *Studies In History and Philosophy of Science Part B: Studies In History and Philosophy of Modern Physics*, vol. 35, pp. 295–315, 01 2004.

[91] H. Qin, S. Zhang, J. Xiao, J. Liu, Y. Sun, and W. Tang, "Why is Boris algorithm so good?," *Physics of Plasmas*, vol. 20, 08 2013.

[92] D. Donnelly and E. Rogers, "Symplectic integrators: An introduction," *American Journal of Physics*, vol. 73, no. 10, pp. 938–945, 2005.

[93] D. Levesque and L. Verlet, "Molecular dynamics and time reversibility," *Journal of Statistical Physics*, vol. 72, pp. 519–537, Aug. 1993.

[94] S. Zenitani and T. Umeda, "On the Boris solver in particle-in-cell simulation," *Physics of Plasmas*, vol. 25, no. 11, p. 112110, 2018.

[95] J. P. Boris, "Relativistic plasma simulation-optimization of a hybrid code," *Proceeding of Fourth Conference on Numerical Simulations of Plasmas*, November 1970.

[96] G. Penn, P. H. Stoltz, J. R. Cary, and J. Wurtele, "Boris push with spatial stepping," *Journal of Physics G: Nuclear and Particle Physics*, vol. 29, pp. 1719–1722, Jul 2003.

[97] R. J. Rowley, "Finite line of charge," *American Journal of Physics*, vol. 74, no. 12, pp. 1120–1125, 2006.

[98] P. H. Stoltz, J. R. Cary, G. Penn, and J. Wurtele, "Efficiency of a Boris-like integration scheme with spatial stepping," *Phys. Rev. ST Accel. Beams*, vol. 5, p. 094001, Sep 2002.

[99] J. Allison *et al.*, "Geant4 developments and applications," *IEEE Transactions on Nuclear Science*, vol. 53, pp. 270–278, Feb 2006.

[100] A. Einstein, "On the electrodynamics of moving bodies," *Annalen Phys.*, vol. 17, pp. 891–921, 1905.

[101] K. Niita *et al.*, "PHITS ver. 3.17 user's manual," tech. rep., JAEA, 2019.

[102] A. M. Adamczyk *et al.*, "NUCFRG3: Light ion improvements to the nuclear fragmentation model," *Nuclear Instruments and Methods in Physics Research Section A*, vol. 678, pp. 21–32, 2012.

[103] R. Serber, "Nuclear reactions at high energies," *Physical Review*, vol. 72, p. 1114, 1947.

[104] D. Mancusi, A. Boudard, J. Cugnon, J.-C. David, P. Kaitaniemi, and S. Leray, "Extension of the Liège Intranuclear-Cascade model to reactions induced by light nuclei," *Physical Review C*, vol. 90, p. 054602, 2014.

[105] Geant4 Collaboration, "Guide for physics lists," tech. rep., Geant4 Collaboration, 2024. Geant4 documentation, version-matched to Geant4 11.0.

[106] A. Ferrari, D. Kiselev, T. Koi, M. Wohlmuther, and J.-C. David, "Po-production in lead: a benchmark between Geant4, FLUKA and MCNPX." arXiv:1806.03732, 2018. Presented at the 13th Meeting of the Task Force on Shielding Aspects of Accelerators, Targets and Irradiation Facilities (SATIF-13), HZDR, Dresden, Germany, Oct. 10–12, 2016.

[107] International Commission on Radiation Units and Measurements, "Measurement of dose equivalents from external photon and electron radiations," Tech. Rep. ICRU Report 47, International Commission on Radiation Units and Measurements, Bethesda, MD, 1992.

[108] J. E. Colwell, S. Batiste, M. Horányi, S. Robertson, and S. Sture, "Lunar surface: Dust dynamics and regolith mechanics," *Reviews of Geophysics*, vol. 45, no. 2, p. RG2006, 2007.

[109] T. J. Stubbs *et al.*, "Dependence of lunar surface charging on solar wind plasma conditions and solar irradiation," *Planetary and Space Science*, vol. 90, pp. 10–27, 2014.

[110] J. S. Halekas, G. T. Delory, R. P. Lin, T. J. Stubbs, and W. M. Farrell, "Lunar surface charging during solar energetic particle events: Measurement and prediction," *Journal of Geophysical Research: Space Physics*, vol. 114, no. A5, p. A05110, 2009.

[111] D. J. Griffiths, *Introduction to Electrodynamics*. Pearson Education, 4th ed., 2013.

[112] Y. Iwamoto *et al.*, "Benchmark study of the recent version of the PHITS code," *Journal of Nuclear Science and Technology*, vol. 54, no. 5, pp. 617–635, 2017.

[113] W. G. Cochran, *Sampling Techniques*. New York: John Wiley & Sons, 3rd ed., 1977.

[114] M. J. Berger *et al.*, "XCOM: Photon cross section database (version 1.5)," 2010. [Online] Available: http://physics.nist.gov/xcom.

[115] J. H. Hubbell and S. M. Seltzer, "Tables of x-ray mass attenuation coefficients and mass energy-absorption coefficients 1 keV to 20 MeV for elements Z = 1 to 92 and 48 additional substances of dosimetric interest," Tech. Rep. NISTIR 5632, National Institute of Standards and Technology, Gaithersburg, MD, May 1995.

[116] J. L. Löwe *et al.*, "Martian proton albedo as signature of near-surface water," *Journal of Geophysical Research: Planets*, vol. 131, no. 6, p. e2026JE009697, 2026. e2026JE009697 2026JE009697.

[117] S. T. Mongelli, J. R. Maiorino, S. Anéfalos, A. Deppman, and T. Carluccio, "Spallation physics and

the ADS target design," *Brazilian Journal of Physics*, vol. 35, no. 3B, pp. 894–898, 2005.

[118] D. Matthiä and T. Berger, "Radiation Exposure and Shielding Effects on the Lunar Surface," *Space Weather*, vol. 22, p. 2024SW004095, Dec. 2024.

[119] S. Blunier, D. Athanasopoulos, C. Dittmar, F. Thoresen, A. Cowley, and A. Fogtman, "Regolith-based lunar habitat for astronaut radiation protection and organ dose assessment," *Planetary and Space Science*, vol. 261, p. 106116, 2025.

[120] M. J. Berger, J. S. Coursey, M. A. Zucker, and J. Chang, "ESTAR, PSTAR, and ASTAR: Computer programs for calculating stopping-power and range tables for electrons, protons, and helium ions (version 1.2.3)," 2005.

Appendix A

Albedo Response Functions

This appendix presents the complete set of PHITS-generated differential number albedo response functions and integrated yield plots referenced in Section 5.2.3, for both incident GCR primary species (proton, ^{4}He) across all 100 simulated incident energies per nucleon. Response functions are ordered by species (proton, then ^{4}He) and by increasing incident energy per nucleon within each species. The integrated yield plots for each species precede the corresponding per-energy response function set.

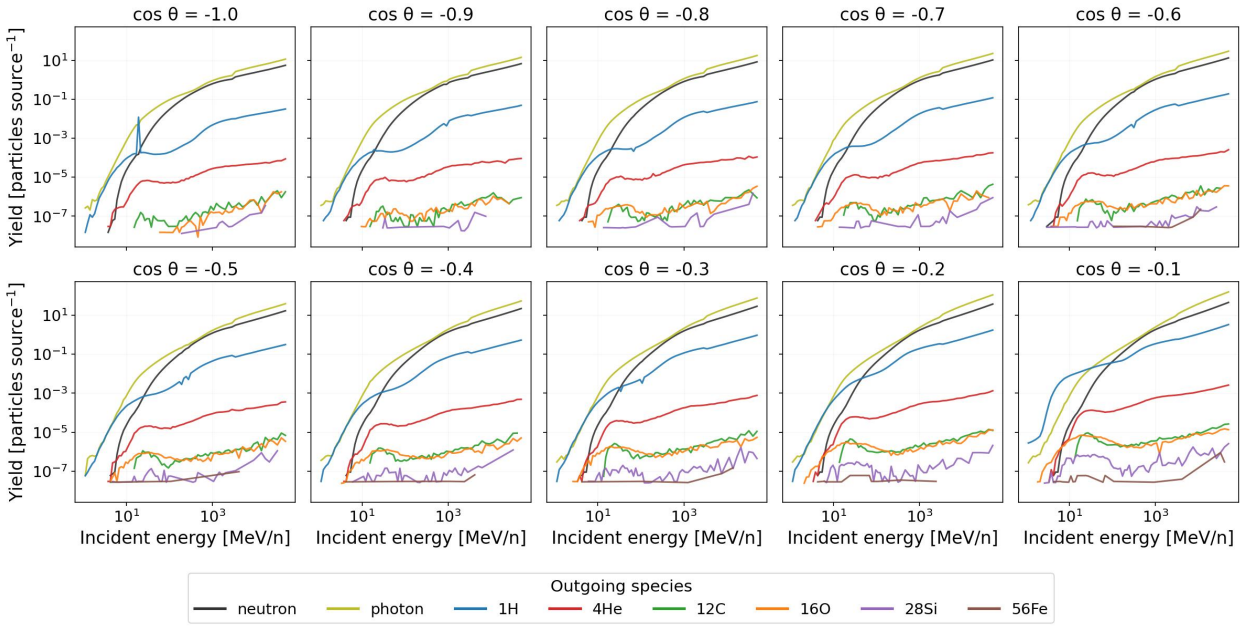


Figure A.1: Integrated outgoing secondary particle yield per source ^{1}H primary as a function of incident energy per nucleon, shown separately for each of the ten simulated incident polar cosine bins ($\cos\theta = -1.0$ to -0.1).

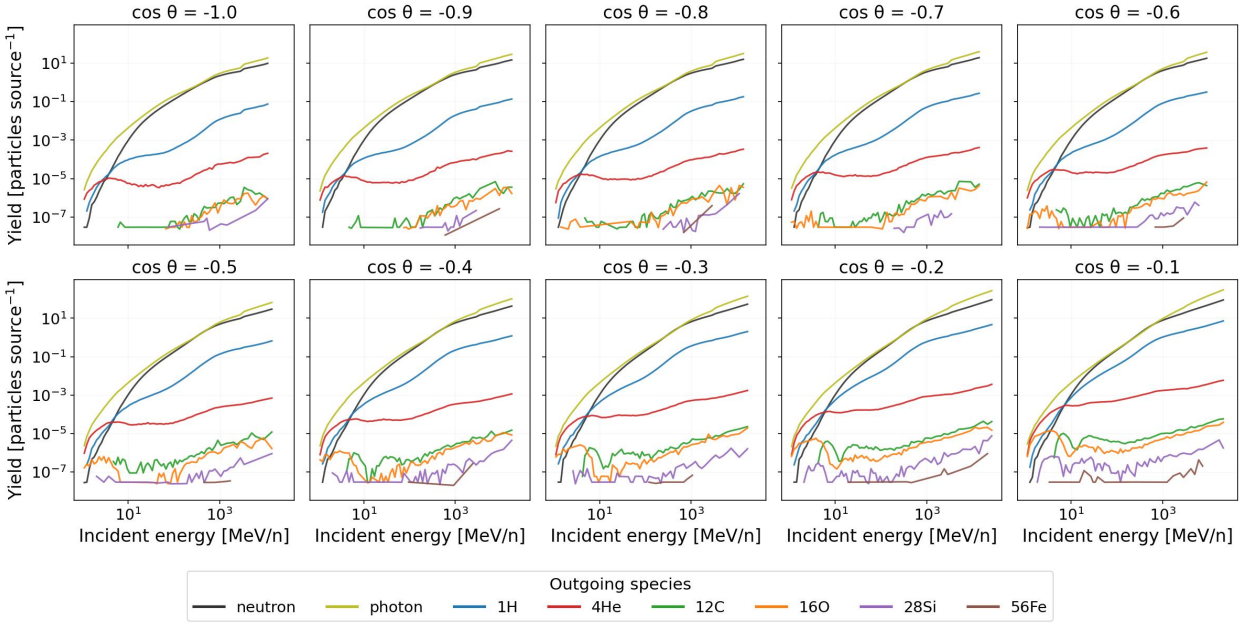


Figure A.2: Integrated outgoing secondary particle yield per source ^{4}He primary as a function of incident energy per nucleon, shown separately for each of the ten simulated incident polar cosine bins ($\cos\theta = -1.0$ to -0.1).

^{1}H Primary Response Functions

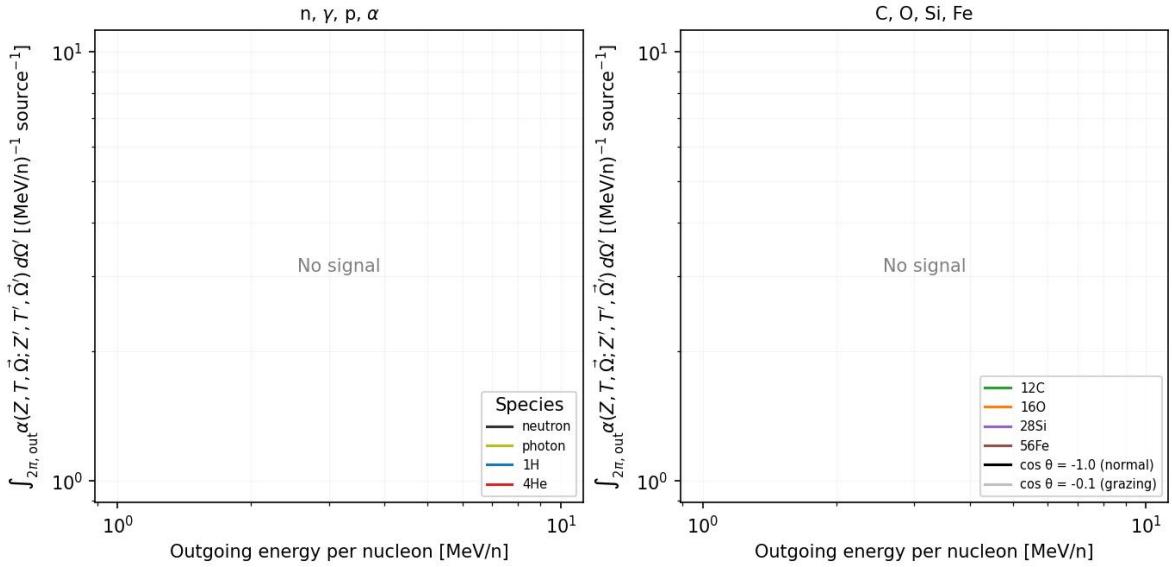


Figure A.3: Differential number albedo response function for a $10\,\mathrm{keV\,n^{-1}}$ ^{1}H primary, shown for all ten simulated incident polar cosine bins ($\cos\theta = -1.0$ to -0.1).

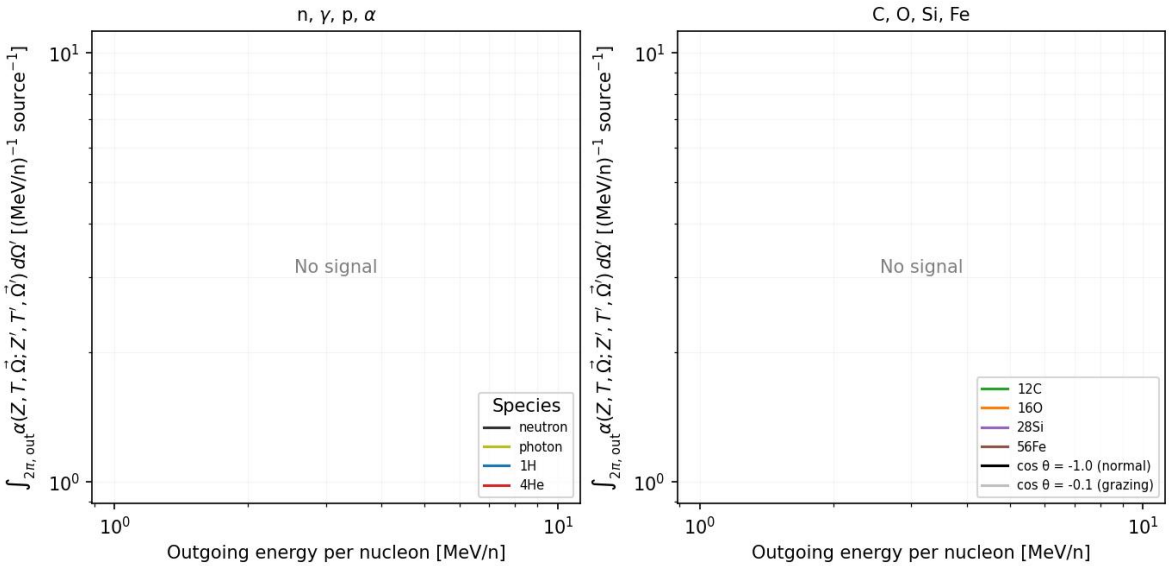


Figure A.4: Differential number albedo response function for a 14.1 keV n^{-1} ^{1}H primary, shown for all ten simulated incident polar cosine bins ($\cos\theta = -1.0$ to -0.1).

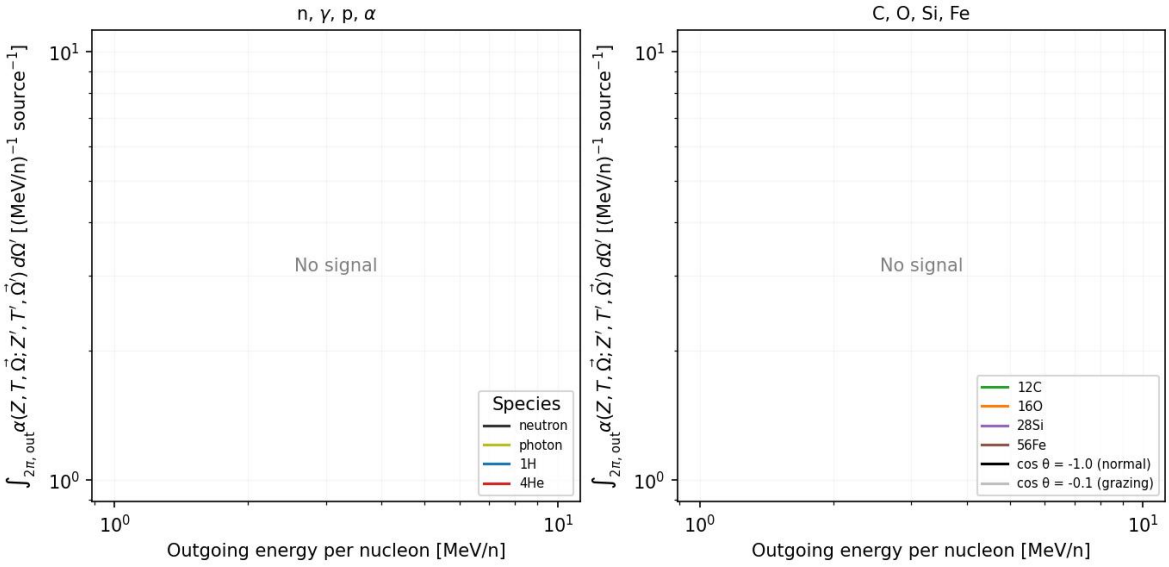


Figure A.5: Differential number albedo response function for a 19.8 keV n^{-1} ^{1}H primary, shown for all ten simulated incident polar cosine bins ($\cos\theta = -1.0$ to -0.1).

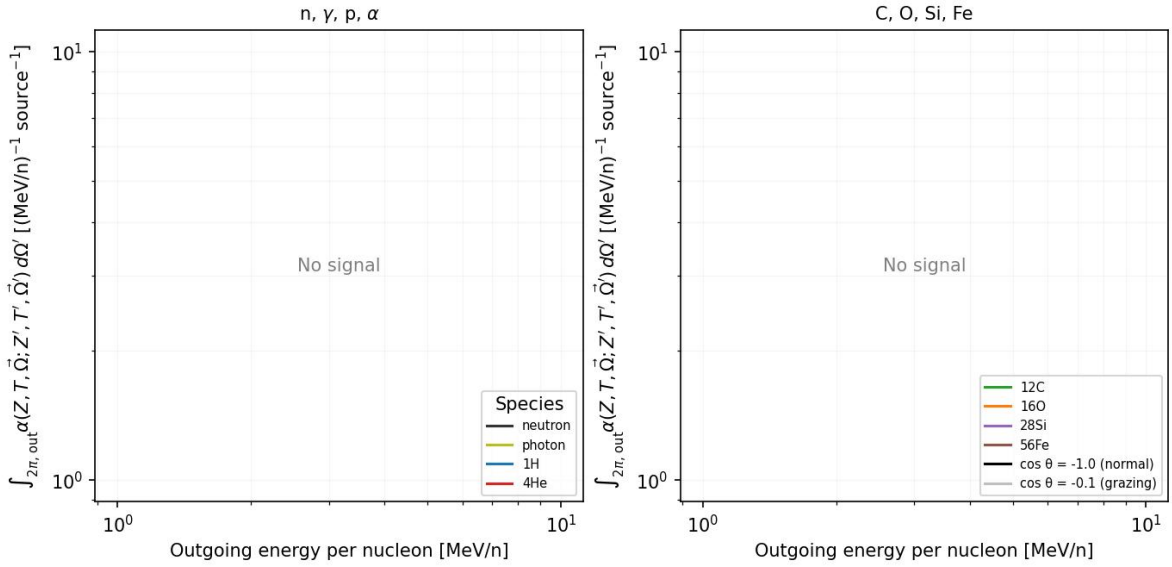


Figure A.6: Differential number albedo response function for a 27.8 keV n^{-1} ^{1}H primary, shown for all ten simulated incident polar cosine bins ($\cos\theta = -1.0$ to -0.1).

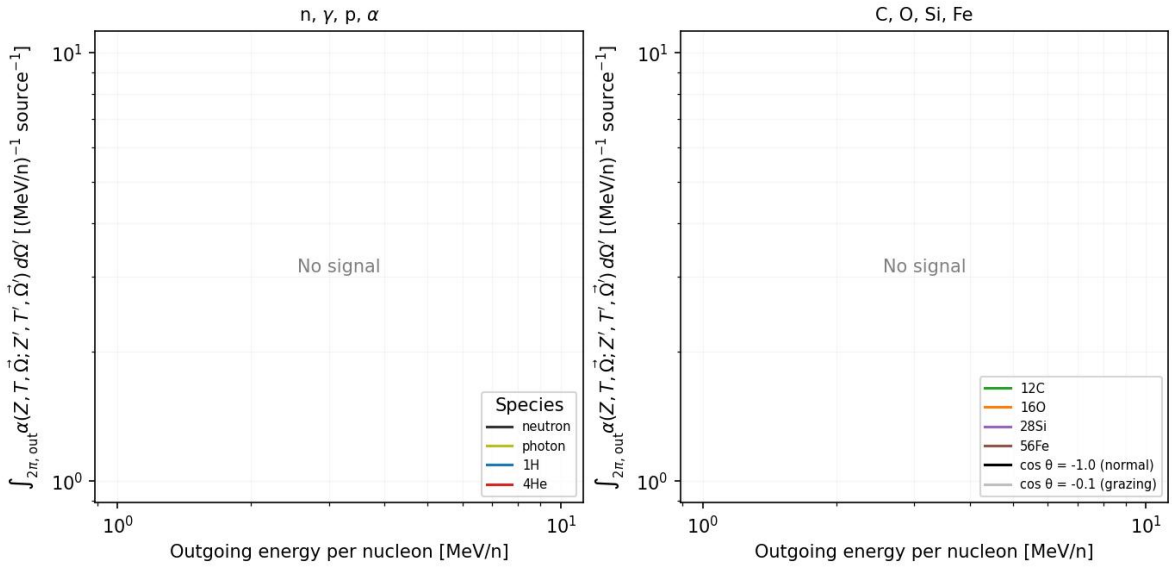


Figure A.7: Differential number albedo response function for a 38.8 keV n^{-1} ^{1}H primary, shown for all ten simulated incident polar cosine bins ($\cos\theta = -1.0$ to -0.1).

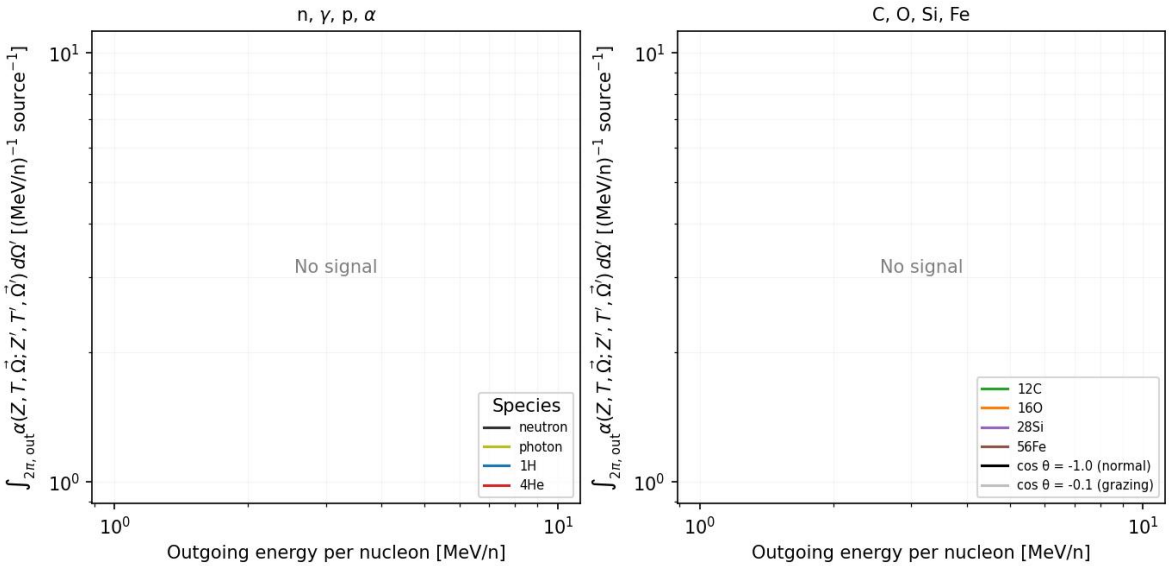


Figure A.8: Differential number albedo response function for a 53.3 keV n^{-1} ^{1}H primary, shown for all ten simulated incident polar cosine bins ($\cos\theta = -1.0$ to -0.1).

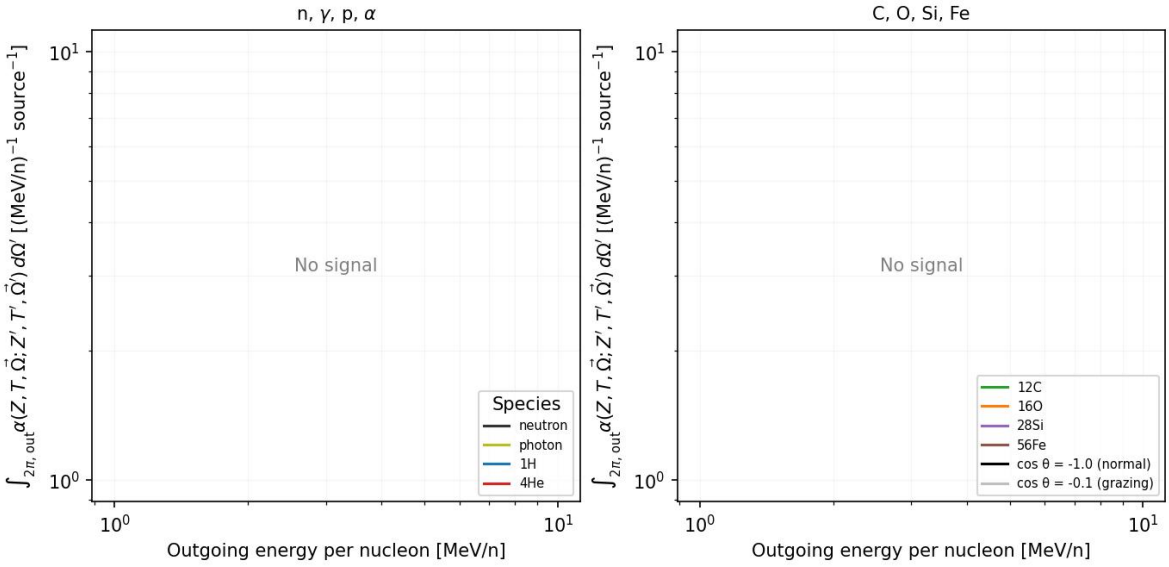


Figure A.9: Differential number albedo response function for a 72 keV n^{-1} ^{1}H primary, shown for all ten simulated incident polar cosine bins ($\cos\theta = -1.0$ to -0.1).

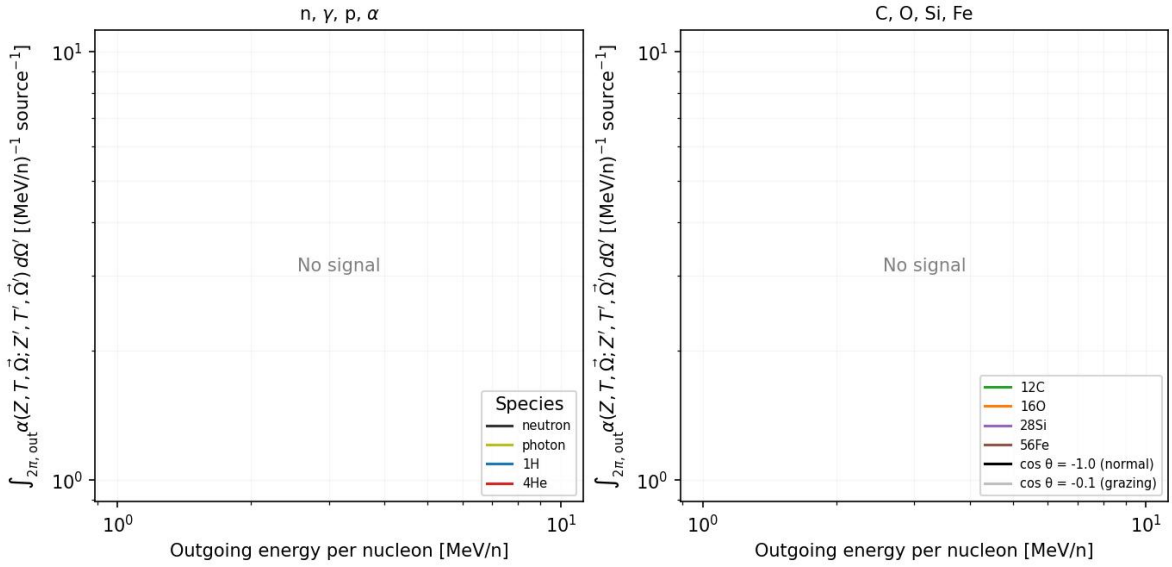


Figure A.10: Differential number albedo response function for a 95 keV n^{-1} ^{1}H primary, shown for all ten simulated incident polar cosine bins ($\cos\theta = -1.0$ to -0.1).

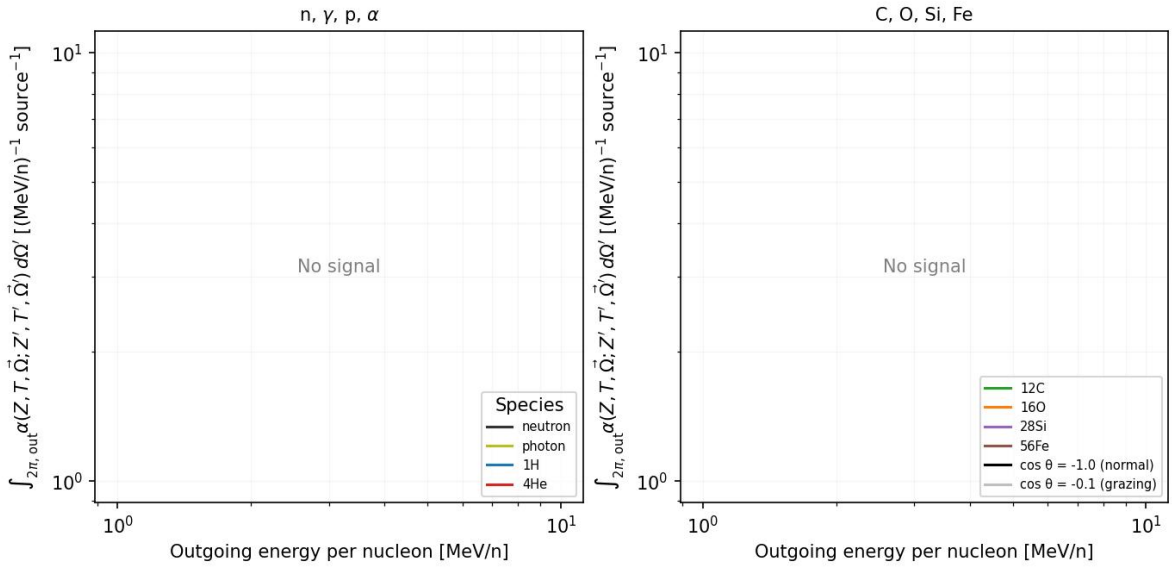


Figure A.11: Differential number albedo response function for a 122 keV n^{-1} ^{1}H primary, shown for all ten simulated incident polar cosine bins ($\cos\theta = -1.0$ to -0.1).

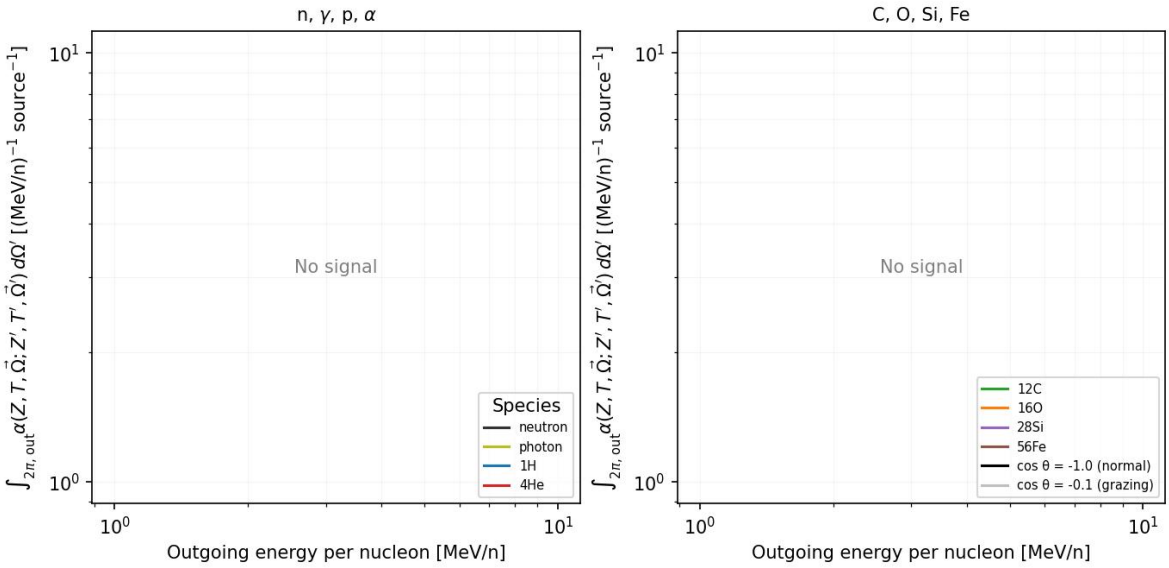


Figure A.12: Differential number albedo response function for a 154 keV n^{-1} ^{1}H primary, shown for all ten simulated incident polar cosine bins ($\cos\theta = -1.0$ to -0.1).

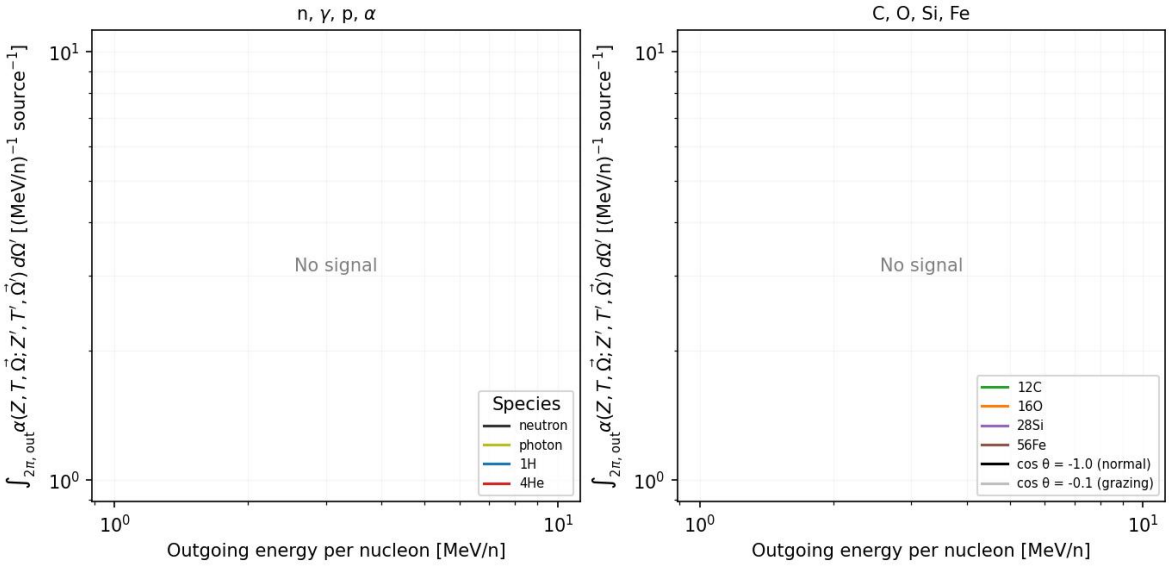


Figure A.13: Differential number albedo response function for a 189 keV n^{-1} ^{1}H primary, shown for all ten simulated incident polar cosine bins ($\cos\theta = -1.0$ to -0.1).

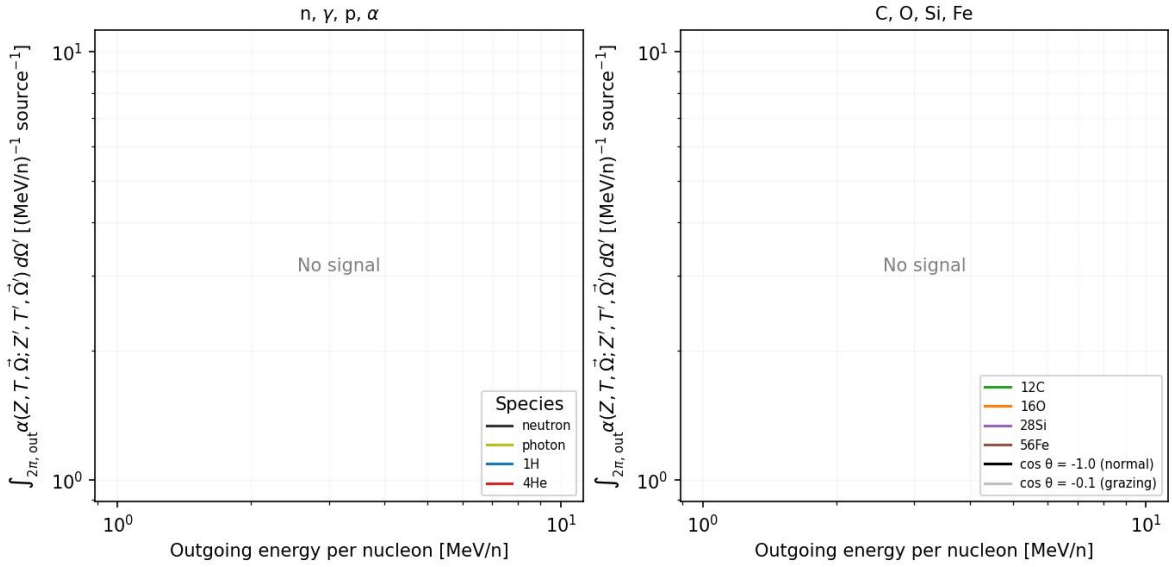


Figure A.14: Differential number albedo response function for a 228 keV n^{-1} ^{1}H primary, shown for all ten simulated incident polar cosine bins ($\cos\theta = -1.0$ to -0.1).

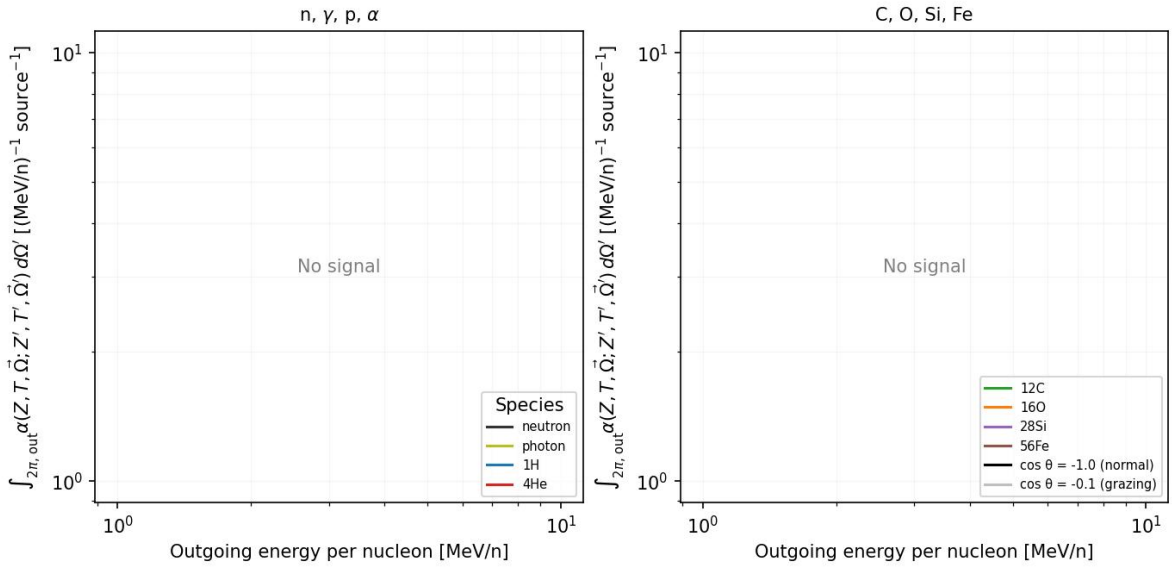


Figure A.15: Differential number albedo response function for a 271 keV n^{-1} ^{1}H primary, shown for all ten simulated incident polar cosine bins ($\cos\theta = -1.0$ to -0.1).

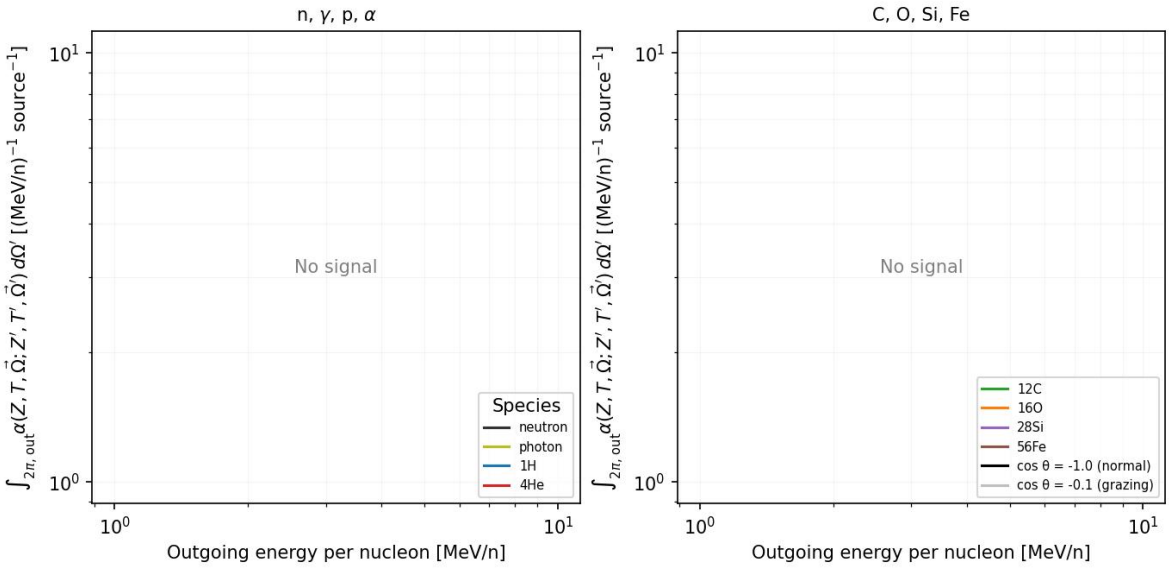


Figure A.16: Differential number albedo response function for a 320 keV n^{-1} ^{1}H primary, shown for all ten simulated incident polar cosine bins ($\cos\theta = -1.0$ to -0.1).

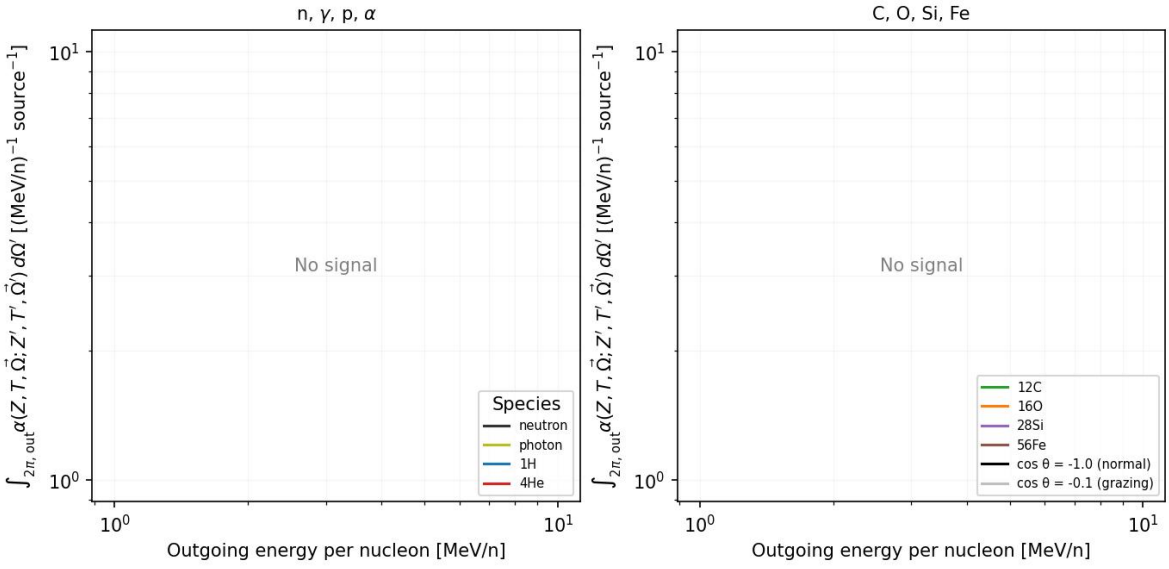


Figure A.17: Differential number albedo response function for a 374 keV n^{-1} ^{1}H primary, shown for all ten simulated incident polar cosine bins ($\cos\theta = -1.0$ to -0.1).

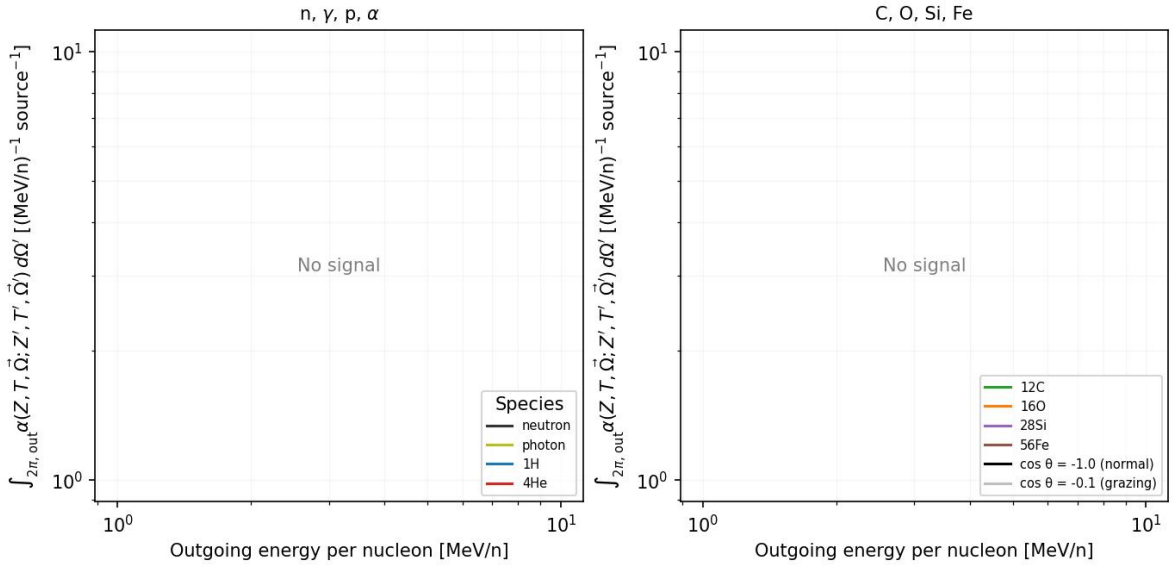


Figure A.18: Differential number albedo response function for a 434 keV n^{-1} ^{1}H primary, shown for all ten simulated incident polar cosine bins ($\cos\theta = -1.0$ to -0.1).

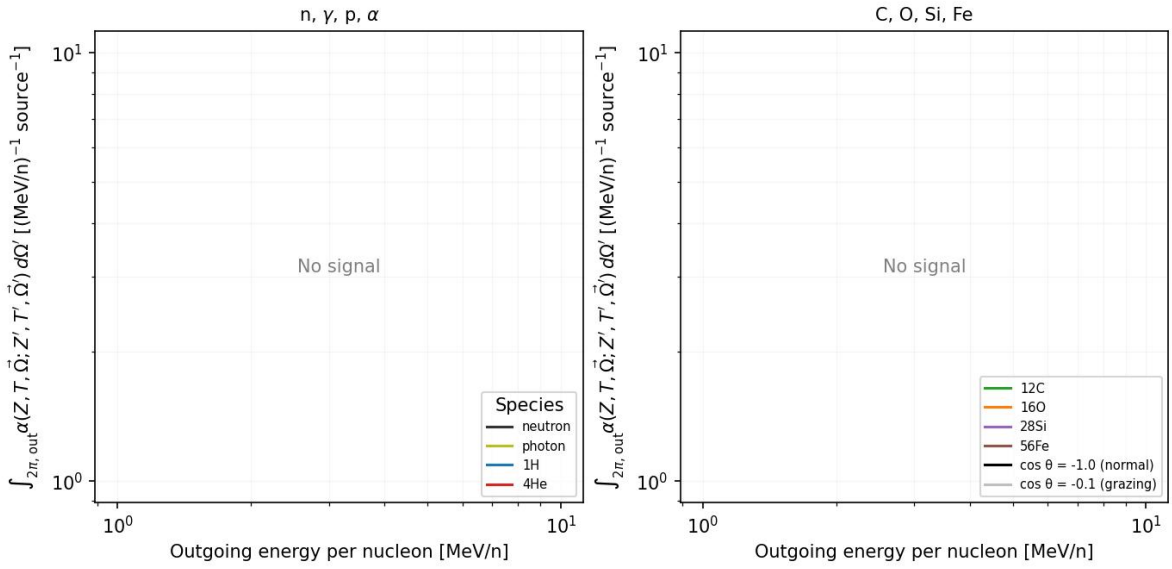


Figure A.19: Differential number albedo response function for a 501 keV n^{-1} ^{1}H primary, shown for all ten simulated incident polar cosine bins ($\cos\theta = -1.0$ to -0.1).

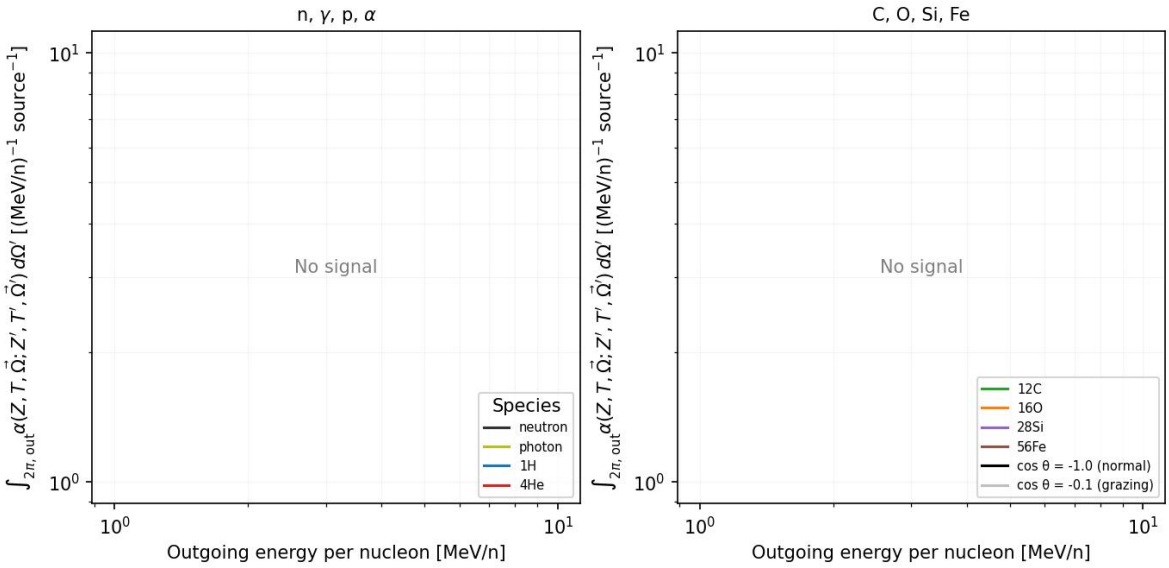


Figure A.20: Differential number albedo response function for a 575 keV n^{-1} ^{1}H primary, shown for all ten simulated incident polar cosine bins ($\cos\theta = -1.0$ to -0.1).

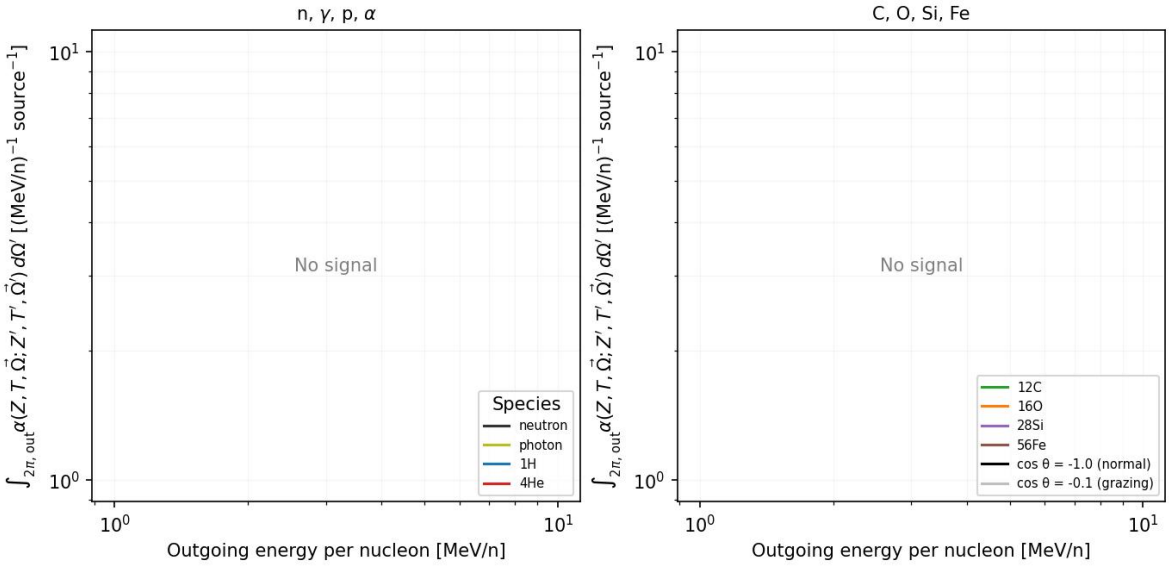


Figure A.21: Differential number albedo response function for a 659 keV n^{-1} ^{1}H primary, shown for all ten simulated incident polar cosine bins ($\cos\theta = -1.0$ to -0.1).

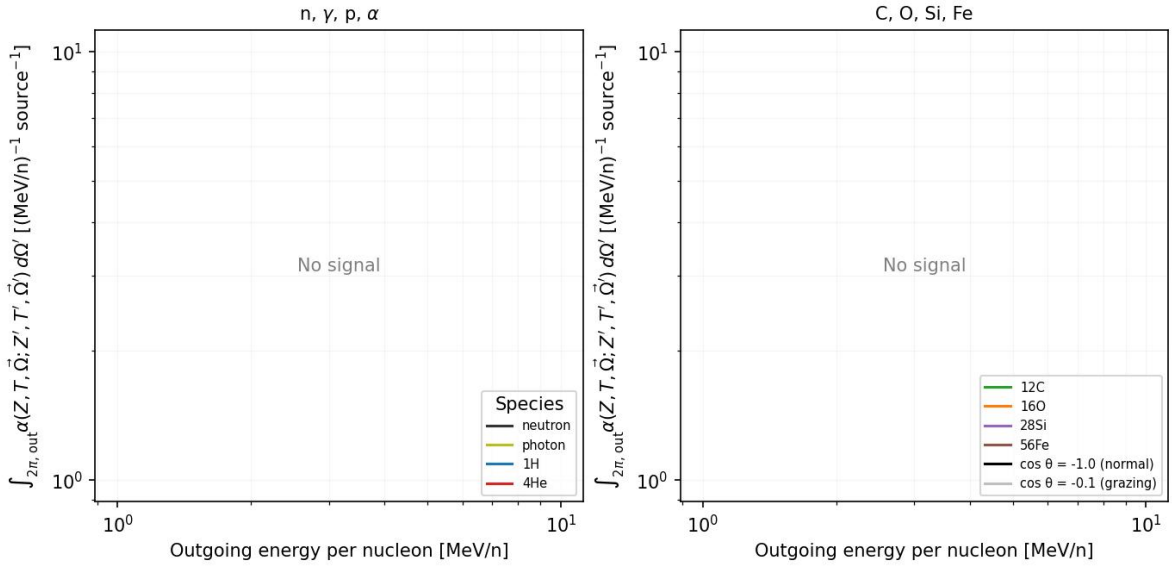


Figure A.22: Differential number albedo response function for a 754 keV n^{-1} ^{1}H primary, shown for all ten simulated incident polar cosine bins ($\cos\theta = -1.0$ to -0.1).

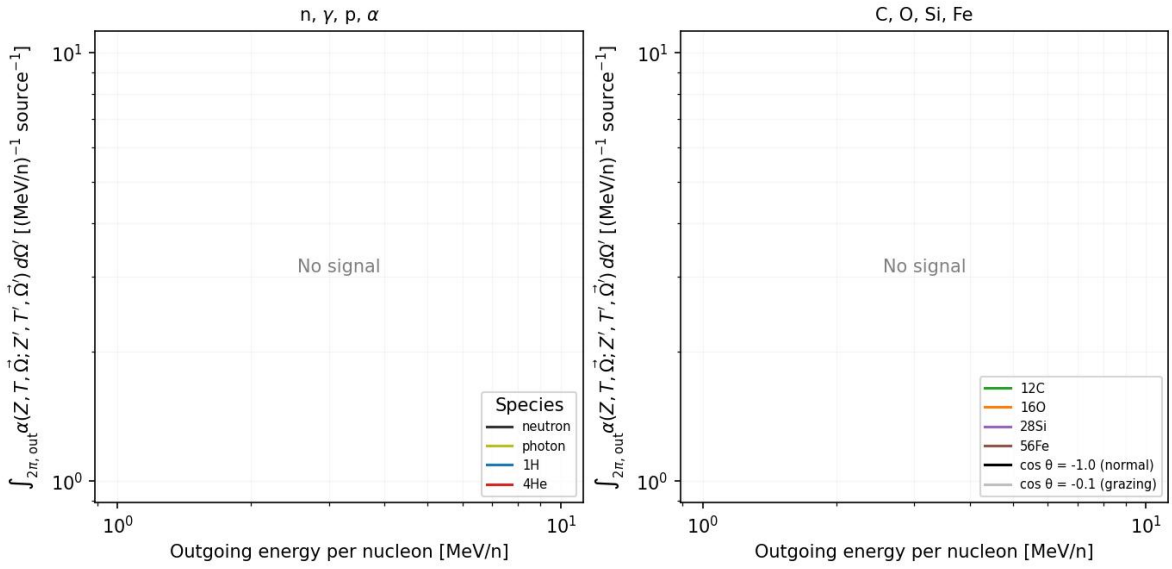


Figure A.23: Differential number albedo response function for a 860 keV n^{-1} ^{1}H primary, shown for all ten simulated incident polar cosine bins ($\cos\theta = -1.0$ to -0.1).

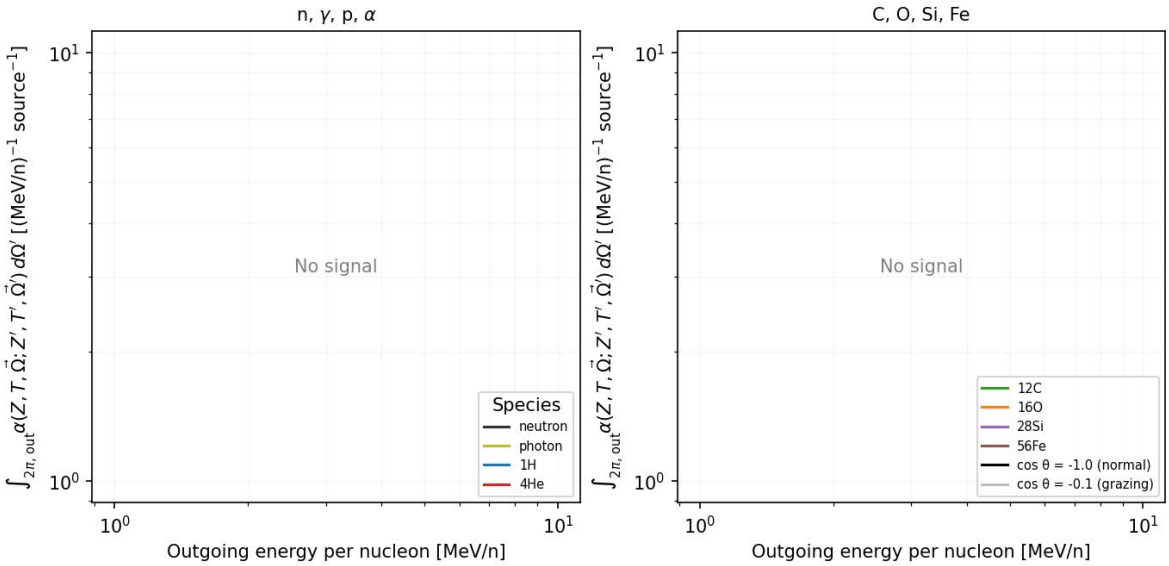


Figure A.24: Differential number albedo response function for a 979 keV n^{-1} ^{1}H primary, shown for all ten simulated incident polar cosine bins ($\cos\theta = -1.0$ to -0.1).

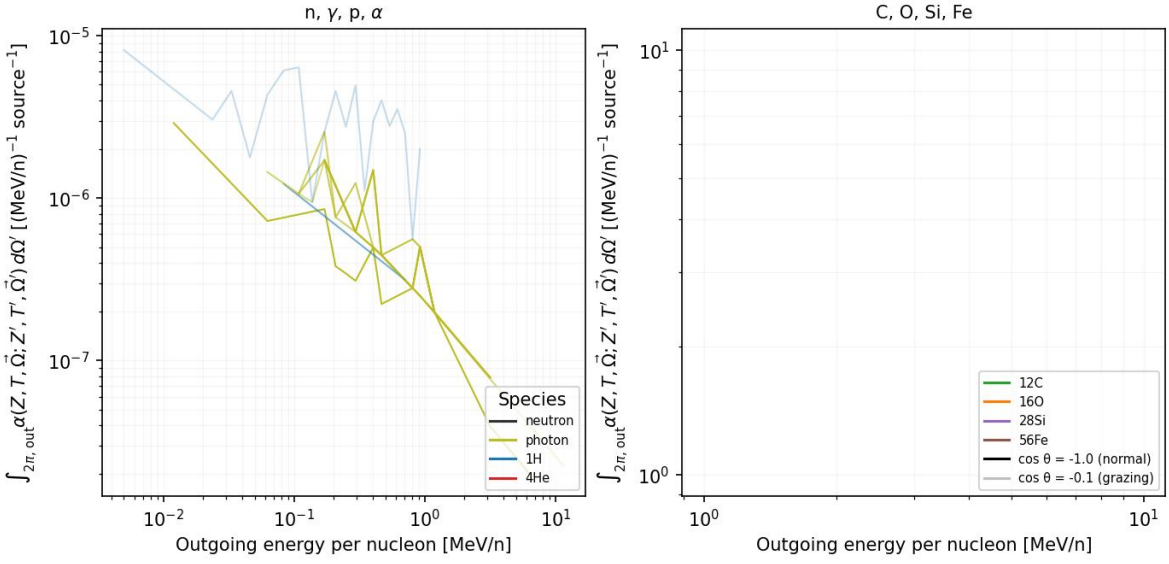


Figure A.25: Differential number albedo response function for a 1.112 MeV n^{-1} ^{1}H primary, shown for all ten simulated incident polar cosine bins ($\cos\theta = -1.0$ to -0.1).

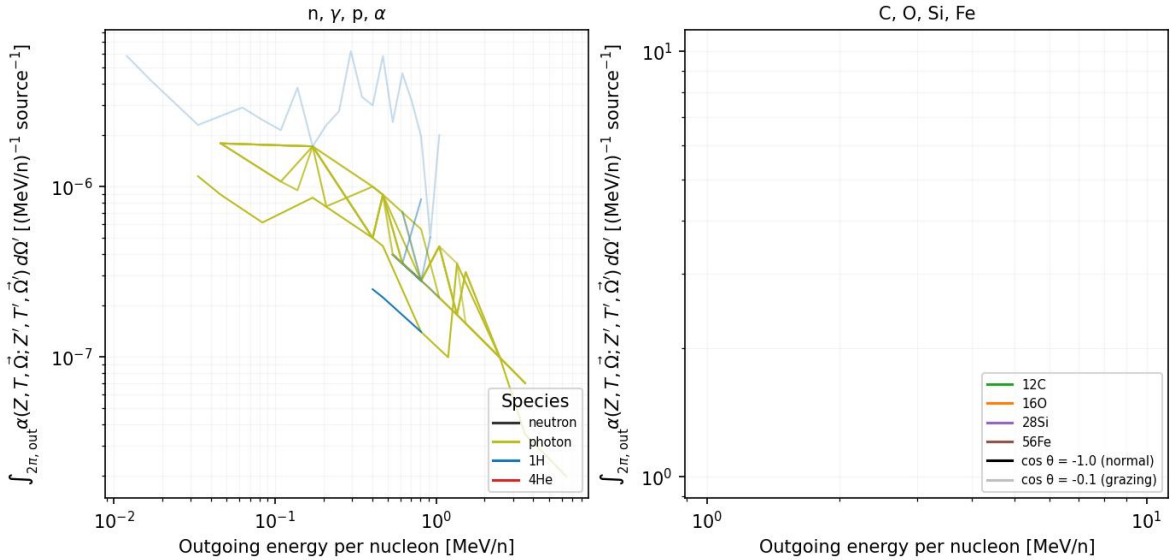


Figure A.26: Differential number albedo response function for a 1.262 MeV n^{-1} ^{1}H primary, shown for all ten simulated incident polar cosine bins ($\cos\theta = -1.0$ to -0.1).

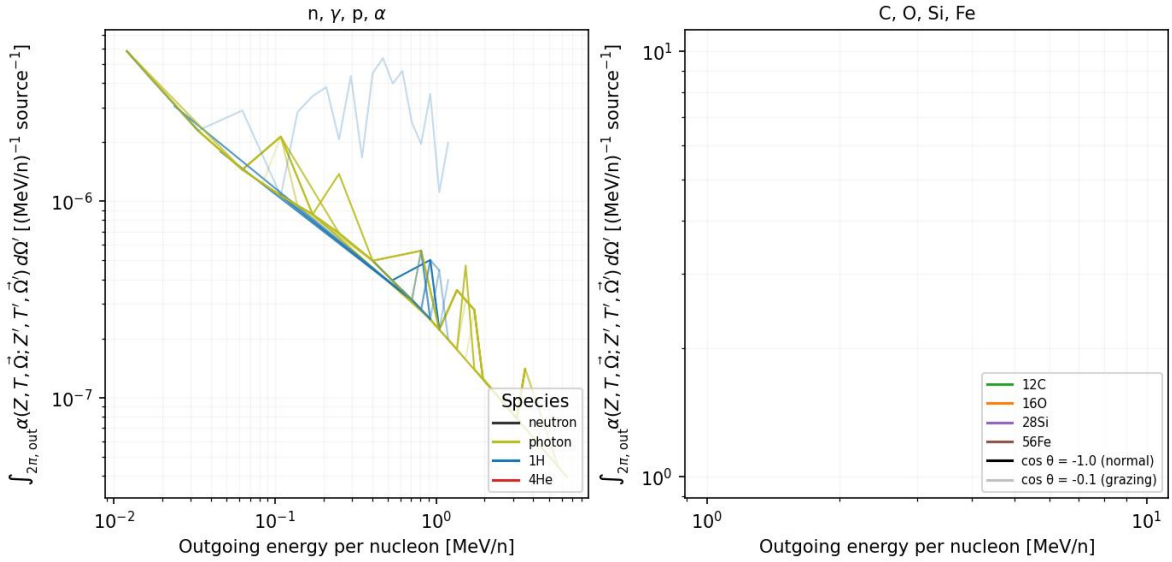


Figure A.27: Differential number albedo response function for a 1.43 MeV n^{-1} ^{1}H primary, shown for all ten simulated incident polar cosine bins ($\cos\theta = -1.0$ to -0.1).

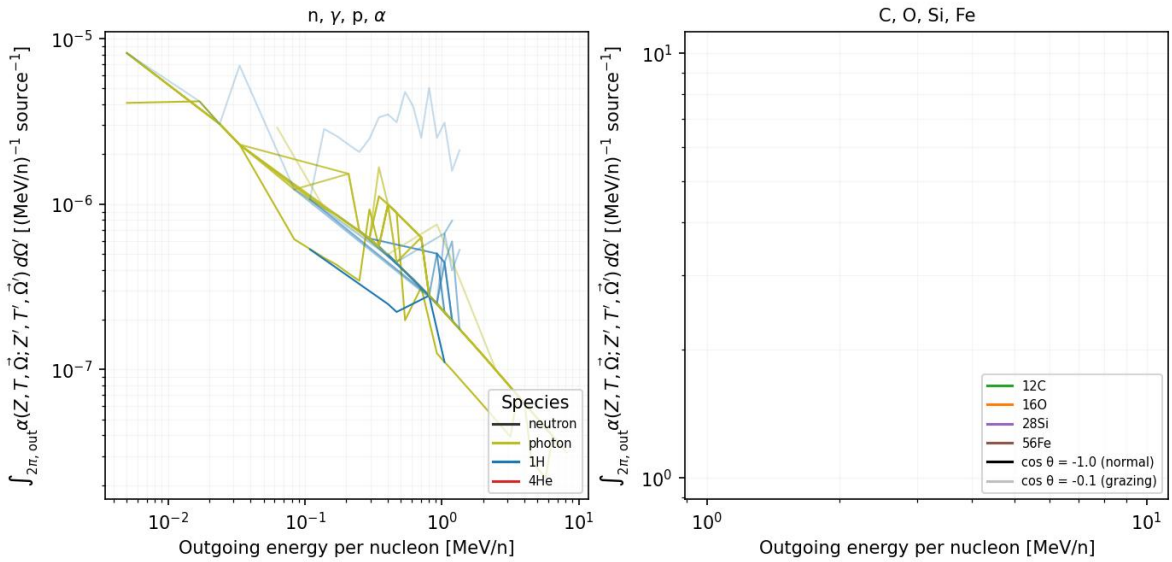


Figure A.28: Differential number albedo response function for a 1.619 MeV n^{-1} ^{1}H primary, shown for all ten simulated incident polar cosine bins ($\cos\theta = -1.0$ to -0.1).

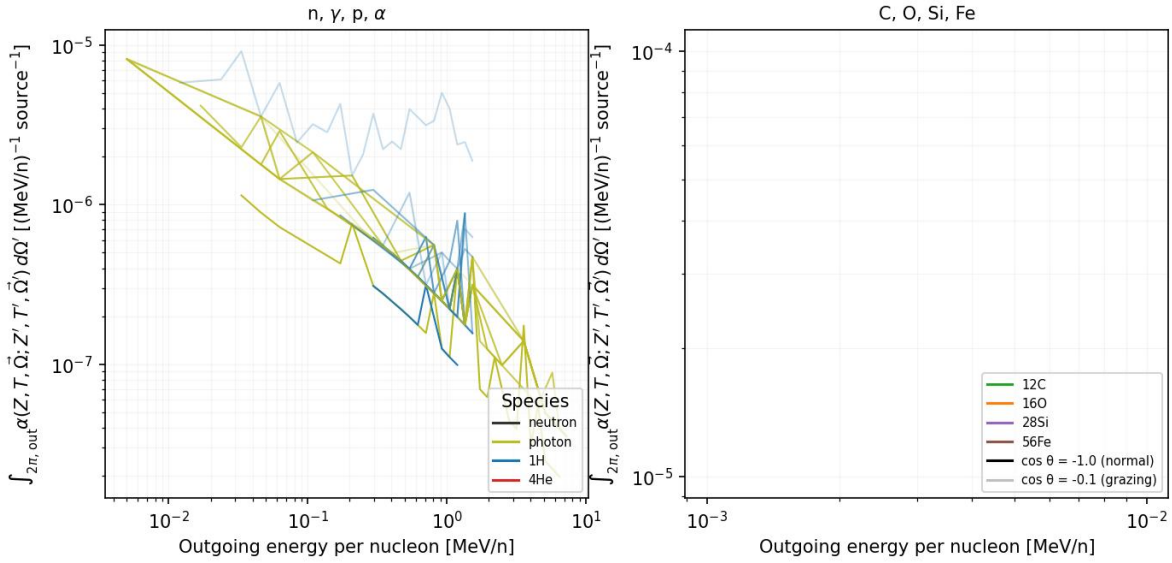


Figure A.29: Differential number albedo response function for a 1.832 MeV n^{-1} ^{1}H primary, shown for all ten simulated incident polar cosine bins ($\cos\theta = -1.0$ to -0.1).

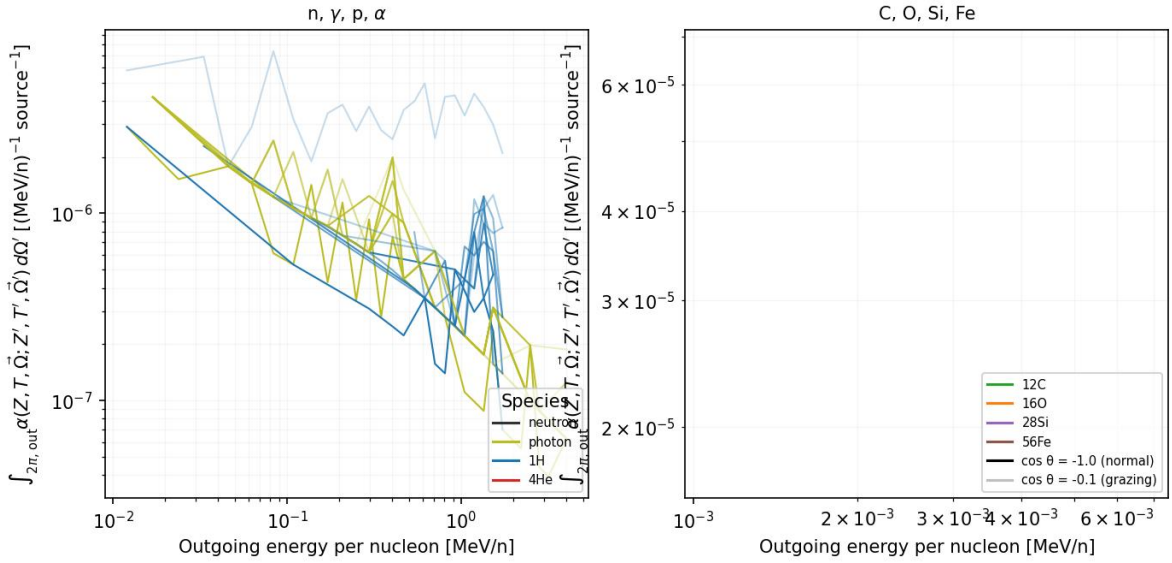


Figure A.30: Differential number albedo response function for a 2.07 MeV n^{-1} ^{1}H primary, shown for all ten simulated incident polar cosine bins ($\cos\theta = -1.0$ to -0.1).

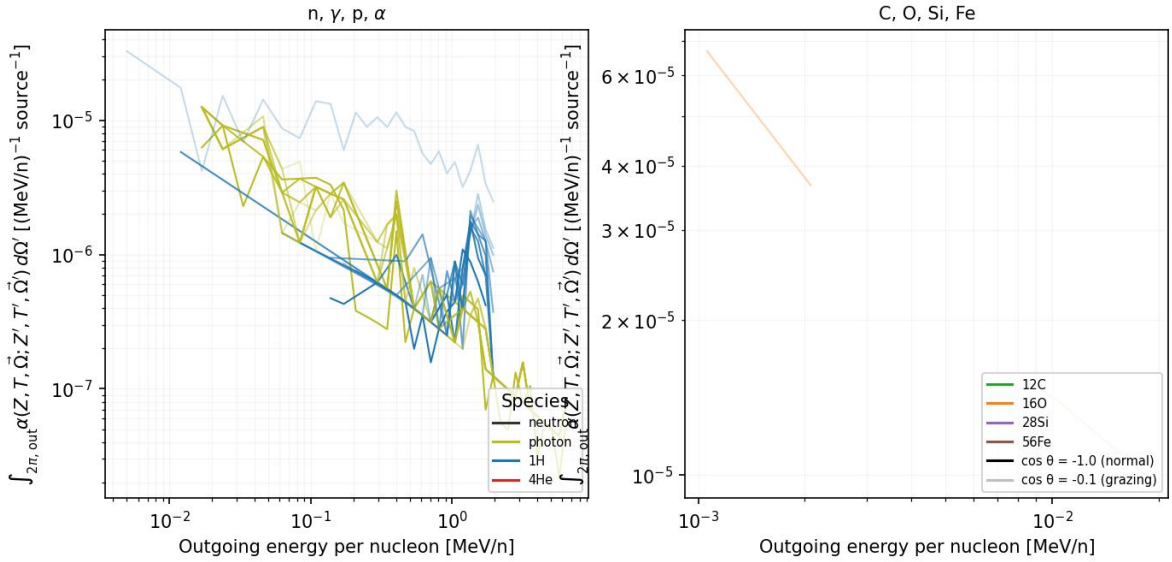


Figure A.31: Differential number albedo response function for a 2.338 MeV n^{-1} ^{1}H primary, shown for all ten simulated incident polar cosine bins ($\cos\theta = -1.0$ to -0.1).

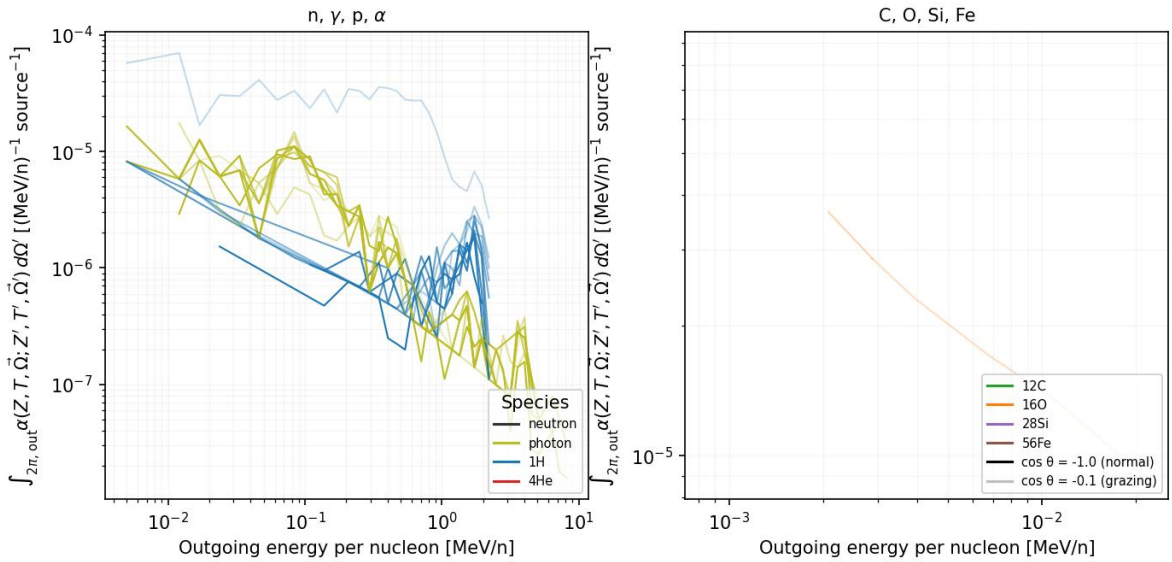


Figure A.32: Differential number albedo response function for a 2.639 MeV n^{-1} ^{1}H primary, shown for all ten simulated incident polar cosine bins ($\cos\theta = -1.0$ to -0.1).

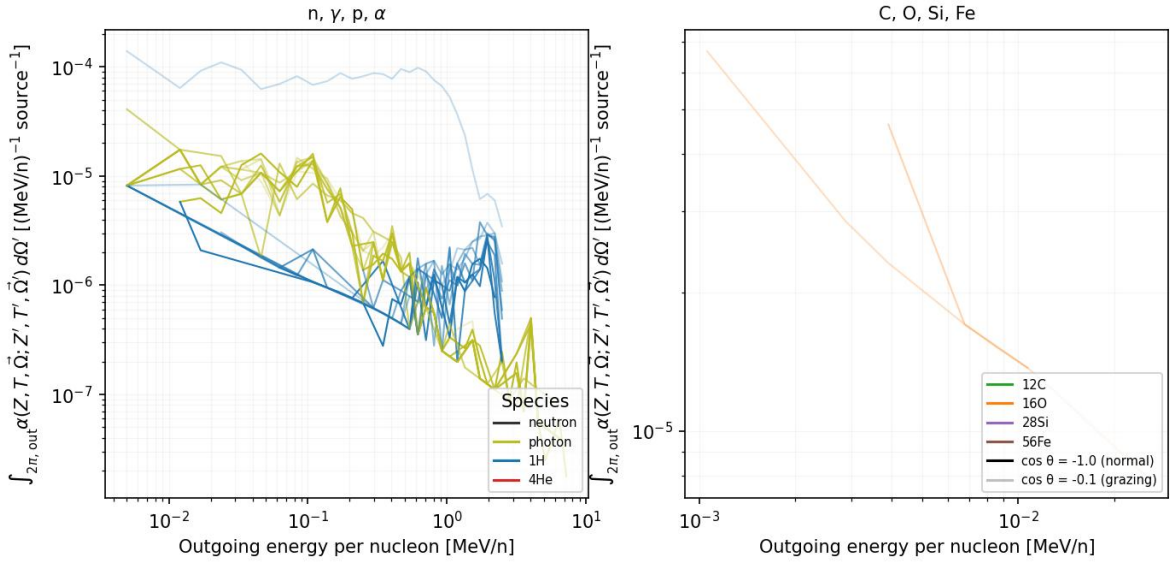


Figure A.33: Differential number albedo response function for a 2.976 MeV n^{-1} ^{1}H primary, shown for all ten simulated incident polar cosine bins ($\cos\theta = -1.0$ to -0.1).

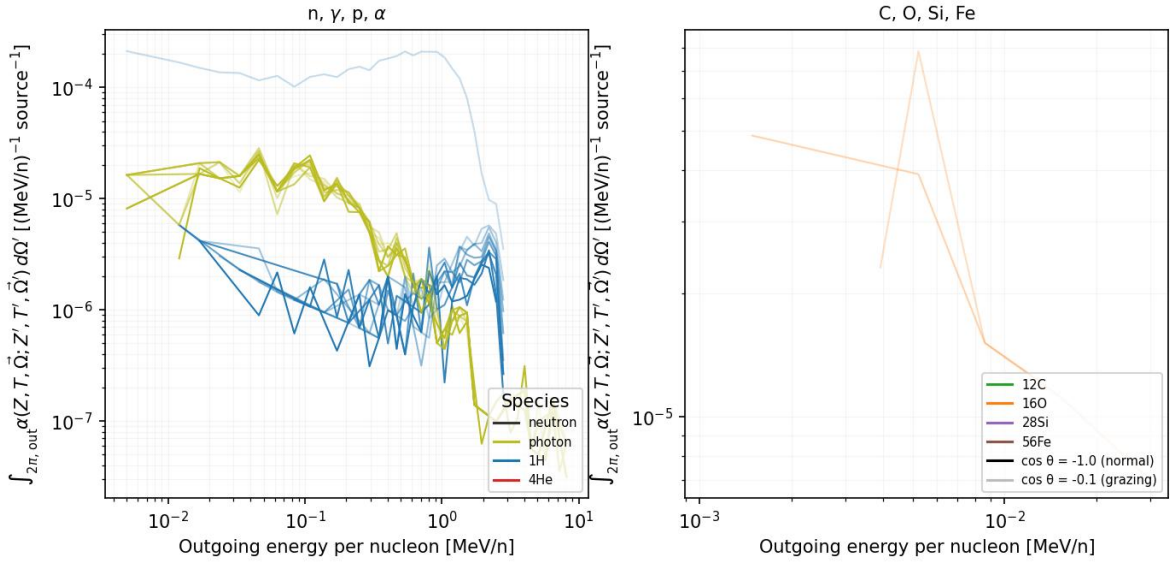


Figure A.34: Differential number albedo response function for a 3.355 MeV n^{-1} ^{1}H primary, shown for all ten simulated incident polar cosine bins ($\cos\theta = -1.0$ to -0.1).

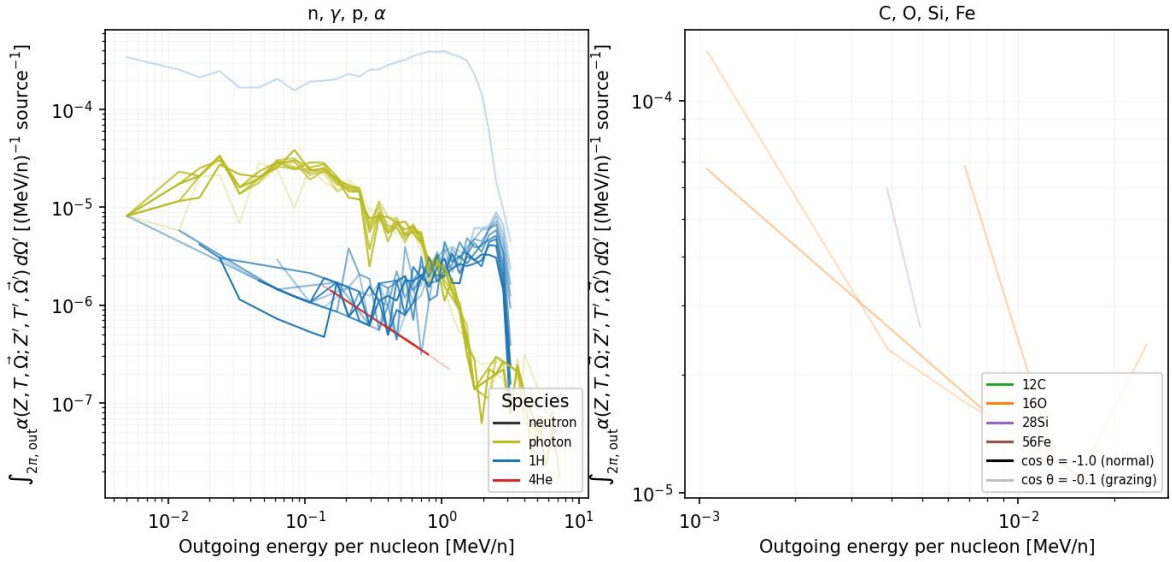


Figure A.35: Differential number albedo response function for a 3.779 MeV n^{-1} ^{1}H primary, shown for all ten simulated incident polar cosine bins ($\cos\theta = -1.0$ to -0.1).

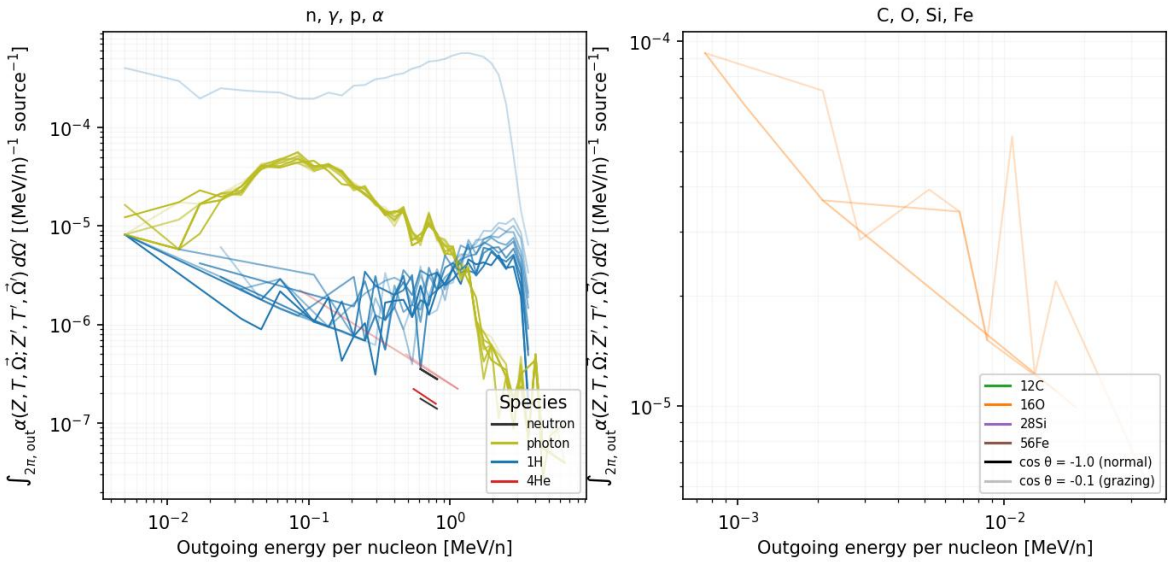


Figure A.36: Differential number albedo response function for a 4.255 MeV n^{-1} ^{1}H primary, shown for all ten simulated incident polar cosine bins ($\cos\theta = -1.0$ to -0.1).

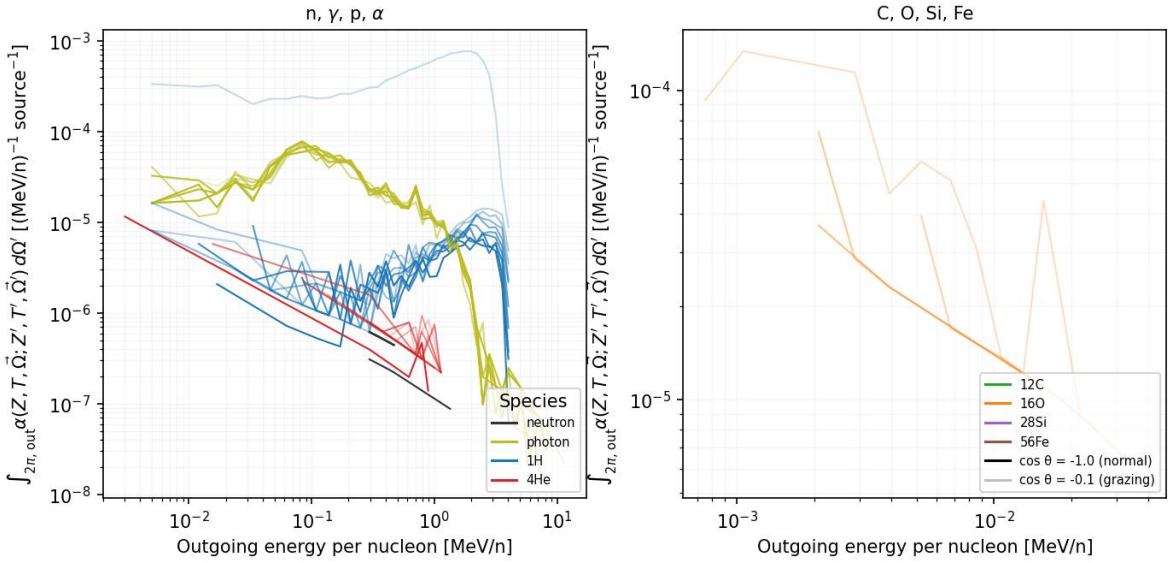


Figure A.37: Differential number albedo response function for a 4.789 MeV n^{-1} ^{1}H primary, shown for all ten simulated incident polar cosine bins ($\cos\theta = -1.0$ to -0.1).

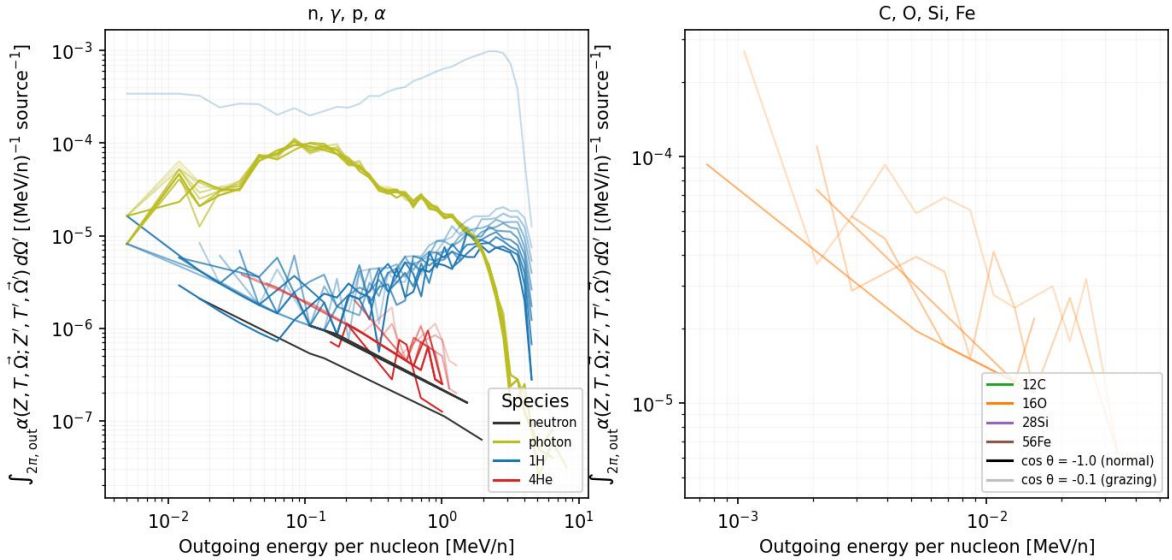


Figure A.38: Differential number albedo response function for a 5.387 MeV n^{-1} ^{1}H primary, shown for all ten simulated incident polar cosine bins ($\cos\theta = -1.0$ to -0.1).

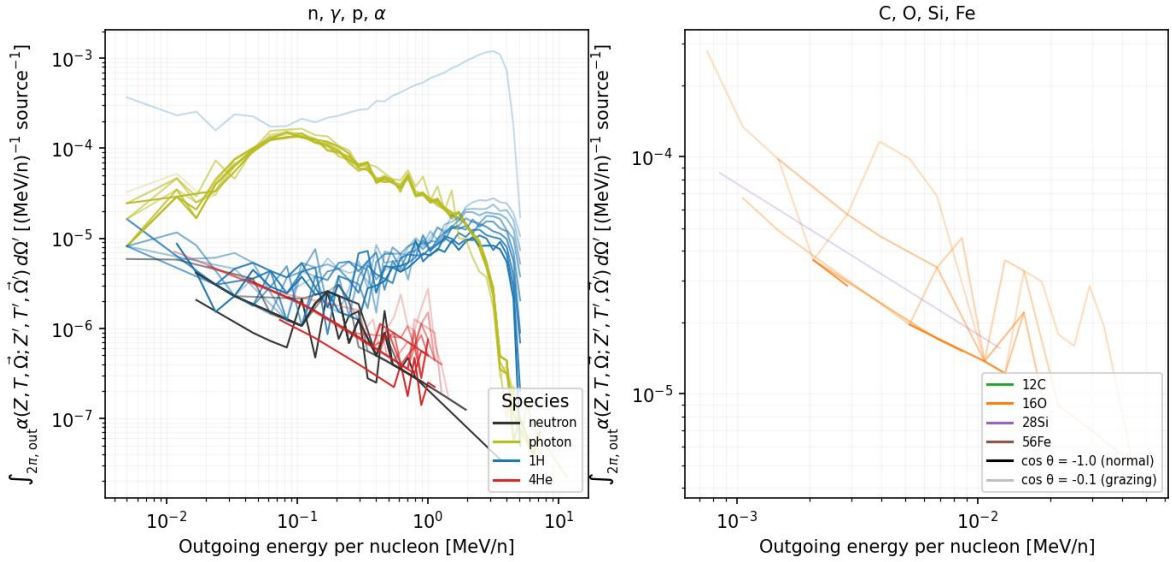


Figure A.39: Differential number albedo response function for a 6.057 MeV n^{-1} ^{1}H primary, shown for all ten simulated incident polar cosine bins ($\cos\theta = -1.0$ to -0.1).

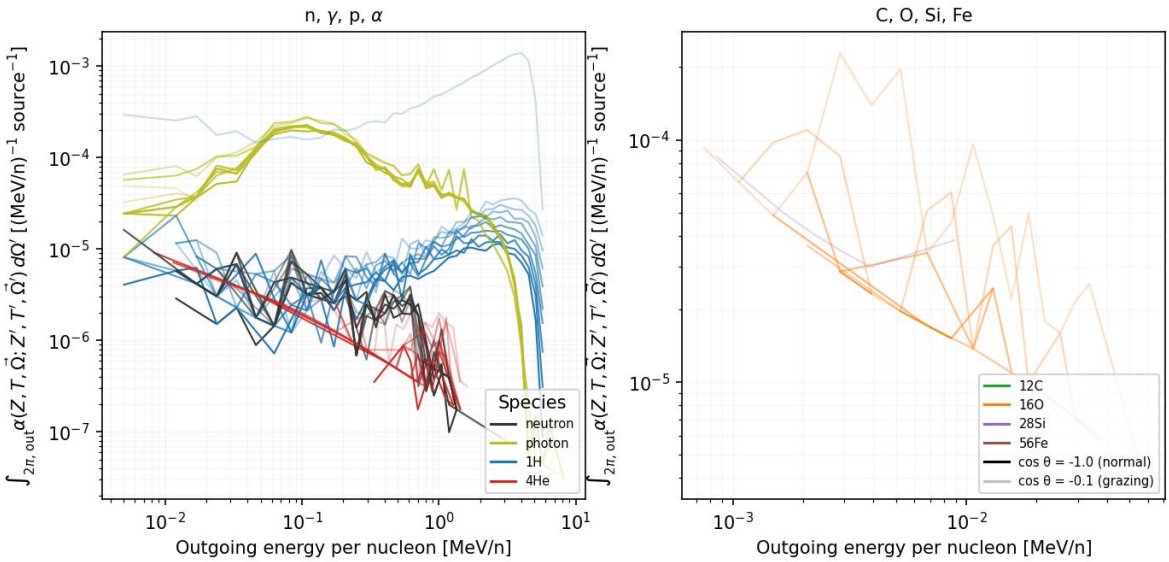


Figure A.40: Differential number albedo response function for a 6.808 MeV n^{-1} ^{1}H primary, shown for all ten simulated incident polar cosine bins ($\cos\theta = -1.0$ to -0.1).

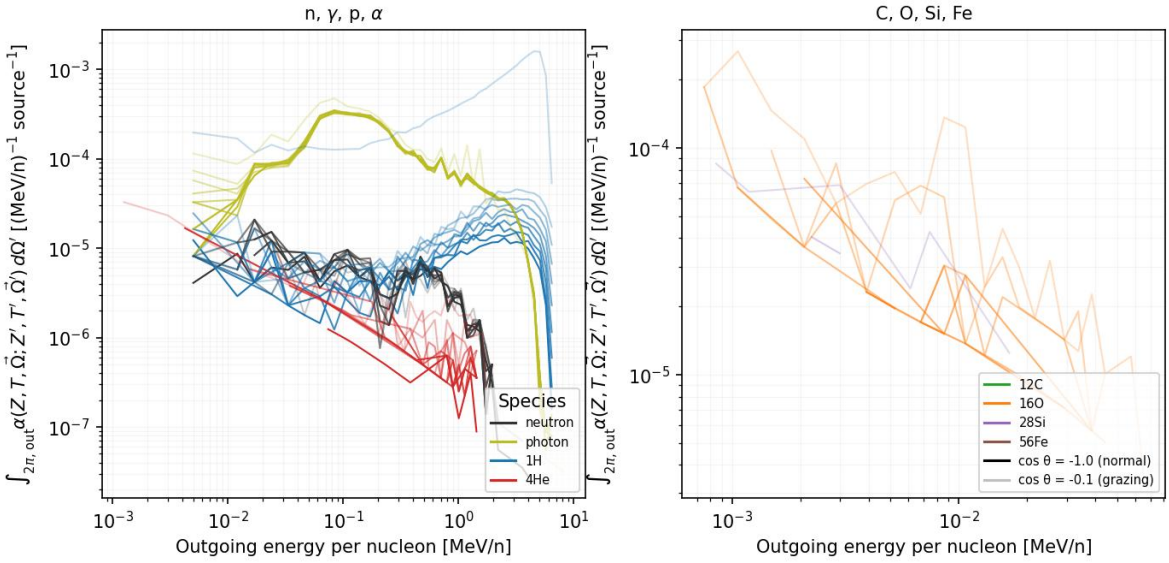


Figure A.41: Differential number albedo response function for a 7.65 MeV n^{-1} ^{1}H primary, shown for all ten simulated incident polar cosine bins ($\cos\theta = -1.0$ to -0.1).

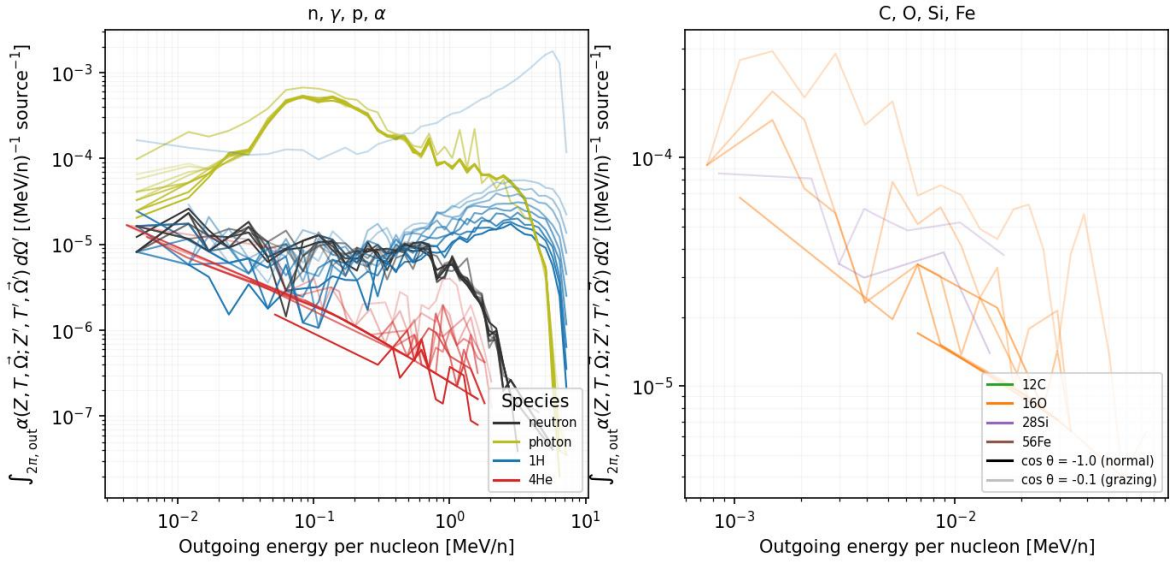


Figure A.42: Differential number albedo response function for a 8.592 MeV n^{-1} ^{1}H primary, shown for all ten simulated incident polar cosine bins ($\cos\theta = -1.0$ to -0.1).

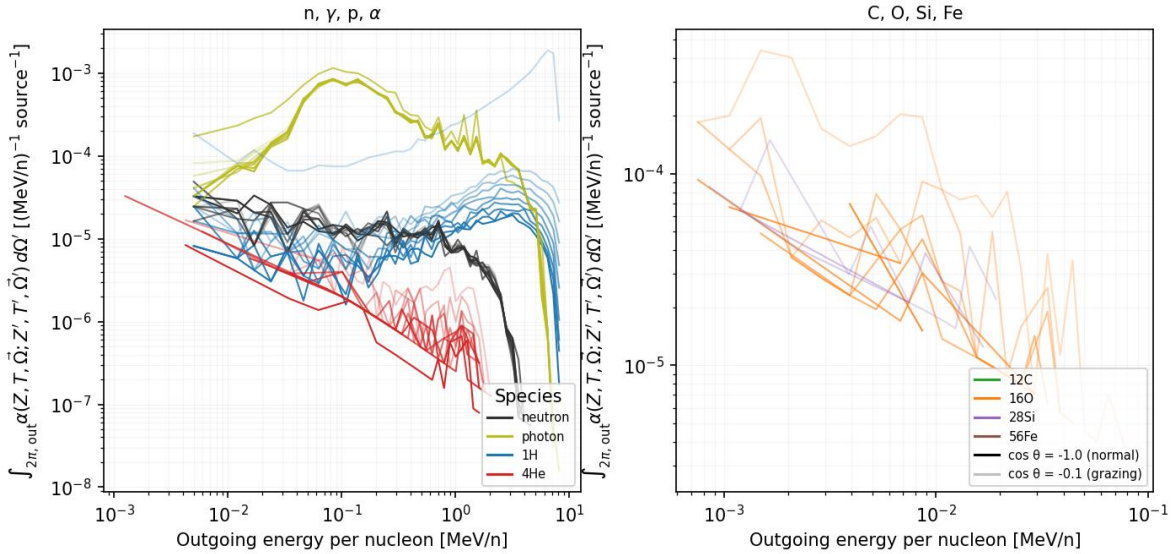


Figure A.43: Differential number albedo response function for a 9.648 MeV n^{-1} ^{1}H primary, shown for all ten simulated incident polar cosine bins ($\cos\theta = -1.0$ to -0.1).

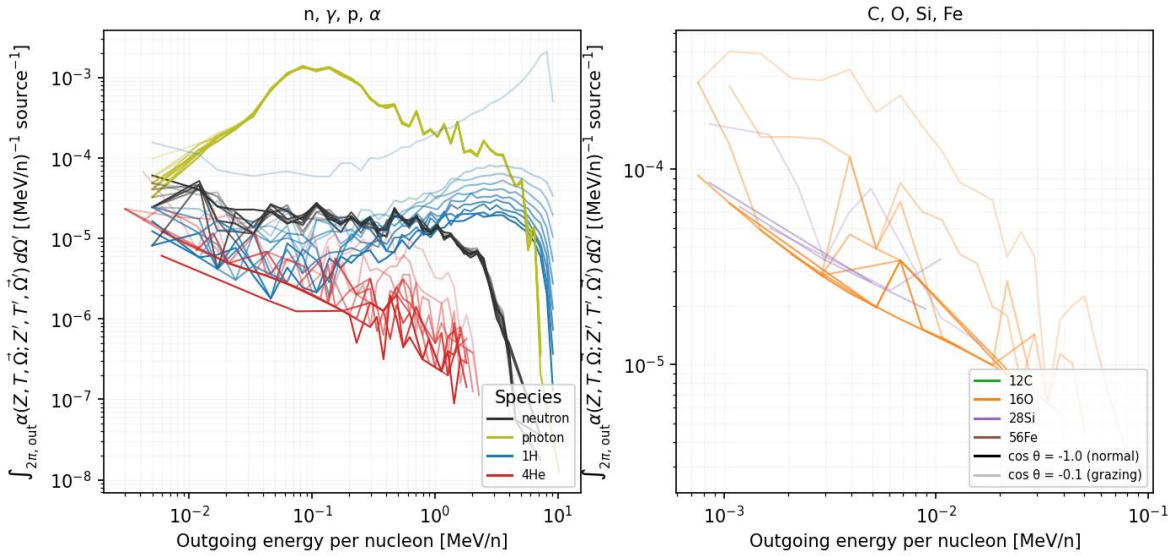


Figure A.44: Differential number albedo response function for a 10.83 MeV n^{-1} ^{1}H primary, shown for all ten simulated incident polar cosine bins ($\cos\theta = -1.0$ to -0.1).

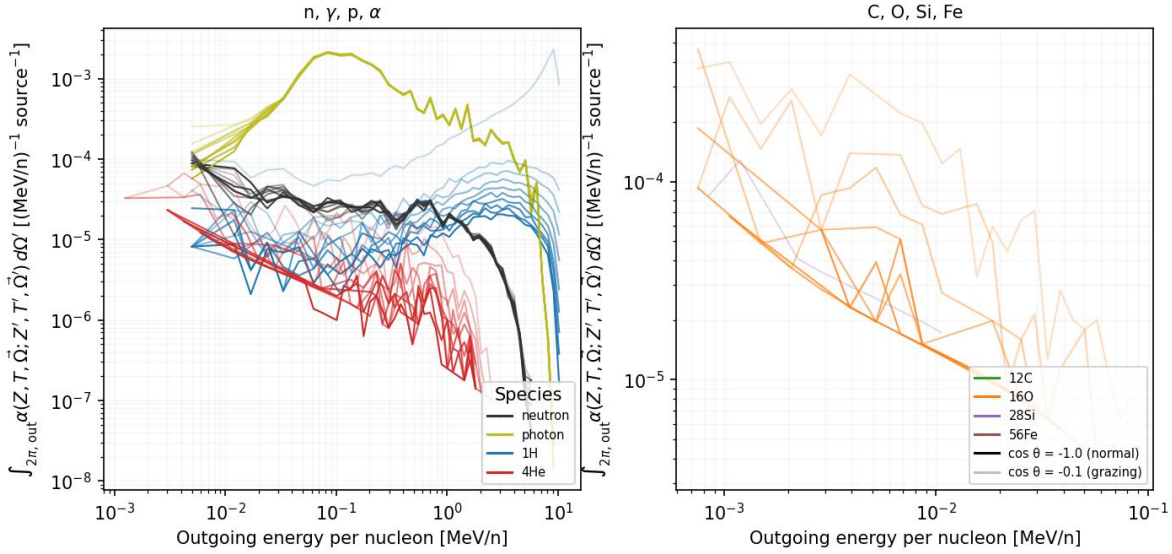


Figure A.45: Differential number albedo response function for a 12.15 MeV n^{-1} ^{1}H primary, shown for all ten simulated incident polar cosine bins ($\cos\theta = -1.0$ to -0.1).

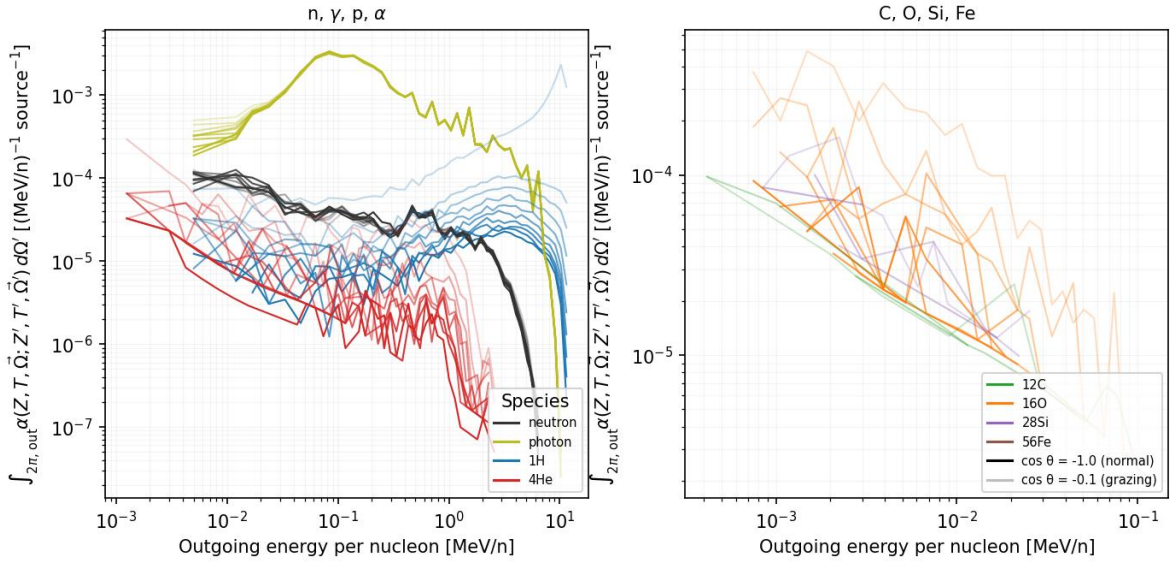


Figure A.46: Differential number albedo response function for a 13.63 MeV n^{-1} ^{1}H primary, shown for all ten simulated incident polar cosine bins ($\cos\theta = -1.0$ to -0.1).

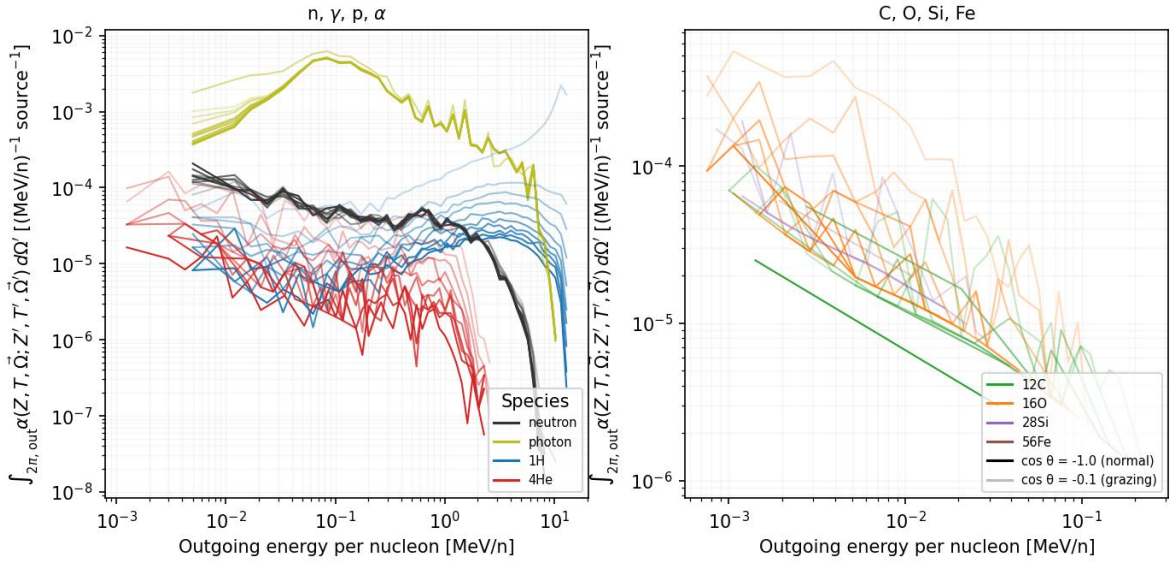


Figure A.47: Differential number albedo response function for a 15.3 MeV n^{-1} ^{1}H primary, shown for all ten simulated incident polar cosine bins ($\cos\theta = -1.0$ to -0.1).

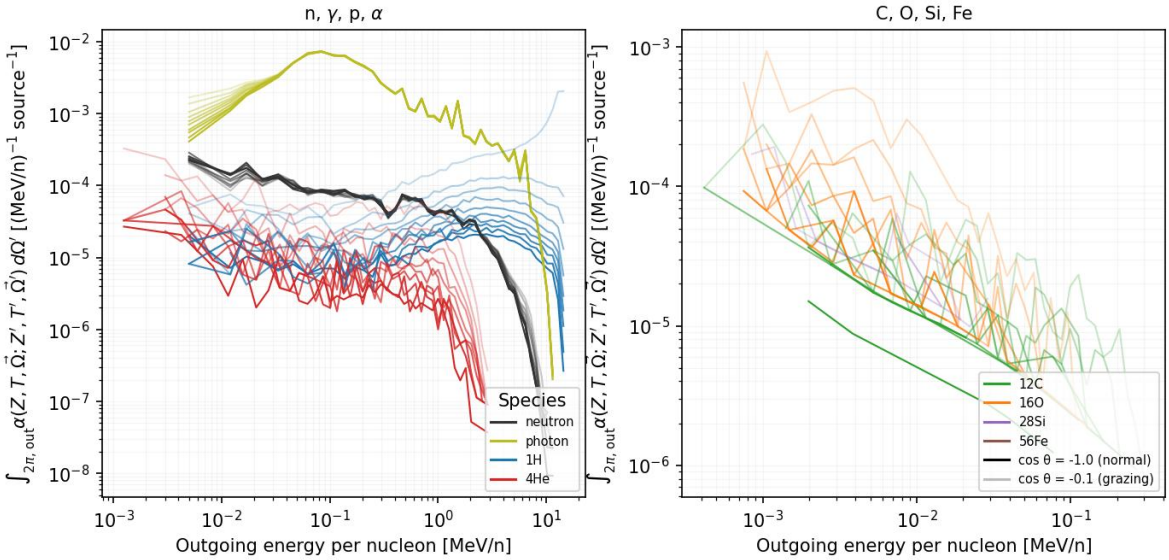


Figure A.48: Differential number albedo response function for a 17.15 MeV n^{-1} ^{1}H primary, shown for all ten simulated incident polar cosine bins ($\cos\theta = -1.0$ to -0.1).

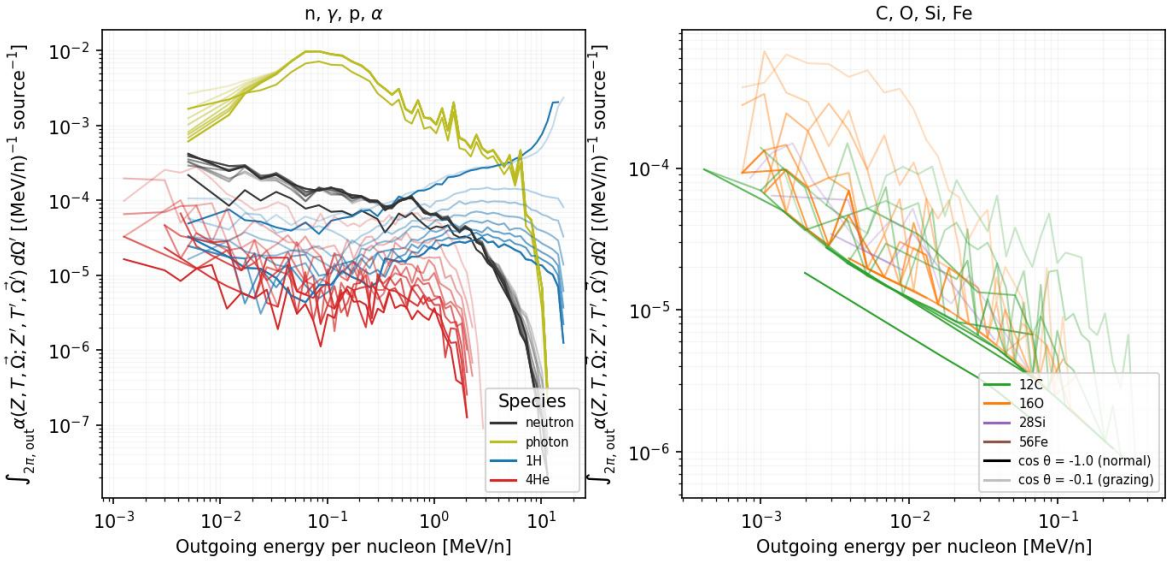


Figure A.49: Differential number albedo response function for a 19.23 MeV n^{-1} ^{1}H primary, shown for all ten simulated incident polar cosine bins ($\cos\theta = -1.0$ to -0.1).

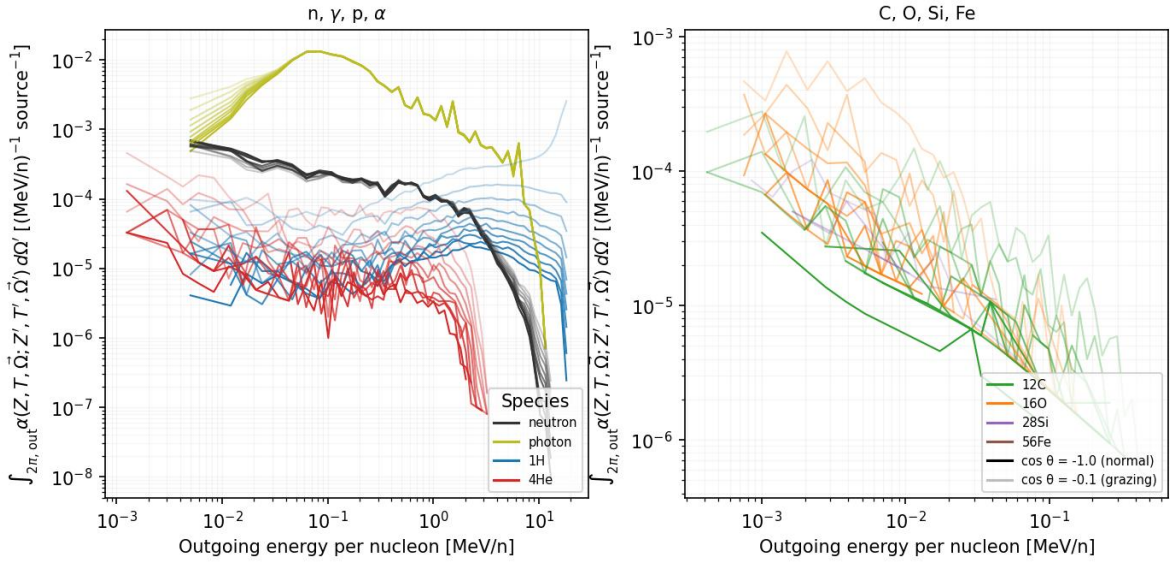


Figure A.50: Differential number albedo response function for a 21.56 MeV n^{-1} ^{1}H primary, shown for all ten simulated incident polar cosine bins ($\cos\theta = -1.0$ to -0.1).

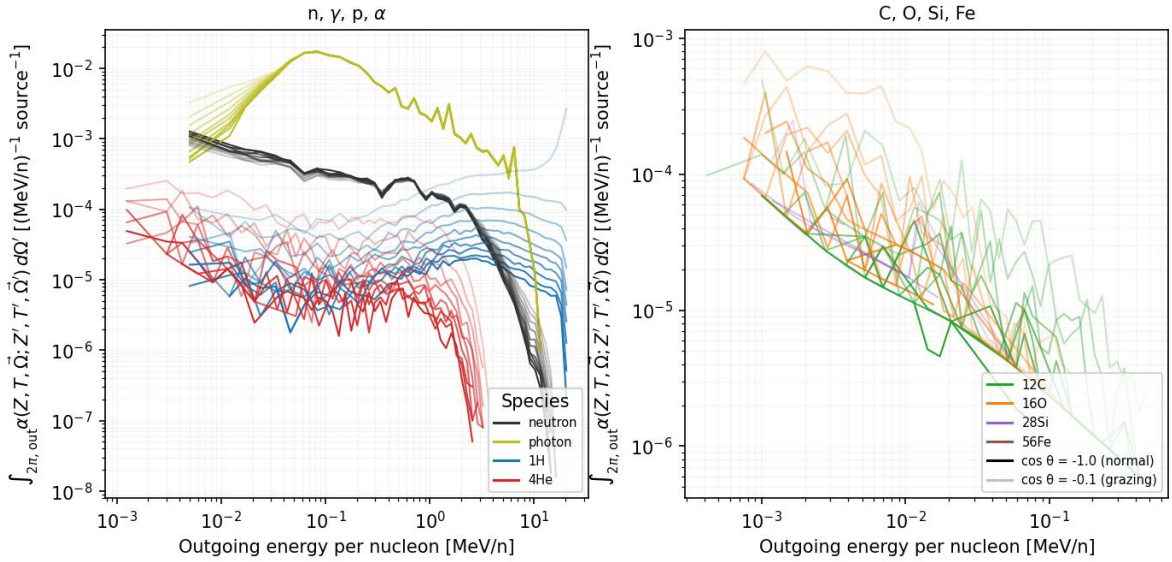


Figure A.51: Differential number albedo response function for a 24.17 MeV n^{-1} ^{1}H primary, shown for all ten simulated incident polar cosine bins ($\cos\theta = -1.0$ to -0.1).

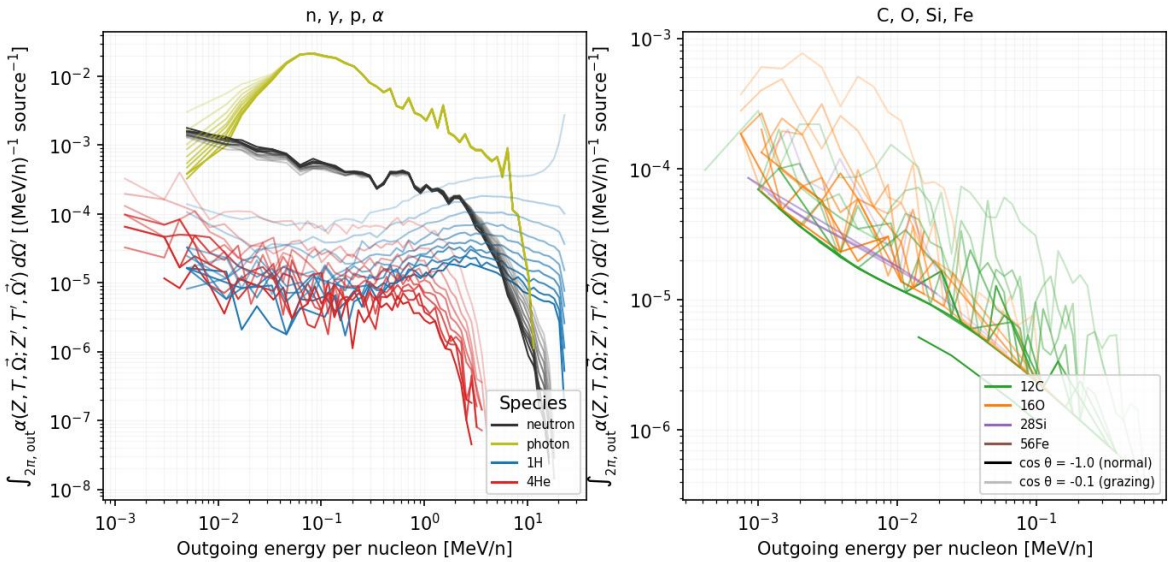


Figure A.52: Differential number albedo response function for a 27.1 MeV n^{-1} ^{1}H primary, shown for all ten simulated incident polar cosine bins ($\cos\theta = -1.0$ to -0.1).

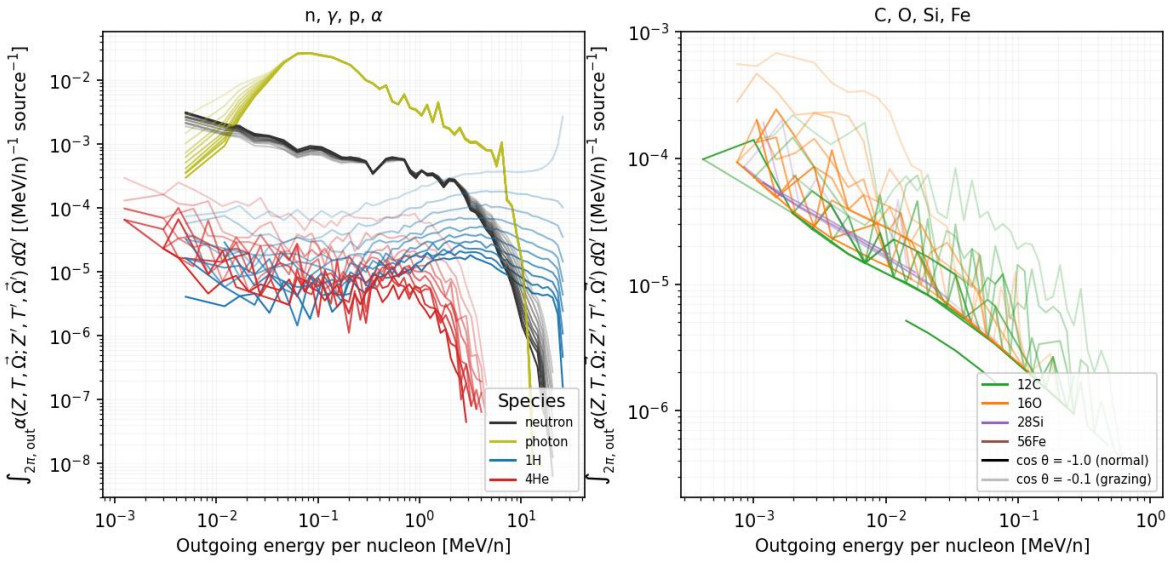


Figure A.53: Differential number albedo response function for a 30.37 MeV n^{-1} ^{1}H primary, shown for all ten simulated incident polar cosine bins ($\cos\theta = -1.0$ to -0.1).

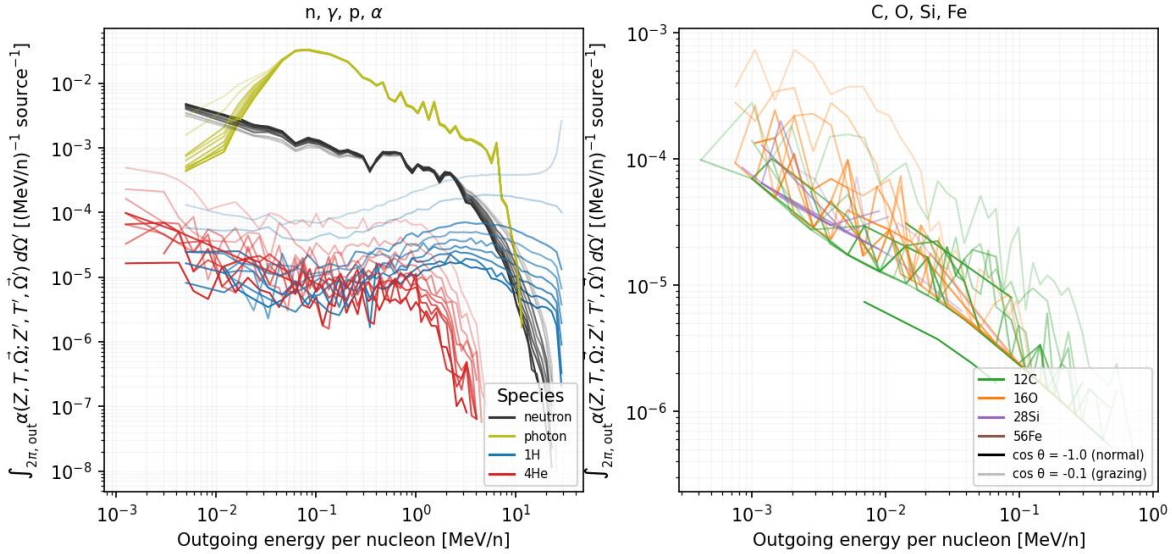


Figure A.54: Differential number albedo response function for a 34.04 MeV n^{-1} ^{1}H primary, shown for all ten simulated incident polar cosine bins ($\cos\theta = -1.0$ to -0.1).

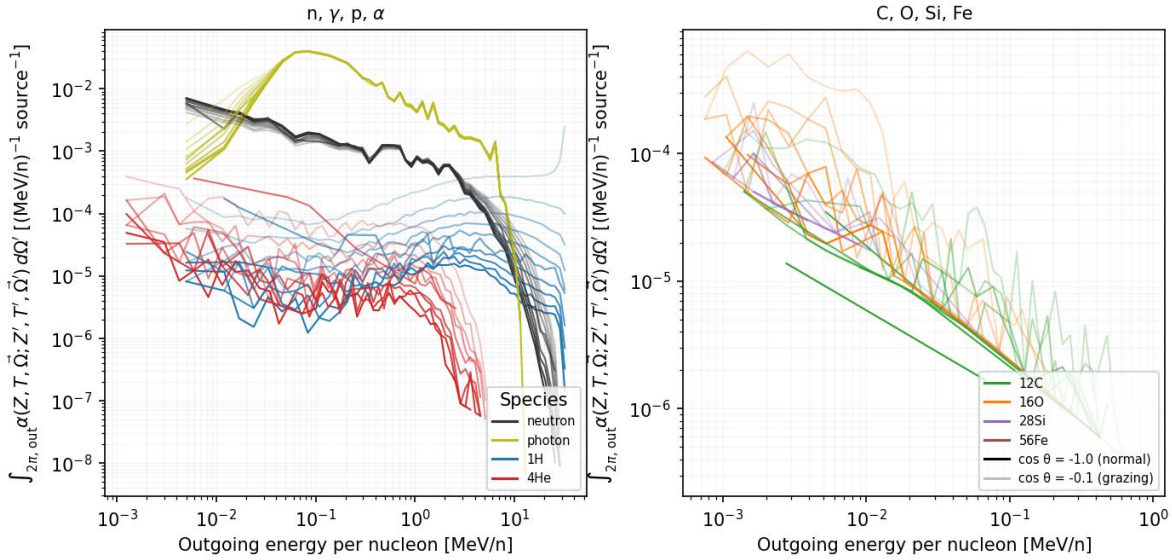


Figure A.55: Differential number albedo response function for a 38.15 MeV n^{-1} ^{1}H primary, shown for all ten simulated incident polar cosine bins ($\cos\theta = -1.0$ to -0.1).

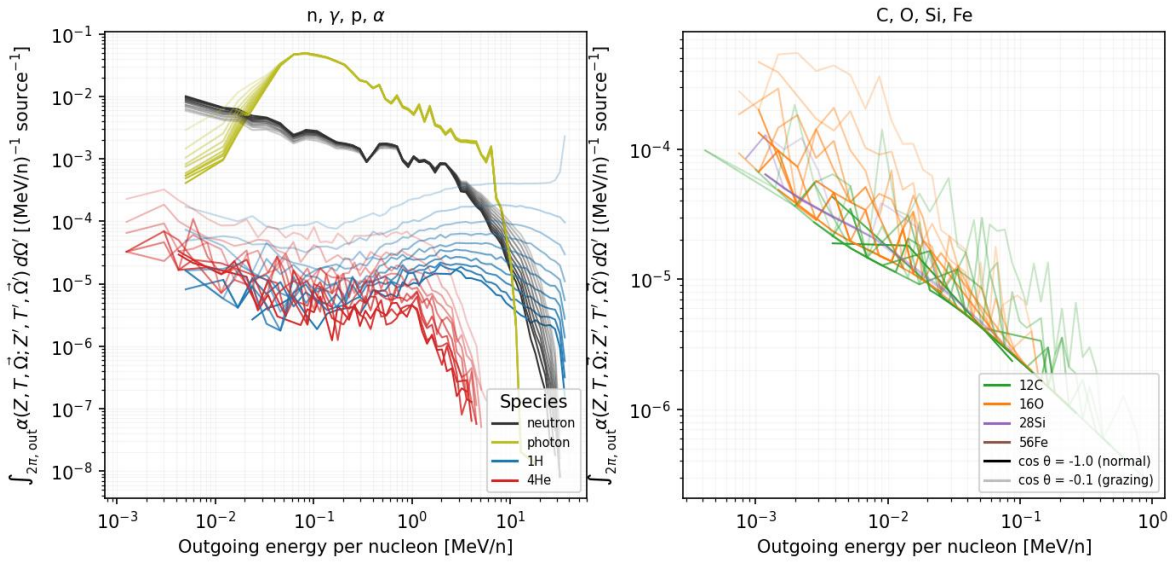


Figure A.56: Differential number albedo response function for a 42.76 MeV n^{-1} ^{1}H primary, shown for all ten simulated incident polar cosine bins ($\cos\theta = -1.0$ to -0.1).

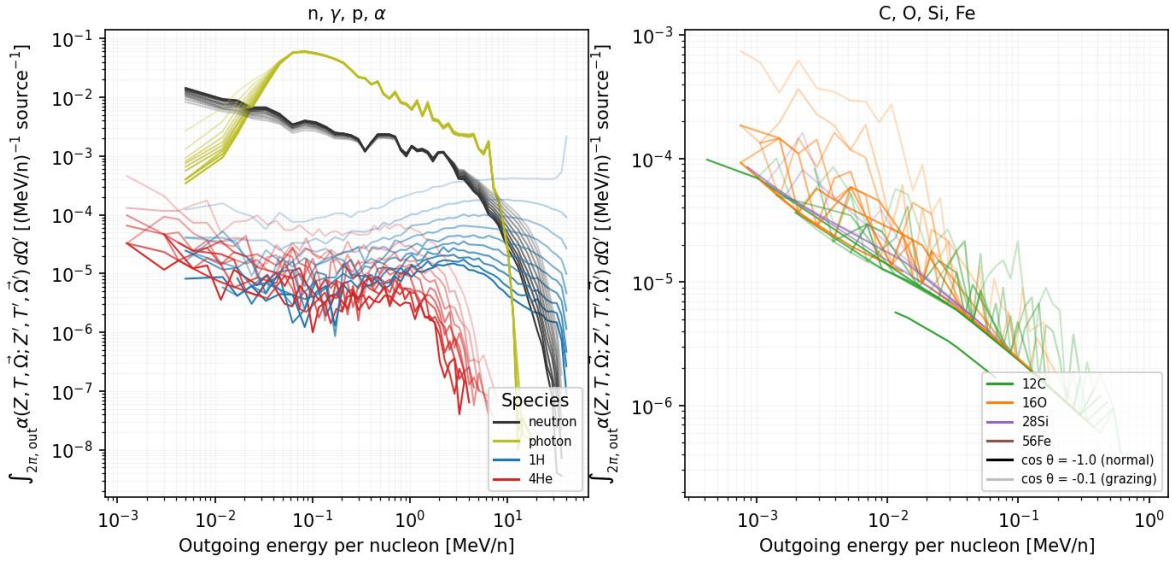


Figure A.57: Differential number albedo response function for a 47.93 MeV n^{-1} ^{1}H primary, shown for all ten simulated incident polar cosine bins ($\cos\theta = -1.0$ to -0.1).

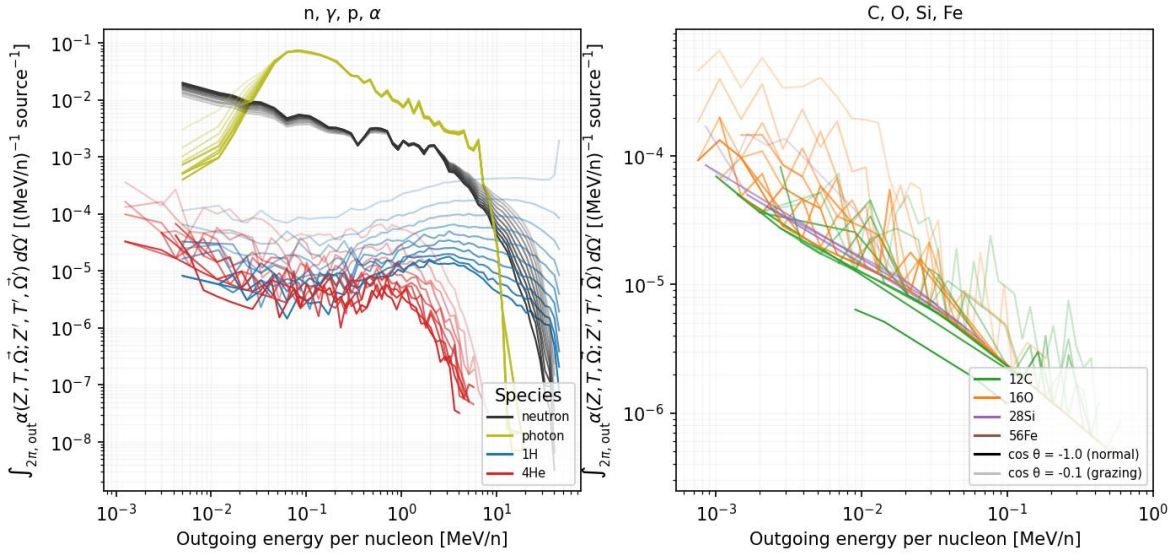


Figure A.58: Differential number albedo response function for a 53.73 MeV n^{-1} ^{1}H primary, shown for all ten simulated incident polar cosine bins ($\cos\theta = -1.0$ to -0.1).

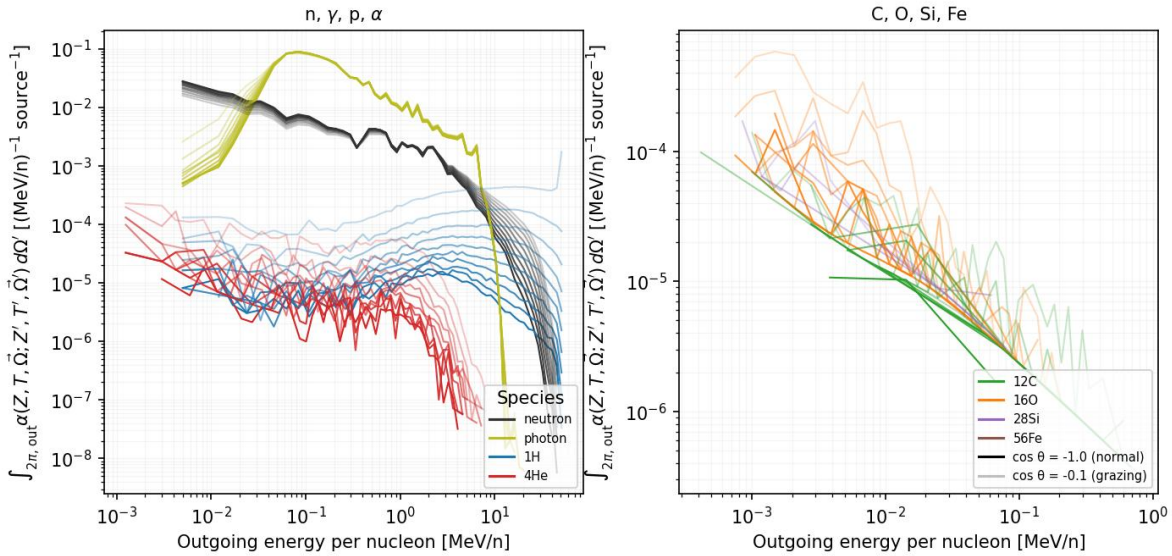


Figure A.59: Differential number albedo response function for a 60.24 MeV n^{-1} ^{1}H primary, shown for all ten simulated incident polar cosine bins ($\cos\theta = -1.0$ to -0.1).

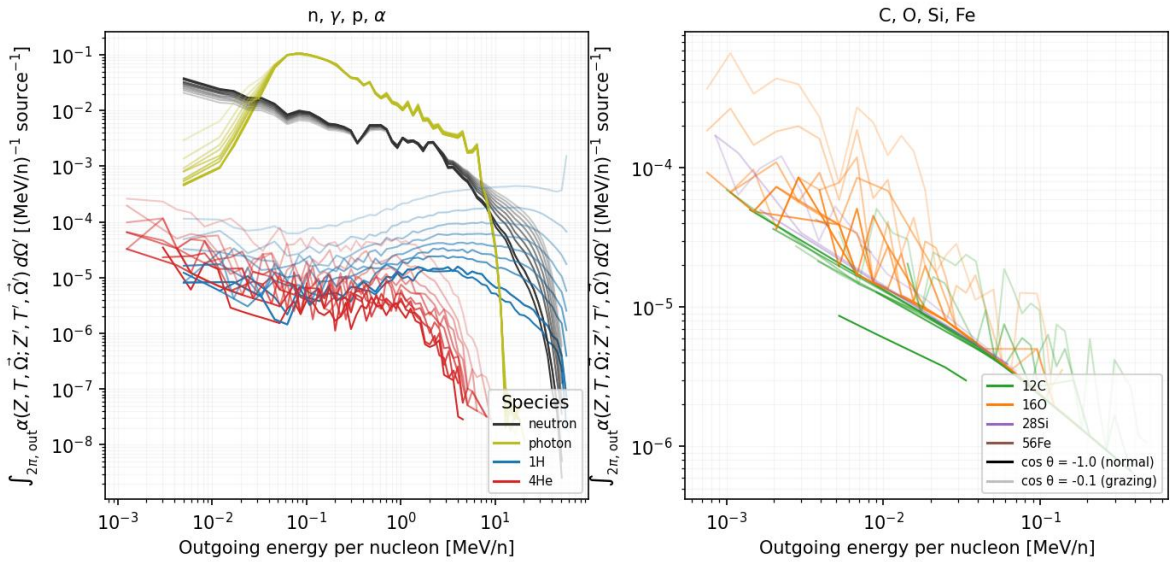


Figure A.60: Differential number albedo response function for a 67.55 MeV n^{-1} ^{1}H primary, shown for all ten simulated incident polar cosine bins ($\cos\theta = -1.0$ to -0.1).

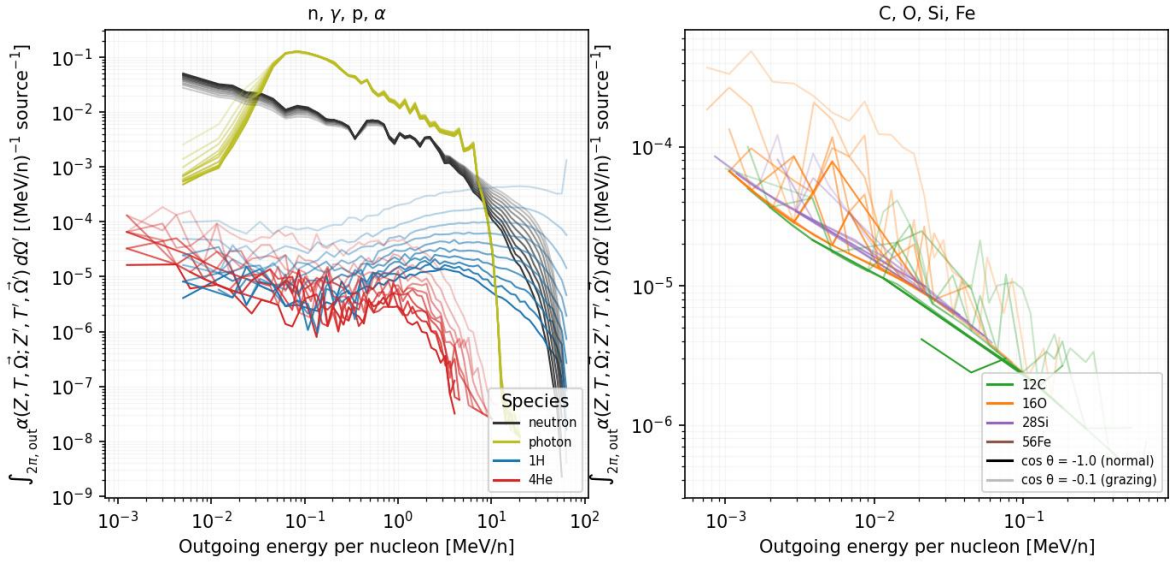


Figure A.61: Differential number albedo response function for a 75.77 MeV n^{-1} ^{1}H primary, shown for all ten simulated incident polar cosine bins ($\cos\theta = -1.0$ to -0.1).

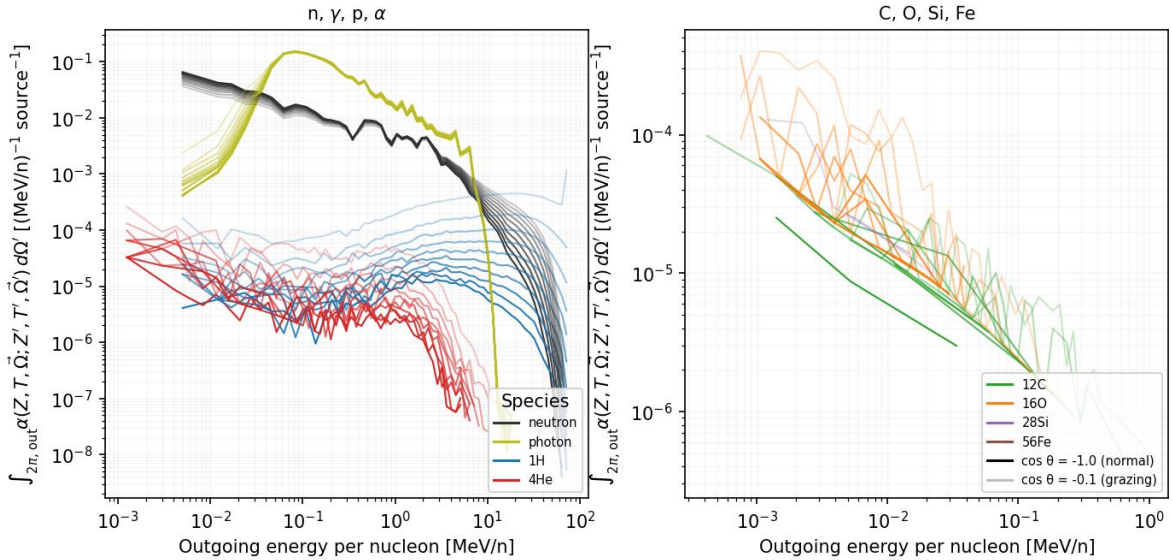


Figure A.62: Differential number albedo response function for a 85.01 MeV n^{-1} ^{1}H primary, shown for all ten simulated incident polar cosine bins ($\cos\theta = -1.0$ to -0.1).

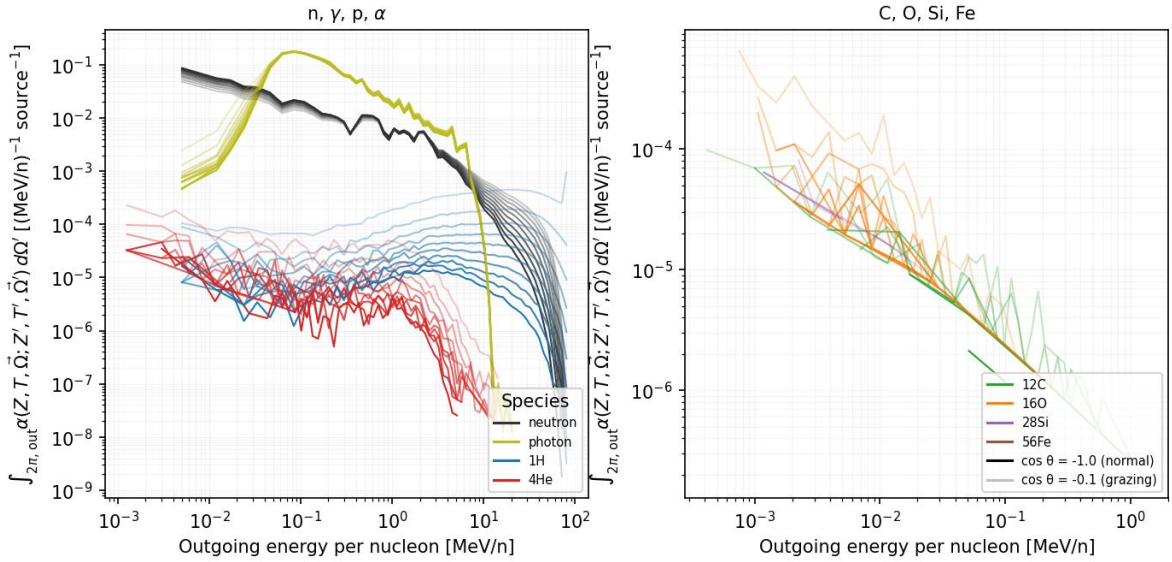


Figure A.63: Differential number albedo response function for a 95.41 MeV n^{-1} ^{1}H primary, shown for all ten simulated incident polar cosine bins ($\cos\theta = -1.0$ to -0.1).

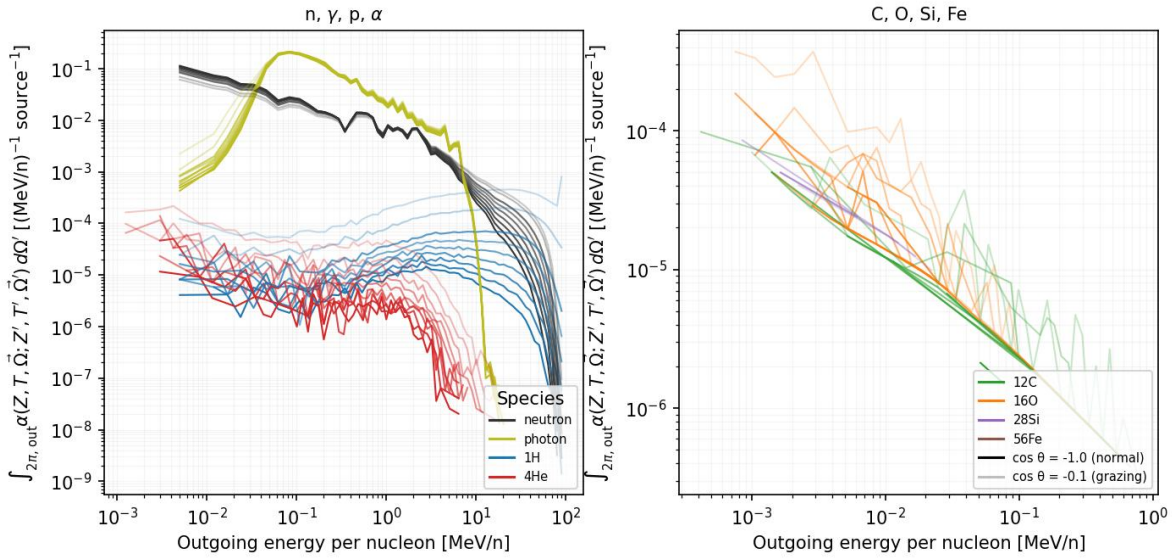


Figure A.64: Differential number albedo response function for a 107.1 MeV n^{-1} ^{1}H primary, shown for all ten simulated incident polar cosine bins ($\cos\theta = -1.0$ to -0.1).

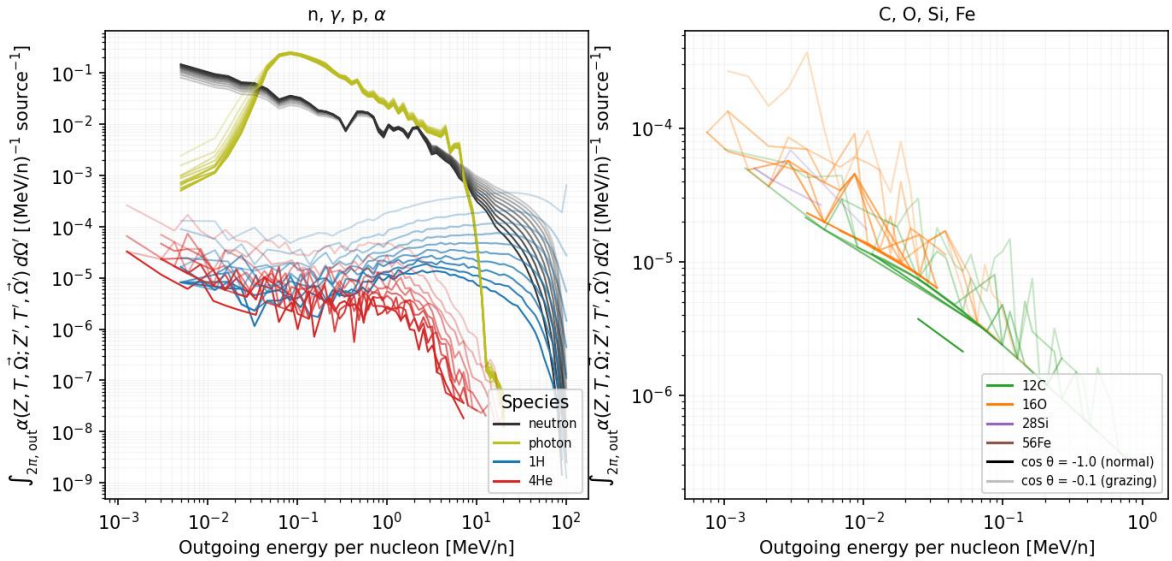


Figure A.65: Differential number albedo response function for a 120.4 MeV n^{-1} ^{1}H primary, shown for all ten simulated incident polar cosine bins ($\cos\theta = -1.0$ to -0.1).

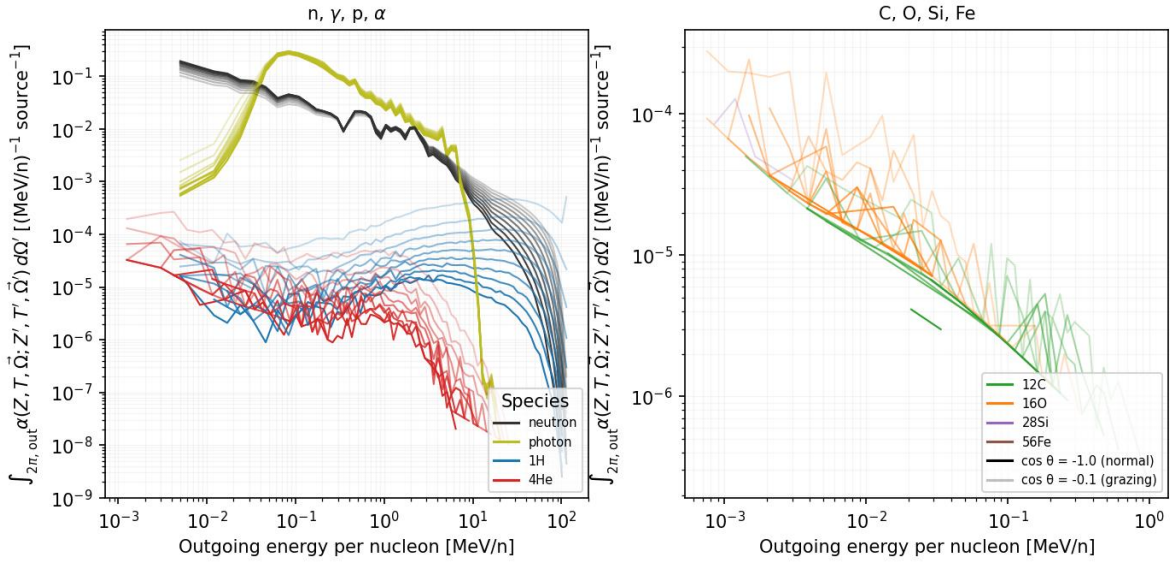


Figure A.66: Differential number albedo response function for a 135.3 MeV n^{-1} ^{1}H primary, shown for all ten simulated incident polar cosine bins ($\cos\theta = -1.0$ to -0.1).

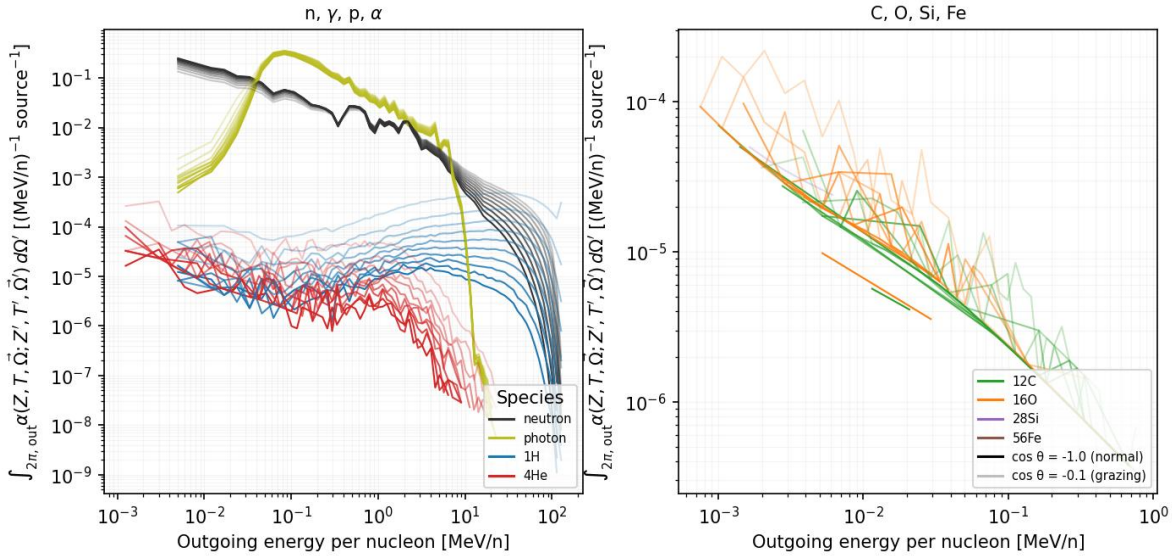


Figure A.67: Differential number albedo response function for a 152.2 MeV n^{-1} ^{1}H primary, shown for all ten simulated incident polar cosine bins ($\cos\theta = -1.0$ to -0.1).

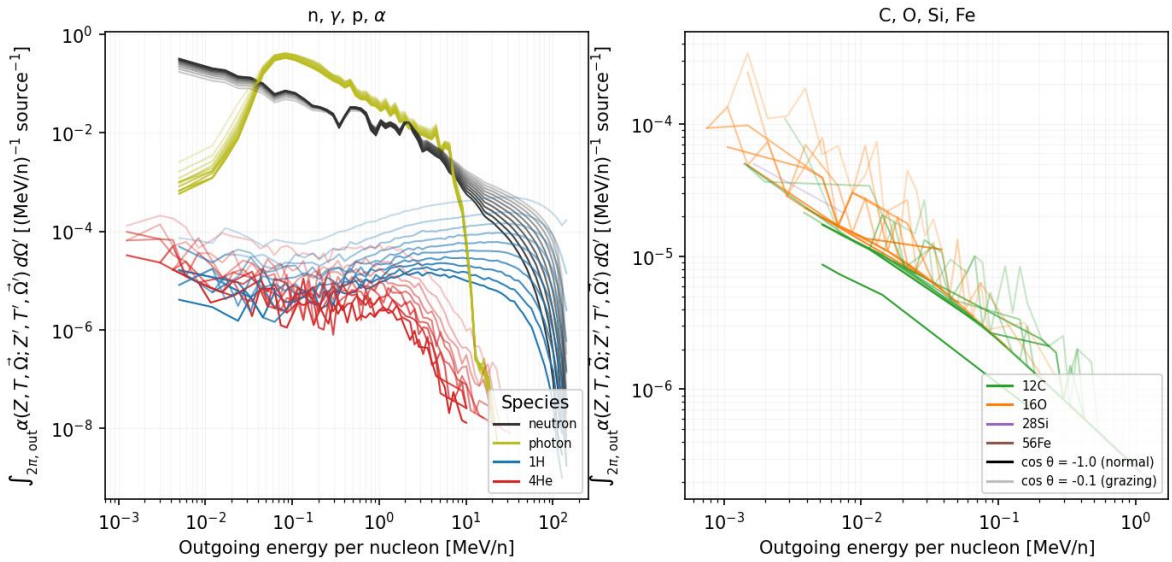


Figure A.68: Differential number albedo response function for a 171.4 MeV n^{-1} ^{1}H primary, shown for all ten simulated incident polar cosine bins ($\cos\theta = -1.0$ to -0.1).

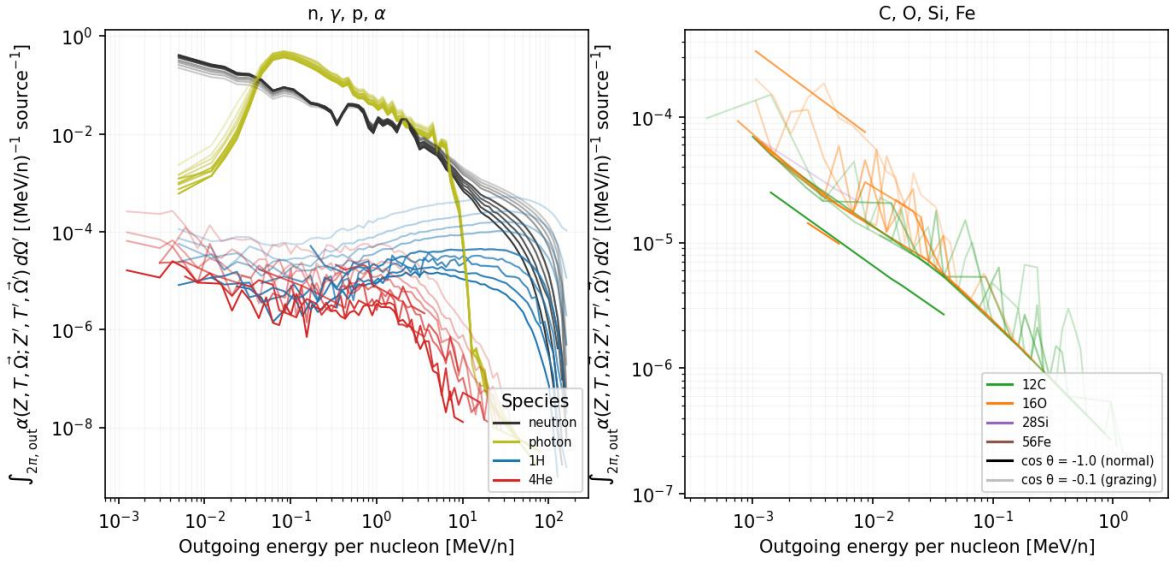


Figure A.69: Differential number albedo response function for a 193 MeV n^{-1} ^{1}H primary, shown for all ten simulated incident polar cosine bins ($\cos\theta = -1.0$ to -0.1).

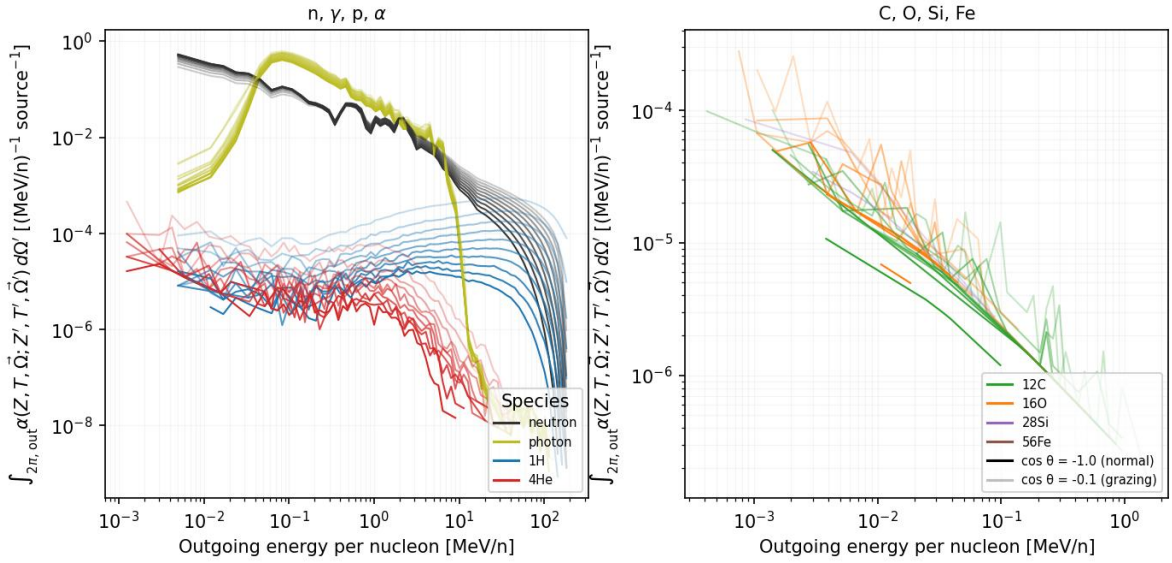


Figure A.70: Differential number albedo response function for a 217.9 MeV n^{-1} ^{1}H primary, shown for all ten simulated incident polar cosine bins ($\cos\theta = -1.0$ to -0.1).

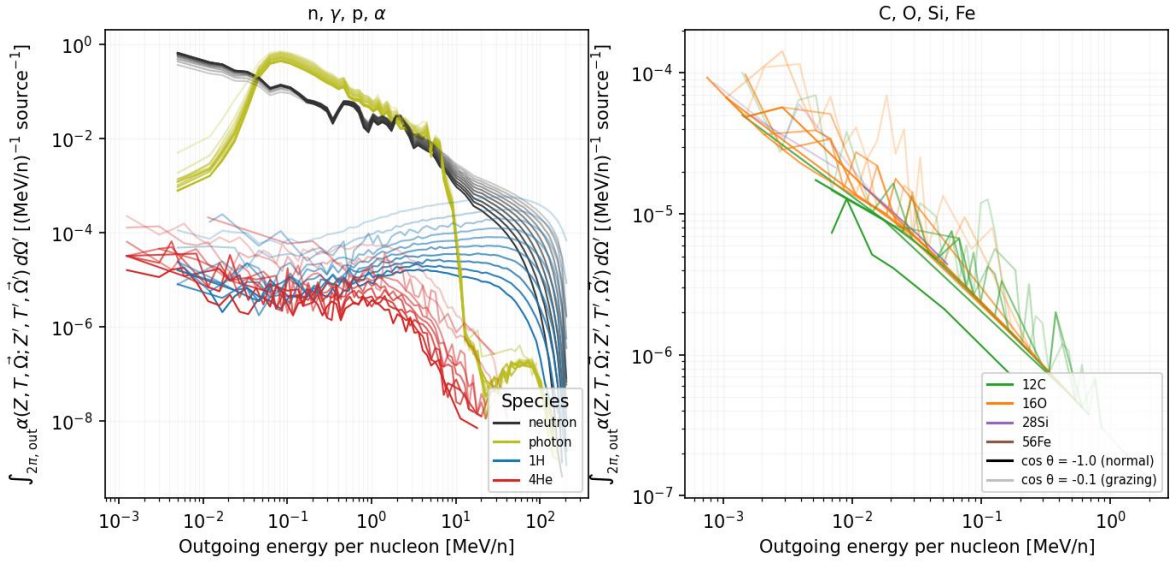


Figure A.71: Differential number albedo response function for a 246.2 MeV n^{-1} ^{1}H primary, shown for all ten simulated incident polar cosine bins ($\cos\theta = -1.0$ to -0.1).

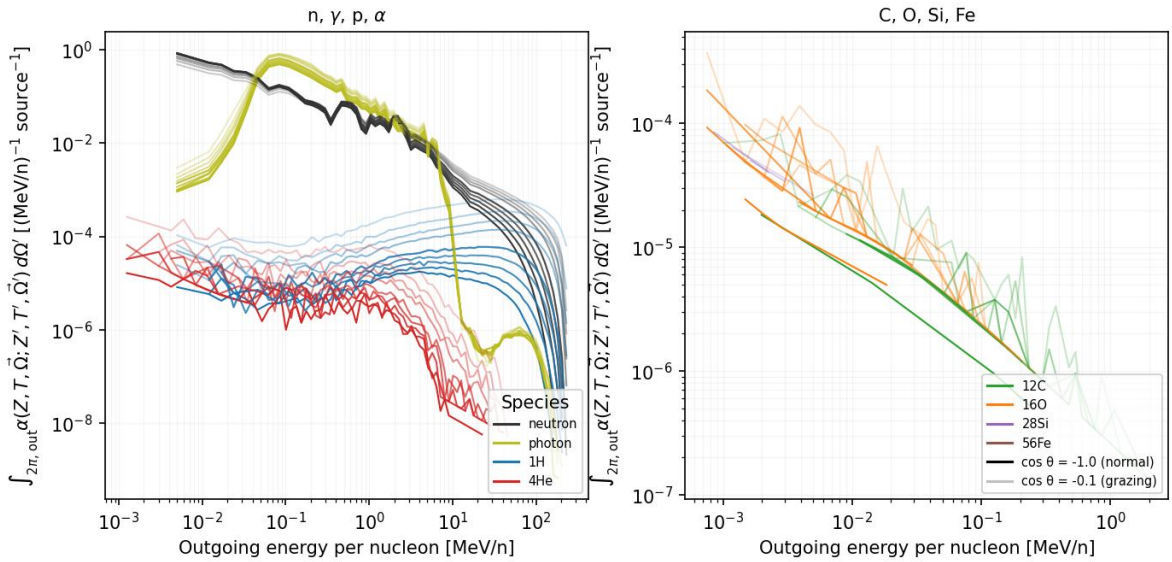


Figure A.72: Differential number albedo response function for a 278.1 MeV n^{-1} ^{1}H primary, shown for all ten simulated incident polar cosine bins ($\cos\theta = -1.0$ to -0.1).

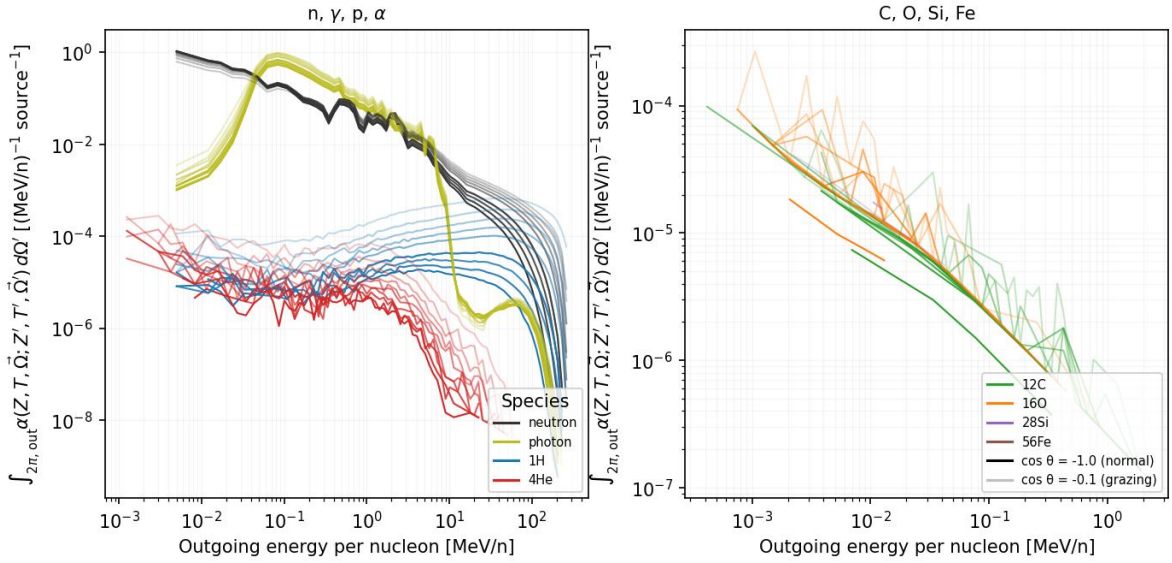


Figure A.73: Differential number albedo response function for a 314.7 MeV n^{-1} ^{1}H primary, shown for all ten simulated incident polar cosine bins ($\cos\theta = -1.0$ to -0.1).

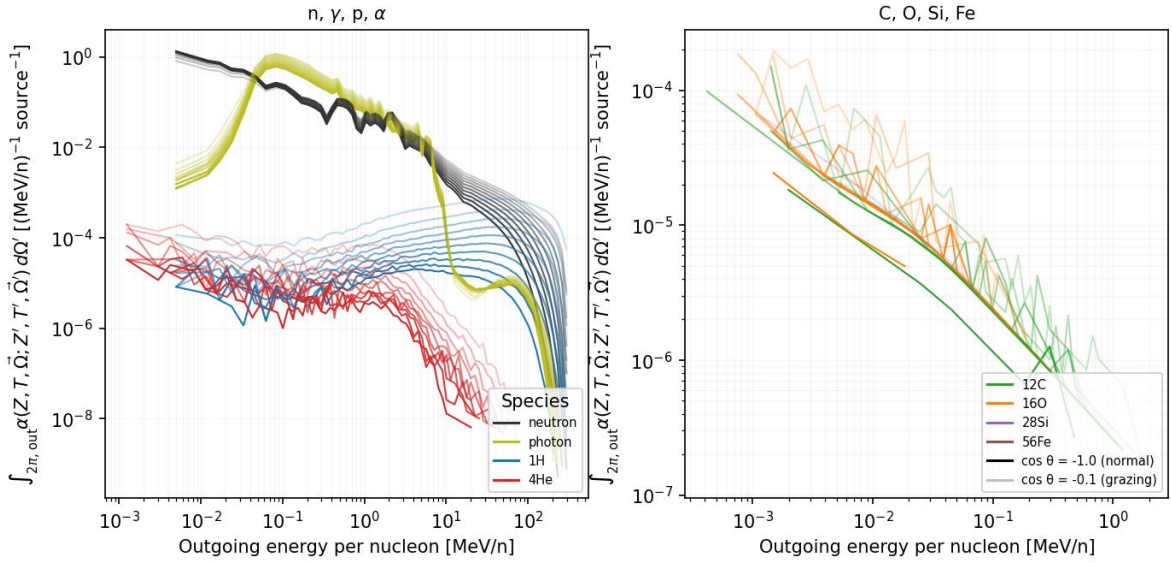


Figure A.74: Differential number albedo response function for a 357.1 MeV n^{-1} ^{1}H primary, shown for all ten simulated incident polar cosine bins ($\cos\theta = -1.0$ to -0.1).

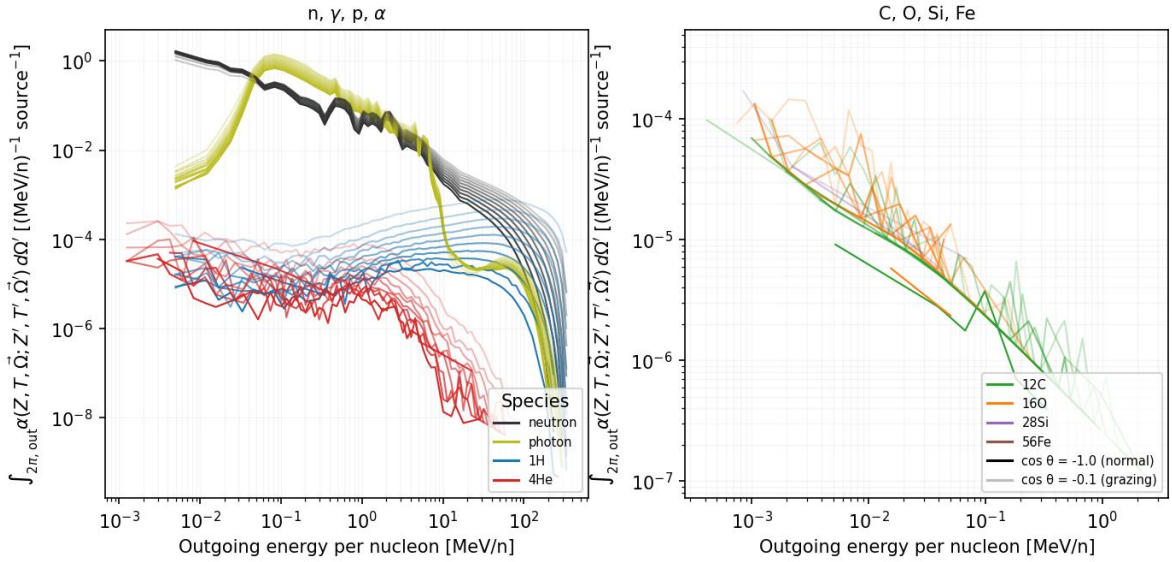


Figure A.75: Differential number albedo response function for a 405.3 MeV n^{-1} ^{1}H primary, shown for all ten simulated incident polar cosine bins ($\cos\theta = -1.0$ to -0.1).

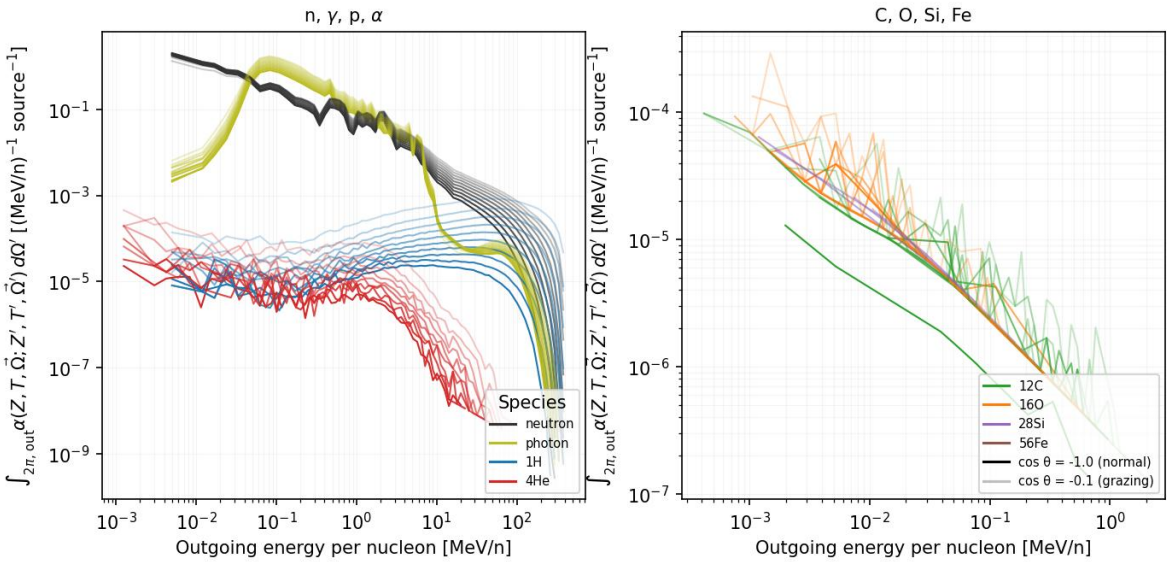


Figure A.76: Differential number albedo response function for a 461.8 MeV n^{-1} ^{1}H primary, shown for all ten simulated incident polar cosine bins ($\cos\theta = -1.0$ to -0.1).

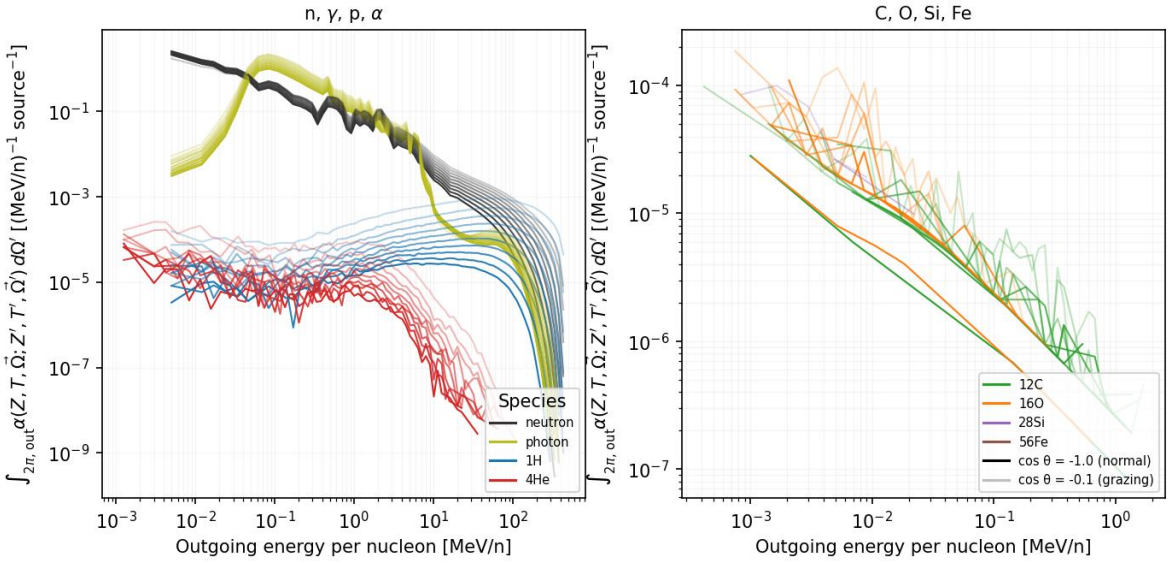


Figure A.77: Differential number albedo response function for a 526.8 MeV n^{-1} ^{1}H primary, shown for all ten simulated incident polar cosine bins ($\cos\theta = -1.0$ to -0.1).

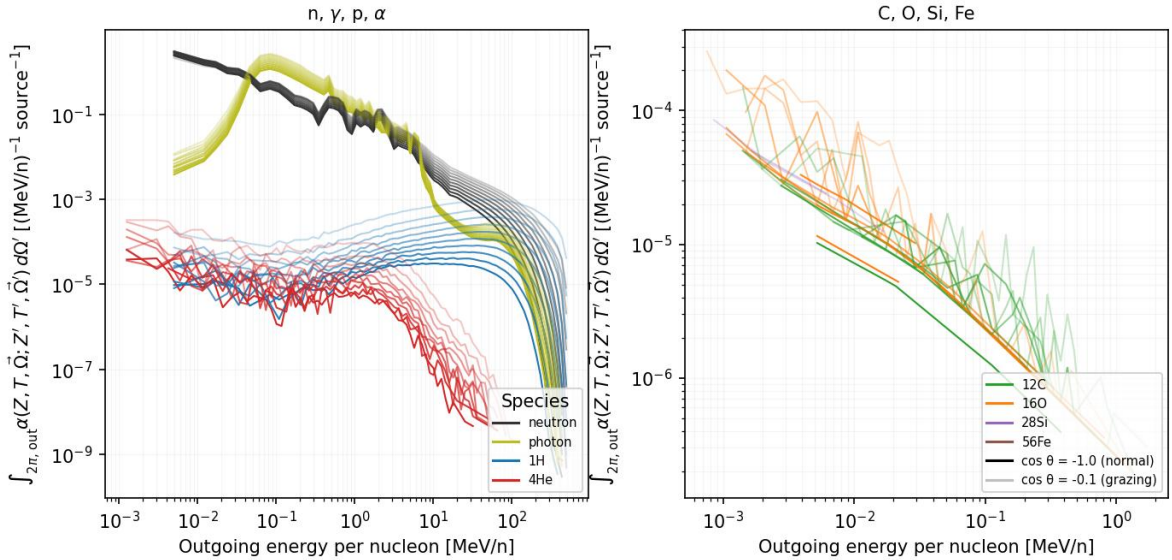


Figure A.78: Differential number albedo response function for a 602.5 MeV n^{-1} ^{1}H primary, shown for all ten simulated incident polar cosine bins ($\cos\theta = -1.0$ to -0.1).

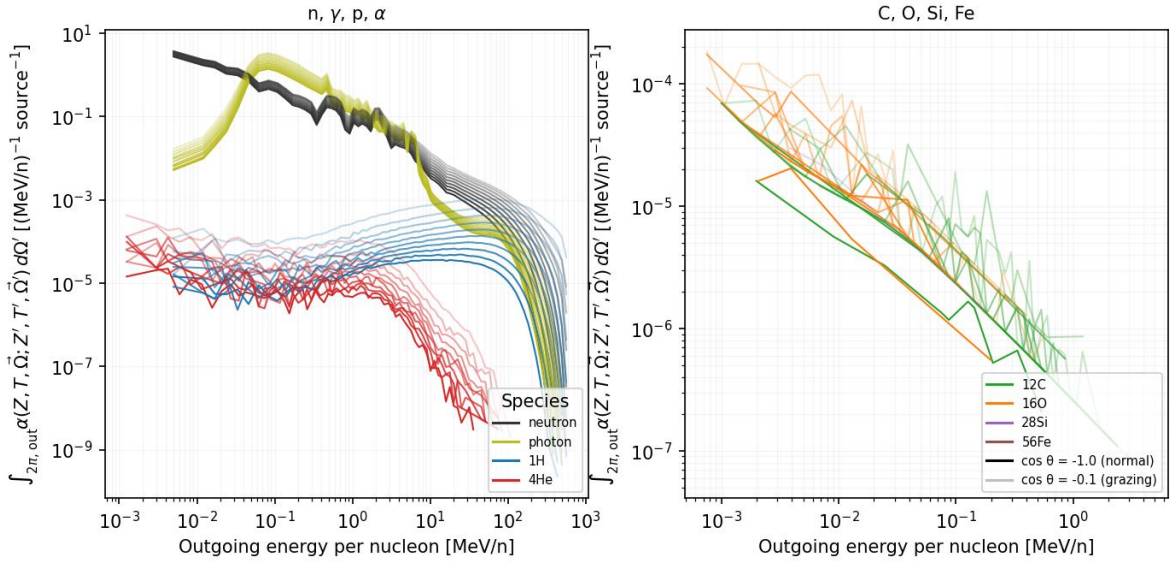


Figure A.79: Differential number albedo response function for a 691.3 MeV n^{-1} ^{1}H primary, shown for all ten simulated incident polar cosine bins ($\cos\theta = -1.0$ to -0.1).

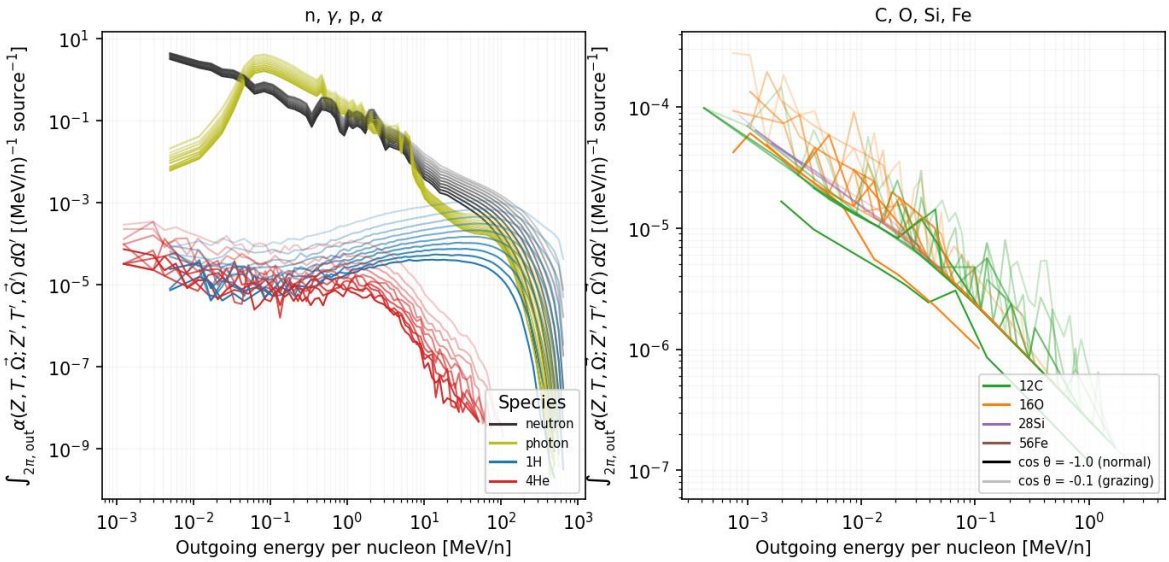


Figure A.80: Differential number albedo response function for a 795.7 MeV n^{-1} ^{1}H primary, shown for all ten simulated incident polar cosine bins ($\cos\theta = -1.0$ to -0.1).

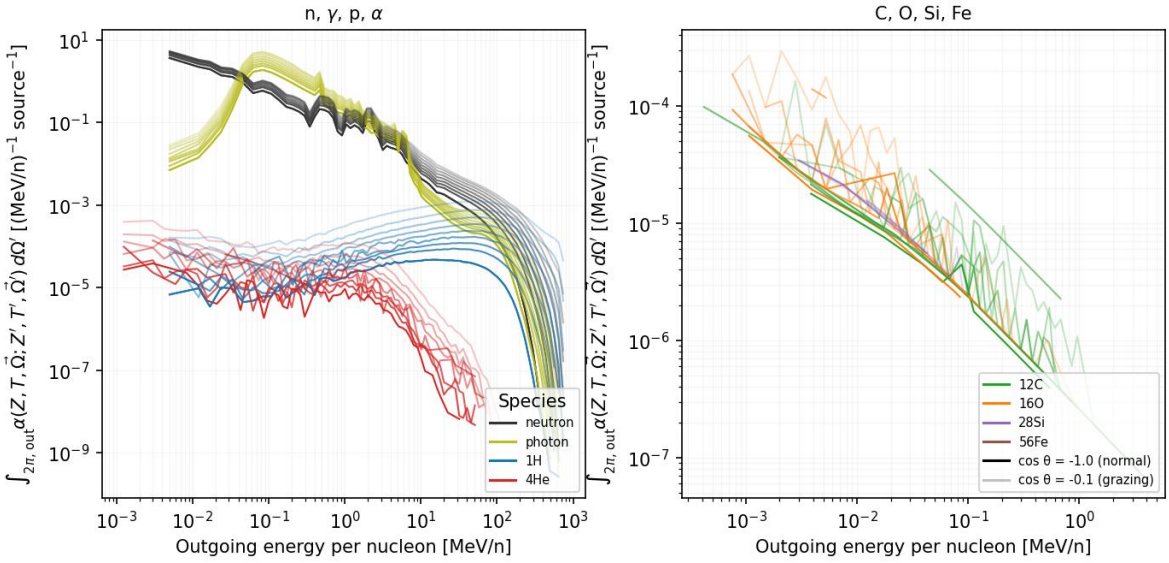


Figure A.81: Differential number albedo response function for a 919.2 MeV n^{-1} ^{1}H primary, shown for all ten simulated incident polar cosine bins ($\cos\theta = -1.0$ to -0.1).

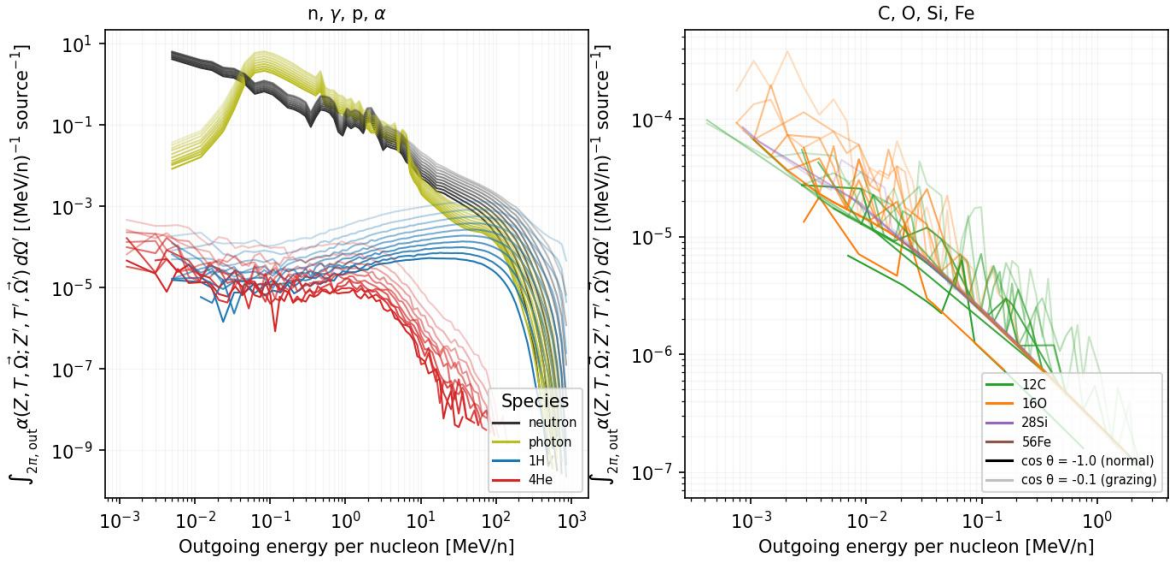


Figure A.82: Differential number albedo response function for a 1.068 GeV n^{-1} ^{1}H primary, shown for all ten simulated incident polar cosine bins ($\cos\theta = -1.0$ to -0.1).

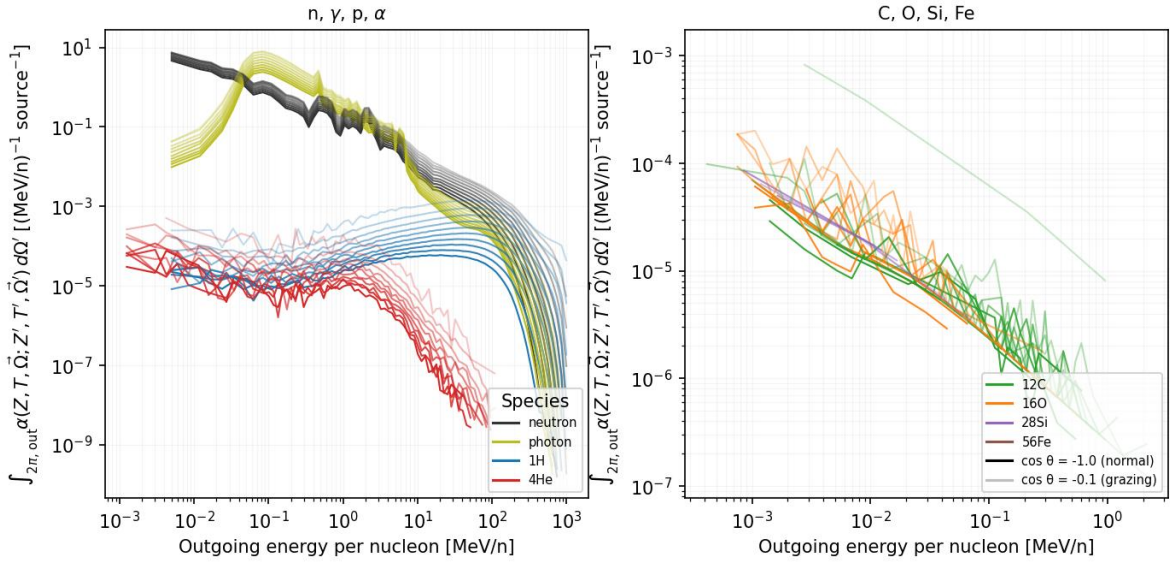


Figure A.83: Differential number albedo response function for a 1.246 GeV n^{-1} ^{1}H primary, shown for all ten simulated incident polar cosine bins ($\cos\theta = -1.0$ to -0.1).

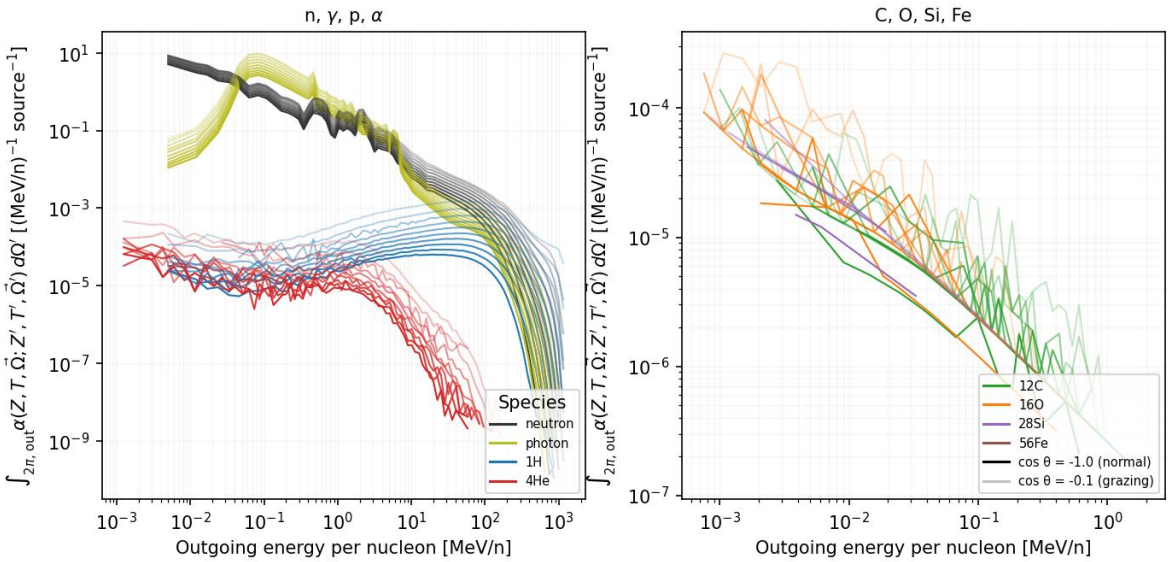


Figure A.84: Differential number albedo response function for a 1.453 GeV n^{-1} ^{1}H primary, shown for all ten simulated incident polar cosine bins ($\cos\theta = -1.0$ to -0.1).

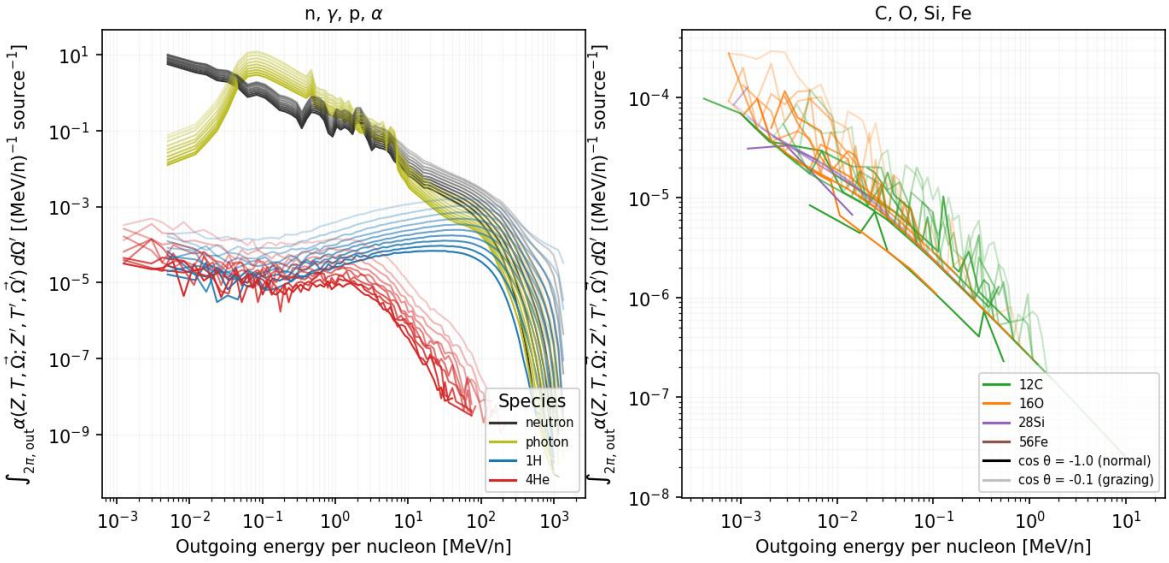


Figure A.85: Differential number albedo response function for a 1.71 GeV n^{-1} ^{1}H primary, shown for all ten simulated incident polar cosine bins ($\cos\theta = -1.0$ to -0.1).

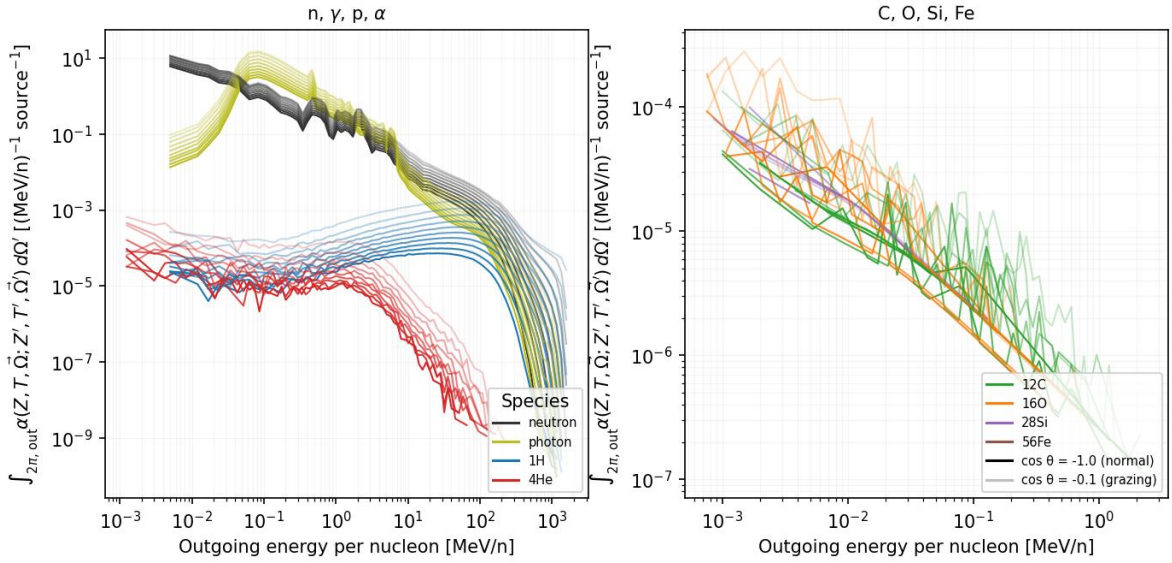


Figure A.86: Differential number albedo response function for a 2.016 GeV n^{-1} ^{1}H primary, shown for all ten simulated incident polar cosine bins ($\cos\theta = -1.0$ to -0.1).

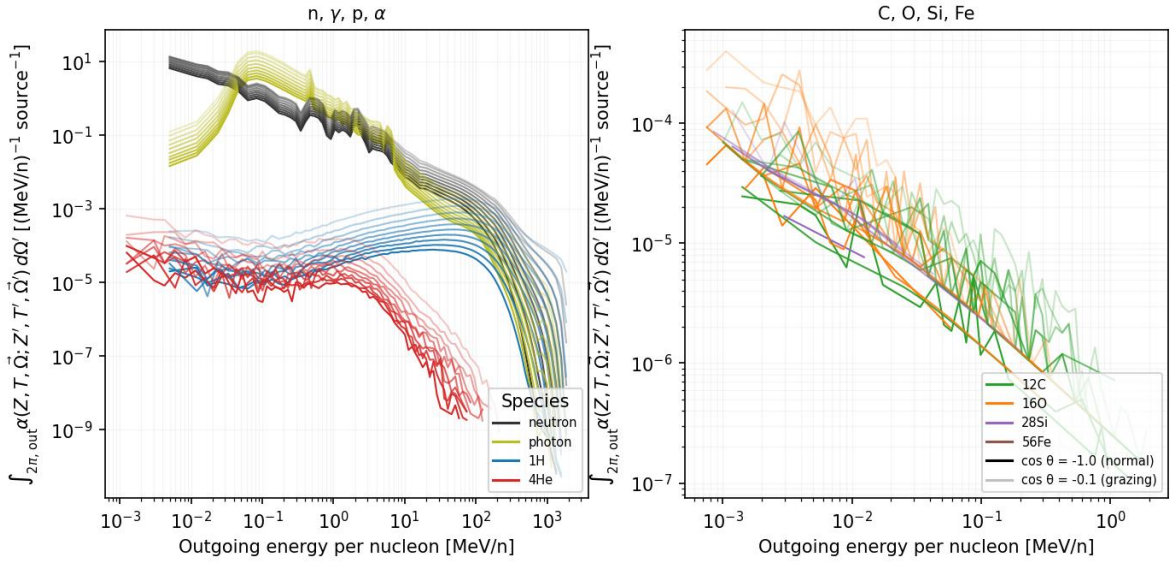


Figure A.87: Differential number albedo response function for a 2.397 GeV n^{-1} ^{1}H primary, shown for all ten simulated incident polar cosine bins ($\cos\theta = -1.0$ to -0.1).

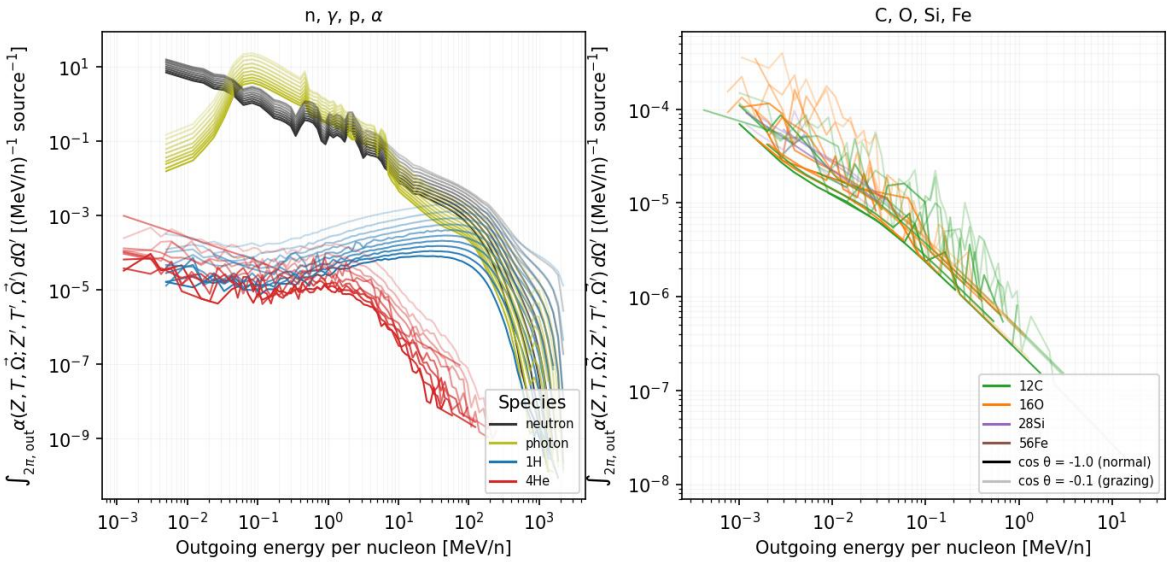


Figure A.88: Differential number albedo response function for a 2.863 GeV n^{-1} ^{1}H primary, shown for all ten simulated incident polar cosine bins ($\cos\theta = -1.0$ to -0.1).

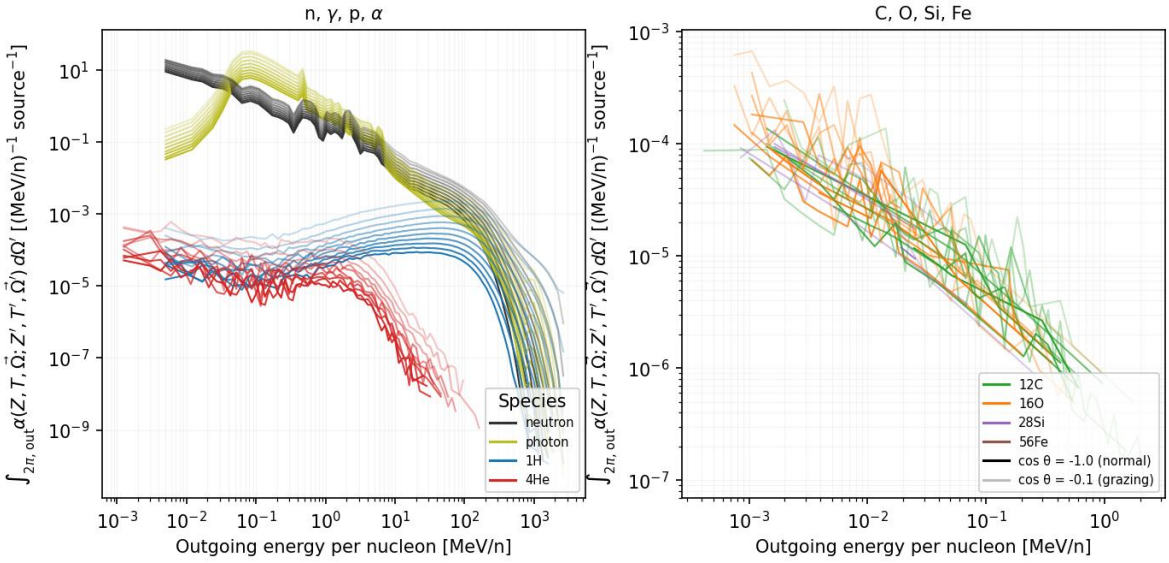


Figure A.89: Differential number albedo response function for a 3.444 GeV n^{-1} ^{1}H primary, shown for all ten simulated incident polar cosine bins ($\cos\theta = -1.0$ to -0.1).

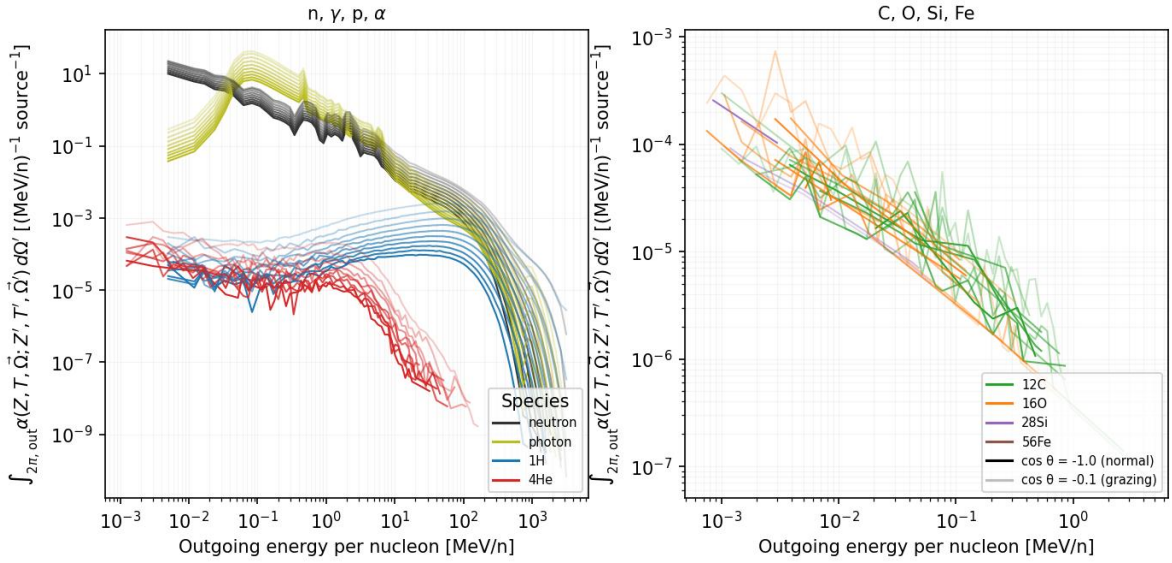


Figure A.90: Differential number albedo response function for a 4.156 GeV n^{-1} ^{1}H primary, shown for all ten simulated incident polar cosine bins ($\cos\theta = -1.0$ to -0.1).

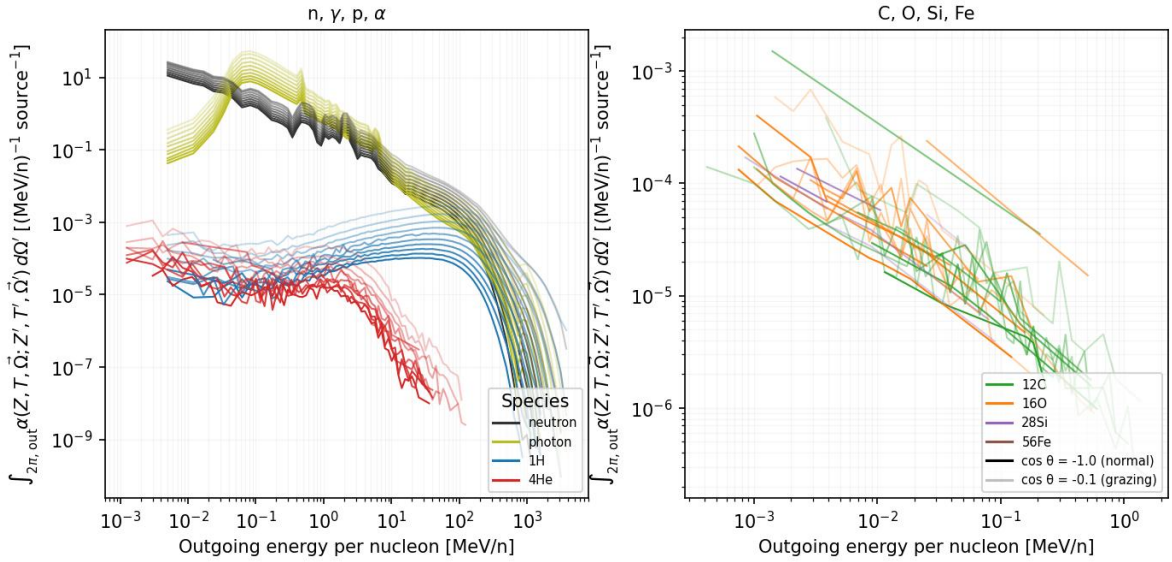


Figure A.91: Differential number albedo response function for a 5.04 GeV n^{-1} ^{1}H primary, shown for all ten simulated incident polar cosine bins ($\cos\theta = -1.0$ to -0.1).

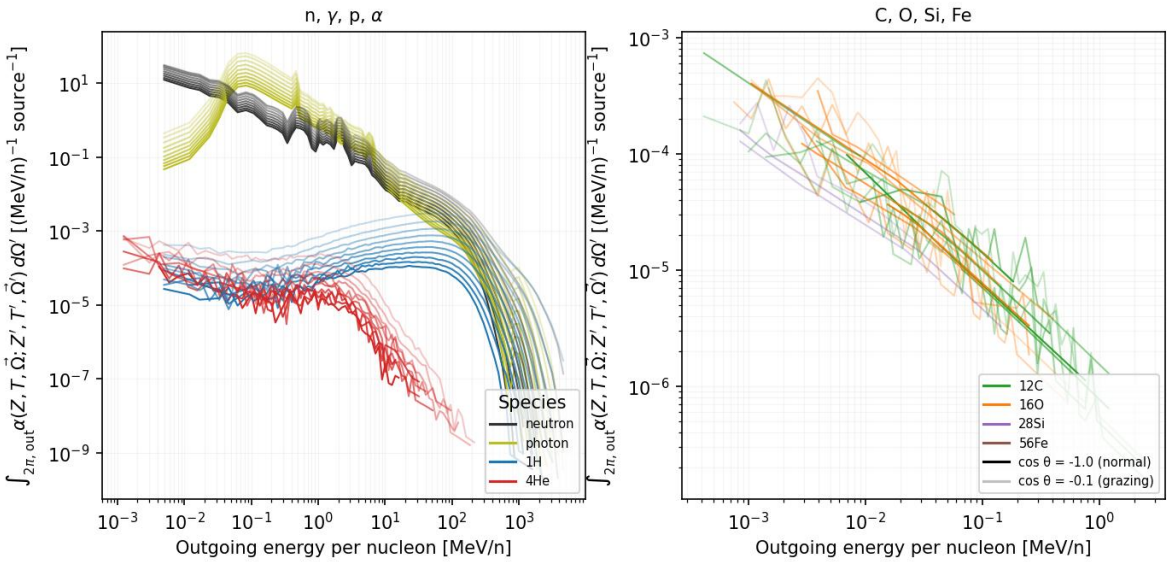


Figure A.92: Differential number albedo response function for a 6.134 GeV n^{-1} ^{1}H primary, shown for all ten simulated incident polar cosine bins ($\cos\theta = -1.0$ to -0.1).

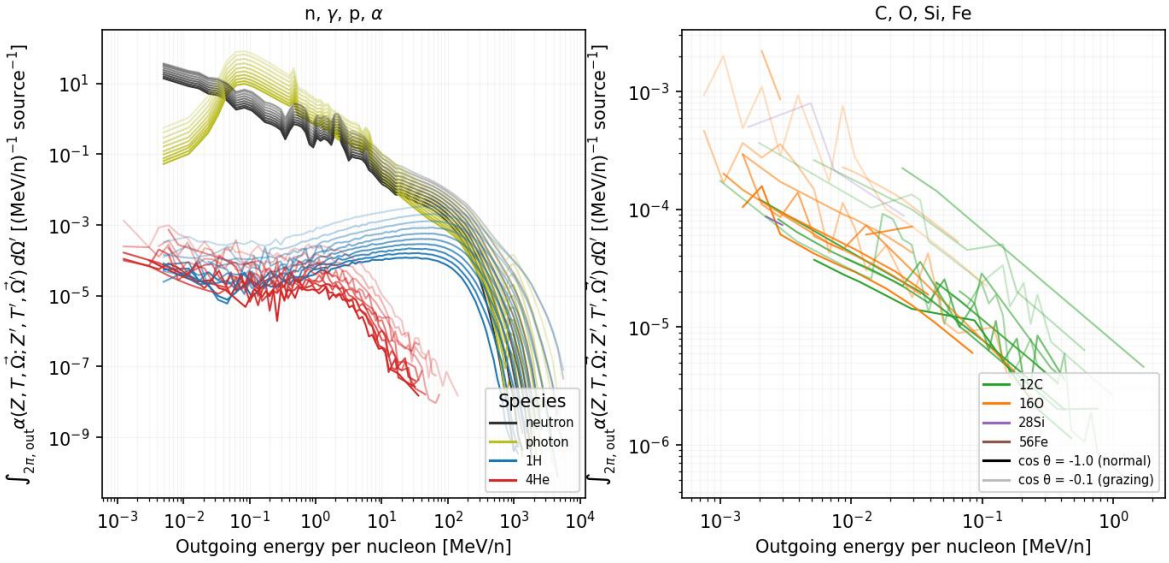


Figure A.93: Differential number albedo response function for a 7.488 GeV n^{-1} ^{1}H primary, shown for all ten simulated incident polar cosine bins ($\cos\theta = -1.0$ to -0.1).

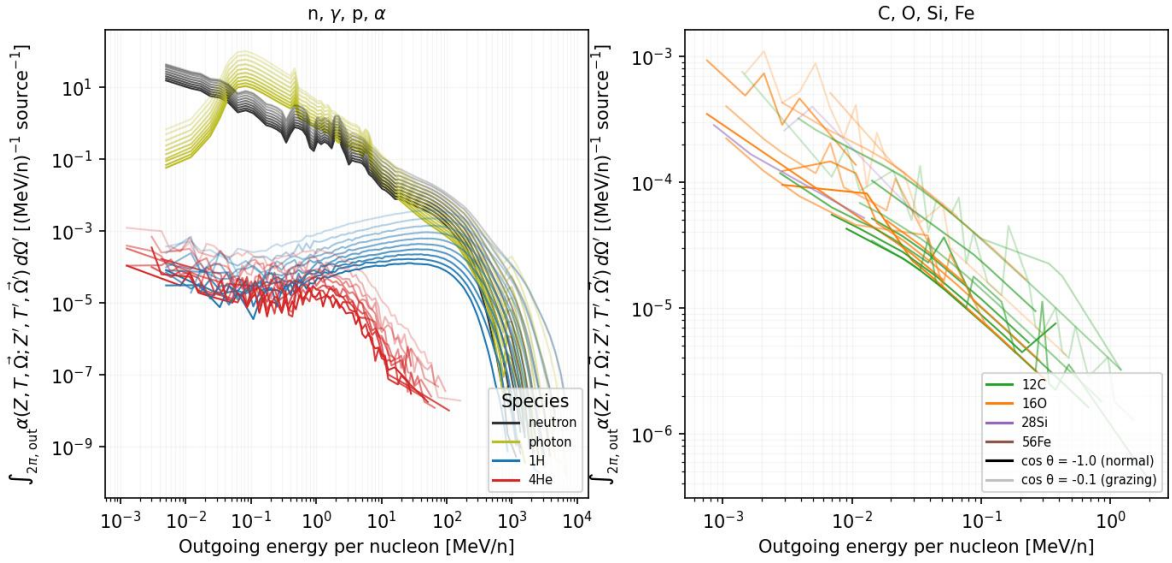


Figure A.94: Differential number albedo response function for a 9.167 GeV n^{-1} ^{1}H primary, shown for all ten simulated incident polar cosine bins ($\cos\theta = -1.0$ to -0.1).

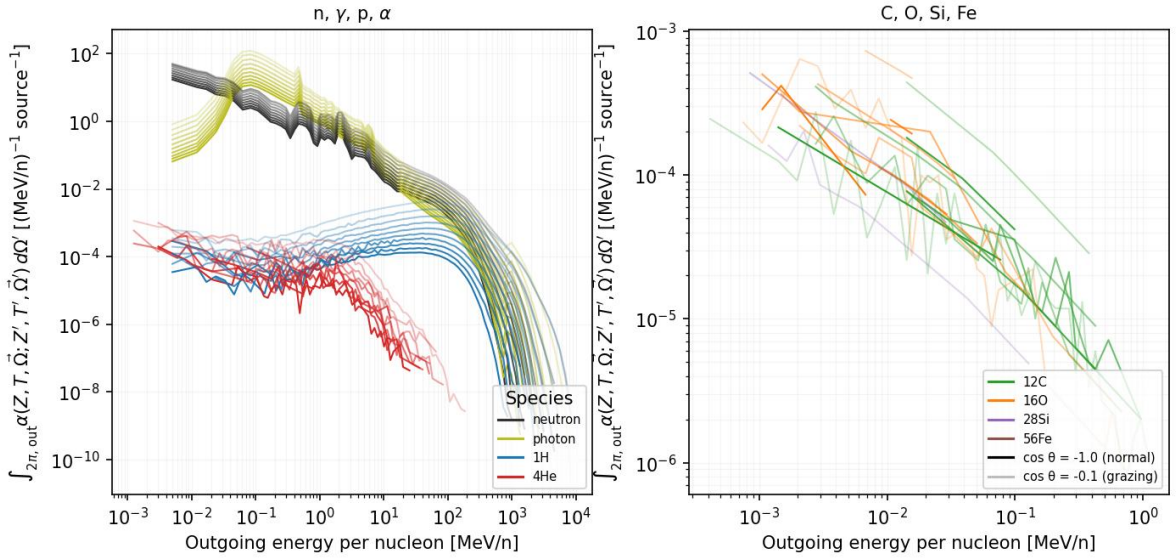


Figure A.95: Differential number albedo response function for a 11.26 GeV n^{-1} ^{1}H primary, shown for all ten simulated incident polar cosine bins ($\cos\theta = -1.0$ to -0.1).

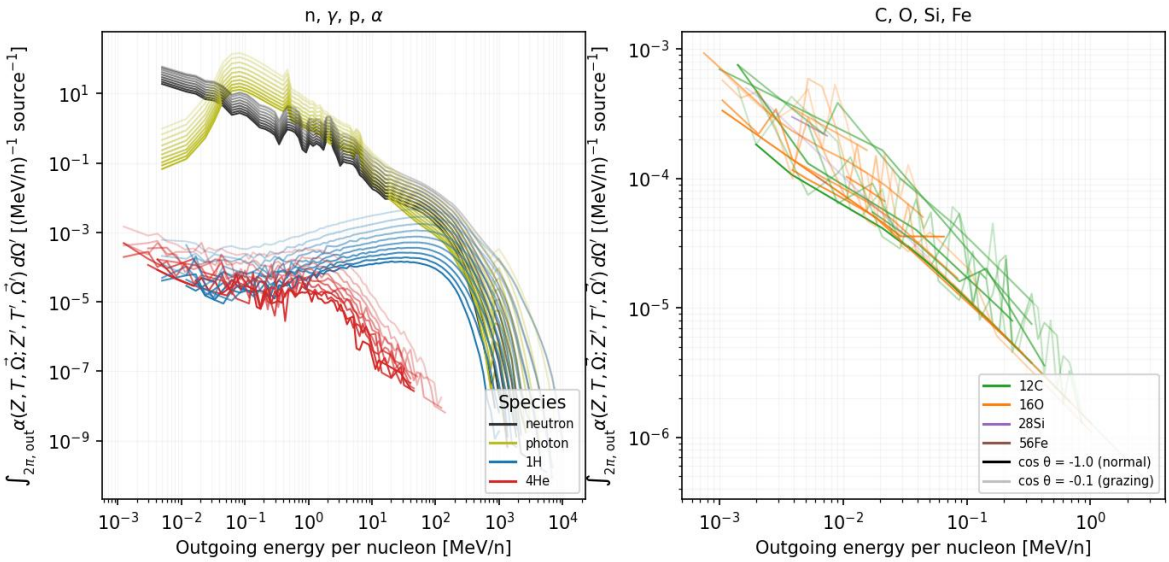


Figure A.96: Differential number albedo response function for a 13.86 GeV n^{-1} ^{1}H primary, shown for all ten simulated incident polar cosine bins ($\cos\theta = -1.0$ to -0.1).

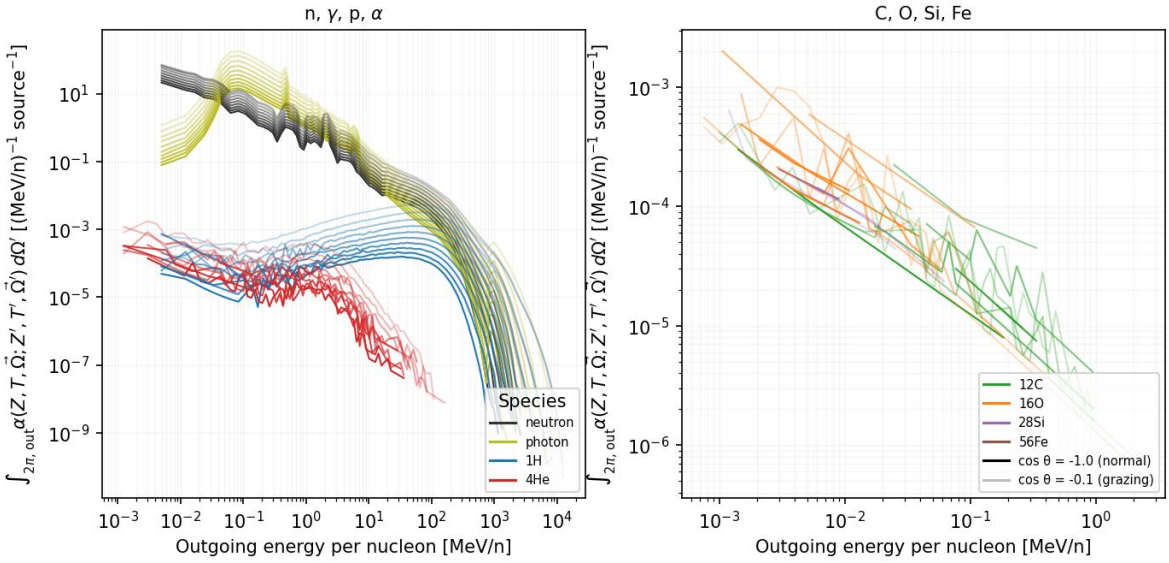


Figure A.97: Differential number albedo response function for a 17.09 GeV n^{-1} ^{1}H primary, shown for all ten simulated incident polar cosine bins ($\cos\theta = -1.0$ to -0.1).

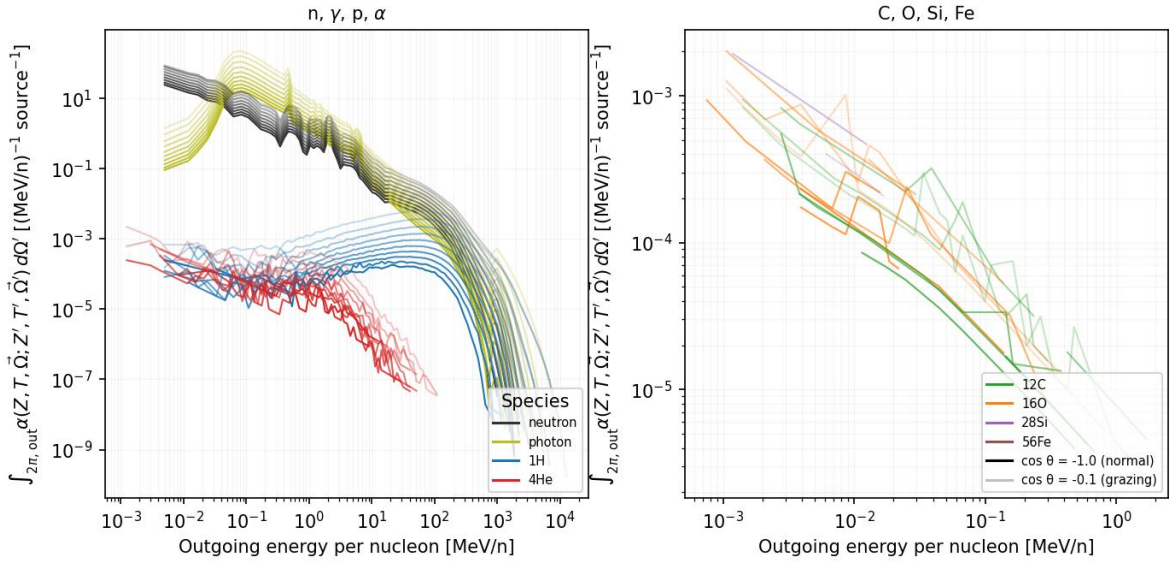


Figure A.98: Differential number albedo response function for a 21.12 GeV n^{-1} ^{1}H primary, shown for all ten simulated incident polar cosine bins ($\cos\theta = -1.0$ to -0.1).

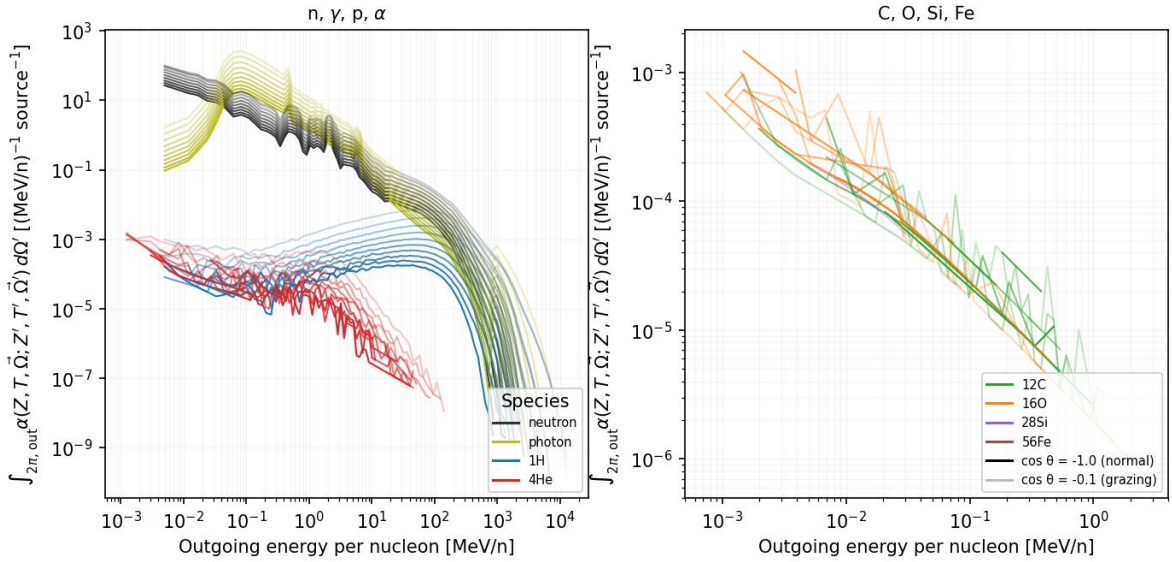


Figure A.99: Differential number albedo response function for a 26.15 GeV n^{-1} ^{1}H primary, shown for all ten simulated incident polar cosine bins ($\cos\theta = -1.0$ to -0.1).

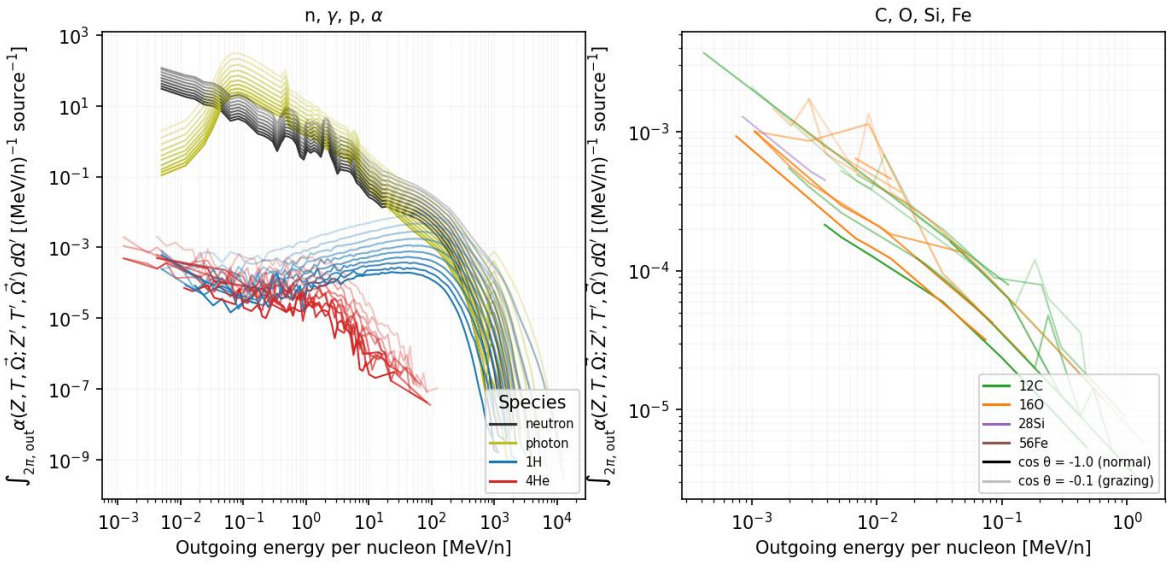


Figure A.100: Differential number albedo response function for a 32.44 GeV n^{-1} ^{1}H primary, shown for all ten simulated incident polar cosine bins ($\cos\theta = -1.0$ to -0.1).

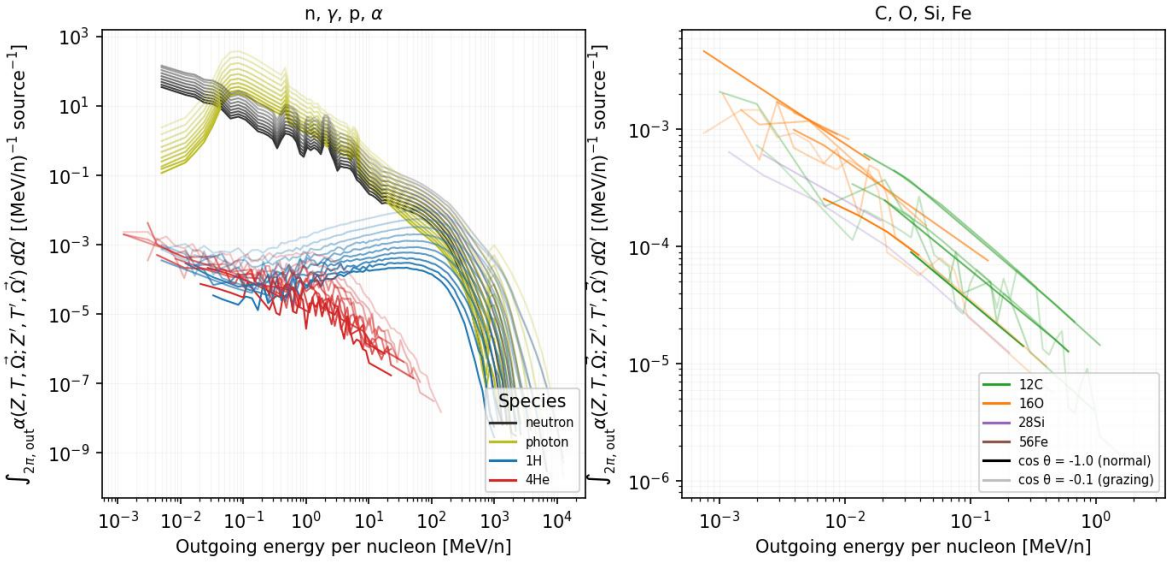


Figure A.101: Differential number albedo response function for a 40.23 GeV n^{-1} ^{1}H primary, shown for all ten simulated incident polar cosine bins ($\cos\theta = -1.0$ to -0.1).

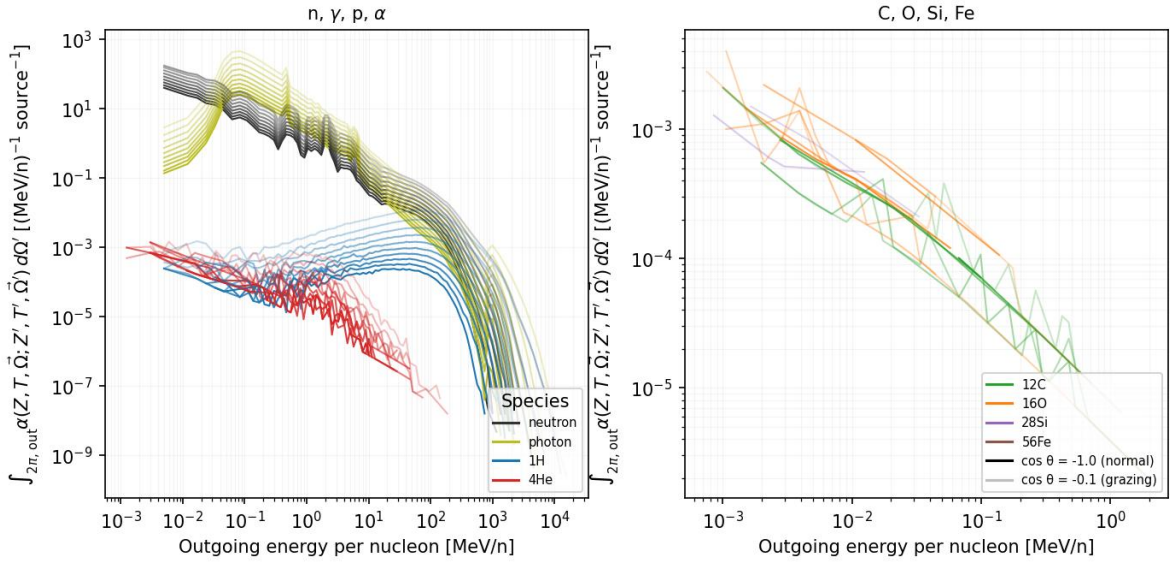


Figure A.102: Differential number albedo response function for a 50 GeV n^{-1} ^{1}H primary, shown for all ten simulated incident polar cosine bins ($\cos\theta = -1.0$ to -0.1).

^{4}He Primary Response Functions

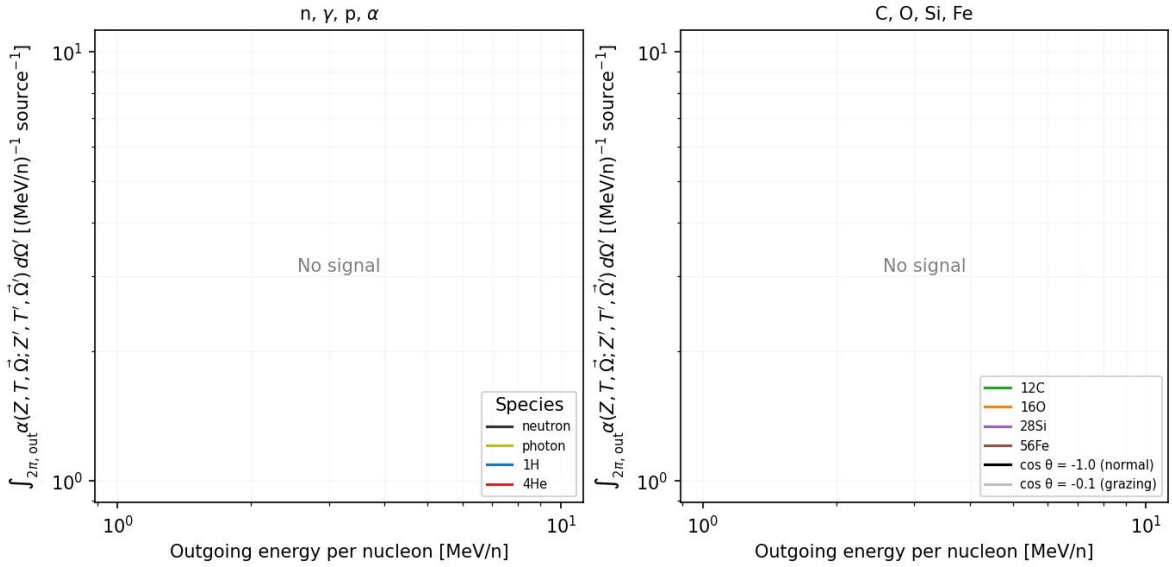


Figure A.103: Differential number albedo response function for a 10 keV n^{-1} ^{4}He primary, shown for all ten simulated incident polar cosine bins ($\cos\theta = -1.0$ to -0.1).

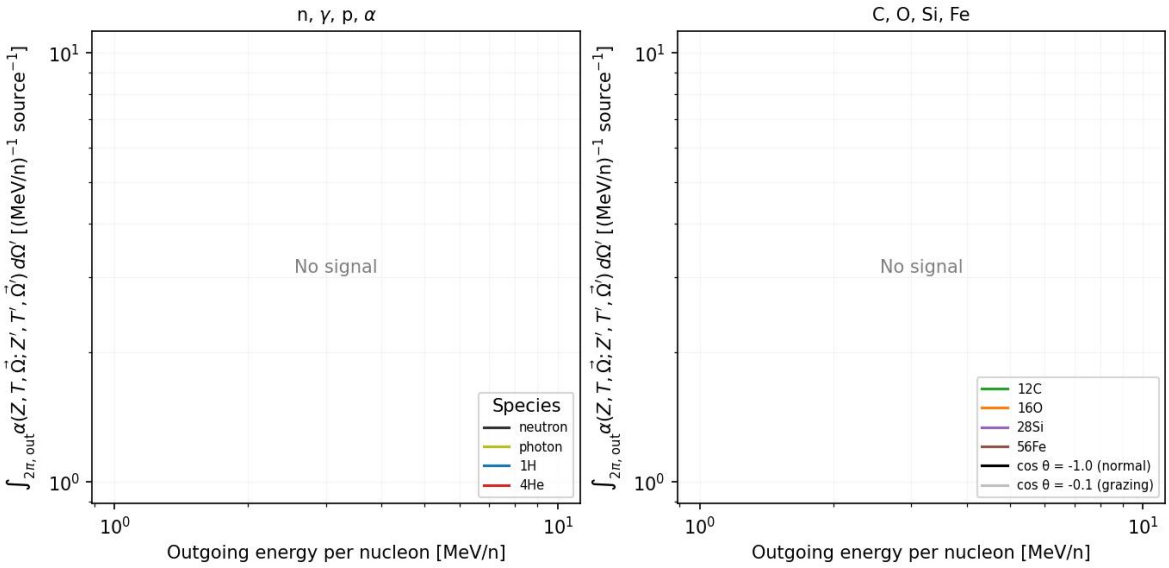


Figure A.104: Differential number albedo response function for a 14.1 keV n^{-1} ^{4}He primary, shown for all ten simulated incident polar cosine bins ($\cos\theta = -1.0$ to -0.1).

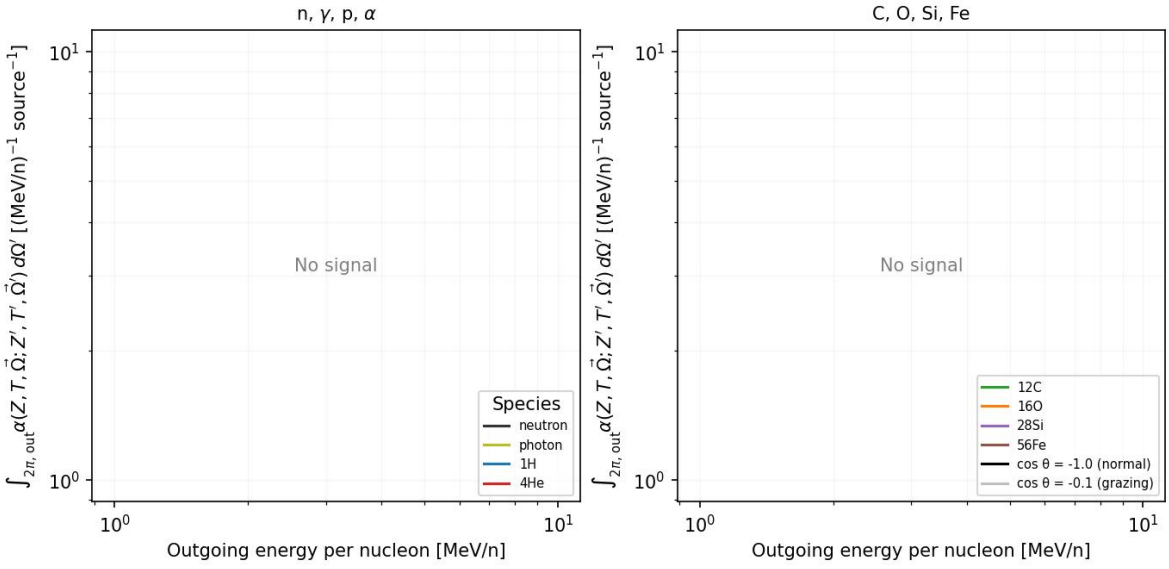


Figure A.105: Differential number albedo response function for a 19.8 keV n^{-1} ^{4}He primary, shown for all ten simulated incident polar cosine bins ($\cos\theta = -1.0$ to -0.1).

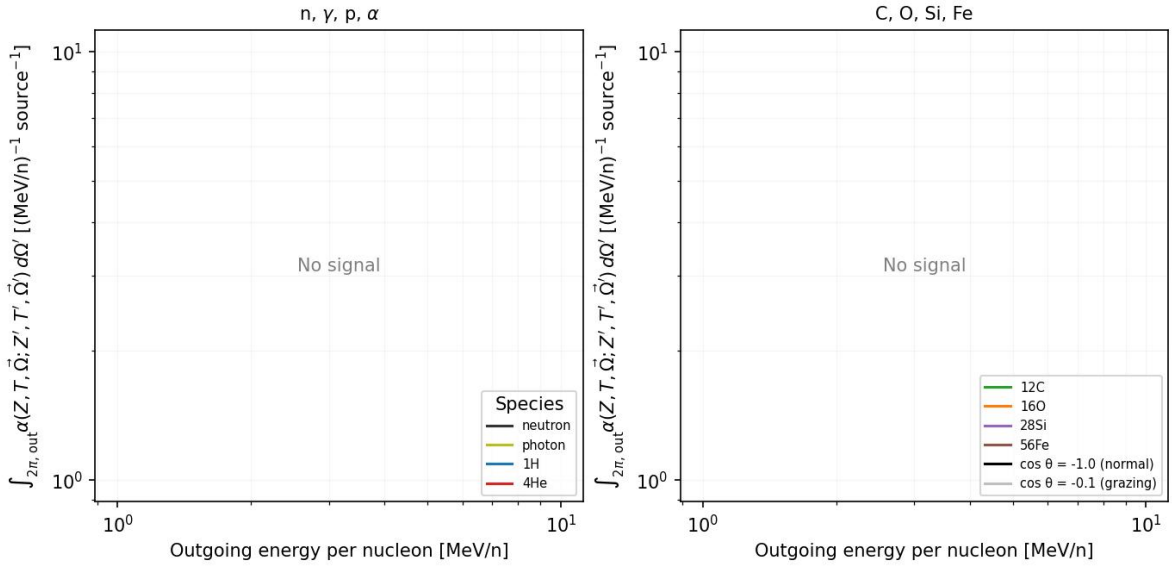


Figure A.106: Differential number albedo response function for a 27.8 keV n^{-1} ^{4}He primary, shown for all ten simulated incident polar cosine bins ($\cos\theta = -1.0$ to -0.1).

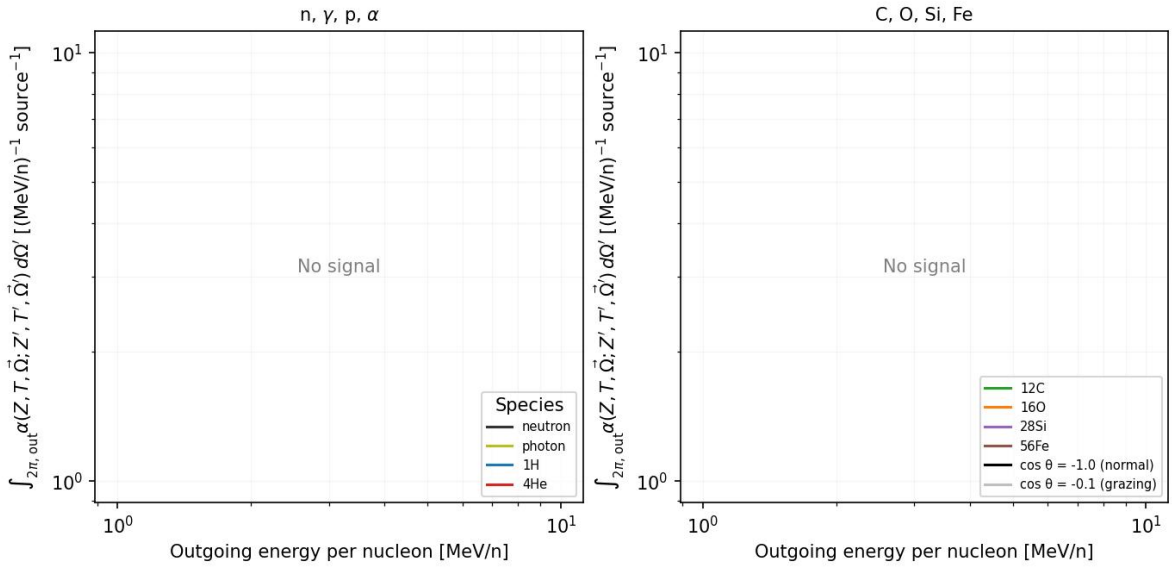


Figure A.107: Differential number albedo response function for a 38.8 keV n^{-1} ^{4}He primary, shown for all ten simulated incident polar cosine bins ($\cos\theta = -1.0$ to -0.1).

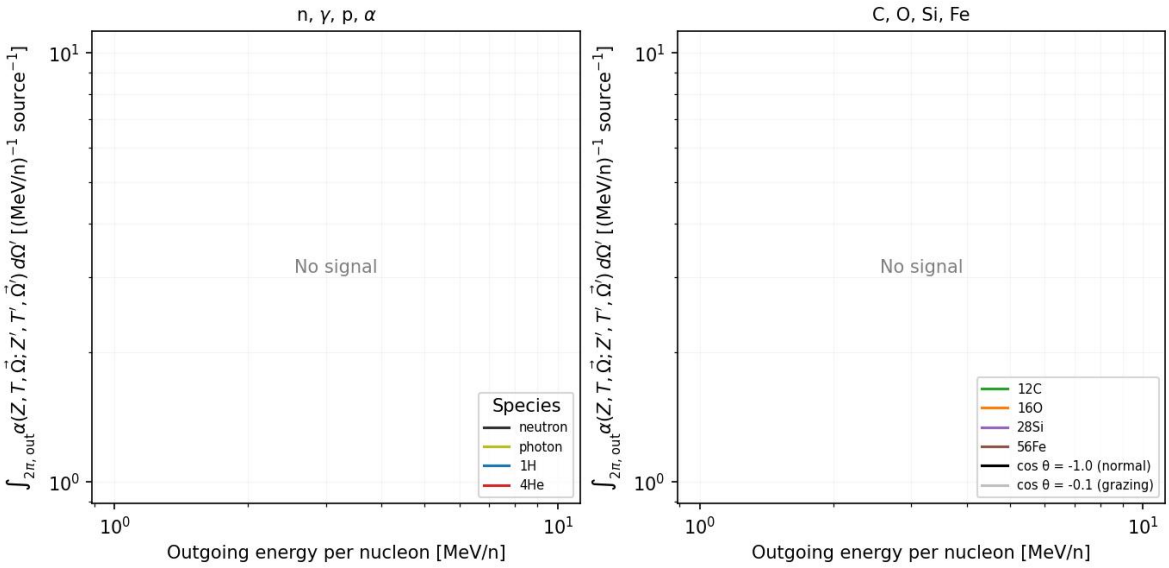


Figure A.108: Differential number albedo response function for a 53.3 keV n^{-1} ^{4}He primary, shown for all ten simulated incident polar cosine bins ($\cos\theta = -1.0$ to -0.1).

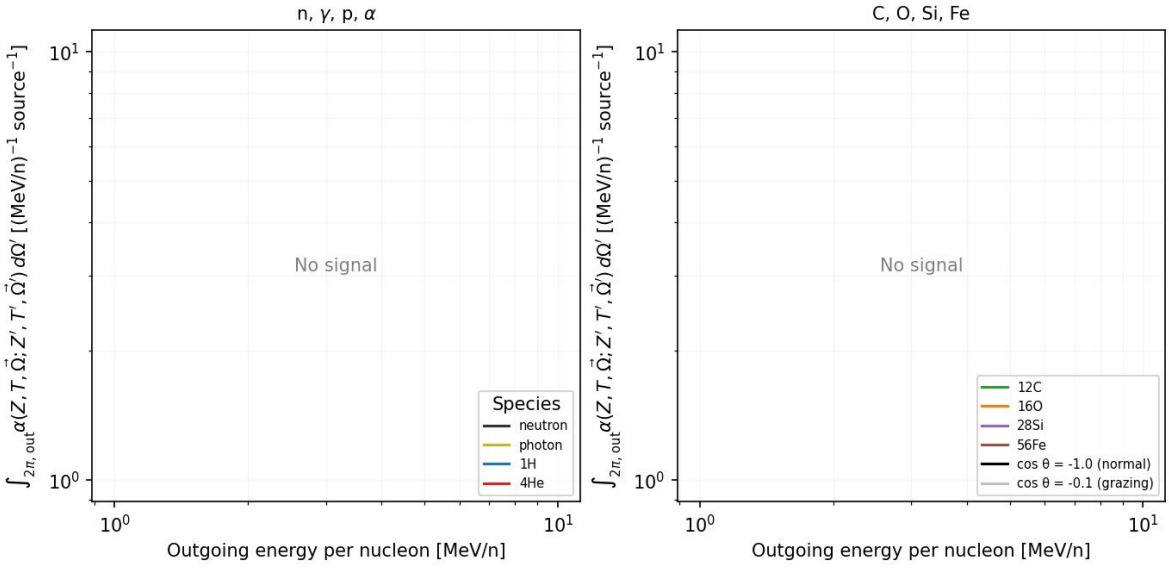


Figure A.109: Differential number albedo response function for a 72 keV n^{-1} ^{4}He primary, shown for all ten simulated incident polar cosine bins ($\cos\theta = -1.0$ to -0.1).

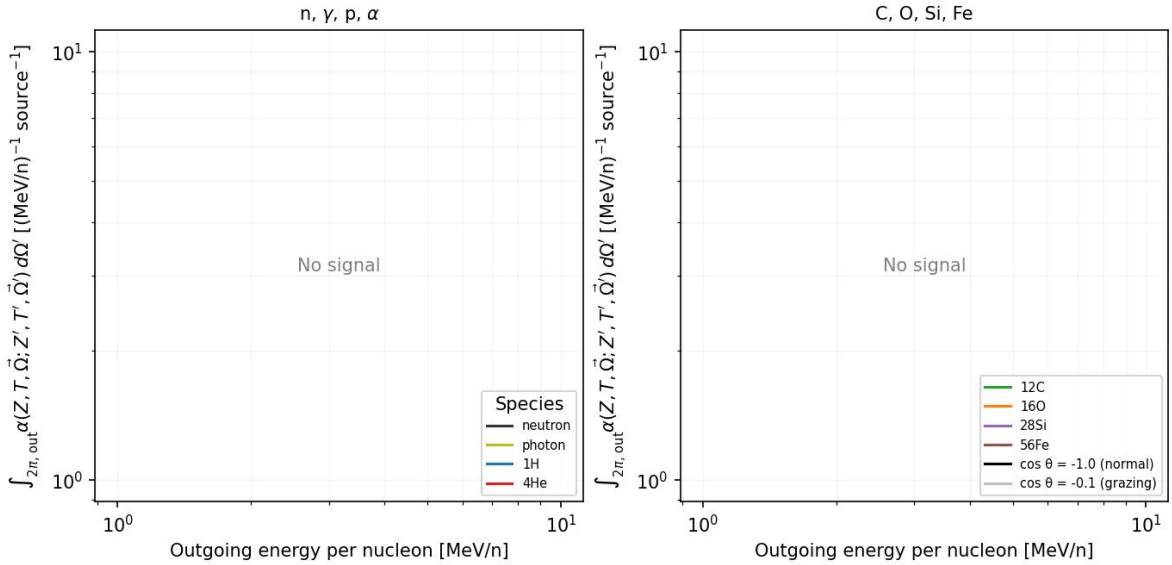


Figure A.110: Differential number albedo response function for a 95 keV n^{-1} ^{4}He primary, shown for all ten simulated incident polar cosine bins ($\cos\theta = -1.0$ to -0.1).

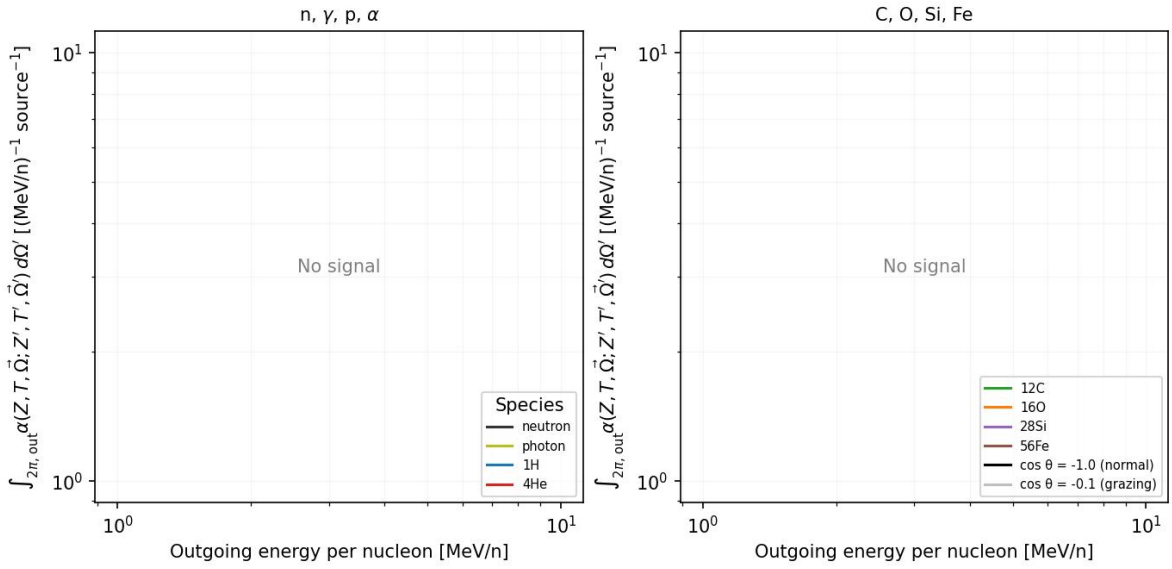


Figure A.111: Differential number albedo response function for a 122 keV n^{-1} ^{4}He primary, shown for all ten simulated incident polar cosine bins ($\cos\theta = -1.0$ to -0.1).

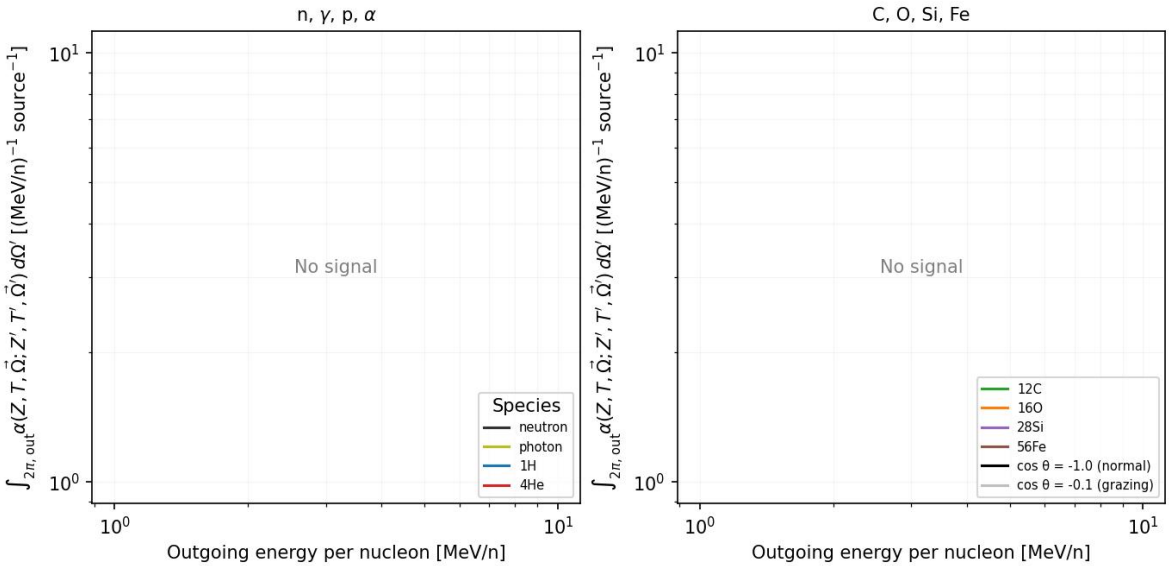


Figure A.112: Differential number albedo response function for a 154 keV n^{-1} ^{4}He primary, shown for all ten simulated incident polar cosine bins ($\cos\theta = -1.0$ to -0.1).

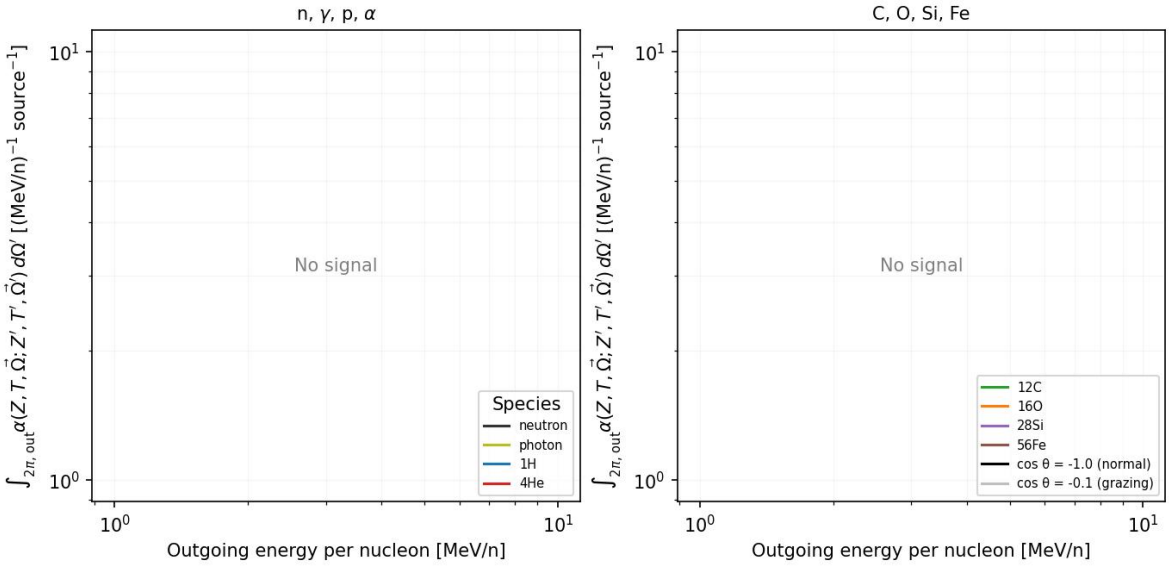


Figure A.113: Differential number albedo response function for a 189 keV n^{-1} ^{4}He primary, shown for all ten simulated incident polar cosine bins ($\cos\theta = -1.0$ to -0.1).

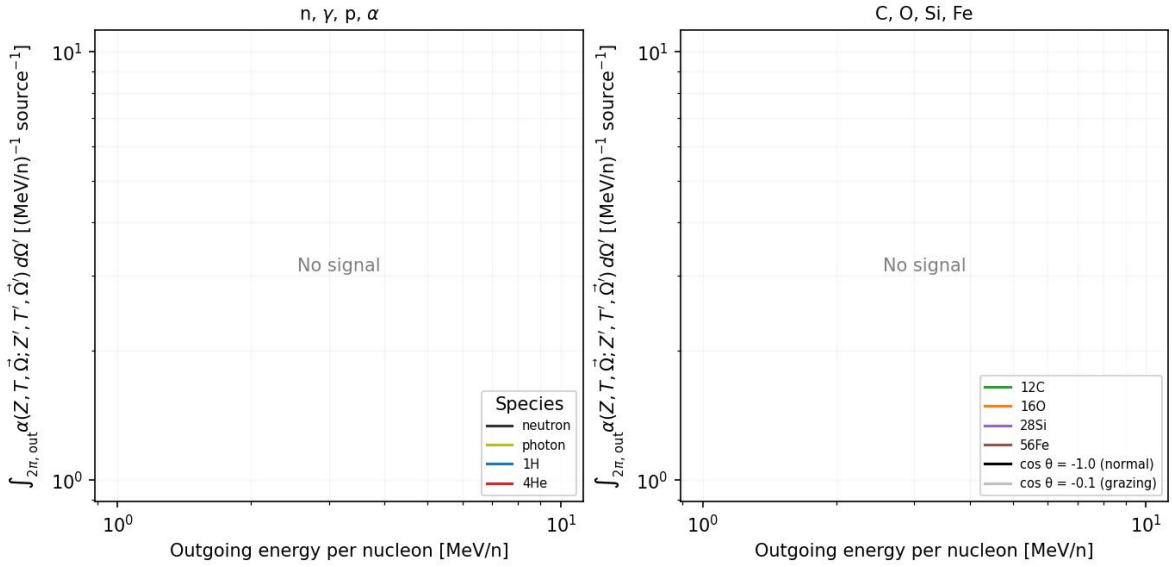


Figure A.114: Differential number albedo response function for a 228 keV n^{-1} ^{4}He primary, shown for all ten simulated incident polar cosine bins ($\cos\theta = -1.0$ to -0.1).

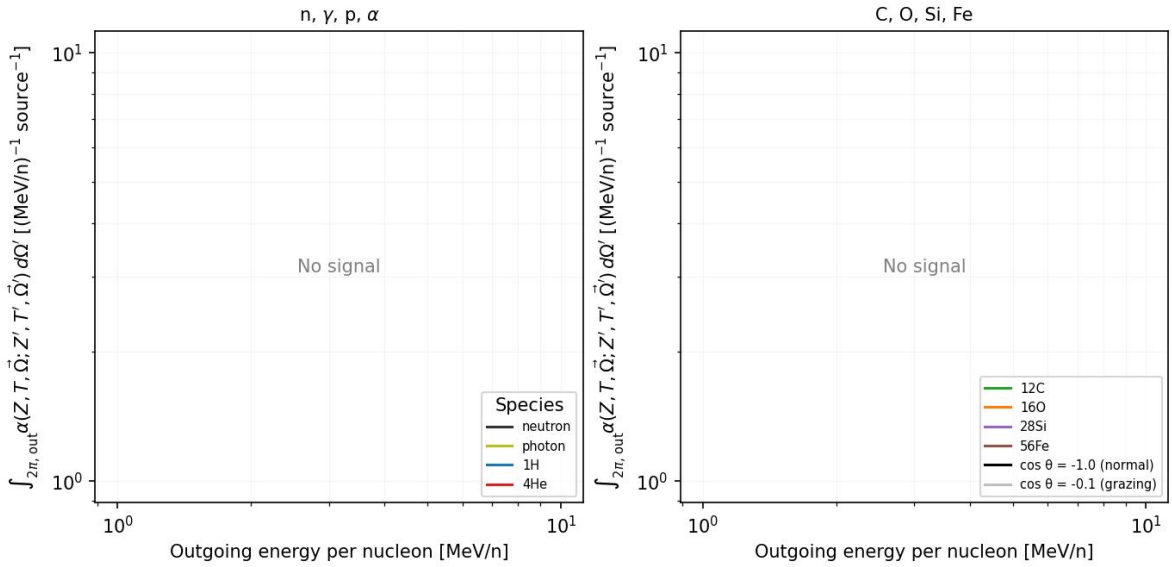


Figure A.115: Differential number albedo response function for a 271 keV n^{-1} ^{4}He primary, shown for all ten simulated incident polar cosine bins ($\cos\theta = -1.0$ to -0.1).

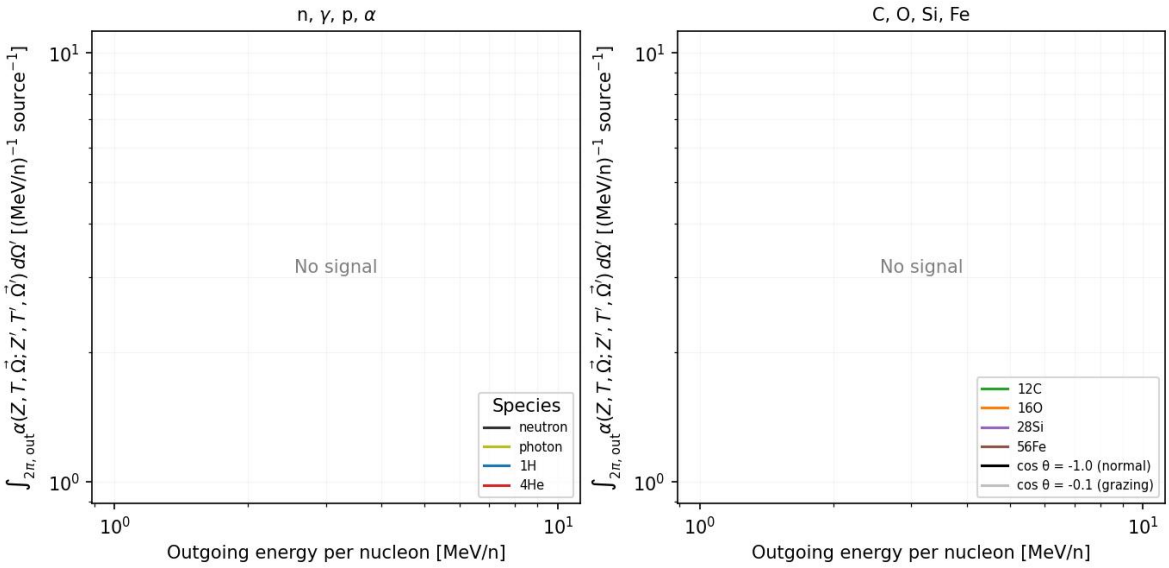


Figure A.116: Differential number albedo response function for a 320 keV n^{-1} ^{4}He primary, shown for all ten simulated incident polar cosine bins ($\cos\theta = -1.0$ to -0.1).

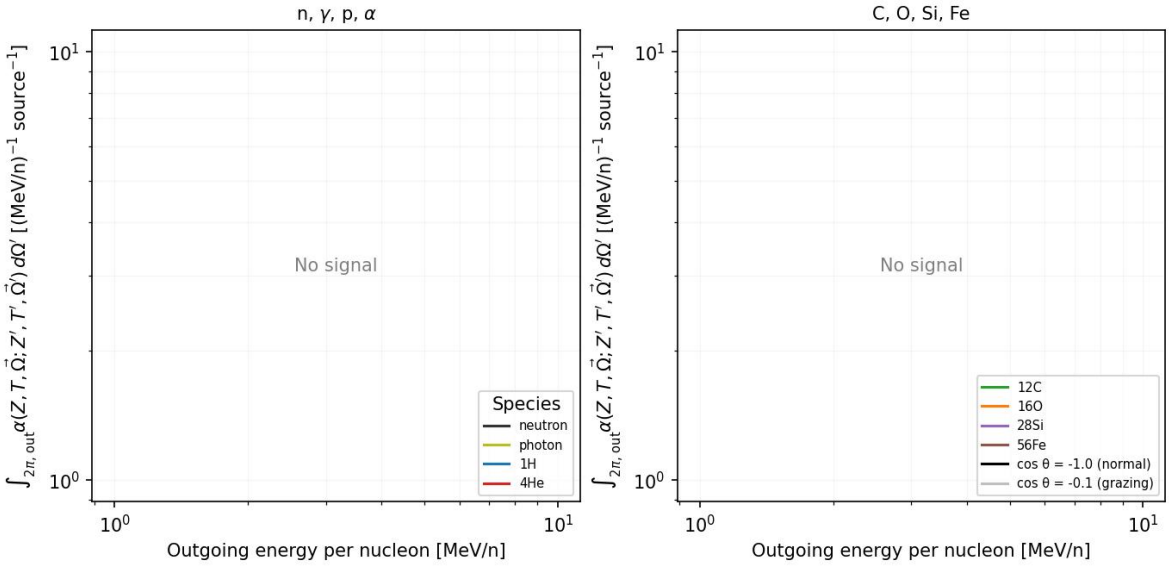


Figure A.117: Differential number albedo response function for a 374 keV n^{-1} ^{4}He primary, shown for all ten simulated incident polar cosine bins ($\cos\theta = -1.0$ to -0.1).

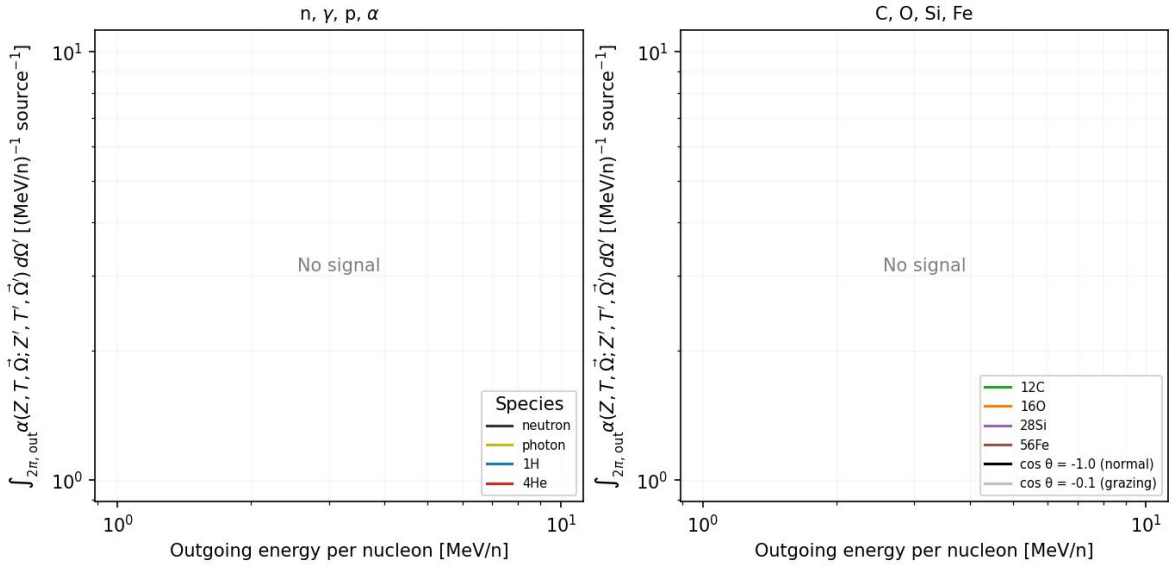


Figure A.118: Differential number albedo response function for a 434 keV n^{-1} ^{4}He primary, shown for all ten simulated incident polar cosine bins ($\cos\theta = -1.0$ to -0.1).

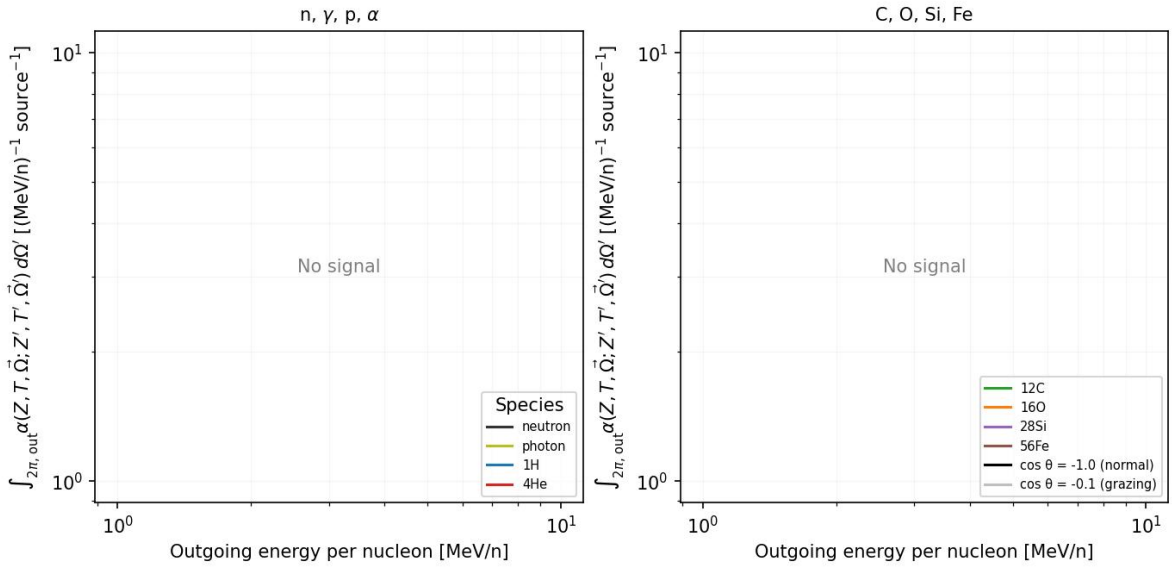


Figure A.119: Differential number albedo response function for a 501 keV n^{-1} ^{4}He primary, shown for all ten simulated incident polar cosine bins ($\cos\theta = -1.0$ to -0.1).

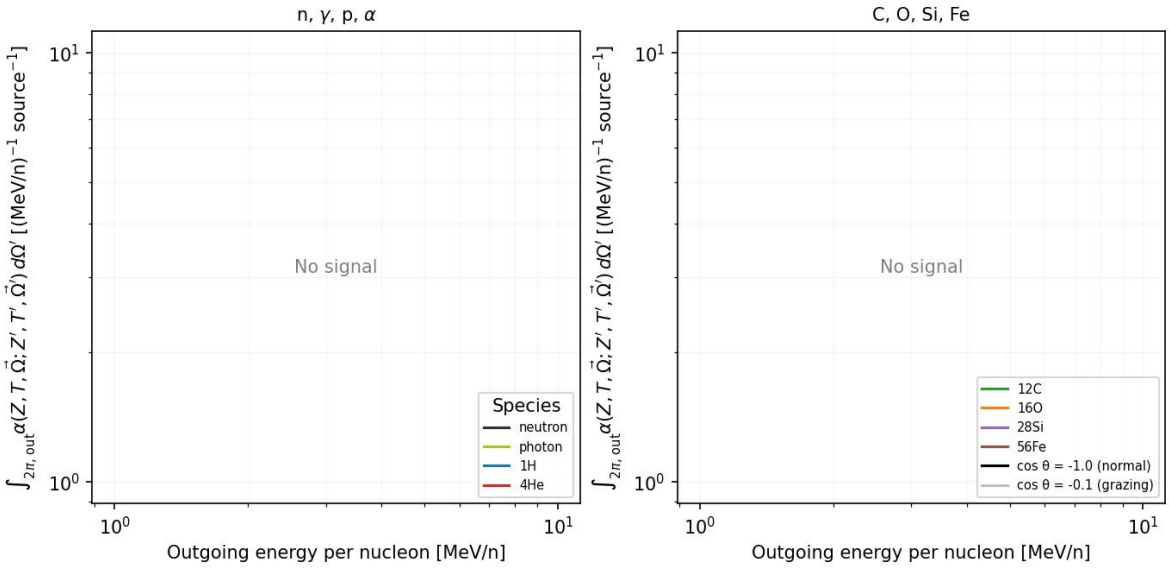


Figure A.120: Differential number albedo response function for a 575 keV n^{-1} ^{4}He primary, shown for all ten simulated incident polar cosine bins ($\cos\theta = -1.0$ to -0.1).

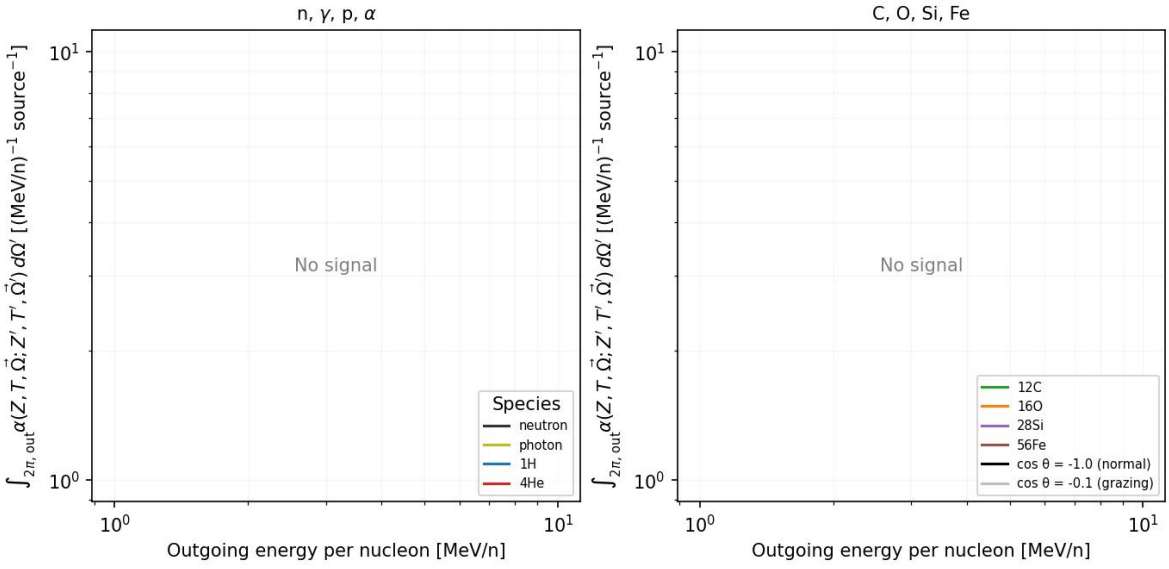


Figure A.121: Differential number albedo response function for a 659 keV n^{-1} ^{4}He primary, shown for all ten simulated incident polar cosine bins ($\cos\theta = -1.0$ to -0.1).

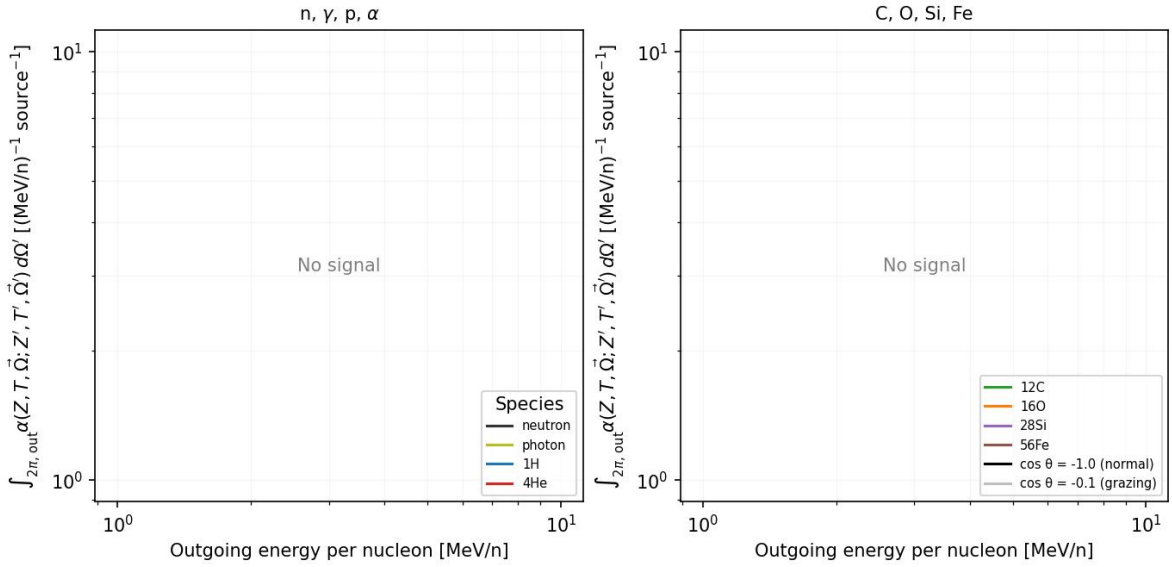


Figure A.122: Differential number albedo response function for a 754 keV n^{-1} ^{4}He primary, shown for all ten simulated incident polar cosine bins ($\cos\theta = -1.0$ to -0.1).

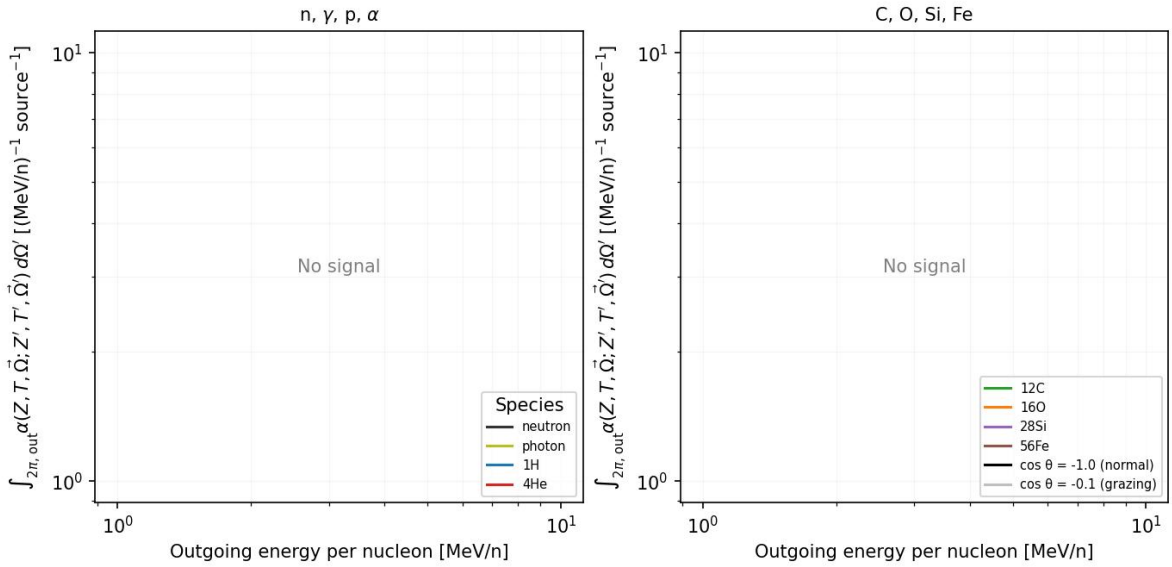


Figure A.123: Differential number albedo response function for a 860 keV n^{-1} ^{4}He primary, shown for all ten simulated incident polar cosine bins ($\cos\theta = -1.0$ to -0.1).

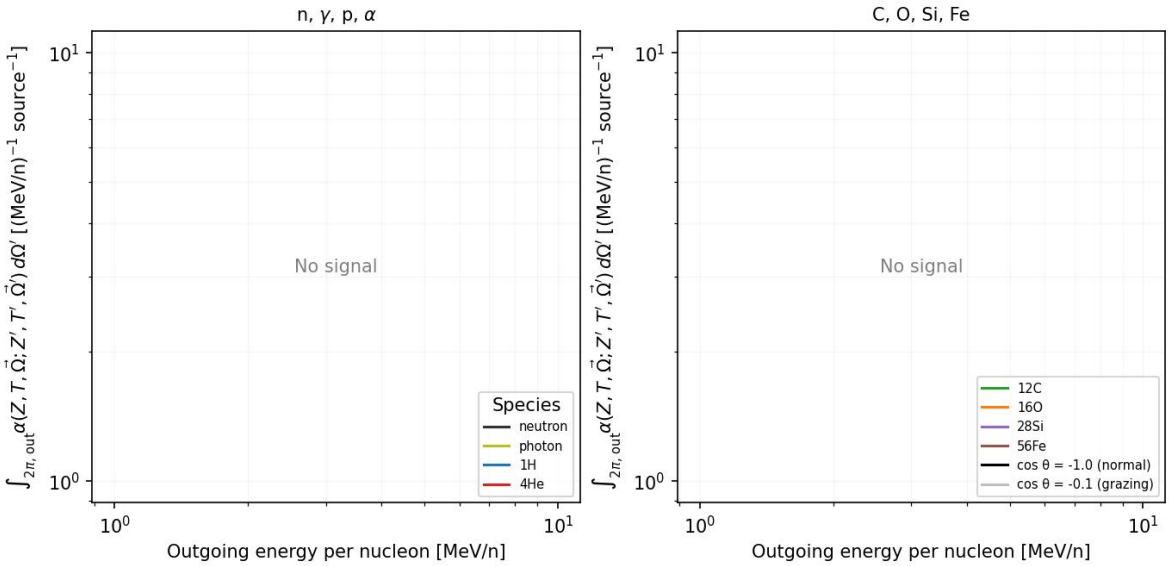


Figure A.124: Differential number albedo response function for a 979 keV n^{-1} ^{4}He primary, shown for all ten simulated incident polar cosine bins ($\cos\theta = -1.0$ to -0.1).

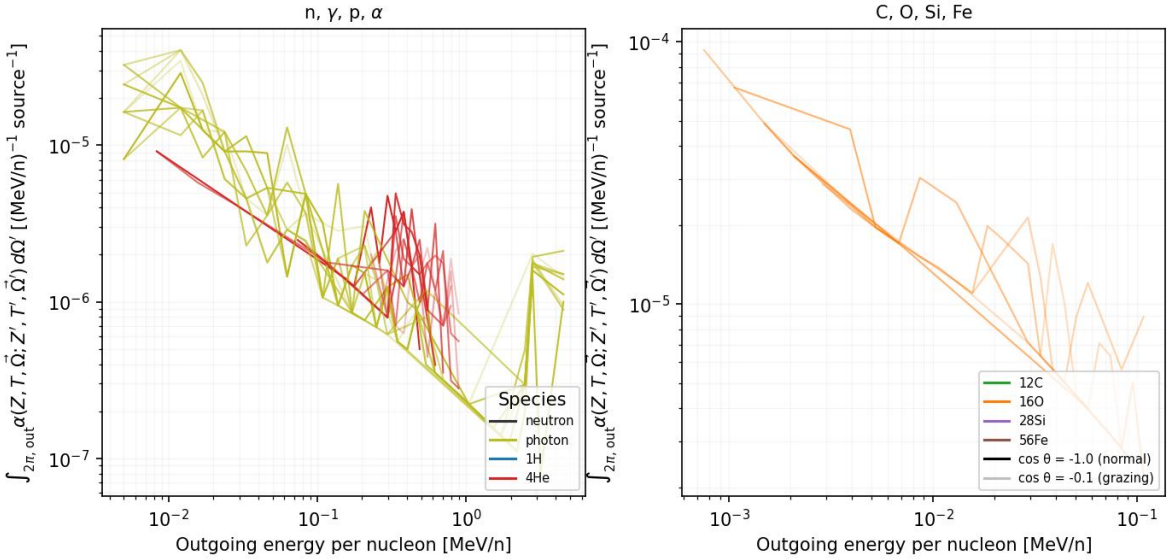


Figure A.125: Differential number albedo response function for a 1.112 MeV n^{-1} ^{4}He primary, shown for all ten simulated incident polar cosine bins ($\cos\theta = -1.0$ to -0.1).

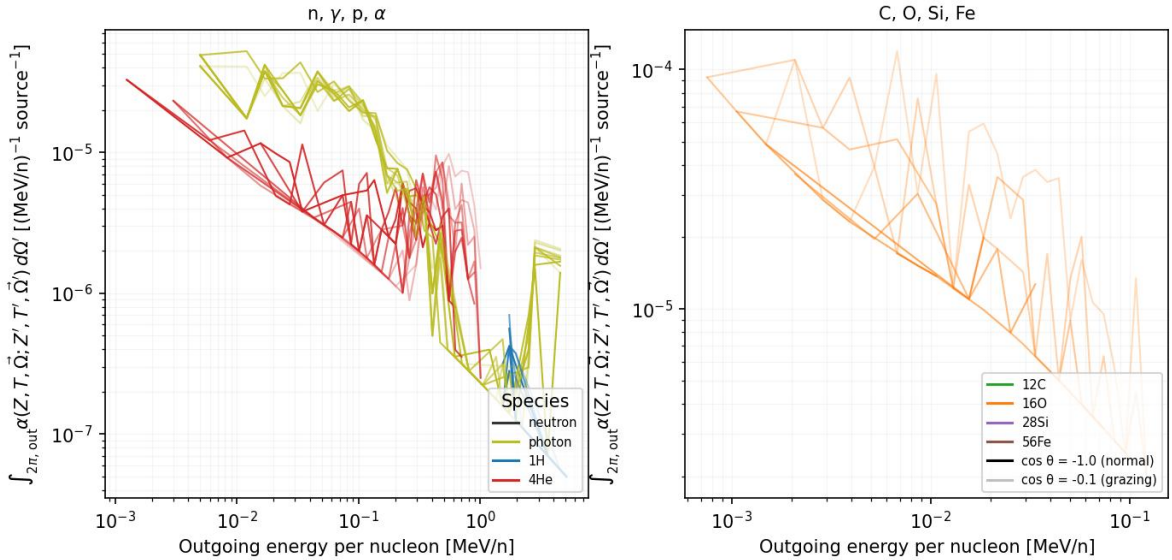


Figure A.126: Differential number albedo response function for a 1.262 MeV n^{-1} ^{4}He primary, shown for all ten simulated incident polar cosine bins ($\cos\theta = -1.0$ to -0.1).

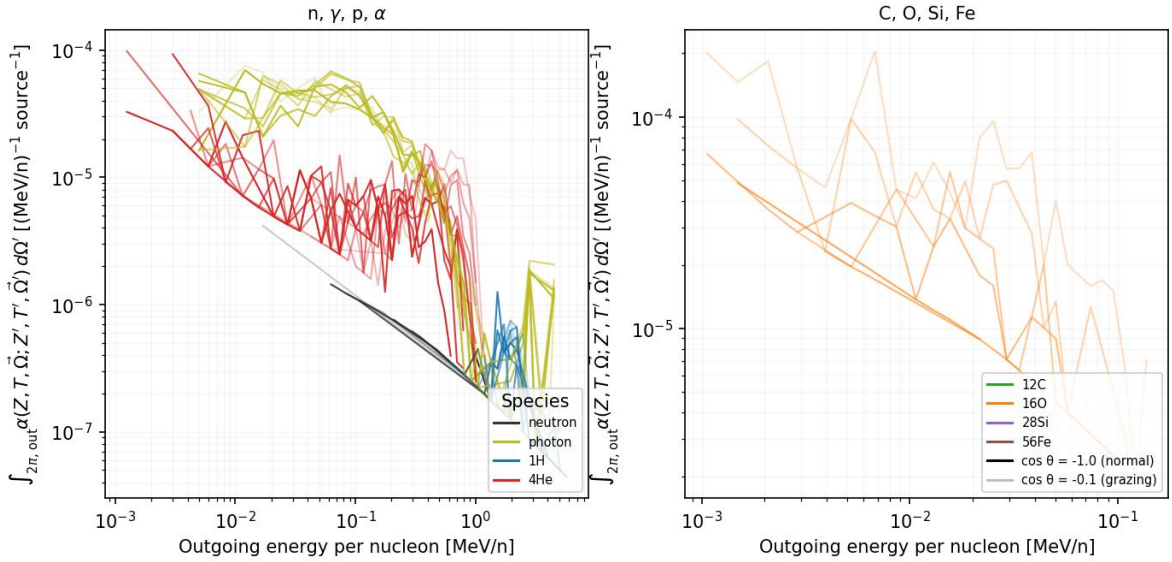


Figure A.127: Differential number albedo response function for a 1.43 MeV n^{-1} ^{4}He primary, shown for all ten simulated incident polar cosine bins ($\cos\theta = -1.0$ to -0.1).

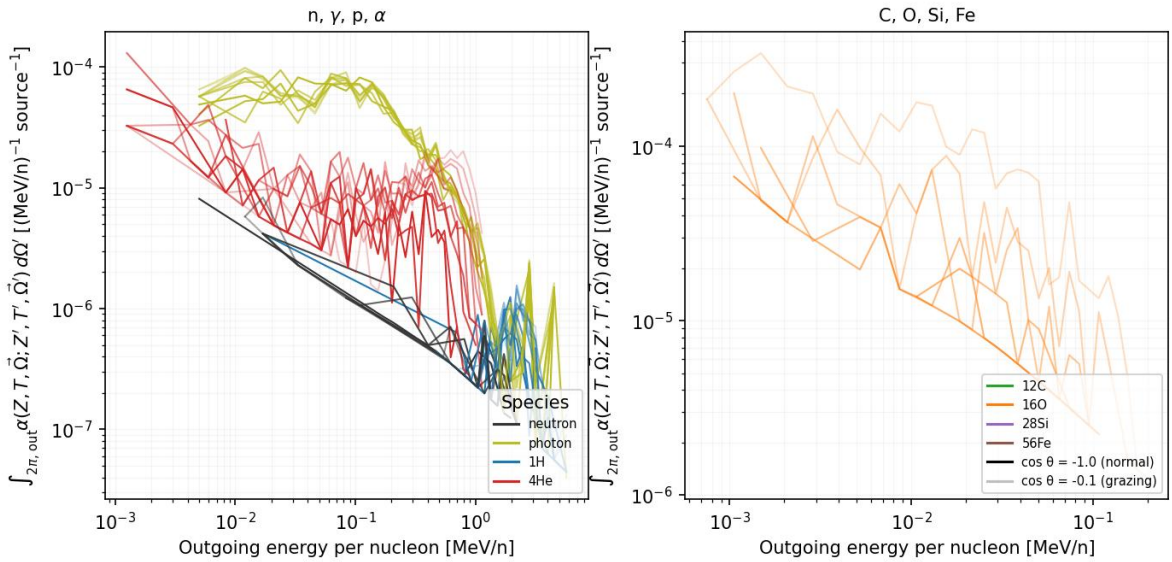


Figure A.128: Differential number albedo response function for a 1.619 MeV n^{-1} ^{4}He primary, shown for all ten simulated incident polar cosine bins ($\cos\theta = -1.0$ to -0.1).

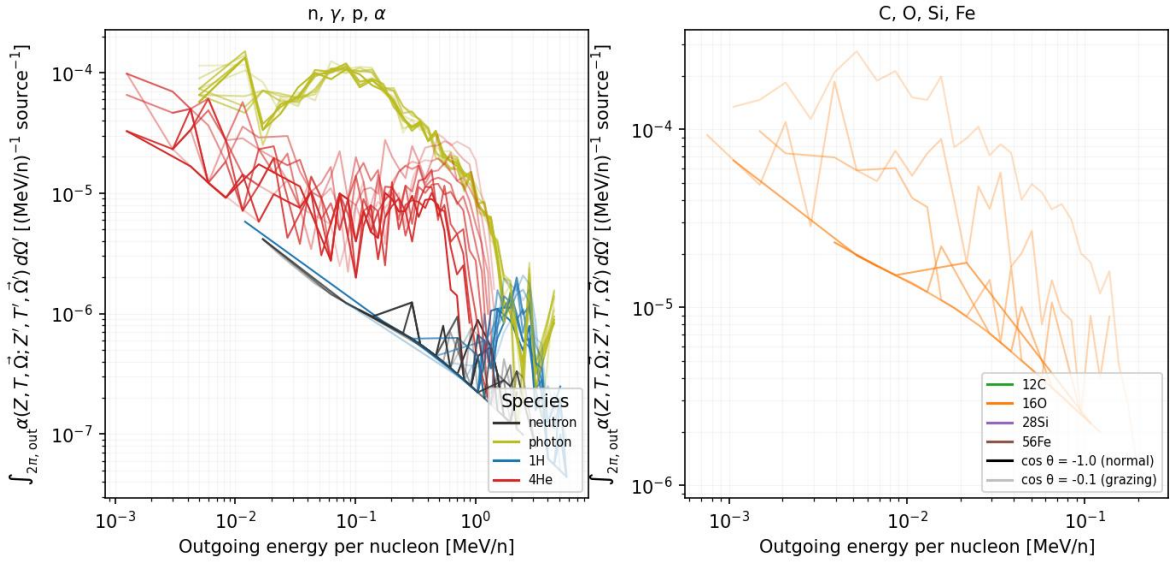


Figure A.129: Differential number albedo response function for a 1.832 MeV n^{-1} ^{4}He primary, shown for all ten simulated incident polar cosine bins ($\cos\theta = -1.0$ to -0.1).

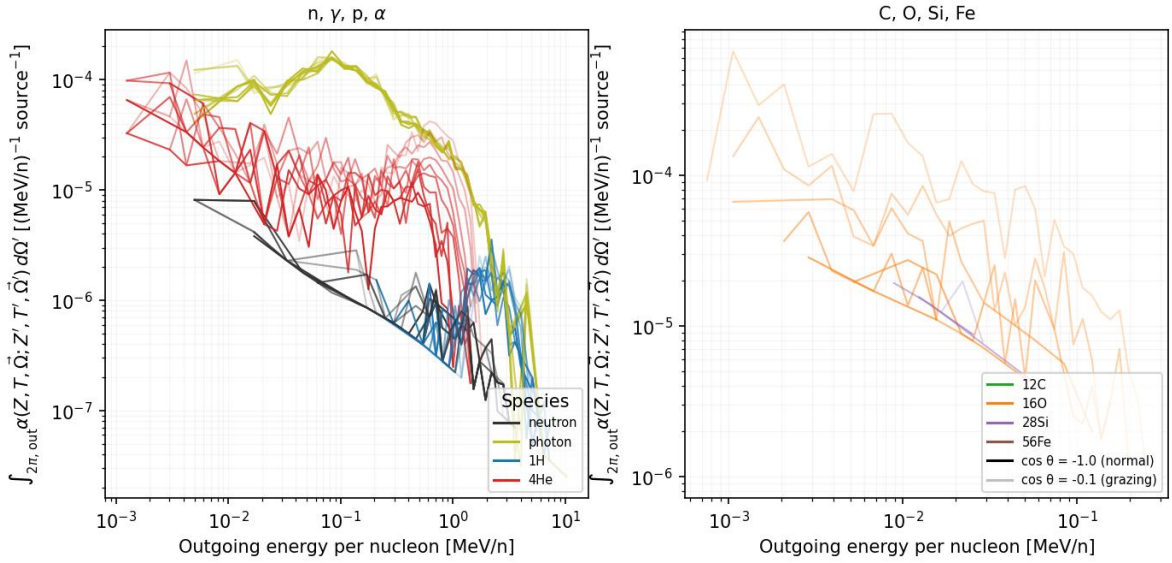


Figure A.130: Differential number albedo response function for a 2.07 MeV n^{-1} ^{4}He primary, shown for all ten simulated incident polar cosine bins ($\cos\theta = -1.0$ to -0.1).

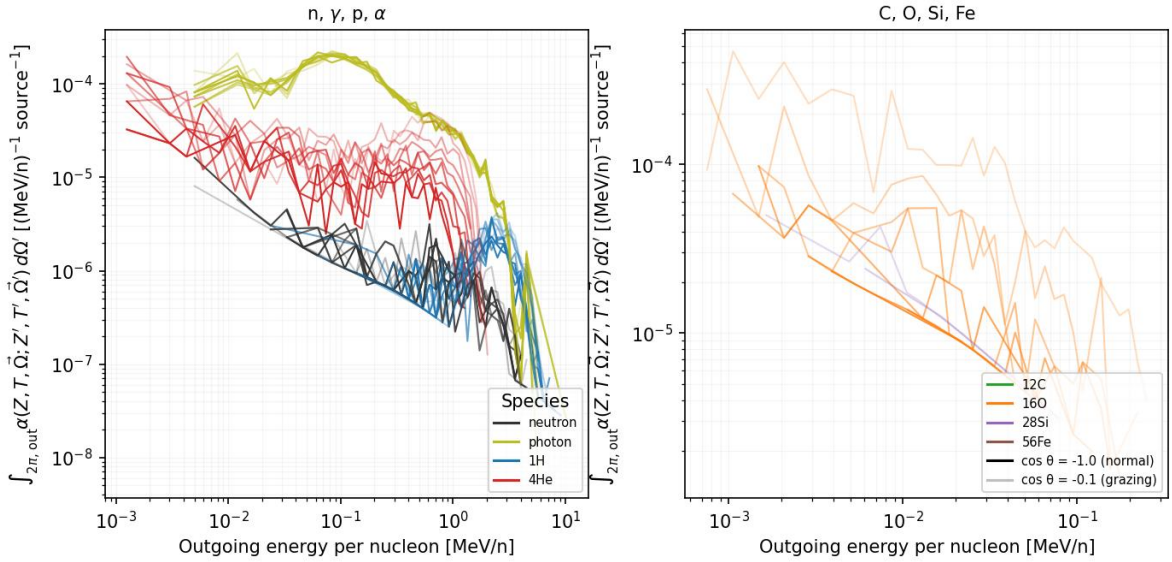


Figure A.131: Differential number albedo response function for a 2.338 MeV n^{-1} ^{4}He primary, shown for all ten simulated incident polar cosine bins ($\cos\theta = -1.0$ to -0.1).

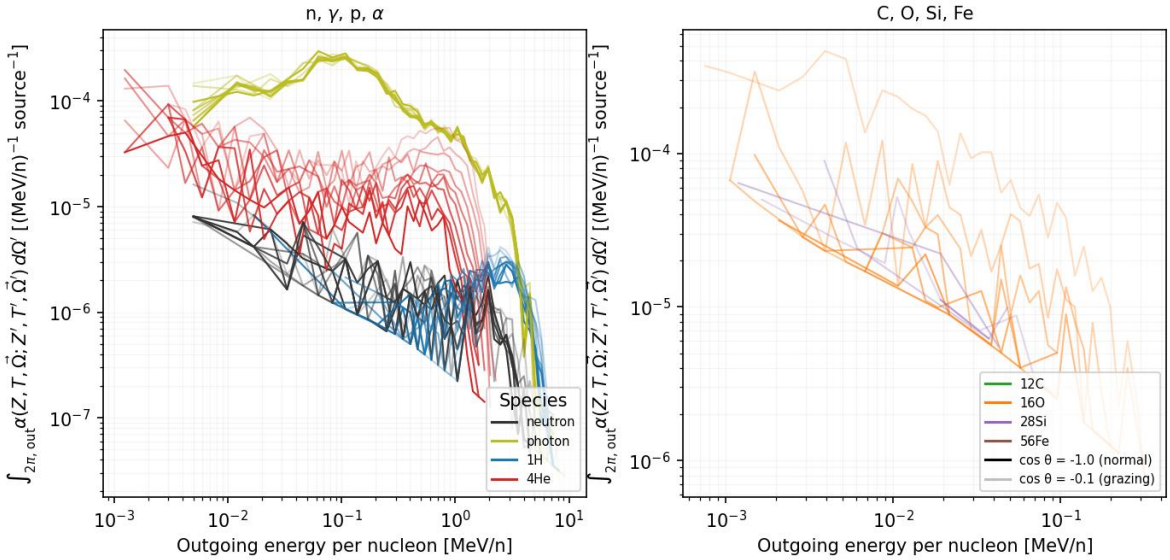


Figure A.132: Differential number albedo response function for a 2.639 MeV n^{-1} ^{4}He primary, shown for all ten simulated incident polar cosine bins ($\cos\theta = -1.0$ to -0.1).

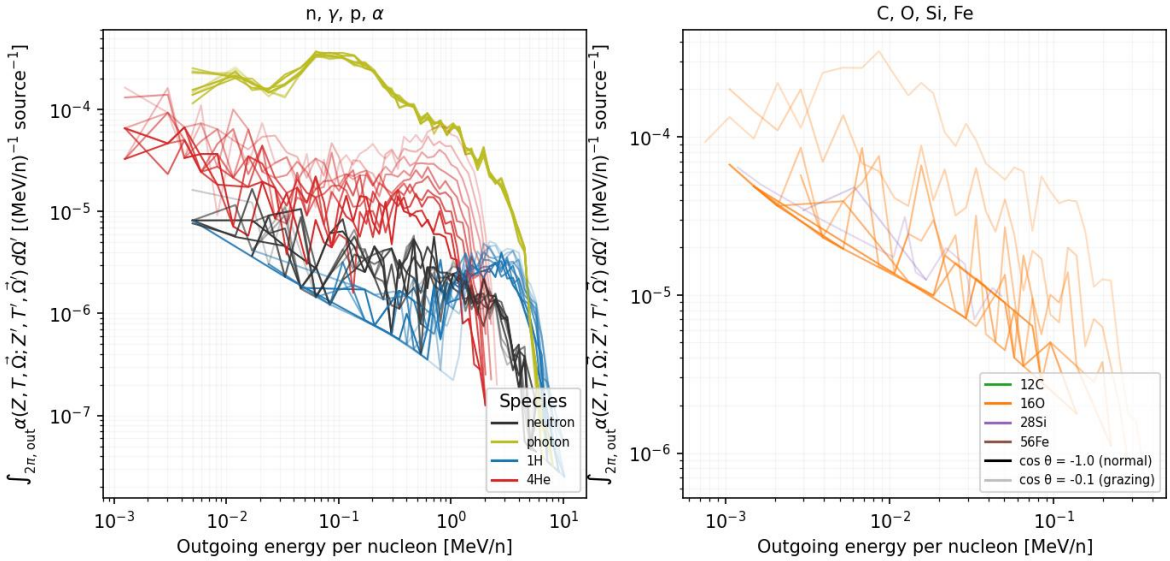


Figure A.133: Differential number albedo response function for a 2.976 MeV n^{-1} ^{4}He primary, shown for all ten simulated incident polar cosine bins ($\cos\theta = -1.0$ to -0.1).

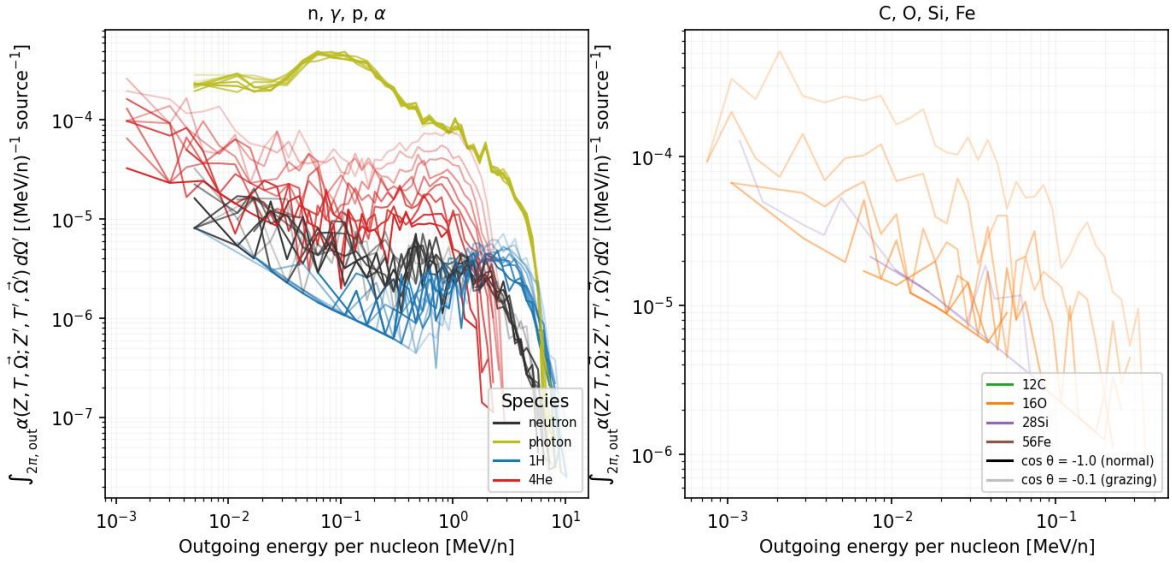


Figure A.134: Differential number albedo response function for a 3.355 MeV n^{-1} ^{4}He primary, shown for all ten simulated incident polar cosine bins ($\cos\theta = -1.0$ to -0.1).

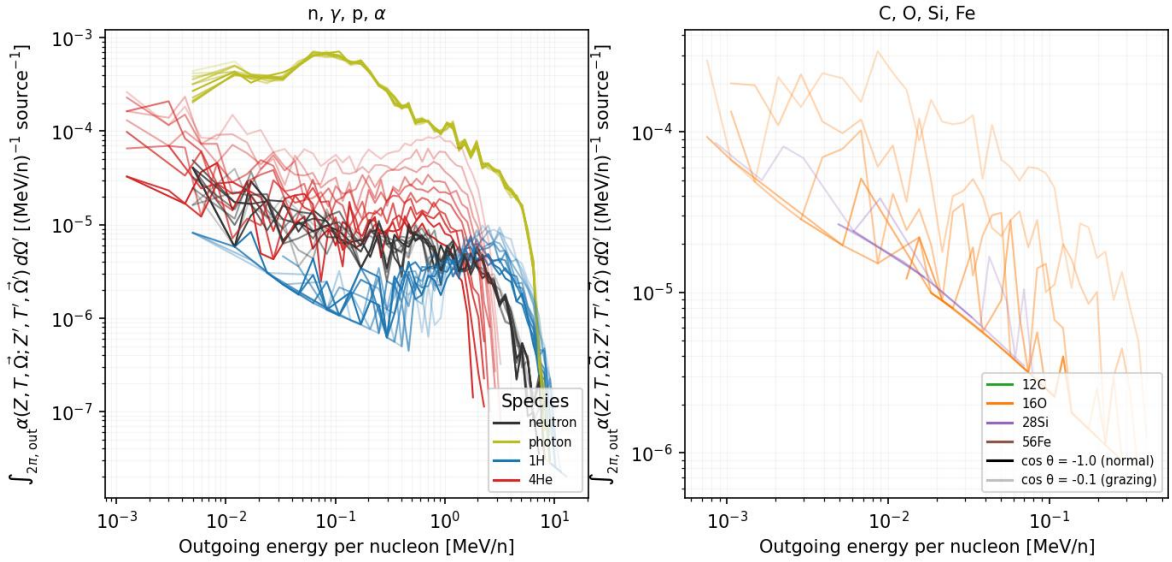


Figure A.135: Differential number albedo response function for a 3.779 MeV n^{-1} ^{4}He primary, shown for all ten simulated incident polar cosine bins ($\cos\theta = -1.0$ to -0.1).

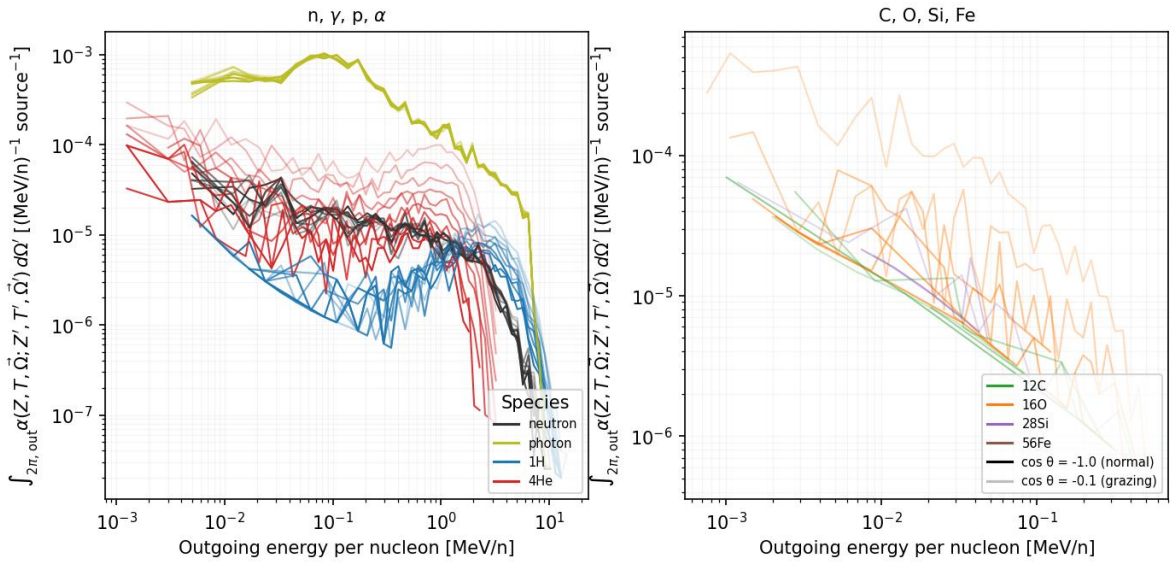


Figure A.136: Differential number albedo response function for a 4.255 MeV n^{-1} ^{4}He primary, shown for all ten simulated incident polar cosine bins ($\cos\theta = -1.0$ to -0.1).

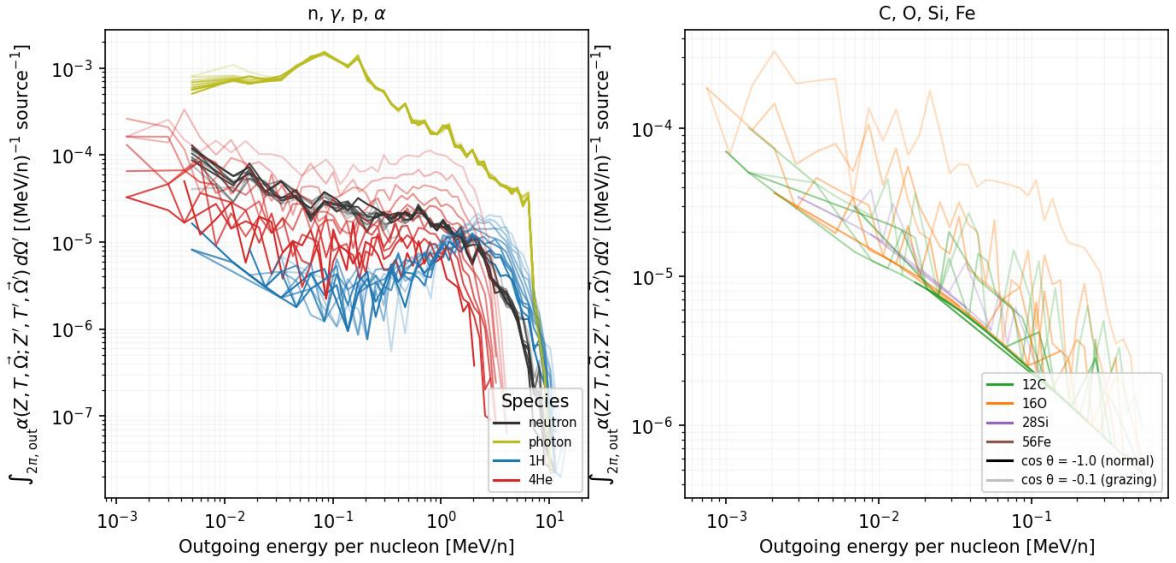


Figure A.137: Differential number albedo response function for a 4.789 MeV n^{-1} ^{4}He primary, shown for all ten simulated incident polar cosine bins ($\cos\theta = -1.0$ to -0.1).

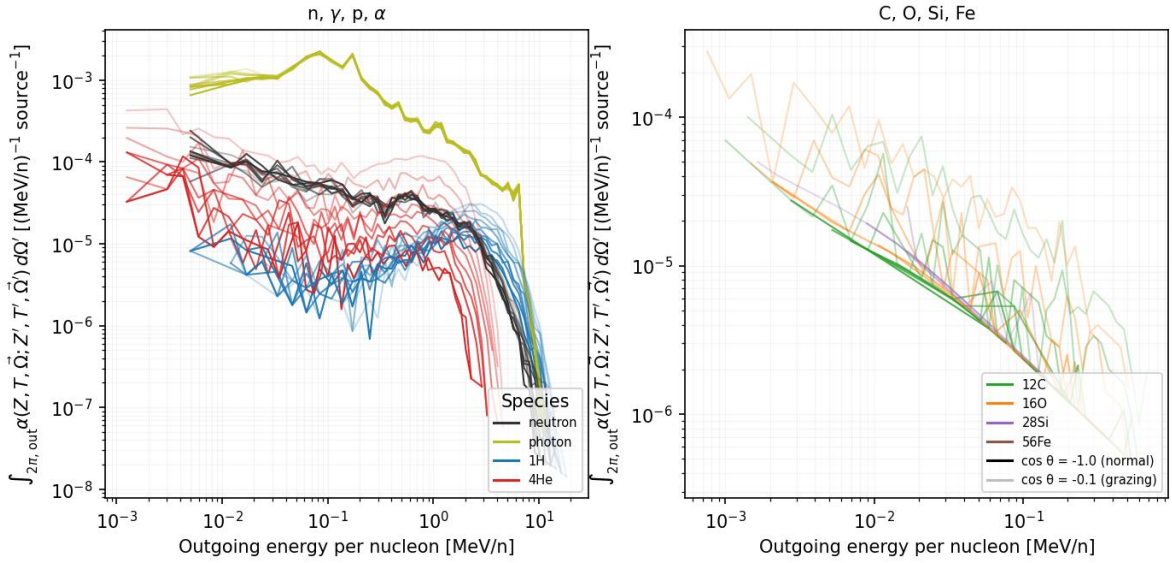


Figure A.138: Differential number albedo response function for a 5.387 MeV n^{-1} ^{4}He primary, shown for all ten simulated incident polar cosine bins ($\cos\theta = -1.0$ to -0.1).

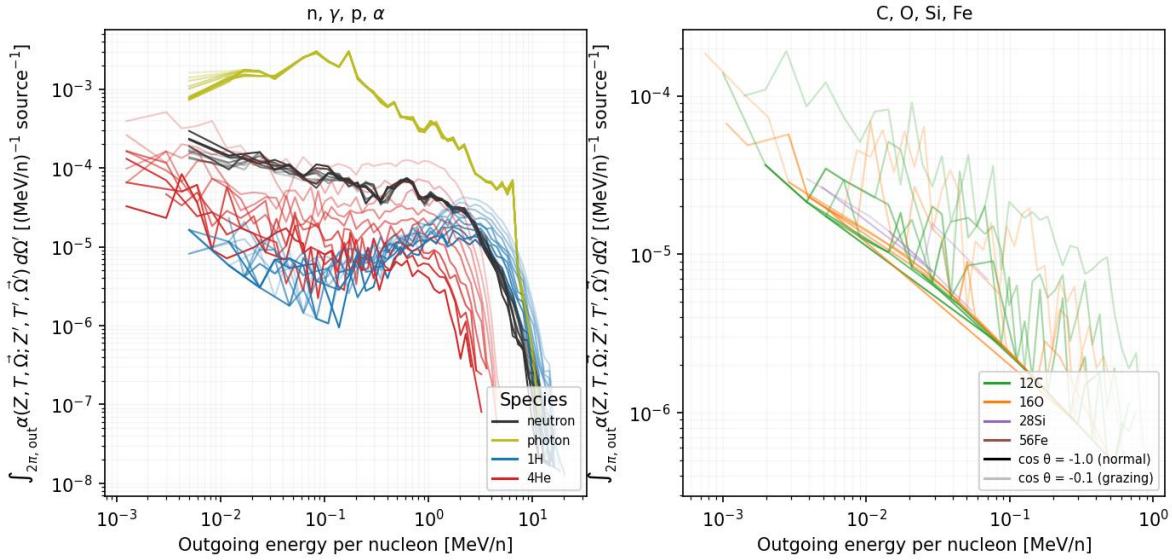


Figure A.139: Differential number albedo response function for a 6.057 MeV n^{-1} ^{4}He primary, shown for all ten simulated incident polar cosine bins ($\cos\theta = -1.0$ to -0.1).

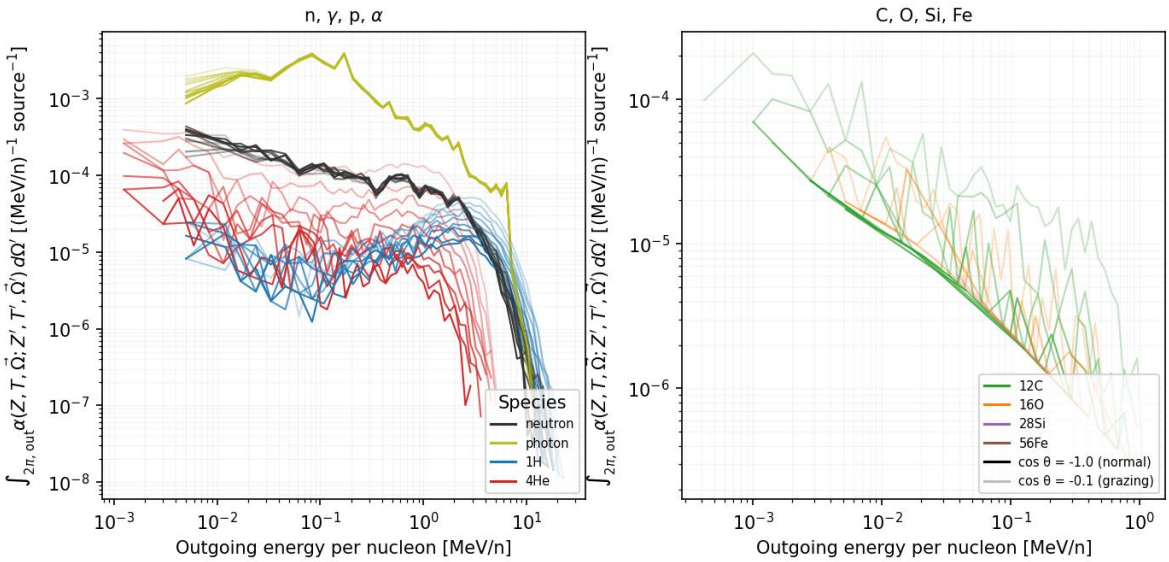


Figure A.140: Differential number albedo response function for a 6.808 MeV n^{-1} ^{4}He primary, shown for all ten simulated incident polar cosine bins ($\cos\theta = -1.0$ to -0.1).

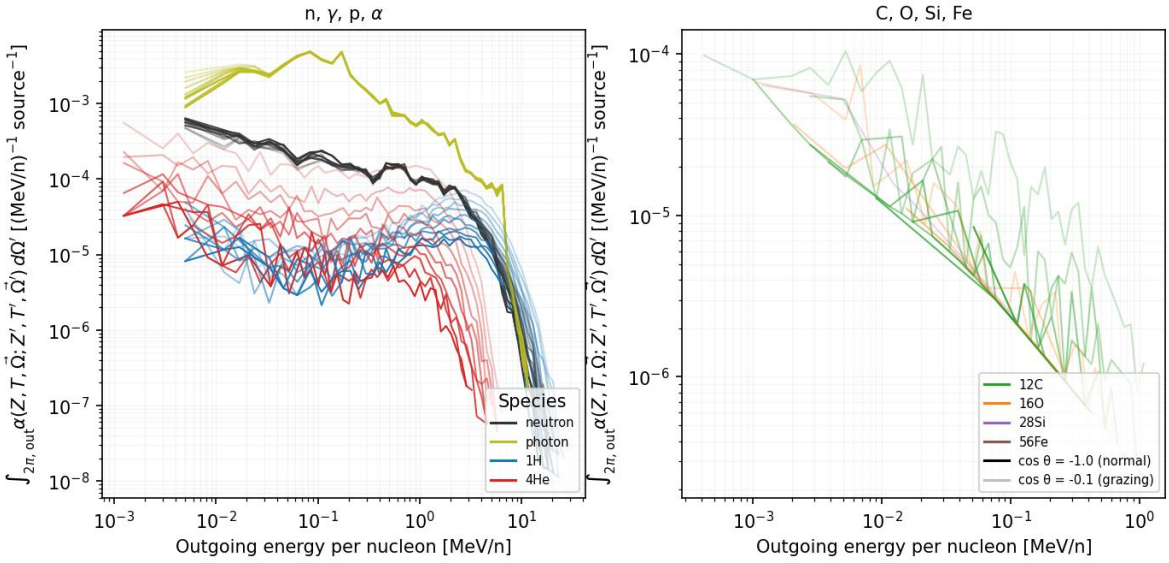


Figure A.141: Differential number albedo response function for a 7.65 MeV n^{-1} ^{4}He primary, shown for all ten simulated incident polar cosine bins ($\cos\theta = -1.0$ to -0.1).

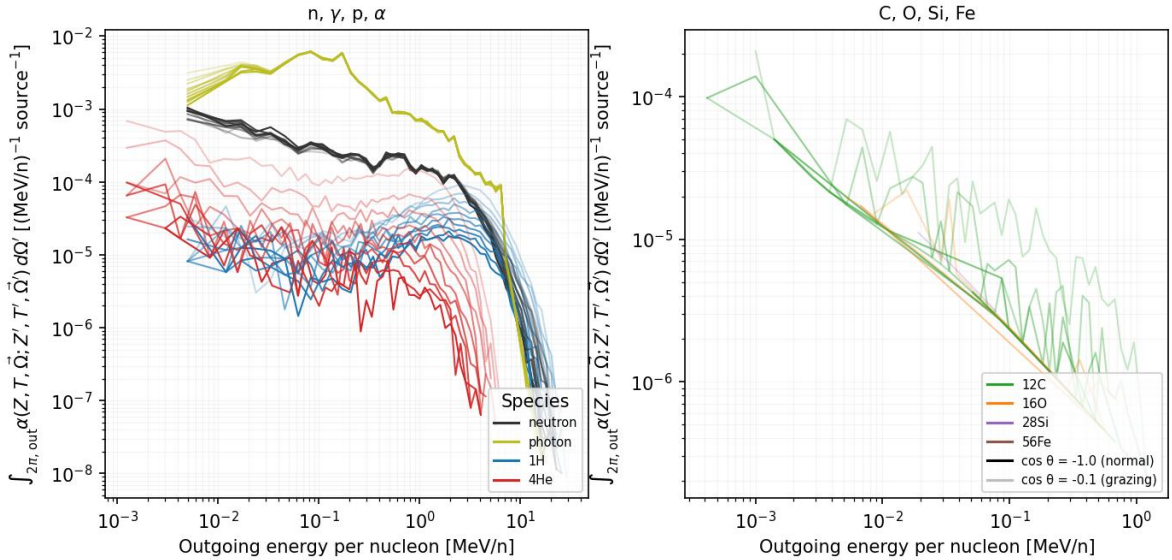


Figure A.142: Differential number albedo response function for a 8.592 MeV n^{-1} ^{4}He primary, shown for all ten simulated incident polar cosine bins ($\cos\theta = -1.0$ to -0.1).

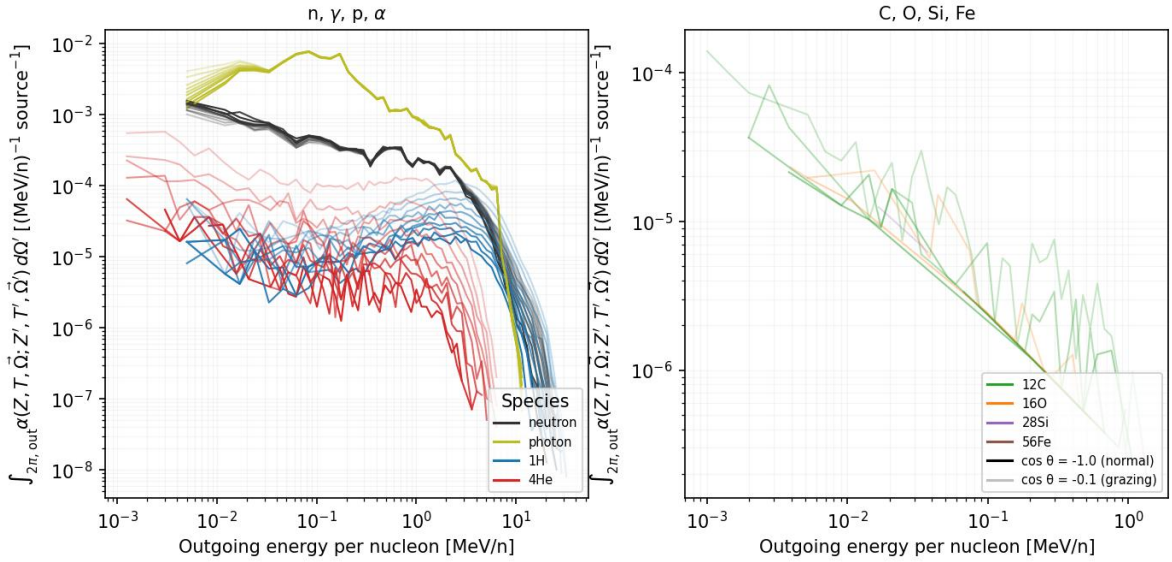


Figure A.143: Differential number albedo response function for a 9.648 MeV n^{-1} ^{4}He primary, shown for all ten simulated incident polar cosine bins ($\cos\theta = -1.0$ to -0.1).

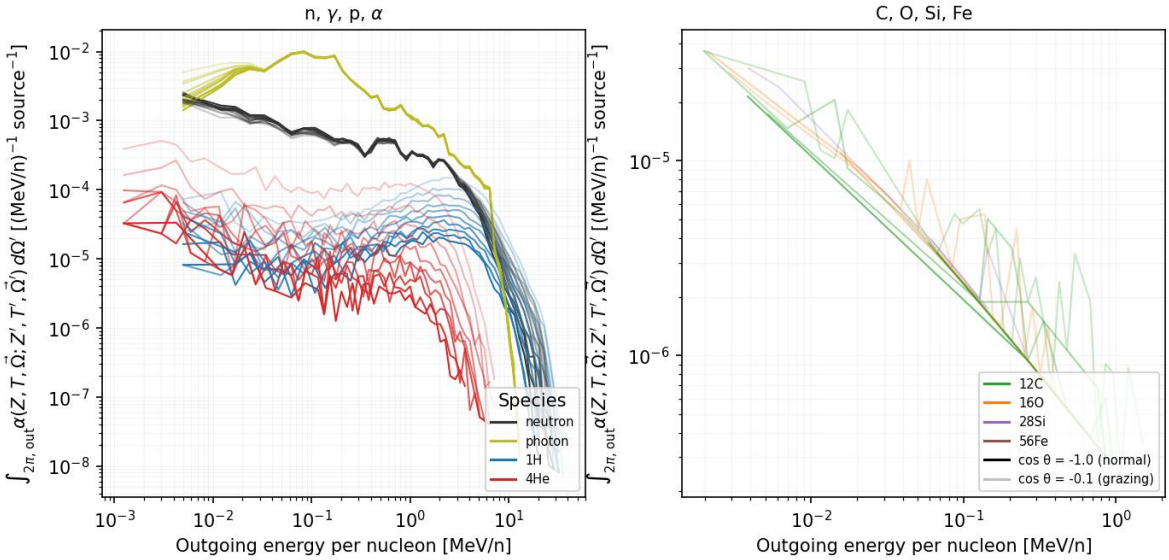


Figure A.144: Differential number albedo response function for a 10.83 MeV n^{-1} ^{4}He primary, shown for all ten simulated incident polar cosine bins ($\cos\theta = -1.0$ to -0.1).

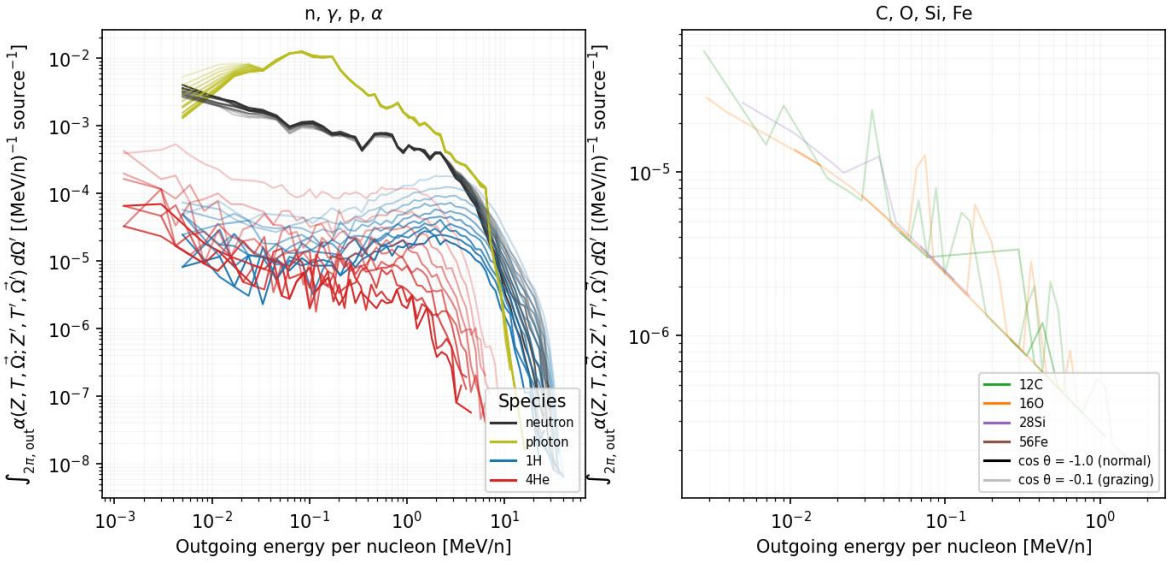


Figure A.145: Differential number albedo response function for a 12.15 MeV n^{-1} ^{4}He primary, shown for all ten simulated incident polar cosine bins ($\cos\theta = -1.0$ to -0.1).

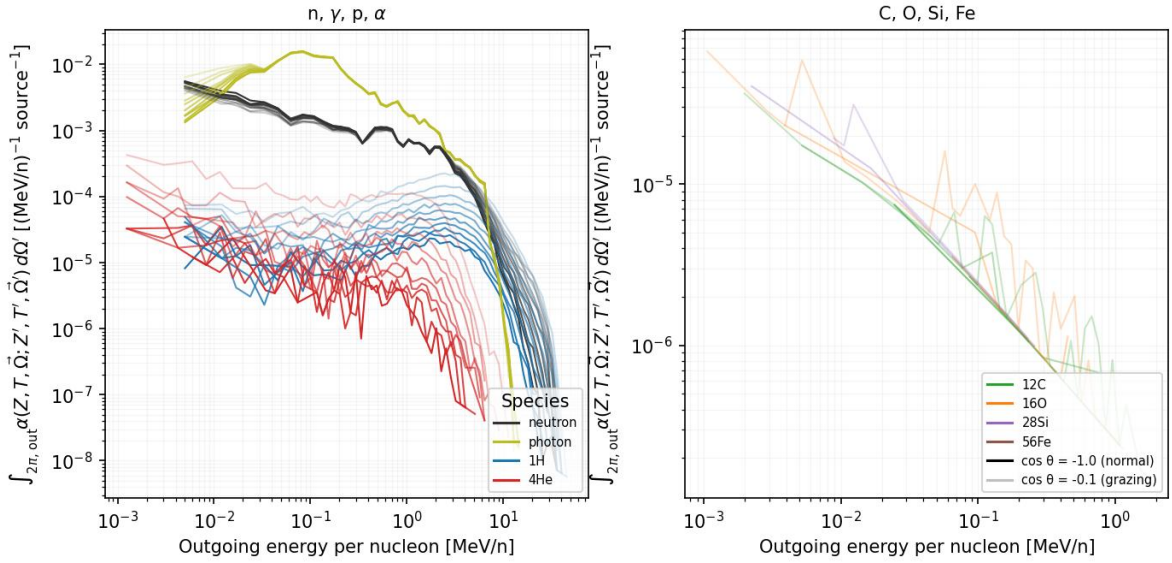


Figure A.146: Differential number albedo response function for a 13.63 MeV n^{-1} ^{4}He primary, shown for all ten simulated incident polar cosine bins ($\cos\theta = -1.0$ to -0.1).

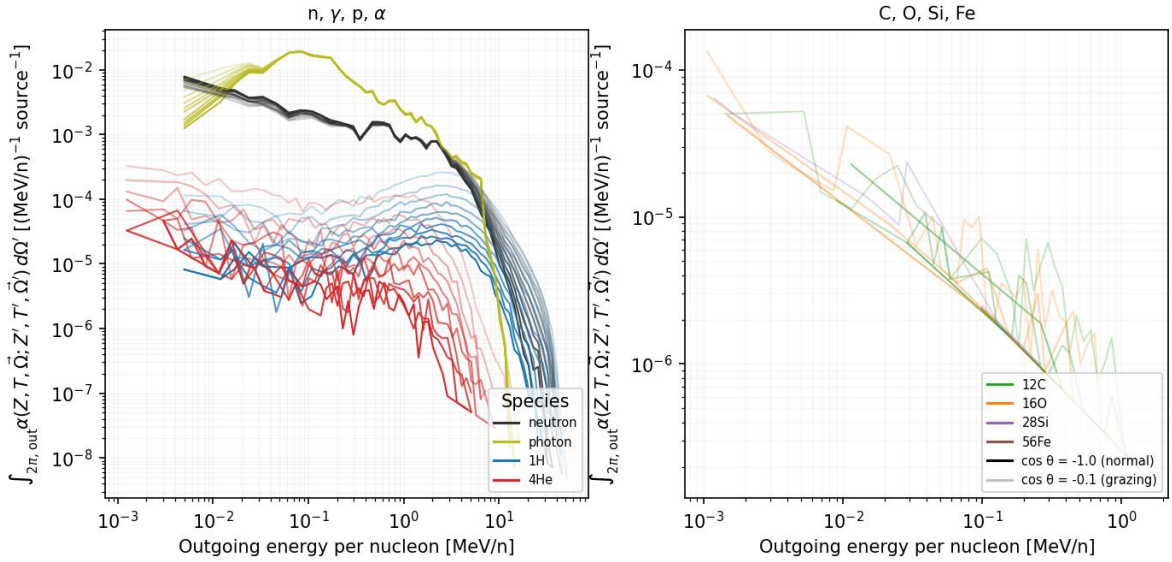


Figure A.147: Differential number albedo response function for a 15.3 MeV n^{-1} ^{4}He primary, shown for all ten simulated incident polar cosine bins ($\cos\theta = -1.0$ to -0.1).

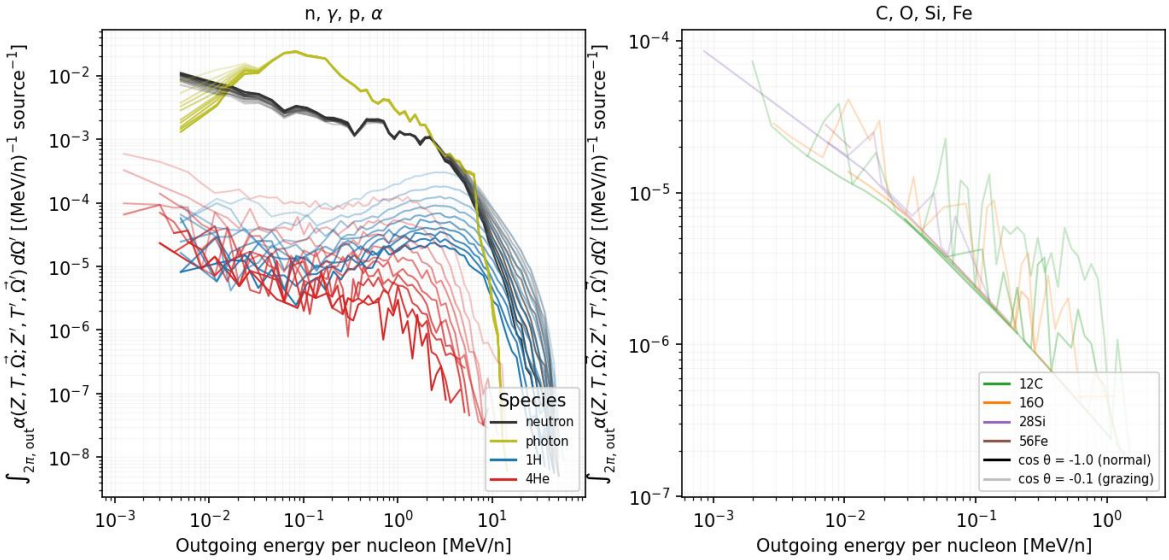


Figure A.148: Differential number albedo response function for a 17.15 MeV n^{-1} ^{4}He primary, shown for all ten simulated incident polar cosine bins ($\cos\theta = -1.0$ to -0.1).

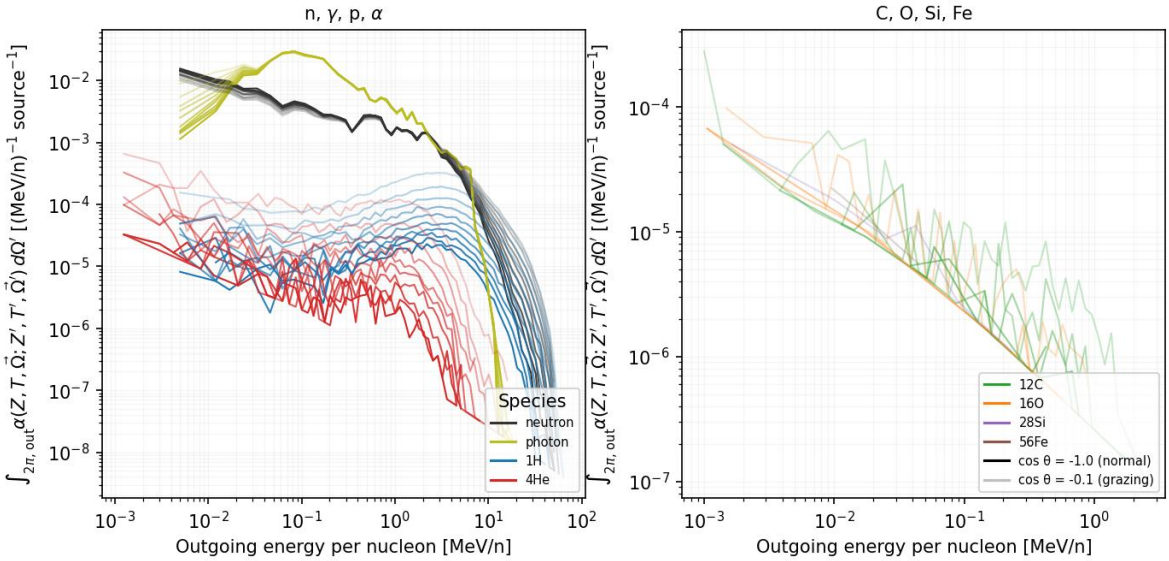


Figure A.149: Differential number albedo response function for a 19.23 MeV n^{-1} ^{4}He primary, shown for all ten simulated incident polar cosine bins ($\cos\theta = -1.0$ to -0.1).

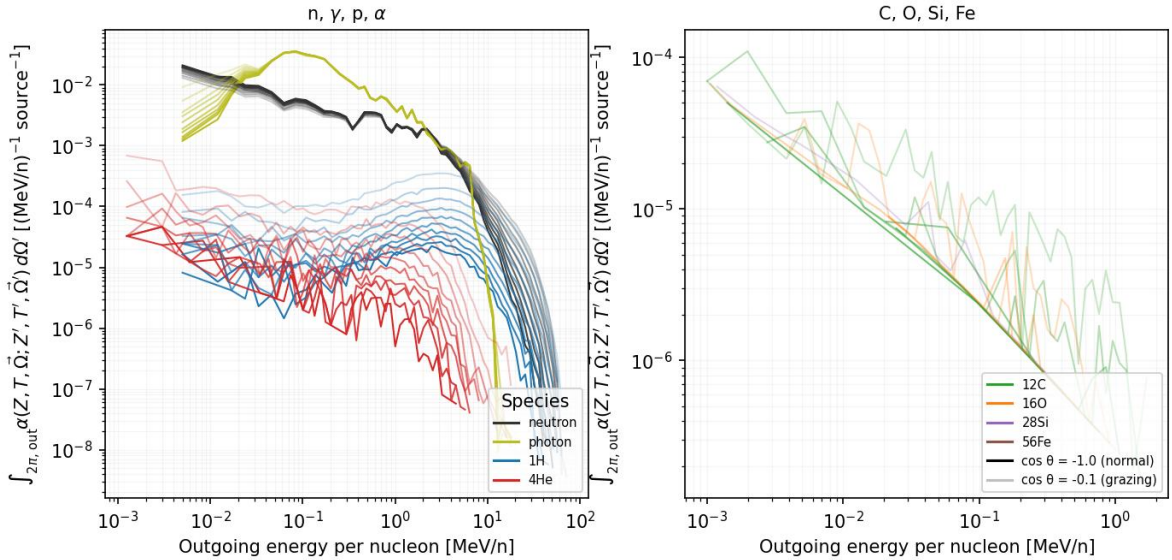


Figure A.150: Differential number albedo response function for a 21.56 MeV n^{-1} ^{4}He primary, shown for all ten simulated incident polar cosine bins ($\cos\theta = -1.0$ to -0.1).

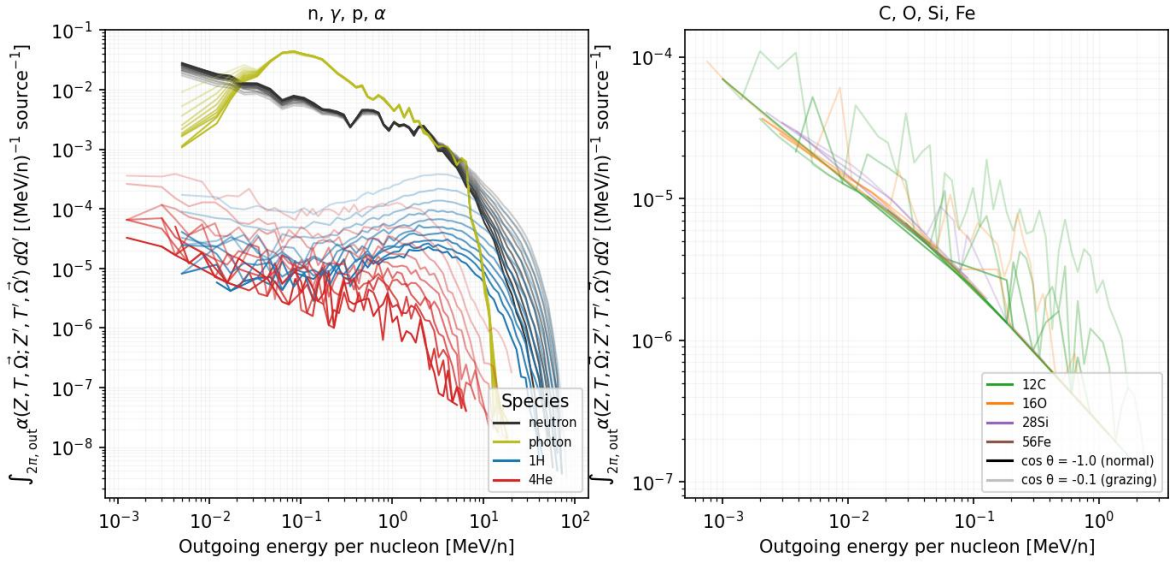


Figure A.151: Differential number albedo response function for a 24.17 MeV n^{-1} ^{4}He primary, shown for all ten simulated incident polar cosine bins ($\cos\theta = -1.0$ to -0.1).

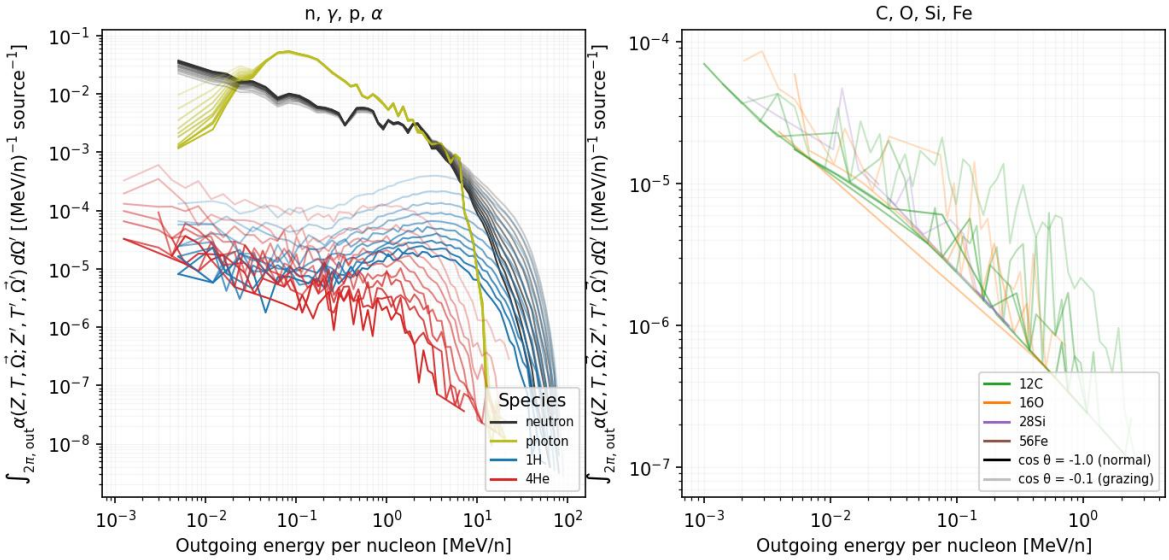


Figure A.152: Differential number albedo response function for a 27.1 MeV n^{-1} ^{4}He primary, shown for all ten simulated incident polar cosine bins ($\cos\theta = -1.0$ to -0.1).

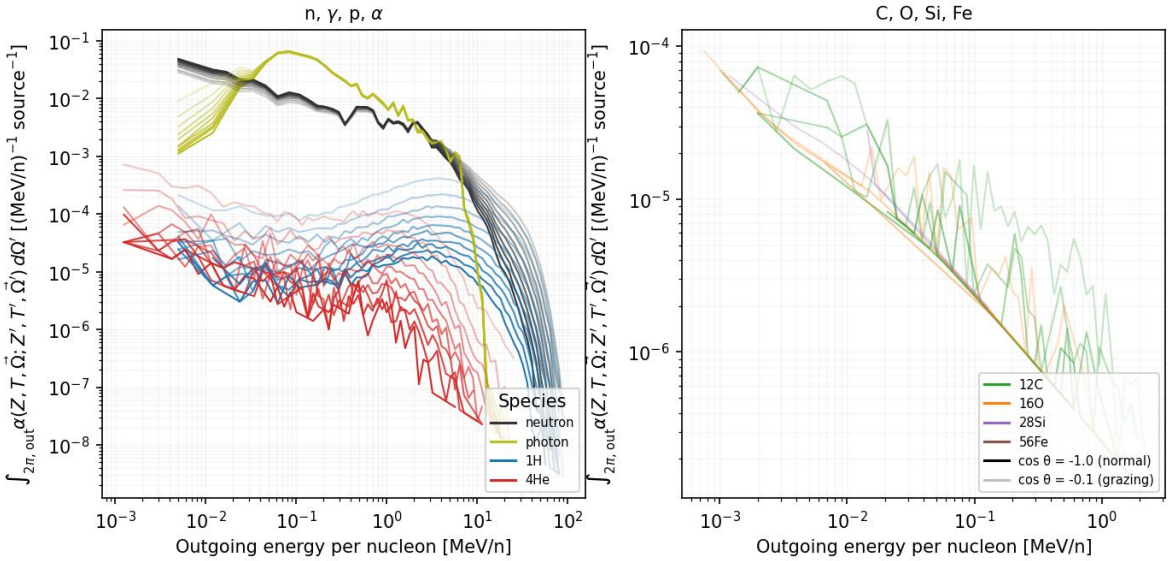


Figure A.153: Differential number albedo response function for a 30.37 MeV n^{-1} ^{4}He primary, shown for all ten simulated incident polar cosine bins ($\cos\theta = -1.0$ to -0.1).

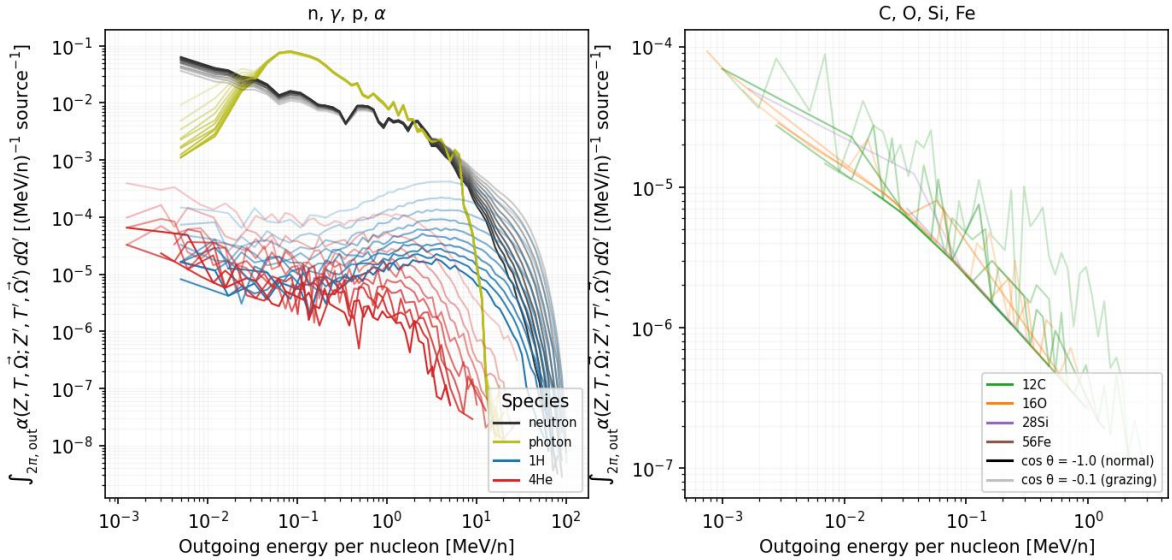


Figure A.154: Differential number albedo response function for a 34.04 MeV n^{-1} ^{4}He primary, shown for all ten simulated incident polar cosine bins ($\cos\theta = -1.0$ to -0.1).

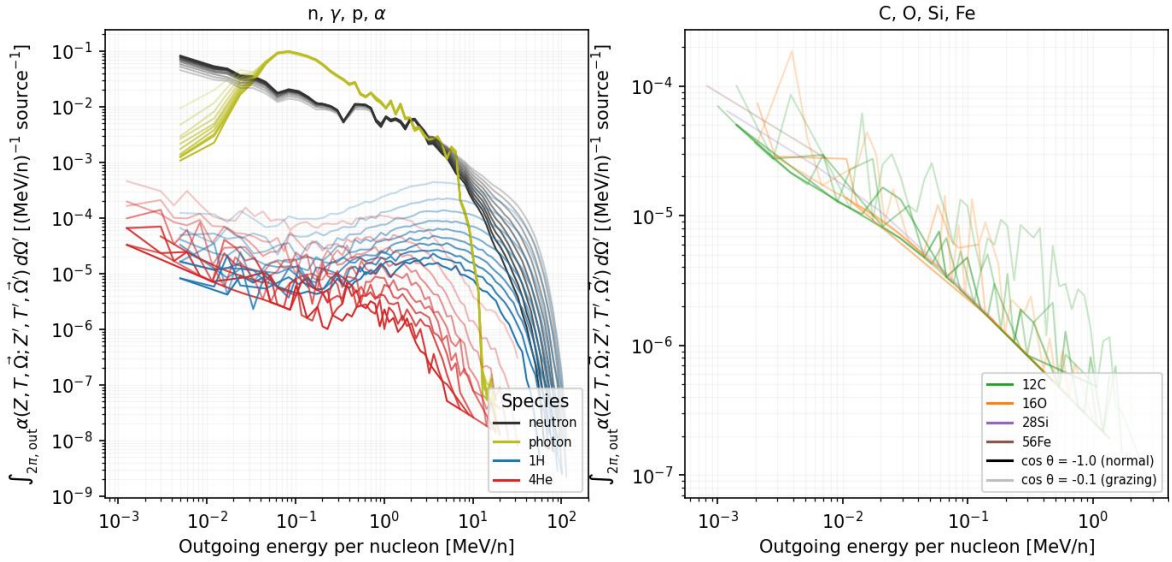


Figure A.155: Differential number albedo response function for a 38.15 MeV n^{-1} ^{4}He primary, shown for all ten simulated incident polar cosine bins ($\cos\theta = -1.0$ to -0.1).

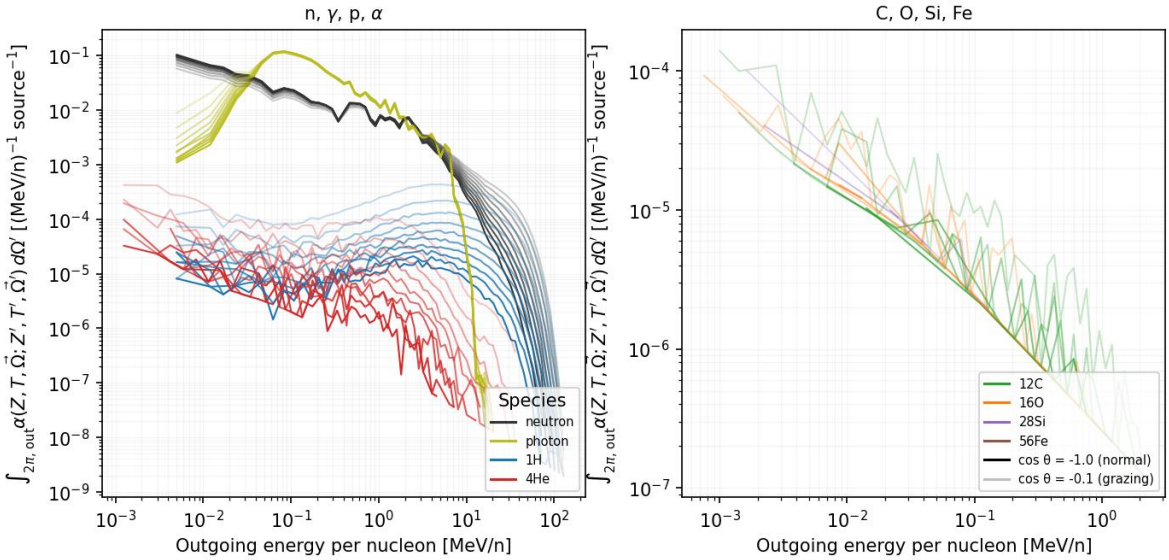


Figure A.156: Differential number albedo response function for a 42.76 MeV n^{-1} ^{4}He primary, shown for all ten simulated incident polar cosine bins ($\cos\theta = -1.0$ to -0.1).

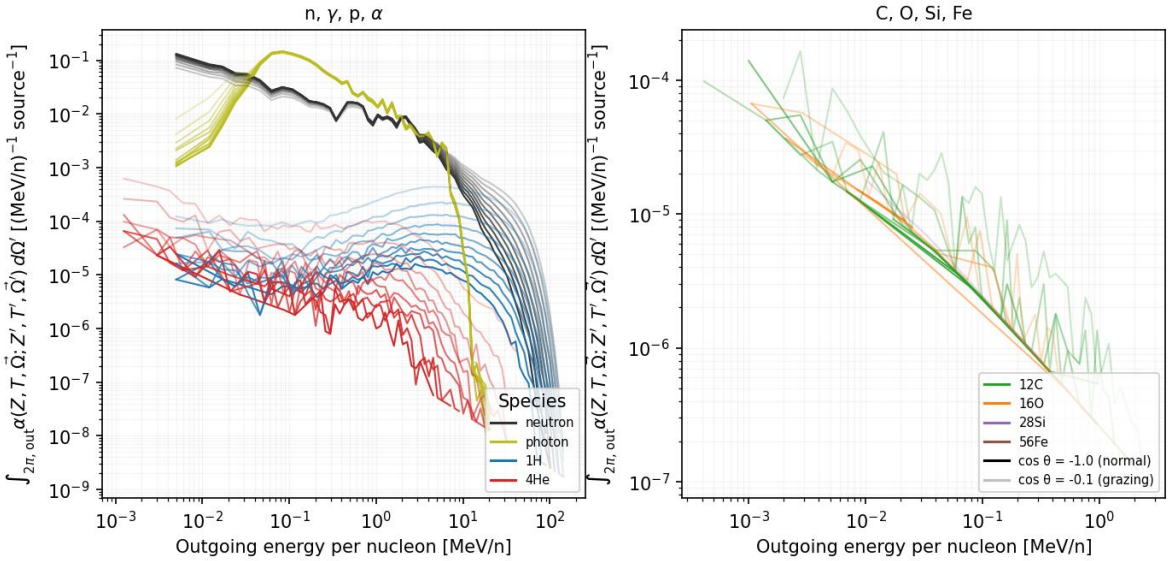


Figure A.157: Differential number albedo response function for a 47.93 MeV n^{-1} ^{4}He primary, shown for all ten simulated incident polar cosine bins ($\cos\theta = -1.0$ to -0.1).

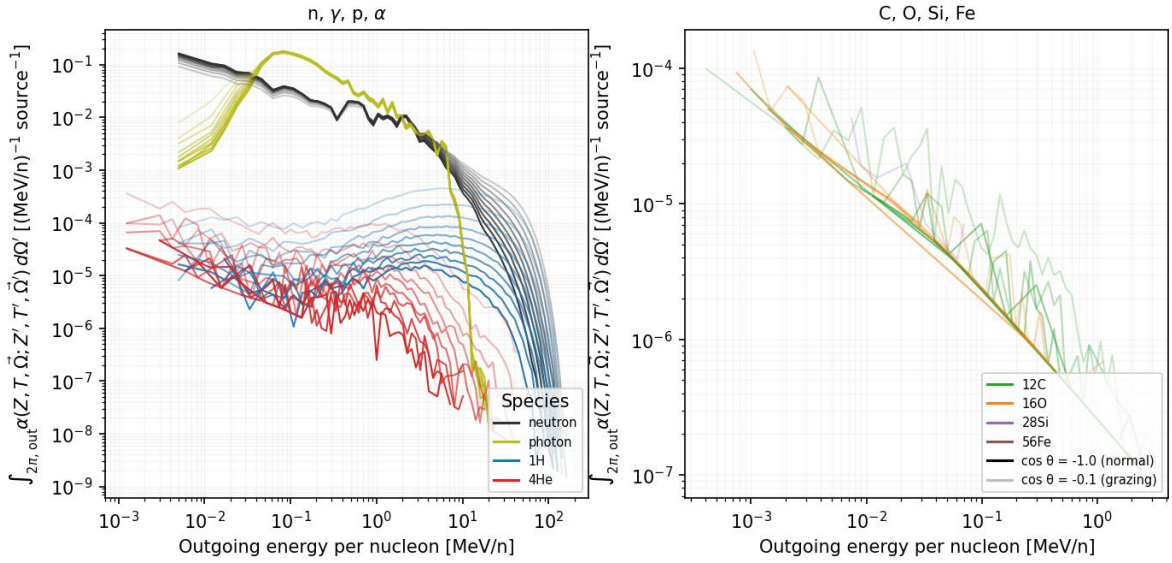


Figure A.158: Differential number albedo response function for a 53.73 MeV n^{-1} ^{4}He primary, shown for all ten simulated incident polar cosine bins ($\cos\theta = -1.0$ to -0.1).

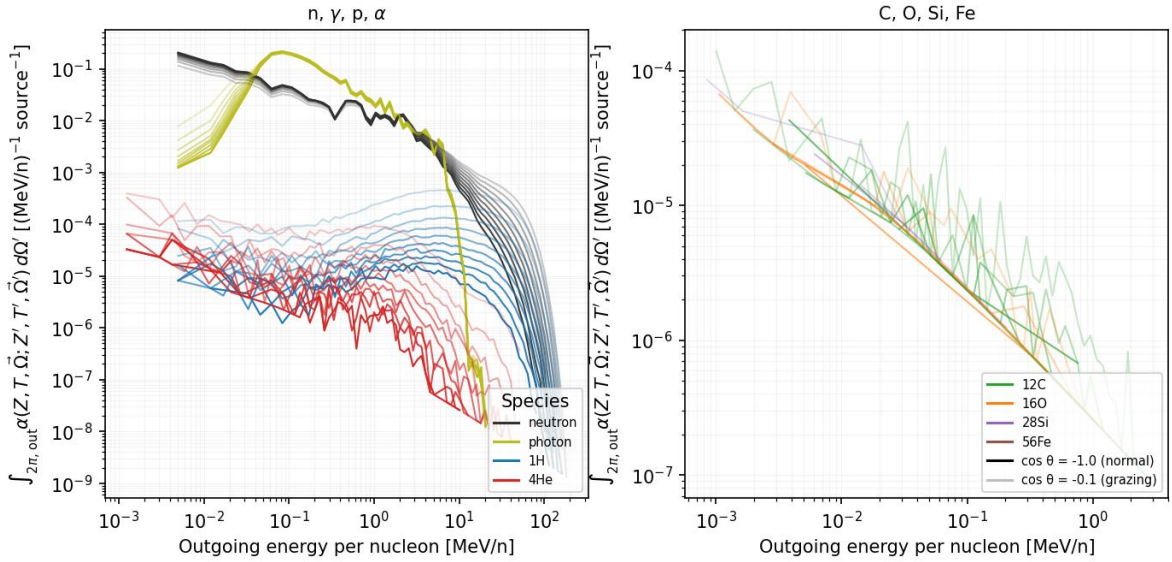


Figure A.159: Differential number albedo response function for a 60.24 MeV n^{-1} ^{4}He primary, shown for all ten simulated incident polar cosine bins ($\cos\theta = -1.0$ to -0.1).

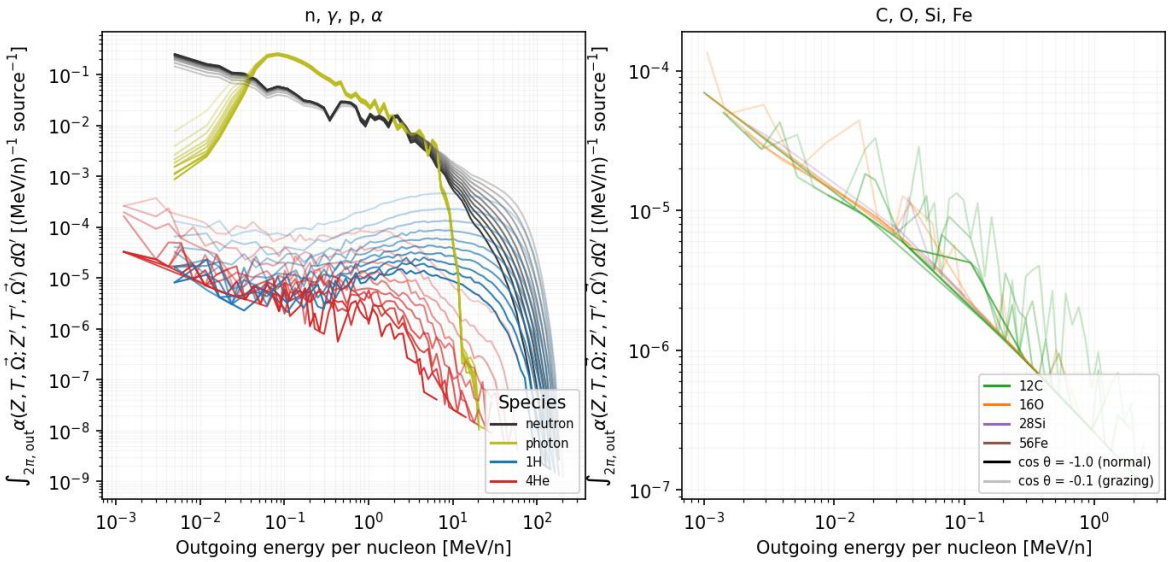


Figure A.160: Differential number albedo response function for a 67.55 MeV n^{-1} ^{4}He primary, shown for all ten simulated incident polar cosine bins ($\cos\theta = -1.0$ to -0.1).

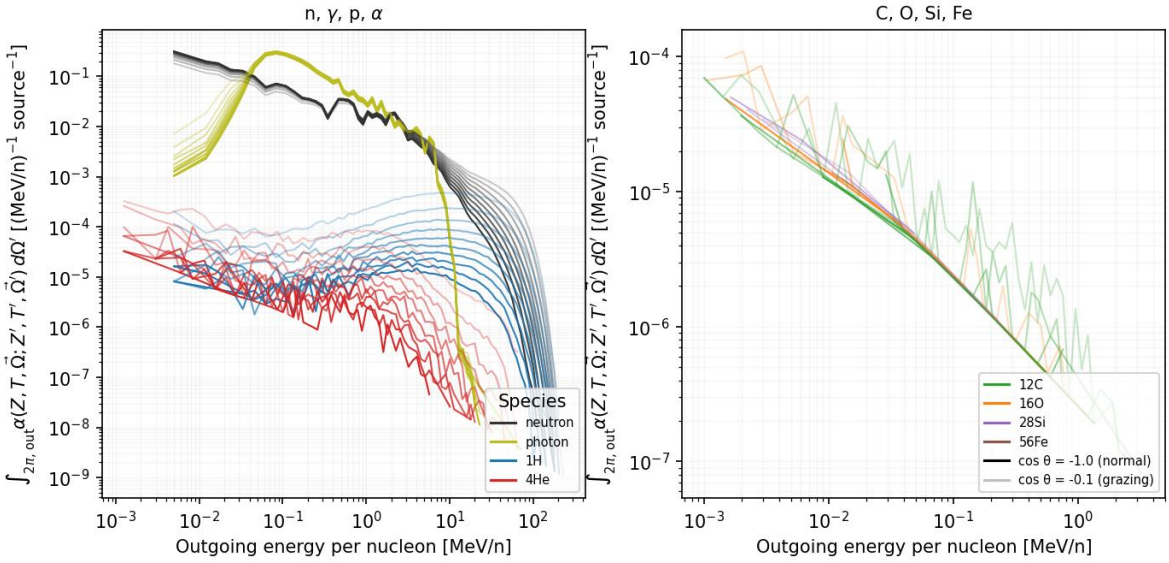


Figure A.161: Differential number albedo response function for a 75.77 MeV n^{-1} ^{4}He primary, shown for all ten simulated incident polar cosine bins ($\cos\theta = -1.0$ to -0.1).

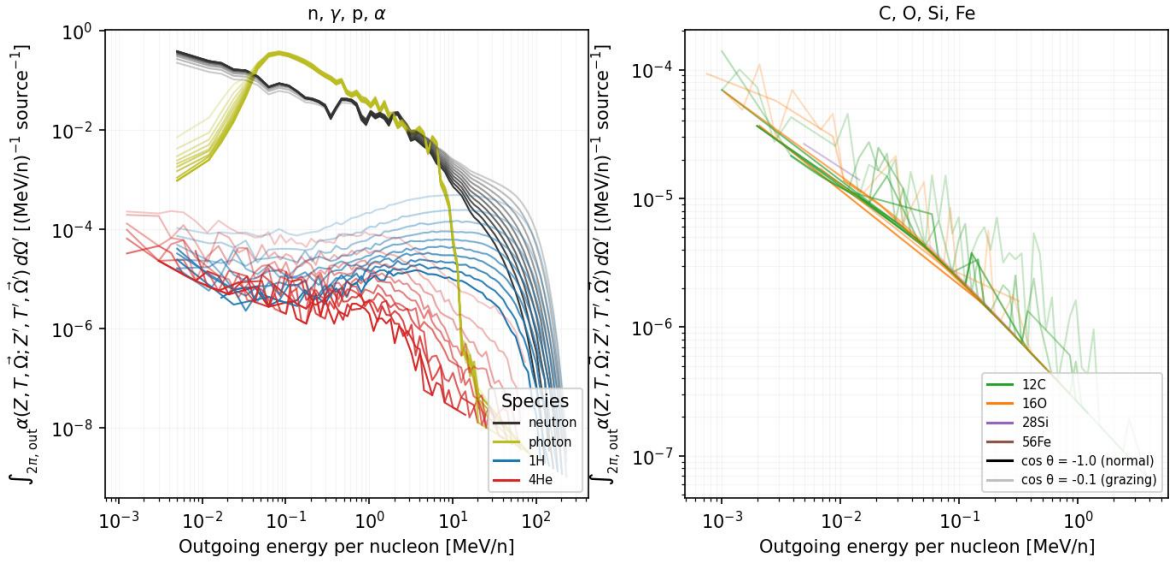


Figure A.162: Differential number albedo response function for a 85.01 MeV n^{-1} ^{4}He primary, shown for all ten simulated incident polar cosine bins ($\cos\theta = -1.0$ to -0.1).

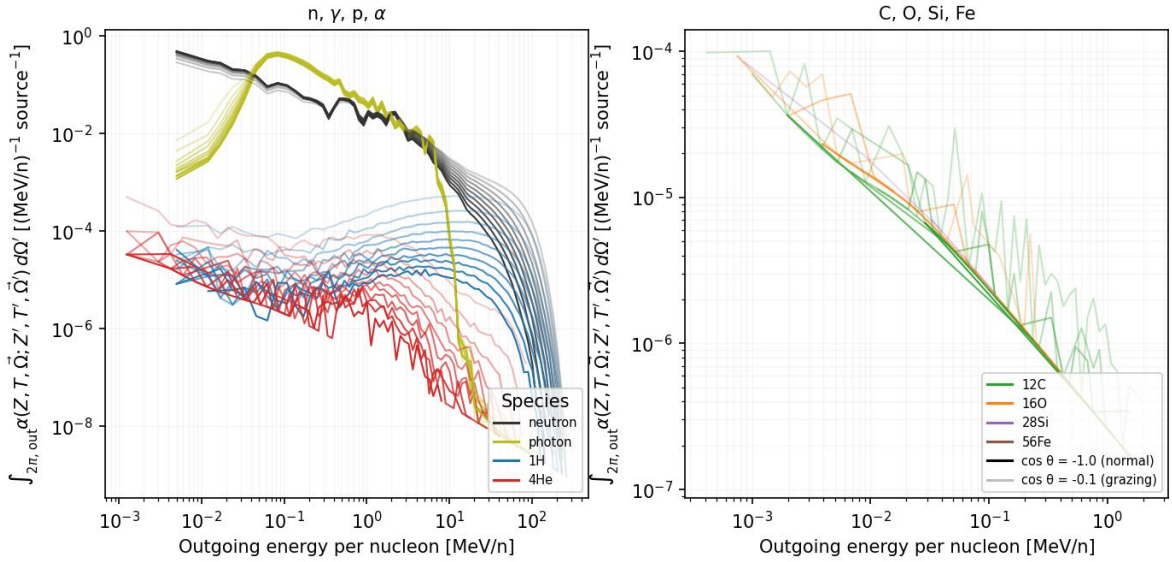


Figure A.163: Differential number albedo response function for a 95.41 MeV n^{-1} ^{4}He primary, shown for all ten simulated incident polar cosine bins ($\cos\theta = -1.0$ to -0.1).

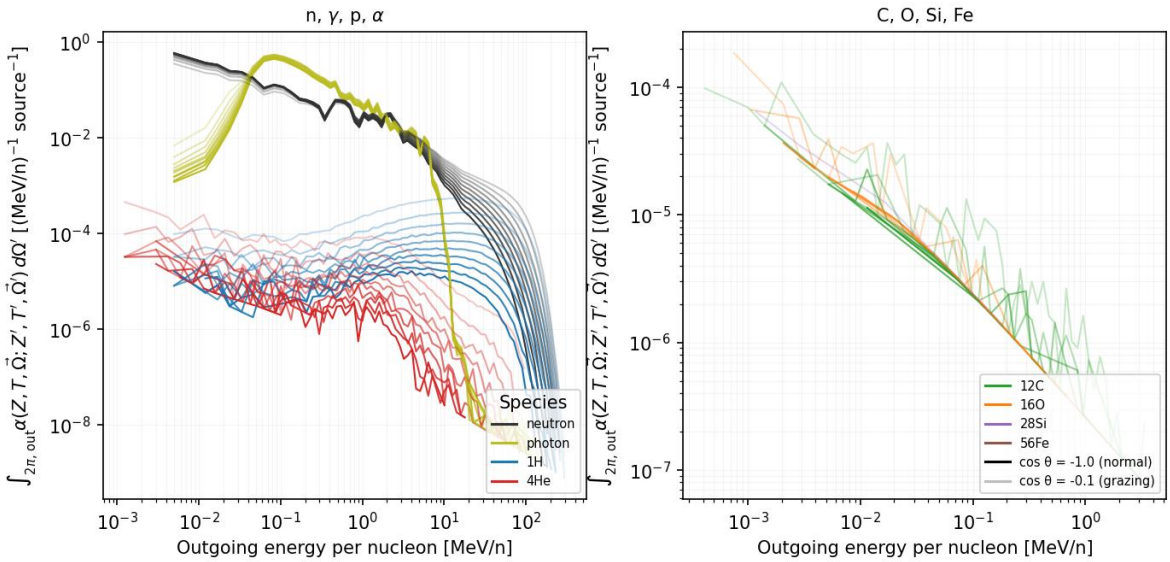


Figure A.164: Differential number albedo response function for a 107.1 MeV n^{-1} ^{4}He primary, shown for all ten simulated incident polar cosine bins ($\cos\theta = -1.0$ to -0.1).

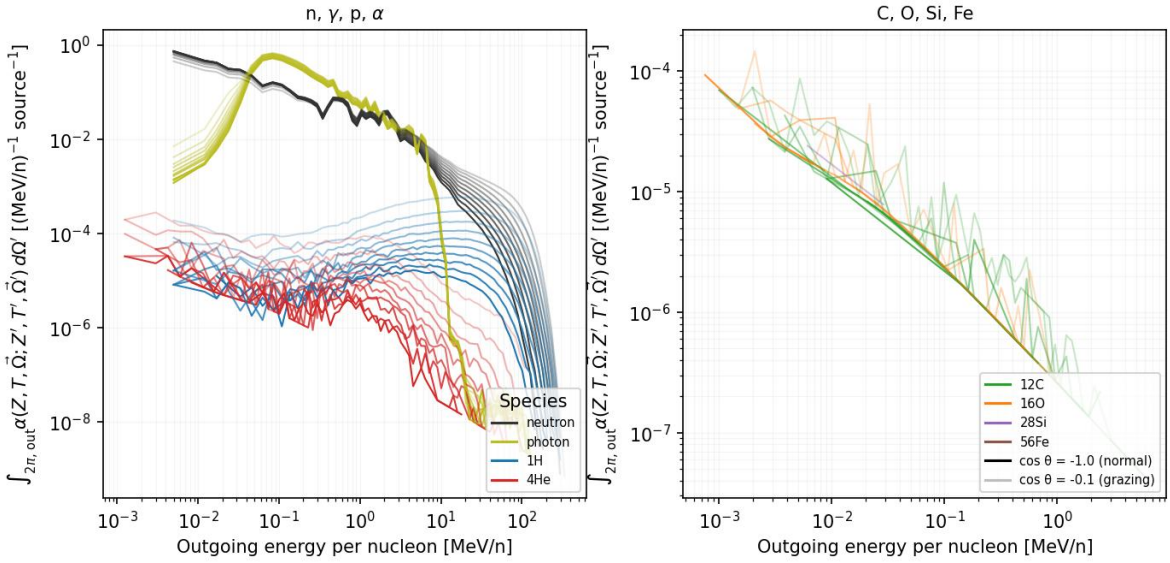


Figure A.165: Differential number albedo response function for a 120.4 MeV n^{-1} ^{4}He primary, shown for all ten simulated incident polar cosine bins ($\cos\theta = -1.0$ to -0.1).

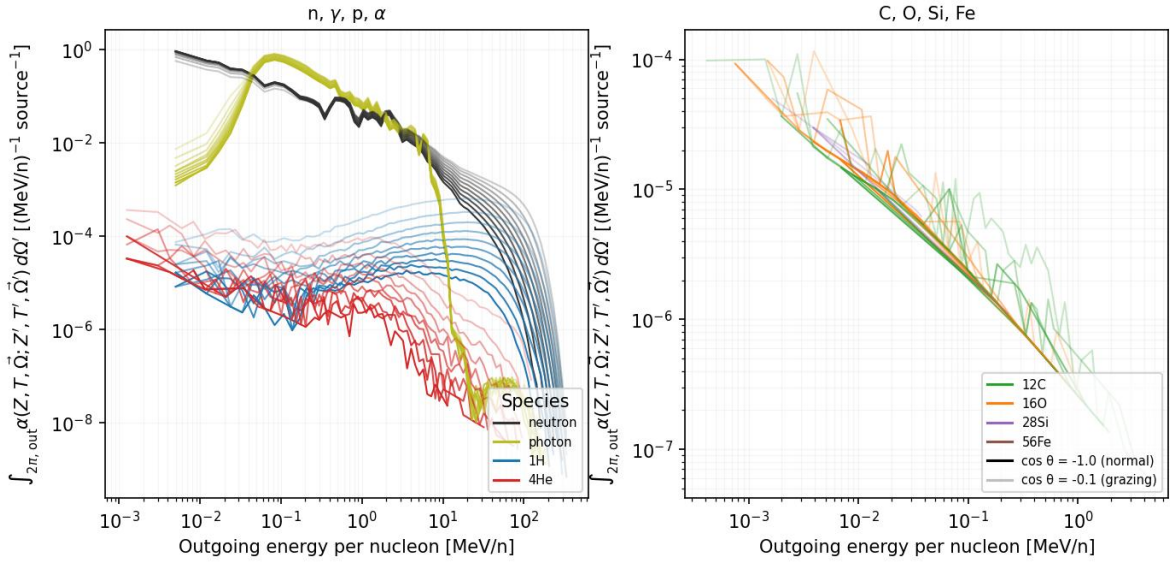


Figure A.166: Differential number albedo response function for a 135.3 MeV n^{-1} ^{4}He primary, shown for all ten simulated incident polar cosine bins ($\cos\theta = -1.0$ to -0.1).

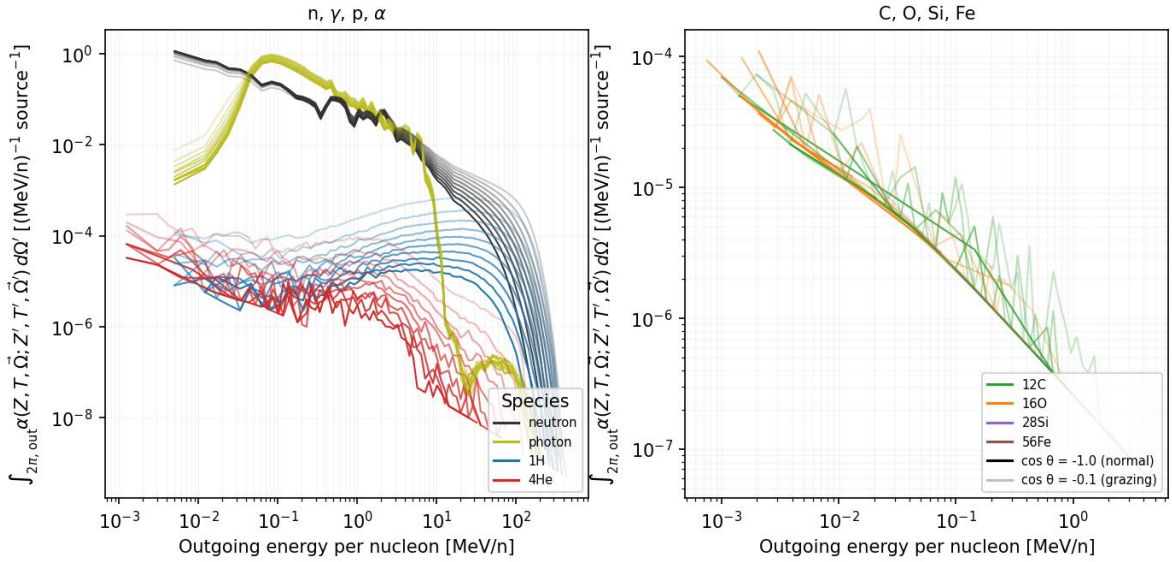


Figure A.167: Differential number albedo response function for a 152.2 MeV n^{-1} ^{4}He primary, shown for all ten simulated incident polar cosine bins ($\cos\theta = -1.0$ to -0.1).

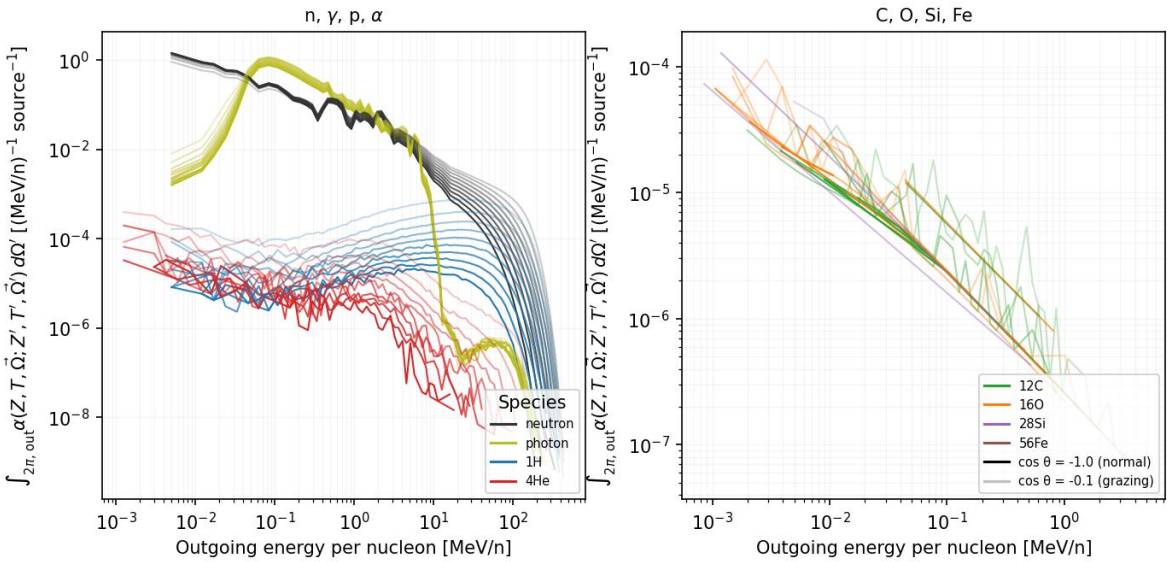


Figure A.168: Differential number albedo response function for a 171.4 MeV n^{-1} ^{4}He primary, shown for all ten simulated incident polar cosine bins ($\cos\theta = -1.0$ to -0.1).

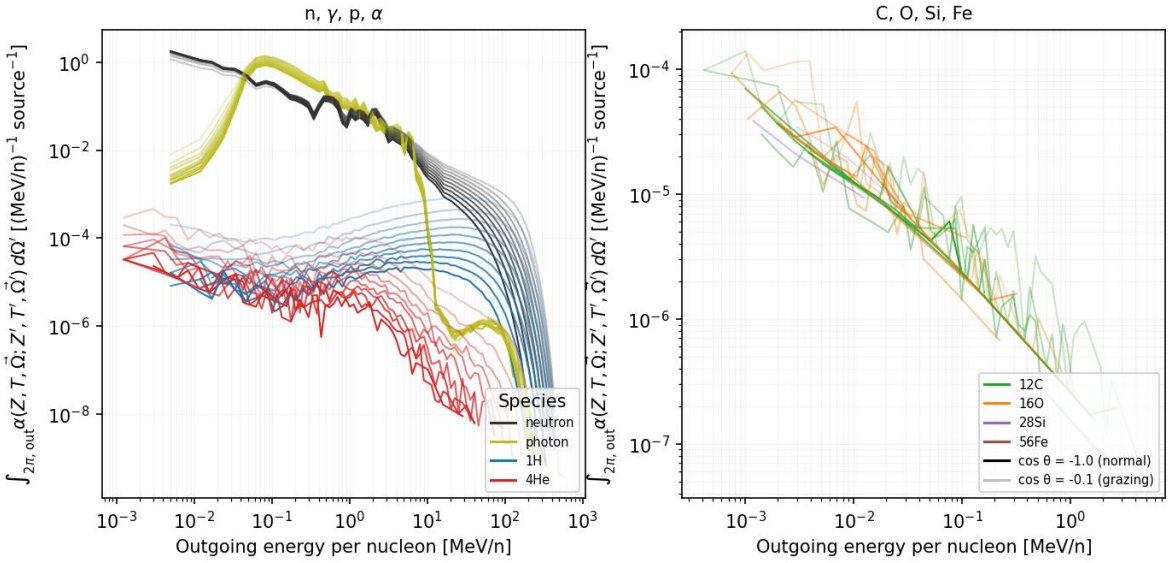


Figure A.169: Differential number albedo response function for a 193 MeV n^{-1} ^{4}He primary, shown for all ten simulated incident polar cosine bins ($\cos\theta = -1.0$ to -0.1).

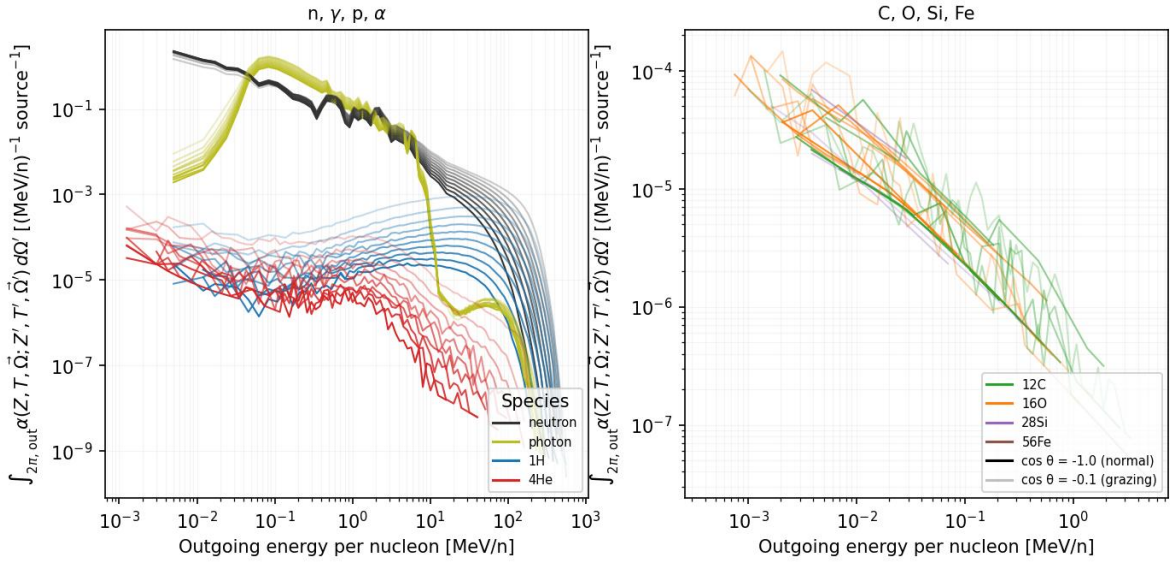


Figure A.170: Differential number albedo response function for a 217.9 MeV n^{-1} ^{4}He primary, shown for all ten simulated incident polar cosine bins ($\cos\theta = -1.0$ to -0.1).

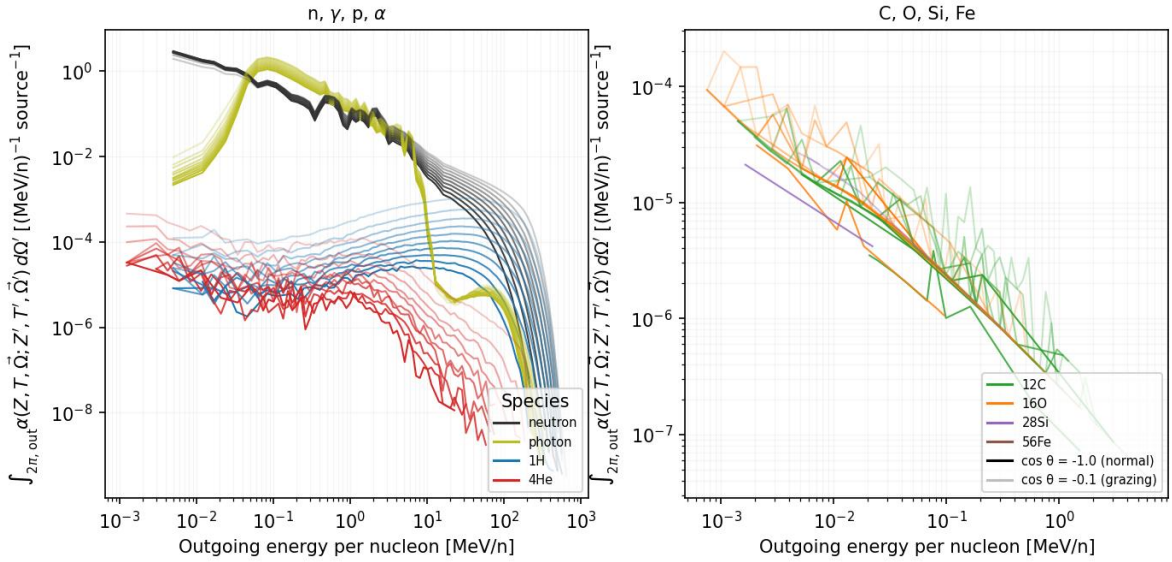


Figure A.171: Differential number albedo response function for a 246.2 MeV n^{-1} ^{4}He primary, shown for all ten simulated incident polar cosine bins ($\cos\theta = -1.0$ to -0.1).

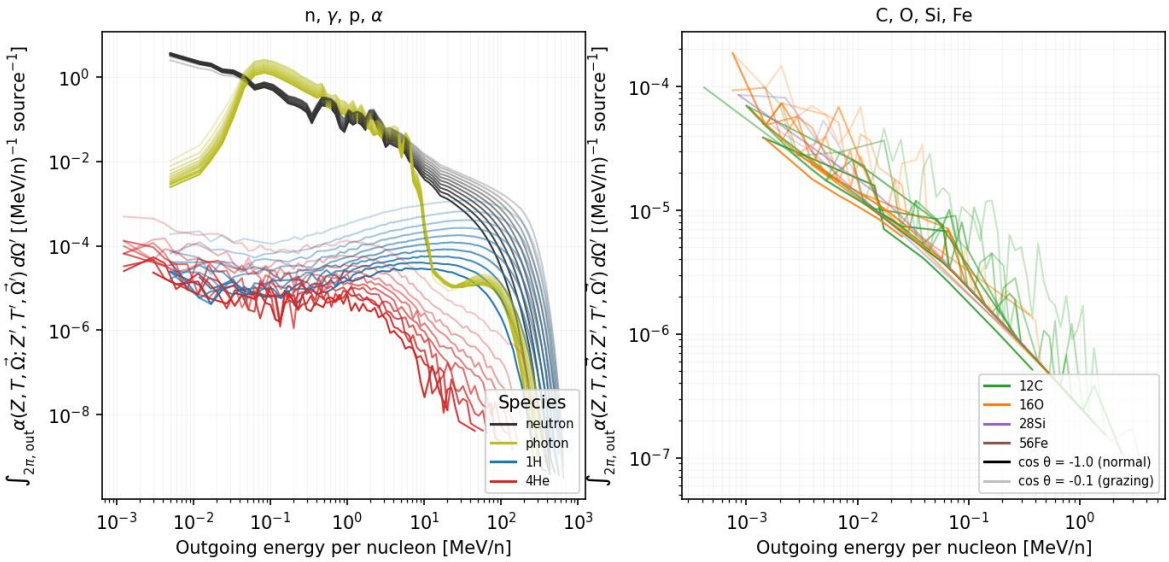


Figure A.172: Differential number albedo response function for a 278.1 MeV n^{-1} ^{4}He primary, shown for all ten simulated incident polar cosine bins ($\cos\theta = -1.0$ to -0.1).

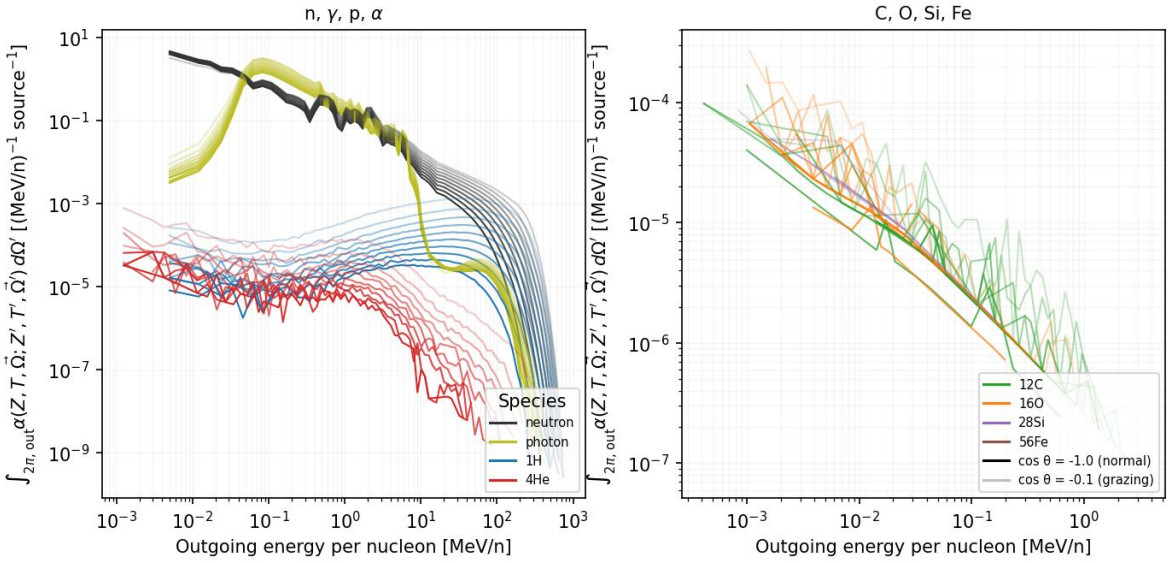


Figure A.173: Differential number albedo response function for a 314.7 MeV n^{-1} ^{4}He primary, shown for all ten simulated incident polar cosine bins ($\cos\theta = -1.0$ to -0.1).

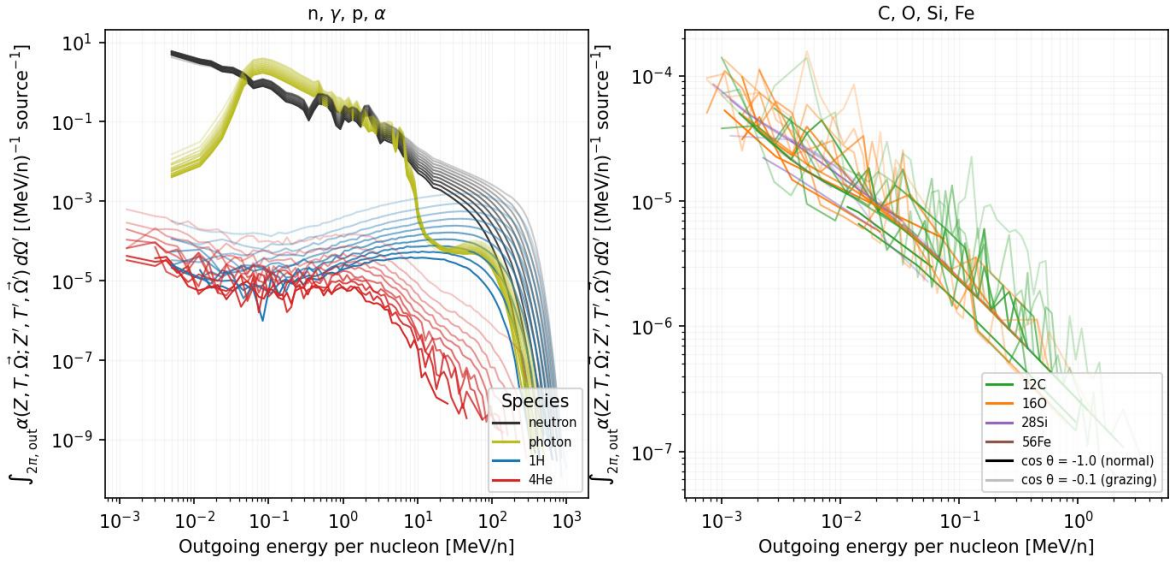


Figure A.174: Differential number albedo response function for a 357.1 MeV n^{-1} ^{4}He primary, shown for all ten simulated incident polar cosine bins ($\cos\theta = -1.0$ to -0.1).

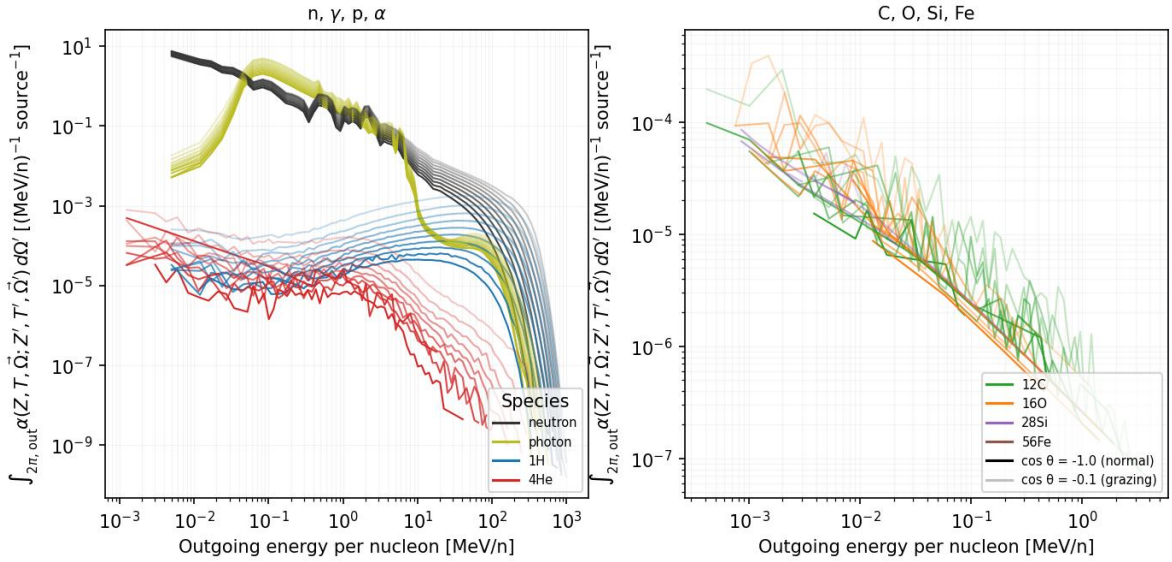


Figure A.175: Differential number albedo response function for a 405.3 MeV n^{-1} ^{4}He primary, shown for all ten simulated incident polar cosine bins ($\cos\theta = -1.0$ to -0.1).

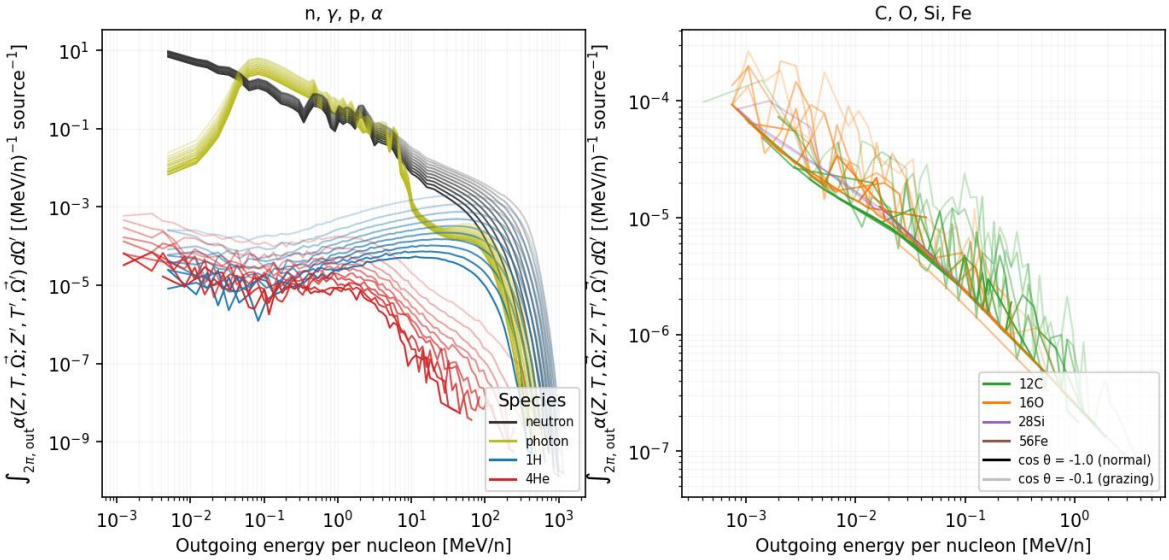


Figure A.176: Differential number albedo response function for a 461.8 MeV n^{-1} ^{4}He primary, shown for all ten simulated incident polar cosine bins ($\cos\theta = -1.0$ to -0.1).

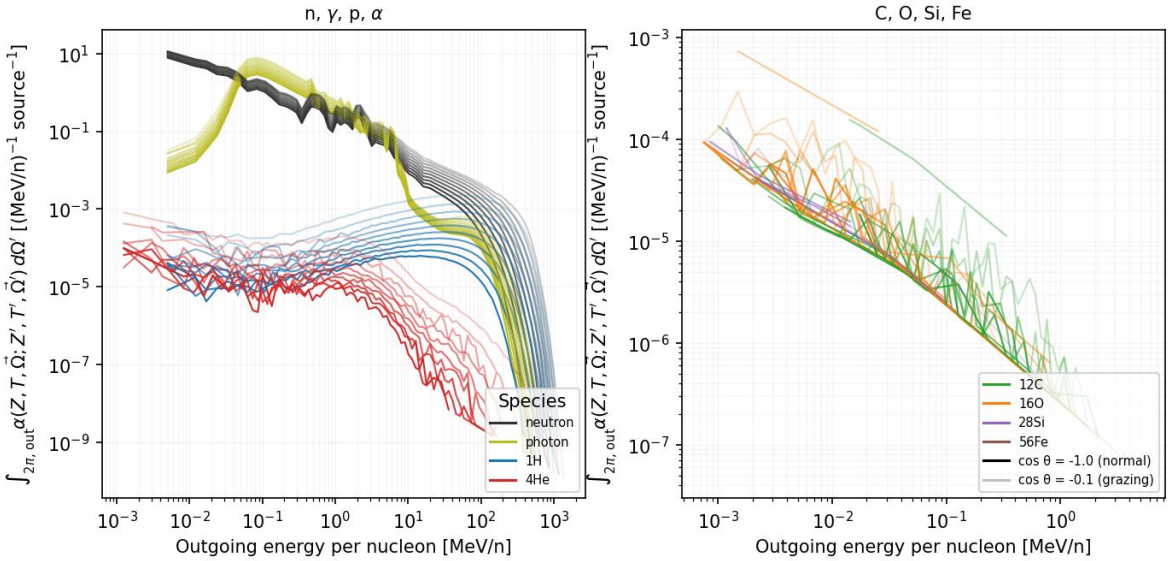


Figure A.177: Differential number albedo response function for a 526.8 MeV n^{-1} ^{4}He primary, shown for all ten simulated incident polar cosine bins ($\cos\theta = -1.0$ to -0.1).

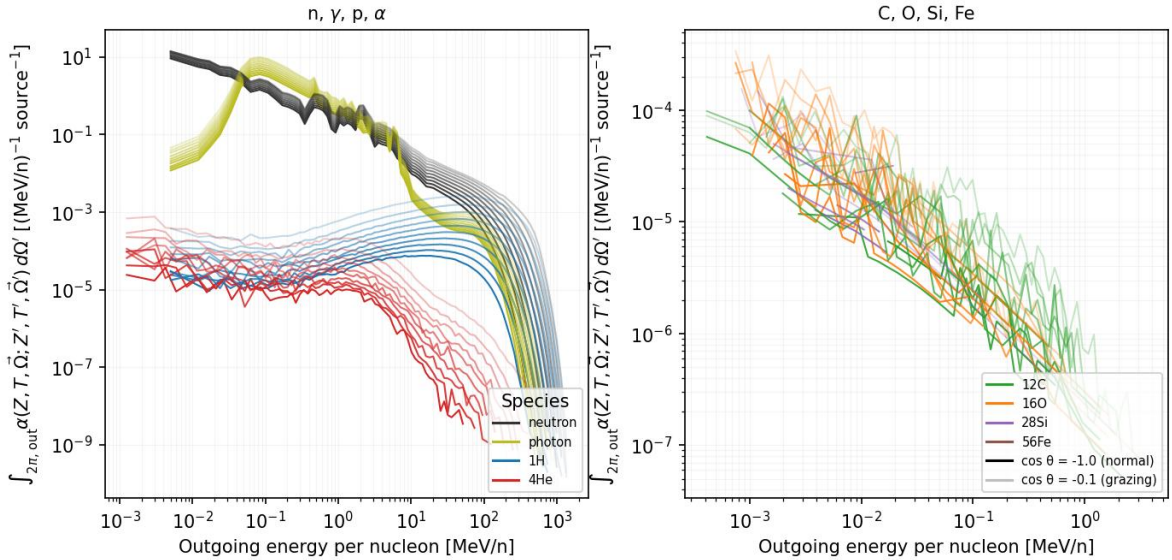


Figure A.178: Differential number albedo response function for a 602.5 MeV n^{-1} ^{4}He primary, shown for all ten simulated incident polar cosine bins ($\cos\theta = -1.0$ to -0.1).

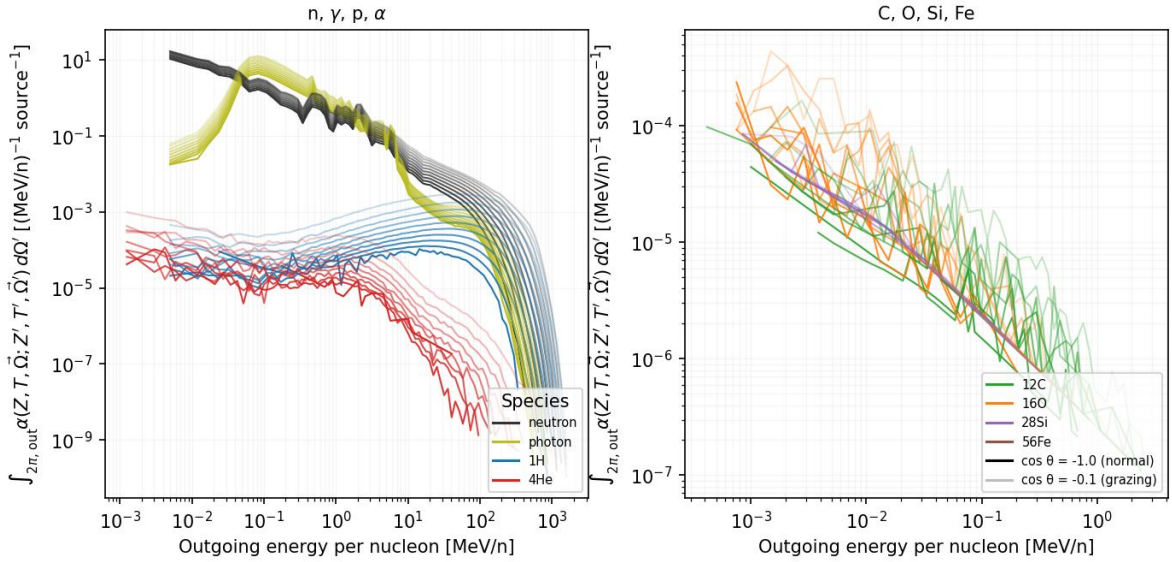


Figure A.179: Differential number albedo response function for a 691.3 MeV n^{-1} ^{4}He primary, shown for all ten simulated incident polar cosine bins ($\cos\theta = -1.0$ to -0.1).

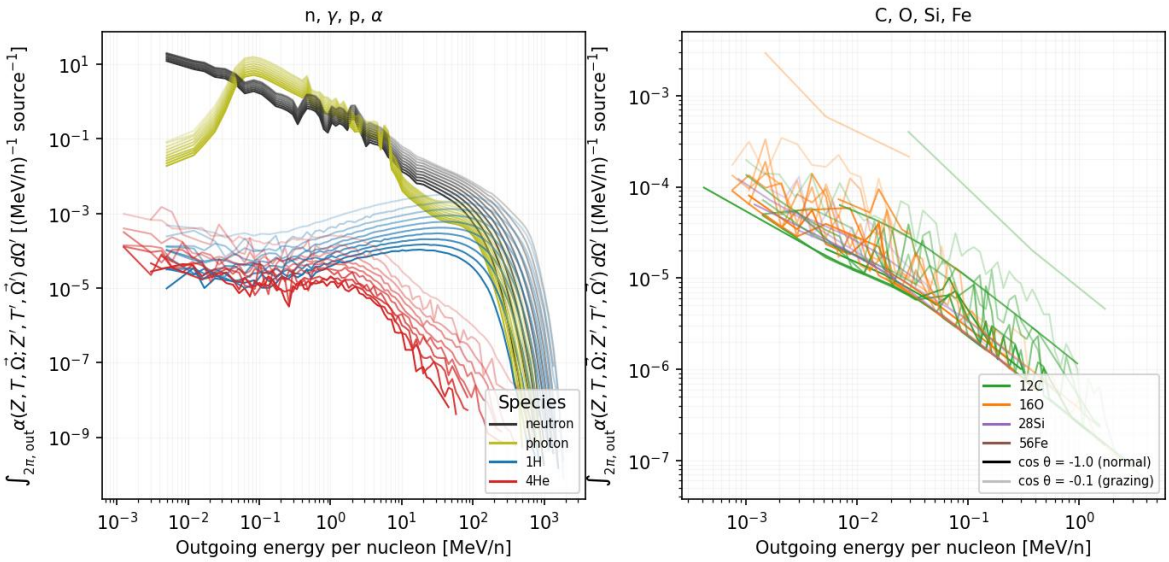


Figure A.180: Differential number albedo response function for a 795.7 MeV n^{-1} ^{4}He primary, shown for all ten simulated incident polar cosine bins ($\cos\theta = -1.0$ to -0.1).

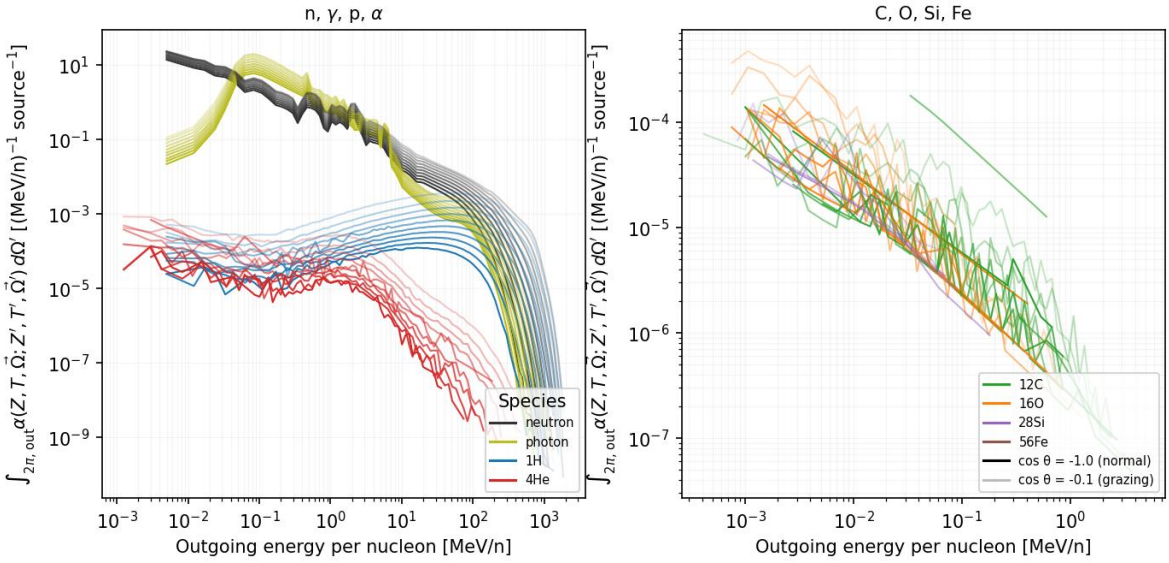


Figure A.181: Differential number albedo response function for a 919.2 MeV n^{-1} ^{4}He primary, shown for all ten simulated incident polar cosine bins ($\cos\theta = -1.0$ to -0.1).

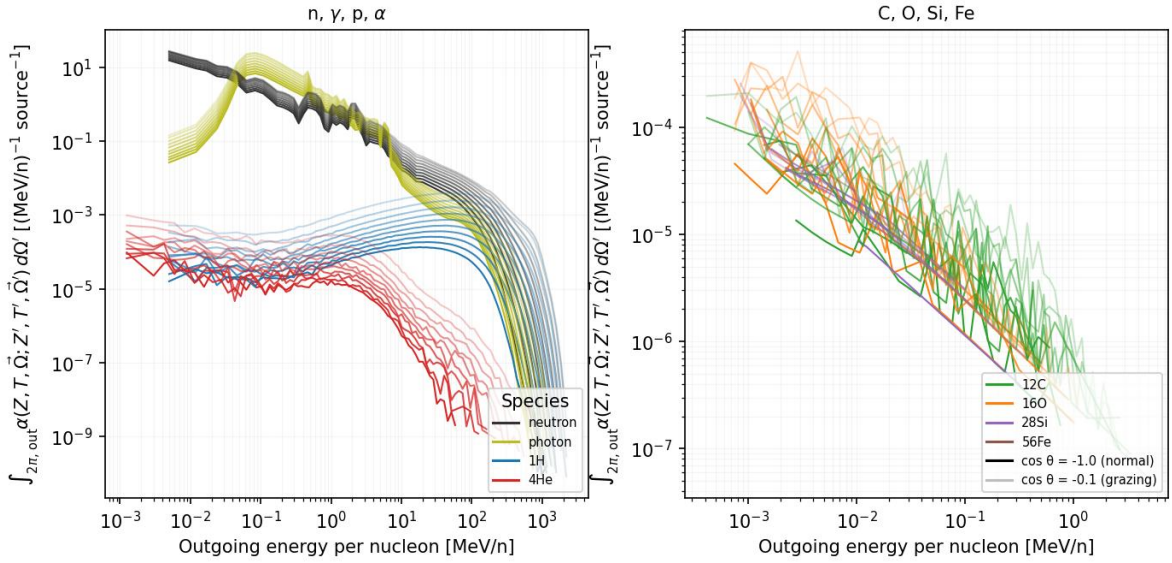


Figure A.182: Differential number albedo response function for a 1.068 GeV n^{-1} ^{4}He primary, shown for all ten simulated incident polar cosine bins ($\cos\theta = -1.0$ to -0.1).

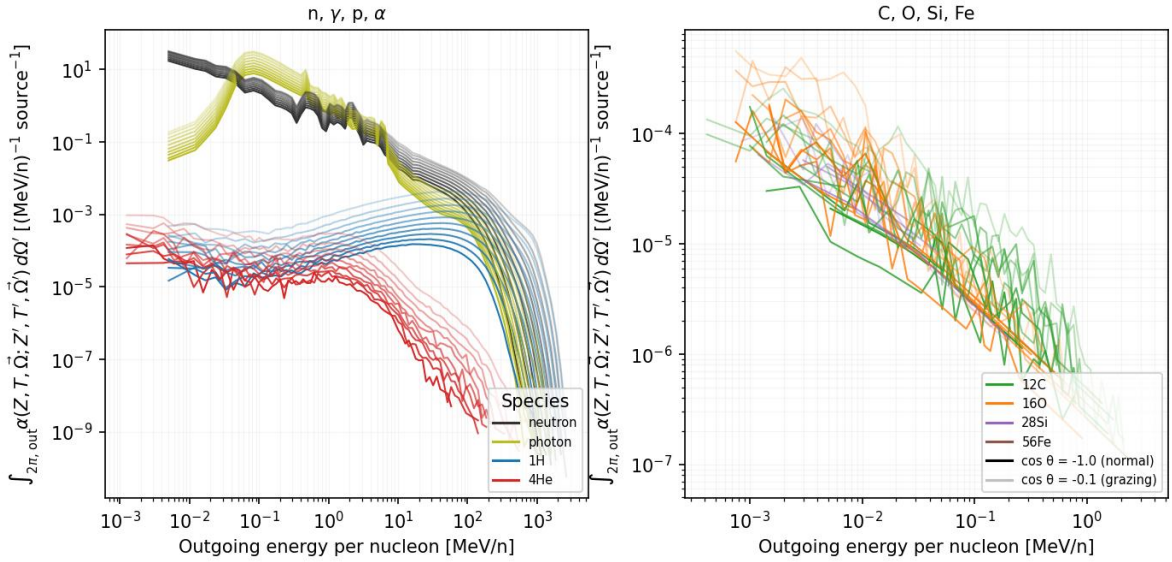


Figure A.183: Differential number albedo response function for a 1.246 GeV n^{-1} ^{4}He primary, shown for all ten simulated incident polar cosine bins ($\cos\theta = -1.0$ to -0.1).

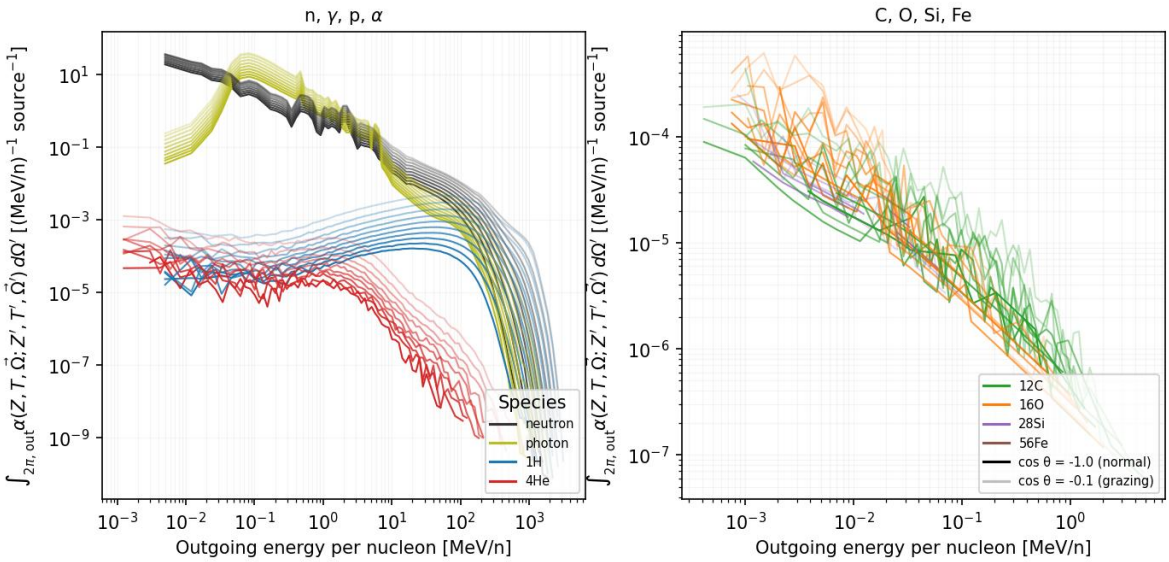


Figure A.184: Differential number albedo response function for a 1.453 GeV n^{-1} ^{4}He primary, shown for all ten simulated incident polar cosine bins ($\cos\theta = -1.0$ to -0.1).

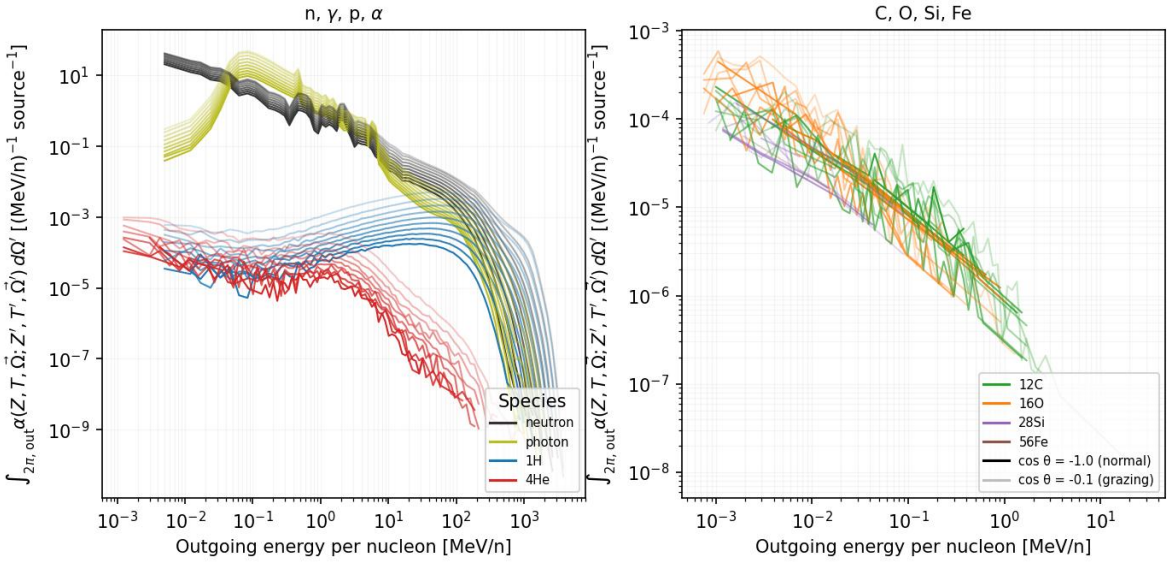


Figure A.185: Differential number albedo response function for a 1.71 GeV n^{-1} ^{4}He primary, shown for all ten simulated incident polar cosine bins ($\cos\theta = -1.0$ to -0.1).

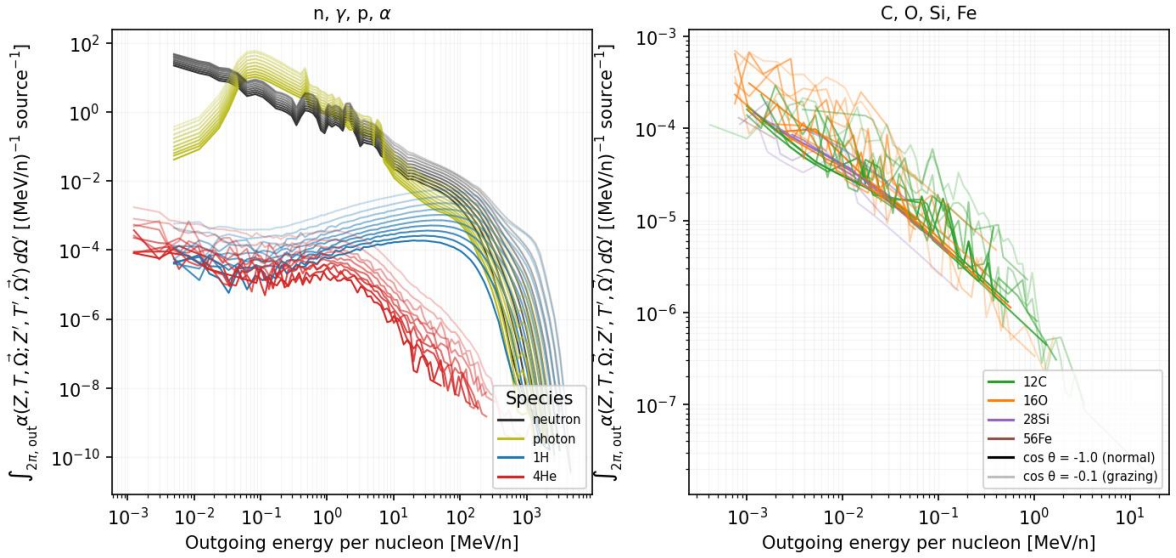


Figure A.186: Differential number albedo response function for a 2.016 GeV n^{-1} ^{4}He primary, shown for all ten simulated incident polar cosine bins ($\cos\theta = -1.0$ to -0.1).

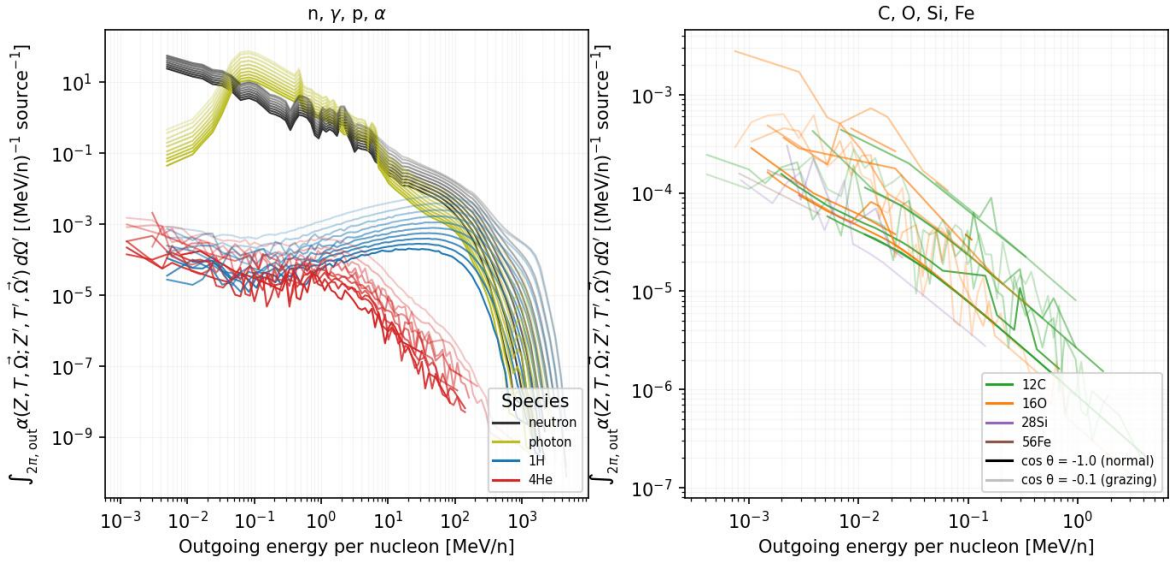


Figure A.187: Differential number albedo response function for a 2.397 GeV n^{-1} ^{4}He primary, shown for all ten simulated incident polar cosine bins ($\cos\theta = -1.0$ to -0.1).

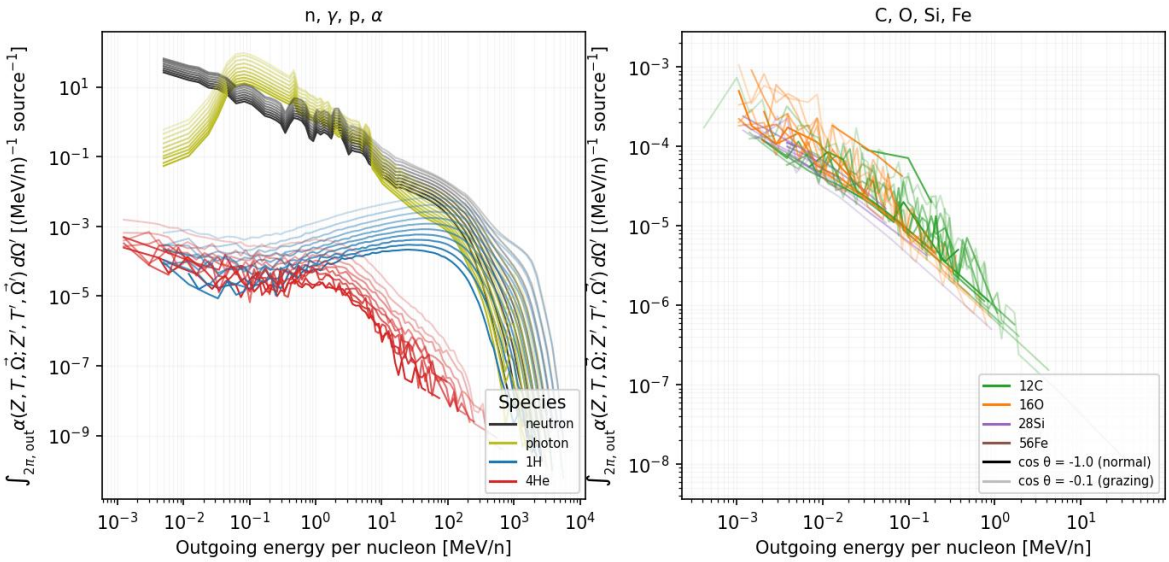


Figure A.188: Differential number albedo response function for a 2.863 GeV n^{-1} ^{4}He primary, shown for all ten simulated incident polar cosine bins ($\cos\theta = -1.0$ to -0.1).

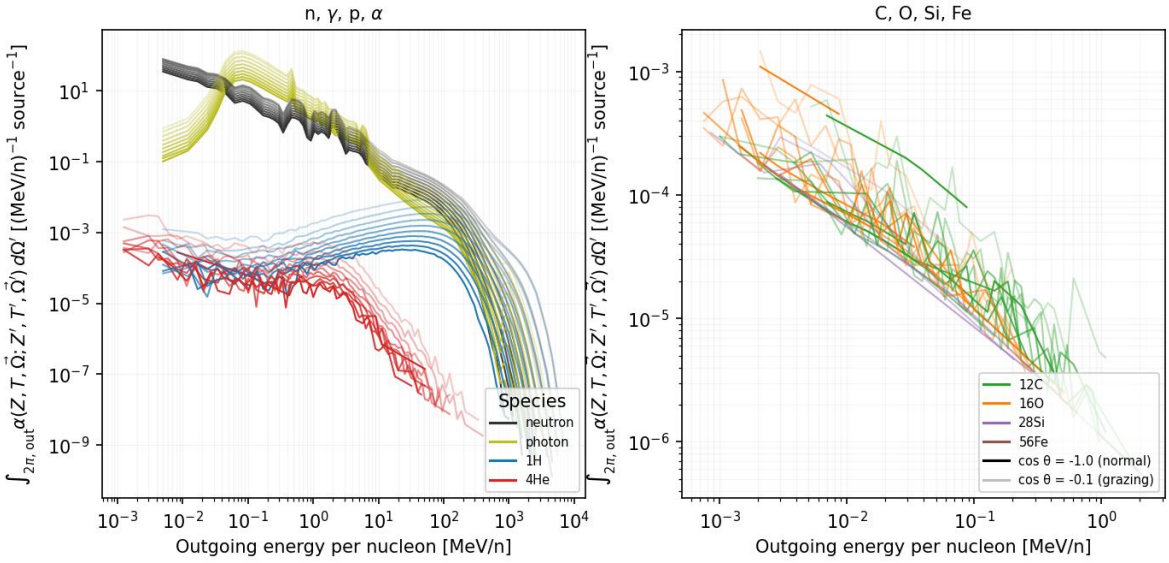


Figure A.189: Differential number albedo response function for a 3.444 GeV n^{-1} ^{4}He primary, shown for all ten simulated incident polar cosine bins ($\cos\theta = -1.0$ to -0.1).

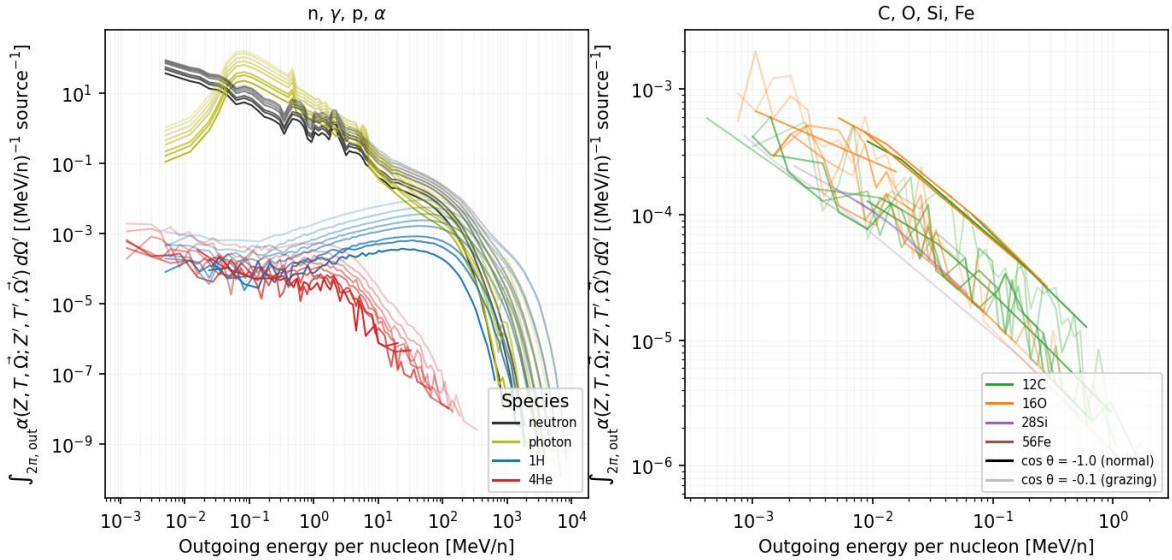


Figure A.190: Differential number albedo response function for a 4.156 GeV n^{-1} ^{4}He primary, shown for all ten simulated incident polar cosine bins ($\cos\theta = -1.0$ to -0.1).

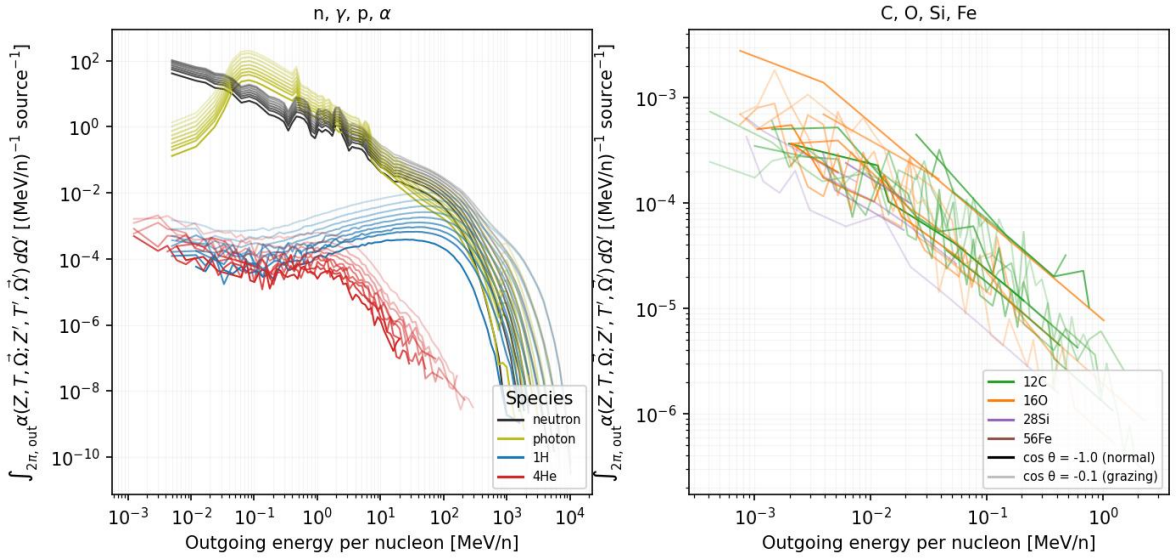


Figure A.191: Differential number albedo response function for a 5.04 GeV n^{-1} ^{4}He primary, shown for all ten simulated incident polar cosine bins ($\cos\theta = -1.0$ to -0.1).

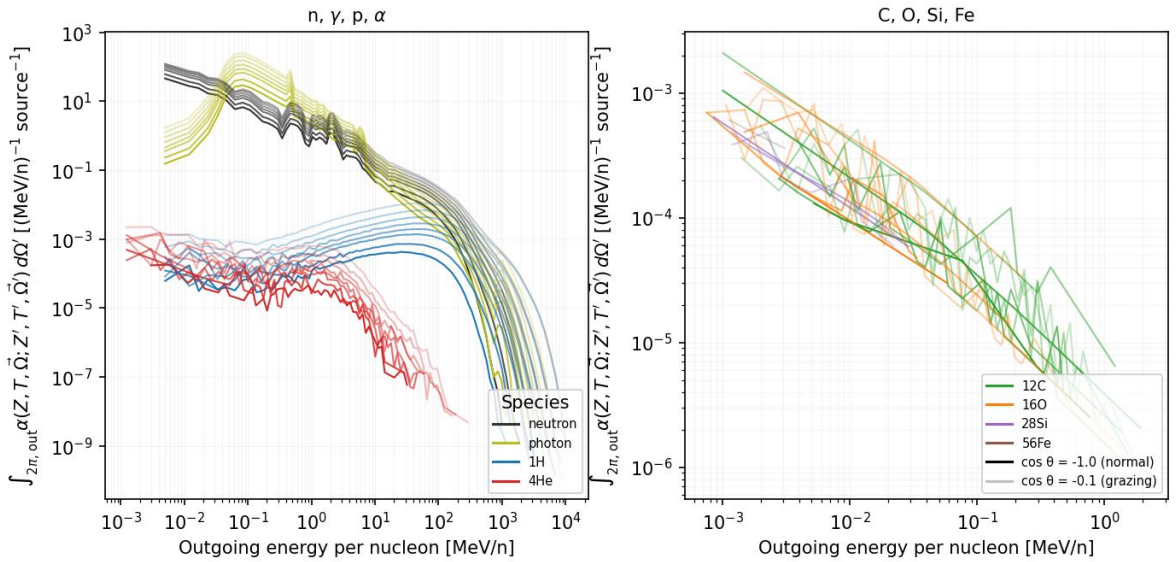


Figure A.192: Differential number albedo response function for a 6.134 GeV n^{-1} ^{4}He primary, shown for all ten simulated incident polar cosine bins ($\cos\theta = -1.0$ to -0.1).

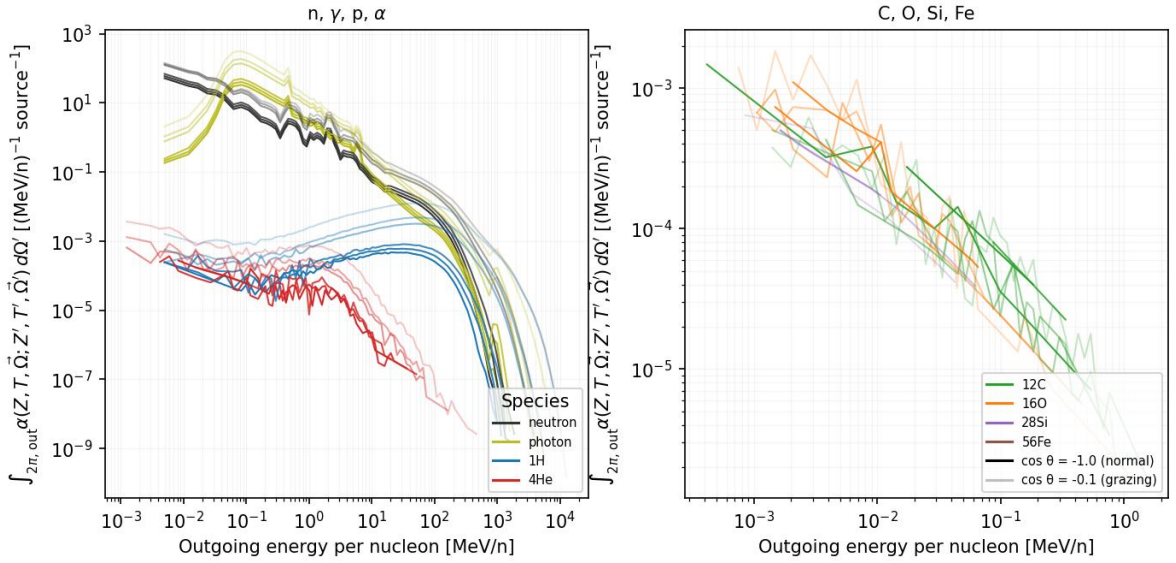


Figure A.193: Differential number albedo response function for a 7.488 GeV n^{-1} ^{4}He primary, shown for all ten simulated incident polar cosine bins ($\cos\theta = -1.0$ to -0.1).

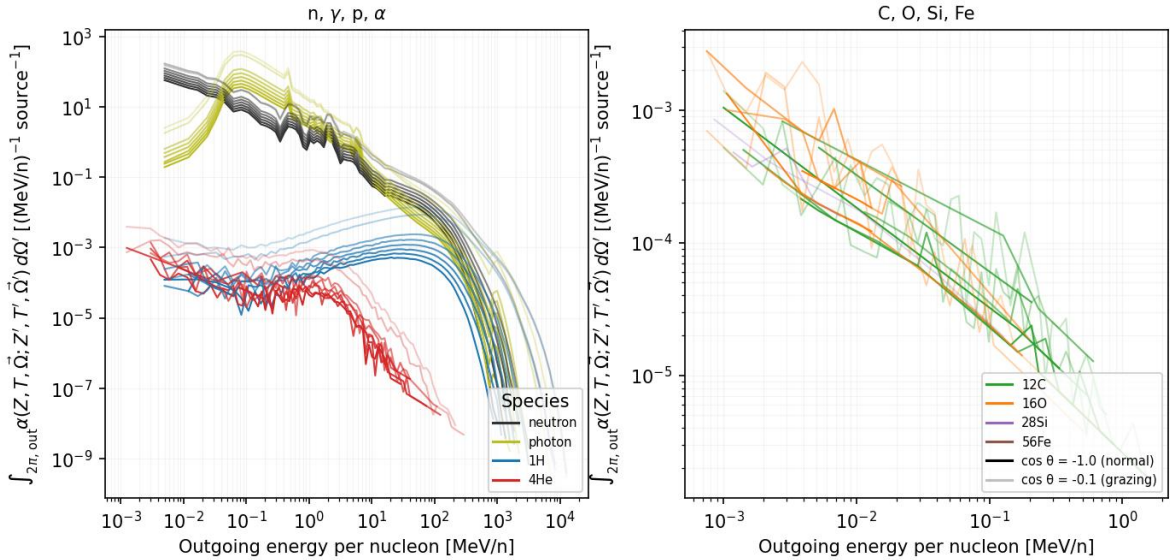


Figure A.194: Differential number albedo response function for a 9.167 GeV n^{-1} ^{4}He primary, shown for all ten simulated incident polar cosine bins ($\cos\theta = -1.0$ to -0.1).

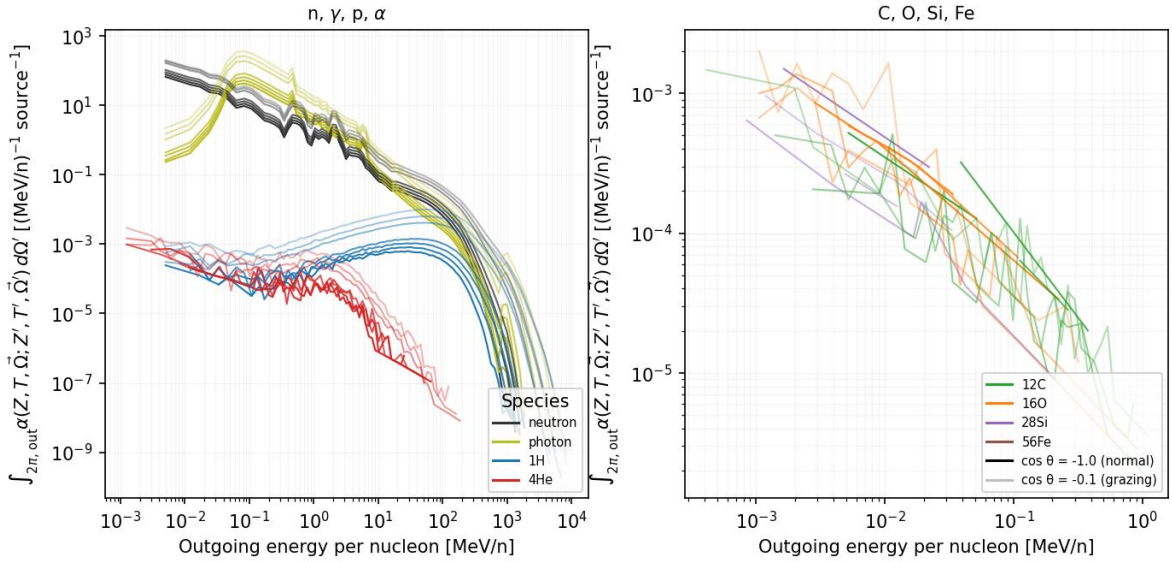


Figure A.195: Differential number albedo response function for a 11.26 GeV n^{-1} ^{4}He primary, shown for all ten simulated incident polar cosine bins ($\cos\theta = -1.0$ to -0.1).

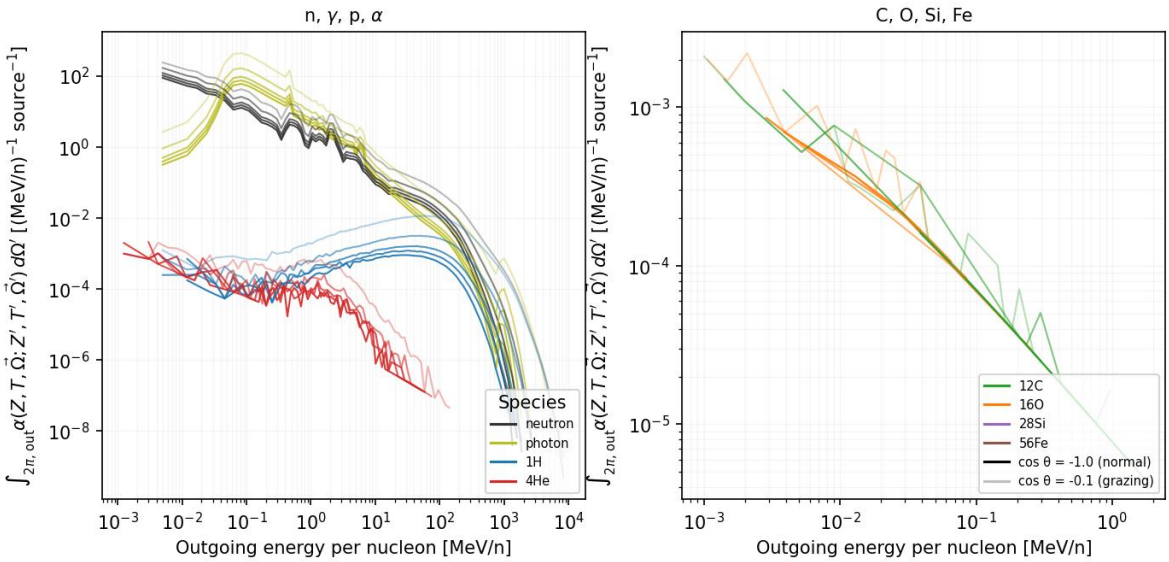


Figure A.196: Differential number albedo response function for a 13.86 GeV n^{-1} ^{4}He primary, shown for all ten simulated incident polar cosine bins ($\cos\theta = -1.0$ to -0.1).

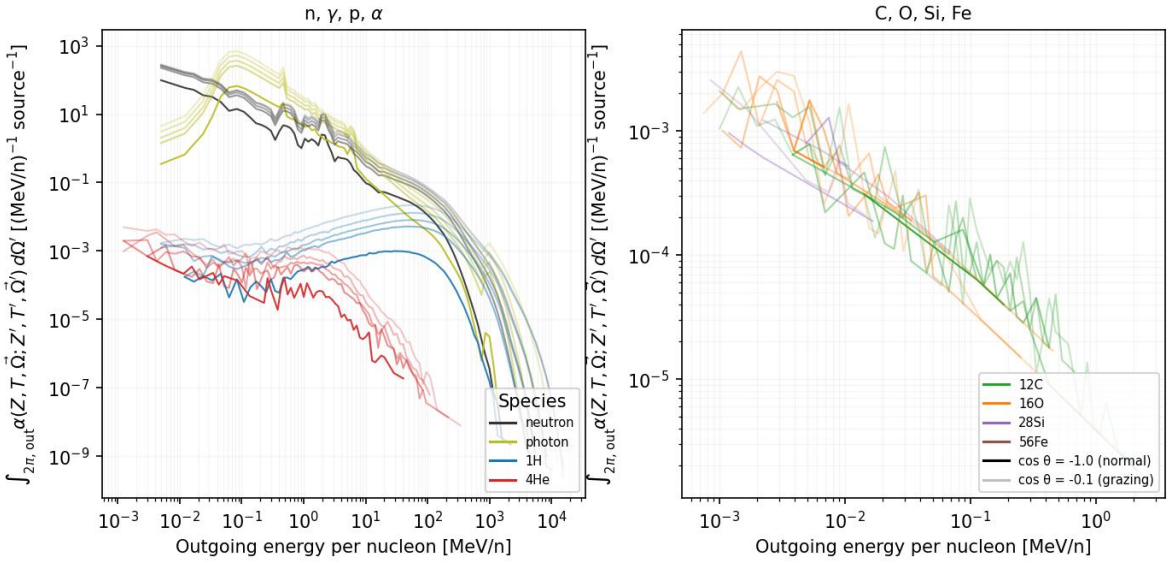


Figure A.197: Differential number albedo response function for a 17.09 GeV n^{-1} ^{4}He primary, shown for all ten simulated incident polar cosine bins ($\cos\theta = -1.0$ to -0.1).

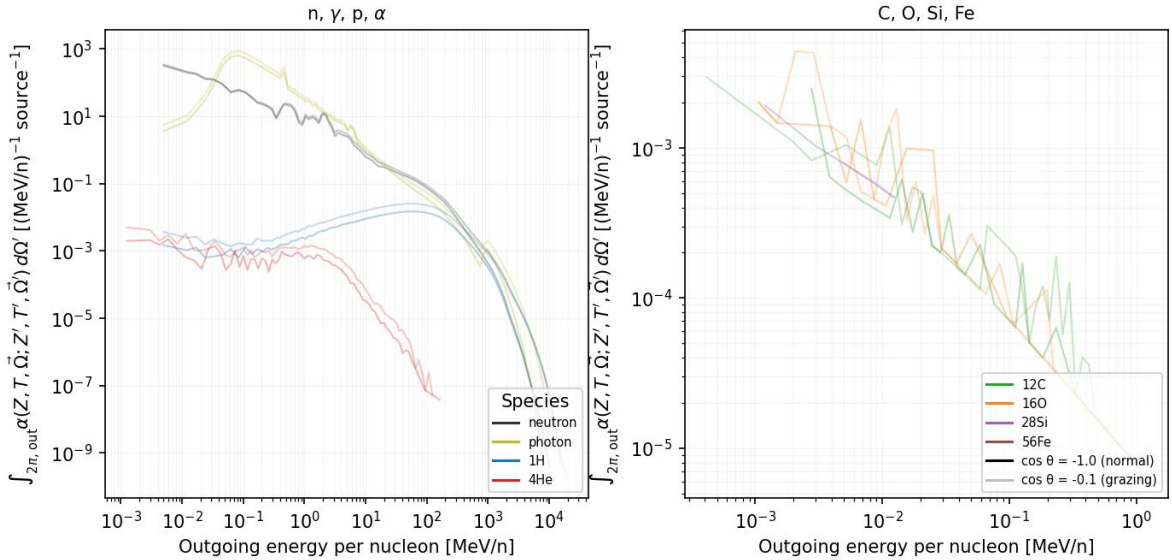


Figure A.198: Differential number albedo response function for a 21.12 GeV n^{-1} ^{4}He primary, shown for all ten simulated incident polar cosine bins ($\cos\theta = -1.0$ to -0.1).

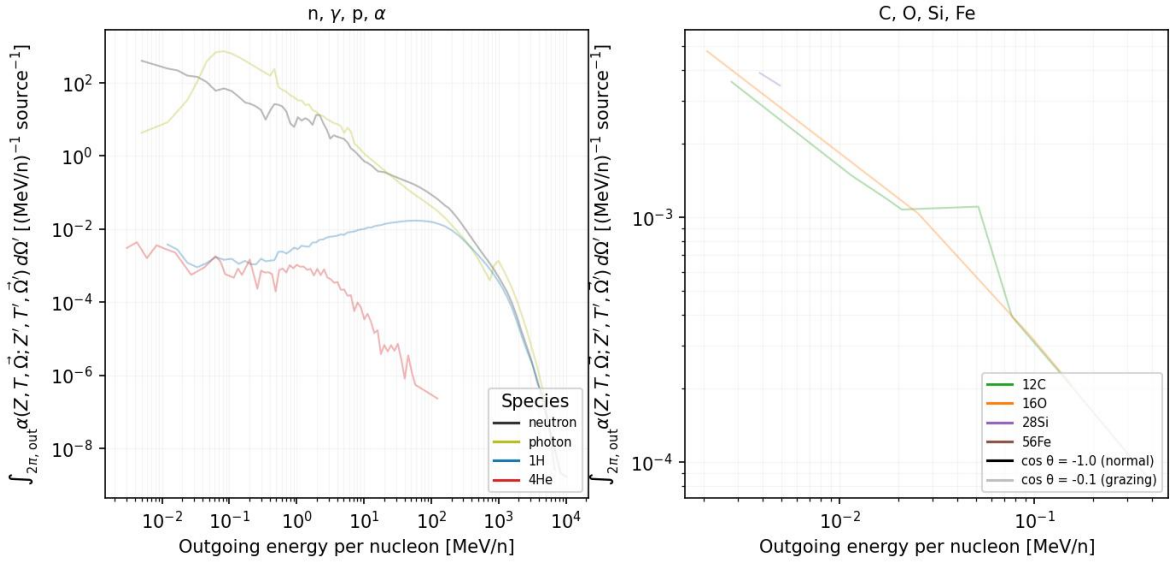


Figure A.199: Differential number albedo response function for a 26.15 GeV n^{-1} ^{4}He primary, shown for all ten simulated incident polar cosine bins ($\cos\theta = -1.0$ to -0.1).

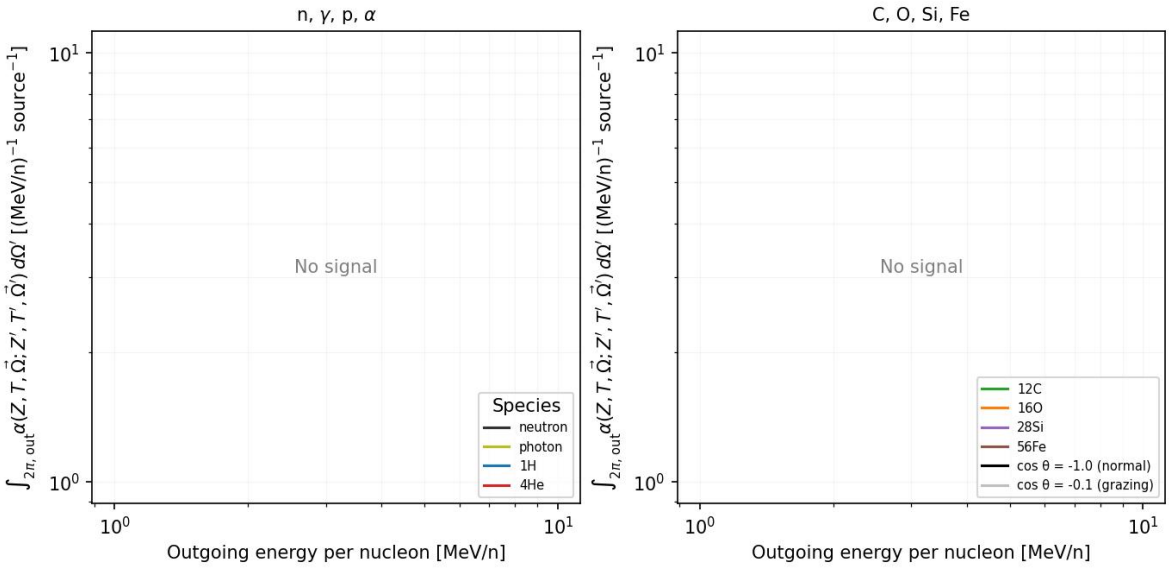


Figure A.200: Differential number albedo response function for a 32.44 GeV n^{-1} ^{4}He primary, shown for all ten simulated incident polar cosine bins ($\cos\theta = -1.0$ to -0.1).

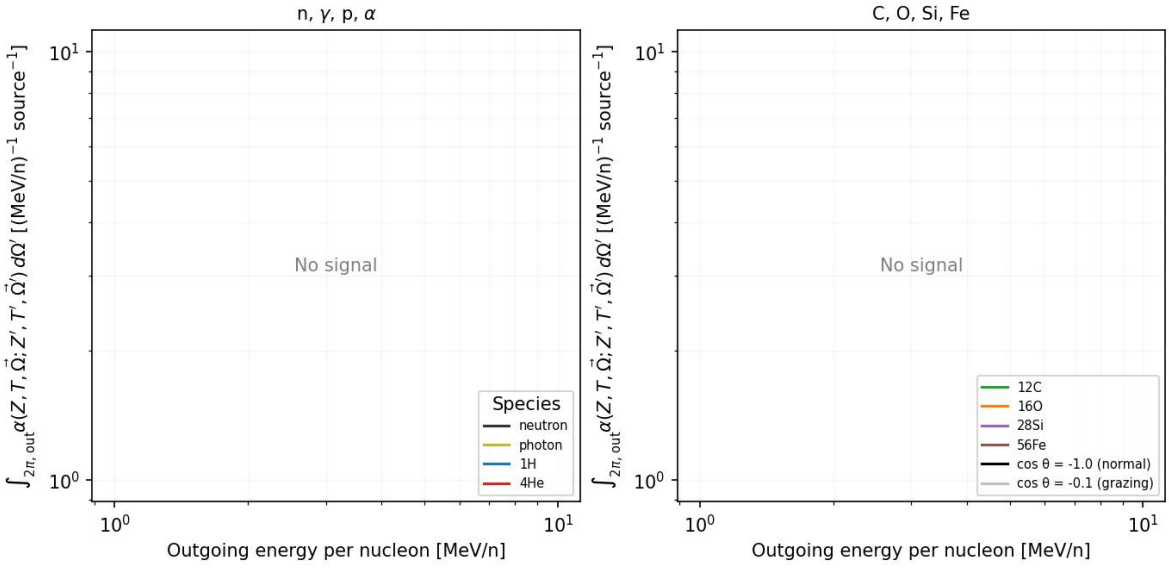


Figure A.201: Differential number albedo response function for a 40.23 GeV n^{-1} ^{4}He primary, shown for all ten simulated incident polar cosine bins ($\cos\theta = -1.0$ to -0.1).

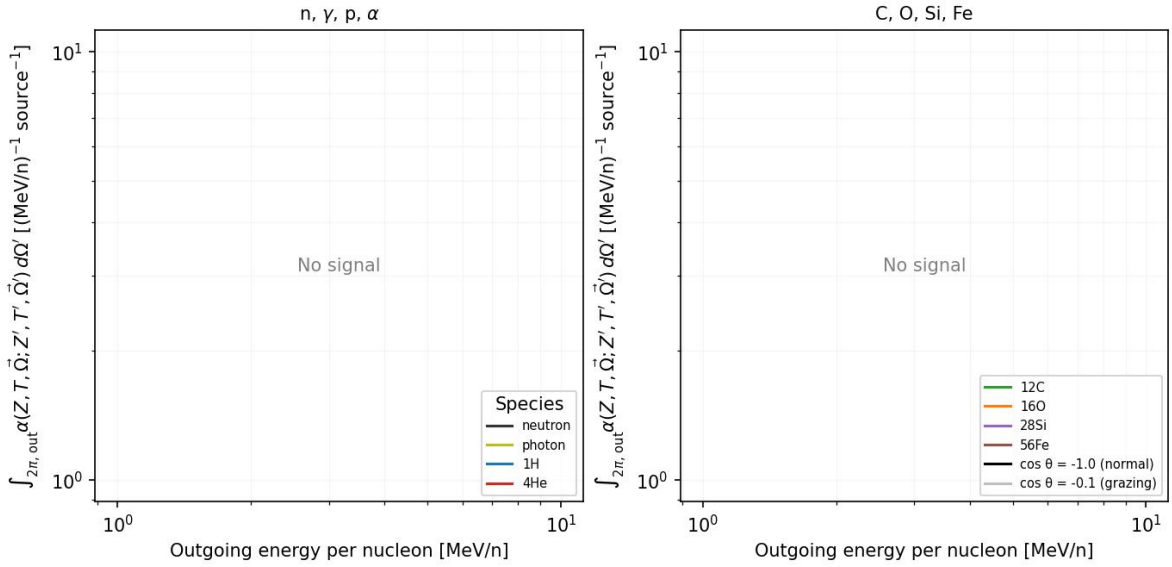


Figure A.202: Differential number albedo response function for a 50 GeV n^{-1} ^{4}He primary, shown for all ten simulated incident polar cosine bins ($\cos\theta = -1.0$ to -0.1).

A.0.1 Primary Flux Distribution at the Dome Surface

A.0.1.1 Primary Hit Distribution—Azimuthal

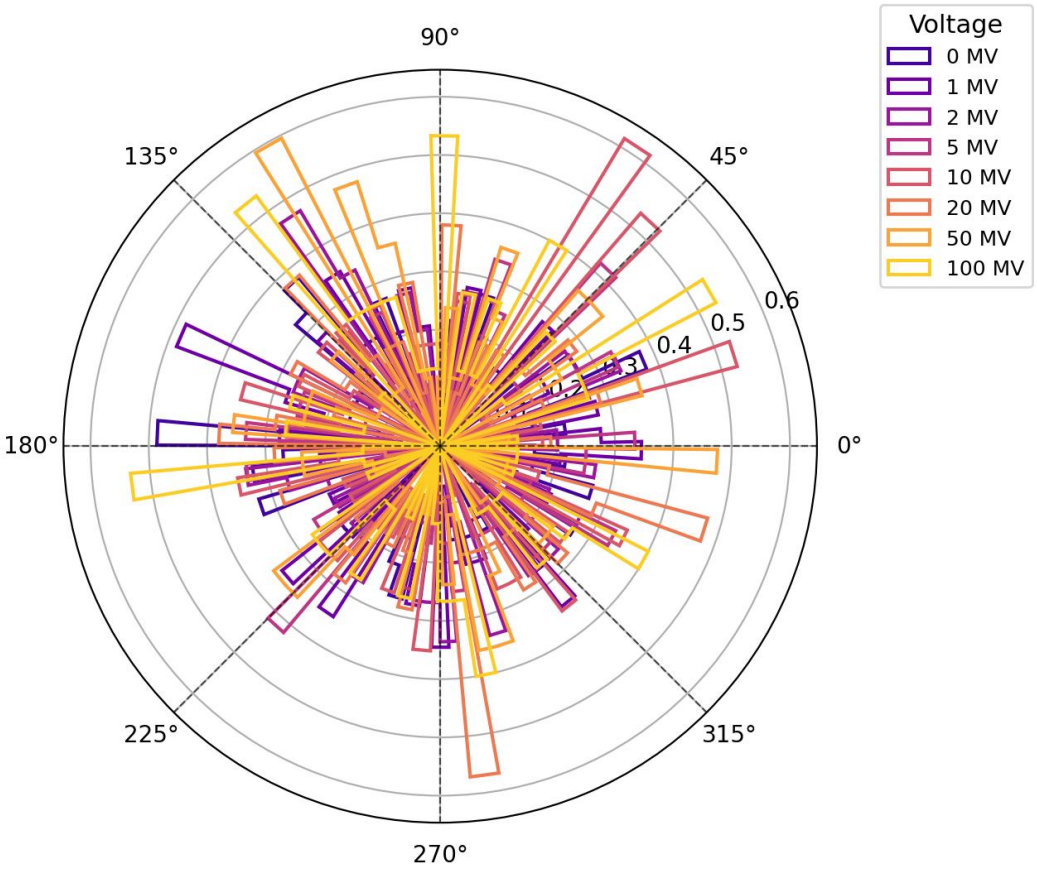


Figure A.203: Azimuthal angle distribution of grazing-incidence (zenith $> 80°$) dome hits for ^{1}H primaries at $0\,\mathrm{g\,cm^{-2}}$ passive shielding, by active shielding voltage. Dashed lines mark the eight perimeter point-charge azimuthal positions.

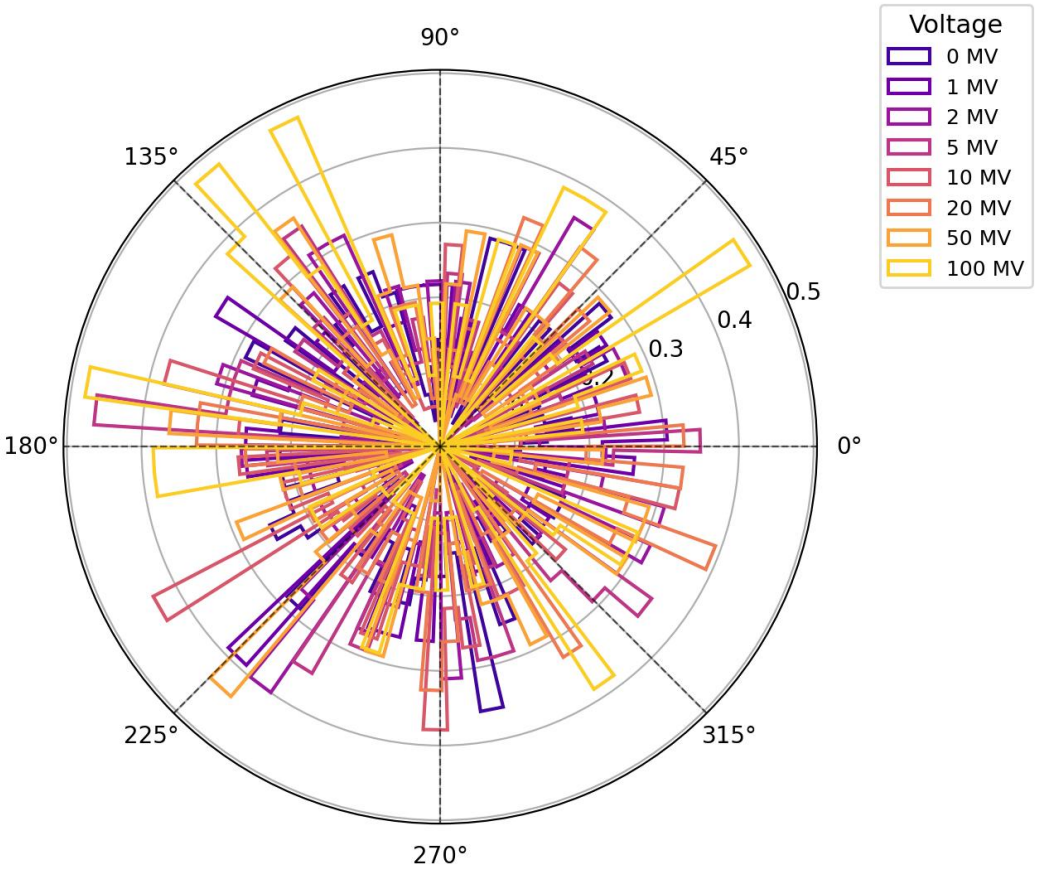


Figure A.204: Azimuthal angle distribution of grazing-incidence (zenith $> 80°$) dome hits for ^{1}H primaries at $10\,\mathrm{g\,cm^{-2}}$ passive shielding, by active shielding voltage. Dashed lines mark the eight perimeter point-charge azimuthal positions.

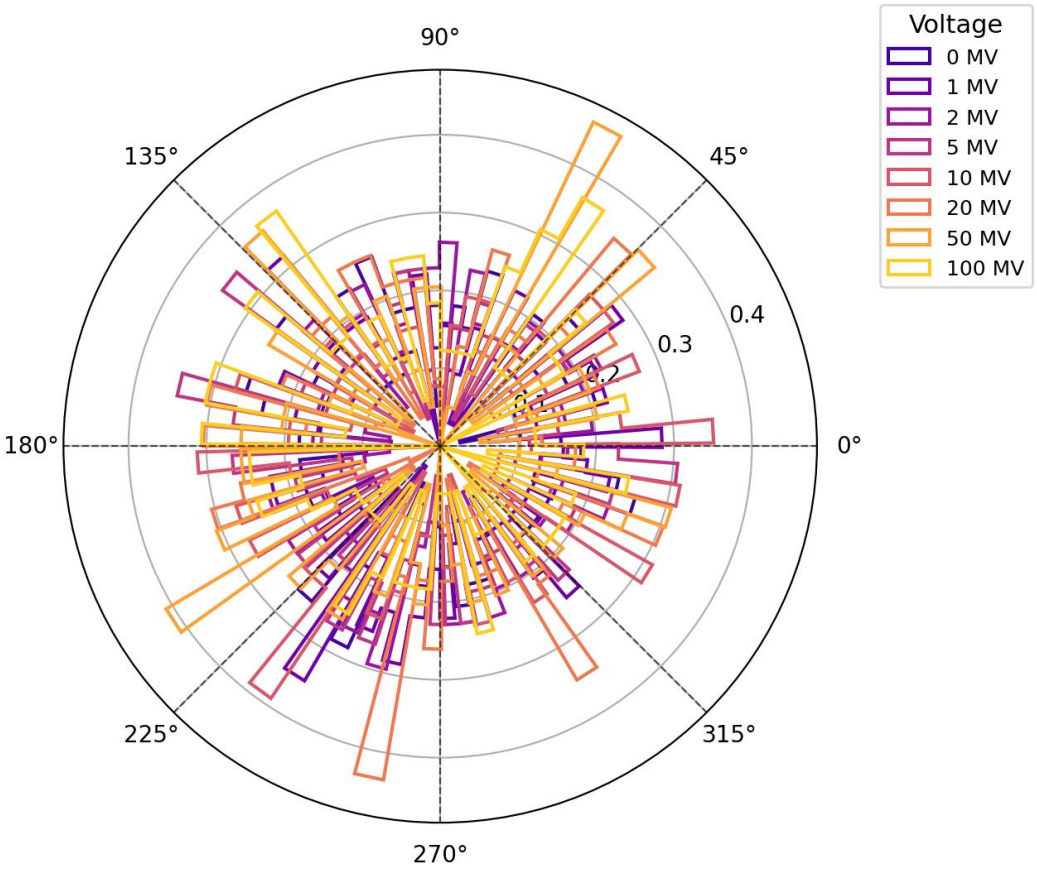


Figure A.205: Azimuthal angle distribution of grazing-incidence (zenith $> 80°$) dome hits for ^{1}H primaries at $20\,\mathrm{g\,cm^{-2}}$ passive shielding, by active shielding voltage. Dashed lines mark the eight perimeter point-charge azimuthal positions.

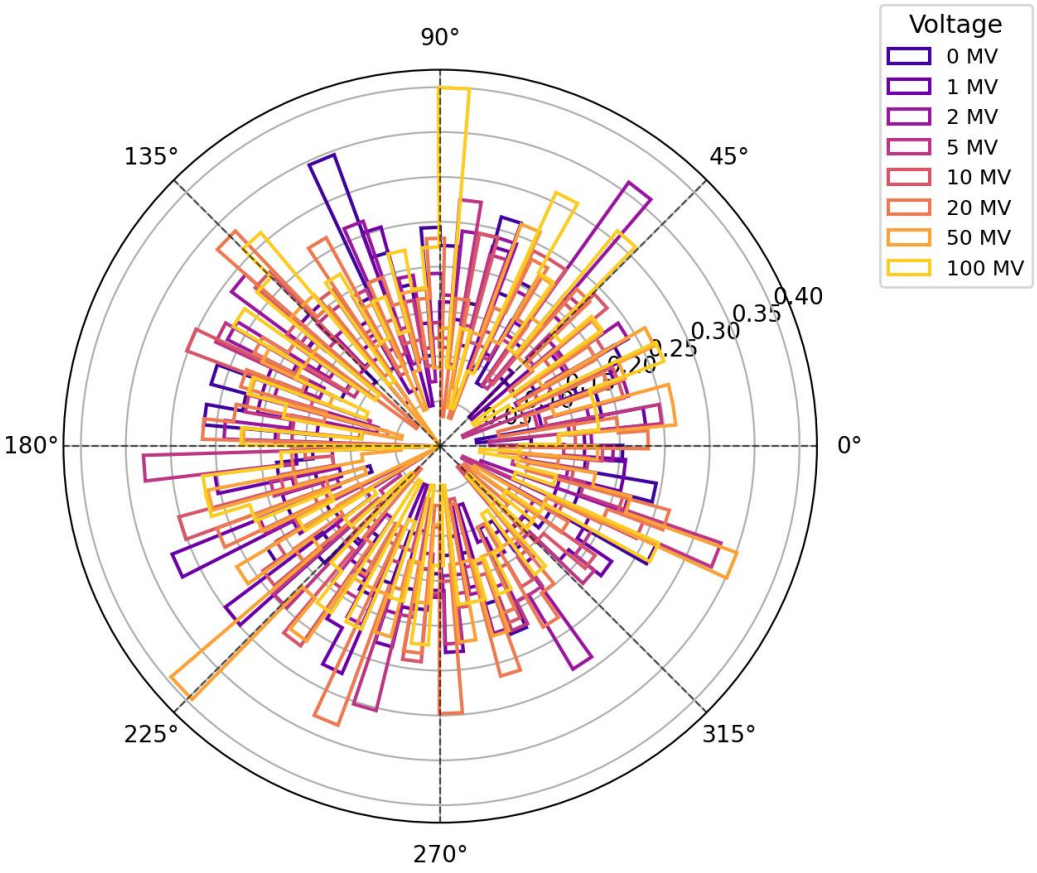


Figure A.206: Azimuthal angle distribution of grazing-incidence (zenith $> 80°$) dome hits for ^{1}H primaries at $30\,\mathrm{g\,cm^{-2}}$ passive shielding, by active shielding voltage. Dashed lines mark the eight perimeter point-charge azimuthal positions.

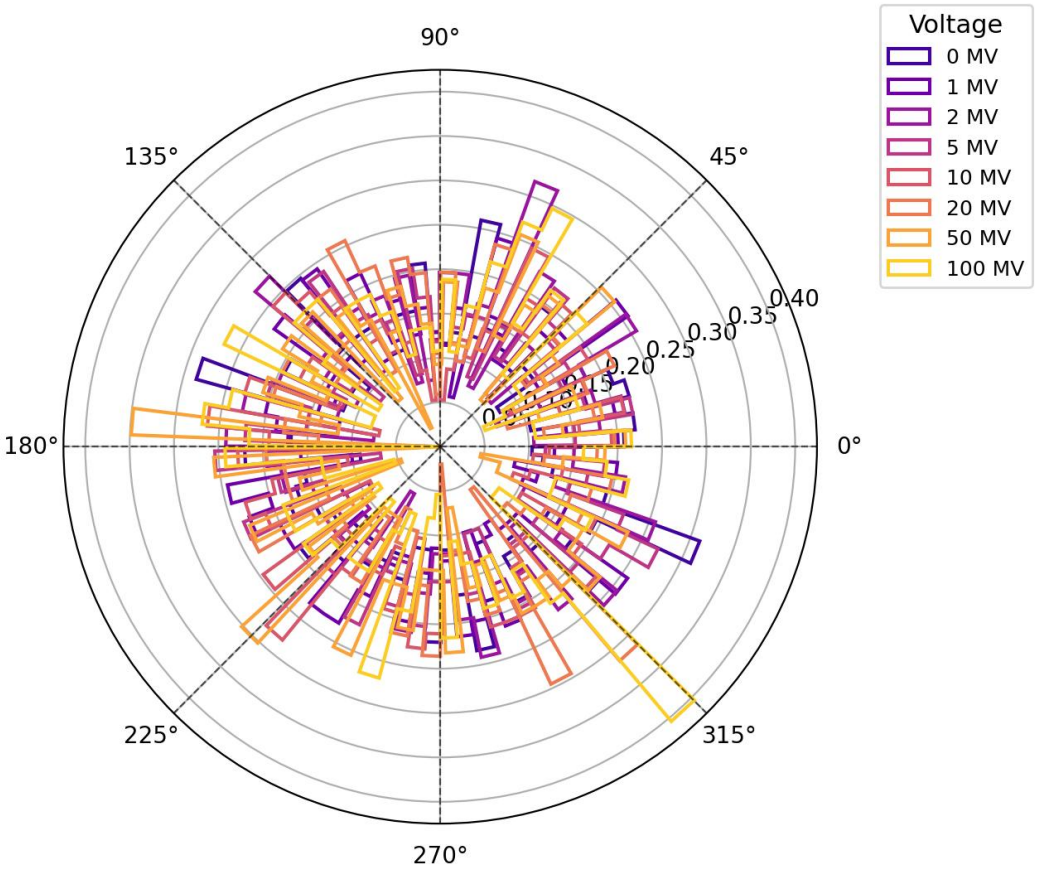


Figure A.207: Azimuthal angle distribution of grazing-incidence (zenith $> 80°$) dome hits for ^{1}H primaries at $50\,\mathrm{g\,cm^{-2}}$ passive shielding, by active shielding voltage. Dashed lines mark the eight perimeter point-charge azimuthal positions.

A.0.1.2 Primary Hit Distribution—Polar

A.0.1.3 Primary Hit Distribution—Map

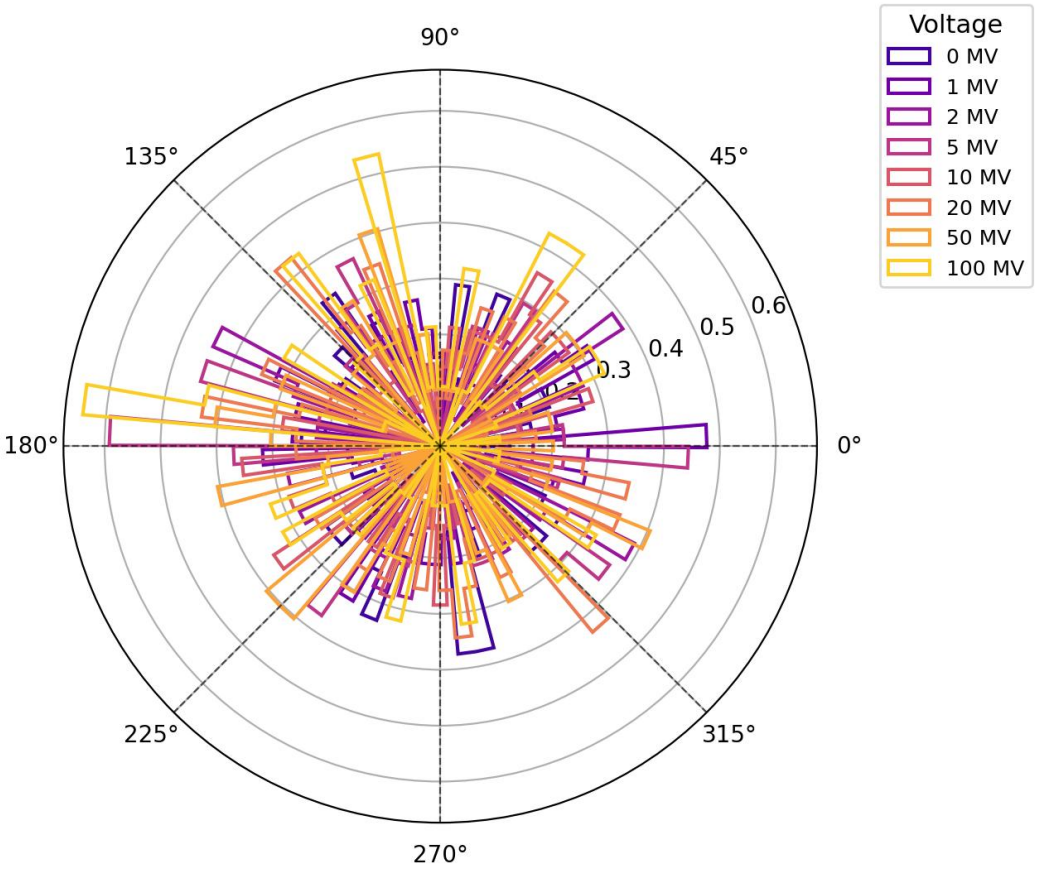


Figure A.208: Azimuthal angle distribution of grazing-incidence (zenith $> 80°$) dome hits for ^{1}H primaries at $5\,\mathrm{g\,cm^{-2}}$ passive shielding, by active shielding voltage. Dashed lines mark the eight perimeter point-charge azimuthal positions.

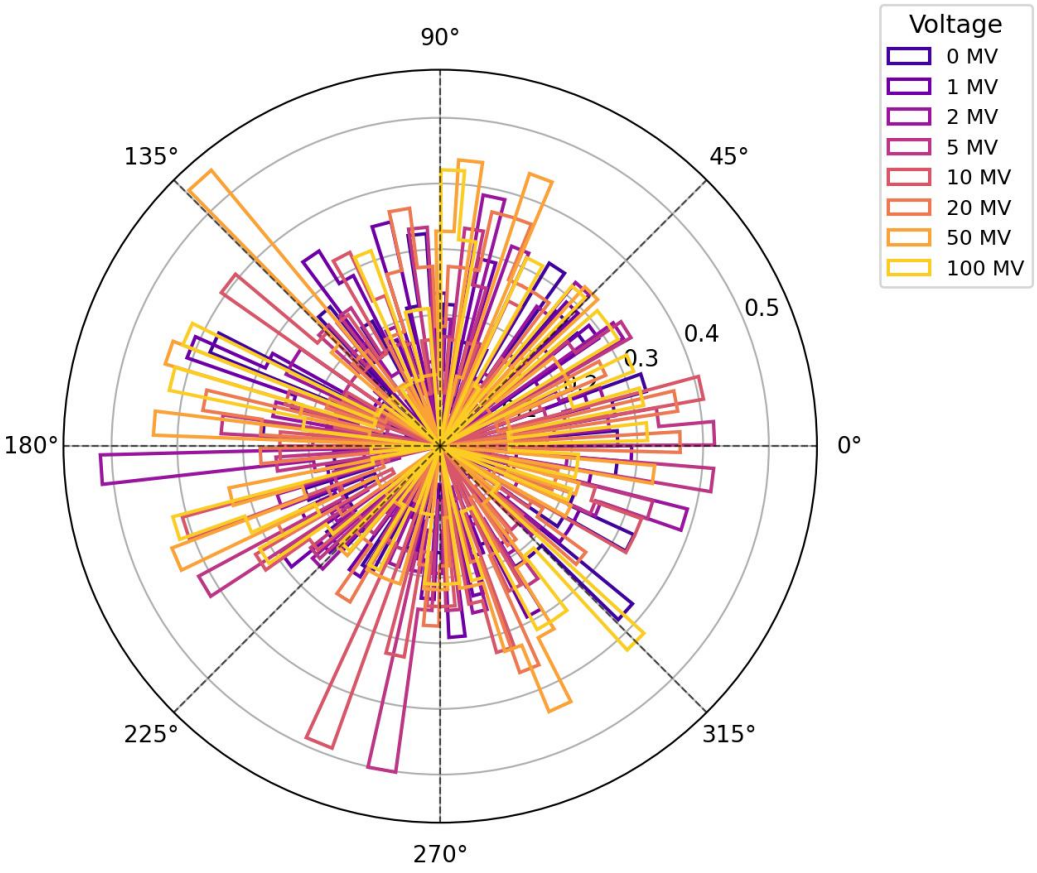


Figure A.209: Azimuthal angle distribution of grazing-incidence (zenith $> 80°$) dome hits for ^{4}He primaries at $0\,\mathrm{g\,cm^{-2}}$ passive shielding, by active shielding voltage. Dashed lines mark the eight perimeter point-charge azimuthal positions.

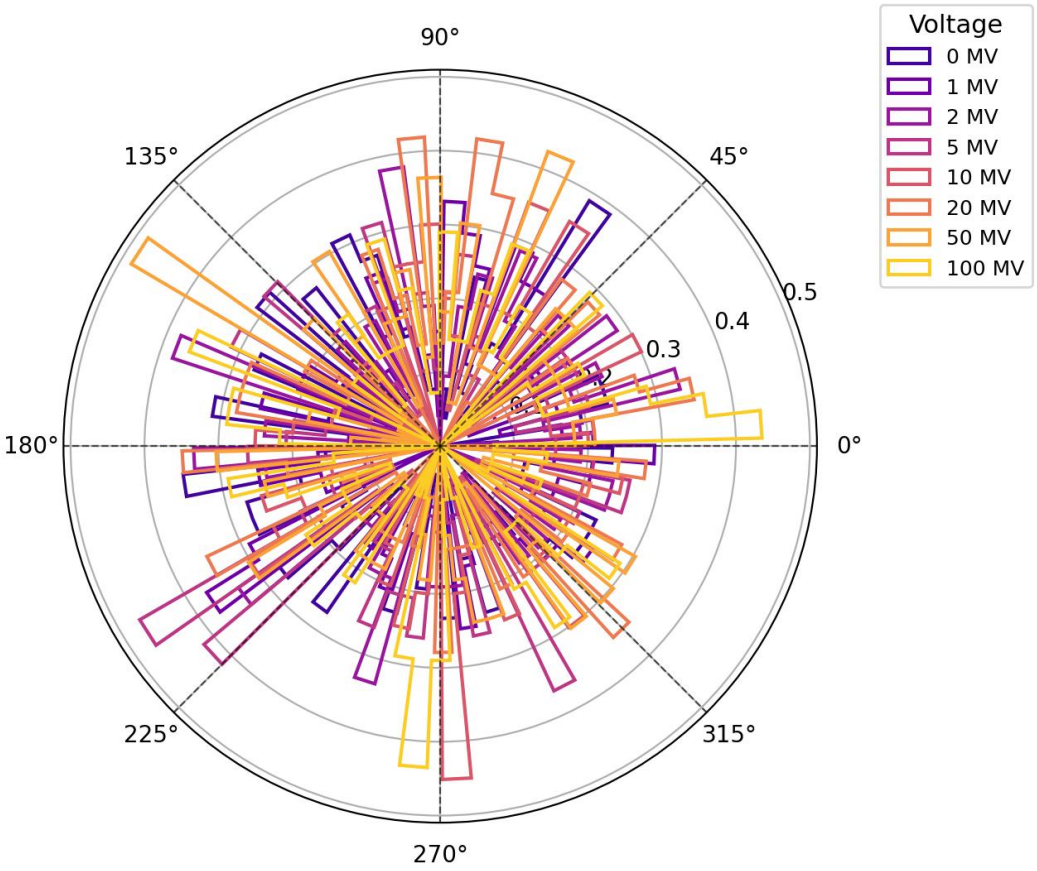


Figure A.210: Azimuthal angle distribution of grazing-incidence (zenith $> 80°$) dome hits for ^{4}He primaries at $10\,\mathrm{g\,cm^{-2}}$ passive shielding, by active shielding voltage. Dashed lines mark the eight perimeter point-charge azimuthal positions.

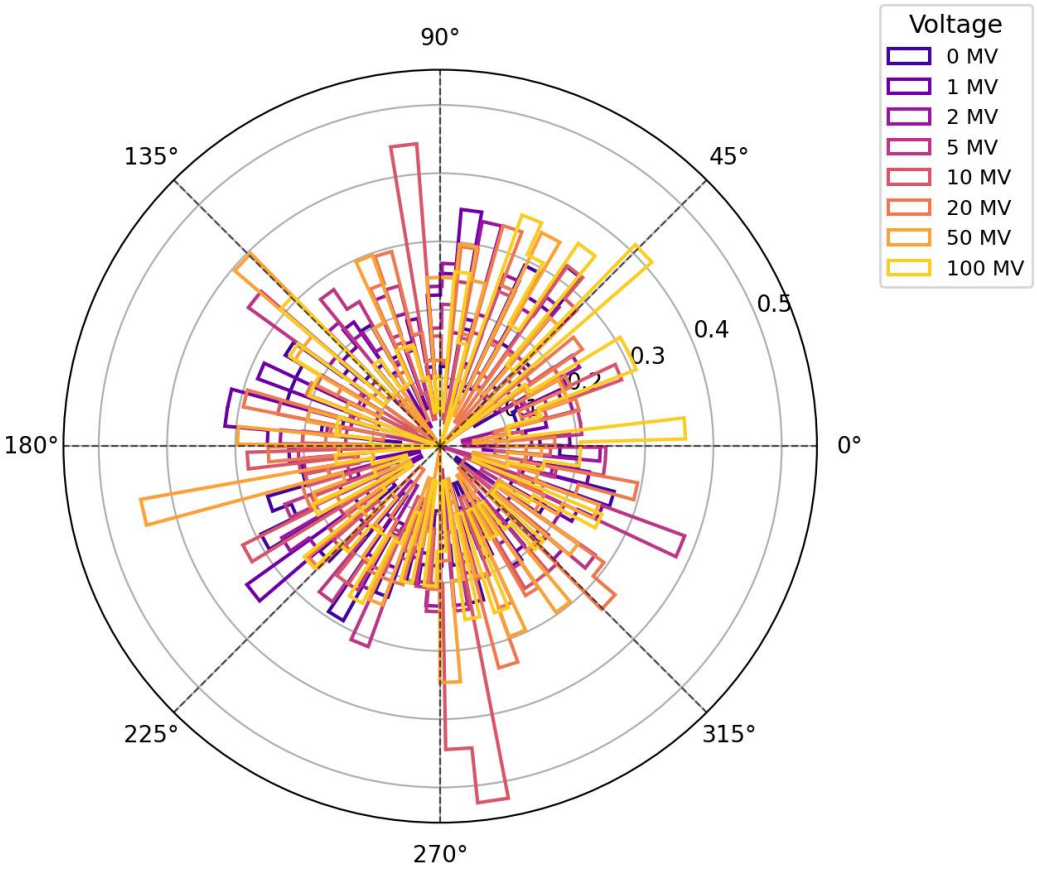


Figure A.211: Azimuthal angle distribution of grazing-incidence (zenith $> 80°$) dome hits for ^{4}He primaries at $20\,\mathrm{g\,cm^{-2}}$ passive shielding, by active shielding voltage. Dashed lines mark the eight perimeter point-charge azimuthal positions.

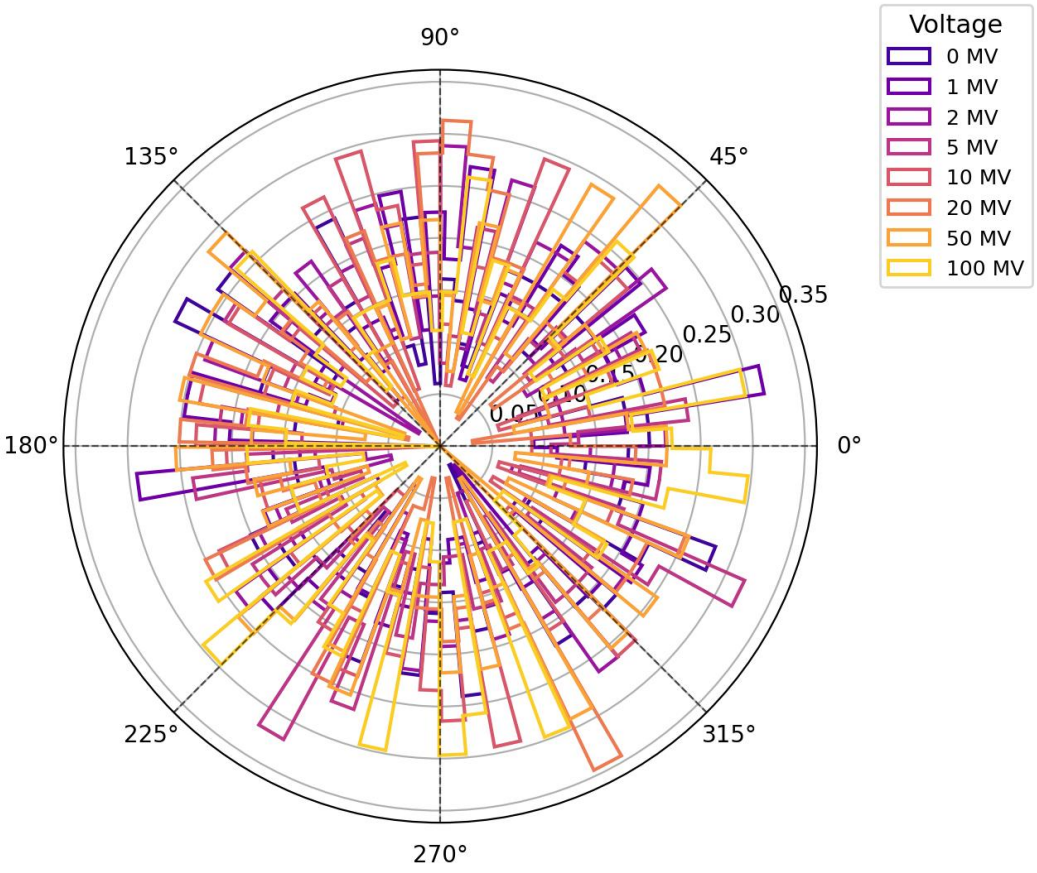


Figure A.212: Azimuthal angle distribution of grazing-incidence (zenith $> 80°$) dome hits for ^{4}He primaries at $30\,\mathrm{g\,cm^{-2}}$ passive shielding, by active shielding voltage. Dashed lines mark the eight perimeter point-charge azimuthal positions.

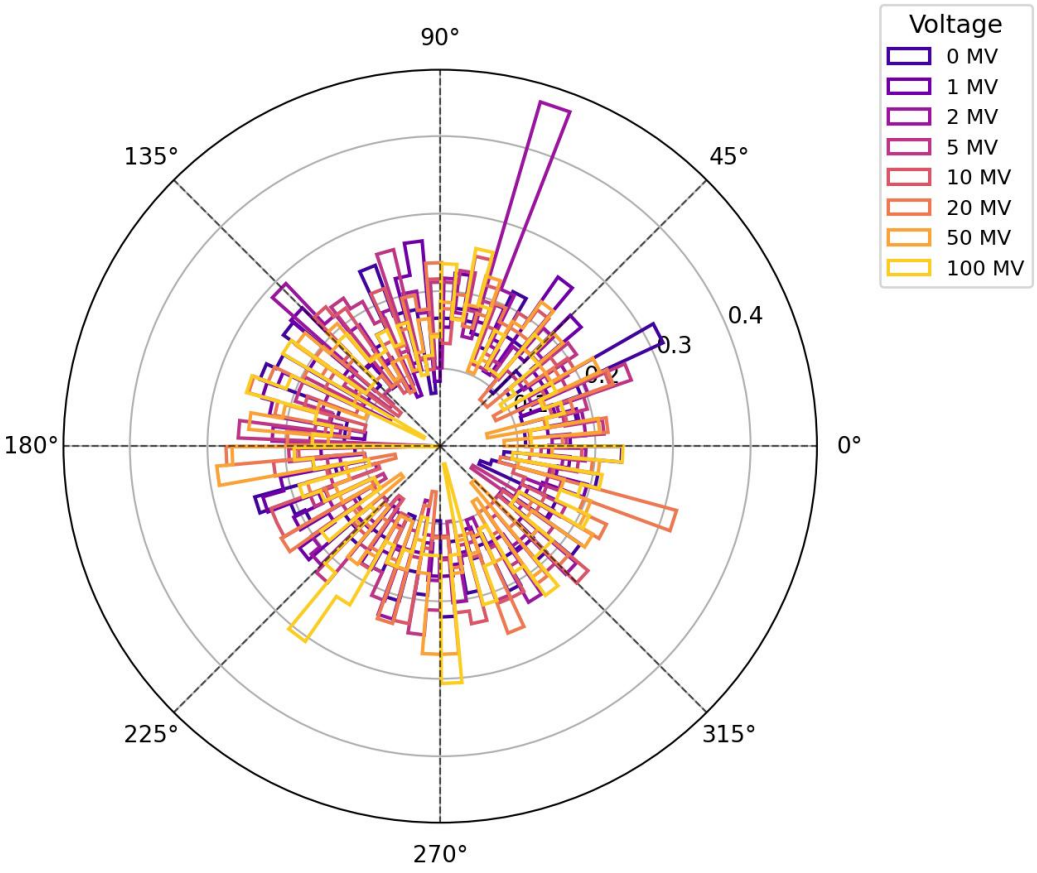


Figure A.213: Azimuthal angle distribution of grazing-incidence (zenith $> 80°$) dome hits for ^{4}He primaries at $50\,\mathrm{g\,cm^{-2}}$ passive shielding, by active shielding voltage. Dashed lines mark the eight perimeter point-charge azimuthal positions.

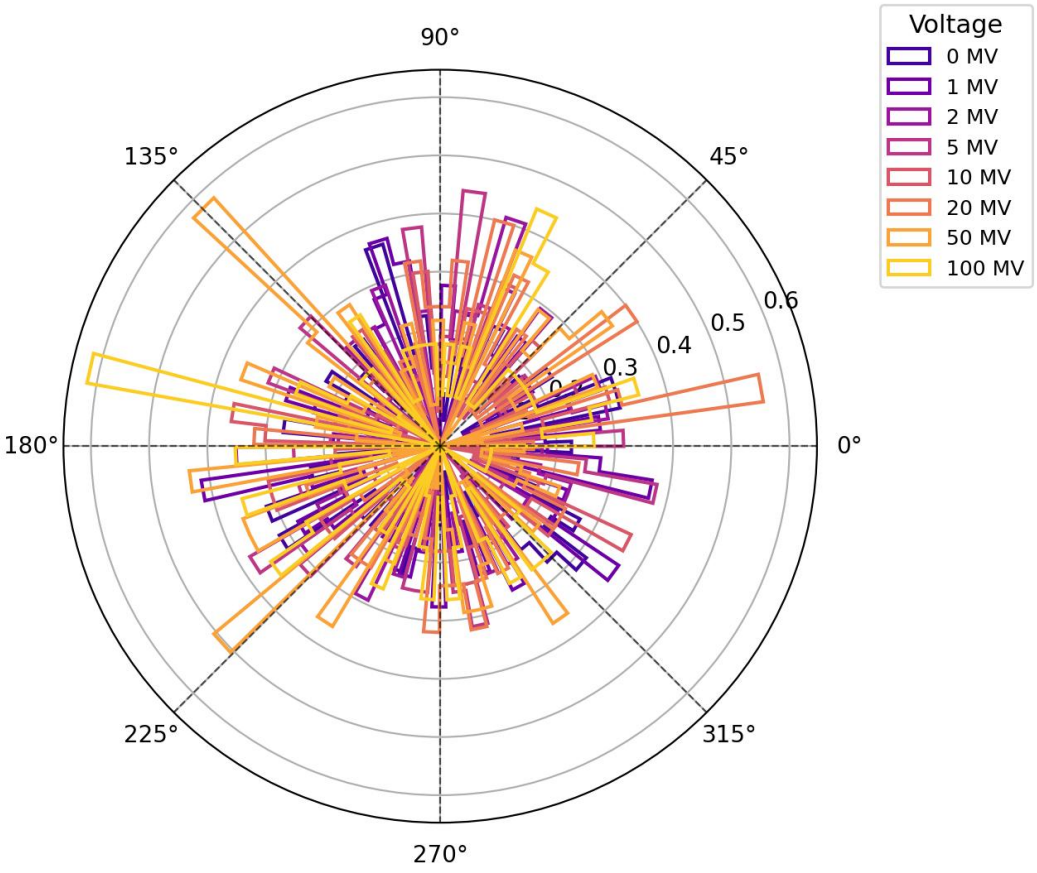


Figure A.214: Azimuthal angle distribution of grazing-incidence (zenith $> 80°$) dome hits for ^{4}He primaries at $5\,\mathrm{g\,cm^{-2}}$ passive shielding, by active shielding voltage. Dashed lines mark the eight perimeter point-charge azimuthal positions.

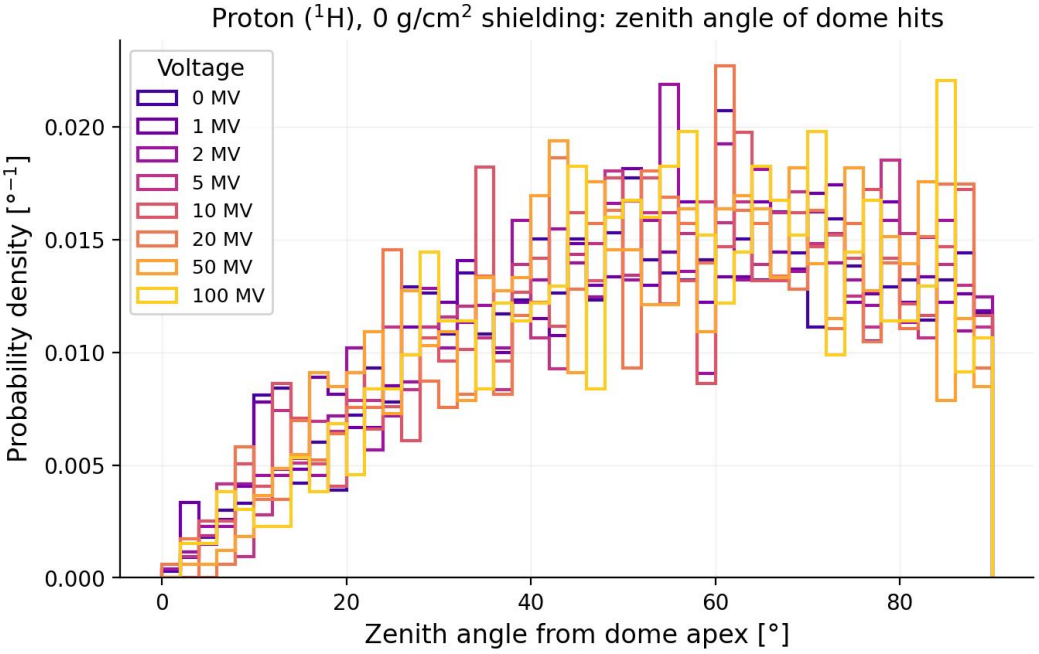


Figure A.215: Polar (zenith) angle distribution of dome hits for ^{1}H primaries at $0\,\mathrm{g\,cm^{-2}}$ passive shielding, by active shielding voltage.

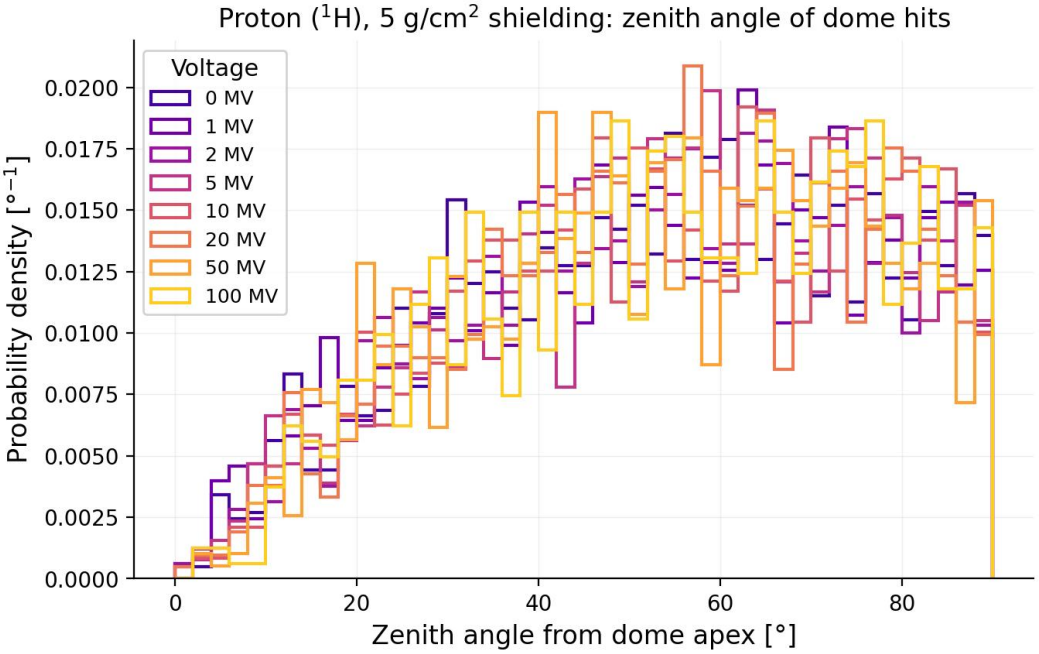


Figure A.216: Polar (zenith) angle distribution of dome hits for ^{1}H primaries at $5\,\mathrm{g\,cm^{-2}}$ passive shielding, by active shielding voltage.

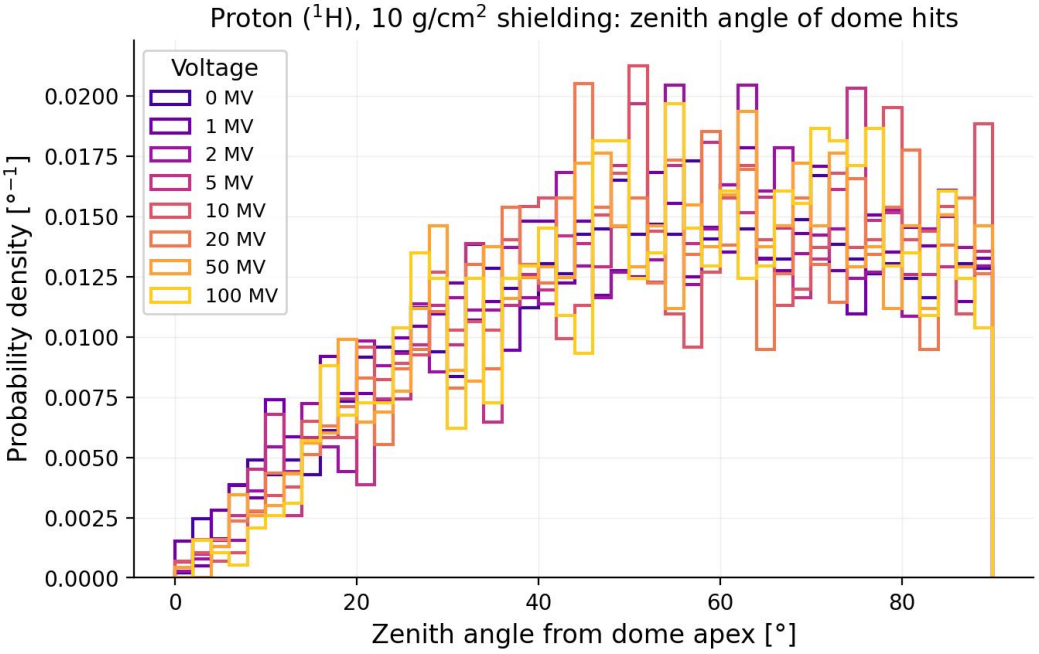


Figure A.217: Polar (zenith) angle distribution of dome hits for ^{1}H primaries at 10 g cm^{-2} passive shielding, by active shielding voltage.

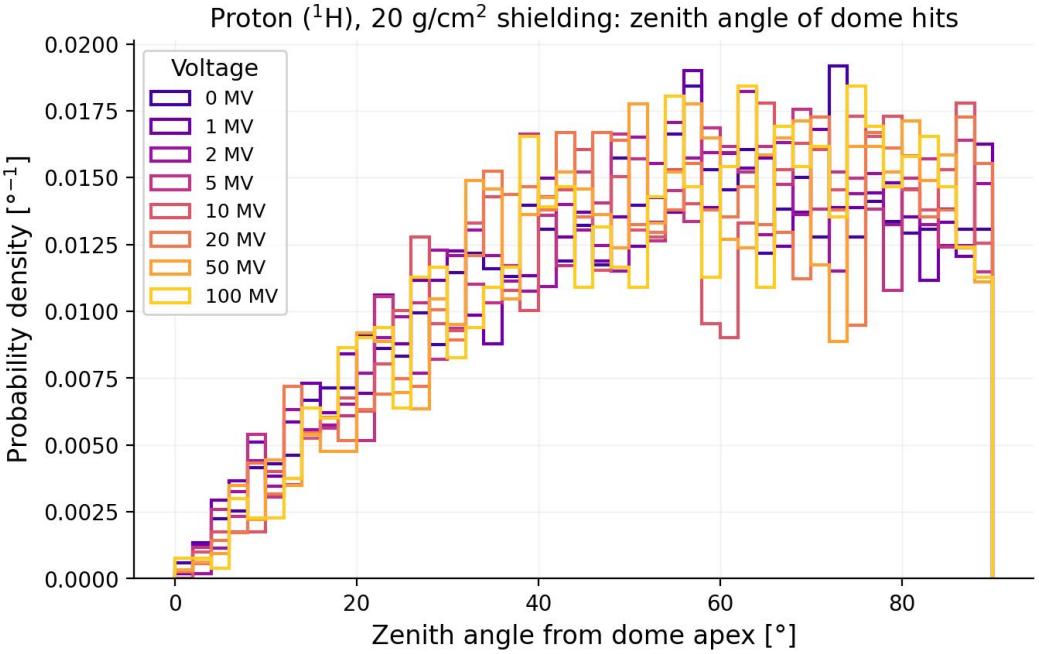


Figure A.218: Polar (zenith) angle distribution of dome hits for ^{1}H primaries at 20 g cm^{-2} passive shielding, by active shielding voltage.

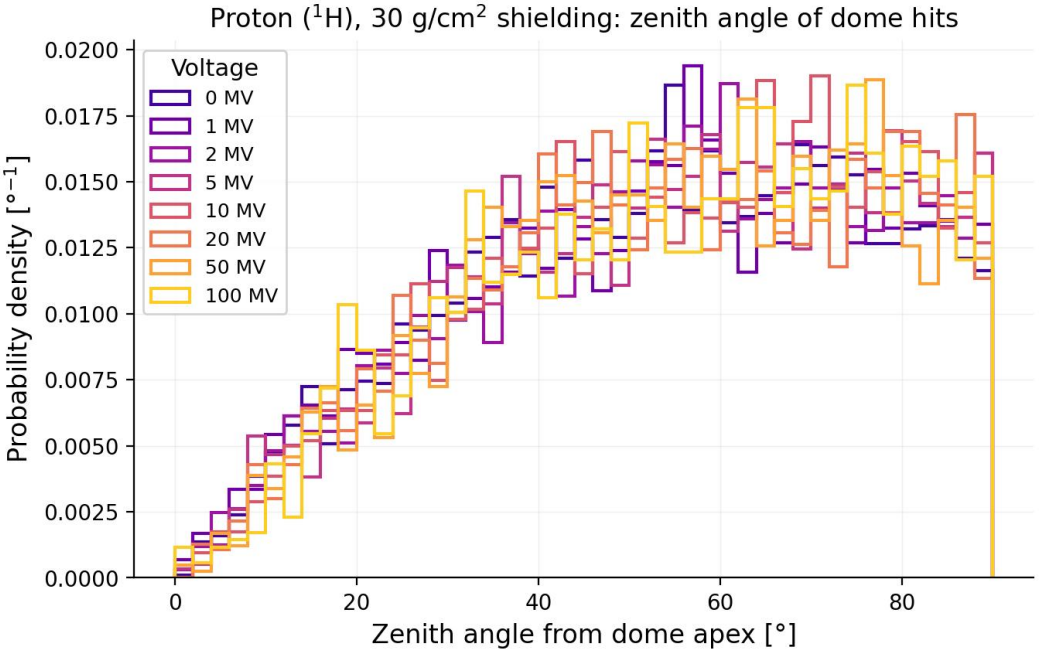


Figure A.219: Polar (zenith) angle distribution of dome hits for ^{1}H primaries at 30 g cm^{-2} passive shielding, by active shielding voltage.

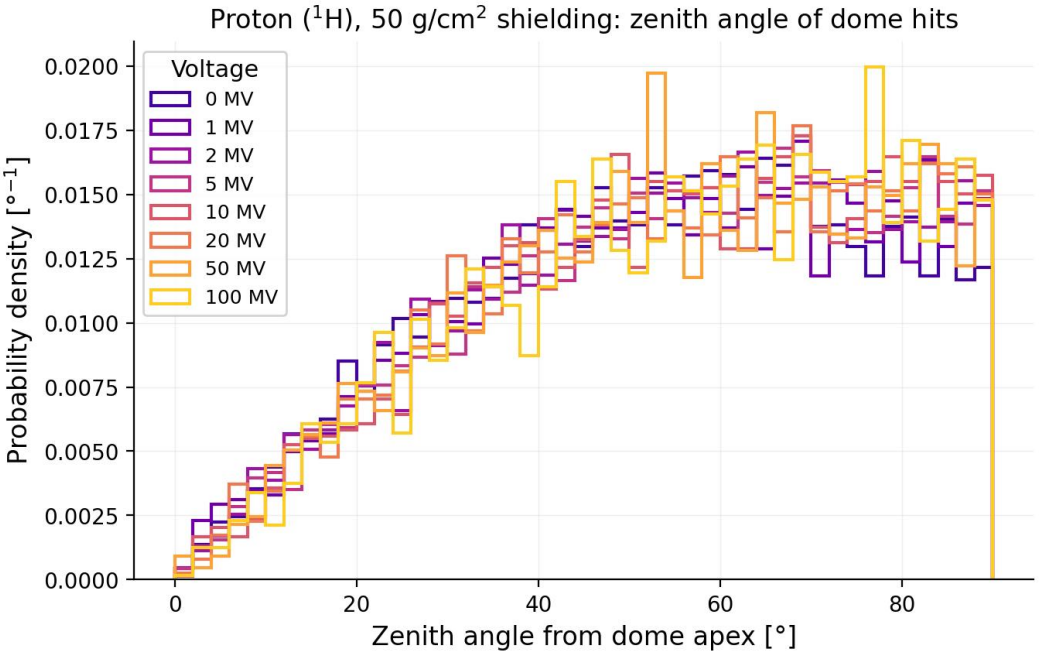


Figure A.220: Polar (zenith) angle distribution of dome hits for ^{1}H primaries at 50 g cm^{-2} passive shielding, by active shielding voltage.

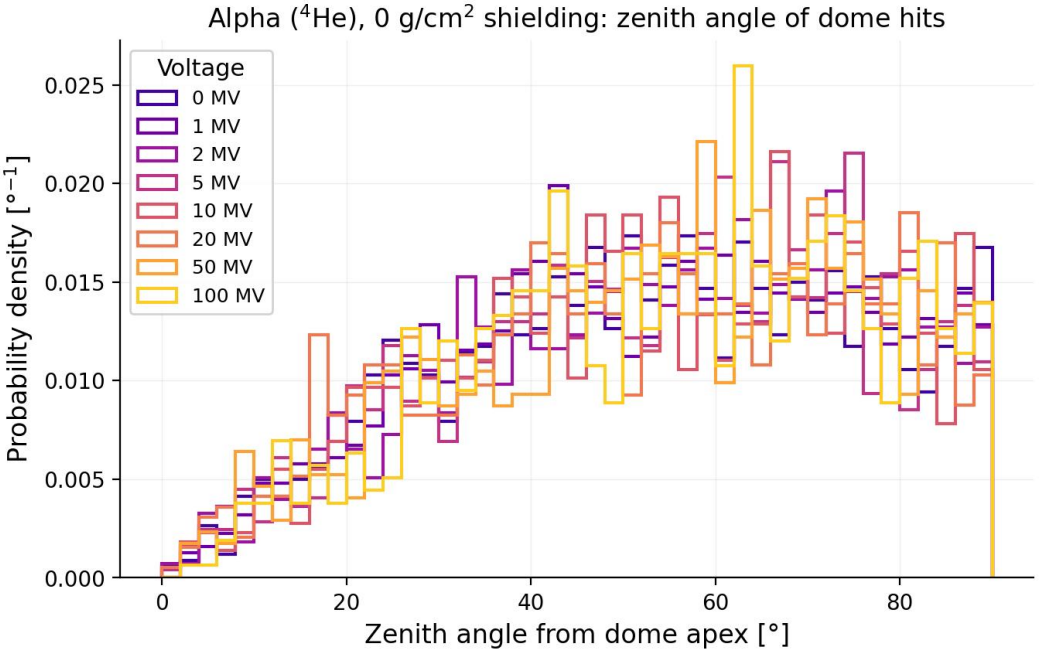


Figure A.221: Polar (zenith) angle distribution of dome hits for ^{4}He primaries at $0\,\mathrm{g\,cm^{-2}}$ passive shielding, by active shielding voltage.

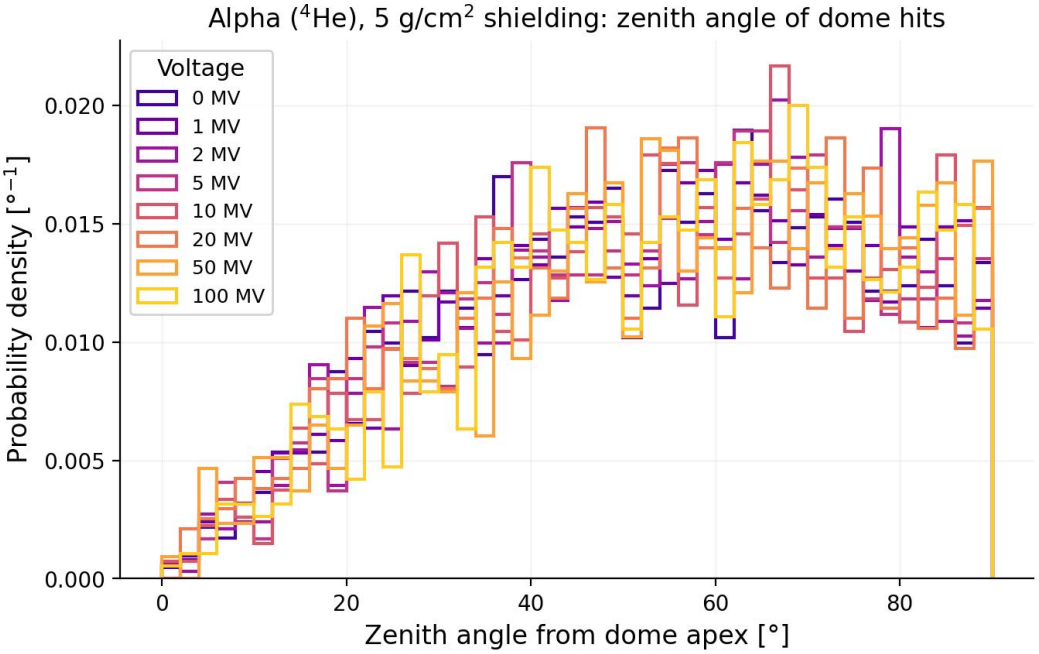


Figure A.222: Polar (zenith) angle distribution of dome hits for ^{4}He primaries at $5\,\mathrm{g\,cm^{-2}}$ passive shielding, by active shielding voltage.

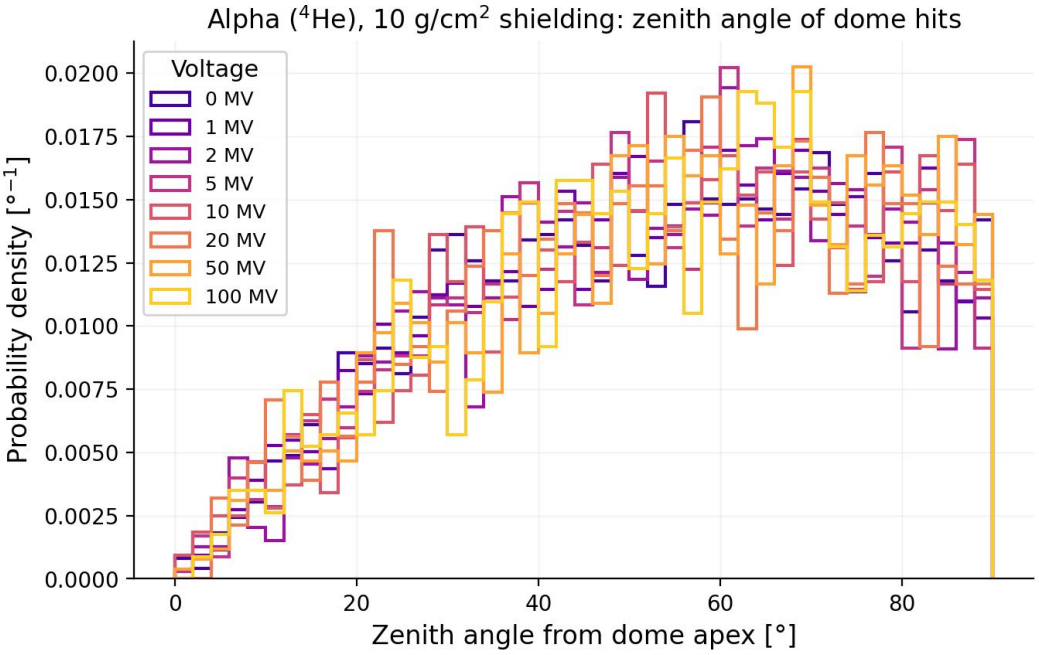


Figure A.223: Polar (zenith) angle distribution of dome hits for ^{4}He primaries at 10 g cm^{-2} passive shielding, by active shielding voltage.

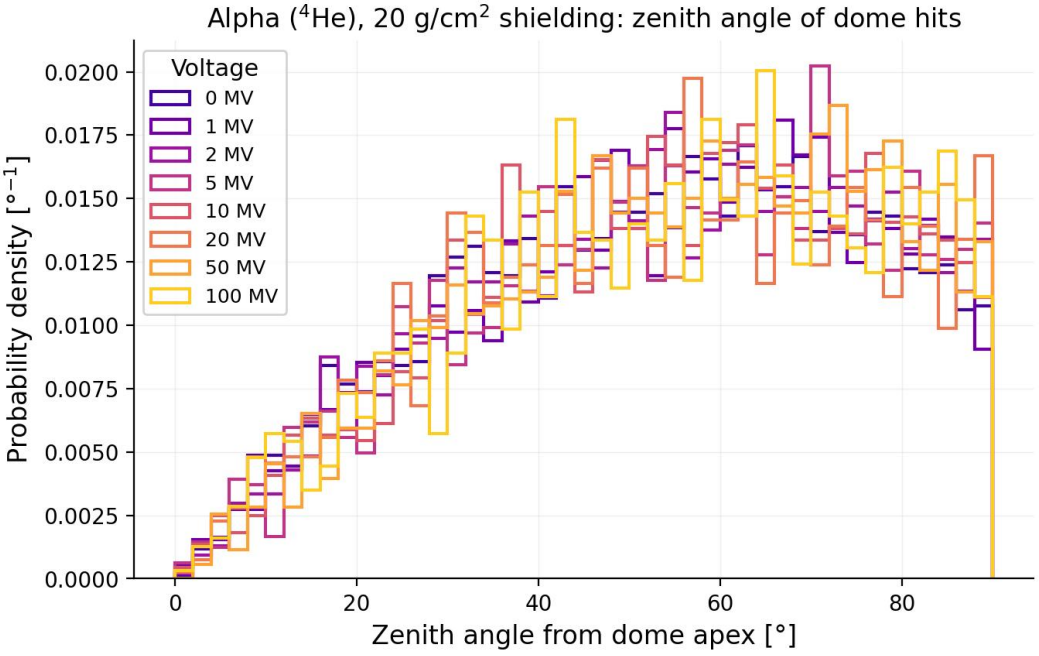


Figure A.224: Polar (zenith) angle distribution of dome hits for ^{4}He primaries at 20 g cm^{-2} passive shielding, by active shielding voltage.

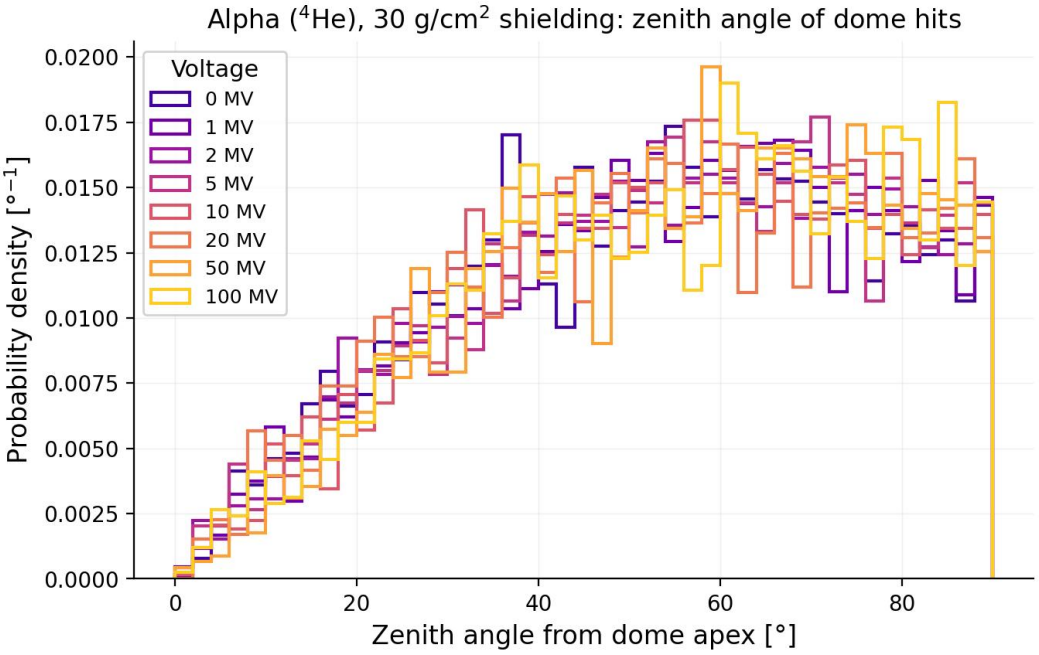


Figure A.225: Polar (zenith) angle distribution of dome hits for ^{4}He primaries at 30 g cm^{-2} passive shielding, by active shielding voltage.

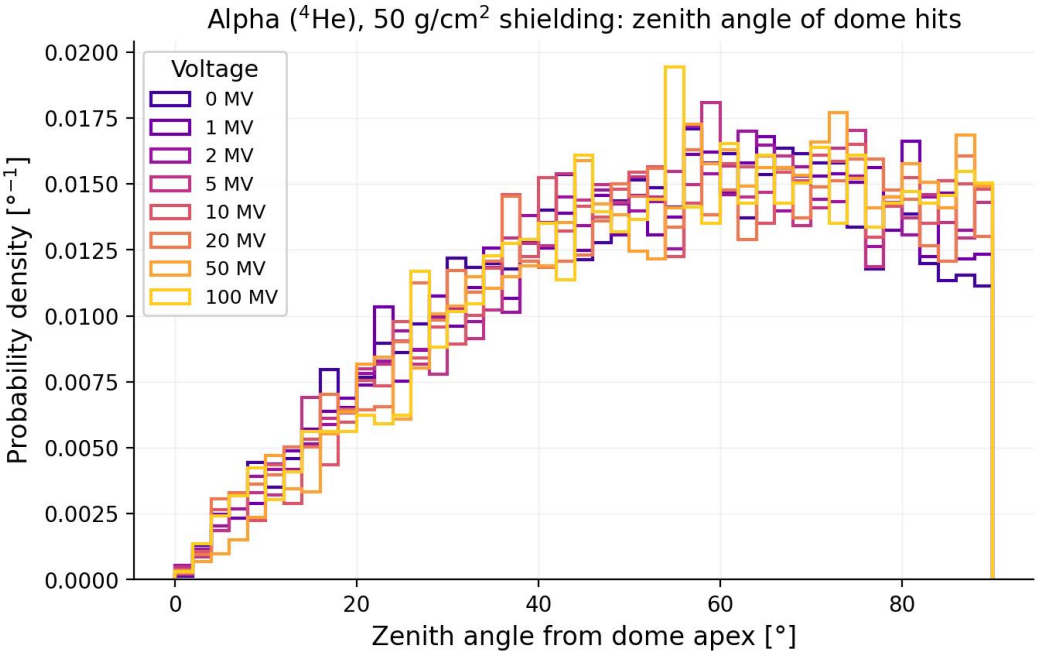


Figure A.226: Polar (zenith) angle distribution of dome hits for ^{4}He primaries at 50 g cm^{-2} passive shielding, by active shielding voltage.

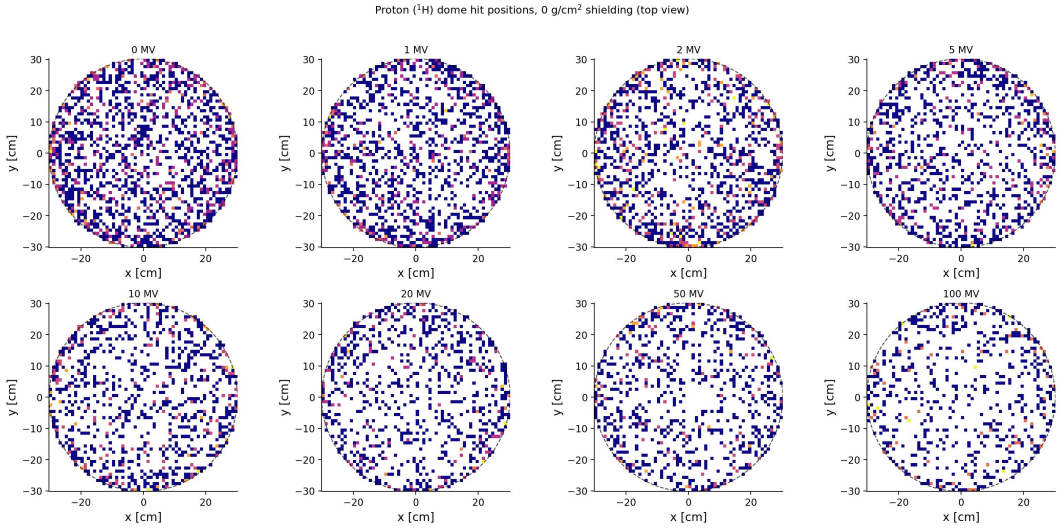


Figure A.227: Spatial distribution of dome hits (top view) for ^{1}H primaries at $0\,\mathrm{g\,cm^{-2}}$ passive shielding, by active shielding voltage.

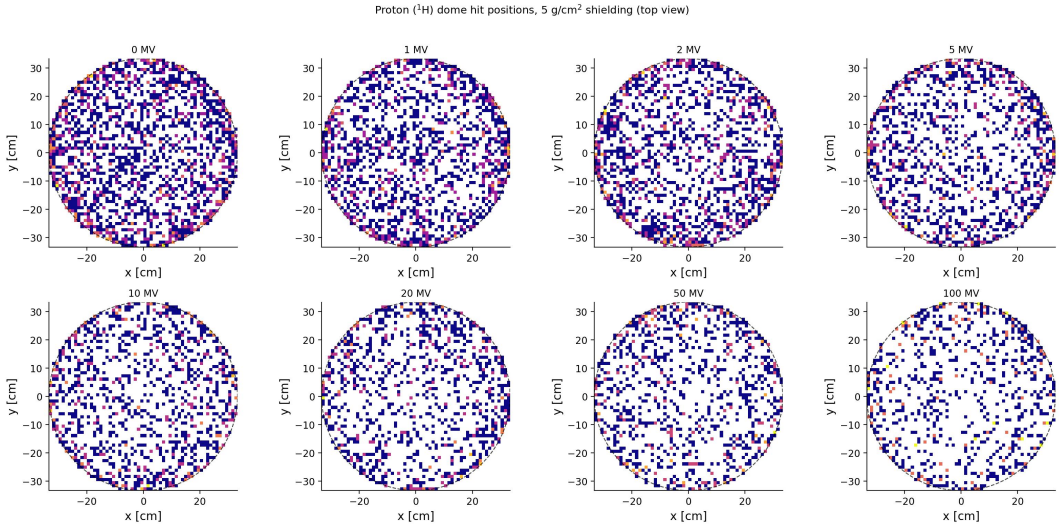


Figure A.228: Spatial distribution of dome hits (top view) for ^{1}H primaries at $5\,\mathrm{g\,cm^{-2}}$ passive shielding, by active shielding voltage.

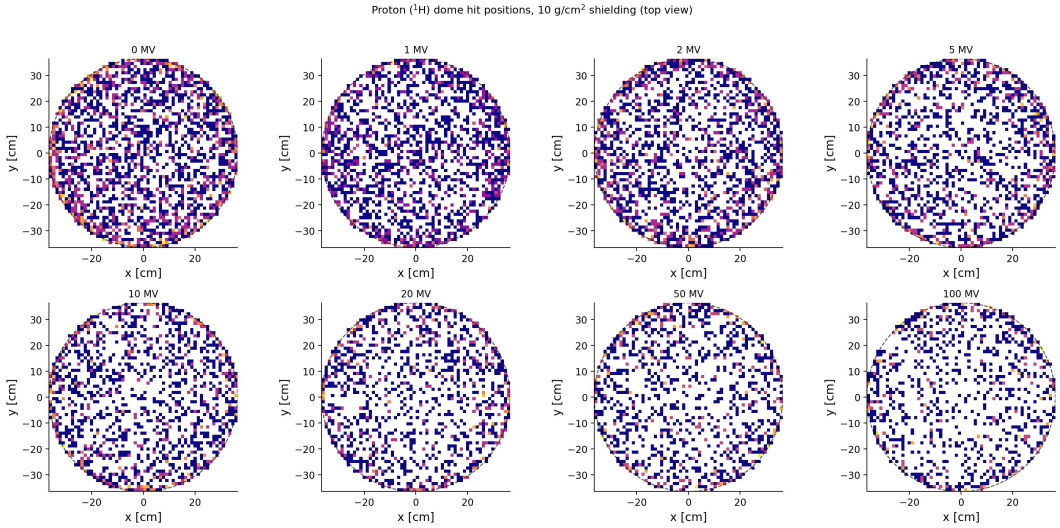


Figure A.229: Spatial distribution of dome hits (top view) for ^{1}H primaries at $10\,\mathrm{g\,cm^{-2}}$ passive shielding, by active shielding voltage.

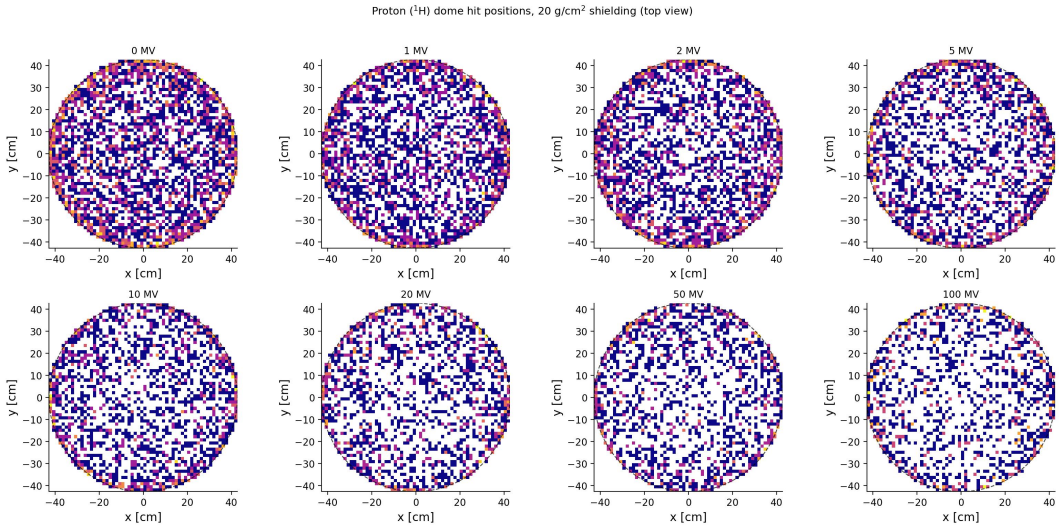


Figure A.230: Spatial distribution of dome hits (top view) for ^{1}H primaries at $20\,\mathrm{g\,cm^{-2}}$ passive shielding, by active shielding voltage.

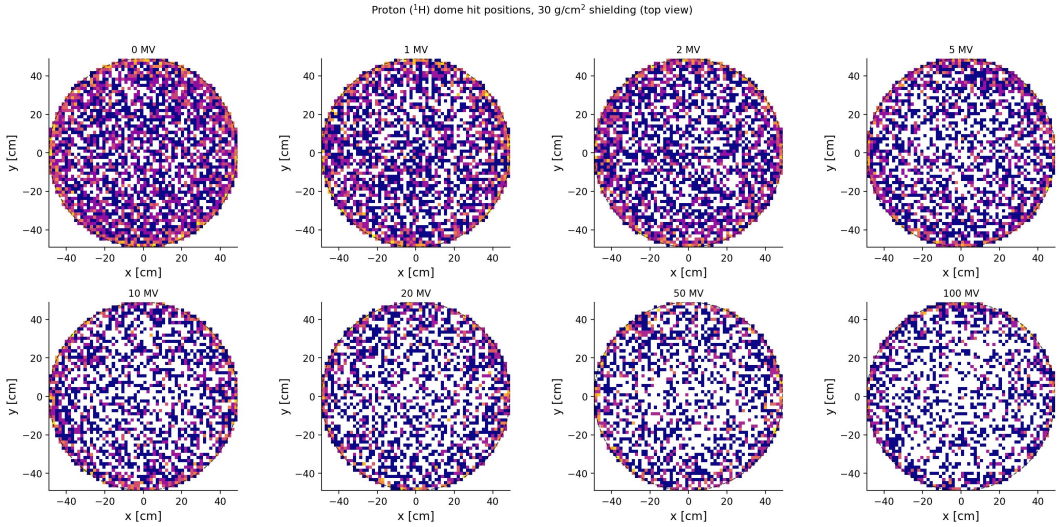


Figure A.231: Spatial distribution of dome hits (top view) for ^{1}H primaries at 30 g cm^{-2} passive shielding, by active shielding voltage.

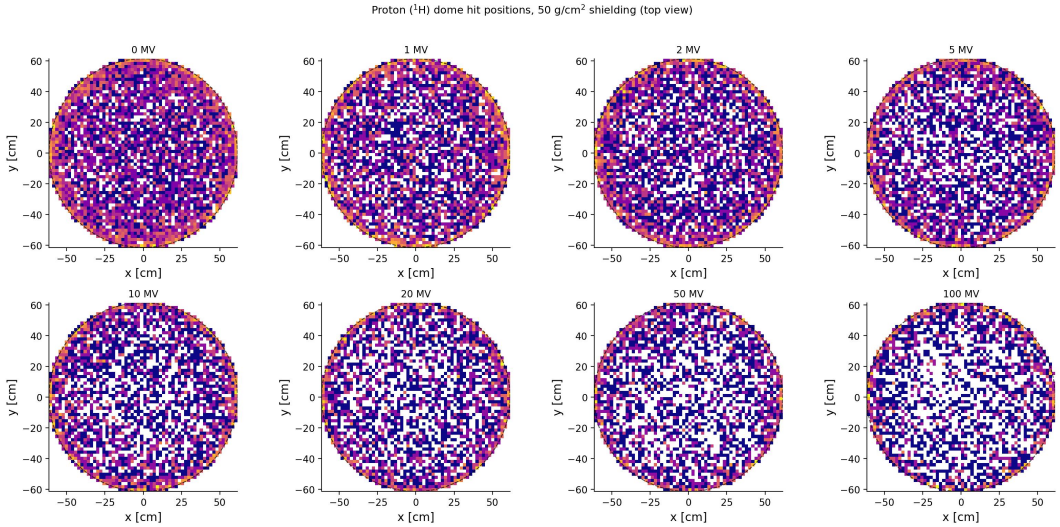


Figure A.232: Spatial distribution of dome hits (top view) for ^{1}H primaries at 50 g cm^{-2} passive shielding, by active shielding voltage.

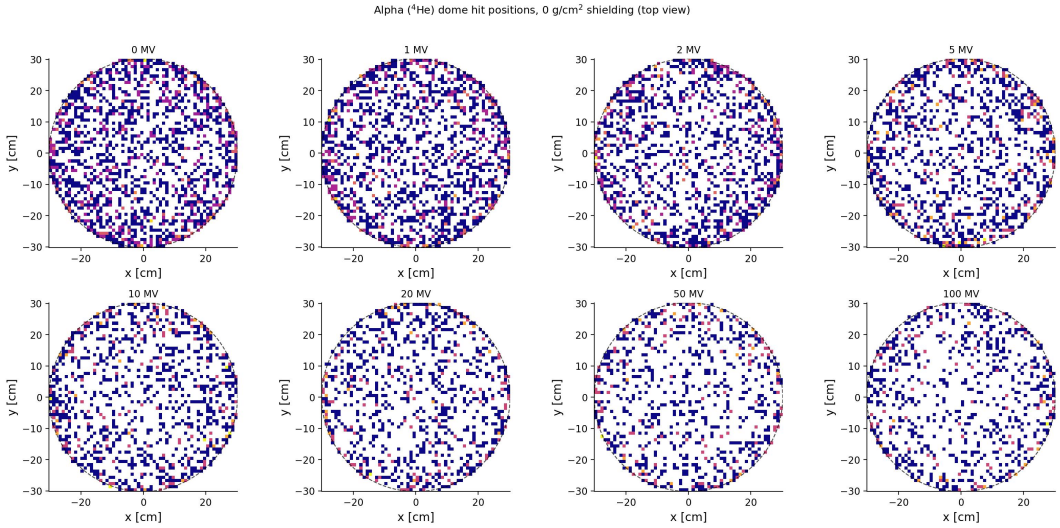


Figure A.233: Spatial distribution of dome hits (top view) for ^{4}He primaries at $0\,\mathrm{g\,cm^{-2}}$ passive shielding, by active shielding voltage.

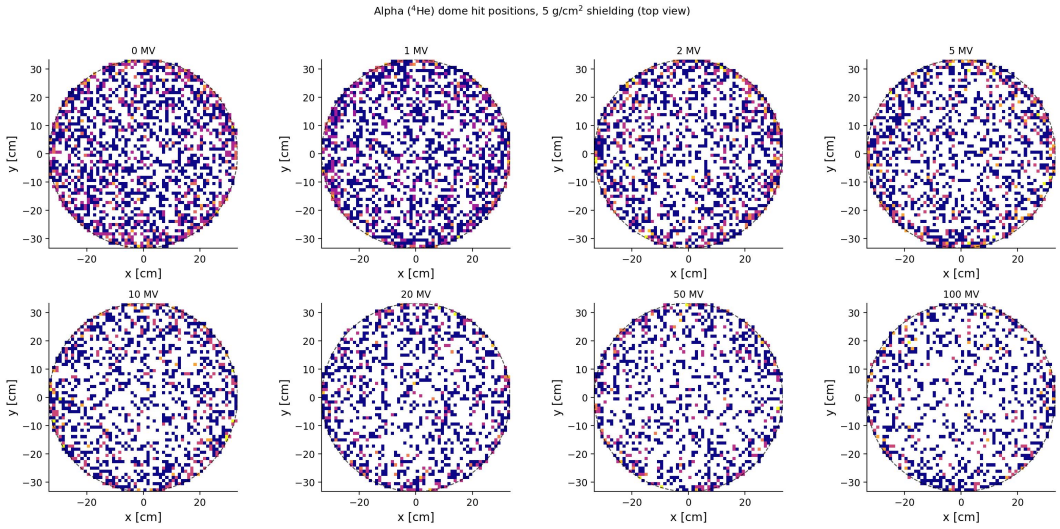


Figure A.234: Spatial distribution of dome hits (top view) for ^{4}He primaries at $5\,\mathrm{g\,cm^{-2}}$ passive shielding, by active shielding voltage.

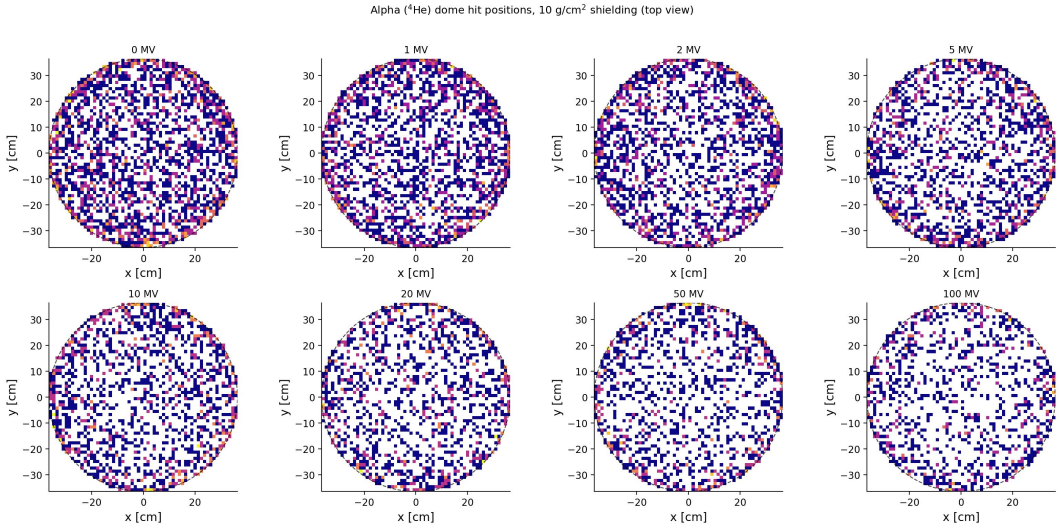


Figure A.235: Spatial distribution of dome hits (top view) for ^{4}He primaries at $10\,\mathrm{g\,cm^{-2}}$ passive shielding, by active shielding voltage.

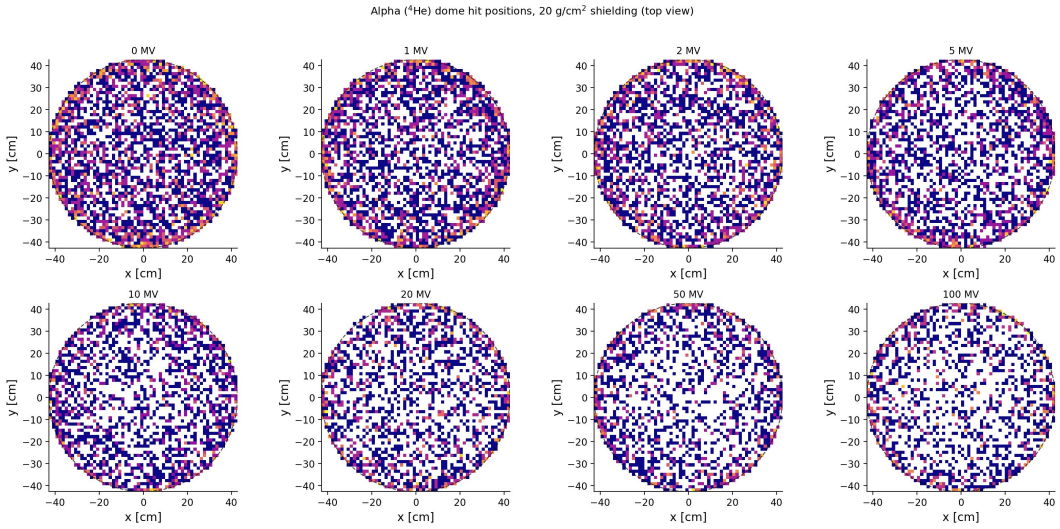


Figure A.236: Spatial distribution of dome hits (top view) for ^{4}He primaries at $20\,\mathrm{g\,cm^{-2}}$ passive shielding, by active shielding voltage.

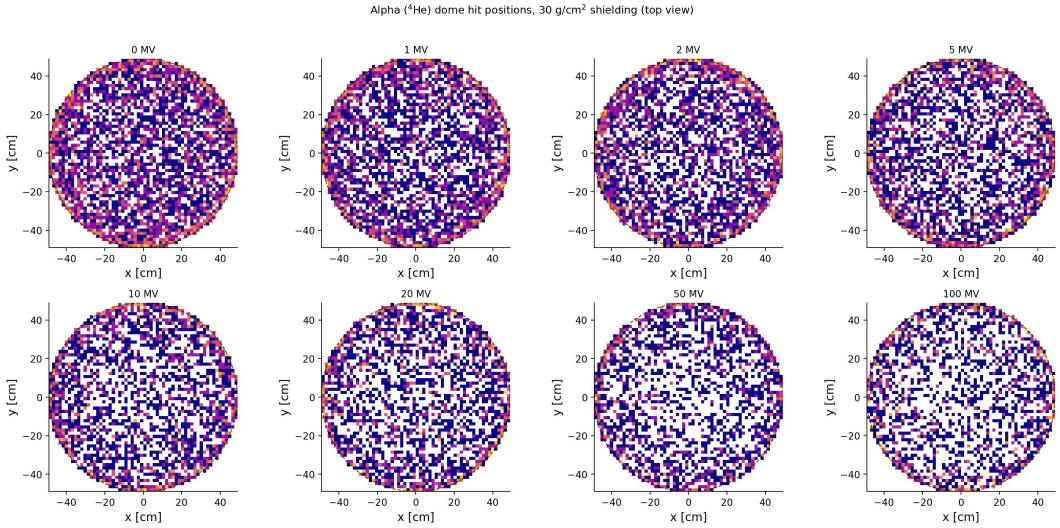


Figure A.237: Spatial distribution of dome hits (top view) for ^{4}He primaries at $30\,\mathrm{g\,cm^{-2}}$ passive shielding, by active shielding voltage.

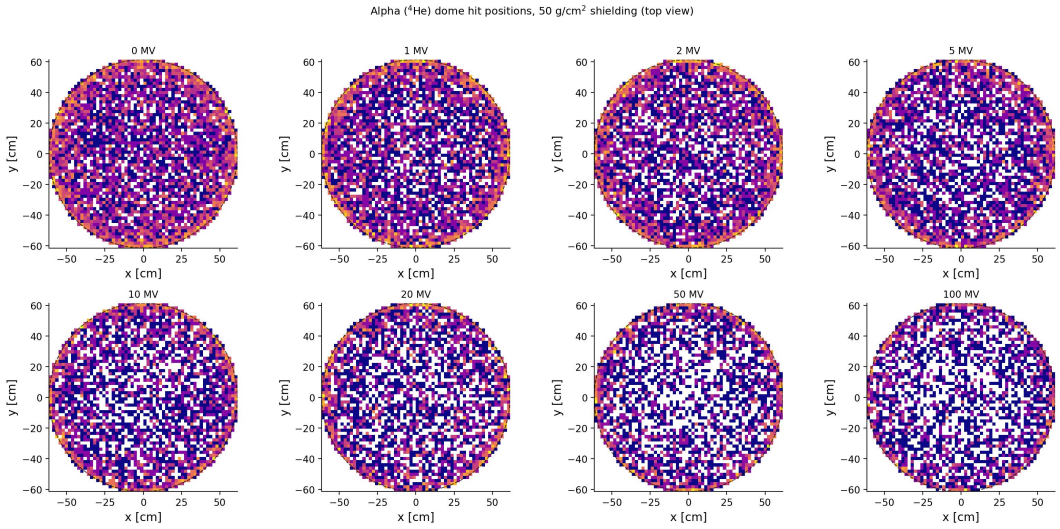


Figure A.238: Spatial distribution of dome hits (top view) for ^{4}He primaries at $50\,\mathrm{g\,cm^{-2}}$ passive shielding, by active shielding voltage.